Development and Application of Human Cortical Organoids: A 1q21.1 Deletion Study

By

Sharna Lunn

A thesis submitted to Cardiff University for the degree of Doctor of Philosophy

December 2022

Abstract

Cerebral organoids are quickly becoming an essential research model in the study of neurodevelopmental disorders. With the aim of generating resources for investigating such neurodevelopmental disorders, new methodology was devised for immunocytochemistry (ICC) quantification of cerebral organoids. A high throughput ICC analysis pipeline was developed, with post-hoc corrections for apoptotic cell death and creation of a universal constant for normalising morphological features and dead cell count data. In addition to these analysis techniques, revised human induced pluripotent stem cell (hIPSC)-derived cortical organoid (hCO) protocols were trialled with the intention of improving on current guided cerebral organoid models. Each protocol's hCOs were scrutinised for dorsal forebrain characteristics such as cortical layering and organised neural progenitors, of which varied significantly between protocols. Extended ROCK inhibition during early hCO differentiation proved counterproductive to developing dorsal forebrain identity. With improved analysis methodologies and a characterised hCO protocol, hCOs were generated from patients of the rare, pathogenic copy number variant (CNV), 1q21.1 deletion (1qDel). 1qDel is associated with developmental delay, intellectual disability, schizophrenia and microcephaly. From the onset of hCO differentiation, 1qDel hCOs were microcephalus until neuronal maturation. As the neuroepithelium developed, 1qDel hCOs also exhibited early neurogenesis and disruption of the cell cycle, hypothesised to be a result of repressed NOTCH and Wnt signalling due to 1qDel. Neuronal maturation alleviated these phenotypes, but expansion of ventral forebrain progenitors at Day 30 was suspected to detrimentally affect cortical layering. By two months of age, 1qDel hCOs were predominantly indistinguishable from controls, with the exception of an increase in GABA-ergic presynaptic markers suggesting an excitatory/inhibitory imbalance in neuronal activity. This is the first *in vitro* example of the frontal lobe-specific microcephaly found in 1qDel patients, as well as providing future insights into CNV-associated cortical dysfunction.

Acknowledgements

This PhD was built on the support, generosity and kindness of others, and I therefore have many individuals I wish to thank.

Within my professional career, I would firstly like to thank my first academic supporter, Dr. Casper Breuker, who I know knows how thankful I am for his encouragement and mentorship during my undergraduate. I hope your family and butterflies are well. Secondly, thank you to Dr. Mercedes Pardo Calvo for giving me my first job in academia at the Sanger Institute. I attribute a lot of my current success to that first foot in the door and your fantastic, patient teaching. I'd like to thank the rag-tag bunch at the CASM Sanger support team too for showing me how a happy working environment can make the world of difference. At Cardiff University, I'd like to thank the Cardiff Student Disability Council and Student Advice for supporting me over the years. I'd like to thank the statistics workshop, particularly Dr. Daniel Farewell, Prof. Peter Morgan and Dr. William Kay, for providing essential help to resolving my countless, awkward data questions and building my confidence in statistics and R. I would also like to thank my supervisory team Dr. Yasir Syed and Prof. Adrian Harwood, as well as my assessor Dr Isabel Garay, for their input throughout this PhD.

I'd like to thank the alumni of the Syed lab, Tanya Singh, Giulia Eminyan and Katrina Savory. Our brief but supportive group was the closest I got to socialising during my PhD and wish it could have lasted. To the Harwood lab, I wish all of you the best in the future and know that you have made the world of difference, particularly in that fateful final lab year by keeping me company and being a surrogate lab family. I also would like to thank Mouhamed Alsaqati especially for your constant sympathy, support & mentorship. I'd like to thank Karolina Dec too, for providing me with a post-COVID social life and wonderful baked goods. I would also like to thank Olena Petter for a leaving speech that deserved an Oscar, and Emma Dalton, a fantastic person as well as lab manager, who I wish all the best for.

On a more personal note, I'd like to thank my friends. Firstly, I'd like to thank Gareth Chapman, the first alum of the Syed lab, who was imperative to the success of this PhD and my training thereof and continues to be a sympathetic ear. To Pete Bradshaw, the smartest man I know, and the only man insane enough to spend evenings pulling apart bad software *for fun*. I would like to thank Bisa Andov for supporting me through my undergraduate and Masters, as well as my PhD, with paradoxically both maximum and minimal judgment. I would also like to thank Bret Sanders for providing me support with light-hearted gossip that brought some very necessary brevity. Lastly, to Katie Norman, my shoulder angel, guilty conscience and childhood best friend. You have been my cheerleading life coach through it all and I aspire to be as kind, forgiving and grounded as

you are. I hope we continue to tackle the world together, for the next 30 years (at least). I thank all of you for your support, love and many eye-watering, belly laughs.

I would like to thank my parents Ian and June, of course. Dad, you have had to withstand countless arguments, rolled eyes, shaking heads and rebellious nature from me, which I inherited from you funnily enough. Mum, you have been every single person I needed in my life for the past 30 years. A confidante, best friend, therapist, a pinnacle of human kindness to try to live up to. You taught me that there is nothing wrong with asking, to stand up for what you believe in (even if it gets you into trouble) and that all I ever need to be is happy. I hope to continue to be a child you can be proud of.

To my partner in crime, Mr. Joel Hyett. You can now claim to have a doctorate, just like you wanted, even if you're only mentioned in one. Moving across a country is no small ask, neither is being the partner to an eccentric scientist. I would have struggled inexplicably without you during this process. You've shared in my joy and pride of my successes. You've been a valiant defender of my skills. You've been forced to stare at data and presentations after a hard day's work, because you know how much this means to me. You've looked after my failing mind and body more times than I care to count. I never thought a person could go through this next to me. But you are not a person; you are Bear and I love you. You'll never know how thankful I am, but I'll spend all my healthy hours trying to show you.

Finally, I would like to dedicate this thesis to my supportive mentor (and cat) Melon. I wish you were able to see the end of this PhD, although I think you would have been angry that dribbling over my keyboard hadn't stopped me writing. You were infinitely better than any other human being, whilst also being a leaky faucet of an animal without concern for anyone other than himself. Miss you buddy.

Glossary of Abbreviations

(ns)	Not significant	IP	Intermediate progenitor
1qDel	1q21.1 deletion	iSVZ	Inner subventricular zone
1qDup	1q21.1 duplication	LCR	Low copy repeat
AD	Area multiplied by cell count	LGE	Lateral ganglionic eminence
AMPA	α-amino-3-hydroxy-5-methyl-4-isoxazolepropionic acid	MCPH	Autosomal recessive primary microcephaly
APD	Area multiplied by perimeter multiplied by cell count	MGE	Medial ganglionic eminence
		MHP	Medial hinge point
aRG	Apical radial glia	miRNA	MicroRNA
ASD	Autism spectrum disorder	NCC	Neural crest cell
BDNF	Brain-derived neurotrophic factor	ND	Neural differentiation
		NDD	Neurodevelopmental disorder
B-hCO	Basic human cortical organoid		
BMP	Bone morphogenetic protein	NE	Neuroectoderm
bp	Base pair	NEC	Neuroepithelial cell
bRG	Basal radial glia	NMDA	N-methyl-D-aspartic acid
cAMP	Cyclic adenosine monophosphate	NPC	Neural progenitor cell
		NTC	Neural tube closure
CC3	Cleaved-caspase 3	oSVZ	Outer subventricular zone
CNV	Copy number variant	PBS	Phosphate-buffered saline
CP	Cortical plate	PFA	Paraformaldehyde
DISC1	Disrupted in schizophrenia 1	PFC	Prefrontal cortex
DLHP	Dorsolateral hinge points	PI	Propidium iodide
DMEM	Dulbecco's modified eagle medium/nutrient mixture F-12	PV	Parvalbumin
		pVIM	Phosphorylated vimentin
DSB	Double-stranded break	qPCR	Quantitative polymerase chain reaction
E/I	Excitatory/inhibitory		
E8F	Essential^{TM} 8 flex	RA	Retinoic acid
EB	Embryoid body	RG	Radial glia
E-EB	Enhanced embryoid body	Ri-EB	ROCKi embryoid body
EGF	Epidermal growth factor	Ri-hCO	ROCKi human cortical organoid
E-hCO	Enhanced human cortical organoid		
		ROI	Region of interest
ER	Endoplasmic reticulum	RT	Room temperature
ESC	Embryonic stem cell	SCZ	Schizophrenia
FGF	Fibroblast growth factor	SFEB	Serum free embryoid body
GABA	γ-aminobutyric acid	SHH	Sonic hedgehog
GDNF	Glial cell-derived neurotrophic factor	SVZ	Subventricular zone
		TAR	Thrombocytopenia-absent radius
GE	Ganglionic eminence		
hCO	Human cortical organoid	TGF-β	Transforming growth factor β
hIPSC	Human induced pluripotent stem cell		
		VZ	Ventricular zone
ICC	Immunocytochemistry	Wnt	Wingless

Table of Contents

List of Tables

List of Figures

1 General Introduction

Currently, more than 50% of the population of middle- to high-income countries will develop a neuropsychiatric disorder in their life time (Trautmann, Rehm and Wittchen, 2016). This amounts to costing on average 4% of the gross domestic product of countries across the EU (Union, 2018). As these conditions are an economic burden in society and highly distressing for the individual, it is paramount to understand how these conditions develop. The relationship between neuropsychiatric disorders and neurodevelopmental disorders (NDDs) was historically proposed a number of decades ago (Weinberger, 1987), and has since been reinforced by studies analysing *in utero* brain development (Owen *et al.*, 2011; Schork *et al.*, 2019), pre- and postnatal environment (Shohat, Ben-David and Shifman, 2017) and cumulative genetic vulnerability (Gray *et al.*, 1991; Cristino *et al.*, 2014). Diagnosis of these conditions is complex and under constant revision (Keeley *et al.*, 2016). Onset of these disorders can occur from early childhood (Davalos *et al.*, 2004; Barnevik Olsson *et al.*, 2013) into adulthood (Sommer *et al.*, 2020), relative to the condition. In recent years, large scale population studies of neurodevelopment have been complemented with high-throughput genetic sequencing data capable of quantifying neuropsychiatric risk (Marshall *et al.*, 2017; Sanders *et al.*, 2017; Zarrei *et al.*, 2019). The summation of this information has led to the understanding that neuropsychiatric disorders, such as autism spectrum disorder (ASD) and schizophrenia (SCZ), can often be traced to altered neurodevelopment (Weinberger, 1987; Cristino *et al.*, 2014; Flaherty and Maniatis, 2020), and are therefore considered NDDs. Recent successes of new methodologies capable of emulating aspects of human neurodevelopment, such as cerebral organoids, have proven fruitful in advancing research on these NDDs (Lancaster *et al.*, 2013; Mariani *et al.*, 2015; Srikanth *et al.*, 2018; Notaras, *et al.*, 2021; Paulsen *et al.*, 2022). Using cerebral organoids, investigations of rare genetic disorders that share similar clinical phenotypic presentation of NDDs could piece together a clearer picture of each NDD's cause and their resulting consequence, as well as potential routes for therapeutics. However, it is necessary to understand how first trimester neurodevelopment occurs typically, in order to determine the anomalies NDDs exhibit.

1.1 First Trimester Mammalian Neurodevelopment: From Neuroectoderm to Neocortex

1.1.1 Designating Mammalian Neuroectoderm

At day 18 post conception (Carnegie stage 8-9), human neurodevelopment begins after gastrulation and development of the notochord. The neural plate begins to form from the surface ectoderm on the dorsal side of the embryo directly above the notochord (Zhang *et al.*, 2010). The neural plate consists of cells that have a number of names within current literature, including neural stem cells or neuroectodermal cells (Zhang *et al.*, 2010; Bond, Bhalala and Kessler, 2012; Thier *et al.*, 2019); in this study they will be termed neuroectodermal cells. The neural plate is distinguishable by its 'thickening', as neuroectodermal cells proliferate exponentially, beginning at the cranial end of the embryo, progressing in a caudal direction and ending at the primitive node (Sutherland, Keller and Lesko, 2020). This is a result of two synchronous processes: morphological manipulation of the designated neuroectodermal cells from cuboidal to columnar (Grego-Bessa *et al.*, 2016) and convergent extension where the neural plate narrows in the mediolateral axis and elongates across the anterior/posterior axis (Ybot-Gonzalez, Savery, *et al.*, 2007; Sutherland, Keller and Lesko, 2020).

The means at which neuroectodermal cells reorganise during convergent extension is relative to the type of organism (Sutherland, Keller and Lesko, 2020). It is believed that mammalian neuroectodermal cells migrate around the outer boundary and intercalate along the midline (Williams *et al.*, 2014), while *Drosophila* and chick neuroectodermal cells remodel via cell-cell junctions (Bertet, Sulak and Lecuit, 2004; Nishimura, Honda and Takeichi, 2012). Distinguishing the neural plate from the surface ectoderm requires crosstalk between multiple morphogens: bone morphogenetic protein (BMP), transforming growth factor-beta (TGF-β), fibroblast growth factor (FGF) and wingless (Wnt). FGF and Wnt signalling act sequentially to spatially localise the rostral/caudal axis of the neural plate (Takata *et al.*, 2017). As it resides above the sonic hedgehog (SHH)-expressing notochord, the midline of the PAX6 positive ($PAX6^+$) neural plate has minimal BMP and TGF-β signalling, but increases substantially on a lateral gradient towards and within the surface ectoderm (Xue *et al.*, 2018). The complex, synchronous modulation of these pathways determines the line of separation between the two ectoderms, otherwise known as the neural plate border. The neural plate border is identifiable by its Pax3, Zic1 and Msx1 expression (Xue *et*

al., 2018). The defined regionalisation of the neural plate, neural plate border and surface ectoderm, signals that the tissues are ready for primary neurulation.

1.1.2 The Process of Primary Neurulation

Primary neurulation is the cellular rearrangement of the neural plate into the neural tube across the embryo, but the process varies relative to the rostral/caudal axis. Cranial (rostral) primary neurulation is the transition of a thickened neural plate into the neural tube via tightly regulated structural remodelling (Figure 1.1) (Sutherland, Keller and Lesko, 2020). The columnar neuroectodermal cells undergo apical constriction to form a pyramidal shape, distinct from the surrounding surface ectoderm. Above the constricting midline and notochord, otherwise known as the neural groove or medial hinge point (MHP), the lateral edges of the neural plate lift upwards, creating neural folds (Figure 1.1.B) (Eom *et al.*, 2012). At the MHP, the neural plate requires the shift of cellular morphology from columnar to pyramidal shape to avoid buckling under mechanical stress (Nikolopoulou *et al.*, 2017). The invagination of the neural plate extends to a large pit across the dorsal midline of the embryo (Nikolopoulou *et al.*, 2017; Sutherland, Keller and Lesko, 2020). Although this morphological restructuring occurs across the cranial and spinal region, in the cranial region the combination of the apposition of the neural folds, cellular morphology shift to pyramidal and progressive apoptosis results in the creation of wedge-shaped dorsolateral hinge points (DLHPs) under each neural fold (Figure 1.1.C) (Yamaguchi *et al.*, 2011; Nikolopoulou *et al.*, 2017).

These DLHPs are exaggerated by biconcave morphology and are influenced by the repression of SHH signalling from the notochord (Ybot-Gonzalez *et al.*, 2002) and BMP antagonism (Ybot-Gonzalez, *et al.*, 2007). With sufficient bending of the neural plate, the surface ectoderm resides on top of the neuroectoderm (NE). The two opposing edges of both ectoderms, either side of the neural groove, gravitate towards one another (Yamaguchi *et al.*, 2011). They meet directly above the MHP (Figure 1.1.D). The two sides of the surface ectoderm conjoin to form the exterior ectoderm, whilst the neural plate edges bond to form a neural tube with a vacant lumen (Figure 1.1.E). This lumen is filled with cerebral spinal fluid and supplies the surrounding apical cells with nourishment and signalling for designating cell fate (Gato *et al.*, 2014). The fusion of surface ectoderm is not instantaneous across the entirety of the embryo, instead favouring

a ‘zipper’ process from the initiation site (Pyrgaki *et al.*, 2010). The surface ectoderm also does not seal completely after fusion. Small ‘open’ regions, termed neuropores, are seen at the cranial and caudal ends of the embryo which close, via cellular protrusions, between Carnegie stage 9-10, signifying the end of primary neurulation (O’Rahilly and Müller, 2002; Pyrgaki *et al.*, 2010). Once closed, the DLHPs devolve into neural crest cells, which then disperse and migrate throughout the cranial region (Figure 1.1.F).

The physical mechanics of primary neurulation are universal across the embryo, although cranial and spinal neurulation do vary. For example, paraxial mesoderm is only found in the spinal region of the embryo (McShane *et al.*, 2015), populating the space otherwise occupied by DLHPs instead with somites, the precursors to the ribs and vertebrae (Morriss-Kay, 1981; Loh *et al.*, 2016). Ultimately, the regional separation of primary neurulation correlates to the neural tube closure (NTC) defects, i.e. exencephaly (cranial) or spina bifida (spinal) (Detrait *et al.*, 2005). These NTC defects are observed in both mouse and human studies, despite cross-species differences; mouse NTC is a ‘buttoning’ process, whilst humans are hypothesised to undergo ‘zipping’ (Pyrgaki *et al.*, 2010). However, the combination of ethics, human foetal tissue research limitations and cross-species differences have slowed neural tube development research. Recent stem cell and organoid developments are capable of bridging the species gap without serious ethical implications (Xue *et al.*, 2018; Thier *et al.*, 2019; Abdel Fattah *et al.*, 2021; Karzbrun *et al.*, 2021; Libby *et al.*, 2021). Such studies have supported both murine and human reports on topics such as actin and N-cadherin bundling constricting cells into a pyramidal shape around the neural tube lumen to form the MHP (Nikolopoulou *et al.*, 2017; Karzbrun *et al.*, 2021), as well as the morphogenic factors contributing to defining the neural plate border (Xue *et al.*, 2018; Thawani and Groves, 2020). With these affirming results, three-dimensional (3D) modelling is likely to become a complimentary tool, alongside *in vivo* modelling, for understanding neural tube development.

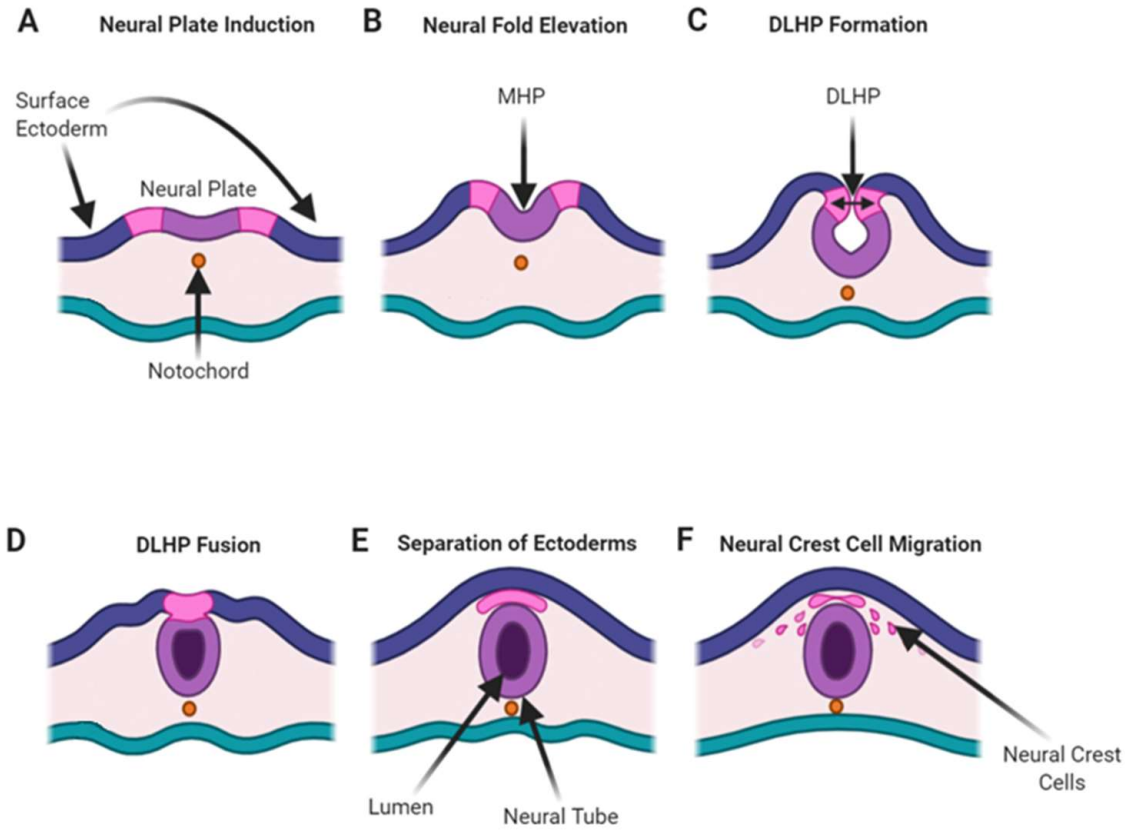

Figure 1.1: Overview of mammalian cranial primary neurulation.
A) Designation of neural plate/surface ectoderm divide. **B)** Elevation of neural folds to form the constricting MHP. **C)** Invagination of neural plate via DLHP bending and apposition of neural folds. **D)** Fusion of DLHP and formation of neural tube lumen. **E)** Fusion of ectoderms into separated tissues: surface ectoderm, neural tube and neural crest cells. **F)** Neural crest cells disperse and begin migration. (Created with BioRender.com free software and adapted).

1.1.3 Allocation of the Dorsal Forebrain

The neural tube progressively closes during Carnegie stages 8-13 (O'Rahilly and Müller, 2002). Once closed, it is termed the neuroepithelium and consists of a one cell-thick border of neuroepithelial cells (NECs), replacing the terminology "neuroectodermal cells" (Subramanian *et al.*, 2017). Segregation of brain regions begins immediately after primary neurulation, dividing the neural tube along the rostral/caudal axis into the prosencephalon (forebrain), mesencephalon (midbrain) and rhombencephalon (hindbrain) (Figure 1.2.A) (Amadei *et al.*, 2022). This is determined by a similar variety of common signalling pathways (BMP, Wnt, SHH and FGF) that are present during primary neurulation, as reviewed by Sidhaye and Knoblich, (2020) (Figure 1.2.A). For example, using a microfluidic-induced Wnt gradient, gene clusters have been found that define

separate regions, i.e. the rostral, $OTX2^+$ prosencephalon expressing FOXG1 and FEZF1, and the caudal, $OTX2^-$ mesencephalon/rhombencephalon expressing GBX2 and HOXB2 (Rifes *et al.*, 2020). Once formed, the prosencephalon undergoes an internal separation into the telencephalon & diencephalon after Carnegie stage 15 (Kobayashi *et al.*, 2016). The telencephalon is of the most interest for this study, as it is responsible for the foundation of the dorsal and ventral forebrain, whilst the diencephalon is the precursor to the thalamic structures, like the hypothalamus (Saito *et al.*, 2018). The telencephalon then differentiates cellular identity and function based on the concentration gradients of signalling pathways such as SHH, BMP and Wnt, across the dorsal/ventral axis (Figure 1.2.A.1) (Tao and Zhang, 2016).

The dorsal and ventral forebrain, also known as the pallium/subpallium, become morphologically and functionally distinct from one another, as the rounded neuroepithelium itself changes shape relative to the location along the rostral/caudal axis (Figure 1.2.A.1-A.2). On the dorsal side of the telencephalon, the roof plate of the neural tube invaginates, becoming a monolayer epithelium containing the choroid plexus, above which the cortical hem sits (Kadoshima *et al.*, 2013). The cortical hem is one of three signalling centres that orientates the forebrain; the other two are the rostrally-located anterior neural ridge and the pallial-subpallial boundary at the medial line between dorsal and ventral telencephalon (Caronia-Brown *et al.*, 2014). During telencephalic development, these three regions act in unison to induce the forebrain's dorsal/ventral and rostral/caudal axis. The cortical hem secretes Wnt and BMP-related proteins, which represses ventral identity in favour of dorsal (Figure 1.2.A.1) (Caronia-Brown *et al.*, 2014) in a similar fashion to the regulation of the dorsal/ventral axis of the neural tube (Horner and Caspary, 2011). The anterior neural ridge secretes key FGF proteins from a region of high concentration (rostral) to low concentration (caudal) across the forebrain (Cajal *et al.*, 2012). Finally, the pallial-subpallial border expresses epidermal growth factor (EGF)-like factors, as well as Wnt inhibitors, to demarcate the dorsal/ventral boundary between forebrain regions (Mallamaci and Stoykova, 2006).

Between the cortical hem and the pallial-subpallial boundary is the dorsal forebrain, which develops into the cerebral cortex proper. It is induced by the high gradient of BMP and Wnt, with a low concentration of SHH (Figure 1.2.A.1) (Tao and Zhang, 2016). It is also defined by several regionally-expressing transcription factors, including PAX6, TBR2, TBR1 and EMX1 (Figure 1.2.B) (Stoykova *et al.*, 2000; Englund *et al.*, 2005; Mallamaci and Stoykova, 2006; Cadwell *et al.*, 2019). The dorsal forebrain houses a diverse array of neural progenitors, descending from the original $PAX6^{+}$ NECs that arise from the neuroepithelium (Ma *et al.*, 2021). Similarly, the variety of post-mitotic neurons produced in the dorsal forebrain are a reflection of the numerous cortical layers characteristic of the cerebral cortex and are glutamatergic and excitatory in nature (Cadwell *et al.*, 2019; Klingler *et al.*, 2021). On the opposing side of the pallial-subpallial border, the ventral forebrain becomes enlarged into two distinct groups, cumulatively called the ganglionic eminence (GE). These two groups are defined as lateral GE (LGE) and the medial GE (MGE). There is also a third GE, which is named the caudal GE due to its more caudal location on the telencephalon (Nery, Fishell and Corbin, 2002).

The GEs are also centres of neural progenitor proliferation and neuron generation, but the variety of types are substantially different than the dorsal forebrain. Neural progenitors in the GE are identifiable by transcription factors, some are shared across the GE (DLX1/2), whilst others are region-specific, such as NKX2.1 for the MGE (Figure 1.2.B) (Germain *et al.*, 2013; Sandberg *et al.*, 2016; Pla *et al.*, 2018; Alzu'bi and Clowry, 2019). The transcription factors expressed by neural progenitor cells of the GE can also affect the specific type of neuron created within this region: γ-aminobutyric acid (GABA)-producing inhibitory interneurons (Ma *et al.*, 2021). GABA-ergic inhibitory interneurons tangentially migrate into the cortical layers of the dorsal forebrain (Tanaka *et al.*, 2006). This migration is key to balancing the excitatory output from glutamatergic, pyramidal neurons that are the dominant majority within the neocortex (Tanaka *et al.*, 2006). The neocortex itself, however, is capable of producing a small population of local GABA-ergic interneurons to aid in the regulation of early cortical circuitry (Tremblay, Lee and Rudy, 2016). Overall, the combined input of these two forebrain regions is required to develop a functional cerebral cortex.

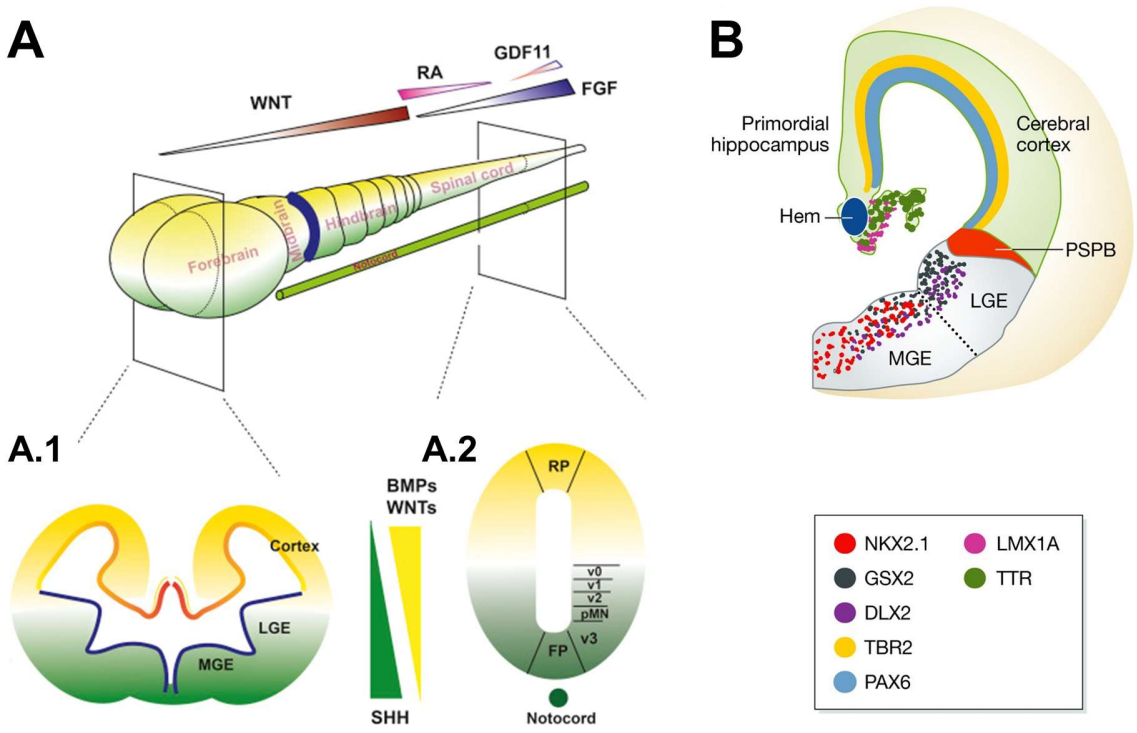

Figure 1.2: Different schematic representations of the dorsal and ventral forebrain.

A) Signalling pathways involved with distinguishing the rostral/caudal axis across the human embryo **(A)** and the dorsal and ventral axis of the forebrain **(A.1)** and other more caudal regions like the spinal chord **(A.2)**. Adapted from (Tao and Zhang, 2016). **B)** Detailed schematic of the mouse forebrain, as well as cellular identity markers for each region. Adapted from (Dias and Guillemot, 2017). Annotations: FP – floor plate, LGE – lateral ganglionic eminence, MGE – medial ganglionic eminence, pMN – motor neuron progenitors, RP – roof plate, PSPB – pallial/subpallial boundary.

1.1.4 Expansion and Lamination of the Neocortex

The development from neural tube to neocortex has evolved in order to maximise production of neurons. In the forebrain, the NECs within the neuroepithelium proliferate exponentially; the quantity of NECs directly relates to neuron count and is considered a key factor in human cortical evolution (Subramanian *et al.*, 2017; Benito-Kwiecinski *et al.*, 2021). In order to instigate neurogenesis in the dorsal forebrain, NECs have to transition to radial glia (RG), initially of the apical variety (aRGs). Both NECs and aRGs are SOX2, NESTIN and PAX6 positive, however aRGs also produce glia-related proteins (GFAP, BLBP and vimentin) whilst NECs do not (Nat *et al.*, 2007). Both neural progenitor cell (NPC) types organise themselves vertically across the neuroepithelium, creating a

pseudo-stratified structure, orientated by an apical-basal axis (reviewed by Götz and Huttner, (2005)). However, the manner in which each NPC type is anchored to the apical edge of the ventricle varies significantly. NECs are bound to their adjacent neighbours by tight junction proteins like ZO1 (Eze *et al.*, 2021). NECs require tight junctions to provide flexibility to alter their shape whilst forming the neural tube (Götz and Huttner, 2005). Conversely, aRGs lose these tight junctions (Aaku-Saraste, Hellwig and Huttner, 1996; Arellano *et al.*, 2021; Eze *et al.*, 2021). Instead, both aRGs and NECs have adherens junctions that act collaboratively with the F-actin belt located at the apical region of the cell to constrict the cell upon instruction (Nishimura, Honda and Takeichi, 2012). The mechanical flexibility junction proteins provide is necessary to adapt to the expanding neocortex and pressure from cerebral spinal fluid in the ventricles (Yamamoto *et al.*, 2013; Guerra *et al.*, 2015).

These scaffolding proteins facilitate interkinetic nuclear migration, whereupon both NECs and aRGs will translocate their nucleus throughout the cell body, the outer processes of which are anchored at the apical and basal edges of the neuroepithelium (Benito-Kwiecinski *et al.*, 2021; Jiang *et al.*, 2021). However, aRGs distinguish themselves from NECs by their fibrous projections during mitosis. As NECs retract their basal process during anaphase and telophase, whilst aRGs' basal process thins significantly but does not retract (Subramanian *et al.*, 2017). NECs also only have basal processes to the edge of the neuroepithelium, whilst RGs' fibres can reach up to the pial surface of the cortex (Nowakowski *et al.*, 2016; Benito-Kwiecinski *et al.*, 2021). The most distinguishing feature between the two NPCs is RGs' proclivity to undergo asymmetric (horizontal or oblique) cell division in a proportion of mitotic events in order to produce intermediate progenitors (IPs), basal radial glia (bRGs) or neurons; NECs only undertake self-proliferative symmetric division (Eze *et al.*, 2021). The rate at which asymmetric RG division occurs is relative to the signalling from the cerebral spinal fluid in the lumen surrounding the apical side of the neocortex (Lehtinen *et al.*, 2011; Ferent, Zaidi and Francis, 2020).

As NECs are replaced with RGs, the neuroepithelium is redefined as the ventricular zone (VZ). The VZ is recognised as one of the main sources of proliferating cells within the developing neocortex. As the number of asymmetrically dividing aRGs increases, layers appear above the VZ to house the new neuronal populations (Figure 1.3). One such layer is the subventricular zone

(SVZ), which interjects between the VZ and the preplate. It harbours descendants of aRGs that have migrated away from the VZ, namely IPs and bRGs. IPs lack apical basal polarity (multipolar) and can be distinguished from RGs by transcription factors such as TBR2 (Kyrousi *et al.*, 2021). IPs are also fated to terminally differentiate into two neurons after migration into the SVZ (Kowalczyk *et al.*, 2009). bRGs, on the other hand, bear a resemblance to aRGs, except for certain distinguishable genes such as *HOPX* (Pollen *et al.*, 2015; Penisson *et al.*, 2019). Despite lacking an apical process, bRGs have a basal process that reaches the pial surface of the neocortex, therefore retaining a unipolar orientation, and can undergo self-renewing asymmetric divisions before terminal neurogenic differentiation (Hansen *et al.*, 2010; Kyrousi *et al.*, 2021). Within the SVZ, a gyrencephalic-specific separation produces an inner (iSVZ) and outer (oSVZ) SVZ, separated by a thin inner fibre layer (Johnson *et al.*, 2018). Although both SVZ layers share similar gene expression profiles (Fietz *et al.*, 2012), the timeline for expanding these regions differ, with populating the oSVZ with bRGs restricted to embryonic development (Martínez-Martínez *et al.*, 2016). The expansion of these regions, particularly the oSVZ, has been correlated to the considerable expansion of neurons in primates (Dehay, Kennedy and Kosik, 2015).

At a similar time to the formation of the SVZ, the preplate forms (Bayatti *et al.*, 2008). The preplate contains pioneer neurons and Cajal-Retzius cells that have migrated from the cortical hem (Meyer *et al.*, 2000; Renner *et al.*, 2017). This is closely followed in development by the creation of the intermediate zone. Although the preplate is a transient structure, the intermediate zone is a perpetual region throughout gestation, separating proliferative regions such as the VZ/SVZ from post-mitotic cortical layers (Molyneaux *et al.*, 2007). It serves as a layer that reorientates incoming multipolar immature neurons from proliferative regions, guided back to a unipolar orientation by RG fibres connected to the pial surface of the cerebral cortex (Hashemi *et al.*, 2017). Above the IZ, the preplate eventually splits into two discrete regions: the subplate, containing pioneer neurons (Judas, Sedmak and Kostovic, 2013; Olson, 2014) and the marginal zone, containing the Cajal-Retzius cells (Costa *et al.*, 2007). Cortical neurons entering or residing in the subplate are often influenced by the migratory afferent fibres of extracortical neurons (Hoerder-Suabedissen and Molnár, 2015). The cortical plate (CP) is the last plate to be formed, located between the subplate and marginal zone. The CP is formed of maturing neurons radially migrating in columns from the proliferative

regions of the VZ/SVZ to their pre-assigned layer. The CP eventually segregates into five layers (VI-II), their identity defined by specific markers determining different neuronal populations. These layers develop sequentially from Layer VI to Layer II, with early born neurons (Layer VI) being physically surpassed by late born neurons (Layer II) in an “inside-out” fashion. Neuronal populations are not necessarily confined to one layer, often overlapping into adjacent layers, such as $CUX1^{+}$ neurons that span Layers II-IV (Nieto *et al.*, 2004). Finally, the marginal zone at the pial surface is redefined as Layer I, still containing Cajal-Retzius cells, but importantly releases the essential neuronal migration protein reelin that orientates radial neuronal migration through cortical columns (Hashimoto-Torii *et al.*, 2008).

The individual processes during the first trimester of human foetal neurodevelopment are innately complex (Figure 1.3). Spanning from neural plate designation to the developing neocortex, signalling pathways and genetic interactions are interconnected to distinguish compartmentalisation of the forming brain, as well as cellular identity (Englund *et al.*, 2005; Ybot-Gonzalez, *et al.*, 2007; Marchal *et al.*, 2009; Zhang *et al.*, 2010; Herrera *et al.*, 2014; Hettige *et al.*, 2022). In scenarios when any of these nodes of communication become faulty, i.e. heritable or *de novo* genetic mutations, it can have long-term impact on neurodevelopment, such as heightening the risk of NDDs (Davalos *et al.*, 2004; Mariani *et al.*, 2015; Srikanth *et al.*, 2018; Palmer *et al.*, 2021).

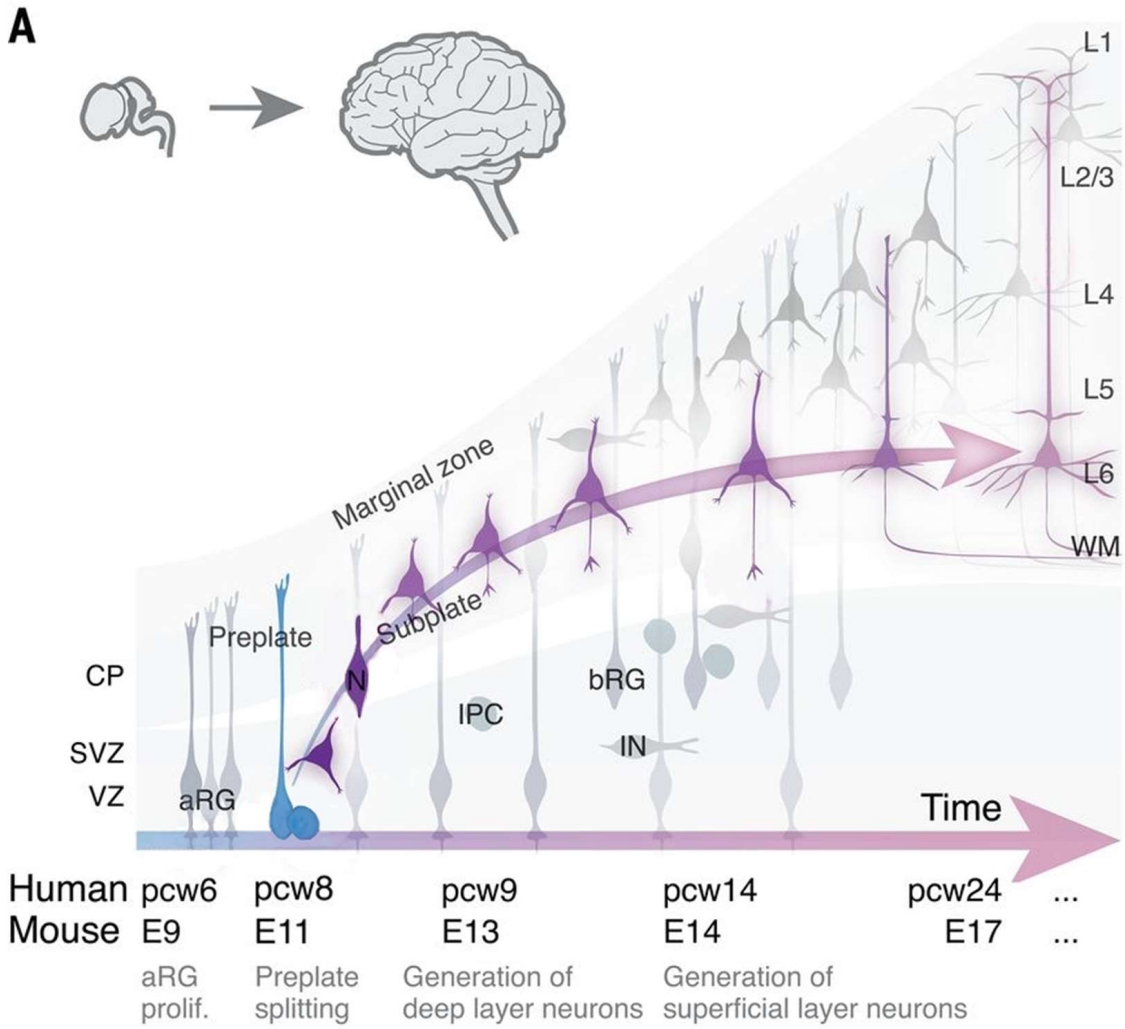

Figure 1.3: Summary of embryonic corticogenesis.
Schematic illustration from development of preplate, subventricular zone and ventricular zone, through to cortical plate (CP) layer separation and white matter development (from intermediate zone). Annotations: aRG – apical radial glia, bRG - basal radial glia, CP - cortical plate, IN – interneuron, IPC - intermediate progenitor cell, PCW – post conception weeks, SVZ - subventricular zone, VZ - ventricular zone, WM - white matter. Adapted from (Klingler *et al.*, 2021).

1.2 Copy Number Variants Contribution to Atypical Neurodevelopment

Abnormal neurodevelopment can be induced by genetic mutations, the likes of which can result in significant structural and functional neurological deficits (Parenti *et al.*, 2020). However, clinical phenotypes vary substantially between each patient due to innate genetic complexity, despite sharing phenotypic similarities such as ASD or SCZ (Crespi, Stead and Elliot, 2010). These difficulties can be overcome by isolating disorders by their shared genetic features, such as patients with copy number variants (CNVs). CNVs are not inherently pathogenic, and are a regular occurrence in human evolution (Sudmant *et al.*, 2015), playing a

significant role in improving human physiology such as through the expansion of specific cortical areas during neurodevelopment (reviewed by Mitchell and Silver, (2018)). CNVs occur typically during meiosis, but can occur somatically (Piotrowski *et al.*, 2008). These variants are usually deletions or duplications, flanked by 'breakpoints'; regions of vulnerable DNA that break apart during chromosomal rearrangement during mitosis, meiosis or quiescence. CNVs tend to occur in low copy repeat (LCR)-rich regions, where mis-selection during recombination is likely, given the LCR's high sequence homology. These errors can occur through different mechanisms during reformation, such as nonallelic homologous recombination, nonhomologous end joining, or fork stalling and template switching (Zhang *et al.*, 2009). The rates of these mechanisms are determined by factors such as the length of the LCR, the distance between the two parent LCRs, as well as the shared homology of the DNA sequence itself (Liu *et al.*, 2011). As sequencing becomes more precise in detailing the complexity and location of CNVs (Zhang *et al.*, 2017), it is clear that, from an evolutionary standpoint, CNVs are a high-risk, high-reward scenario. The former results in detrimental health, whilst the latter is either neutral or more favourable, the likes of which is under positive selection to increase genetic variation and fitness (Vandepoele *et al.*, 2005).

As detailed by Table 1.1, as well as in Takumi and Tamada, (2018) and Sønderby *et al.*, (2022), there is an array of pathogenic CNVs that are associated with NDDs. Other common phenotypes not directly associated with neurology include craniofacial abnormalities, organ variability and muscular/stature issues (Zhao *et al.*, 2020; Edwards *et al.*, 2021).These pathogenic CNVs are relatively rare (≤1%) and can vary in size from >50 base pairs (bps) to ≤3 Mbps (Stone *et al.*, 2008; MacDonald *et al.*, 2013). When reviewing the incidence rate of patients' neurological phenotypes, intellectual disability and/or developmental delay breach the incidence rate threshold of all CNVs referenced in Table 1.1, whilst exhibiting at least one other NDD to a substantial degree is common (Cook and Scherer, 2008; Walsh *et al.*, 2008). However, distinguishing trends in phenotype prevalence is difficult, as cohort sizes can be relatively small (≤10 patients). Furthermore, cohorts can be skewed, knowingly or unknowingly, by geographical, racial or gender bias as a result of minimal sample size. Gene dosage effects also creates phenotypic variability between cohorts with the same CNV architecture (Rice and McLysaght, 2017; Yamasaki *et al.*, 2020; Sønderby *et al.*, 2022). To minimise

unfair weighting of phenotypic representation, Table 1.1 is a collection of pathogenic CNV cohorts containing ≥5 patients, where ≥20% exhibit any one phenotype; this would mean that at least 1 patient within a single cohort of 5 would exhibit the phenotype. Although these CNVs can present a broad spectrum of NDDs significantly above general population level, the intention of Table 1.1 is to show the NDDs of the highest prevalence within a cohort. As well as NDDs, abnormal head size also is a common neurological phenotype in pathogenic CNVs (Sønderby *et al.*, 2022). Certain NDDs that regularly present in CNVs, such as ASD and SCZ, have been associated with head size variance regardless of CNV presence (Ward *et al.*, 1996; Blanken *et al.*, 2018; Wu *et al.*, 2020). These atypical head sizes arise differently depending on the CNV, as each CNV has a unique hallmark on which brain regions are affected by the genetic anomaly (Sønderby *et al.*, 2022). Connecting patient phenotypes such as head size to patient genotypes is one of many avenues that are being explored in CNV research (Chawner *et al.*, 2019), alongside complementary investigations in *in vivo* and *in vitro* models of CNVs (Nomura and Takumi, 2012; Flaherty and Brennand, 2017).

CNVs' usefulness as a model for NDD research is twofold; patients with CNVs are at a considerably greater risk of exhibiting NDDs than the general populace (Zarrei *et al.*, 2019) and multiple NDDs can exist within a singular CNV cohort (Flaherty and Brennand, 2017; Zarrei *et al.*, 2019; Yoon and Mao, 2021). CNVs can therefore be used as investigatory tools to isolate individual NDDs' unique components (Nielsen *et al.*, 2017; Khan *et al.*, 2020; Urresti *et al.*, 2021; Wegscheid *et al.*, 2021) and, in turn, what similarities they share (Moreno-De-Luca *et al.*, 2010; Crespi and Crofts, 2012). For this reason, the reciprocal risk significance of NDDs makes 1q21.1, 15q11.2, 16p11.2 and 22q11.2 favourable choices of CNVs for NDD research e.g. the duplication of 1q21.1 region for ASD and the deletion of 1q21.1 for SCZ (Crespi, Stead and Elliot, 2010).

Table 1.1: List of clinically described CNV disorders associated with NDDs.
Parameters used for review: Cohorts ≥5 patients, tested for at least three of the mentioned phenotypes. Confirmation of NDDs was based on ≥20% incidence in at least one cohort. Expanded list of identified CNVs originally from Takumi and Tamada, (2018). Blank cells are phenotypes either not meeting the criteria or undetermined. Acronyms: DUP - duplication, DEL - deletion, MA - macrocephaly, MI - microcephaly, ASD – autism spectrum disorders, SCZ – schizophrenia, ADHD – attention deficit hyperactivity disorder.

CNV Loci	DEL / DUP	ASD	SCZ	ADHD	Epilepsy/ Seizures	Head size
1q21.1 *(Crespi and Crofts, 2012; Edwards* et al.*, 2021; Modenato* et al.*, 2021)*	DEL		✓	✓	✓	MI
1q21.1 *(Mefford* et al.*, 2008; Modenato* et al.*, 2021)*	DUP	✓		✓		MA
2p16.3 *(Al Shehhi* et al.*, 2019; Alfieri* et al.*, 2020)*	DEL	✓		✓	✓	MA
3q29 *(Ballif* et al.*, 2008; Crespi and Crofts, 2012; Glassford* et al.*, 2016; Sanchez Russo* et al.*, 2021)*	DEL	✓	✓	✓		MI
7q11.23 *(Sanders* et al.*, 2011; Morris* et al.*, 2015)*	DUP	✓		✓		MA
15q11.2 *(Butler, 2017; Baldwin* et al.*, 2021)*	DEL	✓	✓	✓	✓	MI
15q11.2-q13.3 *(Urraca* et al.*, 2013; Conant* et al.*, 2014)*	DUP	✓			✓	
15q13.3 *(Crespi and Crofts, 2012; Lowther* et al.*, 2015)*	DEL		✓		✓	MA/MI
15q13.3 *(Budisteanu* et al.*, 2021)*	DUP	✓			✓	
16p11.2 *(Shinawi* et al.*, 2010; Chung* et al.*, 2021; Modenato* et al.*, 2021)*	DEL	✓		✓	✓	MA

16p11.2 *(Shinawi* et al.*, 2010; Sanders* et al.*, 2011; Modenato* et al.*, 2021)*	DUP	✓	✓	✓	✓	MI
16p13.11 *(Ramalingam* et al.*, 2011; Khattabi* et al.*, 2020)*	DUP	✓		✓	✓	
17q12 *(Moreno-De-Luca* et al.*, 2010; Milone* et al.*, 2021)*	DEL	✓		✓	✓	MA
17q12 *(Milone* et al.*, 2021)*	DUP	✓		✓		
22q11.2 *(Niklasson* et al.*, 2001; Crespi and Crofts, 2012; Taylor* et al.*, 2018; Modenato* et al.*, 2021; Seitz-Holland* et al.*, 2021)*	DEL	✓	✓	✓		MI
22q11.2 *(Crespi and Crofts, 2012; Wenger* et al.*, 2016; Seitz-Holland* et al.*, 2021)*	DUP	✓		✓		
22q13.3 *(Phelan and McDermid, 2011; Levy* et al.*, 2021)*	DEL	✓			✓	

1.2.1 Modelling 1q21.1 Copy Number Variant Pathology

CNVs of the 1q21.1 region substantially increases the likelihood of developing an NDD, but the risk for each NDD varies relative to the rearrangement (Crespi and Crofts, 2012). An assortment of different combinations of CNVs are possible within the 1q21.1 loci, as LCRs span across the majority of the region (Sun *et al.*, 2015). Patients can be categorised into “classes” based on the region affected within the 1q21.1 loci; the thrombocytopenia with absent radius (TAR) or the distal regions (Brunetti-Pierri *et al.*, 2008). These two regions can be affected independently or affected as a whole. Currently, four breakpoints have been identified across the 1q21.1 region, resulting in a recorded total of 5 different combinations of mutations within the 1q21.1 loci (Figure 1.4) (Brunetti-Pierri *et al.*,

2008). Almost all cases affecting both regions have the same mutation, e.g. both the distal and TAR regions are deleted, but it is possible to have a 'complex' TAR region deletion with a duplicated distal region (Brunetti-Pierri *et al.*, 2008). The TAR region is relatively short in comparison to the distal, ~0.4 Mbps in length, and contains ≥14 genes (Rosenfeld *et al.*, 2012). It is predominantly associated with skeletal tissue, limb development and blood composition (Hall, 1987; Houeijeh *et al.*, 2011), with no known connection to NDDs. In contrast, the distal region spans ~2.6 Mbps and has ≥16 genes, the likes of which have been associated with NDDs. Given this affiliation, the focus of this research will be centred on the 1q21.1 distal region mutation, also known as Class I mutations.

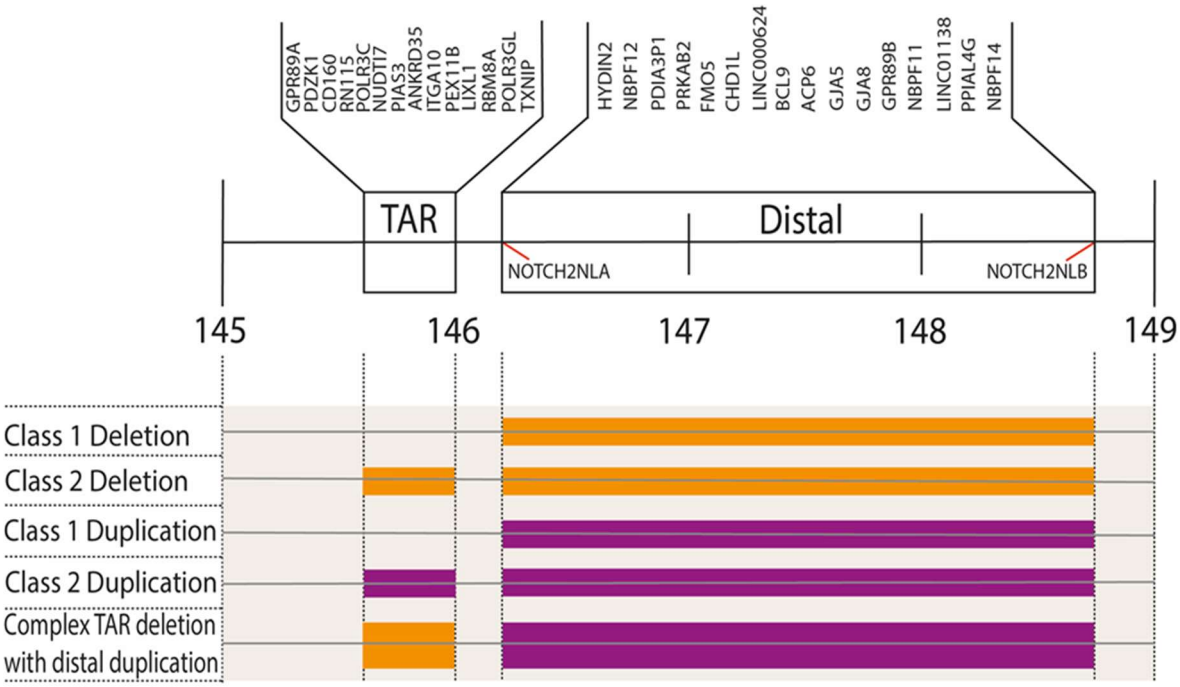

Figure 1.4: Genetic composition and known rearrangements of the distal and TAR regions of the 1q21.1 locus.

1q21.1 TAR region and distal region originally determined by Fiddes, et. al, (2018) and updated distal region determined by flanking breakpoints at *NOTCH2NLA* and *NOTCH2NLB*, as found on UCSC Genome Browser (GRCH38.hg38), accessed in December 2022. Deletion of a region is represented in orange, purple is duplication.

Class I 1q21.1 patients feature facial dysmorphia (>75%), retinal abnormalities (33%), intellectual disability (30%) and cardiac issues (10-25%) (reviewed in an updated Haldeman-Englert and Jewett, (1993)). The deletion and duplication exhibit reciprocal, neurological phenotypes; Class I 1qDel patients have a high incidence of microcephaly (22-72%) with a substantial association

with SCZ and ADHD (Mefford *et al.*, 2008; Stefansson *et al.*, 2008; Stone *et al.*, 2008; Crespi and Crofts, 2012; Bernier *et al.*, 2016; Edwards *et al.*, 2021; Linden *et al.*, 2021). Class I 1q21.1 duplication (1qDup) patients exhibit macrocephaly (26-50%) and high occurrence of ASD (41-50%). These NDDs are the most prominently featured in the CNVs' pathology; all NDDs referred to in Table 1.1, as well as mood disorders such as depression or anxiety, occur within 1q21.1 cohorts at a substantially higher rate than the general population (Crespi, Stead and Elliot, 2010; Crespi and Crofts, 2012; Edwards *et al.*, 2021; Linden *et al.*, 2021).

The differences found in overall intracranial volume and surface area correlate to the relevant abnormal brain size phenotypes found in 1q21.1 patients (Sønderby *et al.*, 2021). The map of differential 1q21.1 gene dosage overlaps with affected surface area, identifying the frontal lobe, particularly the prefrontal cortex (PFC), as vulnerable (Sønderby *et al.*, 2021); this cannot be said of cortical thickness that largely remains unchanged (Sønderby *et al.*, 2021). Mouse models of hemizygous 1qDel mimic the patient phenotype of reduced brain volume (Reinwald *et al.*, 2020), however mice exhibit topological changes only in subcortical regions like the midbrain and striatum, not the PFC (Reinwald *et al.*, 2020). Physiologically, 1qDel mice exhibit sensitivity to dopamine and glutamate modulation via pharmaceutical intervention using agonists (Nielsen *et al.*, 2017) similar to that of SCZ patients (Kapur and Seeman, 2002). Additionally, the cortex of the same mouse model was found to have significant transcriptional overlap with data from post-mortem ASD and SCZ patient brains (Gordon *et al.*, 2021). Interestingly, despite these disparities, there was no difference in functional connectivity and gross behaviour, compared to their control counterparts (Nielsen *et al.*, 2017; Reinwald *et al.*, 2020).

As of yet, there have been no *in vivo* modelling of 1qDup, but recent *in vitro* studies have shown that cortical neurons derived from 1q21.1 patients have diverging phenotypes relative to the rearrangement (Chapman *et al.*, 2021). More Layer VI/V neurons were present in the 1qDel cortical neuron samples, along with electrophysiological properties such as hyperexcitability and longer network bursts (Chapman *et al.*, 2021). The 1qDup neurons however showed none of these characteristics, instead only showing low cortical neuron count and poor synaptic transmission resulting in no electrophysiological activity (Chapman *et al.*, 2021). This study stems from Class I 1q21.1 patients directly and therefore is arguably a closer representation of patient cortical dysfunction than the mouse model.

However, despite *in vitro* results, 1qDup patients are viable and live to adulthood (Brunetti-Pierri *et al.*, 2008; Chapman *et al.*, 2021), and so greater clarity is necessary across research models. With this in mind, future studies of 1q21.1 CNVs should use a multi-modal or all-encompassing model approach. Patient-derived cell lines should also be utilised wherever possible, as important, human-specific, cortical-affecting genes such as the *NOTCH2NL* paralogs (Fiddes *et al.*, 2018; Suzuki *et al.*, 2018) are present within the 1q21.1 region.

1.2.2 Genetic Composition of 1q21.1 Distal Region

Genes within the distal region of the 1q21.1 loci can be separated into distinct categories: protein coding genes of which bear no known, direct interaction with each other, long non-coding genes, and paralogs (Table 1.2) (Yoon and Mao, 2021). Research into the individual functions of some of the protein coding genes is underwhelming. For example, all that is known of *PPIAL4G* is the characteristic function of its gene family, PPIases, that accelerate protein folding, certain members of which have been tied to NDDs (Dunyak and Gestwicki, 2016). Furthermore, ACP6 is required for tumour-associated phospholipid degradation (Chryplewicz *et al.*, 2019), FMO5 abates metabolomic aging (Gonzalez Malagon *et al.*, 2015; Varshavi *et al.*, 2018) and *GPR89B* has minimal clarity on its function; it is assumed to affect pH in the Golgi apparatus (Maeda *et al.*, 2008). Similar can be said of the long non-coding RNAs *PDIA3P1*, *LINC00624* and *LINC01138*, which at present have been solely related to oncogenics (Kong *et al.*, 2017; Zhang *et al.*, 2018; Li *et al.*, 2021).

On the other hand, some of the genes within the 1q21.1 distal region have been examined in greater detail. Two such examples are *GJA5* and *GJA8*, which have been predominantly associated with heart- and eye-related disorders (Ceroni *et al.*, 2019), respectively, including the congenital heart disease reported in 1q21.1 patients (Soemedi *et al.*, 2012). Although neither have been found to be directly connected to neuronal development or function, a protein coded by a member of the same gene family, *GJA1*, has been found to be involved in neural crest migration, causing exencephaly when overexpressed (Ewart *et al.*, 1997) and has a role in astrocytic support to neurons after traumatic brain injury (Ren *et al.*, 2021). A similarly cardiac/neurodevelopment-adjacent 1q21.1 distal region gene is PRKAB2, which regulates AMP-activated protein kinase function in mitochondria (Nagy *et al.*, 2018). Homozygous-null *PRKAB2* mouse models of the

International Mouse Phenotyping Consortium documented early postnatal lethality (preweaning), with differential blood composition distinguishable in the heterozygous equivalent (Groza *et al.*, 2022). Although there were no reported cardiac changes in the mouse model, *PRKAB2* has been found to support development of other mesodermal-lineage tissue, including cardiomyocytes, in human-specific cells (Ziegler *et al.*, 2020). On the other hand, in *Drosophila*, *PRKAB2* also influences neuronal dendrites' structure and cognitive function (Nagy *et al.*, 2018). Again this was not found in *PRKAB2* mutant mice, but *PRKAB1* mutant mice have shown a list of physiological deficits, including several related to neurodevelopment (Dasgupta and Milbrandt, 2009; Groza *et al.*, 2022). Although there may be differences between 1q21.1 CNV models, the fact that all aforementioned *PRKAB2* phenotypes are exhibited in 1q21.1 patients suggests that genes within 1q21.1 distal region may have multiple functions, including heart and brain development.

Certain 1q21.1 genes have been directly attributed to NDDs. Increased prevalence of SCZ has been attributed to common variations of *BCL9* found in geographically different, large population data sets (Li *et al.*, 2011; Xu *et al.*, 2013; Kimura *et al.*, 2015), with notable connection to negative symptoms in SCZ (Xu *et al.*, 2013; Kimura *et al.*, 2015). Although the means by which BCL9 could destabilise typical neurodevelopment is unknown at the moment, BCL9 has been known to be a physical cofactor in the regulation of the neurodevelopmentally-essential β-catenin (Kramps *et al.*, 2002). It does so by compromising the nuclear localisation of β-catenin, thereby preventing binding of TCF/LEF transcription factors resulting in repressed downstream transcription of the Wnt signalling cascade (Brack *et al.*, 2009; Takada *et al.*, 2012). At present, BCL9 is known to contribute to oncogenic phenotypes through its regulation of β-catenin (Takada *et al.*, 2012; Vafaizadeh *et al.*, 2021). As dysregulation of the Wnt signalling pathway has been proven to be indicative of certain NDDs (Dong *et al.*, 2016; Iefremova *et al.*, 2017; Srikanth *et al.*, 2018), the absence or overt presence of a β-catenin cofactor could be contributing to the increased risk of NDDs in 1q patients.

As reviewed by Xiong *et al.*, (2021), *CHD1L* is one of the most well characterised 1q21.1 genes and is known to have multiple functions: a chromatin remodeller during early embryogenesis (Snider *et al.*, 2012; Jiang *et al.*, 2015), acting at sites of DNA damage for repair (Ahel *et al.*, 2009) and modulating cell proliferation and apoptosis in cancer (Sun *et al.*, 2016; Wang *et al.*, 2021). *CHD1L*

is also known to influence β-catenin, and therefore canonical Wnt signalling, in multiple types of cancer (Sun *et al.*, 2016; Liu *et al.*, 2017). In relation to NDDs, studies found that downregulation of *CHD1L* results in failure to form effective neuroepithelium, as *CHD1L* appears to proportionally affect *Pax6* expression (Dou *et al.*, 2017). However, it is not required to maintain mouse embryonic stem cells (ESCs) in culture (Snider *et al.*, 2012; Jiang *et al.*, 2015), therefore it may be a lineage-specific regulator considering its immediacy of disrupting development during neuroectodermal differentiation. Additionally, when phenotyped by the International Mouse Phenotyping Consortium, *Chd1l*$^{-/-}$ mice did not reach weaning stage and had abnormal tail length; there is no phenotypic data available for heterozygous *Chd1l* mice. Furthermore, *CHD1L* shares 59% sequence homology with *CHD1* (Ma *et al.*, 2008), the missense variants of which significantly increase ASD prevalence (Pilarowski *et al.*, 2018). As evidence is found of *CHD1L*'s association with ADHD (Qi *et al.*, 2019), CHD1L is likely to have a similar requirement in neurodevelopment as CHD1.

Table 1.2: Summary of 1q21.1 distal region genes' function between the NOTCH2NLA and NOTCH2NLB breakpoints.

Full names, notes & functions were collected from GeneCard (Stelzer et al., 2016), if not otherwise referenced.

Gene	Full Name	Function
ACP6	Acid Phosphatase 6, Lysophosphatidic	Hydrolyses phospholipids (Chryplewicz *et al.*, 2019), histidine acid phosphatase.
BCL9	B-Cell Lymphoma 9	Localises β-catenin to nucleus (Takada *et al.*, 2012), oncogene (Takada *et al.*, 2012; Vafaizadeh *et al.*, 2021), associated with SCZ (Li *et al.*, 2011).
CHD1L	Chromodomain Helicase DNA Binding Protein 1 Like	DNA helicase, chromatin remodeller (Snider *et al.*, 2012; Jiang *et al.*, 2015), oncogene (Sun *et al.*, 2016; Liu *et al.*, 2017), modulates cell proliferation and apoptosis (Sun *et al.*, 2016; Wang *et al.*, 2021), PAX6 regulator during neuroectodermal differentiation (Dou *et al.*, 2017).

FMO5	Flavin-Containing Dimethylaniline Monoxygenase 5	Mediator of metabolic ageing (Gonzalez Malagon *et al.*, 2015; Varshavi *et al.*, 2018).
GJA5	Gap Junction Protein Alpha 5	Gap junction protein important in atrial fibrillation (Soemedi *et al.*, 2012).
GJA8	Gap Junction Protein Alpha 8	Gap junction protein important in structural integrity of retinal lens (Ceroni *et al.*, 2019).
GPR89B	G Protein-Coupled Receptor 89B	Voltage dependent anion channel required for appropriate Golgi apparatus function (Maeda *et al.*, 2008).
HYDIN2	Hydrocephalus Inducing Homolog 2	Paralog of Hydin. Hypothesized to be a compounding factor in abnormal head size (Brunetti-Pierri *et al.*, 2008) but has been refuted (Dumas *et al.*, 2012; Dougherty *et al.*, 2017; Xavier *et al.*, 2018).
LINC01138	Long Intergenic Non-Protein Coding RNA 1138	Long non-coding RNA, oncogene (Li *et al.*, 2018; Zhang *et al.*, 2018).
LINC00624	Long Intergenic Non-Protein Coding RNA 624	Long non-coding RNA, oncogene (Li *et al.*, 2021).
NBPF11	Neuroblastoma Breakpoint Family Member 11	DUF1220-domain NBPF paralog (Fiddes *et al.*, 2019), related to patient head size (Dumas *et al.*, 2012).
NBPF12	Neuroblastoma Breakpoint Family Member 12	DUF1220-domain NBPF paralog (Fiddes *et al.*, 2019), related to patient head size (Dumas *et al.*, 2012).
NBPF14	Neuroblastoma Breakpoint Family Member 14	DUF1220-domain NBPF paralog (Fiddes *et al.*, 2019), related to patient head size (Dumas *et al.*, 2012).
PPIAL4G	Peptidylprolyl Isomerase A Like 4G	Pseudogene, related to protein folding (Dunyak and Gestwicki, 2016).
PRKAB2	Protein Kinase AMP-Activated Non-Catalytic Subunit Beta 2	Regulatory subunit of AMP-activated protein kinase, involved in metabolism (Dasgupta and Milbrandt, 2009), dendritic modulator and involved in sleep regulation (Nagy *et al.*, 2018), associated with cardiac development (Ziegler *et al.*, 2020).

The paralogs within the 1q21.1 loci are of considerable interest as they are human-specific and have been suggested to affect neurodevelopment. *HYDIN2* is a paralog exclusively expressed in the brain, unlike its ancestral gene *HYDIN* at 16q22.2 that is expressed in the brain as well as other tissues (Davy and Robinson, 2003). *HYDIN2* has been argued to be a dosage-dependent causative factor for abnormal head size in 1q21.1 patients (Brunetti-Pierri *et al.*, 2008) given its relation to *HYDIN;* as its name suggests, mutation of *HYDIN* causes hydrocephaly in mice (Davy and Robinson, 2003). This hydrocephaly is induced by HYDIN's influence on cytoskeletal architecture, e.g. cilia and flagella, as it shares protein domains with the microcephaly-associated ASPM (Ponting, 2006). However, this theory is undermined by several studies; for one, hydrocephaly does not occur in recessive mutations of *HYDIN* in human patients (Olbrich *et al.*, 2012) and so comparison between mouse models and patients should be treated with caution. More recent 1q21.1 copy number arrays have reported no evidence to suggest *HYDIN2* has correlation to pathological brain size abnormalities (Dumas *et al.*, 2012). Most strikingly, a number of studies have shown that 1q21.1 deletion or duplication patients present microcephaly or macrocephaly irrespective of *HYDIN2* copy number variation. Since the original Brunetti-Pierri *et al.*, (2008) publication, revisions to the human genome have significantly changed the arrangement of the 1q21.1 loci so that *HYDIN2* is now within the 1q21.1 distal region. With this misleading assumption, and the following studies that have shown multiple incidences of exceptions to this hypothesis, the proposal that *HYDIN2* had significant involvement in head size is unlikely.

On the other hand, two groups of paralogs in the 1q21.1 distal region have been proven to be essential to human-specific cortical development, having evolved in a parallel duplication event: the *NBPF* and *NOTCH2NL* paralogs (Fiddes *et al.*, 2019). The NPBF paralogs 11, 12 and 14 are human-specific members of the neuroblastoma breakpoint family that encode for the DUF1220 protein domain, which has significant expression in the developing brain (Diskin *et al.*, 2009). In healthy controls and in 1q21.1 cohorts, DUF1220-domain copy number correlates to variable grey matter, unlike any other gene present within the 1q21.1 loci (Dumas *et al.*, 2012). As there are a significant number of paralogous copies of the DUF1220-domain in the 1q21.1 locus, dosage effect on overall head size appears broad and incremental, compared to the impact of deletion or duplication of single copy genes, i.e. *CHD1L* (Dumas *et al.*, 2012).

Dosage of the NOTCH2NL paralogs, *NOTCH2NLA* and *NOTCH2NLB*, is also different in 1q21.1 patients, with copy numbers being reported of 1.5 and 2.5 for deletion and duplication of this region, respectively (Fiddes *et al.*, 2018). This copy number is a result of the paralogs acting as breakpoints flanking the 1q21.1 distal region (Fiddes *et al.*, 2018). The *NOTCH2NL* paralogs have been grouped with other genes such as *ARHGAP11B*, *SRGAP2C* and *TBC1D3*, that are necessary for human-specific cortical development and are descendents of recent segmental duplication events (Dennis and Eichler, 2016). The importance of the *NOTCH2NL* paralogs in early human cerebral development is evident by their influence on NOTCH signalling. Overexpression of *NOTCH2NLB* during early *in vitro* cortical differentiation showed an unbalanced favouring of progenitor over neuronal cell fate, as well as size overgrowth (Fiddes *et al.*, 2018). This is because NOTCH2NLB activates the NOTCH signalling pathway, and in doing so represses neurogenesis and maintaining proliferation of neural progenitors, thereby increasing eventual neuron count (Fiddes *et al.*, 2018). However, NOTCH2NLB only influences aRGs, with no overt effect detected in IPs or bRGs (Suzuki *et al.*, 2018). Further evidence of *NOTCH2NL* paralogs influence on early neurodevelopment can be found in cortical spheroids created in the absence of the *NOTCH2NL* paralogs, where microcephaly phenotypes are seen as early as three days into neuronal differentiation (Fiddes *et al.*, 2018).

Upon consolidation of the genes within the 1q21.1 distal region, these genes are clearly influential to a certain degree when taken as individual entities. However, it is likely that a number of these genes could be working cooperatively, i.e. *NOTCH2NL* and *NBPF* paralogs (Fiddes *et al.*, 2019). It is therefore beneficial to model and analyse how the cluster of 1q21.1 distal region genes function as a collective, in order to disentangle potential networks contributing to the heterogenous phenotypes seen in 1qDel/1qDup patients. This research may then lead to determining the causative factors and pathways for the development of NDDs such as ASD and SCZ, by examining which attributes are unique and which are shared between the two 1q21.1 CNV arrangements.

1.3 Cerebral Organoids Fill a Niche in Neurodevelopmental Research

Historically, *in vivo* research models have been the core tool for investigating NDDs (Aaku-Saraste, Hellwig and Huttner, 1996; Ewart *et al.*, 1997; Horner and Caspary, 2011; Yamaguchi *et al.*, 2011). *In vivo* models exhibit

complex cellular architecture and mixed cell type populations, as well as providing postnatal studies that show behavioural phenotypes (Gonzalez Malagon *et al.*, 2015; Nielsen *et al.*, 2017; Domínguez-Iturza *et al.*, 2019; Silva *et al.*, 2019). However, distinct neurological differences exist between humans and mice, the most common mammalian *in vivo* model (Hodge *et al.*, 2019). Mice do not have separate layers of the SVZ, and as such have a significant reduction in neural progenitor populations such as bRGs (Reillo *et al.*, 2011). In some cases, mouse models can exhibit no discernible phenotype when compared to their human patient counterparts (Pak *et al.*, 2015). Similarly, treatment efficacy can be poor when translated from mouse testing to human clinical trials (Corbett *et al.*, 2015; Schumacher *et al.*, 2016). *In vivo* models also require extensive time and resources to generate successful gene-edited lines. *In vitro* neuronal models on the other hand, have benefitted from the advent of patient-derived hIPSC cultures, thereby retaining a patient's genotype and recapitulating a closer representation of human NDD pathology (Allende *et al.*, 2018; Kathuria *et al.*, 2020; Chapman *et al.*, 2021). However, 2D *in vitro* neuronal cell culture cannot develop 3D, *in vivo*-like structural composition beyond the epithelial-lined neural rosette formation (Chambers *et al.*, 2009). 2D *in vitro* neuronal cell culture also does not have the capacity to develop multiple neural cell types in culture simultaneously; astrocytes and neurons require separate growing conditions in anticipation of co-culture at a later stage (Enright *et al.*, 2020). Even as a monoculture, *in vitro* neurons often require mechanical or pharmacological interference for maturation (Kuijlaars *et al.*, 2016).

In vitro and *in vivo* modelling of NDDs is complemented by *in utero* studies, but they are few and far between. Prenatal human MRI studies are currently limited, both ethically and technologically (Kobayashi *et al.*, 2016), and sibling cohorts can only provide limited prenatal information of NDDs (Zwaigenbaum *et al.*, 2014). Foetal samples are also limited due to ethical implications, with tissue availability relative to elective procedures, and so human-specific investigations of NDDs is slow (Wang *et al.*, 2017; Tian *et al.*, 2022). An alternative model is therefore necessary to expand past the constraints of *in vivo* and *in vitro* modelling, as well as prenatal imaging. 3D, patient-derived, hIPSC-based cerebral organoids have a documented capability to accurately depict early human neurodevelopment (Lancaster *et al.*, 2013; Camp *et al.*, 2015; Fair *et al.*, 2020),

and can be used as a source of otherwise inaccessible information in the pursuit of understanding NDD pathology.

1.3.1 The Evolution and Current State of Cerebral Organoid Culture

The seminal cerebral organoid paper by Lancaster *et al.*, (2013) popularised a new neuroscience research field with the intention of unifying *in vitro* and *in vivo* research. By using a self-patterning, hIPSC-based 3D structure, they proved that it was possible to recapture otherwise unobtainable properties of human brain development *in vitro*, such as human-specific cortical layering (Lancaster and Knoblich, 2014). However, prior to this development, there was already a history of 3D neural aggregates that had shown the validity of using 3D-based models.

One of the earliest recounts of 3D neuronal culturing is the use of neurospheres. Described as an autonomous bundling of cells in a 3D structure, neurospheres are generated from dissociated embryonic and adult neural tissue (Reynolds and Weiss, 1992). Left without adherence supplements, the neurospheres gather into balls of multipotent, self-proliferating neuroectodermal cells (Reynolds and Weiss, 1992; Ostenfeld *et al.*, 2002; Hack *et al.*, 2004). The assay's purpose is to define neuroectodermal cells populations and their characteristics within their former tissues. As proof of their continued pluripotency, a small percentage of neurospheres reform after dissociation (Reynolds and Weiss, 1996). With growth factor manipulation, it was possible to direct neurosphere differentiation past neuroectodermal cells to maturing neurons and oligodendrocytes, although functional capability of either was not investigated (Hack *et al.*, 2004). However, once plated, the neurosphere-derived neuroectodermal cells favoured certain neuronal sub-types with respect to the original tissue (Ostenfeld *et al.*, 2002). Combined with unstandardized protocols that make cross-checking results across studies difficult (Singec *et al.*, 2006), the neurosphere assay fell out of favour.

In its place, the serum-free embryoid body (SFEB) suspension culture model was created (Watanabe *et al.*, 2005). These aggregates built on the neurosphere model by creating embryoid bodies (EBs) from pluripotent embryonic stem cells (ESCs) and then instigating neuroectodermal fate through exogenous manipulation of signalling pathways like Wnt and TGFβ. They were also capable of differentiating into either dorsal or ventral forebrain lineage neural progenitors

while remaining in suspension (Watanabe *et al.*, 2005). By shifting the focus away from understanding the primary tissue and revolving it towards understanding early neurodevelopmental signalling, this model has continued to be beneficial in early stages of central nervous system-related cell culture (Sato *et al.*, 2016; Gunhanlar *et al.*, 2017; Brownjohn *et al.*, 2018), as well as preliminary disease modelling (Garcez *et al.*, 2016). However, SFEBs still have their limitations; albeit capable of generating post-mitotic neuronal or glia cells whilst still in suspension, the neocortical cytoarchitecture and electrophysiological properties are arguably poorly represented . To address these issues, the “quick” SFEB method aimed to improve homogeneity with quick aggregation of EBs (Eiraku *et al.*, 2008). With the addition of an extracellular matrix, more complex, 3D structures proved feasible, such as forming an *in vitro* retinal cup that mimicked the process of *in vivo* retinal development (Eiraku *et al.*, 2011). This was one of the defining results that influenced cerebral organoid culture; the inclusion or exclusion of an extracellular scaffold supplement to facilitate complex morphological development.

Cortical spheroids are neuroectodermally-derived aggregates that have significantly more complexity than their SFEB predecessors but do not use an extracellular scaffold (Paşca *et al.*, 2015). These spheroids can generate both lower and upper layer neurons which are functionally, sporadically active, as well as astrocytes and cells resembling radial glia in VZ-like areas (Paşca *et al.*, 2015). Other studies have manipulated the cortical spheroid model for induction of oligodendrocytes (Madhavan *et al.*, 2018), as well as extending time in culture, producing mature astrocytes that closely resemble purified primary human foetal astrocytes (Sloan *et al.*, 2017). Cortical spheroids have therefore been used in disease modelling such as neuroinflammation (Raasch *et al.*, 2016) and tuberous sclerosis (Blair, Hockemeyer and Bateup, 2018).

Although capable of illustrating rudimentary disease phenotypes, cortical spheroids lack complex cytoarchitecture reminiscent of brain development. Embedding the EBs into an extracellular matrix, such as Matrigel®, provides the additional supplements and scaffolding to support defined polarisation of neural progenitors that cortical spheroids lack (Lancaster *et al.*, 2013). The scaffolding supports neuroepithelium morphology, which can expand with progenitors and neurons specific to a particular brain region, e.g. hippocampus or dorsal forebrain (Dias and Guillemot, 2017; Renner *et al.*, 2017). Such structures made cerebral organoids popular, as they were capable of emulating morphological and cellular

attributes of early human neurodevelopment (Camp *et al.*, 2015; Velasco *et al.*, 2019; Fair *et al.*, 2020). Recycled ideas from other 2D and 3D models formed the basis for significant expansion in the field, creating a plethora of cerebral organoid protocols to choose from. In recent years, however, refinement of these protocols has created distinctive terminology to describe the models to improve scientific communication (Pașca *et al.*, 2022). Cerebral organoids and spheroids have been replaced by whether a “neural” organoid (one of neuroectodermal lineage) is unguided, i.e. self-patterning (Lancaster *et al.*, 2013), or regionalised by exogenous manipulation of multiple signalling pathways, i.e. guided (Qian *et al.*, 2016).

Unguided neural organoids (self-patterned cerebral organoids) are self-explanatory in that minimal exogenous input is provided in culture to endorse multiple brain regions to develop in unison (Lancaster *et al.*, 2013; Dias and Guillemot, 2017). On the other hand, regionalised neural organoid (guided cerebral organoids) protocols often target the neuroectodermal induction stage of culture to establish regional identity, altering early patterning pathways such as Wnt, SHH and BMP. This has led to an array of regionalised neural organoids being modelled, such as midbrain organoids that are capable of creating dopaminergic and neuromelanin-producing neurons (Jo *et al.*, 2016; Qian *et al.*, 2018). Targeting these pathways, as well as adjusting the timeframe of exposure, can result in cerebral spinal fluid-producing choroid plexus (Pellegrini *et al.*, 2020) and hippocampal organoids (Sakaguchi *et al.*, 2015).

To improve the representation of the developing cerebral cortex beyond the default dorsal forebrain identity, ventral forebrain organoids have been created as a source of migrating GABA-ergic interneurons. These ventral forebrain organoids are passively annealed to dorsal forebrain organoids, creating a dorsal-ventral forebrain assembloid (Birey *et al.*, 2017). The GABA-ergic interneurons’ migration can be tracked through the dorsal forebrain organoid whilst maintaining cortical structure (Bagley *et al.*, 2017; Birey *et al.*, 2017; Xiang *et al.*, 2017), thereby improving local neural networks (Xiang *et al.*, 2017). This concept has been similarly replicated for thalamic neurons with success (Xiang *et al.*, 2019). Combining the two concepts of assembloids and secondary, regional developmental organisers has also proven a successful alternative between assembloids and guided neural organoids. Integration of a SHH-emitting, organiser-like EB at the start of dorsal forebrain organoid differentiation provided a

SHH gradient mimicking that of the floor plate of the telencephalic neural tube (Cederquist *et al.*, 2019). This creates a regionalised neural organoid with a gradient-determined segregation of dorsal and ventral forebrain developing in unison, more closely resembling the *in utero* developing forebrain (Stoykova *et al.*, 2000; Tao and Zhang, 2016). This is akin to an unguided neural organoid in its simultaneous development of multiple brain regions within one neural organoid, but the choice of brain regions is specified as opposed to random.

Although comparison between unguided neural organoids and regionalised cortical organoids has, and should continue to be, scrutinised (Velasco *et al.*, 2019), these are relatively new terminological differences, with the vast majority of literature still using the term “cerebral organoid” for either (Bershteyn *et al.*, 2017; Iefremova *et al.*, 2017; Stachowiak *et al.*, 2017; Srikanth *et al.*, 2018; Zhang *et al.*, 2019). In this study, the term cerebral organoid will continue to be used in this manner, unless specifically stated otherwise. The dorsal forebrain regionalised neural organoids created in this study will be specifically referred to as human cortical organoids (hCOs) to denote which brain region and cell origin they are related to.

1.3.2 Cerebral Organoids are Capable of Emulating Key Elements of Neocortical Development

Cerebral organoids are most well known for their mimicry of telencephalic development, more precisely the dorsal forebrain. These organoids are capable of recapitulating specific developmental events with relative accuracy, including proteomic (Nascimento *et al.*, 2019; Notaras, *et al.*, 2021), epigenetic (Luo *et al.*, 2016), transcriptomic (Kathuria *et al.*, 2020; Kim *et al.*, 2020; Gordon *et al.*, 2021; Uzquiano *et al.*, 2022) and electrophysiological traits (Fair *et al.*, 2020; Schröter *et al.*, 2022) of the first trimester or later. They do not, however, follow the *in vivo* neurodevelopmental stages as previously described. Although cerebral organoids do develop NECs (Subramanian *et al.*, 2017), they do not undergo primary neurulation or form a neural tube (Renner *et al.*, 2017; Rifes *et al.*, 2020; Benito-Kwiecinski *et al.*, 2021; Giandomenico, Sutcliffe and Lancaster, 2021; Wu *et al.*, 2021). Instead, cerebral organoids form numerous circular facsimiles of the dorsal forebrain, otherwise known as neuroepithelial loops (Krefft *et al.*, 2018). These telencephalic-originating neuroepithelial loops are able to be formed in the absence of primary neurulation due to the signalling pathways modulated

endogenously or externally guided (Lancaster *et al.*, 2013, 2017; Mariani *et al.*, 2015; Rosebrock *et al.*, 2022). These loops begin as small neural rosettes, similar to those characteristic of 2D *in vitro* neuronal culture (Figure 1.5.A) (Fedorova *et al.*, 2019). Embedding in scaffolding gel greatly improved the size, complexity and maturity of these loops (Chen *et al.*, 2021; Rosebrock *et al.*, 2022).

Within the first month of culture, cerebral organoids' neuroepithelial loops consists of aRGs, developed from the original NECs, arranged in a VZ-like pseudo-stratified neuroepithelium (Figure 1.5) (Subramanian *et al.*, 2017). The neuroepithelial loop also has apical/basal polarity, punctuated by an apical edge consisting of tight and adherens junction proteins and actin bundling (Iefremova *et al.*, 2017; Odenwald *et al.*, 2017; Zhang *et al.*, 2019; Wang *et al.*, 2020). This facilitates characteristic traits of NPCs within the cerebral organoid, including interkinetic nuclear migration of aRGs (Bershteyn *et al.*, 2017; Subramanian *et al.*, 2017) and symmetric/asymmetric cell division of a variety of NPCs, including aRGs, bRGs and IPs (Lancaster *et al.*, 2013; Bershteyn *et al.*, 2017; Iefremova *et al.*, 2017; Fischer *et al.*, 2022; Rosebrock *et al.*, 2022). The presence of neuroepithelial loops is a clear indicator of successful induction of telencephalic differentiation, as is FOXG1 expression (Mariani *et al.*, 2015; Lancaster *et al.*, 2017; Gomes *et al.*, 2020; Wang *et al.*, 2022). Discrimination between dorsal and ventral forebrain is determined by PAX6/TBR2/EMX1 or NKX2.1/GSX2/DLX2 expression, respectively (Figure 1.2.B) (Mariani *et al.*, 2015; Lancaster *et al.*, 2017; Gomes *et al.*, 2020; Wang *et al.*, 2022). Although it is the aim of both unguided and guided cerebral organoids to be predominantly dorsal forebrain in identity (Lancaster *et al.*, 2017), ventral forebrain progenitors and neurons still represent a minority of the cellular composition within both types of cerebral organoid (Bagley *et al.*, 2017; Wang *et al.*, 2022).

As cerebral organoids mature, they develop additional layers reflecting neocortical development, including the SVZ, CP and marginal zone (Figure 1.5.B). However, there is minimal evidence to support that cerebral organoids develop an *in vivo*-like intermediate zone or a preplate before forming a CP or marginal zone (Lancaster *et al.*, 2013, 2017; Giandomenico, Sutcliffe and Lancaster, 2021). Cerebral organoids have proven to accurately separate the oSVZ from the iSVZ, as well as generate bRGs, features that are specific to primates and not feasible in 2D *in vitro* neuronal culture (Otani *et al.*, 2016; Bershteyn *et al.*, 2017; Subramanian *et al.*, 2017; Fischer *et al.*, 2022; Rosebrock *et al.*, 2022). Within the

developing CP, Layer II-VI neurons are visible above the SVZ in cerebral organoids after radial migration of neurons (Lancaster *et al.*, 2013, 2017; Giandomenico *et al.*, 2019). However, cerebral organoids' CP-like region is substantially less uniform in its segregation of cortical layers than its *in vivo* counterpart, with significant overlap between upper and lower layer neurons (Nieto *et al.*, 2004; Englund *et al.*, 2005; Li *et al.*, 2017; Giandomenico *et al.*, 2019; Notaras, *et al.*, 2021; Rosebrock *et al.*, 2022). On the other hand, Cajal-Retzius cells line the top of the CP-like region, having developed in early stages and migrated upwards, similarly to human neurodevelopment (Lancaster *et al.*, 2017; Renner *et al.*, 2017). After a significant period of maturation (≥2 months), astrocytes span the cortical plate region (Paşca *et al.*, 2015; Sloan *et al.*, 2017; Giandomenico, Sutcliffe and Lancaster, 2021); it takes specific enrichment to produce oligodendrocytes (Madhavan *et al.*, 2018; Kim *et al.*, 2019). Despite maturation, cerebral organoids are currently incapable of undergoing gyrification whilst in a free-form setting (Li *et al.*, 2017), however different formats of culturing have shown success (Karzbrun *et al.*, 2018). Long term maturation of cerebral organoids exhibit functionally active neurological networks that are responsive to typical neuromodulators, i.e. TTX (Fair *et al.*, 2020; Samarasinghe *et al.*, 2021; Schröter *et al.*, 2022; Sharf *et al.*, 2022). Unfortunately, maturation of such networks have either no or few GABA-ergic inhibitory interneurons or thalamocortical neurons and so require fusion with an alternative organoid to form an assembloid in order to emulate such properties (Bagley *et al.*, 2017; Birey *et al.*, 2017; Xiang *et al.*, 2017, 2019). Cerebral organoids are also missing other non-dorsal forebrain-originating cell types, including microglia, endothelial cells and neural crest cells that would otherwise be present during neurodevelopment (reviewed by Wörsdörfer *et al.*, (2020)).

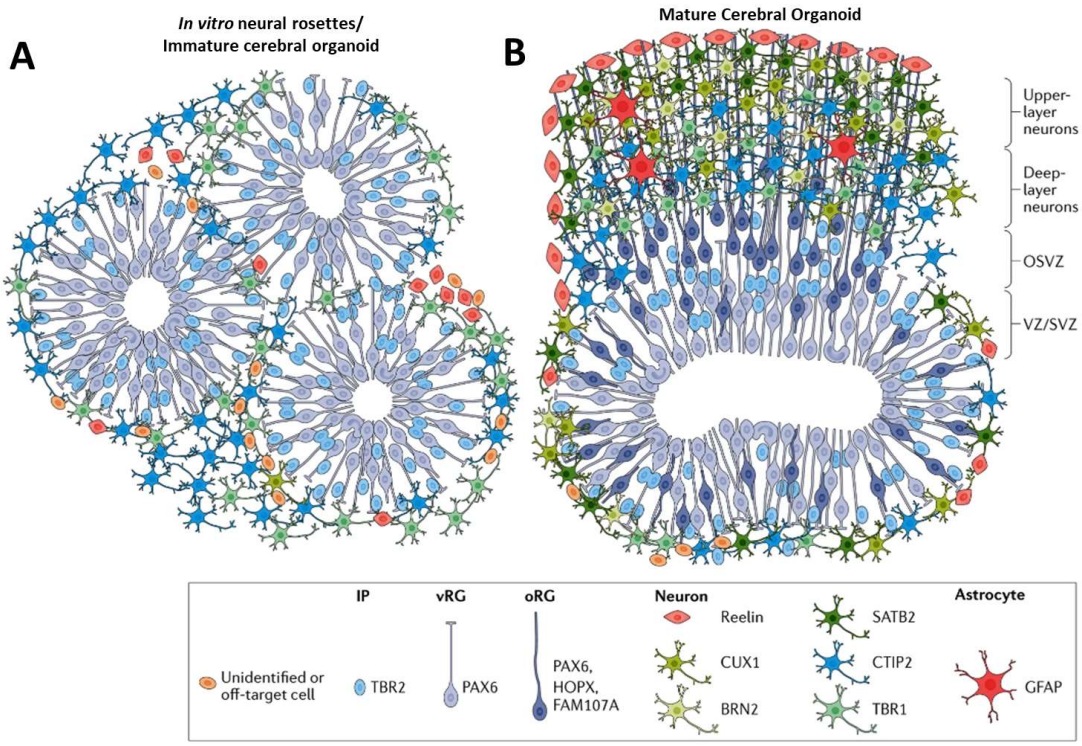

Figure 1.5: Neocortical development as depicted *in vitro* and in cerebral organoids.

Schematic representation of cellular composition of *in vitro* neural rosettes, as well as immature cerebral organoids **(A)** and mature cerebral organoid composition **(B)**. Both images adapted from Di Lullo and Kriegstein, (2017). Acronyms: VZ – ventricular zone, SVZ – subventricular zone, oSVZ – outer subventricular zone, vRG – ventral radial glia, oRG – outer radial glia, IP – intermediate progenitor cell.

As cerebral organoids are limited in their scope of emulating neurodevelopment, assumptions are required when using cerebral organoids as a research model. Firstly, replicability of the cerebral organoids themselves has been a consistent argument against their use (Yoon *et al.*, 2019; Hernández *et al.*, 2021). However, inter- and intra- batch heterogeneity has improved substantially with the refinements in protocols over recent years (Velasco *et al.*, 2019; Giandomenico, Sutcliffe and Lancaster, 2021; Rosebrock *et al.*, 2022). Cerebral organoids are also in a consistent state of stress that detrimentally affects cell type specification (Bhaduri *et al.*, 2020). It is hypothesised that the free-floating environment instigates increases cell stress, as well as the absence of *in utero* environmental cues (Bhaduri *et al.*, 2020). An additional cause of stress in maturing cerebral organoids is the exponentially expanding dead core. This expansion is a combination of hypoxia and limited range of nutrient diffusion (Giandomenico *et al.*, 2019; Choe *et al.*, 2021). No other known research model

has inadvertent, experimentally-induced cell death; dead *in vitro* cells detach from the plastic and are lost during culture, whilst *in vivo* studies have minimal observable cell death, as glia and macrophages disseminate dead cells (Vanden Berghe *et al.*, 2013). Cerebral organoids lack the necessary cell populations to remove cells trapped in the expanding core, with the exception of astrocytes which are confined within the live cell population (Dezonne *et al.*, 2017). Although there have been attempts to circumvent this issue experimentally through microfluidics or integration of endothelial cells, these methods are in their infancy and have arguable limitations of their own, such as financial and technical accessibility (Raasch *et al.*, 2016; Ao *et al.*, 2020; Salmon *et al.*, 2022). The absence of vascularisation is a significant hinderance to current methods as the organoids become limited in size, relying on diffusion through the organoid's surface as the sole means of nutrient uptake (Choe *et al.*, 2021). Current solutions for this issue include oscillating suspension culture to improve permeation of nutrients, whilst increasing surface area also has been trialled, such as organotypic slice culture (Qian *et al.*, 2020) and bisection (Velasco *et al.*, 2019; Choe *et al.*, 2021).

Overall, cerebral organoids are capable of generating complex 3D cytoarchitecture with multiple co-existing cell types, whilst being of human origin and emulating human-specific features. Cerebral organoids are therefore a significant leap in bridging the gap between the limitations between 2D *in vitro* hIPSC-derived neuronal monoculture and 3D *in vivo* modelling. Although cerebral organoids are still limited in both application and generation (Mansour *et al.*, 2018; Velasco *et al.*, 2019; Albanese *et al.*, 2020; Bhaduri *et al.*, 2020; Hernández *et al.*, 2021), their strengths have been advantageous to disease modelling research, such as exploring mechanisms of microcephaly (Lancaster *et al.*, 2013; Li *et al.*, 2017; Zhang *et al.*, 2019; Martins *et al.*, 2022).

1.3.3 Cerebral Organoids as a Tool for Disease Modelling

Cerebral organoids' ability to develop simplified cortical structures have made them a popular research model for both post- and prenatal diseases. In the context of postnatal disease, glioblastoma multiforme, for example, is a poorly understood and highly fatal form of cancer, where prognosis has not improved substantially for a number of years due to lack of accurate tissue models. Using cerebral organoids, it has been possible to model the invasion of glioma stem cells and their formation into patient phenotype-like tumours (Ogawa *et al.*, 2018;

Linkous *et al.*, 2019; Krieger *et al.*, 2020). Importantly, these 3D glioblastoma models replicate the poor drug efficacy seen *in vivo* (Bian *et al.*, 2018; Linkous *et al.*, 2019). As glioblastomas also show variable aggression in their pathogenesis with respect to the patient's age (Morgan *et al.*, 2017), affected cerebral organoids at four months showed the glioma stem cells exhibited more infiltrative growth than that of the one-month affected cerebral organoid (Linkous *et al.*, 2019). Cerebral organoids also act as useful tools for age-related neurodegenerative disorders, such as Alzheimer's disease or frontotemporal dementia. Using hIPSCs either derived from patients or those harbouring high-risk genes, the resulting cerebral organoids exhibited phenotypes characteristic of neurodegenerative diseases such as increases in amyloid beta protein (Gonzalez *et al.*, 2018) and hyperphosphorylated tau protein (Raja *et al.*, 2016; Bowles *et al.*, 2021), with abnormalities in amyloid beta uptake from microglia similar to *in vivo* (Lin *et al.*, 2018). Arguably, age-related disease modelling in cerebral organoids has questionable biological relevance given the cerebral organoid's inability to undergo gyrification (Li *et al.*, 2017; Karzbrun *et al.*, 2018), develop white matter without external influences (Madhavan *et al.*, 2018; Cullen *et al.*, 2019) or questionable similarity to the adult cortex (Dezonne *et al.*, 2017; Logan *et al.*, 2020; Gordon *et al.*, 2021).

On the other hand, cerebral organoids' capability of representing early neurodevelopmental structures make them a popular choice for prenatal disease modelling. Investigating microcephaly was one of the first applications of cerebral organoids, providing vital evidence in the pathology of the Zika virus. Zika-infected cerebral organoids reflected the microcephalus outcome observed in affected mothers' children in a way that was unobtainable in 2D *in vitro* neuronal culture (Qian *et al.*, 2016; Gabriel *et al.*, 2017; Lage *et al.*, 2019). Other microcephaly-related genetic disorders exhibit a similar disruption of NPCs to that of the Zika virus in cerebral organoids (Lancaster *et al.*, 2013; Li *et al.*, 2017; Fiddes *et al.*, 2018; Zhang *et al.*, 2019; Wang *et al.*, 2020; Dhaliwal *et al.*, 2021; Urresti *et al.*, 2021). For example, microcephaly-associated *ASPM* mutations modelled in cerebral organoids result in a lack of VZ and oSVZ formation, and thereby cortical morphology is disrupted (Li *et al.*, 2017). Cerebral organoids' proficiency to emulate early morphological phenotypes expands to other forms of faulty structural development, including macrocephaly (Allende *et al.*, 2018; Sawada *et al.*, 2020; Zhang *et al.*, 2020; Urresti *et al.*, 2021), lissencephaly (Bershteyn *et al.*,

2017) and neuronal heterotopia (Klaus *et al.*, 2019). Cerebral organoids have also been a tool for examining the neurodevelopmental roots of ASD & SCZ. First trimester, in particular, has been referred to as a vulnerable stage for developing high-risk abnormalities for these NDDs (Schork *et al.*, 2019); this is the niche developmental stage that cerebral organoids have been proven to accurately represent (Camp *et al.*, 2015; Luo *et al.*, 2016; Qian *et al.*, 2016; Nascimento *et al.*, 2019; Logan *et al.*, 2020). Sequencing studies in ASD-related cerebral organoids have provided a script of common molecular targets that span ASD, SCZ and bipolar disorder (Wang *et al.*, 2017). Twin-study design has been useful in limiting the genetic heterogeneity of the disorders when modelling SCZ in cerebral organoids (Sawada *et al.*, 2020). However, even in minimal genetic heterogeneity, disorganised proliferation and/or apoptosis of NPCs and disruption of cortical organisation is a frequent narrative in studies of SCZ in cerebral organoids (Stachowiak *et al.*, 2017; Srikanth *et al.*, 2018; Notaras *et al.*, 2021), suggesting this cellular behaviour to be a universal SCZ phenotype. ASD appears to have a similar theme of dispersed localisation and abnormal ratios of radial glia to neurons. CNVs such as 17q11.2 microdeletion (Wegscheid *et al.*, 2021) and 16p11.2 (Urresti *et al.*, 2021), in both its deletion and duplication forms, display similar phenotyes, alongside high ASD-penetrance NDDs like fragile X syndrome (Kang *et al.*, 2021) and individual high-risk ASD genes such as *RAB39B* (Zhang *et al.*, 2020) and *CHD8* (Wang *et al.*, 2017).

Excitatory/inhibitory (E/I) imbalance of neurotransmitters is also a common feature of ASD pathology but the type of presentation found in ASD-modelling cerebral organoids varies depending on the genotype: accelerated neuronal maturation (Urresti *et al.*, 2021), hyperexcitation (Kang *et al.*, 2021), and overproduction (Mariani *et al.*, 2015) or underproduction of GABA-ergic interneurons, alongside emulating patient resistance to modulating glutamate receptors (Kang *et al.*, 2021), have all been reported. Correspondingly, proof of E/I imbalance in SCZ-based cerebral organoids has been reported using RNA sequencing (Kathuria *et al.*, 2020) and bioenergetic analysis (Dutta *et al.*, 2020), with either abnormal abundance of GABA-ergic inhibitory interneurons (Srikanth *et al.*, 2018; Sawada *et al.*, 2020) or mature neuronal loss (Stachowiak *et al.*, 2017; Notaras, *et al.*, 2021).

As cerebral organoid-based disease modelling studies multiply, the collection of phenotypes paint a picture of converging and diverging molecular and

cellular phenotypes of NDDs. This is a key complication in modelling multi-faceted NDDs, but as the closest approximation to a patient's development at present, cerebral organoids are closing gaps in research that would otherwise be unobtainable. Although research into cerebral organoids' propensity to replicate brain oscillation patterns is in its infancy (Samarasinghe *et al.*, 2021), the application of this research model into NDD research will provide the multi-tier observation very much required to affirm treatment efficacy (Bian *et al.*, 2018; Linkous *et al.*, 2019; Kang *et al.*, 2021). Cerebral organoids' ability to be derived from human patients and develop a rudimentary, electrophysiologically-active neocortex have made them an ideal model to recapitulate NDD phenotypes observed in pathogenic CNVs (Khan *et al.*, 2020; Urresti *et al.*, 2021; Wegscheid *et al.*, 2021). As such, cerebral organoids were a rational choice of research model to document if 1qDel phenotypes arise during early neurodevelopment.

1.4 Research Aims & Hypothesis

The overall aim of this research is to illustrate the requirement for comprehensive human cortical organoid (hCO) protocol validation, as well as updating hCO analysis techniques. This will ensure that 1qDel patient's cortical development is recapitulated as accurately as is feasible in a hCO and analysed with minimally-biased approaches. The intention of modelling 1qDel in hCOs is to identify the mechanisms contributing to 1qDel patient phenotypes of microcephaly and SCZ.

The hypothesis for this body of work is that, with suitable experimental and analytical methodology, hCOs can successfully embody elements of 1qDel patient pathophysiology. Firstly, upon review of *in vitro*, *in vivo* and cerebral organoid studies (Nieto *et al.*, 2004; Kadoshima *et al.*, 2013; Lancaster *et al.*, 2017; Chapman *et al.*, 2021; Eze *et al.*, 2021), it is hypothesised that ICC and morphological analysis can be substantially improved by developing quantification techniques that can evaluate a whole section of a hCO with minimal bias using a high throughput analysis pipeline and post hoc adjustments for cell death. Secondly, it is hypothesised that select elements of current cerebral organoid differentiation protocols can be amalgamated together to produce a high quality hCO protocol (Lancaster and Knoblich, 2014; Bagley *et al.*, 2017; Birey *et al.*, 2017; Lancaster *et al.*, 2017; Sloan *et al.*, 2018; Velasco *et al.*, 2019; Yakoub and Sadek, 2019; Sivitilli *et al.*, 2020; Giandomenico, Sutcliffe and Lancaster, 2021).

Lastly, using new analysis techniques and an assessed hCO protocol, it is hypothesised that 1qDel hCOs will mimic certain 1qDel patient phenotypes, e.g., microcephaly and cortical dysfunction, similarly to other CNV cerebral organoid studies (Khan *et al.*, 2020; Urresti *et al.*, 2021; Wegscheid *et al.*, 2021).

2 General Methodology

2.1 Cell & Cortical Organoid Culture

2.1.1 hIPSC Generation, Maintenance & Storage

Control hIPSC lines used in this report originated from healthy individuals with no known CNVs or psychiatric risk mutations and were unrelated to any other cell line: Control #1 – IBJ4, see Plumbly *et al.*, (2019), and Control #2 – HPSI1013i-Wuye purchased from HipSci, Wellcome Trust Sanger Institute, Cambridge, UK. One Class 1 1q21.1 distal deletion cell line was derived from an unrelated patient referred to in Table 2.1. 1qDel patient-derived hIPSCs were generated by Dr. Craig Joyce and Dr. Gareth Chapman using the CytoTune™-IPS 2.0 Sendai reprogramming kit (ThermoFisher Scientific) from fibroblasts collected and maintained by Dr. Craig Joyce. DNA was isolated via the DNeasy Blood & Tissue Kit (Qiagen™) according to the manufacturer's recommended protocol. This was necessary for sequencing to confirm the CNV diagnosis. Sequencing and CNV calling was performed by Dr. Elliot Rees.

Table 2.1: Information of 1q21.1 deletion patient from which "Deletion #1" hIPSC line was derived.

Cell Line	IQ	Clinical Symptoms	1q21.1 Mutation Coordinates
Deletion #1	78	Adjustment disorder, cardiac: deformed valve, narrowing of aorta, thyroid problems, hearing difficulties, sleep apnoea	chr1:146330584 - 147825662

hIPSCs were seeded on Geltrex™ (Gibco™) coated plates which were prepared to the manufacturer's guidelines at a 1:100 dilution in DMEM/F12 (Gibco™) one hour before use. hIPSCs were maintained with Essential 8™ Flex (Gibco™) (E8F) at 37°C, 5% CO_2 with full media changes every 2 days. Passaging was conducted at 60-70% confluency or <6 days since last passage. Cells were washed with phosphate-buffered saline (PBS) (Gibco™), followed by incubation with Versene solution (Gibco™) for 1 minute at 37°C then aspirated. A volume of E8F media was added to the aspirated well, manually scratched with a 5 mL serological plastic pipette and transferred to a pre-coated plate. If hIPSCs required clearing of differentiated cells, hIPSCs were passaged with EZ-LiFT™ (Millipore™) instead of Versene, to ensure ≥90% purity of stem cells. To perform EZ-LiFT™ (Millipore™), hIPSCs were washed with PBS and incubated with pre-warmed EZ-LiFT™ for 2 minutes at 37°C. Pre-warmed Dulbecco's Modified Eagle Medium: Nutrient Mixture F12 (DMEM/F12) (Gibco™) was added to the EZ-LiFT™/cell solution at a 10:1 ratio. hIPSCs were then spun at 120 rcf for 5 minutes and resuspended in E8F media at a 1:2 ratio and plated on Geltrex™-coated plates.

For cryostorage, hIPSCs were incubated with RevitaCell™ (ThermoFisher Scientific) at a 1:100 dilution, 1 hour before freezing preparation. The hIPSCs were detached from the pre-coated plates as if passaging, with 500 µL of E8F added prior to manual scratching per cryovial. An equal volume of cryopreservation media (80% E8F/20% dimethyl sulfoxide (Sigma-Aldrich™) is added dropwise to the cell/E8F solution, for a final concentration of 10% dimethyl sulfoxide. The cell solution was then separated into 1 mL aliquots in the cryovials, frozen at -80°C in an isopropanol-surrounded vessel for 24-72 hours prior to liquid nitrogen storage.

Defrosting required retrieval of cryovials from liquid nitrogen onto dry ice (-20°C). Cryovials were treated individually and partially defrosted in a 37°C water bath. Cells were diluted incrementally with pre-warmed E8F for a final 1:10 dilution and centrifuged at 120 rcf for 5 minutes. The supernatant was aspirated and replaced by 2 mL of pre-warmed E8F media containing 1:100 dilution of RevitaCell™. The total volume of cells was then plated on 1 well of a 6 well Geltrex™-coated plate. Cells were incubated for 2 days before resuming standard maintenance.

2.1.2 Cortical Organoid Differentiation

Prior to hCO differentiation, hIPSCs had to be 50-70% confluency with large, preferably non-overlapping colonies, with ≥90% stem cell purity. hIPSCs were only used for differentiations after ≥2 passages had passed after thawing and after ≥2 passages with Versene only, with passage numbers ranging from 15 to 40 post-reprogramming. All hCOs were generated with the same batch lot of Matrigel™ (Corning™) across multiple bottles. Three different hCO protocols were trialled and analysed to determine their viability as models for investigation (Section 4), however, the Enhanced protocol was used throughout this study and therefore will be described below.

The type of well used to generate Enhanced embryoid bodies (E-EBs) has been shown to affect differentiation (Sivitilli *et al.*, 2020) and therefore the V-shaped, manually coated AggreWell800™ plate (STEMCELL Technologies™) was used. On Day 0, the 24 well AggreWell800™ plate was prepped using the Anti-Adherence Rinsing Solution (STEMCELL Technologies™) as per the manufacturer's instructions. hIPSCs were washed with PBS and disassociated into a single-cell suspension with pre-warmed Accutase™ for 9-12 minutes at 37°C. The Accutase™ was deactivated with pre-warmed E8F at a 1:4 ratio, and the cell solution was centrifuged at 120 rcf for 5 minutes. The supernatant was aspirated, and cells were resuspended in 2 mL of AggreWell™ EB formation media (STEMCELL Technologies™). hIPSCs were counted by 60 µm Scepter™ cell counter sensor in a Scepter™ 2.0 automatic cell counter, counting those between the size range of 10.09 µm to 18.07 µm. The single-cell solution was diluted so that $1.2x10^6$ cells were seeded into one well of a 24 well AggreWell800™ plate, supplemented with additional AggreWell™ EB formation media, 10 µM Y-27632 (Stratech™) and 1% antibiotic/antimyotic (Sigma-Aldrich™) to a total volume of 2 mL, and then readily mixed. The AggreWell800™ plate was spun at 100 g for 3 minutes and incubated for 24 hours at 37°C, 5% CO_2. Y-27632 was added as per manufacturer's instructions to prevent anoikis and promote cell-cell contact (Horiguchi *et al.*, 2014), thereby generating EBs that aggregated within 24 hours. Although it has been argued whether Y-27632 is necessary (Pettinato, Wen and Zhang, 2014), pilot studies using the AggreWell™ system informed this study that Y-27632 was required to form uniform EBs.

On Day 1, E-EBs were individually plated in 500 µL of AggreWell™ EB formation media in 24 well ultra-low attachment plates (Corning™). Day 3 was a half media change of EB formation media. Day 5, 7 and 9 required full media changes of fresh NE induction media (Table 2.2). On Day 11, E-EBs were then referred to as Enhanced hCOs (E-hCOs). Day 11 E-hCOs were isolated individually onto parafilm, all culture media was removed and they were embedded into 40 µL of 4°C Matrigel™ (Corning™). The droplets were incubated at 37°C, 5% CO_2 for 30 minutes. The E-hCO/Matrigel™ droplet was detached from parafilm, returned to the original well with a full media change to neuronal differentiation (ND) media (Table 2.2). Every two days, starting on Day 11 and ending on Day 21, there were half media changes of ND media. On Day 21, three to four hCOs of the same line and differentiation were grouped into one well of a low-attachment 6 well plate (Corning™) with a full media change to 6 mL of maturation media and placed on an oscillator set at 85 rpm within an 37°C, 5% CO2 incubator. Specifically for the Enhanced protocol, 20 ng/mL of brain-derived neurotrophic factor (BDNF) was added to maturation media changes on Day 21 and 25. An 80% maturation media change was performed on day 21 every 4 to 6 days until Day 60.

Table 2.2: Base composition of hCO differentiation media.

NE Media	ND Media	Maturation Media
97% DMEM/F12	48.5% DMEM/F12	48% DMEM/F12
1% N2 supplement	48.5% Neurobasal medium	48% Neurobasal medium
1% GlutaMAX	1% B27 supplement without retinoic acid (RA)	1% B27 supplement with retinoic acid
1% Non-essential amino acids	1% GlutaMAX	1% GlutaMAX
10 µM SB-431542	0.5% N2 supplement	1% Antibiotics
100 nM LDN-193189	0.5% Non-essential amino acids	0.5% N2 supplement
	0.00035% β-mercaptoethanol	0.5% Non-essential amino acids

	3 µg/mL Insulin	0.00035% β-mercaptoethanol
	20 ng/mL Epidermal growth factor (EGF)	3 µg/mL Insulin
	20 ng/mL Thermally stable basic FGF	10 µM Cyclic adenosine monophosphate (cAMP)
		10 µM Ascorbic acid

2.2 Sample Analysis

2.2.1 Brightfield Imaging Acquisition

hCO morphology was individually tracked and imaged via brightfield microscopy from Day 1 (Enhanced Protocol) or Day 5 (Basic & ROCKi Protocol). Images were recorded every 2 days until Day 21, then recorded collectively as a batch, at Day 30 and Day 60. Measurements of area were conducted using raw bright field images and OrganoSeg (Borten *et al.*, 2018) in the first instance, using the specific settings (Table 2.3).

Table 2.3: OrganoSeg settings for bright field imaging hCO quantification

Day 1 to 9	Day 11 to 21
Out of focus correction	DIC correction
Size threshold = 5000	Size threshold = 2500
Window size = 100	Window size = 20
Intensity threshold = 0.1	Intensity threshold = 0.4

All Day 30 and Day 60 images, along with any Day 21 or earlier images where boundaries could not be defined, were measured manually based on visible boundaries using ImageJ (Schneider, Rasband and Eliceiri, 2012).

2.2.2 RNA extraction, Complementary DNA synthesis and Quantitative PCR Analysis

hCOs were removed from media, washed with PBS, and frozen at -80^{o}C for at least 24 hours. hCOs were clustered in groups of two at Days 5 & 11, whilst Day 21, 30 & 60 hCOs were treated individually. RNA was extracted using either the RNeasy Micro Kit (Qiagen™) for Day 5 and 11 or the GenElute™ Mammalian Total RNA Miniprep Kit (Sigma-Aldrich™) for Day 21, 30 and 60. Kits were used according to manufacturers' guidelines and eluted with either 14 µL or 30 µL of

elution buffer, respectively. Complementary DNA (cDNA) synthesis was conducted on 0.1-2 µg of RNA using the Applied Biosystems™ High-Capacity cDNA Reverse Transcription Kit according to manufacturer's guidelines. This was diluted with 1x Tris-EDTA buffer to a working concentration of 100 ng/µL of cDNA. Quantitative polymerase chain reactions (qPCRs) were conducted using 100 ng cDNA, 2x qPCRBIO SyGreen Blue Mix Hi-ROX Master mix (PCR Biosystems™), MilliQ water and 400 nM primers (Table 2.15) on an Applied Biosystems™ StepOnePlus™ machine. Primers were validated by melt curve analysis and gel electrophoresis for proof of correct amplified material. PCR conditions were as follows: initial denaturation at 95ºC for 2 minutes, with 40 cycles of denaturation at 95ºC for 5 seconds and annealing at 60ºC for 30 seconds. Threshold cycle (CT) value was extrapolated from the logarithmic slope at 0.2 threshold. Three technical replicates were run per gene and outliers were removed based on CT value. CT values of technical replicates were averaged before statistical analysis.

2.2.3 Immunocytochemistry Analysis

Day 21, 30 & 60 hCOs were prepped and stored via an adapted protocol by Xiang *et al.*, (2017). In summary, hCOs were removed from media, washed in PBS multiple times, and fixed in 3.7% PFA for 1 hour at 4ºC. After incubation, hCOs were washed in PBS multiple times and then incubated in 30% sucrose (filtered) solution for ≥24 hours at 4ºC until sunk. After sucrose incubation, hCOs were briefly dried and mounted into an OCT-filled mould (Aston Pharma™) and snap frozen in a liquid nitrogen bath. Moulds were left overnight at -80ºC and then transferred to -20ºC, 24 hours before cryosectioning. Cryosections were cut at 10 µm on a Leica CM1900 cryostat at -20ºC onto sequentially numbered slides, 10 slides with 3 sections on each, resulting in a 100 µm difference between each section on a slide. Sectioned samples were left to dry for 30 minutes before storage at -80ºC.

2.2.3.1 Immunocytochemistry Protocol

For ICC staining, only hCO cryosections that represented the middle portion of the hCO were used where possible. These were briefly dehydrated on a 70ºC heat-block and washed with PBS. Sections were drawn around using a hydrophobic pen and then treated as required (Table 2.4).

Table 2.4: ICC protocols used for hCO slide staining.

	Nuclei-localising only ICC staining	Nuclei & cell surface/cytoplasmic localising ICC staining
Day 1	Block in 0.5% Triton X-100 in PBS for 1 hour at room temperature (RT). Overnight primary antibody incubation at 4°C in 0.5% Triton X-100, 5% donkey serum and PBS.	Block in 0.1% Tween in PBS for 1 hour at RT. Overnight primary antibody incubation at 4°C of non-nuclear antibodies in 0.1% Tween, 5% donkey serum and PBS.
Day 2	Wash. Secondary antibody incubation in PBS at RT for 1 hour. Wash. Incubation of DAPI (1 µg/mL) in PBS for 5 minutes at RT. Wash. Mount.	Wash. Secondary antibody incubation in PBS at RT for 1 hour. Wash. Block in 0.5% Triton X-100 in PBS for 1 hour at RT. Overnight primary antibody incubation at 4°C of nuclear stains in 0.5% Triton X-100, 5% donkey serum and PBS.
Day 3	N/A	Wash. Secondary antibody incubation in PBS at RT for 1 hour. Wash. Incubation of DAPI (1 µg/mL) in PBS for 5 minutes at RT. Wash. Mount.

All washes were conducted with PBS, a minimum of three times, in Coplin jars on an oscillator at ≥50 rpm, at RT and for 10 minutes each; after secondary incubation, opaque Coplin jars were used. All slides were mounted with Prolong™ Glass Antifade Mountant (Invitrogen™). A glass coverslip was laid on top of the slides and incubated overnight at RT in the dark to cure. After curing, slides were imaged on a Zeiss Axioscan Z1.

2.2.3.2 TUNEL Assay

The DeadEnd™ Fluorometric TUNEL system kit was used as per the manufacturer's guidelines, including a non-enzymatic control. Samples were mounted and imaged between 24 to 48 hours after mounting using a Zeiss Axioscan Z1 as recommended.

2.2.3.3 Immunocytochemistry Image Acquisition

ICC-stained hCO slides were mounted in the Zeiss Axioscan Z1 as per manufacturer's guidelines. Using ZEN Blue 3.2© (Zeiss) software, a universal scan profile was generated and applied to each stained hCO slide (Table 2.5). The scan profile was altered for each slide to encompass the coarse focus range of each slice of a hCO. This was followed by changes in fluorescent exposure times of each channel; exposure time was kept consistent for each primary antibody. Once the scan profile was completed, the slides were then scanned using a 20x objective. No-primary-antibody controls were imaged for each secondary antibody used to confirm antigen-specific fluorescence intensity when a primary antibody is present.

Table 2.5: Scan profile settings for Zeiss Axioscan Z1 for hCO ICC imaging.

Settings	Details
Tissue Detection	Automatic mode, marker recognition method
Course Focus	Brightfield light path, 10x focus, hCO focus range ±50 µm, 10 µm intervals, support point distribution strategy: 10 points.
Fine Focus	DAPI light path (50% power, 30 ms), 20x focus, automatic focus, 10 µm range, 2 µm interval, sampling – fine, sharpness measure set – FFT, support point distribution strategy: 10 points.
Fluorescence	DAPI light path (50% power, 30 ms), 20x focus, other channels vary for power and exposure, full Z-stack per channel: range 8-12 µm, 2 µm interval.

2.2.3.4 Immunocytochemistry Image Processing

High throughput quantification of hCO ICC was performed using ZEN Blue 3.2© (Zeiss), ImageJ (Schneider, Rasband and Eliceiri, 2012) and CellProfiler (McQuin *et al.*, 2018). Figure 2.1 illustrates the workflow for preparation and analysis of ICC images of hCOs. ZEN Blue 3.2© (Zeiss) was used by the Zeiss Axioscan Z1 to produce a raw image, which was then condensed into a single z-slice image of each individual channel using weighted average, orthogonal projection. ImageJ was used to edit the image in preparation of quantification (Schneider, Rasband and Eliceiri, 2012). A duplicated, high fluorescence DAPI image of the hCO was used to manually draw a hCO perimeter. Overlaying this template on the raw image, the "PrepImage" macro measured the area and

perimeter of a hCO, as well as removed fluorescence outside the perimeter (Table 2.6). The “PrepImage” image was then inputted into the appropriate CellProfiler (McQuin *et al.*, 2018) pipeline. CellProfiler pipelines were designed to generate masks that identified primary objects by different thresholding strategies to distinguish nuclei borders, relative to the strength of the signal: Global Otsu (strong signal) or Robust Background (weaker signal). Additionally, nuclei size was used for nuclei-bound staining; nuclei size was determined by randomised measurements of diameter of DAPI-stained cell nuclei (±20%) using ImageJ (Schneider, Rasband and Eliceiri, 2012).

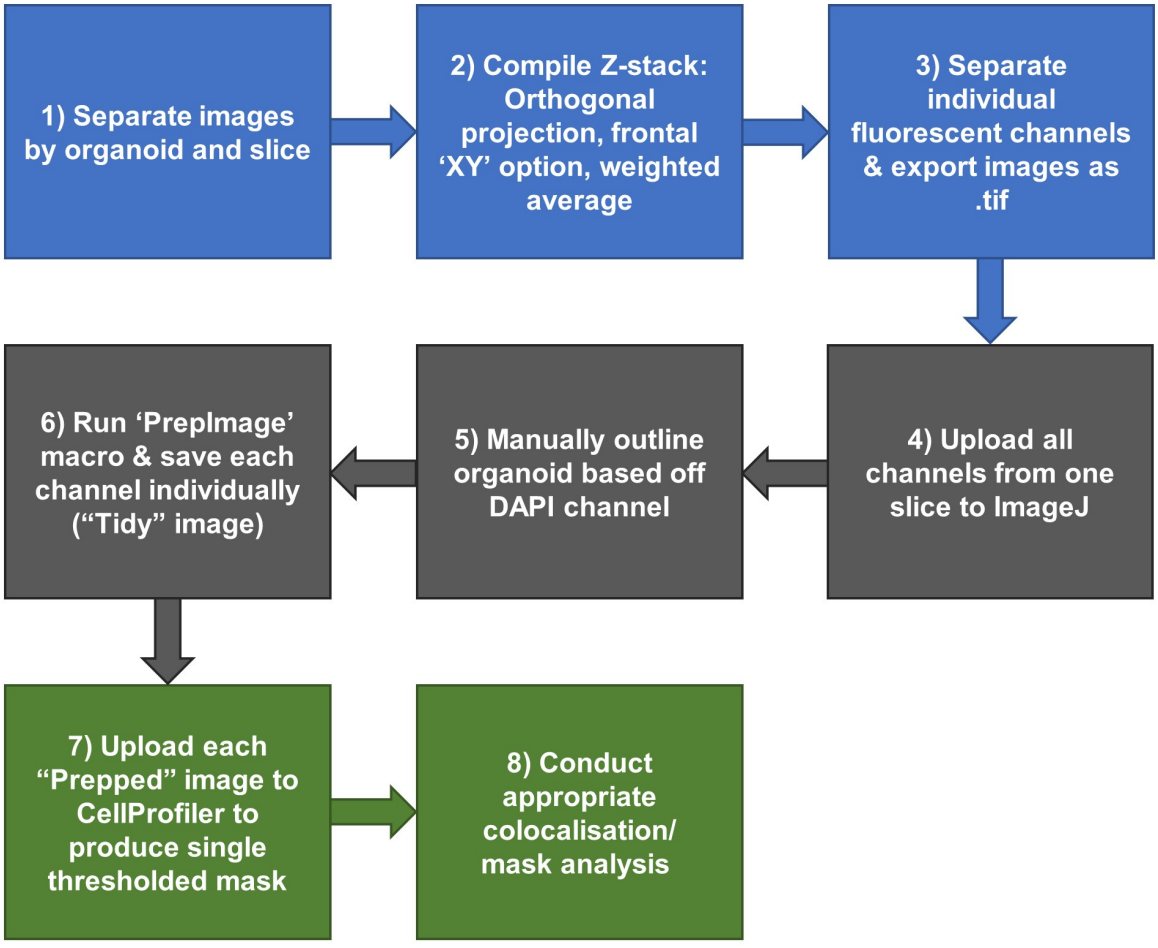

Figure 2.1: Workflow for analysis of hCO ICC images.
Colours dictate software used: Zen Blue 3.2 © (blue), ImageJ (grey) (Schneider, Rasband and Eliceiri, 2012) and CellProfiler (green) (McQuin *et al.*, 2018).

To reduce the likelihood of inaccurate co-localisation, all identified nuclear objects were individually shrunk to a central point within the object and then expanded by 5 pixels to produce a mask. Each protein of interest's mask had to colocalise with the corresponding DAPI mask to be considered genuine; any identified primary objects that did not colocalise with DAPI were discarded. Only masks of $DAPI^+$/$protein^+$ were used for counting and further colocalisation analysis. Pipelines were kept consistent across images for each protein of interest, and settings were decided after trialling settings across ICC images from different cell lines, protocols and timepoints.

Table 2.6: "PrepImage" macro used in ImageJ on images in preparation for input into Cellprofiler pipelines.

```
//draw a perimeter around duplicated high fluorescence DAPI image of hCO
and copy perimeter for unedited image
run("Restore Selection");
title = getTitle();
run("Clear Outside");
run("Crop");
run("Measure");
run("Restore Selection");
saveAs("Tiff", "D:/Output/"+title);
close()
```

Table 2.7: Image J macros used for specific ICC analysis of hCOs.

"DCX Coverage" Macro	*//Switch on Area fraction* *//load previous "Prepped" image and copy outline* *run("8-bit");* *setAutoThreshold("Default dark no-reset");* *run("Threshold...");* *setThreshold(50, 200);* *//setThreshold(50, 200);* *run("Convert to Mask");* *run("Close");* *run("Restore Selection");* *run("Measure");* *close();*

“Lumen Skeleton” Macro	*title = getTitle();*
	run("Merge Channels...");
	run("Stack to RGB");
	waitForUser; //load ROI manager, draw and add all ROIs, change the properties to line width 1 & colour white
	//click the image
	run("Duplicate...", " ");
	run("Select All");
	run("Clear", "slice");
	run("Select None");
	run("From ROI Manager");
	roiManager("Set Color", "white");
	roiManager("Set Line Width", 1);
	run("Flatten");
	saveAs("Tiff", "D:/Output/"+title+"LS");
	roiManager("Measure");
	selectWindow("Results");
	saveAs("Results", "D:/Output/"+title+"Results.csv");
	close("");*
	selectWindow("Results");
	run("Clear Results");
	roiManager("Select All");
	roiManager("Delete");

For quantifying DCX area coverage, the same workflow depicted in Figure 2.1 was used for both the DAPI and DCX channels of the hCO section with adjustments. The DAPI channel was adapted to produce a count of DAPI only, a mask was not generated. For the DCX channel, the “Identify Primary Objects” module was replaced by “Threshold” using Robust Background thresholding strategy to produce a thresholded image of DCX. The thresholded DCX image was loaded into ImageJ alongside the original DAPI “PrepImage”. The manual outline drawn in the DAPI “PrepImage” was copied, and then the “DCX coverage” macro was run on the thresholded DCX image to determine the quantity of DCX coverage of a hCO (Table 2.7).

To count and measure lumens, as well as count phosphorylated vimentin positive (pVIM$^{+)}$ cells localisation to the lumens, the same approach as described in Figure 2.1 was used for the colocalised staining of DAPI$^+$/SOX2$^+$/pVIM$^+$/ZO1$^+$, i.e. 5 pixel central point masks, except for the ZO1 channel. Additionally, a DAPI mask was created to retain the shape of the thresholded DAPI$^+$ cell nuclei (Figure 2.2.A). This DAPI mask was then related as a child object to thresholded, centralised point masks of the parents objects of pVIM aggregation and SOX2 (Figure 2.2.A-B). This produced "filled in" masks denoting the location and shape of all DAPI$^+$ cells, with the DAPI$^+$/pVIM$^+$ or DAPI$^+$/SOX2$^+$ cells artificially coloured. Finally, the ZO1$^+$ channel was thresholded and artificially coloured to create a mask, similarly to the DCX mask (Figure 2.2.C). All three masks of Figure 2.2.A-C were merged to act as a guide to manually define the vacuous space (lumen) in ImageJ (Figure 2.2.E).

The criteria for determining a lumen were: a vacuous space that is circular in nature, surrounded by perpendicularly orientated DAPI$^+$ cells that are predominantly SOX2$^+$, to denote live cells of NPC identity. In addition, ZO1$^+$ traces should be visible around the outline of the lumen. This was to best reflect observations from in raw images (Figure 2.2.F). In cases of low fluorescence such as older hCO sections from the Basic protocol, the SOX2$^+$ or ZO1$^+$ masks were treated as preferable, but not necessary. These manually drawn masks of lumens were termed "lumen skeletons" (Figure 2.2.D) and were created using the "Lumen Skeleton" macro (Table 2.7), wherein quantity and area of lumens were recorded, whilst producing a skeletal mask of lumens. To ascertain the number of M phase cells localised to the lumens, the "lumen skeleton" and DAPI$^+$/pVIM$^+$ "filled in" mask were converted into objects. Using the CellProfiler "MeasureObject Neighbours" module, the quantity of DAPI$^+$/pVIM$^+$ "filled in" cells that were 50 pixels (two nuclei lengths) away from the lumen skeleton were counted as "apically-bound NPCs".

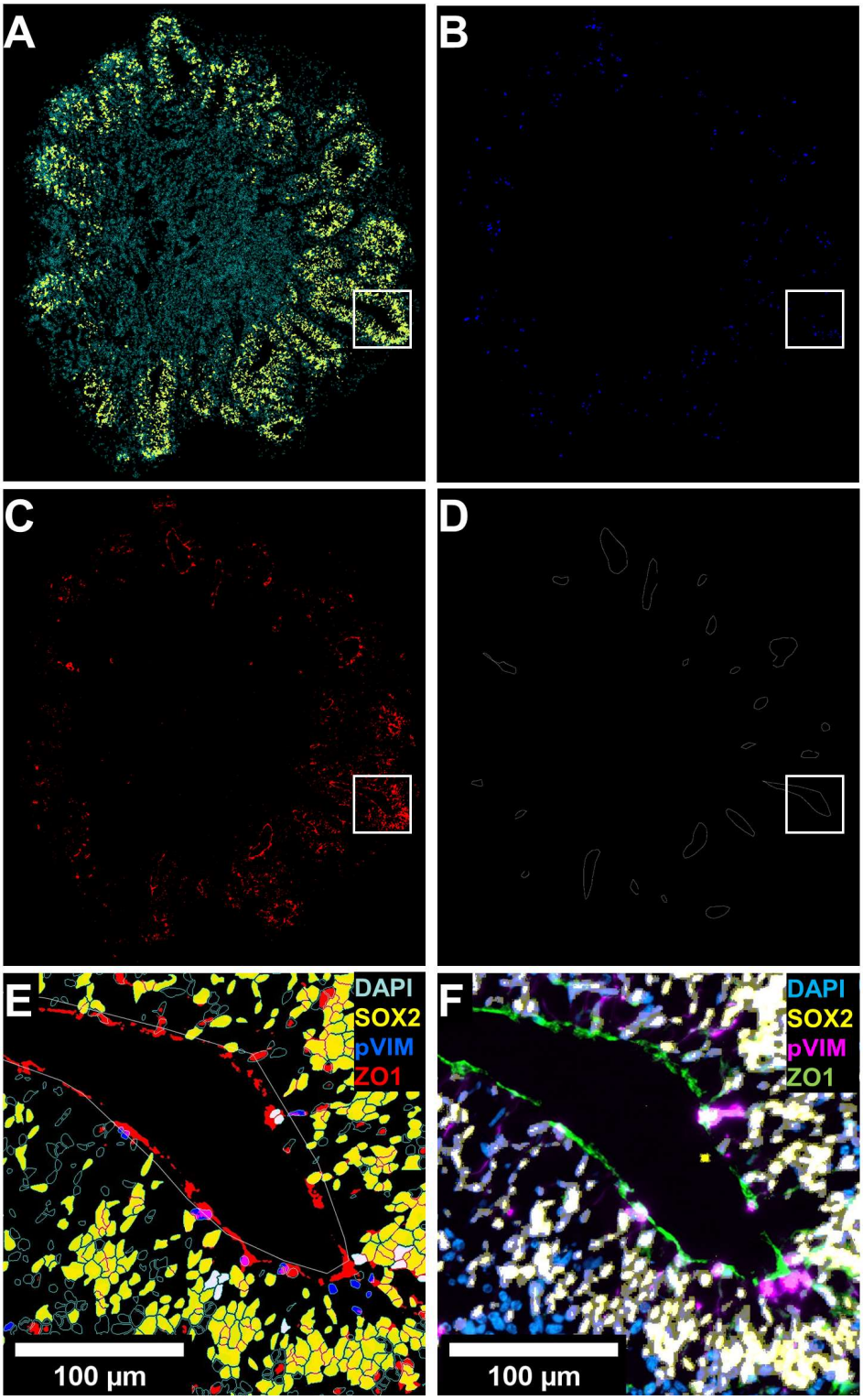

Figure 2.2: Masks used to determine lumen count and area, as well as M phase NPC localisation.

A) Mask containing outlined DAPI$^+$ cells and yellow, "filled in" DAPI$^+$/SOX2$^+$ cells. **B)** Mask of blue, "filled in" DAPI$^+$/pVIM$^+$ cells. **C)** Mask of thresholded ZO1. **D)** Mask of "lumen skeleton" determined by a composite of **(A-C)**. **E)** Composite of annotated region from **(A-D)**, close up 250 µm x 250 µm square. **F)** Image of region represented in **(E)** prior to input into CellProfiler (fluorescence increased for display). Scale bar = 100 µm.

2.2.4 Enhanced Cortical Organoid Replicate Design

Design of replicates for the Enhanced protocol were defined as: a minimum of three cell lines (two control and one patient), with two independent differentiations per cell line, each containing a minimum of three hCOs per type of analysis (Table 2.8). Any missing samples during differentiation are as a result of technical issues and not a deliberate choice.

Table 2.8: Available replicates for Enhanced hCO protocol analysis.

Enhanced hCO Protocol		Day 0	Day 5	Day 11	Day 21		Day 30		Day 60	
		qPCR	qPCR	qPCR	qPCR	ICC	qPCR	ICC	qPCR	ICC
Independent Differentiation #1	Control #1	✓	✓	✓	✓	✓	✓	✓	✓	✓
	Control #2	✓	✓	✓	✓	✓	✓	✓	✓	✓
	Deletion #1	✓	✓	✓	✓	✓	✓	✓	✓	✓
Independent Differentiation #2	Control #1	✓	✓	✓	✓	✓	✓	✓	✓	✓
	Control #2	✓	✓	✓	✗	✗	✗	✗	✗	✗
	Deletion #1	✓	✓	✓	✗	✗	✗	✗	✗	✗

2.2.5 Statistical Methodology

To fully utilise all available samples and in the absence of multiple independent differentiations, each organoid was used as a biological replicate for statistics, as opposed to technical replicates. The type of statistical test used per analysis is referred to in figure legends. Statistical analysis and graphs were produced using Prism Software Version 8.3 (GraphPad) & RStudio (Team, 2019). A lack of significance (ns) is only referenced in figures that have two categories and do not have numerous comparisons within one figure; in all other circumstances, only statistically significant results are referenced in a figure.

The standard of qPCR analysis was performed on a minimum of 3 hCOs per independent differentiation. For relative quantification of qPCR results, GAPDH was the chosen housekeeping gene and ΔCT and relative fold change were calculated by Pfaffl method (Pfaffl, 2001). Samples that were undetectable, i.e., over 40 CTs, were given a hypothetical figure of [40-CT_{GAPDh}] where necessary for statistical comparison. qPCR data is presented as $2^{-\Delta CT}$ with $2^{\pm CI}$ error bars; all qPCR statistics were based on Δ CT values and Δ CT standard deviation, unless otherwise stated.

ICC quantification of sections was performed on a minimum of 2 sections per hCO and a minimum of 3 hCOs per differentiation. Count data averaged across technical replicates were rounded up to the nearest whole integer. For live cell count data, CC3 estimations were predicted using linear regression analyses, specific to timepoint, genotype and protocol (Figure 3.9 and 3.10 and Supplementary Figures 5 and 7). These predictions were made using the total $CC3^+/DAPI^+$ cell count against the sum of area, perimeter and DAPI count (APD) multiplied together. Apoptotic estimations drawn from these regressions were deducted from total cell count, leaving a total non-apoptotic cell count. Live cell count data were taken as a percentage from the total non-apoptotic cell count. Cell death was not incorporated into analysis of dead cell count data, i.e., CC3, TUNEL and p53/KI67 analysis, as well as non-count data such as DCX coverage of area, lumen area or lumen count. Instead, these measurements were normalised to the hCO's respective APD and compared either in t-test/One-Way ANOVAs or in general linear mixed effects models to derive statistical significance.

Lumen area required a general linear mixed effects model that incorporated hierarchal random effects' structure to avoid pseudoreplication of the same lumen

across multiple ICC sections. Details of each formula used for lumen area comparison can be found in relevant figure legends. Morphometric analysis of hCO growth also required general linear mixed effects models to incorporate repeat batch measurements, interactions and random variables. Details of each formula for hCO growth can be found in Supplemental Figures 1-4 and 7. All second order interactions were included in each model and then removed if there was no significant effect on hCO size. Both examples of linear mixed effects models established statistical significance using estimated marginal means derived from optimised models.

2.3 Materials

2.3.1 Consumables

Table 2.9: List of inert consumables used in this research.

Item	Supplier	Product Code
6 well plates	StarLab	CC7682-7506
1 mL Tips (Sterile)	Starlab	S1112-1720
200 µl Tips (Sterile)	Starlab	S1111-1700
10 µl Tips (Sterile)	Starlab	S1111-3700
50 mL Tubes	Greiner	227261
15 mL Tubes	Fisher Scientific	11765075
25 mL Stripettes	Fisher Scientific	11517752
10 mL Stripettes	Fisher Scientific	11839660
5 mL Stripettes	Fisher Scientific	11829660
1 mL Tips	StarLab	S1161-1720
200 µL Tips	StarLab	S1163-1700
10 µL Tips	StarLab	S1161-3700
1 mL Filter tips	StarLab	S1122-1730
200 µL Filter tips	StarLab	S1120-8710
20 µL Filter tips	StarLab	S1123-1710
1.5 mL Tubes	Fisher	11569914
2 mL Tubes	Fisher	11579914
Cryovials	Starlab	E3110-6122
PCR tubes (Singles)	StarLab	I1402-8108
PCR tubes (Rows)	StarLab	I1402-3700
Autoclave tape	Fisher	12370489
Trypan blue	Thermo	15250061
Haemocytometer	Fisher Scientific	13444890
800 24 Well AggreWell plates	StemCell Tech	34815
Low attachment 24 well plates	Corning	CC228
Filter units	Thermofisher	151-4020
Low attachment 6 well plates	Corning	CC227

Parafilm	Sigma-Aldrich	P7793-1EA
Petri dishes	Starlab	CC7682-3394
Hydrophobic pen	VectorLabs	310018

2.3.2 Cell Culture Material

Table 2.10: List of cell culture reagents used in this research

Items	Supplier	Product Code
Ethanol	VWR	85823.36
Versene	Thermofisher	15040033
EZ LiFT	Sigma-Aldrich	SCM139-100ML
AggreWell Rinsing Solution	StemCell Tech	07010
Accutase	StemCell Tech	07920
AggreWell EB Formation Media	StemCell Tech	05893
Y-27632	Stratech	S1049
DMEM/F12	Thermofisher	11540566
N2	Fisher Scientific	15410294
BSA (sterile)	Sigma-Aldrich	A8412-100mL
Glutamax	Thermofisher	35050061
Non-essential amino acids	Thermofisher	11140050
Matrigel	Corning	354277
Neurobasal Media	Thermofisher	21103049
B27 -RA	Thermofisher	15440584
B27 +RA	Thermofisher	17504044
Antibiotic	Sigma-Aldrich	A5955-100ML
Trilineage kit	StemCell Tech	05230
PBS	Fisher Scientific	14190169
Geltrex	Fisher Scientific	A1413302
E8F	Thermofisher	A2858501
SB431542	Stratech	S1067
LDN193189	Cambridge Biosi	SM23-1
cAMP	Sigma-Aldrich	D0260
Ascorbic acid	Sigma-Aldrich	A4403
BDNF	Cambridge Biosi	GFH1AF
EGF	R&D	236-EG-200
Basic FGF	R&D	233-FB-025
Thermally stable basic FGF	Gibco	PHG0368
Insulin	Sigma-Aldrich	I9278-5mL
β-mercaptoethanol	Gibco	31350010
Dimethyl sulfoxide	Sigma-Aldrich	D4540-100ML
RevitaCell	Thermofisher	A2644501

2.3.3 Molecular Biology Reagents

Table 2.11: List of molecular biology reagents used in this research

Items	Supplier	Product Code
DAPI	Sigma-Aldrich	D9542-10MG
Low melting point Agarose	Thermofisher	10143954
RNA extraction kit	Sigma-Aldrich	RTN70-1KT
cDNA reverse transcription kit	Thermofisher	4368814
qPCR plates	StarLab	E1403-7700
qPCR plate film	StarLab	E2796-9795
qPCRBIO SyGreen Blue Mix Hi-ROX	PCR Biosystems	PB20.16-51
Optimal cutting temperature compound	Aston Pharma	KMA-0100-00A
Anti-roll plates	SLS	12083049
Glass slides	Fisher Scientific	11976299
Glass coverslips (50 mm)	VWR	ECN 631-1574
Microtome blades	Fisher Scientific	12191830
Slide boxes	VWR	HECH42704003
Sucrose	Sigma-Aldrich	S7903
Embedding moulds	VWR	720-0821
Paraformaldehyde	Sigma-Aldrich	16005-1KG-R
Donkey serum	Sigma-Aldrich	D9663
Triton X-100	Sigma-Aldrich	T9284-100ML
Tween-20	Sigma-Aldrich	P7949
Tris-EDTA buffer	Sigma-Aldrich	T9285
ProLong™ Glass Antifade Mountant	Thermofisher	P36984
RNA micro extraction kit	Qiagen	74004
Sybr Safe	Invitrogen	S33102
Ethanol	Merck	34852-2.5L-M
PBS tablets	Sigma-Aldrich	P4417-100TAB

2.3.4 Immunocytochemistry Antibodies

Table 2.12: List of ICC antibodies used in this research

Antibody	Product Code	Supplier	Species	Concentration
BRACHYURY	SC374321	Santa Cruz	Mouse	1:250
CLEAVED-CASPASE 3	9661S	CellSignalling	Rabbit	1:500
CTIP2	Ab18465	Abcam	Rat	1:250
CXCR4	AB124824	Abcam	Rabbit	1:250
DCX	4604S	CellSignalling	Rabbit	1:500
FOXG1	AB196868	Abcam	Rabbit	1:500
KI67	AB15580	Abcam	Rabbit	1:500

NKX2.1	AB76013	Abcam	Rabbit	1:250
P53	AF1355	R&D	Goat	1:250
PAX3	MAB2457-SP	R&D	Mouse	1:250
PHOSPHORYLATED-VIMENTIN	AB217673	Abcam	Rabbit	1:1000
SOX17	AB84990	Abcam	Mouse	1:250
SOX2	MAB2018	R&D	Mouse	1:250
TBR2	AB23345	Abcam	Rabbit	1:100
ZO1	AB190085	Abcam	Goat	1:250
488-Donkey	A21202	Thermofisher	Mouse	1:1000
488-Donkey	A21208	Thermofisher	Rat	1:1000
488-Donkey	A32814	Thermofisher	Goat	1:1000
555-Donkey	A31572	Thermofisher	Rabbit	1:1000
647-Donkey	A32787	Thermofisher	Mouse	1:1000

2.3.5 qPCR Primers

Table 2.13: List of qPCR primers used in this research

Target	Forward Sequence (5'-3')	Reverse Sequence (5'-3')
ACP6	AGATGGCAGTAGGCCCATTC	ACAGCTTTCTGATCTTGTCGG
BCL9	GGCCATACCCCTAAAGCACTC	CGGAAATACTTCGCTCCCTTTT
CHD1L	GCTATGAGCGTGTGGATGGTT	TGCTGTTAAGTTCATGCCAACTC
CTIP2	CTCCGAGCTCAGGAAAGTGTC	TCATCTTTACCTGCAATGTTCTCC
CUX1	GCTCTCATCGGCCAATCACT	TCTATGGCCTGCTCCACGT
CXCR4	CCCTCCTGCTGACTATTCCC	TAAGGCCAACCATGATGTGC
DCX	CCTTGGCTAGCAGCAACAGT	CCACTGCGGATGATGGTAA
DLX1	CCATGCCAGAAAGTCTCAACA	GGCCCAAACTCCATAAACACC
FOXA2	TGCACTCGGCTTCCAGTATG	CGTGTTCATGCCGTTCATCC
FOXG1	CCCTCCCATTTCTGTACGTTT	CTGGCGGCTCTTAGAGAT
GAD65	GGCTTTTGGTCTTTCGGGTC	GCACAGTTTGTTTCCGATGCC
GAD67	GCCAGACAAGCAGTATGATGT	CCAGTTCCAGGCATTTGTTGAT
GAPDH	CTGGTAAAGTGGATATTGTTGCCAT	TGGAATCATATTGGAACATGTAAACC
GJA5	GCTGCCAGAATGTCTGCTAC	GGTACTCGTAAGAGCCAGAGC
GJA8	GACCCTGCTGAGGACCTACAT	CCCAACTCCATCACGTTGAG
GPR89B	GGAGTGACTCTCATGGCTCTT	TGTTATGCACTTCCCCCTTCT
GRIA1	TGCTTTGTCGCAACTCACAGA	GGCATAGACTCCTTTGGAGAAC
GRIN 1	CTACCGCATACCCGTGCTG	GCATCATCTCAAACCACACGC

HOPX	CCCTTTTCTCTTCCCCGTCT	ACTCGAGCAAGGACCTGAAA
HOXB2	CCTAGCCTACAGGGTTCTCTC	CACAGAGCGTACTGGTGAAAAA
KI67	TCCTTTGGTGGGCACCTAAGACCTG	TGATGGTTGAGGTCGTTCCTTGATG
KLF4	CCACCCACACTTGTGATTACG	GCGGGCGAATTTCCATC
LHX6	TGAGAGTCAGGTACAGTGCG	GCCCATCCATATCGGCTTTGA
MAP2	CTGCTTTACAGGGTAGCACAA	TTGAGTATGGCAAACGGTCTG
NANOG	TCTGCAGAGAAGAGTGTCGC	AGAGTAAAGGCTGGGGTAGGT
NCAM	ACATCACCTGCTACTTCCTGA	CTTGGACTCATCTTTCGAGAAGG
NESTIN	TCCAGAAACTCAAGCACCA	AAATTCTCCAGGTTCCATGC
NKX2.1	CGCATCCAATCTCAAGGAAT	TGTGCCCAGAGTGAAGTTTG
OCT4	TTGATCCTCGGACCTGGCTAAG	GAACTCATACGGCGGGGG
OLIG2	CAGAAGCGCTGATGGTCAT	CGGCAGTTTTGGGTTATTC
P53	GCTGCTCAGATAGCGATGGT	CACGCACCTCAAAGCTGTTC
PAX3	AGCCGCATCCTGAGAAGTAA	CTTCATCTGATTGGGGTGCT
PAX6	CAACTCCATCAGTTCCAACG	TGGATAATGGGTTCTCTCAAACTCT
PRKAB2	ATGCGTTTCGATCTGAGGAAAG	GGTTCAGCATAACATGGTTGGG
REELIN	TCCGGGACAAGAATACCATGT	CCAAATCCGAAAGCACTGGAA
S100β	TGGCCCTCATCGACGTTTTC	ATGTTCAAAGAACTCGTGGCA
SATB2	CCGCACACAGGGATTATTGTC	TCCACTTCAGGCAGGTTGAG
SOX17	GTGGACCGCACGGAATTTG	GGAGATTCACACCGGAGTCA
SOX2	GAGTGGAAACTTTTGTCCGAGA	GAAGCGTGTACTTATCCTTCTTCAT
TBR1	GGGCTCACTGGATGCGCCAAG	TCCGTGCCGTCCTCGTTCACT
TBR2	CCGGGCACCTATCAGTACAG	GGTTGCACAGGTAGACGTG
TBXT	TATGAGCCTCGAATCCACATAGT	CCTCGTTCTGATAAGCAGTCAC
VGAT	CCGAGTGGTGAACGTAGCG	GTGGCGATAATGGACCAGGAC
VGLUT1	CGACGACAGCCTTTTGTGGT	GCCGTAGACGTAGAAAACAGAG
VGLUT2	GGGAGACAATCGAGCTGACG	CAGCGGATACCGAAGGAGATG
VIM	GGACCAGCTAACCAACGACA	AAGGTCAAGACGTGCCAGAG

3 Assessing Stem Cells, Experimental Design and Analysis Techniques for Cerebral Organoid Research

3.1 Introduction

Cerebral organoids are predominantly associated with intra- and inter-batch variation (Velasco *et al.*, 2019; Yoon *et al.*, 2019; Hernández *et al.*, 2021), and so it is necessary to minimise any sources of variability to provide the best reflection of the mimicked cerebral cortex tissue. In the first instance, high quality stem cells are required, of which should be pluripotent and with minimal heterogeneity, however the choice of starting stem cell material is relative to which origin best supports the research question: human ESCs or hIPSCs. Both categories of stem cells can exist in either naïve (preimplantation epiblast) or primed state (post-implantation epiblast), depending on how they are maintained in culture (Kilens *et al.*, 2018).

These states are defined by specific transcription factors and cell cycles (Messmer *et al.*, 2019), and if they are capable of maintaining pluripotency throughout self-renewal after inhibition of the MEK/ERK signalling pathway (Bayerl *et al.*, 2021). Human ESCs are harvested from the inner cellular mass of pre-implantation blastocysts, whilst hIPSCs are artificially reprogrammed somatic cells, using methods such as ectopic expression of the Yamanaka factors (Huang *et al.*, 2009). Both types of stem cells are expected to express these factors, as they are responsible for transcriptionally and translationally regulating pluripotency (Huang *et al.*, 2009). Two of the key members of this network are SOX2 and OCT4, transcription factors responsible for maintenance of pluripotency across both naïve and primed pluripotent states in stem cells, and therefore can be termed “universal” stem cell markers (Merino *et al.*, 2014). Furthermore, they can act independently, or form a regulatory complex, have similar binding preference to the enhancer regions of a shared pool of target genes (Bayerl *et al.*, 2021). This is in opposition to the naïve-associated transcription factors, such as KLF4 and KLF17, which are more likely to bind to promoter regions and share considerably fewer target genes than SOX2 and OCT4 (Bayerl *et al.*, 2021). An important master pluripotency transcription factor, NANOG, is not considered a Yamanaka factor but is essential to maintaining pluripotency, particularly in maintaining a naïve stem cell state (Abranches *et al.*, 2014; Acampora *et al.*, 2017) and is

capable of self-regulating, arguably independently, of SOX2 and OCT4 (Navarro *et al.*, 2012; Swaidan *et al.*, 2020).

Each type of stem cell has their own drawback; human ESCs have ethical complications due to the human embryo retrieval necessary for cell line generation, whilst hIPSCs retain epigenetic markers from the original tissue from which the cells were harvested (reviewed by Khoo *et al.*, (2020)). Furthermore, hIPSCs derived from female donors are vulnerable to X-inactivation erosion in culture (Brenes *et al.*, 2021). Although hIPSCs have these issues, they can be ameliorated with thorough validation, using sequencing to monitor genomic and epigenomic changes, as well as consistent methods of reprogramming, and using suitable culturing conditions to maintain a specific stem cell state (Scesa, Adami and Bottai, 2021). The decision between using human ESCs or hIPSCs is driven by the research question, although hIPSCs are often chosen as they are an effective, patient-specific model, competent at replicating complex disease pathology as they retain patient phenotype (Allende *et al.*, 2018; Chapman *et al.*, 2021). In this instance, hIPSCs were chosen for this research due to the accessibility to proband samples and the minimal ethical implications thereof, but with the intention of undertaking significant assessment to ensure pluripotency of stem cell lines.

Homogenous, pluripotent stem cells, either human ESCs or hIPSCs, are required for efficient EB generation, the first step in cerebral organoid differentiation. EBs are capable of self-aggregation in supplemented stem cell media, with the expectation of maintaining pluripotency (Jennifer Antonchuk *et al.*, 2010; Boxman *et al.*, 2016). Despite the lack of external patterning, however, current studies illustrate that there are significant transcriptional changes undertaken over time that cause EBs to lose their pluripotent nature (Boxman *et al.*, 2016; Kim *et al.*, 2020). Non-stem cell fate cell populations can occur over a range of time depending on the methodologies, notably between 3 to 8 days (Boxman *et al.*, 2016; Kim *et al.*, 2020; Tremble *et al.*, 2021). Many studies have converged on the cellular identity of EBs as a result of long term culture: a heterogenous mix of all three developmental lineages, ectoderm, mesoderm and endoderm (Boxman *et al.*, 2016; Kibschull *et al.*, 2016; Lancaster *et al.*, 2017; Kim *et al.*, 2020; Tremble *et al.*, 2021). This is beneficial in research scenarios dedicated to embryo development as it replicates *in utero* development, however, this is an issue for translational research questions requiring a pluripotent or

lineage-specific EB. It also poses questions as to when a disease model phenotype may occur, as this could be relative to the cellular identity of the EB. Examples of phenotypes arising during the EB stage of differentiation are limited, as cerebral organoid studies focus predominantly on ≥1 month old cerebral organoids. However, available information supports investigation of early timepoints in developmental disorders (Dang *et al.*, 2016; Iefremova *et al.*, 2017; Li *et al.*, 2017). In order to design research suitable for investigating the microcephaly-associated 1qDel (Sønderby *et al.*, 2021), it was therefore necessary to identify the cellular composition of early timepoints in hCO differentiation, including EBs.

Once EBs are generated, differentiation of cerebral organoids can begin. Although there are multiple methods of generating cerebral organoids (Lancaster and Knoblich, 2014; Watanabe *et al.*, 2017; Giandomenico, Sutcliffe and Lancaster, 2021), there are common characteristics that define a cerebral organoid, including visible characteristic morphology, such as neuroectodermal border clearing or neuroepithelial loops (Lancaster and Knoblich, 2014; Lancaster *et al.*, 2017; Sloan *et al.*, 2018). These external observations are examined in greater detail in Section 4 in figures such as Figure 4.3, but these external morphological changes are reflective of the internal development of key cerebral organoid cytoarchitecture, which can be evaluated using ICC (Bershteyn *et al.*, 2017; Albanese *et al.*, 2020; Beghin *et al.*, 2022). However, cerebral organoid morphology changes substantially over the stages of differentiation, and so quantifying these characteristics is complex. Morphological comparisons across timepoints can be difficult if restricted to particular structures, as features such as lumen shape vary over time (Sivitilli *et al.*, 2020). On the other hand, manually counting nuclei or fluorescently covered areas of a whole cerebral organoid section can be artificially skewed by the dead core found in ≥1 month old, maturing cerebral organoids, as well as greatly time-consuming (Giandomenico, Sutcliffe and Lancaster, 2021).

Few studies have achieved ICC imaging and analysis of a whole cerebral organoid (Albanese *et al.*, 2020; Adhya *et al.*, 2021). Instead, it has been favourable to adopt either manual counting (Iefremova *et al.*, 2017; Mansour *et al.*, 2018; Klaus *et al.*, 2019; Zhang *et al.*, 2019; Dong *et al.*, 2021; Kang *et al.*, 2021) or fluorescent intensity quantification strategies (Klaus *et al.*, 2019), determining areas of interest randomly or by constraining to specific cellular structures, such as

the VZ. An inexpensive automated solution for analysing whole cerebral organoid sections is not currently available, nor is a post-imaging correction for the dead core for cell count analysis. A combination of pre-existing software, such as ImageJ (Schneider, Rasband and Eliceiri, 2012), Zen Blue™ and CellProfiler (McQuin *et al.*, 2018), could be a successful approach in forming a high-throughput, ICC quantification pipeline. This pipeline could automatically gather data on metrics related to morphology, e.g., vacuous spaces, cell count, area, perimeter, for use in further analysis. However, if this universal data is not sufficient to reliably negate the dead core of each ICC image of a cerebral organoid, one or more cell death markers will be required to quantify cell death. These markers should be applicable to ICC experiments and capable of distinguishing between deliberate, programmed cell death or cells that have died due to hypoxia/malnutrition caused by methodological limitations. Choosing appropriate representation of cell death requires an understanding the shared and divisive characteristics of multiple types of cell death.

Programmed cell death, otherwise known as apoptosis, is an integral process necessary for maintaining cellular health. As reviewed by D'Arcy, (2019), apoptosis is initiated by one of two pathways, the intrinsic or extrinsic. The initiation of the intrinsic pathway of apoptosis is a response to significant internal damage of an individual cell caused by external stressors, e.g. UV radiation. Occurrence of such stressors destabilises the equilibrium between pro- and anti-apoptotic factors governed by the BCL-2 protein family (Kuwana and Newmeyer, 2003). Pro-apoptotic factors overwhelm this system and integrate into the mitochondrial membrane, causing overt permeability and depolarisation (Kuwana and Newmeyer, 2003). Compromised mitochondria is the signature of mid-stage, intrinsic-led apoptosis, and causes the release of specific proteins, like cytochrome c, that form an apoptosome complex (H. Dehkordi *et al.*, 2020). The apoptosome induces cleavage of one of the initiator caspases, procaspase-9.

With the activation of one of the initiation caspases, the intrinsic pathway converges with the extrinsic pathway hereafter. In contrast, the extrinsic pathway is initiated by stress signalling from 'death' ligands like FasL to neighbouring cells (Yuan *et al.*, 2018). The reception of these ligands can culminate in the creation of a death inducing signalling complex, with the objective of cleaving procaspase-8. This occurs in the early stages of apoptosis, as opposed to the mid-stage like in the intrinsic pathway, as the extrinsic pathway does not require mitochondrial

degradation in order to supply the components necessary for cleaving initiation procaspases (Deng *et al.*, 2017). Once activated, initiator caspases, caspase-8 and caspase-9 from the extrinsic and intrinsic pathways, respectively, will cleave the effector caspases, caspase-3, -6 and -7, thereby inducing late-stage apoptosis. Late-stage, caspase-dependent apoptosis is characterised by DNA fragmentation, caused by translocation of endonuclease G from mitochondria to nucleus (Kitazumi and Tsukahara, 2011). This is coupled with effector caspases alleviating inhibition of DNA-fragmentation-factor proteins (Kitazumi and Tsukahara, 2011). Similarly, the effector caspases cleave inactive ROCK1 into its active form, causing membrane blebbing (Coleman *et al.*, 2001). Total cell volume shrinks significantly, before forming apoptotic bodies from the blebbed membrane, which contain degraded cellular components (Núñez *et al.*, 2010). Apoptotic bodies, or cells in execution phase, are engulfed by recruited macrophages to avoid triggering surrounding cells into apoptosis.

Necrosis, on the other hand, is the result of a community of cells collectively undertaking unprogrammed cell death in the event of sudden, extreme disruption in cellular environment, e.g., hypoxia, chemical damage, extreme heat, etc. Necrosis follows a relatively opposite approach to apoptosis; the plasma membrane becomes more permeable and forms blebs resulting in the cell and its organelles swelling (oncosis) (D'Arcy, 2019). The plasma membrane eventually ruptures, releasing all cellular contents into the surrounding extra-cellular matrix (D'Arcy, 2019). The blebbing of the plasma membrane sets up a positive-feedback loop that causes the collapse of calcium homeostasis and membrane-bound ionic pumps, thereby generating reactive oxygen species (reviewed by Moujalled, Strasser and Liddell, (2021)). During necrosis, DNA can be both fragmented or digested/lysed prior to nuclear rupture (Takada, Watanabe and Mizuta, 2020). There is currently no known cellular signalling machinery for unprogrammed necrosis and therefore no cell surface or protein markers are available, however it is known that necrosis instigates a pro-inflammatory response by releasing damage-association molecular pattern proteins, which recruit phagocytes to the point of cell injury (Kayagaki *et al.*, 2021).

Apoptosis and necrosis do share some similar cellular features, such as nuclear condensation and DNA fragmentation. Necrosis is not always unprogrammed, and more evidence is being provided that different types of necrosis are heavily regulated, e.g. necroptosis and pyroptosis (Berghe *et al.*,

2010; Jiang *et al.*, 2020). Like that of the extrinsic pathway of apoptosis, necroptosis is instigated by death ligands received at the plasma membrane. However, the post-translational modifications of an affected protein, RIP1, determines the cellular outcome. Polyubiquitination maintains cell survival, whilst deubiquitination results in caspase-associated apoptosis and deubiquitination combined with phosphorylation creates a 'necrosome' complex that causes caspase-independent necroptosis (Berghe *et al.*, 2014; Oliveira, Amaral and Rodrigues, 2018). Similar to necroptosis and necrosis, pyroptosis undergoes the same physiological events of cell swelling and membrane permeabilisation and therefore is considered a necrotic process (Wang *et al.*, 2017; Yuan *et al.*, 2020; Jiang *et al.*, 2020). On the other hand, pyroptosis' defining feature is that it is triggered by proinflammatory signalling, as opposed to cellular injury, but is caspase-dependent, marking it as a distinct mode of cell death compared to apoptosis and necrosis (Wang *et al.*, 2017; Jiang *et al.*, 2020; Yuan *et al.*, 2020). Necroptosis and pyroptosis are distinguishable methodologically from necrosis and apoptosis by either quantifying the necroptosis executioner protein MLKL, or by the activation of caspase 1, 11, 4 or 5, respectively (Jiang *et al.*, 2020; Cotsmire, Szczerba and Jacobs, 2021).

What has been previously referred to as necrosis can also be termed primary necrosis, as necrosis can also proceed apoptosis in the absence of phagocyte recruitment in a process known as secondary necrosis. Secondary necrosis is characterised similarly to the end stages of primary necrosis, necroptosis and pyroptosis: cell lysis via disrupted calcium homeostasis (Schwab *et al.*, 2002) and lysosomal and plasma membrane permeabilisation (Berghe *et al.*, 2010; Wickman *et al.*, 2013). Secondary necrosis is often only observed in disease pathologies that have repressed immunological capabilities such as cancerous tumours being treated with radiotherapy (Rogers *et al.*, 2017). Secondary necrosis can occur when activated caspase-3 disrupts calcium homeostasis increasing plasma membrane permeability (Schwab *et al.*, 2002). Activated caspase-3 can also cleave a protein responsible for apoptotic body formation, DFNA5, into a fragment that targets the plasma membrane for lysis (Rogers *et al.*, 2017). Secondary necrosis is not currently perceived as an immediate switch from apoptosis, but a gradual transition. The plasma membrane of apoptotic bodies gradually loses membranal integrity over time, in the process releasing immunogenic signals into the extracellular matrix. In the absence of a response

from phagocytes, the membrane continues to disintegrate and the apoptotic bodies undertake secondary necrosis (Wickman *et al.*, 2013). Although there is no known evidence of cerebral organoids exhibiting secondary necrosis, they undergo apoptosis in a developmentally-relevant manner (Zhang *et al.*, 2019) and also could undergo one, or many, forms of hypoxic-induced cell death within the dead core, such as necroptosis, pyroptosis or primary/secondary necrosis, but which, if at all, is unknown.

In summation, prior to designing a new cerebral organoid protocol, one must determine all facets of an experimental design for disease modelling, including stem cell quality, EB cellular identity and quantification methodologies. Stable, homogenous, pluripotent stem cells are a necessity for successful differentiation of cerebral organoids; in this scenario control hIPSCs from healthy donors were chosen as source material to best recapitulate patient phenotypes. The cellular identity of EBs will influence the temporal design of disease modelling experiments, so as to capture the anticipated microcephaly phenotype of 1qDel. Finally, current cerebral organoid ICC analysis is constrained to biased selection of areas of interest and/or avoiding the dead core issue; both elements could be mitigated with improvements in methodology. These improvements would be designed to quantify cerebral organoids with less bias whilst representing a full section of a cerebral organoid.

3.2 Research Aims & Hypothesis

The aim of this chapter was to confirm the pluripotency of hIPSCs prior to differentiation and to identify cellular identity of EBs in the chosen cerebral organoid protocol. Furthermore, a high-throughput ICC pipeline capable of quantifying whole sections of cerebral organoids was to be created and tested, with flexible analysis parameters to mitigate for morphological differences and the dead core.

The hypothesis for this chapter was that the hIPSCs chosen for this research were pluripotent; the cell lines used in this research had had previous assessment of Yamanaka factors (Chapman *et al.*, 2021). Additionally, current literature suggests that EBs are not analogous to hIPSCs and so it is believed that Day 5 EBs will represent a multipotent, not pluripotent, cellularly diverse aggregate (Boxman *et al.*, 2016; Kibschull *et al.*, 2016; Lancaster *et al.*, 2017; Kim *et al.*, 2020; Tremble *et al.*, 2021). Furthermore, it was hypothesised that a high-

throughput system for quantifying whole cerebral organoid ICC images was feasible by combining current quantification methodologies and software used for *in vitro* neurons and *in vivo* mouse brain (Schneider, Rasband and Eliceiri, 2012; McQuin *et al.*, 2018). Manipulation of universal measurements from cerebral organoids was suggested as a method to produce a normalising constant capable of quantifying morphology and cell count. Finally, it was anticipated that maturing cerebral organoids exhibit one or more of types of cell death in the hypoxic, nutrient-deficient core, as well as the physiologically-relevant apoptosis in predetermined regions such as outside the VZ (Daviaud *et al.*, 2019; Zhang *et al.*, 2019). It was therefore believed necessary to try different methods of cell death assay to determine the quantity and type of cell death occurring within a cerebral organoid. If feasible, this data would be integrated into the high-throughput ICC system to adjust total cell count for accurate quantification of live cell populations.

3.3 Methodology

All methodologies referred to in this chapter stem from the General Methodology (Section 2) except trilineage assessment of hIPSC lines as detailed below.

Expanding upon Dr. Gareth Chapman's assessment of the presence of Yamanaka factors in the hIPSC lines used in this research (Chapman *et al.*, 2021), validation of the stem cell quality of the hIPSC lines required proof of their capability to differentiate into the three developmental lineages: ectoderm, mesoderm and endoderm. Following the STEMdiff™ Trilineage Differentiation Kit (STEMCELL Technologies™) manufacturers protocol, hIPSCs were washed in PBS and single cell disassociated via pre-warmed Accutase™ (STEMCELL Technologies™) incubation for 10 minutes at 37°C. Accutase™ was deactivated with the addition of DMEM-F12 at a 1:5 ratio. Cells were pelleted at 120 rcf for 5 minutes, supernatant removed, and either resuspended in 1 mL of E8F media (for mesoderm and endoderm lineages) or in the STEMdiff™ Trilineage Ectoderm media (for ectodermal lineage), both of which had the addition of 1:100 dilution of antibiotic/antimycotic solution (Sigma-Aldrich™) and 10 µM Y-27632 (Stratech™). The cells were then plated on Geltrex-coated glass coverslips at the designated quantities with reference to their intended lineage, i.e., 400,000 cells per well for endoderm and ectoderm lineages, 100,000 cells per well for mesodermal lineage per well of a 24 well plate. After 24 hours, all media was replaced and only the

relevant lineage media supplied in the STEMdiff™ Trilineage Differentiation Kit was used with no additional components. Media was changed every day for a total of either 4 days (endoderm/mesoderm lineages) or 6 days (ectoderm) in STEMdiff™ Trilineage media after seeding. These collection dates were one day shorter than recommended. Samples were collected for either qualitative ICC staining or quantitative qPCR analysis.

For qualitative ICC assessment, hIPSCs were washed in PBS and incubated with 3.7% paraformaldehyde (PFA) (Sigma-Aldrich™) for 15 minutes at RT. Cells were washed in PBS and stored in excess PBS at 4°C until stained. For ICC staining, samples were incubated with blocking solution (5% donkey serum, 0.01% Triton X-100 and PBS) for 1 hour at RT. Blocking solution was replaced with fresh blocking solution containing the recommended dilution of primary antibody and incubated overnight at 4°C. After 24 hours, cells were washed with PBS and incubated with a solution of PBS and secondary antibody at the recommended dilution for 1 hour at RT in darkness. After 1 hour, samples were washed with PBS, incubated with DAPI (10 ng/mL) for 5 minutes at RT in darkness, and then washed again. Coverslips were mounted with Fluoromount™ Aqueous Mounting Medium (ThermoFisher Scientific) before sealing with clear nail varnish. Z-stacks of images were taken on a Leica DMI600B Inverted Timelapse microscope and presented as a maximum projection of each channel.

In preparation for qPCR analysis, cells were washed in PBS and disassociated via Accutase™ incubation for 10 minutes at 37°C. Accutase™ was deactivated with the addition of DMEM-F12 at a 1:5 ratio. Cells were pelleted at 120 rcf for 5 minutes and supernatant was aspirated. Separate wells of the same condition were combined to increase cell quantity for RNA extraction. Cells were stored at -80°C until RNA extraction. RNA extraction, cDNA synthesis and qPCR analysis were conducted as described in Section 2.2.2. Reference to replicates in trilineage qPCRs equate to technical replicates, which were used for statistical analysis and data presentation.

3.4 Results

3.4.1 Trilineage Assessment of Human Induced Pluripotent Stem Cells

The STEMdiff™ Trilineage Differentiation Kit (STEMCELL Technologies™) was used to confirm pluripotency by differentiating the hIPSC lines used in this study into the three developmental lineages of ectoderm, mesoderm and endoderm (Figure 3.1, 3.2 and 3.3). After seeding, exposure to specific differentiation media instigated neural rosette formation in ectodermal samples and lifting/curling of cells in mesodermal samples, whereas endodermal cells remained visibly unchanged. Cell lines Control #1 and Deletion #1 (Figure 3.1 and 3.3, respectively) showed universal gene upregulation and visible protein expression of the corresponding markers: *PAX6* and *NESTIN* (*NES*) for ectoderm, *TBXT* and *CXCR4* for mesoderm and *SOX17* and *CXCR4* for endoderm. All genes translate for proteins with corresponding names, except *TBXT* which encodes for the protein BRACHYURY. Control #2 showed a downregulation of *NES* transcription in the ectodermal sample which is not ideal for ectodermal differentiation, but exhibited neural rosette morphology, visible expression of PAX6 and nestin at protein level and upregulated *PAX6* transcription (Figure 3.2). The data and images presented in this Section (Section 3.4.1) were included as supplementary information for the Chapman *et al.*, (2021) publication, but in a different format.

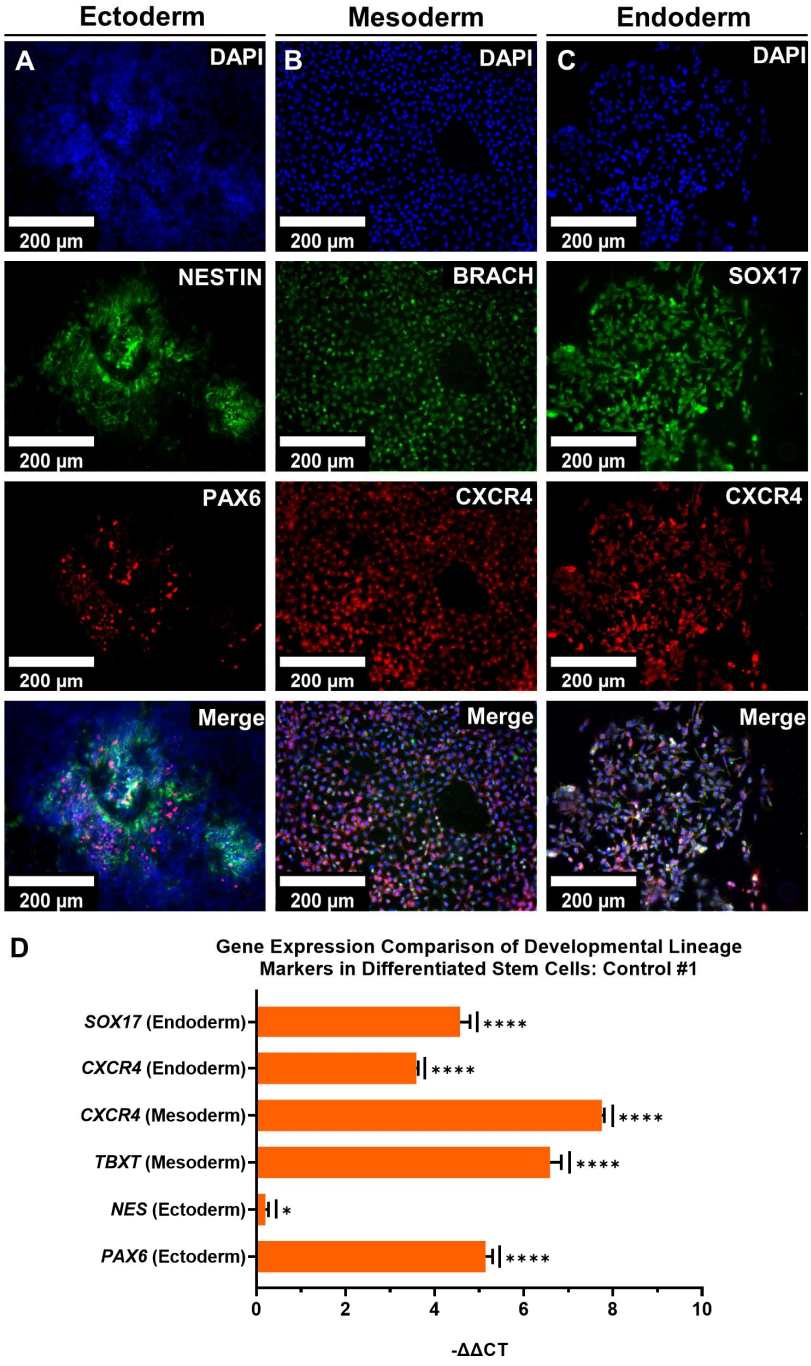

Figure 3.1: Control #1 hIPSCs proved pluripotent by differentiating into the three major developmental lineages of ectoderm, mesoderm and endoderm. Representative fluorescent images of trilineage-differentiated cells defined by the expression of lineage-appropriate proteins. **Column A)** ectodermal (PAX6 and NESTIN), **Column B)** mesodermal (BRACHYURY and CXCR4), and **Column C)** endodermal (SOX17 and CXCR4). Protein expressed referenced in image, scale bar = 200 µm. **D)** Transcription of developmental lineage-associated genes in trilineage-differentiated cells. Data is presented as fold change (-ΔΔCT), relative to undifferentiated hIPSCs, ±95% CIs, (n≥3 CT replicates). Statistical analysis was conducted on dCTs using a mixed model with Geisser-Greenhouse correction, with Holm-Šídák correction for post-hoc tests; *p=<0.05, ****p=<0.0001.

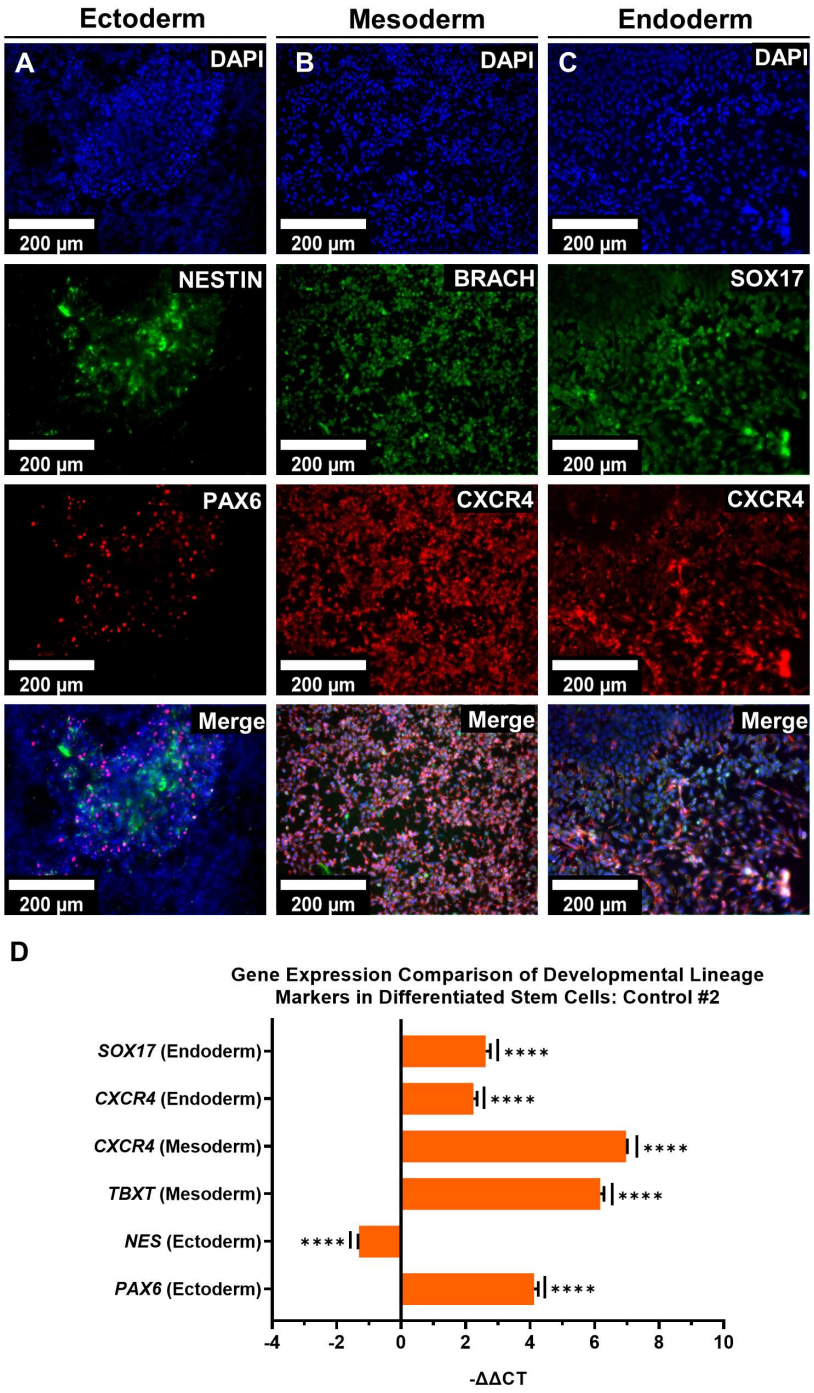

Figure 3.2: Control #2 hIPSCs proved pluripotent by differentiating into the three major developmental lineages of ectoderm, mesoderm and endoderm. Representative fluorescent images of trilineage-differentiated cells defined by the expression of lineage-appropriate proteins. **Column A)** ectodermal (PAX6 and NESTIN), **Column B)** mesodermal (BRACHYURY and CXCR4), and **Column C)** endodermal (SOX17 and CXCR4). Protein expressed referenced in image, scale bar = 200 µm. **D)** Transcription of developmental lineage-associated genes in trilineage-differentiated cells. Data is presented as fold change (-ΔΔCT), relative to undifferentiated hIPSCs, ±95% CIs, (n≥3 CT replicates). Statistical analysis was conducted on dCTs using a mixed model with Geisser-Greenhouse correction, with Holm-Šídák correction for post-hoc tests; *p=<0.05, ****p=<0.0001.

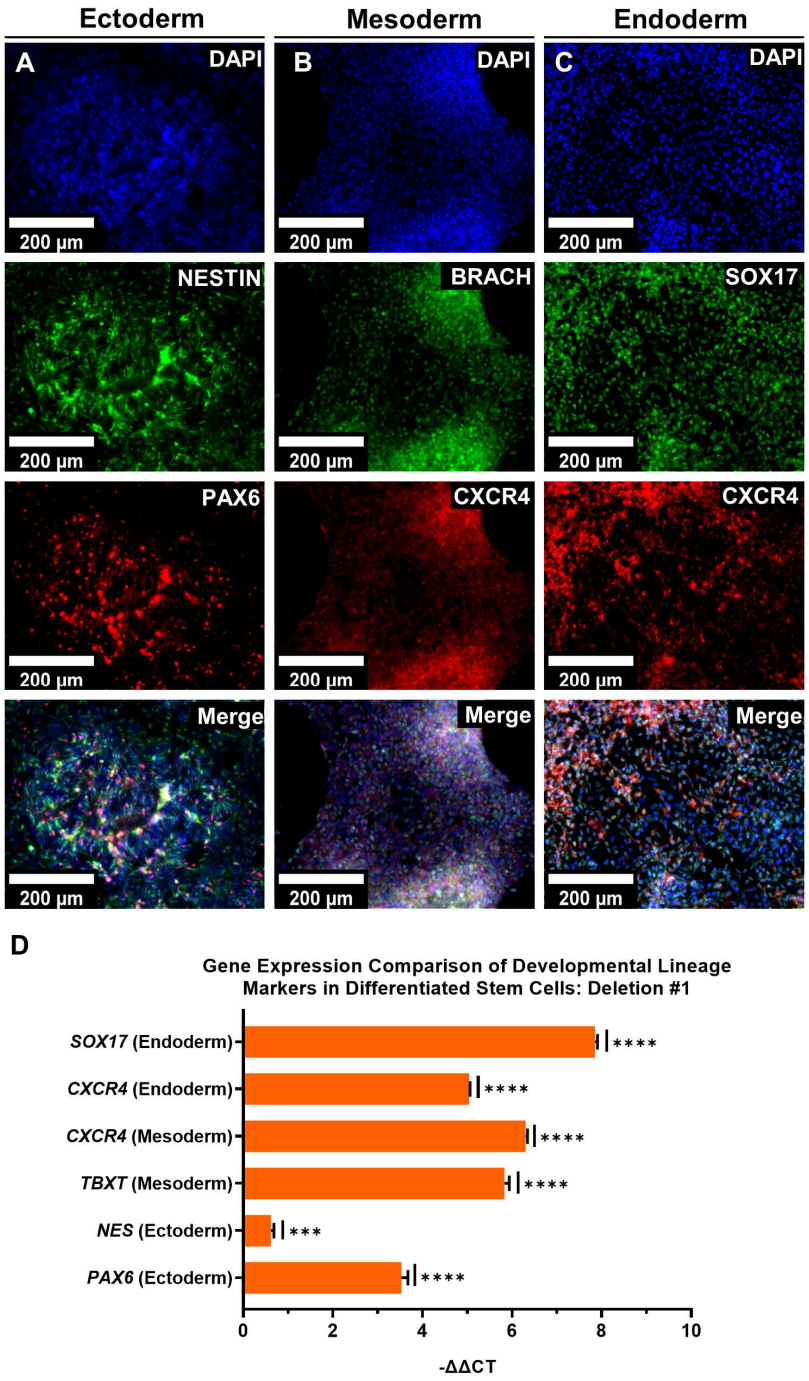

Figure 3.3: Deletion #1 hIPSCs proved pluripotent by differentiating into the three major developmental lineages of ectoderm, mesoderm and endoderm. Representative fluorescent images of trilineage-differentiated cells defined by the expression of lineage-appropriate proteins. **Column A)** ectodermal (PAX6 and NESTIN), **Column B)** mesodermal (BRACHYURY and CXCR4), and **Column C)** endodermal (SOX17 and CXCR4). Protein expressed referenced in image, scale bar = 200 µm. **D)** Transcription of developmental lineage-associated genes in trilineage-differentiated cells. Data is presented as fold change (-ΔΔCT), relative to undifferentiated hIPSCs, ±95% CIs, (n≥3 CT replicates). Statistical analysis was conducted on dCTs using a mixed model with Geisser-Greenhouse correction, with Holm-Šídák correction for post-hoc tests; *p=<0.05, ****p=<0.0001.

3.4.2 Embryoid Bodies are a Multipotent, but Ectodermally-Fated, Aggregate

Day 5 EBs were created from Control #1 and #2 hIPSCs and made using the Enhanced Protocol (E-EBs). To identify cellular identity of Day 5 EBs, they were compared to both hIPSCs and Day 11 Enhanced hCOs (E-hCOs). Compared to hIPSCs, significant increases in universal stem cell markers *SOX2* and *OCT4* transcription were observed in Day 5 E-EBs. Neuroectodermal and neurogenesis markers were also significantly upregulated (*PAX6, NES* and *NCAM*) (Figure 3.4.C). On the other hand, the naïve stem cell markers *NANOG* and *KI67* were significantly downregulated, as was the endodermal marker *SOX17* (Figure 3.4.A-B). The transcription factor *PAX3,* responsible for neural plate border organisation (Xue *et al.*, 2018) and a marker of neural crest cells (Mehler *et al.*, 2020; So *et al.*, 2020), was also significantly upregulated in Day 5 E-EBs (Figure 3.4.C). However, there was no change in transcription of cell cycle markers (*KI67* and *P53*) (Figure 3.4.D), nor the mesodermal marker *TBXT* (Figure 3.4.B).

Day 11 E-hCOs that had undergone neuroectodermal induction for 6 days were presented alongside Day 5 E-EBs and hIPSCs for comparison. Day 11 E-hCOs had significantly depleted *OCT4* expression compared to hIPSCs and Day 5 E-EBs (Figure 3.4.A). Although neuroectodermal/neurogenesis markers such as *PAX6, NES* and *NCAM* were elevated at Day 5, this substantially increased after neuroectodermal induction at Day 11 (Figure 3.4.C). There was also an increase in *KI67* transcription at Day 11 compared to Day 5 E-EBs (Figure 3.4.D). When viewed in comparison with neuroectodermal E-hCOs and hIPSCs, Day 5 E-EBs were neither hIPSCs nor hCOs. Instead, Day 5 E-EBs retained transcriptional indicators of multipotency, but were exhibiting neuroectodermal gene regulation.

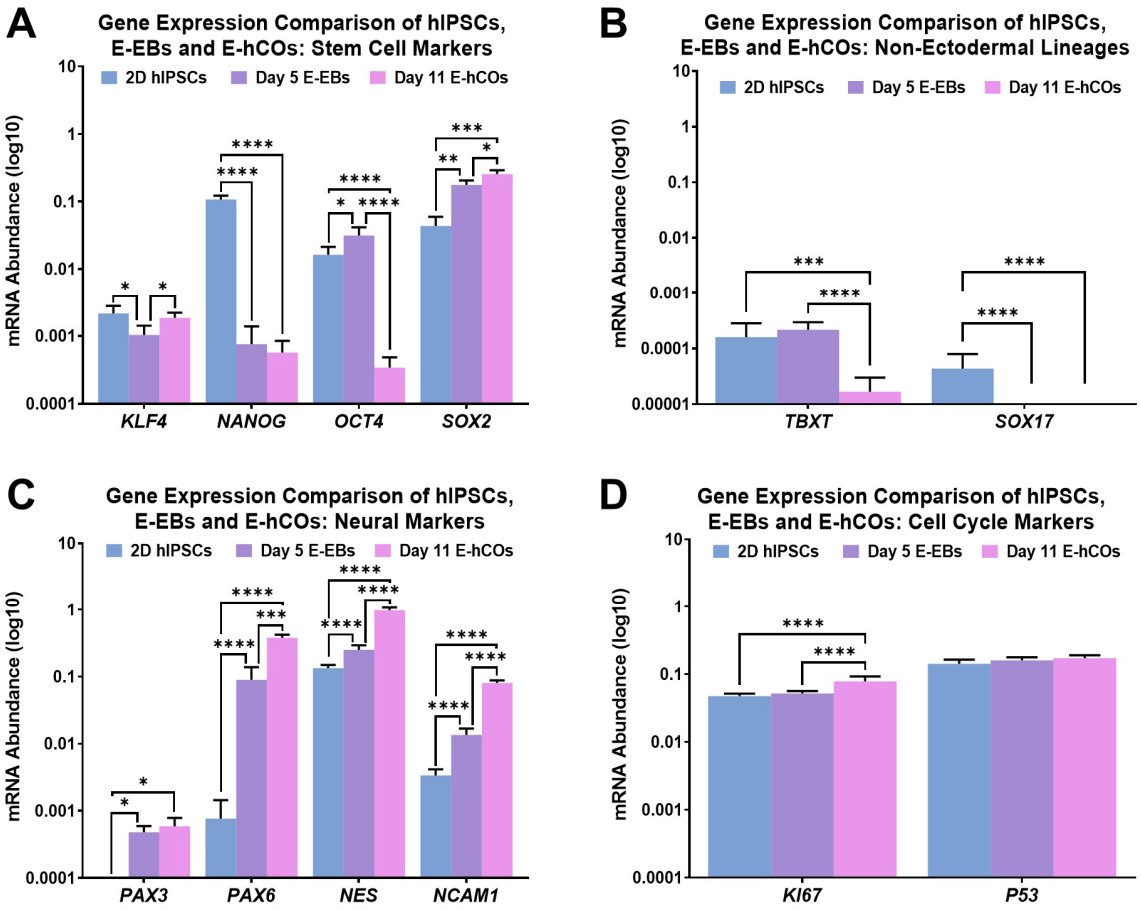

Figure 3.4: Day 5 E-EBs represented multipotent, neuroectodermally fated aggregates.

Each graph compares hIPSCs, Day 5 E-EBs and Day 11 E-hCOs of both Control #1 and #2 combined across specific clusters of genes defined by identity: **(A)** stem cell (*KLF4, NANOG, OCT4* and *SOX2*), **(B)** non-ectodermal lineages (*TBXT* and *SOX17*), **(C)** neural (*PAX3, PAX6, NES* and *NCAM1*) and **(D**) cell cycle *(KI67* and *P53*). Data is presented as relative mRNA abundance ($2^{-\Delta CT}$, $\pm 2^{-CI}$), (n≥3 wells/6 independent EBs/3 independent E-hCOs). Statistical analysis was conducted on dCTs using a two-way ANOVA with Geisser-Greenhouse correction with Holm-Šídák correction for post-hoc tests; unlabelled=not significant, *p=<0.05, **p=<0.005, ***p=<0.0005, ****p=<0.0001.

3.4.3 Assessing Possible Methods of Normalising Immunocytochemistry Analysis

In order to achieve the stated aims of this research, hCOs structural morphology and proteins of interest would be compared using ICC across timepoints, protocols and genotypes. However, to compare whole hCO sections across timepoints, the dead core present in hCOs needed to be eliminated. In the absence of any known method suitable to correct for the dead core in ICC analysis of whole hCO sections, one option investigated was to create a “live cell space” relative to the depth of diffusion, guided by perpendicular measurements of the hCO perimeter (Figure 3.5.A). This would exclude any cells outside the diffusion range, i.e., the dead core, leaving a portion of live tissue normalised to the hCO size. This “live cell space” was created by shrinking a replica of the hCO perimeter to a given size to match cardinal points representing the depth of diffusion. This was then deleted from ICC images prior to quantification. However, there were a variety of unresolvable issues when attempting to apply this method. Firstly, the method requires a uniform shape (Figure 3.5.A), of which a hCO is not (Figure 3.5.B). Without a uniform shape, using the same cardinal points results in unequal space surrounding the measurement (Figure 3.5.B). The template did not fit the perimeter correctly, which would result in disproportional measurements of the “live cell space”. Readjusting the cardinal points to be perpendicular to random locations on the outer perimeter of the hCO had a similarly poor outcome (Figure 3.5.B). The difficulties of determining where the cardinal points should be located along the perimeter became significantly worse around curves, as the template could not be readjusted to have the same depth of diffusion to suit all three perpendicular-to-perimeter angles (Figure 3.5.B). In this circumstance, the hCO’s non-uniform shape means that this method of determining the dead core was not fit for purpose.

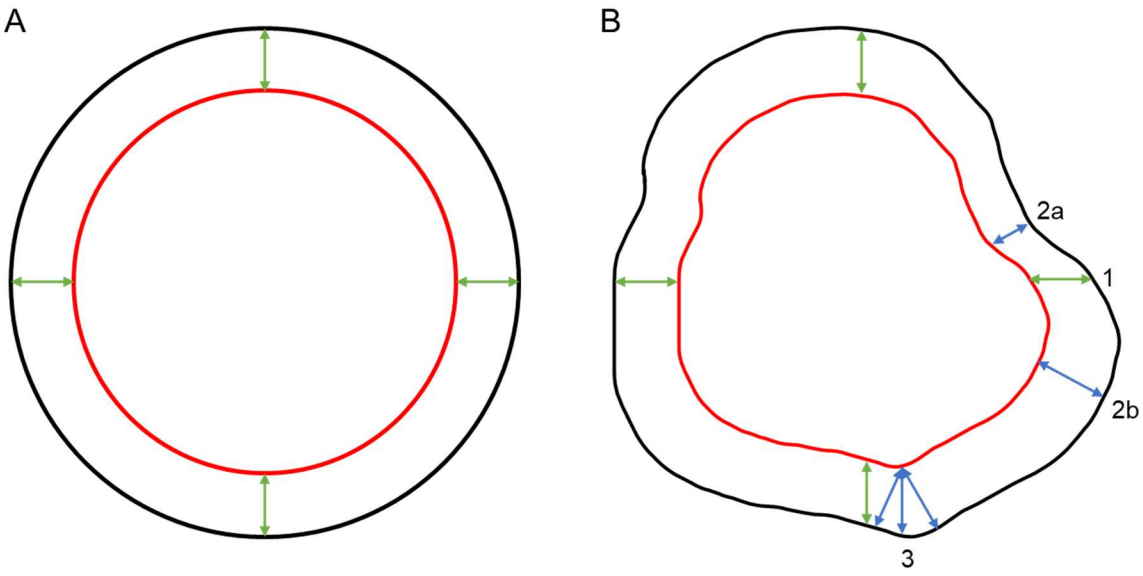

Figure 3.5: Cerebral organoid's shape rendered a perimeter-based removal of the dead core inviable.

Schematic representation of a perimeter-based, predictive dead core template in hCOs. **A**) Uniform circle with arrows of identical length (green) set in a cardinal pattern, identifying the live cell space between the outer surface perimeter (black) and inner dead core perimeter (red). **B**) Using same methods as (**A**) to produce a dead core template of a Day 30 control E-hCO. Issues annotated: **1**) unequal space surrounding cardinal points, **2**) when random cardinal points are set to the outer perimeter, they can either be under (**a**) or over (**b**) representing the live cell space, and **3**) it is possible to inaccurately represent live cell space depending on what angle the cardinal point is set to.

An alternative option to the "live cell space" idea was to make a "live cell count". This would be determined by deducting the quantity of dead cells from the overall cell count, predicted by a pre-calculated total cell death based off cell death-specific ICC staining. Count values of proteins of interest could be documented as a proportion of the "live cell count". Predicted cell death could be estimated from measurements universal to all hCOs. The same measurements could be used to normalise more morphological/non-count data, such as lumen count. Current methodologies for analysing count or morphological data rely on normalising information to one common measurement, i.e., area, perimeter or cell count (Iefremova *et al.*, 2017; Mansour *et al.*, 2018; Klaus *et al.*, 2019; Zhang *et al.*, 2019; Dong *et al.*, 2021; Kang *et al.*, 2021). However, only using one measurement can prove flawed (Figure 3.6). Normalising to area ignores that some hCOs may have increased diffusion due to an expanded perimeter, or not

take into account variable cell density or internal cytoarchitectural organisation (Figure 3.6.A-C). Normalising to perimeter could be considered reasonable given its relation to surface area and therefore exposure to nutrients, however it again does not accommodate for internal characteristics, such as cell count (Figure 3.6.A-C). The relationship between area and perimeter is also inconsistent; a given perimeter can increase whilst maintaining a constant area (Figure 3.6.B), whilst a given area can only increase alongside an increase in perimeter (Figure 3.6.D). Finally, normalising to cell count can cause issue particularly when looking across timepoints. Although a hCO may be larger due to maturity, the cell count can be substantially skewed by variable cell density, complex internal morphology such as multi-cell thick VZ but vacuous lumens, as well as an increased dead-to-live cell ratio (Figure 3.6.D). Overall, one, sole measurement appears an unfit choice for normalising ICC quantification of a whole hCO section.

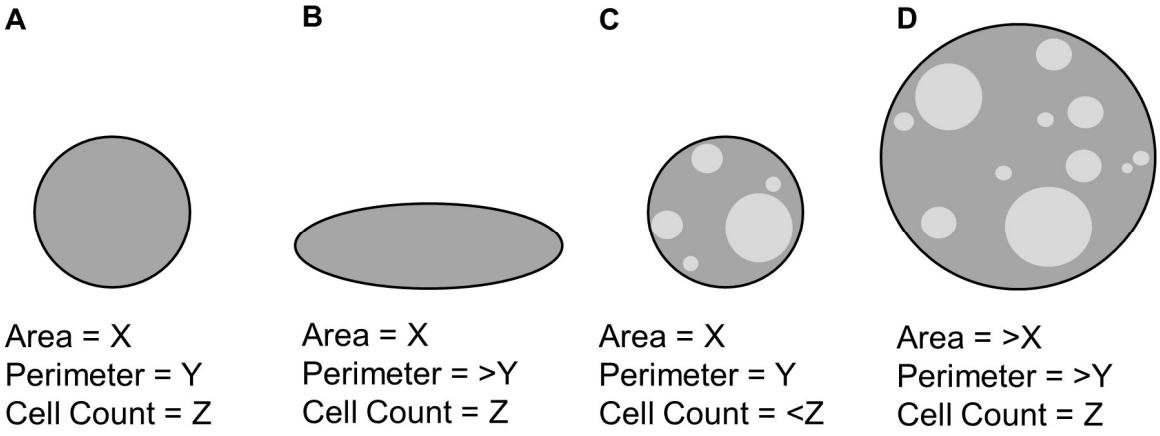

Figure 3.6: Area, perimeter and cell density were biased methods of normalising ICC images of whole hCO sections.

Schematic examples of varying internal and external information that may vary from a uniform, spherical hCO **(A)**, including flattened hCOs **(B)**, spherical hCOs with variable density of cells (represented as light grey circles) **(C)** or larger, spherical hCOs with variable density of cells **(D)**.

A better approach to finding a measurement that can be used as a "normalising constant" would be to analyse the relationships these measurements have with one another in actual hCOs. The three chosen universal measurements of area, perimeter and total cell count (determined by total $DAPI^+$ count) of Control #1 and #2 E-hCOs at Day 21, 30 and 60 were compared in multiple linear regression analysis (Figure 3.7). Across the three timepoints, there was significant positive correlation (R^2 value) when comparing each individual measurement to each other, most notably area against cell count across all three timepoints (R^2=0.799 to 0.968) (Figure 3.7.A, 3.7.D and 3.7.G). However, not all of these relationships significantly deviated from an R^2 value of 0, such as Day 21 area against perimeter (R^2=0.524) (Figure 3.7.C). It was noted that across all three timepoints, perimeter has the poorest relationship to cell count, even when significantly deviating from zero (R^2=0.642 to 0.786) (Figure 3.7.B, 3.7.E and 3.7.H).

The linear regression analyses in Figure 3.7 led to the suggestion that area, perimeter and total cell count ($DAPI^+$ count) could be unified into a normalising constant that maximises information available for normalising hCO ICC quantitative count and morphological analysis. Based off the analysis of individual measurement relationships in Figure 3.7, two combinations of unified constant were examined in the context of cell death marker analysis: area multiplied by cell count (referred to as AD) due to its aforementioned high correlation (Figure 3.7.A, 3.7.D and 3.7.G), and area, perimeter and cell count multiplied together (referred to as APD) as an all-encompassing constant. These two unified constants were also compared to individual measurements to illustrate the improvements a unified constant could make in predicting cell count.

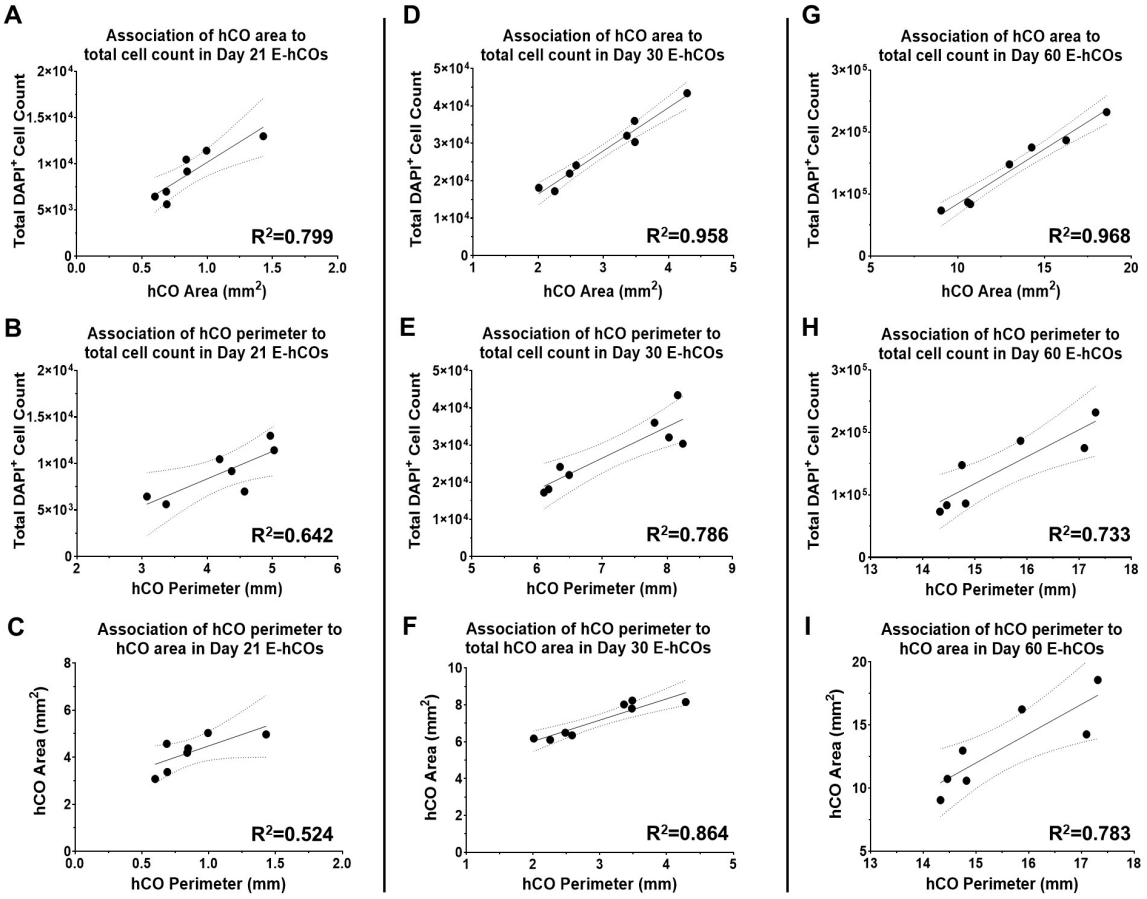

Figure 3.7: Inconsistent correlations found between area, perimeter and cell density of cerebral organoids across different timepoints.

Linear regression graphs of the three universal measurements, area, perimeter and total cell count ($DAPI^+$ count) in Control #1 and #2 E-hCOs. **A)** Day 21 – Area against total cell count: F(1,5)=19.9, p=0.007, **B)** Day 21 – Perimeter against total cell count: F(1,5)=8.981, p=0.03, **C)** Day 21 – Perimeter against area: F(1,5)=5.514, p=0.066. **D)** Day 30 - Area against total cell count: F(1,6)=135.5, p=<0.0001, **E)** Day 30 - Perimeter against total cell count: F(1,6)=22.04, p=0.003, **F)** Day 30 - Perimeter against area: F(1,6)=38.05, p=0.0008. **G)** Day 60 - Area against total cell count: F(1,5)=149.8, p=<0.0001, **H)** Day 60 - Perimeter against total cell count: F(1,5)=18.03, p=0.008, **I)** Day 60 - Perimeter against area: F(1,5)=13.73, p=0.014. Bold line represents line of best fit, dashed lines represent 95% CIs, R^2 value is referenced within image.

3.4.4 How to Predict Cell Death in the Cerebral Organoid Core

With the knowledge of the relationship between the universal measurements present in a hCO, the next step was to apply and examine each measurement in the context of investigating and quantifying the hCO dead core. Using one of these measurements, it could be possible to determine a formula capable of predicting a total cell death count that included the hCO core, and apply it to any hCO section regardless of ICC antibodies used. To achieve this, it was necessary to assess a suitable method of labelling the different types of cell death.

The apoptotic marker cleaved-caspase 3 (CC3) (Jiang *et al.*, 2020) was chosen as a starting point. In E-hCOs, apoptotic cells were labelled by CC3 where nuclei appear condensed/undertaking pyknosis (Figure 3.8.A and 3.9.A). These cells were observed both around the ventricles and non-uniformly across the E-hCOs at Day 21. The pattern of expression of CC3 around the ventricles continued throughout the other timepoints, but at Day 30, CC3 was also found in the centre of the E-hCO, signifying a collection of apoptotic cells resembling the beginning of the dead core (Figure 3.8.B and 3.9.B). By Day 60, CC3 was present over a large area of the E-hCO but not uniformly, with variable fluorescence across areas within the core (annotated - Figure 3.8.C).

When reviewing how well the universal measurements correlate to $DAPI^{+}/CC3^{+}$ count in Control #1 E-hCOs, the uniformed constant of APD had consistently high R^2 values, with the highest average R^2 value across timepoints of all five metric analyses (R^2=0.971), and when n>3 E-hCOs, the association was statistically different from an R^2 value of 0 (Figure 3.10.J and 3.10.O). Where n=3 E-hCOs, the association was not statistically significant (Figure 3.10.E), however the substantial F values provided confidence in the association to derive predictions of cell apoptosis. The same cannot be said of Control #2 E-hCOs, where cell count had the highest average R^2 value (R^2=0.951), however APD had the second highest average R^2 value (R^2=0.91). Due to minimal replicates (n=3 hCOs), no analysis in Figure 3.11 achieved significant deviation from zero, despite substantial F and R^2 values. It was noted that area had an exceptionally poor relationship to CC3 count in Control #2 E-hCOs at Day 60 specifically (R^2=0.051) (Figure 3.11.L). These results coincided with the substantial differences found in fluorescence intensity between Control #1 and Control #2 E-hCOs. However. the appropriate localisation of the CC3 to pyknotic nuclei around ventricles, as well as

in amassed central areas in Day 30 and Day 60 E-hCOs, indicated that CC3 is highlighting the anticipated total cell death.

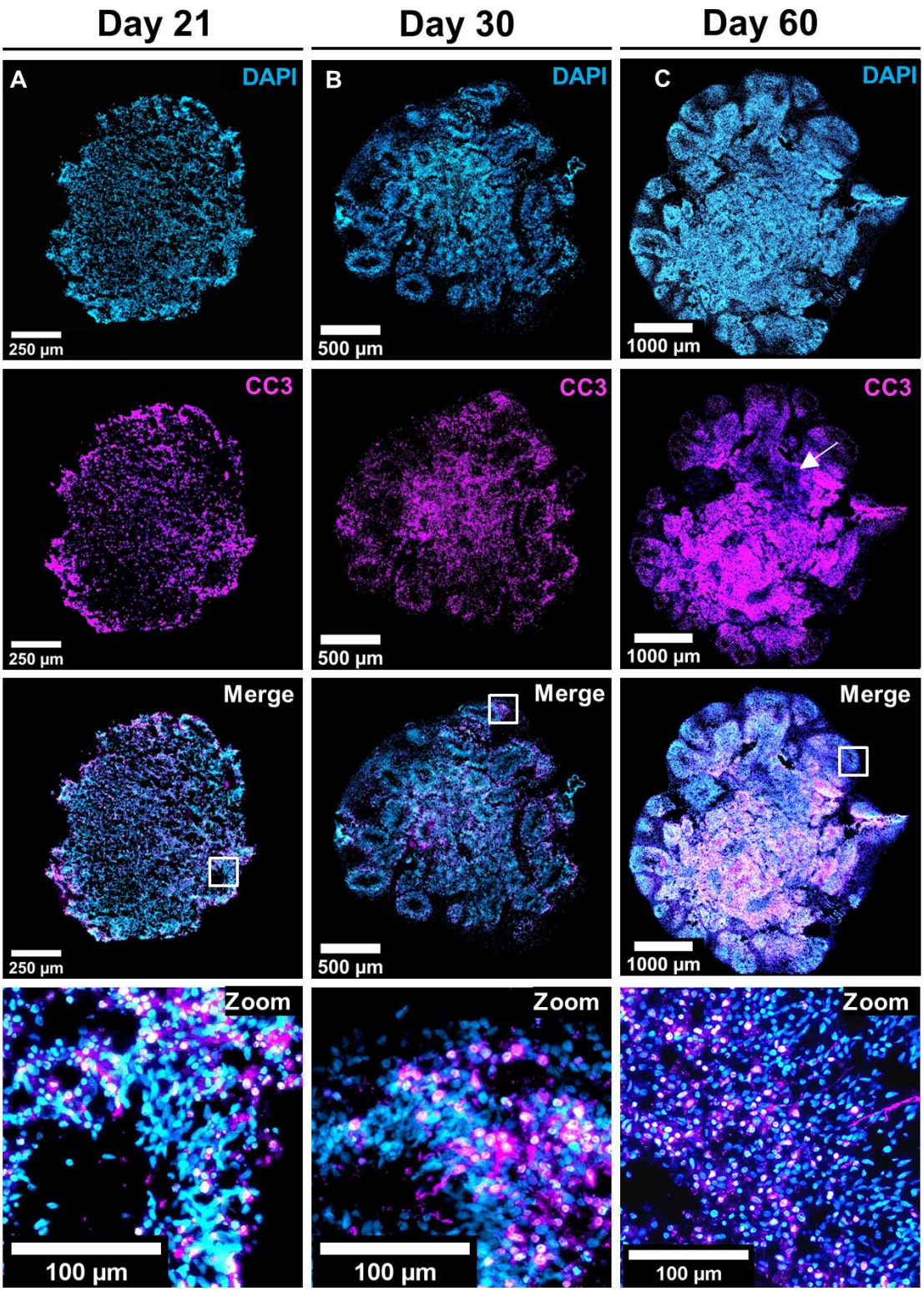

Figure 3.8: Cleaved-caspase 3 was localised to apoptotic cells around the VZ and the dead core of Control #1 E-hCOs.

Representative fluorescent images of Control #1 E-hCOs at Day 21 **(Column A),** Day 30 **(Column B)** and Day 60 **(Column C),** stained for either DAPI or CC3; whole E-hCO merged fluorescent images annotated with white box signifying zoomed region of interest (ROI). White arrow annotation points to areas of low fluorescence (**Figure 3.10**). Protein expressed referenced in image, scale bar = 250/500/1000 µm (full image) or 100 µm (zoomed ROI).

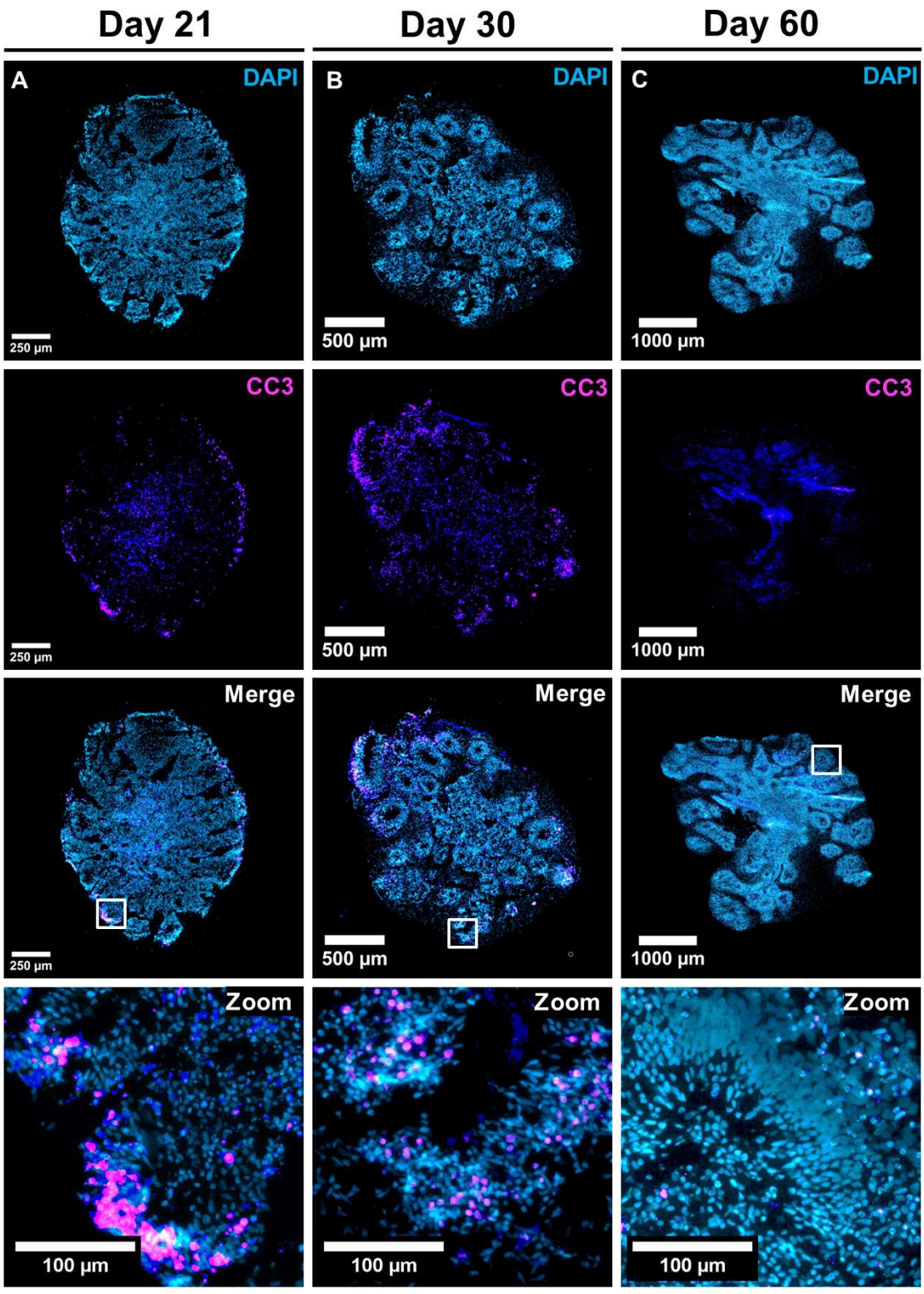

Figure 3.9: Cleaved-caspase 3 was localised to apoptotic cells around the VZ and the dead core of Control #2 E-hCOs.

Representative fluorescent images of Control #2 E-hCOs at Day 21 **(Column A),** Day 30 **(Column B)** and Day 60 **(Column C),** stained for either DAPI or CC3; whole E-hCO merged fluorescent images annotated with white box signifying zoomed region of interest (ROI). White arrow annotation points to areas of low fluorescence (**Figure 3.10**). Protein expressed referenced in image, scale bar = 500 µm (full image) or 100 µm (zoomed ROI).

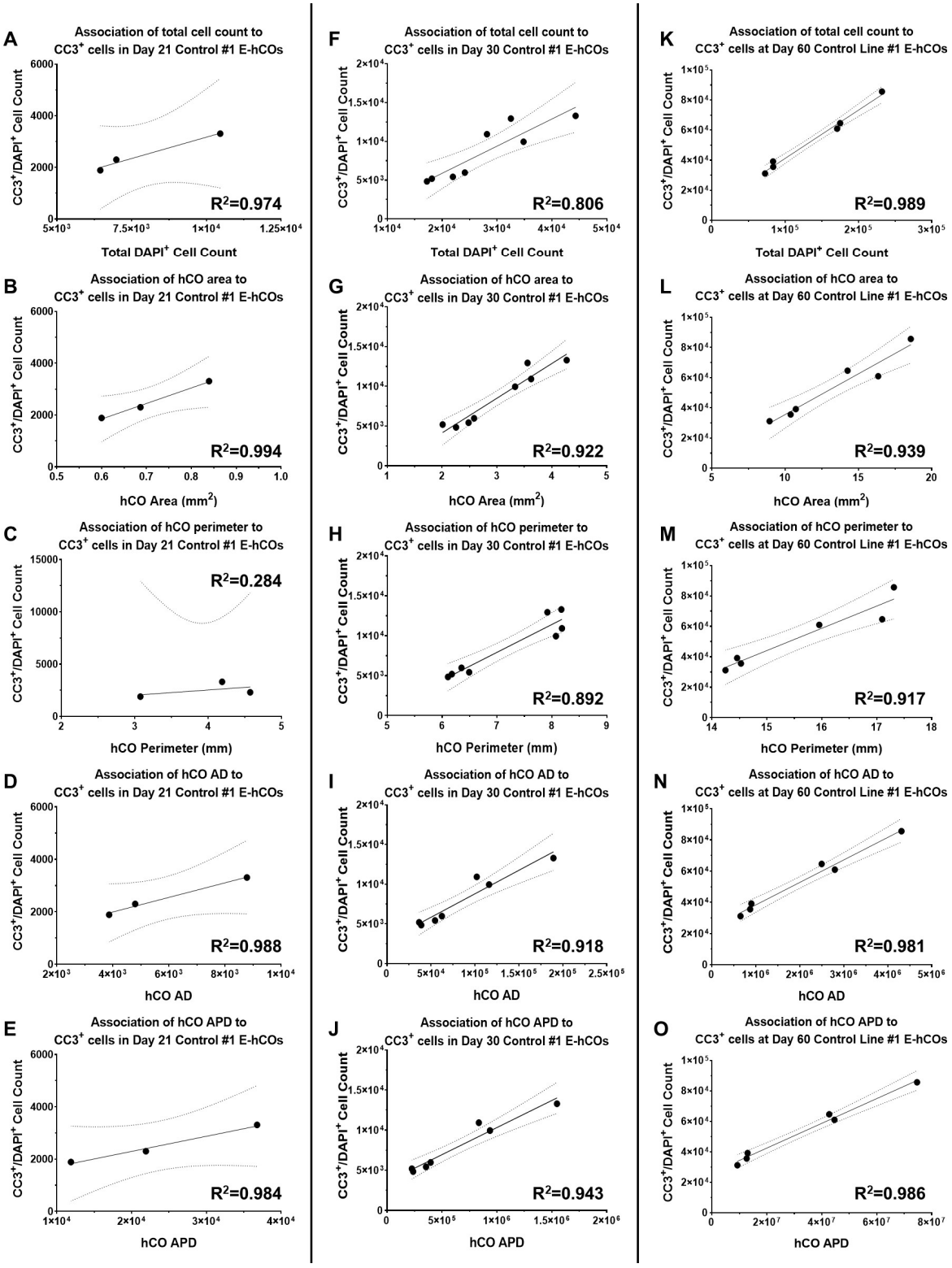

Figure 3.10: APD outperformed individual measurements and AD for correlation with total CC3 count in Control #1 E-hCOs across three timepoints.

Figure legend on following page.

Figure 3.10 (above): APD outperformed individual measurements and AD for correlation with total CC3 count in Control #1 E-hCOs across three timepoints. Linear regression analysis of cleaved-caspase 3 count against individual measurements, area multiplied by cell count (AD) and area, perimeter and total cell count multiplied together (APD) of Day 21, Day 30 and Day 60 Control #1 E-hCOs. **A)** Day 21 - Total cell count: F(1,1)=36.84, p=0.104, **B)** Day 21 - Area: F(1,1)=161.7, p=0.05, **C)** Day 21 - Perimeter: F(1,1)=0.396, p=0.642, **D)** Day 21 – AD: F(1,1)=84.79, p=0.069, **E)** Day 21 – APD: F(1,1)=63.25, p=0.08, **F)** Day 30 - Total cell count: F(1,6)=24.99, p=0.003, **G)** Day 30 – Area: F(1,6)=71.32, p=0.0002, **H**) Day 30 – Perimeter: F(1,6)=49.51, p=0.0004, **I)** Day 30 – AD: F(1,6)=56.01, p=0.0007, **J)** Day 30 – APD: F(1,6)=82.22, p=0.0003, **K)** Day 60 – Total cell count: F(1,4)=342.7, p=<0.0001, **L)** Day 60 – Area: F(1,4)=61.67, p=0.0014, **M)** Day 60 – Perimeter: F(1,4)=43.98, p=0.0027, **N)** Day 60 – AD: F(1,4)=200.8, p=0.0001, **O)** Day 60 – APD: F(1,4)=285.8, p=<0.0001. Bold line represents line of best fit, dashed lines represent 95% CIs, R^2 value is referenced within image.

Figure 3.11 (below): APD outperformed individual measurements and AD for correlation with total CC3 count in Control #2 E-hCOs across three timepoints. Linear regression analysis of cleaved-caspase 3 count against individual measurements, area multiplied by cell count (AD) and area, perimeter and total cell count multiplied together (APD) of Day 21, Day 30 and Day 60 Control #2 E-hCOs. **A)** Day 21 - Total cell count: F(1,1)=36.84, p=0.104, **B)** Day 21 – Area: F(1,1)=161.7, p=0.05, **C)** Day 21 – Perimeter: F(1,1)=0.396, p=0.642, **D)** Day 21 – AD: F(1,1)=84.79, p=0.069, **E)** Day 21 – APD: F(1,1)=63.25, p=0.08, **F)** Day 30 – Total cell count: F(1,1)=10.19, p=0.193, **G)** Day 30 – Area: F(1,1)=58.64, p=0.083, **H)** Day 30 – Perimeter: F(1,1)=0.607, p=0.579, **I)** Day 30 – AD: F(1,1)=15.00, p=0.161, **J)** Day 30 – APD: F(1,1)=30.40, p=0.114, **K)** Day 60 – Total cell count: F(1,1)=29.05, p=0.117, **L)** Day 60 – Area: F(1,1)=49.15, p=0.090, **M)** Day 60 – Perimeter: F(1,1)=1.395, p=0.447, **N)** Day 60 – AD: F(1,1)=155.4, p=0.051, **O)** Day 60 – APD: F(1,1)=71.20, p=0.075. Bold line represents line of best fit, dashed lines represent 95% CIs, R^2 value is referenced within image.

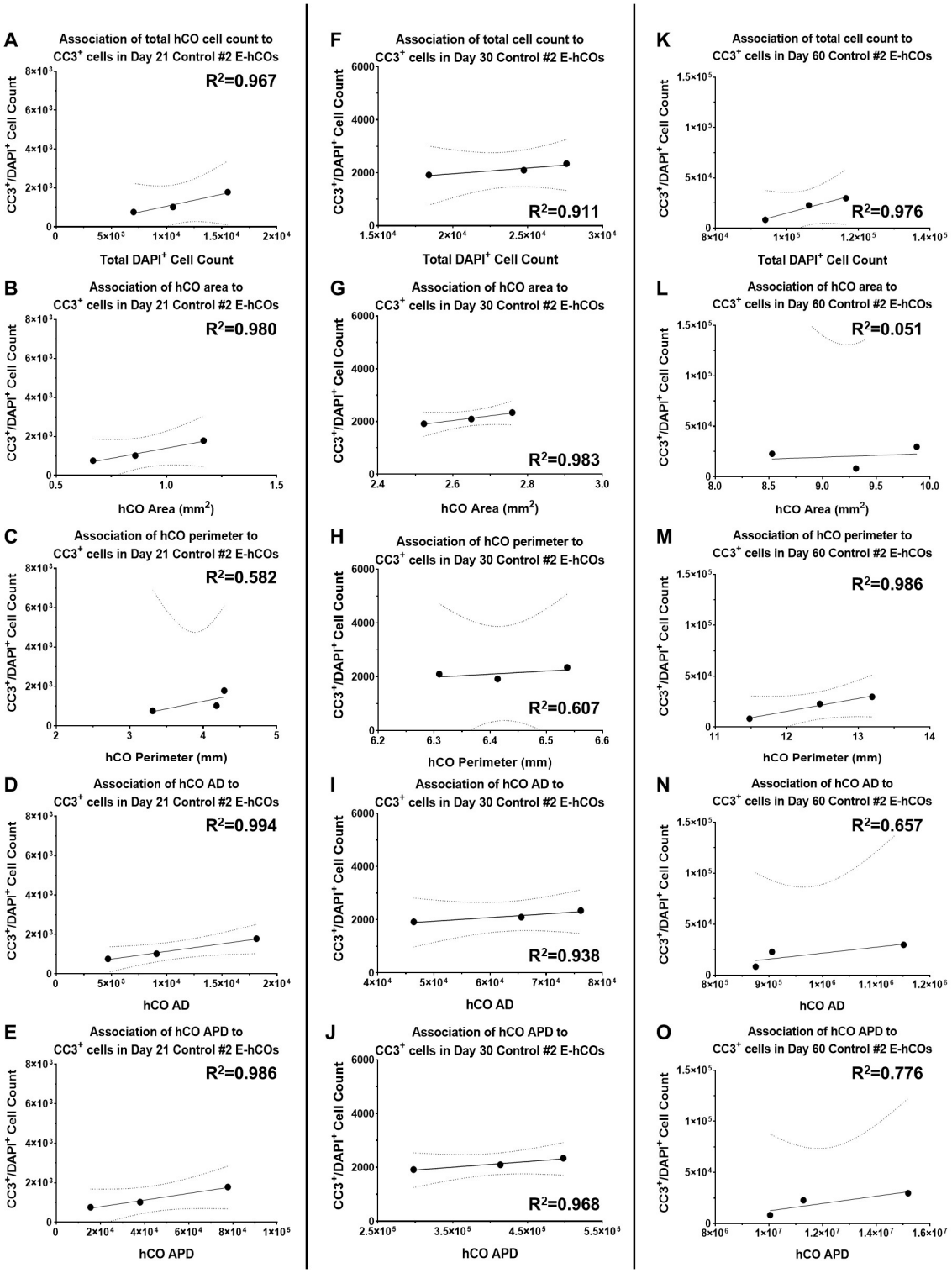

Figure 3.11: APD outperformed individual measurements and AD for correlation with total CC3 count in Control #2 E-hCOs across three timepoints.

Figure legend on previous page.

For comparison with CC3, an alternative cell death assay, the TUNEL assay, was examined. The TUNEL assay is designed to bind fluorescently-tagged dUTPs to DNA double stranded breaks (DSBs), a characteristic present in apoptosis and necrosis (Perry, Epstein and Gelbard, 1997). Similarly to CC3 in E-hCOs, TUNEL bonded to condensed nuclei, perceived to be apoptotic cells, that surrounded ventricles. TUNEL also bound to a significant number of nuclei present in the dead core, albeit with CC3-like regions of variable fluorescence intensity (Figure 3.12 and 3.13). Additionally, there was a reduction in fluorescence intensity of TUNEL in Control #2 E-hCOs compared to Control #1 E-hCOs across all timepoints, similar to what was observed in CC3 staining (Figure 3.12 and 3.13).

The linear regression analysis of TUNEL count against the universal measurements had a similar pattern to what was observed in CC3 analyses. In Control #1 E-hCOs (Figure 3.14), APD had the highest average R^2 value (R^2=0.695), as well as having the only regression that significantly deviated away from zero (Figure 3.14.E). It was noticeable that Control #1 Day 30 E-hCOs had particularly low R^2 values (R^2=≤0.284) for all metrics against TUNEL count, compared to other timepoints and Control #2 E-hCOs (Figure 3.14.F-J and Figure 3.15). In Control #2 (Figure 3.15), R^2 values were substantially higher across all measurements and timepoints compared to Control #1, but APD had the second lowest average R^2 value (R^2=0.838), whereas AD had the highest (R^2=0.906). However, F and p values were limited due to replicate number and no singular regression deviated significantly from zero.

The intention of these cell death assays was to create a post-hoc adjustment to total cell count across all ICC slides of hCOs, including those that had not been stained for either CC3 or TUNEL. It was therefore essential to choose the normalising constant with the highest average R^2 value to ensure prediction of cell death was as accurate as possible. In light of the outcomes of these cell death assays, APD was considered the best choice of normalising constant. In almost all regression analyses conducted across both CC3 and TUNEL investigations, APD had a high average R^2 value compared to AD or individual measurements and when n>3 E-hCOs, the regression significantly deviated from zero.

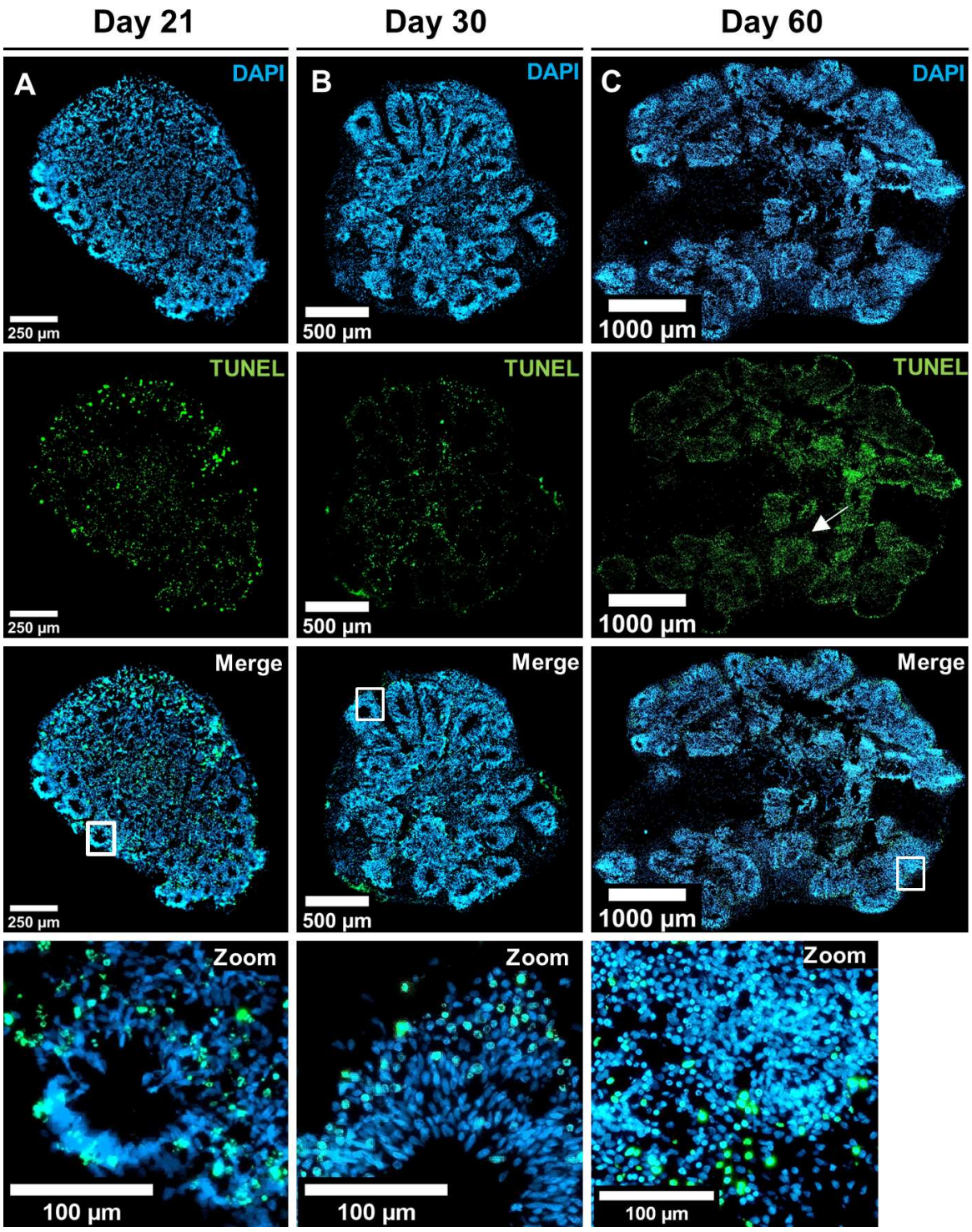

Figure 3.12: TUNEL staining was localised to both apoptosis around the VZ and the dead core of E-hCOs.

Representative fluorescent images of Control #1 E-hCOs at Day 21 **(Column A),** Day 30 **(Column B)** and Day 60 **(Column C),** stained for either DAPI or TUNEL; whole E-hCO merged fluorescent images annotated with white box signifying zoomed region of interest (ROI). White arrow annotation points to areas of low fluorescence (**Figure 3.10**). Protein expressed referenced in image, scale bar = 250/500/1000 µm (full image) or 100 µm (zoomed ROI).

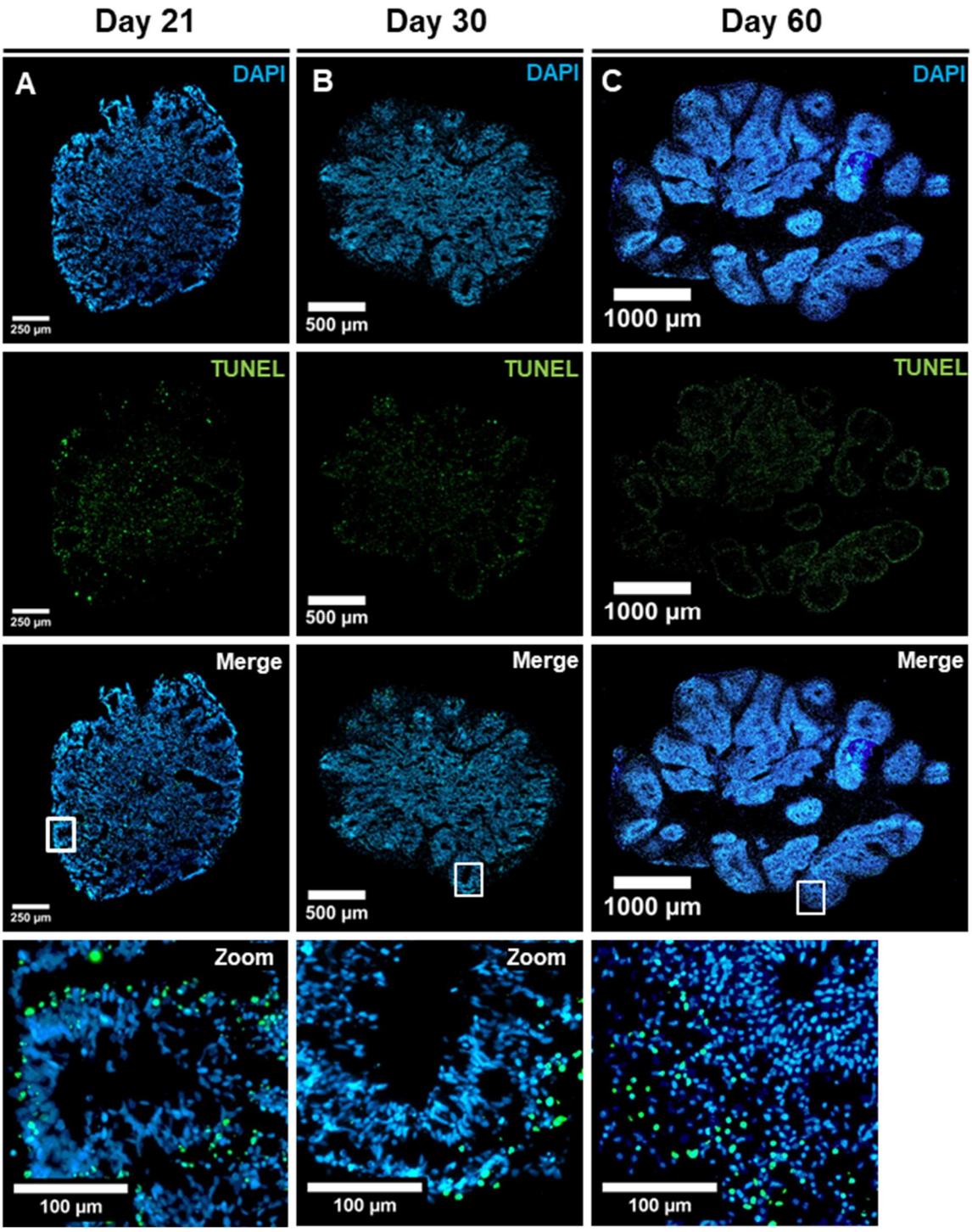

Figure 3.13: TUNEL staining was localised to both apoptosis around the VZ and the dead core of E-hCOs.

Representative fluorescent images of Control #2 E-hCOs at Day 21 **(Column A),** Day 30 **(Column B)** and Day 60 **(Column C),** stained for either DAPI or TUNEL; whole E-hCO merged fluorescent images annotated with white box signifying zoomed region of interest (ROI). White arrow annotation points to areas of low fluorescence (**Figure 3.10**). Protein expressed referenced in image, scale bar = 250/500/1000 µm (full image) or 100 µm (zoomed ROI).

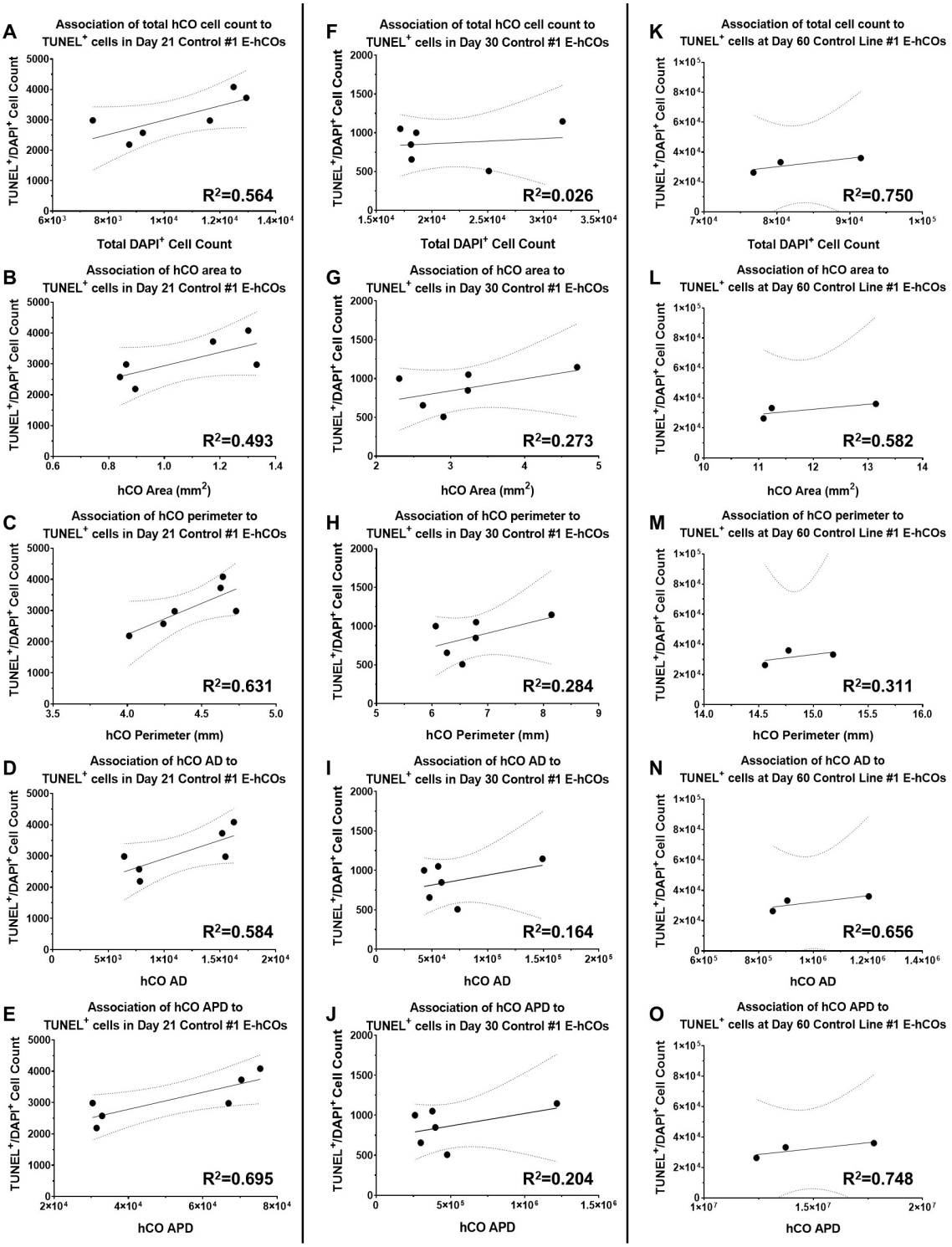

Figure 3.14: APD outperformed individual measurements and AD for correlation with total TUNEL count in Control #1 E-hCOs across three timepoints.

Figure legend on proceeding page.

Figure 3.14 (above): APD outperformed individual measurements and AD for correlation with total TUNEL count in Control #1 E-hCOs across three timepoints.

Linear regression analysis of TUNEL count against individual measurements, area multiplied by cell count (AD) and area, perimeter and total cell count multiplied together (APD) of Day 21, Day 30 and Day 60 Control #1 E-hCOs. **A)** Day 21 - Total cell count: $F(1,4)=5.178$, $p=0.085$, **B)** Day 21 – Area: $F(1,4)=3.895$, $p=0.120$, **C)** Day 21 – Perimeter: $F(1,4)=6.841$, $p=0.059$, **D)** Day 21 – AD: $F(1,4)=5.613$, $p=0.077$, **E)** Day 21 – APD: $F(1,4)=9.095$, $p=0.039$, **F)** Day 30 – Total cell count: $F(1,4)=0.106$, $p=0.761$, **G)** Day 30 – Area: $F(1,4)=1.499$, $p=0.288$, **H)** Day 30 – Perimeter: $F(1,4)=1.589$, $p=0.276$, **I)** Day 30 – AD: $F(1,4)=0.785$, $p=0.426$, **J)** Day 30 – APD: $F(1,4)=1.022$, $p=0.369$, **K)** Day 60 – Total cell count: $F(1,1)=3.005$, $p=0.333$, **L)** Day 60 – Area: $F(1,1)=1.394$, $p=0.447$, **M)** Day 60 – Perimeter: $F(1,1)=0.450$, $p=0.624$, **N)** Day 60 – AD: $F(1,1)=1.904$, $p=0.399$, **O)** Day 60 – APD: $F(1,1)=2.960$, $p=0.335$. Bold line represents line of best fit, dashed lines represent 95% CIs, R^2 value is referenced within image.

Figure 3.15 (below): APD underperformed for correlation with total TUNEL count in Control #2 E-hCOs across three timepoints.

Linear regression analysis of TUNEL count against individual measurements, area multiplied by cell count (AD) and area, perimeter and total cell count multiplied together (APD) of Day 21, Day 30 and Day 60 Control #2 E-hCOs. **A)** Day 21 - Total cell count: $F(1,1)=14.91$, $p=0.161$, **B)** Day 21 – Area: $F(1,1)=1.955$, $p=0.395$, **C)** Day 21 – Perimeter: $F(1,1)=49.07$, $p=0.090$, **D)** Day 21 – AD: $F(1,1)=4.924$, $p=0.270$, **E)** Day 21 – APD: $F(1,1)=3.482$, $p=0.313$, **F)** Day 30 – Total cell count: $F(1,1)=19.75$, $p=0.141$, **G)** Day 30 – Area: $F(1,1)=164.0$, $p=0.05$, **H)** Day 30 – Perimeter: $F(1,1)=12.14$, $p=0.178$, **I)** Day 30 – AD: $F(1,1)=23.01$, $p=0.131$, **J)** Day 30 – APD: $F(1,1)=20.53$, $p=0.138$, **K)** Day 60 – Total cell count: $F(1,2)=4.552$, $p=0.167$, **L)** Day 60 – Area: $F(1,2)=14.31$, $p=0.063$, **M)** Day 60 – Perimeter: $F(1,2)=1.943$, $p=0.298$, **N)** Day 60 – AD: $F(1,2)=9.723$, $p=0.089$, **O)** Day 60 – APD: $F(1,2)=7.214$, $p=0.115$. Bold line represents line of best fit, dashed lines represent 95% CIs, R^2 value is referenced within image.

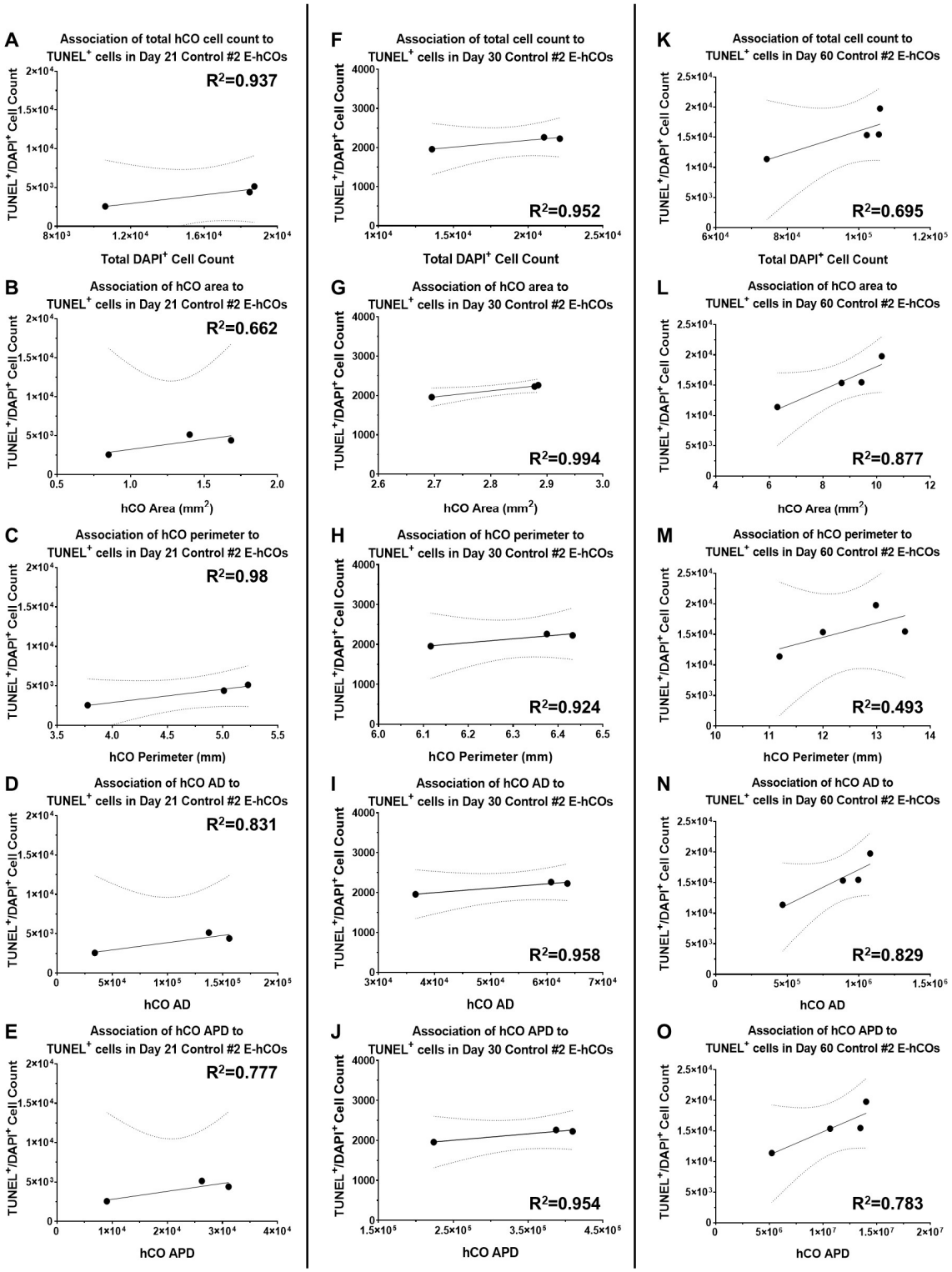

Figure 3.15: APD underperformed for correlation with total TUNEL count in Control #2 E-hCOs across three timepoints.

Figure legend on previous page.

In review of the two cell death markers, CC3 was considered a better choice for cell death analysis, as the predictive accuracy was predominantly higher and more consistent than the TUNEL assay. It was, however, important to confirm if CC3 and TUNEL target the same cells, so as not to misrepresent cell death values. Additionally, it was important to establish if using APD would distort the representation of either cell death assay. Comparing these two investigations simultaneously, it was possible to determine how CC3 and TUNEL relate to one another, as well as how singular measurements, such as total cell count, can skew the outcome (Figure 3.16). Qualitatively, there was little difference between TUNEL and CC3 in their localisation (Figure 3.8 - 3.9 and 3.12 – 3.13). However, distinct differences between CC3 and TUNEL count were visible, either when taken as a percentage of the total cell count or when normalised to APD. Firstly, the cell line-specific variation in total cell count at Day 21 for Control #2 (Figure 3.16.A) disappeared when the same count values were normalised to APD (Figure 3.16.D), resulting in no differences between CC3 and TUNEL for every observed timepoint of Control #2. Secondly, the disparity between CC3 and TUNEL in Control #1 at Day 30 was consistently observed in both total cell count (Figure 3.16.B) and when normalised to APD (Figure 3.16.E). Furthermore, in Control #1 Day 21 E-hCOs, when normalised to APD, CC3 followed the Day 30 trend and was similarly increased when compared to TUNEL (Figure 3.16.D). Despite cell line-specific exceptions, these results supported the idea that the TUNEL assay and CC3 staining labels the same type of dead cells, apoptotic cells. These observations also supported the use of the APD over singular measurements to mitigate any single measurement bias when normalising live cell count data, as well as quantifying cell death or other non-cell count data.

As count data was to be used significantly throughout this research, it was necessary to see how the cell death “adjustment” would affect both the quantity and variance of live cell populations. Using one of the prolifically expressed proteins found in the forebrain, FOXG1, as a proxy for live cells, it was clear that the CC3-associated cell death adjustment to total cell count made a significant difference to the representative percentage of FOXG1 in an E-hCO (Figure 3.17). The significant increase in FOXG1 percentage was consistent for both cell lines across all three timepoints, excluding Control #2 at Day 60 (Figure 3.17.C). It was also noted that the variance in the data was maintained after adjustment for CC3-

associated cell death. APD-predicted CC3-associated adjustment to total cell count was therefore considered a closer representation of the total “live” cell count and a better choice for normalising raw count data than using unadjusted total cell count.

However, the quantity of CC3 cells was not considered an adequate reflection of the anticipated total cell death (Figure 3.16); based on Figure 3.8 and 3.12, an estimated ≥50% of the cellular mass of the E-hCO was within the dead core region. Similarly, after cell death adjustment, FOXG1 represented less than half of the total cell population at Day 60 (Figure 3.17.C). To investigate why a large percentage of cells were unaccounted for, the regions that showed uneven fluorescence in CC3 and TUNEL imaging were scrutinised (Figure 3.8, 3.12 and 3.18). In the unevenly fluorescing dead core regions of the apoptotic marker-stained Control #1 E-hCO (Figure 3.18), close inspection of the cell nuclei portrayed a heterogenous mix of apoptotic-labelled and unlabelled cells. Apoptotic nuclei were identifiable by CC3 or TUNEL, as well as the spherical, rounding of the nuclei (pyknosis) and DNA condensation, represented by high DAPI fluorescence. $DAPI^{+}/CC3^{-}$ and $DAPI^{+}/TUNEL^{-}$ nuclei were not undergoing pyknosis, but instead had low and uneven DAPI fluorescence intensity, inconsistent distribution of DNA and appeared lysed in areas (Figure 3.18). This illustrated that both cell death assays were not representing this secondary population of caspase-independent dead cells within the dead core. Without a known means of quantifying this cell population in an ICC format, it was only possible to quantify a hCO’s total apoptotic cell count using CC3 staining, as opposed to a total cell death count.

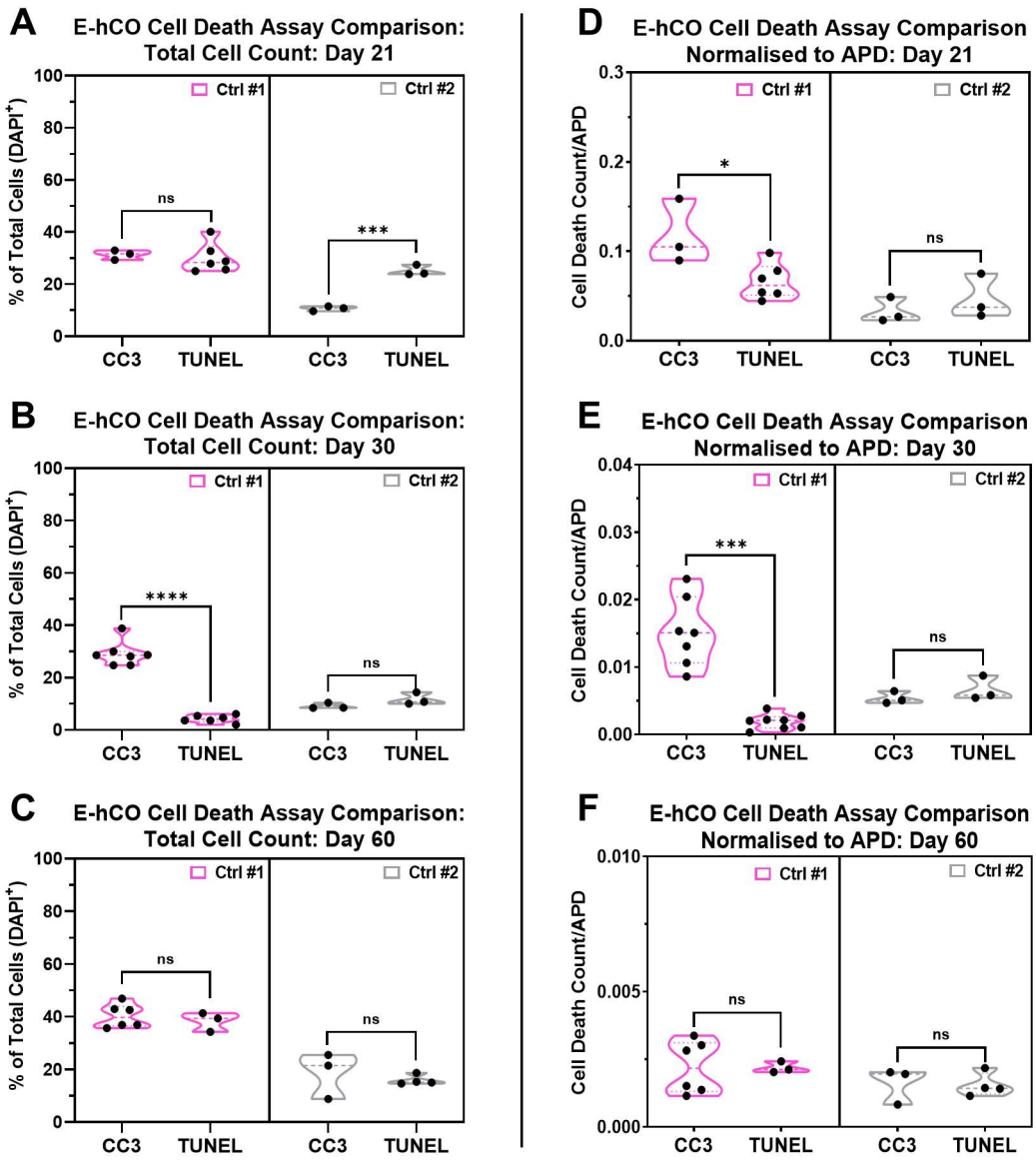

Figure 3.16: CC3 and TUNEL did not consistently share values over time, but APD mitigated single measurement bias for both cell death assays.

Comparison of TUNEL and CC3 assays in E-hCOs for total cell count and when normalised to APD, at Day 21, Day 30 and Day 60. Truncated violin plots, separated by control cell line, of $CC3^+$ /$DAPI^+$ and $TUNEL^+$ /$DAPI^+$ in Day 21, Day 30 and Day 60 E-hCOs as a percentage of total cell count **(A-C)** or normalised to APD **(D-F)**. Statistical analysis conducted using unpaired, two-tailed t-tests with Welch's correction; ns=not significant, *p=<0.05, **p=<0.005, ***p=<0.0005, ****p=<0.0001.

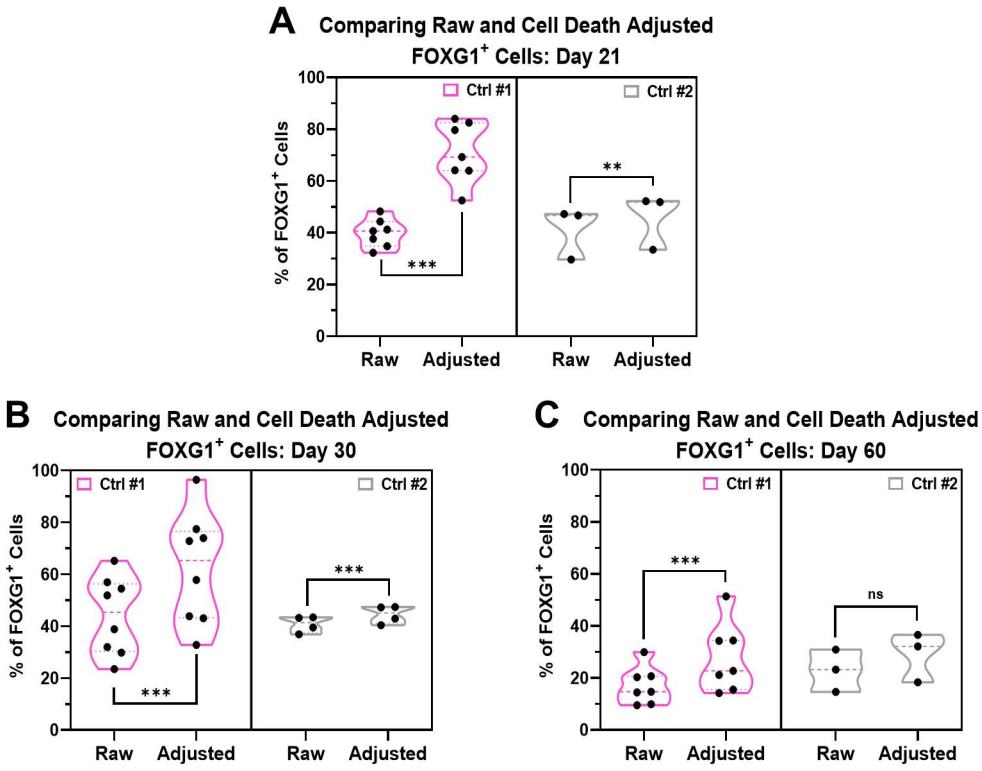

Figure 3.17: Proof-of-concept analysis for cell death adjustment using CC3/APD predicted values illustrated cell death adjustment significantly increased live cell population but retained data variance.

Comparison of FOXG1$^+$ cells as a percentage of total cell count ("raw") or as a percentage of the adjust cell count that has removed the APD-predicted CC3 count ("adjusted") in E-hCOs. Truncated violin plots, separated by control cell line, of Day 21 **(A)**, Day 30 **(B)** and Day 60 **(C)** E-hCOs. Statistical analysis conducted using paired, two-tailed t-tests; ns=not significant, *p=<0.05, **p=<0.005, ***p=<0.0005, ****p=<0.0001.

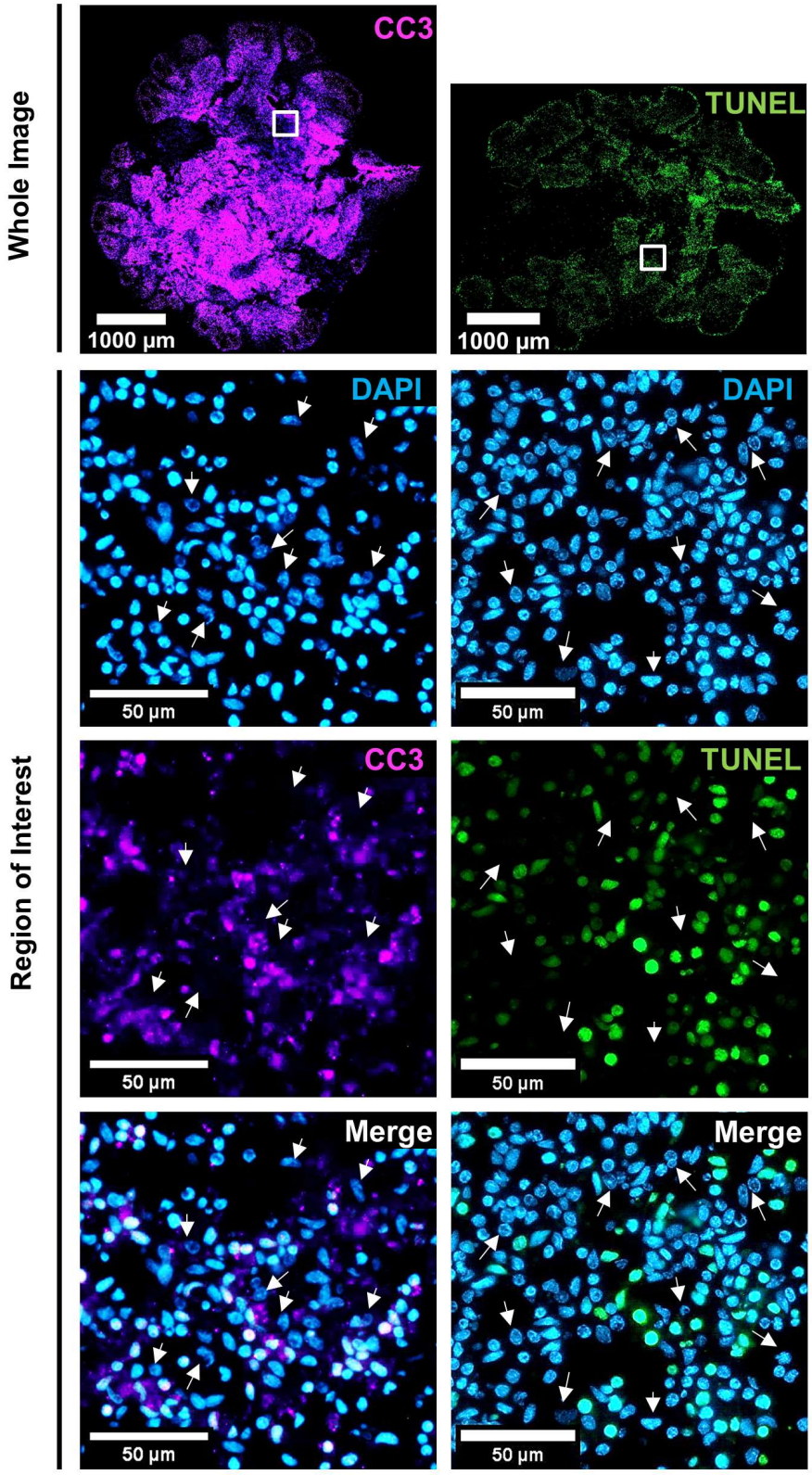

Figure 3.18: Unlabelled nuclei in dead E-hCO core exhibited abnormal morphology. Whole section fluorescent images from Figure 3.8 (CC3) and Figure 3.11 (TUNEL) with isolated regions of interest to examine the uneven fluorescence in the dead E-hCO core. White box annotations indicate regions of interest, white arrow annotations represent DAPI+/TUNEL- or DAPI+/CC3- nuclei. Protein expressed referenced in image, scale bar = 1000 µm or 50 µm.

3.5 Discussion

3.5.1 Assessment of Human Induced Pluripotent Stem Cell Lines Confirms Pluripotency

hIPSCs pluripotency is relative to the cell culture in which they are kept (Kilens *et al.*, 2018), but there is no specific information about E8F's influence on stem cell identity. The results of Figure 3.4 indicated that E8F media maintained a heterogenous mix of naïve (*KLF4* and *NANOG*) and universal pluripotency stem cell markers (*OCT4* and *SOX2*), with low expression of developmental lineage-specific transcription factors (*PAX6, TBXT* and *SOX17*). However, both Control #1 and #2 hIPSCs transcribed *NES* to a significant level, an intermediate filament gene associated with the neuroectodermal lineage (D'Aiuto *et al.*, 2014) (Figure 3.4.C). The expression of nestin was localised specifically to the neural rosette formations in ectodermal cells from the hIPSC lines, differentiated using the trilineage kit (Figure 3.1.A, 3.2.A and 3.3.A). These rosette formations were not observed in the undifferentiated hIPSC lines used in this research, and so it is likely that *NES* is only transcribed but not translated.

The trilineage assessment confirmed the pluripotency of the stem cells used in this study, however, in ideal circumstances, there would have been three independent differentiations of each lineage for each cell line. Days in culture were also reduced by one day each compared to the kit instructions, as mesodermal cells would lift off and be lost by Day 5, leaving no cells behind for analysis. The reduction in *NES* in Control #2 is of concern (Figure 3.2.A), as it was the only cell line across all 3 cell lines tested that exhibited a decrease in any lineage marker. However, previous research in 2D neuronal models that used Control #2 had no known significant disparities in data when compared to Control #1 (Chapman *et al.*, 2021).

3.5.2 Day 5 Embryoid Bodies are Neither Human Induced Pluripotent Stem Cells Nor Neuroectodermal Spheroids

The comparison of transcriptional profiles of hIPSCs, Day 5 E-EBs and Day 11 E-hCOs illustrated a significant shift in cell fate relative to the change in culturing method, from 2D hIPSCs to their 3D E-EB counterparts (Figure 3.4). This shift was anticipated based off previous literature (Kibschull *et al.*, 2016; Kim *et al.*, 2020; Tremble *et al.*, 2021), however, what exactly was occurring in this study's E-EBs was not immediately obvious.

One explanation is that the stem cell population had transitioned from a state of naïve to primed stem cells upon changing to non-adherent culture. This was suggested as, at Day 5, E-EBs had significantly upregulated transcription of the universal stem cell markers *OCT4* and *SOX2*, whereas the naïve-specific *NANOG* and *KLF4* were significantly downregulated (Figure 3.4.A). Mouse embryos and ESCs present similar patterns when the stem cells transition from a naïve to a primed state (Kalkan *et al.*, 2017). Other hIPSC-derived EBs also replicate this outcome after 7 days of serum-based self-directed differentiation (Kibschull *et al.*, 2016). There was also evidence of a delayed response in transcriptional downregulation between *NANOG,* and *OCT4* and *SOX2* (Figure 3.4.A). In mouse IPSC-derived EBs, *NANOG* transcription dropped from substantial to residual levels three days post-EB formation as stem cells transitioned away from a naïve state; *OCT4*, on the other hand, did not significantly reduce until seven days post-EB formation (Tremble *et al.*, 2021). The hypothesis of transitioning between states of pluripotency is also supported by the downregulation of *NANOG*, as *NANOG* expression is still present but low in primed stem cells (Abranches *et al.*, 2014; Acampora *et al.*, 2017). However, when reviewing *KLF4* expression, it is not as simple. *KLF4* expression is low in naïve hIPSCs compared to other naïve transcription factors of the same gene family, i.e. *KLF17* (Abdyyev *et al.*, 2020; Dodsworth *et al.*, 2020). *KLF4* transcription was downregulated in Day 5 E-EBs, a result expected if the EB was residing in a primed stem cell state. Surprisingly, at Day 11, *KLF4* expression resolved to an expression akin to hIPSC; it was not apparent in this study why the Day 11 E-hCOs would increase transcription of *KLF4* post-neuroectodermal induction.

An alternative interpretation to the naïve-to-primed stem cell theory, is that E-EBs are undergoing spontaneous neuroectodermal differentiation as a response to reorganising the cells into a 3D format. The transcriptional pattern of acute *NANOG* downregulation and a delayed *OCT4* response post-EB formation reflected what has been previously observed in spontaneously differentiating EBs (Tremble *et al.*, 2021). There is further evidence to this theory when investigating ectodermal lineage markers. Alongside *SOX2* upregulation, *PAX6*, *NES* and *NCAM* transcription was also significantly increased at Day 5 (Figure 3.4.C), all of which are neuroectodermal, intermediate filament and neurogenesis markers, respectively. hIPSC-derived EBs that undertook self-directed differentiation with FBS reported significant increases in *NCAM* and *PAX6* after 7 days of culture, but

NES remained unchanged (Kibschull *et al.*, 2016). However, other studies on hIPSC-derived EBs showed evidence of increased expression of all three developmental lineages relatively equally, including $PAX6^+$ cells, after 4-6 days of self-directed patterning (Xie *et al.*, 2017; Abdyyev *et al.*, 2020). In line with this evidence, the mesodermal marker *TBXT* was expressed equally in hIPSCs and Day 5 E-EBs (Figure 3.4.B), which would be expected to reduce if E-EBs pluripotency was being lost to the neuroectodermal fate.

A further conflicting point of evidence to both hypotheses is that *KI67* transcription increased after neuroectodermal induction at Day 11 (Figure 3.4.D). KI67 expression in any cycling cell fluctuates relative to the cell cycle process, i.e. high during active mitosis, low during interphase; it is not expressed in G_0 quiescent cells. The cell cycle of hIPSCs is 16-18 hours (Ghule *et al.*, 2011), but could vary between naïve and primed states similar to human ESCs (Messmer *et al.*, 2019). On the other hand, if Day 5 E-EBs are transitioning to a neuroectodermal fate, that identity could be neuroepithelial cells (NECs). NECs' cell cycle is considerably shorter (~8 hours) during early development and becomes longer at later stages due to an extension of the G_1 phase (Liu *et al.*, 2019). This would lead to the belief that *KI67* transcription would be higher if significant NECs were present, as cells are entering mitosis more often. The lack of increased *KI67* transcription in Day 5 E-EBs would imply that the original assumption of a naïve-to-primed stem cell shift is correct. On the other hand, it is also possible that the change in *KI67* transcription only occurs at Day 11 because, like hIPSCs, two states of NECs are represented: primitive and mature/definitive. Originally defined by their lack of requirement for EGF and FGF *in vitro* unlike their mature counterparts (Hitoshi *et al.*, 2004), primitive NECs retain a level of multiipotency akin to stem cells (Lee *et al.*, 2010), whilst also expressing elements of NECs such as *SOX1* and *NES* expression (Akamatsu *et al.*, 2009). A different NEC state could influence *KI67* transcription, although the changes in cell cycle length between hIPSCs and NECs does not specify the state of either (Ghule *et al.*, 2011; Liu *et al.*, 2019).

Other notable cell cycle mediators, *P53* and *PAX3*, were included in the assessment as both have key roles in the development of neural tube disorders (Pani, Horal and Loeken, 2002; Wang *et al.*, 2017). Although the first 11 days of hCO culture are not representative of neural tube development, they do undertake similar morphological processes, such as forming a circular ring of NECs (Adhya

et al., 2021; Beghin *et al.*, 2022). In Day 5 E-EBs, the lack of change to *P53* transcription was likely a representation of minimal change in *P53*-dependent apoptosis and cellular stress during differentiation (Figure 3.4.D) (Haronikova *et al.*, 2019). *PAX3* transcription, on the other hand, significantly increased after 3D aggregation (Figure 3.4.C). PAX3 is a transcription factor that aids in forming the neural plate border, facilitates cell apoptosis during NTC and is a marker of neural crest cell progenitors (Pani, Horal and Loeken, 2002; Britton *et al.*, 2019; Mehler *et al.*, 2020; So *et al.*, 2020). It is minimally expressed in hIPSCs (Kobayashi *et al.*, 2020) and so the increase in *PAX3* transcription from Day 5 onwards indicates that neuroectodermal borders were being set and neural rosettes are likely in the process of being formed.

Although it is unknown exactly when neural rosettes form in the Enhanced protocol, by Day 11 neural rosettes are visible on the surface of E-hCOs (Figure 5.2.A); studies have shown neural rosette formation on the surface of spheroids after a similar period of neuroectodermal induction to Day 11 E-hCOs (Adhya *et al.*, 2021; Beghin *et al.*, 2022). Previous studies have shown that EBs that spontaneously differentiate do not immediately form the characteristic rosettes of *in vitro* neuroectoderm, despite $PAX6^{+}$ cells being found on the surface (Abdyyev *et al.*, 2020). This would suggest that primitive NECs do not form characteristic rosettes until exogenous induction to a neuroectodermal fate; currently there are five known stages of neural rosette formation, transitioning from stem cell to NEC identity, that could include the various states of both cell types (Hříbková *et al.*, 2018).

In review, there are three proposed identities of Day 5 E-EBs: primed hIPSCs, spontaneously differentiating cells or primitive NECs. Firstly, primed hIPSCs would not express neuroectodermal markers to the level observed in Day 5 E-EBs (Ragheb *et al.*, 2020). There is more evidence to support spontaneous differentiation than primed hIPSCs, as mesodermal and ectodermal lineage markers' expression is either equal or greater than their hIPSC counterpart, but there is also substantially greater neuroectodermal representation. This is in opposition to what certain EB studies have concluded, that in the absence of exogenous, directed patterning, EBs form all three developmental lineages equally in an attempt to mimic early embryogenesis (Kibschull *et al.*, 2016; Kim *et al.*, 2020; Tremble *et al.*, 2021). The lack of the endodermal marker *SOX17* (Figure 3.4.B), as well as *OCT4* expression not reducing significantly (Figure 3.4.A), would

suggest that the Day 5 E-EBs were still multipotent to a degree. Primitive NECs ignore the drawbacks presented by the other two theories; primitive NECs retain stem cell-like multipotency but are predominately neural fated.

In conclusion, it is clear that refinement of EB generation is necessary. Despite improvements to the methodology, EB generating kits do not succeed in stabilising the stem cell state of aggregated cells, even when cultured over a short time (Figure 3.4) (Antonchuk *et al.*, 2010). It was, however, useful to compare Day 5 E-EBs to Day 11 E-hCOs to clarify the success of exogenous neuroectodermal induction. Considerable reduction in other developmental lineages (*TBXT, SOX17*), pluripotency markers (*NANOG* and *OCT4*) and significantly high neural marker expression all point to the homogenous, mature NEC identity of Day 11 E-hCOs (Figure 3.4.A-C). With the assumptions generated here about both Day 5 E-EBs and Day 11 E-hCOs, timepoint choice for modelling 1qDel could be more informed. Any translational research interested in early developmental patterning, particularly of ectodermal lineage, should therefore make allowances to assess EBs to record any significant changes and adapt experiments accordingly.

3.5.3 Successful Development of a Universal Cerebral Organoid Immunocytochemistry Pipeline and Normalising Constant

There is minimal literature addressing analysis of the internal cytoarchitecture of a cerebral organoid (Albanese *et al.*, 2020), particularly in a whole E-hCO section format. Multiple iterations of ideas capable of normalising an ICC-stained E-hCO section were pursued in this study through a series of informed trial and error, including the “live cell space”, individual measurements and AD/APD concepts. The exploration of current methods of ICC normalisation, and their flaws (Figure 3.5 and 3.6), was key to finding a suitable normalising measurement. Investigating the relationships of each measurement illustrated that the two most common means of normalising ICC measurements of cerebral organoids, by area or by cell count, were significantly correlated to one another (Figure 3.7.A, 3.7.D and 3.7.G). Similarly, the pair performed well singularly or combined together (AD) in linear regression analysis with the two cell death assays, CC3 and TUNEL, for both control E-hCOs (Figure 3.10, 3.11, 3.14 and 3.15). This confirms that, although not ideal, current literature using either metric for normalising ICC data is justifiable (Iefremova *et al.*, 2017; Mansour *et al.*, 2018; Klaus *et al.*, 2019; Zhang *et al.*, 2019; Dong *et al.*, 2021; Kang *et al.*, 2021).

However, using APD suits the requirements for a normalising constant for a whole E-hCO ICC section better than individual measurements, as it is able capable of buffering for any singular measurement when they sporadically underperform in regression analyses, i.e. cell count (Figure 3.14.F), area (Figure 3.11.L) and perimeter (Figure 3.10.C and Figure 3.15.M). It also showed consistently high R^2, F and p values (when n>3 E-hCOs) relative to the singular measurements and AD in regression analysis when applied to both cell death assays for both control cell lines (Figure 3.10, 3.11 and 3.14), with the exception of the TUNEL assay of Control #2 (Figure 3.15). Retrieving the information required for APD also requires minimal additional input and the variables can be collected from any ICC stain run through this study's ICC analysis pipeline. Perimeter and area can be measured automatically in the "PrepImage" macro, after manual drawing of a hCO's perimeter, which was required for image preparation prior to quantification. Centralised, 5-pixel DAPI masks are also required for all ICC analysis to determine accurate localisation of proteins of interest, and therefore total cell count is gathered without additional effort as well.

However, the high throughput ICC analysis pipeline still has room for improvement. Automation of drawing the outline of a E-hCO would be ideal and quicken the process considerably. Attempts were made to do so using plugins and macros such as FindEdges in ImageJ, but unfortunately the cell nuclei were not compact enough for clear edges to be found. A possible starting point to find edges automatically could be using a methodology similar to that of the MeasureObjectNeighbours module found in CellProfiler (McQuin *et al.*, 2018). A specific distance in pixels between one cell nuclei to another could determine the definition of a hCO's perimeter, although it may become difficult in cases of large lumen sizes or hCO damage from cryopreservation/cryosectioning. In the meantime, manual annotation should continue to be used.

The next iteration of this type of method would be to scale up from 2D sections of whole E-hCOs to using light-sheet microscopy with cleared E-hCOs to produce 3D ICC images. This has been conducted successfully in both small spheroids (Dekkers *et al.*, 2019) and larger cerebral organoids (Albanese *et al.*, 2020). To current knowledge, the study of Albanese *et al.*, (2020) is similar in aim to this chapter in providing an in-depth method in which to investigate spatial organisation of cerebral organoid cytoarchitecture. The SCOUT method proposed in this study requires access to specialist technology which may not be possible in

all labs and does not dictate a method of which to determine the dead cerebral organoid core. It did, however, illustrate that the internal morphology of a cerebral organoid varies relative to what z-slice is chosen for analysis, which was proven to affect the outcome of results (Albanese *et al.*, 2020). Using the APD metric to predict cell death for adjusting total live cell count, as well as normalising dead cell count and morphological data, aids in reducing this bias, as does choosing E-hCO sections from similar z-stacks for each ICC analysis. In the absence of such specialist equipment, the APD metric could be adapted to suit 3D ICC image acquisition, by replacing area with volume and perimeter with surface area. In its current state, the APD metric is capable of normalising ICC quantitative analysis but remains flexible for future development.

3.5.4 Cerebral Organoid Cores: Half Apoptotic, Half Necrotic

The purpose of creating the normalising constant was to find a method of normalising ICC analysis of whole E-hCO sections, with the intent to use it for predicting total cell death. This would produce a live cell count value with which to determine proportionality of cellular identities in the live cell populations. When reviewing the outcomes between the two chosen assays of CC3 and TUNEL, it is clear they are both able to identify apoptotic cells but do not fulfil the aim of capturing total cell death.

Current studies have made the assumption that the cerebral organoid core is purely apoptotic, caused by hypoxia and malnutrition (Choe *et al.*, 2021), and so CC3 staining was trialled first. CC3 is a mid-stage apoptotic marker that is integral to both the extrinsic and intrinsic apoptosis pathway. In Day 21 and Day 30 E-hCOs, CC3 predominantly colocalised to cells undergoing pyknosis, i.e. nuclear shrinkage, most commonly associated with apoptosis (Figure 3.8.A-B and 3.9.A-B). These cells localised to outside of the VZ/SVZ regions of E-hCOs, similar to what is observed in cerebral organoid papers (Daviaud *et al.*, 2019; Zhang *et al.*, 2019; Anastasaki *et al.*, 2020; Delepine *et al.*, 2021; Cakir *et al.*, 2022). Quantity of CC3 as a coverage of total cell count also mirrored published cerebral organoid findings at both Day 30 (Y. Li *et al.*, 2017; Daviaud *et al.*, 2019; Cho *et al.*, 2021) and Day 60 (Shi *et al.*, 2020; Kim *et al.*, 2021; Cakir *et al.*, 2022). However, CC3 was visibly smeared in the dead core of the E-hCOs (Figure 3.8.C) or had variable fluorescence intensity between cell lines (Figure 3.8 and 3.9); these issues were recognised in the pipeline. Nuclei-sized CC3 objects had to overlap with nuclei-

sized DAPI objects in a 5-pixel space in order to be considered valid, whilst thresholds were set to appropriately encompass what was considered genuine staining and avoid over/under representation.

As previously mentioned, the TUNEL assay was also chosen for total cell death quantification, as it uses fluorescently tagged dUTPs to highlight DNA DSBs, a feature of both apoptosis and necrosis (Zhivotosky and Orrenius, 2001; Didenko, Ngo and Baskin, 2003; Higuchi, 2003). TUNEL has been used in the past for identifying necrosis (Zhivotosky and Orrenius, 2001; Didenko, Ngo and Baskin, 2003; Higuchi, 2003; Zhao *et al.*, 2021). However, in recent years, TUNEL has more readily been used for apoptosis quantification (Terashi *et al.*, 2019; Hsu *et al.*, 2020; Choe *et al.*, 2021; Zhang *et al.*, 2021), and instead necrosis has been identified using nuclei morphology-based identification using stains such as Trypan Blue (Perry, Epstein and Gelbard, 1997), haematoxylin and eosin staining (Elmore *et al.*, 2016) or propidium iodide (PI) staining (Sawai and Domae, 2011). Cerebral organoid studies have shown that $TUNEL^+$ apoptosis localises outside the VZ, similar to what was observed around ventricles of E-hCOs (Figure 3.12 and 3.13) (Lancaster *et al.*, 2013; Mansour *et al.*, 2018; Zhang *et al.*, 2019; Wegscheid *et al.*, 2021). There was also a significant proportion of $TUNEL^+$ cells in the E-hCO core (Figure 3.12 and 3.13), which was comparable to other cerebral organoid studies (Choe *et al.*, 2021), indicating that TUNEL identifies the apoptotic features of the dead core similarly to CC3. Although no known studies have used a more morphologically-encompassing metric like APD, cerebral organoid publications that use TUNEL assays have similar percentage values of $DAPI^+/TUNEL^+$ to E-hCOs at Day 30 (Figure 3.16.B) (Allende *et al.*, 2018; Mansour *et al.*, 2018; Zhang *et al.*, 2019; Wegscheid *et al.*, 2021) and at Day 60 (Figure 3.16.C) (Cakir *et al.*, 2022).

This leads to the question as to whether TUNEL highlights necrosis in cerebral organoids. CC3 is a well characterised apoptotic marker and so was used as a guideline to confirm if TUNEL was successfully identifying necrosis and/or apoptosis. However, in this study, it is clear that TUNEL does not mark necrotic cells, instead labelling apoptotic cells, as the nuclei localisation predictions and count values were very similar to CC3 (Figures 3.8, 3.9, 3.12, 3.13 and 3.16); $DAPI^+/TUNEL^+$ values were slightly lower, which has been observed previously in similar comparisons (Duan *et al.*, 2003; Srikanth *et al.*, 2018; Wegscheid *et al.*, 2021). Upon comparison of the $DAPI^+$ nuclei in particular, $TUNEL^+$ or $CC3^+$ nuclei

had high DAPI^{+} intensity with spherical or small, fragmented, pyknotic nuclei, whereas unlabelled nuclei were swollen, misshapen, with uneven and faded fluorescence (Figure 3.18). One hypothesis is that these are unlabelled cells undergoing karyolysis, a unique feature of necrotic cells (Elmore *et al.*, 2016), where the DNA is degraded by nucleases whilst retained in the nuclear membrane (Rahimi *et al.*, 2018). This would be a possible answer as to why we see inconsistent TUNEL intensity in non-pyknotic nuclei (Figure 3.17.B), that the E-hCOs core is undertaking secondary necrosis (Sachet, Liang and Oehler, 2017). Comparison of the features of unlabelled nuclei in the dead core of the E-hCO (Figure 3.18 - annotated) to other examples of the nuclei of karyolitic cells, including neurons, supports this theory, as they display similar nuclear morphology (Li *et al.*, 2012; Rogers *et al.*, 2017). Additionally, the observed CC3 smear-like ICC staining in the E-hCO core was unlikely to be a technical issue, as additional care was taken to sufficiently wash slides. The smear effect could be a reflection of CC3 being released into the extracellular matrix by the lysis of originally caspase-dependent apoptotic turned secondary necrotic cells. Although the possibility of this occurring has not been found in current literature, these hypotheses follow the narrative that cellular components are lost to surrounding extracellular matrix in necrosis (reviewed by Silva, (2010)).

It is unsurprising to observe necrotic cells in the E-hCO core, but the results of Figure 3.17 and 3.18 produces a second question: why aren't all the cells in the E-hCO core necrotic. To answer this question, it is useful to estimate how the E-hCO core is likely to develop; no known cerebral organoid research papers have investigated this. One possibility is that older cells are involuntarily forced towards the E-hCO core as new cells are created in the VZ areas. These older cells would undertake apoptosis initially, as the restriction of oxygen and nutrients is gradual and not an immediate, extreme event which would instigate unprogrammed necrosis (D'Arcy, 2019). This was supported by observations of apoptotic cells congregating more prolifically than unlabelled cells at the boundary between live and dead regions of the E-hCO (Figure 3.8, 3.9, 3.12 and 3.13). However, in the absence of an immunological response, these apoptotic cells are compelled to initiate secondary necrosis. *In vitro* neurons are known to be resistant to hypoxic environments and can take up to 24 hours in a hypoxic environment to be negatively affected (Chen *et al.*, 2014). Similarly, the transition from apoptosis to secondary necrosis is not immediate and can also take up to 24 hours (Rogers *et*

al., 2017). During this transition, nuclei can retain pyknosis morphology, prior to membranal degradation that causes karyolysis (Rydell-Törmänen, Uller and Erjefält, 2006), so it is possible that not all $CC3^+$ or $TUNEL^+$ nuclei are apoptotic, some may be early secondary necrotic. It is therefore plausible that the 10% change of total CC3 count observed in an E-hCO from Day 30 to Day 60 (Figure 3.16.A-C) represents the shift between apoptotic cells degrading naturally (Day 30) to apoptotic cells degrading naturally and undertaking secondary necrosis (Day 60). This secondary necrosis hypothesis would explain why there is a heterogenous mix of apoptotic and necrotic-presenting cells in the core; other cerebral organoids have shown that not all cells within the core are $TUNEL^+$ (Choe *et al.*, 2021). It could take a possible 48 hours before cells undertake secondary necrosis, roughly 6 times longer than the proliferation rate of NECs (Liu *et al.*, 2019), and so dying cells will be regularly replenished in the hCO core. With no coordination of movement other than the constant, forced migration of dying cells, the cells that are karyolitic become mixed with newly apoptotic cells in the dead core.

In order to confirm this hypothesis, and fulfil the original aim of a total cell death count, an adapted approach to cell death analysis is necessary. There are few options to simultaneously capture all types of cell death in a high throughput, fluorescent system. There are no known markers that distinguish between apoptosis and necrosis without a significant margin for error (Vanlangenakker, Vanden Berghe and Vandenabeele, 2012). To further this study, a viable next step could be to quantify apoptosis and necrosis by manually counting specific features of nuclei in haematoxylin and eosin staining (Elmore *et al.*, 2016). Another alternative would be to use a combination of PI and CC3 in ICC analysis. PI is membrane impermeable and so should not integrate into the nuclei of live or apoptotic cells, but should bind to secondary necrotic, karyolitic nuclei. The combination of these two markers should segregate cell populations into three discrete groups: live ($DAPI^+/CC3^-/PI^-$), apoptotic ($DAPI^+/CC3^+/PI^-$), and secondary necrotic ($DAPI^+/CC3^-/PI^+$). Combining the apoptotic and secondary necrotic count values would results in a total dead cell count, leaving the total live cell count value available for normalising live count data. With the current method of using CC3 only, proof-of-concept analysis using FOXG1 staining demonstrated that the removal of the APD-predicted CC3-dependent apoptosis count significantly adjusts the cell count percentage to a closer representation of the total live cell

count without distorting the variance of the data (Figure 3.17). However, the average percentage of FOXG1$^+$ cells reduced over time, drastically so at Day 60 as the dead core expands (Figure 3.17.C). Evidently APD-predicted CC3 count can only be considered an improvement, as opposed to a solution, for accommodating for the dead core in cerebral organoids.

The overarching result of investigating E-hCO cell death is that CC3 and TUNEL are not suitable total cell death markers, as they are only capturing apoptotic population present in the E-hCO core. An additional result of this analysis is the recognition of cell line-specific differences with respect to mode of cell death assay, regardless of the mechanism in which one normalises the count values (Figure 3.16), i.e., Control #1 Day 30. Considering this change is not observed in Control #2 E-hCOs, one explanation for this disparity is that more cells entering apoptosis but not reaching the late, TUNEL$^+$ DNA fragmentation stage at Day 21 and 30 of Control #1 E-hCOs. Because of these significant differences in cell death, control cell lines should be kept separate during analysis so as not to skew conclusions. However, the fact that the results of both CC3 staining and TUNEL assay analysis reflect similar apoptosis studies in aforementioned cerebral organoid literature indicates that the E-hCOs are of comparable quality to current cerebral organoid methodologies.

As a result of these conclusions, assumptions were made for all following ICC analysis. Firstly, the linear regression analyses support the use of APD as a metric for apoptotic cell count prediction and may also be used for dead cell count and morphological data. Secondly, CC3 and TUNEL are both suitable assays for apoptosis, however CC3 against APD was to be used for predicting total apoptotic cell count of E-hCOs due to its superior linear regression results and TUNEL was to be used for DNA DSB analysis when appropriate. Thirdly, due to the significant difference in apoptosis quantity, each cell line would be treated individually and not clustered by genotype. Lastly, there was to be no cross-timepoint comparison for analysis; this would be inaccurate due to the morphological differences between E-hCOs of different timepoints, as well as the time-dependent presence of the dead core. However, the trends found across each timepoint would be comparable. Once a validated approach to identifying unlabelled cells is discovered, this information could easily be integrated into the data gathered in this study, thereby allowing for analysis of temporal changes of proteins of interest.

3.6 Conclusion

It is clear that many experiments and analytical considerations are necessary for designing cerebral organoid research. Firstly, hIPSC lines require validation of their pluripotency; the cell lines assessed within this research were capable of trilineage differentiation. Secondly, information on the cell identity of early stages of hCO differentiation can influence experimental decisions with regards to timepoint analysis, particularly when modelling NDDs. Differentiation of hIPSCs to EBs created a shift in cell identity from stem cell pluripotency to multipotent primitive NECs, in keeping with current knowledge of EB culture. Furthermore, cerebral organoid analysis methodology can be improved upon by incorporating multiple measurements into one normalising constant. APD was an improved measure of normalising total hCO sections, capable of producing ICC results that are comparable across genotypes, protocols and timepoints. Finally, attempts to rectify the dead core conundrum in whole hCO ICC analysis transitioned into formulating a total apoptotic cell count after analysis of two common cell death markers CC3 and TUNEL. CC3 was capable of estimating total apoptotic count value using APD, of which will be removed from an E-hCO's total cell count prior to statistical calculations of live cell populations (Figure 3.15). In summation, assumptions made about the experimental design and analysis of cerebral organoids should be revisited regularly for revision with the aid of new technologies and insight to benefit future disease modelling.

4 The Great, the Good and the Ugly: Cortical Organoid Protocol Development

4.1 Introduction

There is no singular, universal dorsal forebrain-specific cerebral organoid protocol currently available, as the protocols evolve quickly. This lack of continuity presented an opportunity to create a new cerebral organoid protocol that it is capable of accomplishing this research's aims; to generate a stable hCO capable of mimicking dorsal forebrain development for future use in disease modelling. Using the framework of current cerebral organoid protocols (Lancaster and Knoblich, 2014; Bagley *et al.*, 2017; Birey *et al.*, 2017; Lancaster *et al.*, 2017; Sloan *et al.*, 2018), protocol design choices were made, resulting in the generation of three new hCO protocols. These new hCO protocols required in-depth validation to confirm the quality of the hCO with regards to accurately recapitulating dorsal forebrain development.

4.1.1 Reviewing Key Choices for Designing a Cortical Organoid Protocol

After identifying the choice of stem cell source, it is necessary to determine how to create the 3D, free-floating aggregates. There are multiple methods in which to create EBs, including specialised EB-generating equipment, such as AggreWell™ systems, using gravity to encourage aggregation ('hanging drop') or self-aggregation in low-attachment plates. The latter two methods have high variability in embryoid body formation, which can drastically impact reproducibility (Sivitilli *et al.*, 2020). As a result, V-bottomed wells, like the Aggrewell™, were found to be the best in creating uniform EBs when compared to all other methods (Sivitilli *et al.*, 2020). EB seeding density varies amongst protocols, but 0.9-1x10^4 cells per EB is a common seeding density (Bhaduri *et al.*, 2020; Zhao *et al.*, 2020; Sawada *et al.*, 2020; Rosebrock *et al.*, 2022). However, in Lancaster *et al.*, (2017), a range of EB seeding densities were trialled, including 0.9x10^4 cells per EB. 10 days post-seeding, and after neuroectodermal induction, EBs that were seeded with ≤2000 cells were found to be less stable, whilst EBs with a ≥4500 cell seeding density hosted small cell populations of other developmental lineages. These results illustrate that the current default of using 0.9x10^4 cells for EB seeding density is not ideal and should be avoided. Instead, evidence suggests 3000-4000

cells is the optimal seeding density for homogenous neuroectodermal differentiation.

To support EB generation, the additive Y-27632 was also included in seeding media. Y-27632 is a Rho kinase inhibitor and is used in stem cell culture for increasing viability and surface attachment (Claassen, Desler and Rizzino, 2009). It is commonly added in cerebral organoid studies as it alters the actin cytoskeleton in a manner that facilitates EB generation (Vaezi *et al.*, 2002; Lancaster and Knoblich, 2014; Lancaster *et al.*, 2017; Giandomenico, Sutcliffe and Lancaster, 2021). Certain studies have proven a lack of requirement of Y-27632 during EB generation (Pettinato, Wen and Zhang, 2014), but it is still used in most instances as modelling diseases in cerebral organoids can be difficult due to EB fragility (Bhaduri *et al.*, 2020). The length of exposure to Y-27632 differs between cerebral organoid protocols and methods of EB generation, varying between 24 hours (Cederquist *et al.*, 2019) to 6 days (Xiang *et al.*, 2017; Sloan *et al.*, 2018; Velasco *et al.*, 2019; Zhang *et al.*, 2019) prior to neuroectodermal induction. Based on the presented studies, 3000-4000 human induced pluripotent stem cells (hIPSCs) were seeded in V-bottom AggreWell™ EB-generating plates for this study. As the AggreWell™ system suggests addition of Y-27632 for 24 hours, whilst current cerebral organoid literature suggests between 24 hours to 5-6 days, both of these suggestions were trialled in the different cerebral organoid protocols presented in this study.

With EB generation methodology chosen, the next step is to choose the type of cerebral organoid protocol, but this depends on the research question. Cerebral organoids that are unguided are preferable given the standardised protocol and minimal technical skill necessary in comparison to other methods (Lancaster *et al.*, 2013) and the close association to foetal brain development (Camp *et al.*, 2015). However, unguided cerebral organoids have various different brain regions developing together unlike *in utero* development, as well as other populations of non-ectodermal cells like skeletal and digestive tissue and microglia. Low reproducibility is the most common issue with the unguided cerebral organoids due to this unguided self-organisation (Velasco *et al.*, 2019). The guided/directly patterened cerebral organoids, on the other hand, have reduced intra- and inter-batch heterogeneity, minimised influence from different brain regions and improved accuracy of developing specific populations of neuronal sub-types (Velasco *et al.*, 2019).

In order to create dorsal forebrain-specific hCOs, the selective cortical patterning system of dual SMAD inhibition was adapted from 2D neuron culture (Chambers *et al.*, 2009). Dual SMAD inhibition, a term used for the inhibition of both BMP and TGF-β signalling effectors, has been a cornerstone of neuroectodermal/neuronal *in vitro* differentiation, as it was proven that inhibiting one of the two SMAD pathways was not sufficient for highly effective differentiation in 2D stem cell cultures (Chambers *et al.*, 2009). In the absence of BMP-driven SMAD signalling, neuroectodermal induction occurs via BMP-independent FGF expression but with lower fidelity (LaVaute *et al.*, 2009). In some circumstances, BMP inhibition can be replaced with Wnt inhibition to create telencephalic neuroectodermal cell identity (Kadoshima *et al.*, 2013; Xiang *et al.*, 2017), or all three antagonists can be combined to improve hCO development (Rosebrock *et al.*, 2022). Dual SMAD inhibition has proven capable of producing cortex-like structures after months of maturation (Paşca *et al.*, 2015), and is significantly more replicable within and across differentiations than unguided cerebral organoids (Velasco *et al.*, 2019). When reviewing the means of generating a hCO, the majority of guided cerebral organoid protocols have combinations of at least two SMAD inhibitors, such as SB-431542, dorsomorphin, A83-01 and LDN-193189, to induce neural ectoderm (Qian *et al.*, 2016; Bagley *et al.*, 2017; Birey *et al.*, 2017; Xiang *et al.*, 2017; Sloan *et al.*, 2018). The dual SMAD strategy was implement as the TGF-β inhibitor SB-431542 and the BMP4 inhibitor LDN-193189 had been used in previous *in vitro* 1qDel literature (Chapman *et al.*, 2021).

To achieve the characteristic cerebral organoid ventricular structure, hCOs required a basement matrix. The basement matrix used in the majority of cerebral organoid studies is Matrigel® (Daviaud *et al.*, 2019; Delepine *et al.*, 2021; Kyrousi *et al.*, 2021; Sharf *et al.*, 2022) which is composed of extracellular matrix components extracted from Engelbreth-Holm-Swarm tumours of mice: laminin (60%), collagen IV (30%), entactin (8%) and heparin sulfate proteoglycan perlecan (2-3%) (Aisenbrey and Murphy, 2020). However, the origins of Matrigel® make it an unfavourable choice when aiming for reproducibility in 3D culture. The inherent heterogeneity of the tumours can lead to heterogeneity between batches of Matrigel®, each lot with varying ratios of components and their isoforms (reviewed by Aisenbrey and Murphy, (2020)). There are successful biological and synthetic alternatives to Matrigel™ used for 2D *in vitro* cultures, including Geltrex (Chapman *et al.*, 2021) and poly(ethylene glycol)-peptide based hydrogels, the latter of which

is proving successful in non-cerebral organoid culture (Cruz-Acuña *et al.*, 2017, 2018). Application of hydrogels in cerebral organoids is still under investigation (Lindborg *et al.*, 2016; Chen *et al.*, 2021), and therefore cannot be considered as a viable alternative at this time. However, once validated, these synthetic alternatives will provide control over stiffness, degradation and chemical composition, minimising replicability issues, thereby rendering Matrigel® obsolete.

After Matrigel® embedding, neuroepithelial loop formation is facilitated in a composite media used in pre-neurogenic *in vitro* neuronal culture (Lancaster and Knoblich, 2014; Chapman *et al.*, 2021), as well as additional reagents, such as insulin, EGF or FGF. Insulin-associated growth factors plays a major role in regulating NPC cell division in the dorsal forebrain (Hodge, D'Ercole and O'Kusky, 2004). Insulin is therefore necessary to maintain *in vitro* NPC cultures, and by extension cerebral organoids; in its absence, NPCs undergo severe apoptosis and delayed growth (Rhee *et al.*, 2013; Lancaster *et al.*, 2017). EGF and FGF signalling is also essential to 2D and 3D neuronal culture (Zhao *et al.*, 2019; Rosebrock *et al.*, 2022), as they are both necessary for different populations of NPCs in the telencephalon, and coexist at a similar time period in development (E7.5-E8.5) (Tropepe *et al.*, 1999). Both EGF and FGF stimulate self-renewal of NPCs, whilst FGF shortens the cell cycle and increases the fraction of cells that are mitotically active. Addition of these reagents is therefore useful during the neural differentiation stage of hCO differentiation to expand and support the NPC population. However, basic FGF has a distinctly shorter half-life when placed under heat stress than its thermally-stable equivalent, and there is a greater reliance on exogenous heparin for inducing FGF receptor signalling; heparin is an additive found in multiple cerebral organoid protocols (Lancaster and Knoblich, 2014; Kang *et al.*, 2021; Kyrousi *et al.*, 2021; Sharf *et al.*, 2022). To avoid unnecessary use of heparin, thermally stable FGF should be used in cerebral organoid culture where possible, including the trialled hCO protocols. Lastly, the length of neural differentiation varies amongst cerebral organoid protocols, between 4 – 18 days (Birey *et al.*, 2017; Lancaster *et al.*, 2017; Albanese *et al.*, 2020). In the trialled hCO protocols, neural differentiation length was flexible and adjusted based on visible changes, but kept within known limits.

During neuronal maturation, a composite of additives is often included in cerebral organoid protocols to support neuronal development, including cAMP, ascorbic acid, BDNF and glial cell-derived neurotrophic factor (GDNF). cAMP

improves functionality of voltage-gated sodium and potassium channels in mature neurons, as well as facilitates complex dendritic morphology (Lepski *et al.*, 2013; Piguel *et al.*, 2022). Ascorbic acid is the reduced form of vitamin C, of which is at high concentration in the foetal brain (Castro *et al.*, 2001). When supplemented in *in vitro* culture, ascorbic acid alleviates NPC's reactive oxidative stress thereby activating Wnt signalling, which in turn instigates neuronal differentiation (Rharass *et al.*, 2017). BDNF is expressed predominantly by astrocytes and supports neuronal maturation by regulating synaptic transmission and the release of glutamate (Romanos *et al.*, 2019; Fernández-García *et al.*, 2020; Farhy-Tselnicker *et al.*, 2021). Finally, GDNF is found in the marginal zone of the neocortex and the VZ of the MGE, where it is vital for the tangential migration of GABA-ergic interneurons (Pozas and Ibáñez, 2005).

Although exogenous cAMP and ascorbic acid broadly benefit all cell types in a maturing cerebral organoid, GDNF and BDNF are more specific to certain cell types. Cerebral organoids have a small population of GABA-ergic interneurons, whilst astrocytes do not arise in cerebral organoids until ≥45 days into culture (Gonzalez *et al.*, 2018; Arzua *et al.*, 2020; Gordon *et al.*, 2021; Huang *et al.*, 2022). This length of time is in keeping with *in vitro* astrocyte-generating protocols that report requiring a minimum of 6 weeks to produce $GFAP^+$ astrocytes (Chandrasekaran *et al.*, 2016), as *in vivo* gliogenesis follows neurogenesis, beginning as progenitors in the oSVZ (Fu *et al.*, 2021). The addition of both GDNF and BDNF significantly improved gliogenesis in cerebral organoids (Watanabe *et al.*, 2017). However, due to fiscal constraints and anticipated glutamatergic neuronal identity, only BDNF was chosen to be included in neuronal maturation media where possible; cAMP and ascorbic acid were included in neuronal maturation media for all hCO protocols.

Lastly, the culturing method of maturation varies between cerebral organoid protocols. Originally, Erlenmeyer flasks were used to circulate media to improve diffusion of nutrients into the cerebral organoid (Lancaster and Knoblich, 2014). Over time, this method has fallen out of favour due to its requirement for significant volumes of media, as well as the increased variance between batches in different flasks (Quadrato *et al.*, 2017). No known literature has examined the effect of different techniques for maturing cerebral organoid culture, however the evolution of certain protocols' methods, such as the Lancaster and Knoblich, (2014) to the Giandomenico, Sutcliffe and Lancaster, (2021) would suggest that the transition

from Erlenmeyer flasks to orbital shaking is a beneficial one. To identify how significant this difference was, both forms of maturation culture was trialled in the hCO protocols.

Protocol and experimental design are determined by the limitations of time, cost and availability of resources against the anticipated scope of answering the desired research questions. In this research, informed choices of methodology, as well as validation of the system, was essential prior to investigating the effect of 1qDel on neurodevelopment.

4.1.2 What Defines a Dorsal Forebrain Cortical Organoid?

With the cerebral organoid type and key methodological factors decided upon, hCO protocols could be designed. Consolidating cerebral organoid protocols that have characteristic dorsal forebrain attributes with low variability provided the foundation for creating three unique hCO protocols (Lancaster and Knoblich, 2014; Bagley *et al.*, 2017; Birey *et al.*, 2017; Lancaster *et al.*, 2017; Sloan *et al.*, 2018). However, there are few detailed evaluations to distinguish cerebral organoid quality (Sivitilli *et al.*, 2020), instead providing limited “anticipated results” as a basis for cerebral organoid evaluation (Lancaster and Knoblich, 2014; Paşca *et al.*, 2015; Giandomenico, Sutcliffe and Lancaster, 2021). With limited specification as to what parameters a cerebral organoid should adhere to, it was deemed necessary to produce assessment guidelines, with which to determine the hCO protocol’s characteristics (Figure 4.1 and Table 4.1). Designating what was considered essential in a hCO’s development was compiled and adapted from previous cerebral organoid literature that focussed on both protocol design and disease modelling of similar NDDs to 1qDel (Lancaster and Knoblich, 2014; Bagley *et al.*, 2017; Birey *et al.*, 2017; Iefremova *et al.*, 2017; Lancaster *et al.*, 2017; Sloan *et al.*, 2018; Velasco *et al.*, 2019; Yakoub and Sadek, 2019; Zhang *et al.*, 2019; Sivitilli *et al.*, 2020; Giandomenico, Sutcliffe and Lancaster, 2021; Urresti *et al.*, 2021).

Figure 4.1 (below): Qualitative assessment criteria for hCOs from previous cerebral organoids literature.

A) Day 5 EBs after initial formation in non-binding (NB) V-shaped wells, scale bar = 250 µm (Sivitilli *et al.*, 2020). **B)** Neuroepithelial loop formation (annotated) at Day 13 of cerebral organoid differentiation, scale bar = 1 mm (Giandomenico, Sutcliffe and Lancaster, 2021). **C)** A mature 5-week cerebral organoid with lobular structures (annotated), scale bar = 500 µm (Giandomenico, Sutcliffe and Lancaster, 2021). **D)** Suboptimal Day 5 EBs after initial formation in NB, U-bottom wells, scale bar = 250 µm (Sivitilli *et al.*, 2020). **E)** Unwanted outgrowth of cells (arrowhead) outside satisfactory neuroepithelial loops (arrows) in a Day 14 cerebral organoid, scale bar = 200 µm (Lancaster and Knoblich, 2014). **F)** Destructive fluid-filled cystic formation (annotated) in a Day 55 cerebral organoid (Giandomenico, Sutcliffe and Lancaster, 2021), scale bar = 500 µm. **G)** Distinction between VZ ($PAX6^+$), SVZ ($TBR2^+$) and CP ($CTIP2^+$)-like structures in a 10-week-old cerebral organoid, scale bar = 100 µm (Bershteyn *et al.*, 2017). **H)** M phase NPCs ($pVIM^+/SOX2^+$) bound to apical edge (PKC^+) of lumen in a 5 week old cerebral organoid, scale bar = 100 µm (Bershteyn *et al.*, 2017). **I)** Presynaptic markers (SYN1) on mature neurons (MAP2) in a Day 80 cerebral organoid, scale bar = 2 µm (Yakoub and Sadek, 2019). **J)** Development of a whole cerebral organoid, including dead core, over the course of three months, with NPCs ($SOX2^+$) and upper- ($SATB2^+$) and lower- ($CTIP2^+$) layer neurons, scale bar = 500 µm (Sivitilli *et al.*, 2020). All images adapted for clarity from referenced papers.

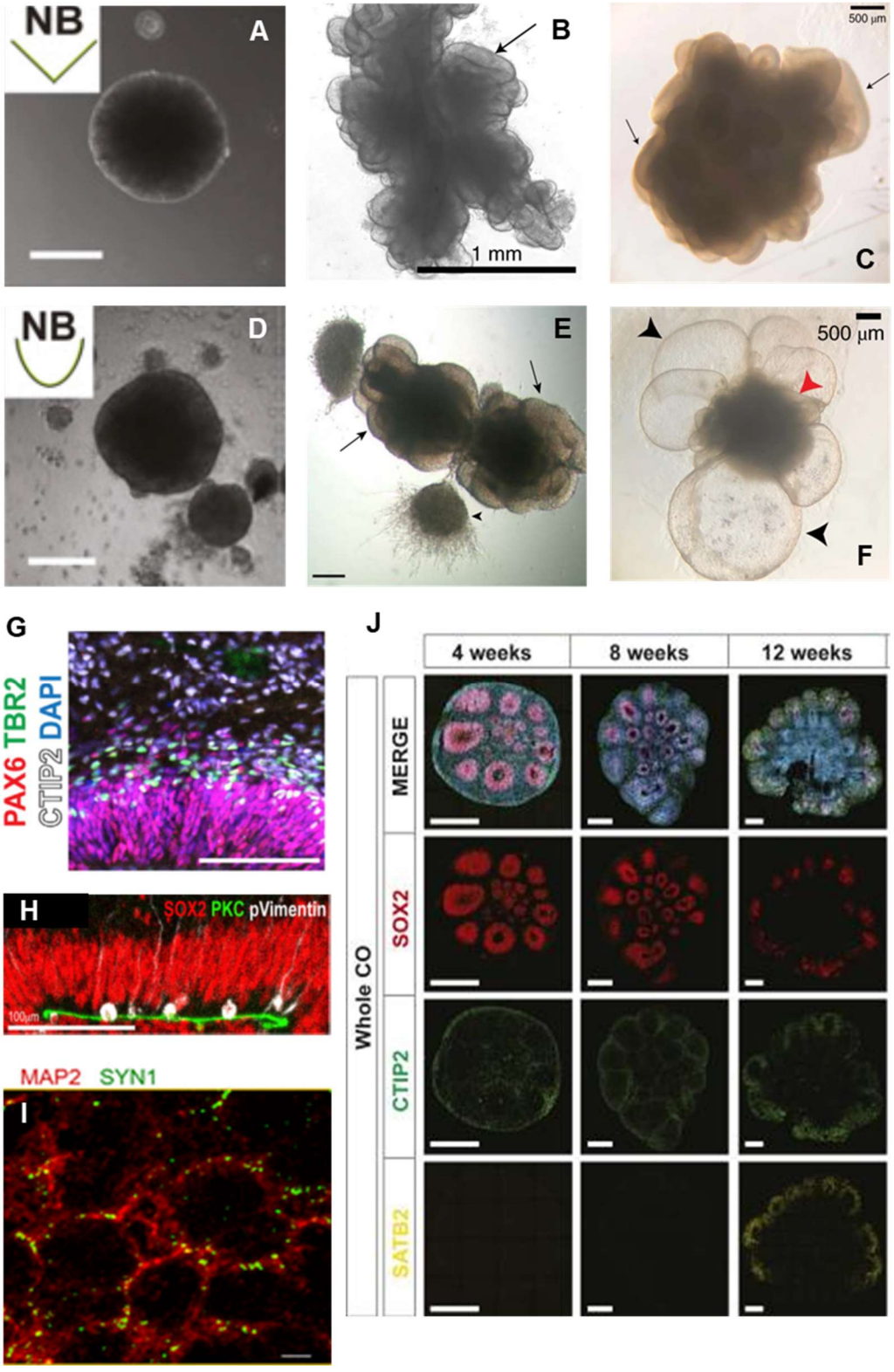

Figure 4.1: Qualitative assessment criteria for hCOs from previous cerebral organoids literature.

Figure legend on previous page.

Table 4.1: Quantitative and qualitative attributes required of hCOs.

hCO Feature
1) External morphology that represents the four developmental stages: EB, neuroectodermal induction, neuronal differentiation and maturation (Figure 4.1.A-4.1.C).
2) Numerous lumens, defined by ZO1/β-catenin/actin, surrounded by proliferative ($KI67^+$) orientated NPCs ($SOX2^+$), with a proportion of M phase ($pVIM^+$) cells bound at the apical lumen edge (Figure 4.1.H).
3) High to low ratio of dorsal forebrain to ventral forebrain progenitors. Furthermore, minimal representation of non-telencephalic regions.
4) Defined, discrete regions reminiscent of the neocortex, including a VZ, SVZ and CP (Figure 4.1.G & 4.1.J).
5) Enrichment of mature glutamatergic cortical neuronal populations (Figure 4.1.I).
6) Minimal intra- and inter-batch variation across the aforementioned assessments. Minimal differences between cell lines of the same genotype.

Although how cerebral organoids model dorsal forebrain development has been previously discussed in Section 1.3.2, there were specific attributes that were isolated as key to generating successful hCOs. Firstly, all hCOs should reach key developmental stages in due course, although exact timepoints differs between cerebral organoid protocols (Table 4.1.1). Beginning with EB formation, EBs should have prolific expression of stem cell markers such as *SOX2* and *OCT4*. Visually, they should be relatively perfect spheres to ensure even distribution of nutrients and appropriate cell composition (Figure 4.1.A). If there is significant cell death, polarised budding or irregular density then the EBs will be considered invalid and removed (Figure 4.1.D) (Sivitilli *et al.*, 2020). The next developmental stage is neuroectodermal induction, upon which the EB is now referred to as a hCO as it is being exogenously directed towards a neuroectodermal fate. Dual SMAD inhibition-guided neuroectodermal induction is designed for forebrain-specific differentiation (Chambers *et al.*, 2009; M. Zhang *et al.*, 2018), with which a clearly defined internal border of radially-organised pseudostratified neuroepithelium is considered a sign of successful neuroectodermal induction (Lancaster and Knoblich, 2014). After neuroectodermal induction, the hCO is

embedded in Matrigel® to support neuroepithelial loop formation. These loops form over the course of 6-12 days post-embedding and should be visible under bright-field microscopy (Figure 4.1.B) (Lancaster and Knoblich, 2014; Giandomenico, Sutcliffe and Lancaster, 2021). A lack of neuroepithelial loops is a sign of poor neuroectodermal induction, as is the presence of neuroepithelial loops alongside branched bundles of cells (see annotations, Figure 4.1.E) (Lancaster and Knoblich, 2014). Once provided with RA, the visible appearance of the hCO should rapidly change into dense, lobe-like structure as neurons mature (Giandomenico, Sutcliffe and Lancaster, 2021). This is the stage at which cystic issue can arise (Figure 4.1.F). Although the exact cause of the swelling of neuroepithelial loops is unknown, it is believed to be a stress response to poor dorsal forebrain differentiation (Lancaster and Knoblich, 2014; Giandomenico, Sutcliffe and Lancaster, 2021), for example, a cyst can be a representation of the cerebral spinal fluid sac present in choroid plexus organoids (Pellegrini *et al.*, 2020). However, minor cystic formation is not uncommon and so only 'destructive' cyst formation was considered unfavourable; destructive cysts were defined as those that caused hCOs to be heavily damaged, such as that shown in Figure 4.1.F (Giandomenico, Sutcliffe and Lancaster, 2021).

After the hCO exhibits characteristic cerebral organoid morphology under bright field imaging, the internal cellular organisation becomes the next major point of assessment (Table 4.1.2). The key characteristic that separates hCOs from their *in vitro* counterparts is their capability to develop self-contained regions of neuronal development, the neuroepithelial loops. The expectation for hCOs is that numerous neuroepithelial loops are visible externally during early neuronal differentiation (Figure 4.1.B), which then become more internalised during maturity (Figure 4.1.J). Neuroepithelial loops, or 'ventricles', should have specific characteristics that reflect human neocortical development. Starting from the inside-out, the apical edge of the lumen needs to be clearly defined by actin bundling (Karzbrun *et al.*, 2018) as well as tight/adherens junction proteins (Iefremova *et al.*, 2017). The lumens are surrounded by perpendicularly-orientated nuclei of NECs, which are replaced by aRGs in later development; both NPCs are $SOX2^{+}$/$PAX6^{+}$ (Figure 4.1.G and 4.1.J) (Arai and Taverna, 2017; Krefft *et al.*, 2018). These orientated NPCs form the basis of the VZ, the majority of which are mitotically active ($KI67^{+}$) (Zhang *et al.*, 2019; Sawada *et al.*, 2020). They should also be densely compacted and striated, with NPCs undergoing the M phase of

mitosis at the apical edge of the lumen, indicative of the cells' interkinetic nuclear migration observed in the VZ of the *in vivo* neocortex (Figure 4.1.H) (Bershteyn *et al.*, 2017; Iefremova *et al.*, 2017). It should be noted that other progenitors, including $TBR2^+$ IPs, and $HOPX^+$ bRGs are not bound to the apical edge of the VZ, and so are anticipated to be present and mitotically active in the SVZ during maturity (Kelava *et al.*, 2022).

Neuroepithelial loops are indicative of dorsal forebrain induction (Lancaster and Knoblich, 2014), however this identity still requires confirmation (Table 4.1.3). Representation from the midbrain, hindbrain, hypothalamus and choroid plexus is unlikely, as they all have significant adaptations to their protocols that separate them from telencephalic organoids within the first two weeks of differentiation (Qian *et al.*, 2018; Pellegrini *et al.*, 2020; Valiulahi *et al.*, 2021). Ventral forebrain, on the other hand, could be represented in hCOs (Iefremova *et al.*, 2017). Dorsal forebrain is the default identity for dual-SMAD inhibited cerebral organoids, as ventral forebrain organoids require SHH agonists and/or Wnt antagonists to deviate away from dorsal forebrain lineage (Bagley *et al.*, 2017; Cederquist *et al.*, 2019; Kim *et al.*, 2019). However, even in dorsal forebrain organoids there is an anticipated level of neuronal heterogeneity, as it is known that some hIPSC lines can be predisposed to "ventralisation" during differentiation (Yoon *et al.*, 2019). It was therefore essential to assess the representation of the ventral forebrain in all trialled hCO protocols to determine correct forebrain axis identity.

With confirmation of dorsal forebrain identity and presence of developing ventricles, discrete populations of specific cell types should be separating into distinct layers as the hCO matures, akin to the developing cortical layers of the human neocortex (Table 4.1.4). ≥2 months old organoids have proven that more complex cortical layering is achievable, including upper ($SATB2^+$) and lower layer ($CTIP2^+$) neurons (Figure 4.1.J) (Lancaster *et al.*, 2013; Renner *et al.*, 2017; Pollen *et al.*, 2019; Qian *et al.*, 2020; Rosebrock *et al.*, 2022). The expectation of the two-month hCO differentiation was to observe a minimum of three separate layers: a VZ consisting of apical-basal orientated $SOX2^+$ NPCs, a SVZ containing $TBR2^+$ IPs and a CP region with $CTIP2^+$ Layer V neurons (Figure 4.1.G and 4.1.J). Layer V $CTIP2^+$ neurons were chosen for analysis as they are not found in the preplate (Alsanie *et al.*, 2020), unlike $TBR1^+$ neurons (Englund *et al.*, 2005), and were therefore easily distinguishable from the SVZ, whilst being abundant in ≤2 month old cerebral organoids (Qian *et al.*, 2016; Bershteyn *et al.*, 2017; Zhang *et*

al., 2019; Kitahara *et al.*, 2020). Although these layers are intended as distinct, there should be a proportion of overlap in identity as cells transition from progenitors to neurons (Qian *et al.*, 2020). The emulation of the human cortical layering structure is essential to any prospective disease modelling, including Fragile X syndrome (Kang *et al.*, 2021), autism (Mariani *et al.*, 2015; Zhang *et al.*, 2020), microcephaly (Li *et al.*, 2017; Wang *et al.*, 2020; Sun *et al.*, 2020) and macrocephaly (Zhang *et al.*, 2020).

As discussed previously, NDDs have been associated with cortical dysfunction in the form of an E/I ratio abnormality in mature glutamatergic and GABA-ergic interneurons (Sun *et al.*, 2019; Chapman *et al.*, 2021; Toritsuka *et al.*, 2021). In order to appropriately replicate such phenotypes, hCOs need to produce the excitatory, glutamatergic cortical neurons that represent a large proportion of those present in the neocortex (Vigneault *et al.*, 2015). However, similarly to the expectation of forebrain progenitor heterogeneity, it is also anticipated that a proportion of mature neurons within a hCO will be GABA-ergic interneurons as *in vitro* cultures of glutamatergic cortical neurons can house a percentage of GABA-ergic interneurons (Wu *et al.*, 2007; Shcheglovitov *et al.*, 2013; Xu *et al.*, 2016). This is not to the detriment of the hCO, as both are required to support a functioning neural network (Rubin, Abbott and Sompolinsky, 2017). There are a variety of methods to quantify neuronal identity including transcriptional analysis, such as RNAseq (Mariani *et al.*, 2015; Paulsen *et al.*, 2022), and protein analysis, such as ICC (Figure 4.1.I) (Yakoub and Sadek, 2019; Sawada *et al.*, 2020) or Western Blotting (Zhao *et al.*, 2020). In this circumstance, significant mRNA abundance of markers for pan-neuronal maturity and glutamatergic synapses was considered the baseline for hCO validation.

Finally, variation in cerebral organoids can be interpreted in a multitude of ways, including inter-batch (across multiple differentiations), intra-batch (within a singular differentiation) or within-genotype variability (across multiple cell lines) (Bhaduri *et al.*, 2020; Rosebrock *et al.*, 2022). Experimental variability is not a unique feature of cerebral organoids, and both *in vivo* and *in vitro* have similar issues (Wu *et al.*, 2007; Kafkafi *et al.*, 2018; Hirsch and Schildknecht, 2019; Burke *et al.*, 2020). However, these research fields are applying improvements to address the “replicability crisis” (Morrison *et al.*, 2016; Dhamne *et al.*, 2017; Volpato *et al.*, 2018; von Kortzfleisch *et al.*, 2020). Cerebral organoids have been put under similar scrutiny as they become more prolific in research, designing

experiments to both identify (Velasco *et al.*, 2019; Yoon *et al.*, 2019; Hernández *et al.*, 2021) and reduce (Sivitilli *et al.*, 2020) such variability. Current cerebral organoid literature trends towards a minimum of two differentiations of two cell lines per genotype of interest (Lancaster *et al.*, 2013; Klaus *et al.*, 2019; Zhang *et al.*, 2019; Samarasinghe *et al.*, 2021); this was set as the aim for each hCO protocol. As inter- and intra-batch variation is associated with methodological expertise (Morrison *et al.*, 2016; Volpato *et al.*, 2018; von Kortzfleisch *et al.*, 2020), a specific interest was taken for the influence of within-genotype variability between the two control cell lines in this study (Yoon *et al.*, 2019; Hernández *et al.*, 2021).

With an evidence-based criteria for determining the quality of a hCO, as well as tested, new ICC analysis methodologies, it was possible to scrutinise each newly-created hCO protocol for the required cerebral organoid attributes.

4.1.3 Research Aims & Hypothesis

The aim of this chapter was to assess different hCO protocols with the intention of establishing a stable, dorsal forebrain-like hCO, of which the characteristics have been validated by literature-led guidelines.

The hypothesis of this chapter was that each hCO protocol would be capable of generating the core properties of the developing human neocortex, including primitive neocortical layering and appropriate cellular diversity. This hypothesis was based on the fact that each hCO protocol was based on pre-existing methodology of stable and reproducible cerebral organoids (Lancaster and Knoblich, 2014; Bagley *et al.*, 2017; Bershteyn *et al.*, 2017; Birey *et al.*, 2017; Iefremova *et al.*, 2017; Lancaster *et al.*, 2017; Sloan *et al.*, 2018; Velasco *et al.*, 2019; Yakoub and Sadek, 2019; Sivitilli *et al.*, 2020; Giandomenico, Sutcliffe and Lancaster, 2021; Urresti *et al.*, 2021). It was anticipated that there would be variance in attributes between hCOs from different protocols, but how and why these attributes may appear was unknown. It was also expected that different control cell lines may introduce heterogeneity within a single hCO protocol. The hCO protocol chosen for disease modelling would be that which best reflected the predetermined attributes dictated in Table 4.1.

4.2 Methodology

4.2.1 Cortical Organoid Protocols

Three hCO protocols were reviewed in this chapter: Basic, ROCKi and Enhanced. The hCO differentiation media composition and methods of generating and culturing cerebral organoids were the same as the Enhanced protocol (Section 2.1.2) for Basic and ROCKi unless otherwise stated; an overview of the protocols is summarised below, specific changes to the protocol were reported in Sections 4.2.1.1-4.2.1.2.

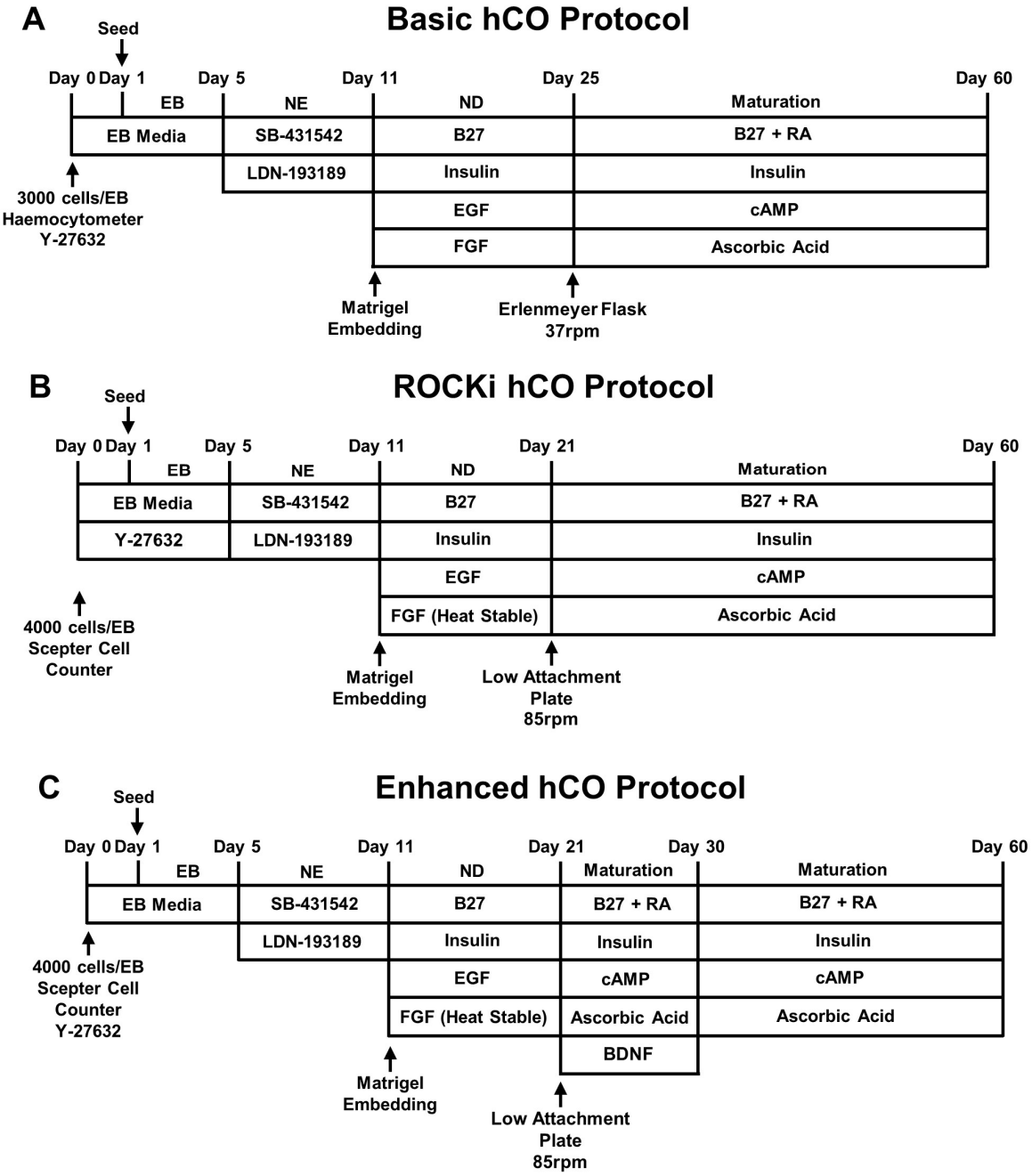

Figure 4.2: Summary figure for the three trialled hCO differentiation protocols. Timepoints (Days), stage-specific culture reagents and differing methodological practises are referenced in images. Protocols represented: **A)** Basic, **B)** ROCKi and **C)** Enhanced. Acronyms: EB – embryoid body, NE – neuroectodermal induction, ND – neural differentiation.

4.2.1.1 Cortical Organoid Protocol: Basic

Basic hCOs (B-hCOs) had significant changes to protocol compared to the Enhanced protocol (Section 2.1.2). Firstly, cell counting for EB seeding was conducted manually using Trypan Blue dye (ThermoFisher Scientific) and a glass haemocytometer. The single-cell solution was also diluted to represent 3000 cells per EB, in contrast to the Enhanced protocol's 4000. Secondly, the length of the ND phase was extended by four days, with maturation induction at Day 25 as opposed to Day 21. Additionally, the thermally stable FGF used in the ND media was replaced with a basic FGF equivalent at the same concentration (20 ng/mL). BDNF was not included in maturation media. At Day 25, all hCOs of the same line and differentiation were grouped into an Erlenmeyer flask containing 100 mL maturation media and placed on an electronic spinner at 35 rpm within a 37°C, 5% CO_2 incubator; an 80% maturation media change was performed every 4 to 6 days to Day 60.

4.2.1.2 Cortical Organoid Protocol: ROCKi

ROCKi hCOs (Ri-hCOs) were generated similarly to the Enhanced protocol (Section 2.1.2), with two key exceptions: fresh 10 µM Y-27632 (Stratech™) was added to AggreWell™ EB formation media on Day 1 and 3, and BDNF was not included in maturation media.

4.2.2 Cortical Organoid Analysis

All methodologies mentioned in Section 2.2 were used throughout this chapter with the exception of the TUNEL assay (Section 2.2.3.2). Comparisons of hCO protocols was only conducted on data from the same cell line. APD of hCOs was used for normalising non-count or non-live cell count data where mentioned and was specific to cell line and protocol. ICC quantification of live cell counts was reported as a percentage of non-apoptotic cells, determined by subtracting cell line- and protocol-specific, APD-predicted, CC3-based apoptosis values from total DAPI count (B-hCOs – Supplementary Figure 5.A-B, Ri-hCOs – Supplementary Figure 5.C-D and E-COs – Figure 3.9.E, 3.9.J, 3.9.O, 3.10.E, 3.10.J and 3.10.O).

4.2.3 Basic and ROCKi Cortical Organoid Replicate Design

Design of control replicates for the Enhanced protocol were defined previously as a minimum of two cell lines with two independent differentiations per cell line, each containing a minimum of three hCOs per type of analysis (Section 2.2.4). B-hCO and Ri-hCO analysis was designed with the intention of replicating this design (Table 4.2-4.3); any missing samples during differentiation are as a result of technical issues and not a deliberate choice.

Table 4.2: Available replicates for Basic hCO protocol analysis.

Basic hCO Protocol		Day 30		Day 60	
		qPCR	ICC	qPCR	ICC
Independent Differentiation #1	Control #1	✓	✓	✓	✕
	Control #2	✓	✕	✕	✕

Table 4.3: Available replicates for ROCKi hCO protocol analysis.

ROCKi hCO Protocol		**Day 30**		**Day 60**	
		qPCR	ICC	qPCR	ICC
Independent Differentiation #1	Control #2	✓	✓	✓	✓
Independent Differentiation #2	Control #2	✓	✕	✓	✓

4.3 Results

4.3.1 Cortical Organoids' Growth is Relative to Cell Line and Protocol

As hCOs go through a series of developmental stages during hCO differentiation, the area of each individual hCO was documented from Day 5 EB to Day 21 hCO, to monitor possible developmental stage-specific size changes. Simlar morphological characteristics were found in B-hCOs and E-hCOs, the likes of which are indicative of successful hCO differentiation (Figure 4.3). These included smooth, rounded EB formation at Day 5, edge clearing and polarised budding, characteristic of NE induction at Day 11 and neuroepithelial loop formation with visible lumens at the end of the ND stage at Day 21 (Figure 4.1.A-C). Comparison of the two cell lines, Control #1 and #2, in both the Basic and

Enhanced protocols showed that both cell lines followed the expected hCO development (Figure 4.3). Control #2 Ri-hCOs displayed no visible difference with other hCO protocols of the same cell line (Figure 4.3). However, inconsistent cell density and misshapen edges indicated poor NE induction at Day 11; by Day 21, Control #2 Ri-hCOs were visibly larger than the other hCO protocols with no clear neuroepithelial loops (Figure 4.3).

Longitudinal analysis of hCO area over two of the differentiation phases, NE and ND, showed distinct differences between hCO protocols and cell lines (Figure 4.4). When comparing hCO protocols using Control #1, E-hCOs surpassed B-hCOs in area only at the ND phase of development (Figure 4.4.A). Protocol comparison of those using Control #2 illustrated a distinctive separation between all three protocols at both phases of development, except between Ri-hCOs and E-hCOs at the NE phase (Figure 4.4.B). Although B-hCOs' and E-hCOs' area differed, they followed a similar pattern of growth, whilst Ri-hCOs logarithmic expansion in area in the ND phase resulted in the observed large size at Day 21 (Figure 4.3). Furthermore, comparison of control cell lines of both B-hCOs and E-hCOs resulted in similar outcomes; Control #1 and #2 were significantly different from one another at both the NE and ND phases of development (Figure 4.4.C-D).

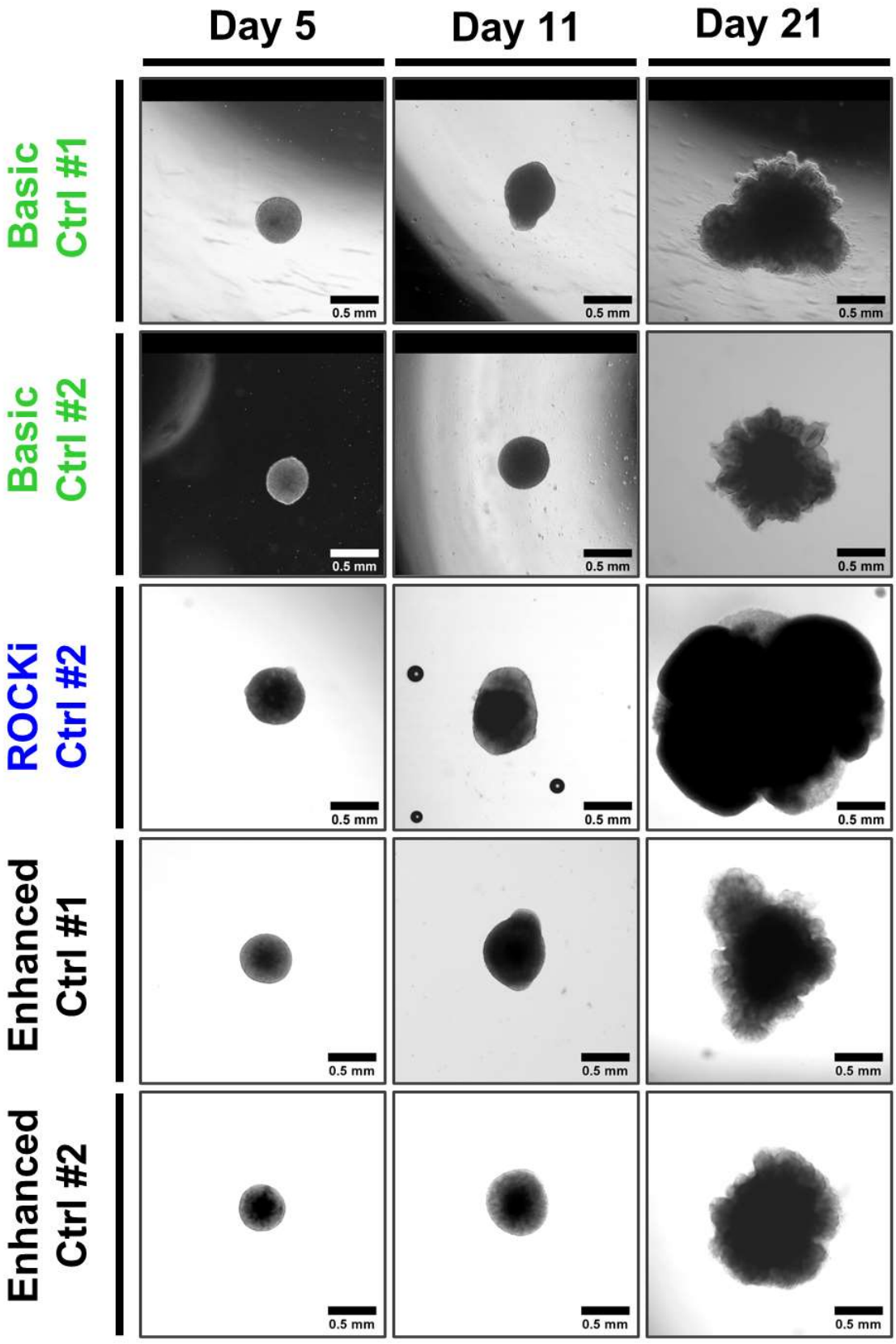

Figure 4.3: Irrespective of cell line, B-hCOs and E-hCOs visibly mirrored cerebral organoid characteristics over time; Ri-hCOs grew into an unspecified mass. Bright-field images of key stages of early hCO differentiation, including Day 5 (EB), Day 11 (NE) and Day 21 (ND), across Basic, ROCKi or Enhanced protocols. hCO protocol and control cell line used referenced in image. Scale bar = 500 μm.

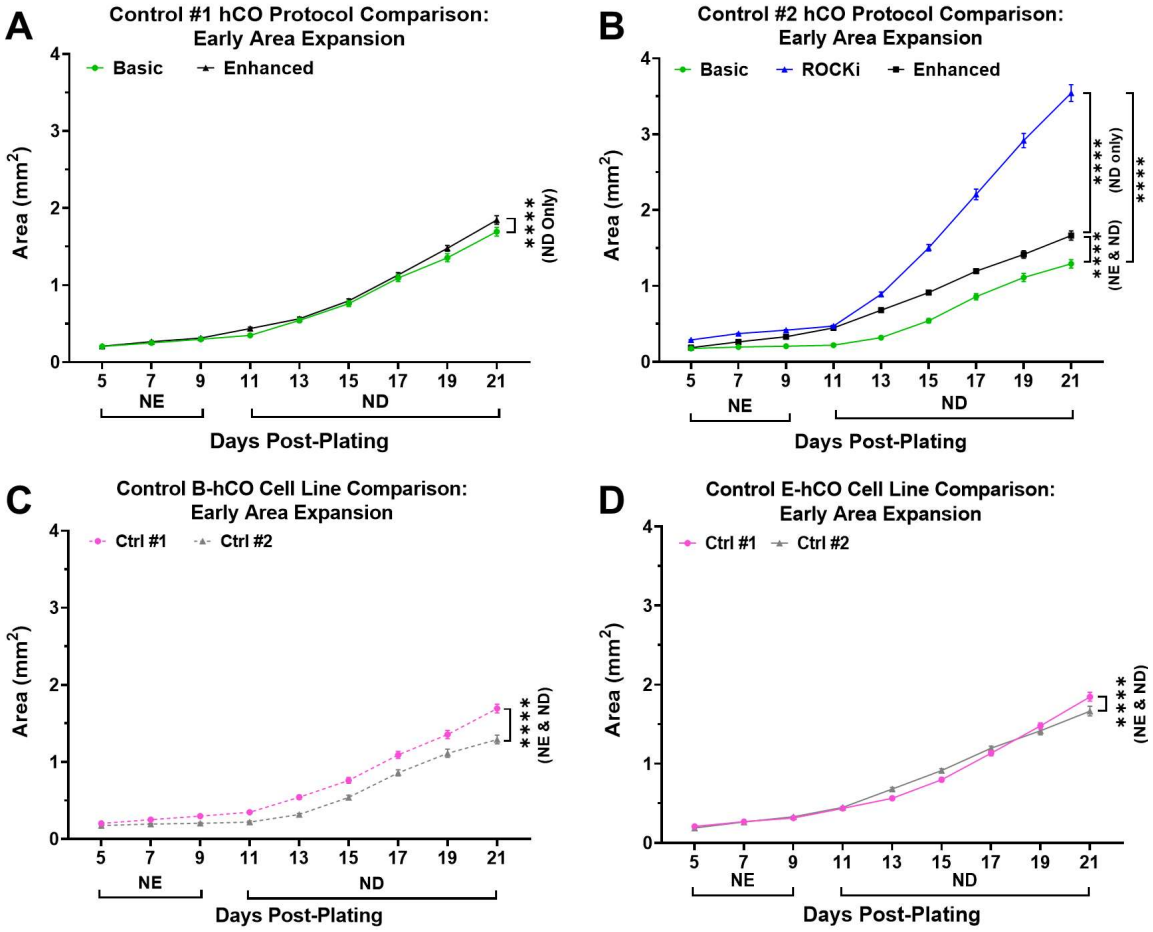

Figure 4.4: Longitudinal analysis of early hCO development proved that each cell line and hCO protocol varied in growth across multiple stages of hCO differentiation.

Growth of area during early hCO differentiation for either hCO protocol comparison using Control #1 **(A)** or Control #2 **(B)**, or comparing control cell lines in B-hCOs **(C)** or E-hCOs **(D).** Data for area was collected from individually-tracked, repeat-batch bright field imaging; mean ±95% CI presented in line graphs. Statistical analysis used mixed effects models on datasets of ≥18 independent hCOs per group (for full information of models see Supplementary Figure 1-4). After two-way ANOVA determined significant variation among conditions, pairwise, Tukey-corrected post-hoc comparison, that accommodated for interaction with Media, was used to determine significant differences in area between hCO protocol or cell line, relative to either the NE or ND stages of hCO differentiation; unlabelled=not significant, ****p=<0.0001.

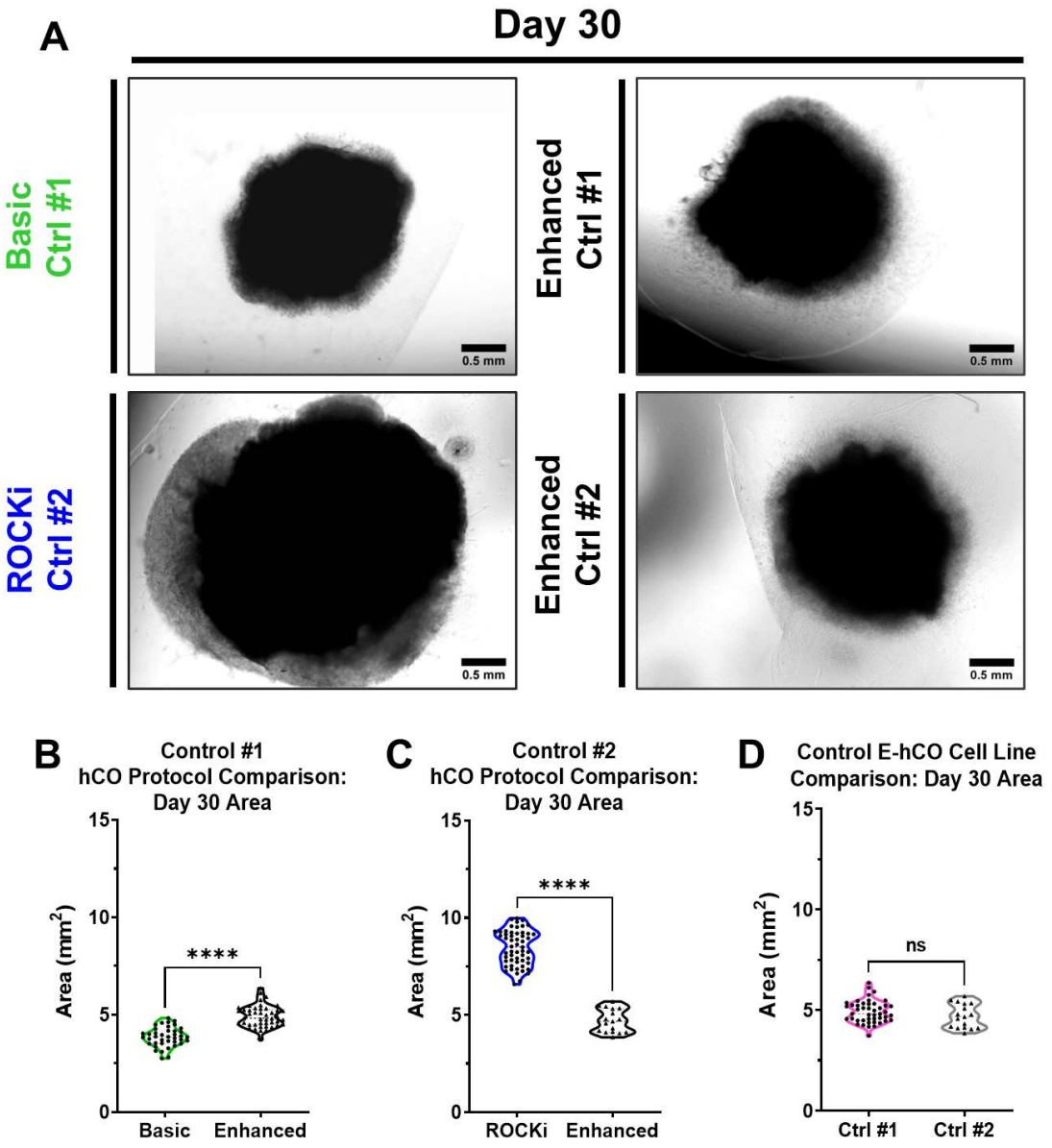

Figure 4.5: Day 30 E-hCOs were larger than B-hCOs, but smaller than Ri-hCOs; no significant differences in area found between control E-hCOs.

A) Bright-field images of Day 30 hCOs from across Basic, ROCKi or Enhanced protocols. hCO protocol and control cell line used referenced in image. Scale bar = 500 µm. **B-D)** Truncated violin plots of hCO area at Day 30, comparing either hCO protocols using Control #1 **(B)** or Control #2 **(C)**, or comparing E-hCOs from both control cell lines **(D)**. Statistical analysis conducted using unpaired, two-tailed t-tests with Welch's correction. All data used n≥17 independent hCOs per group; ns=not significant, ****p=0.0001.

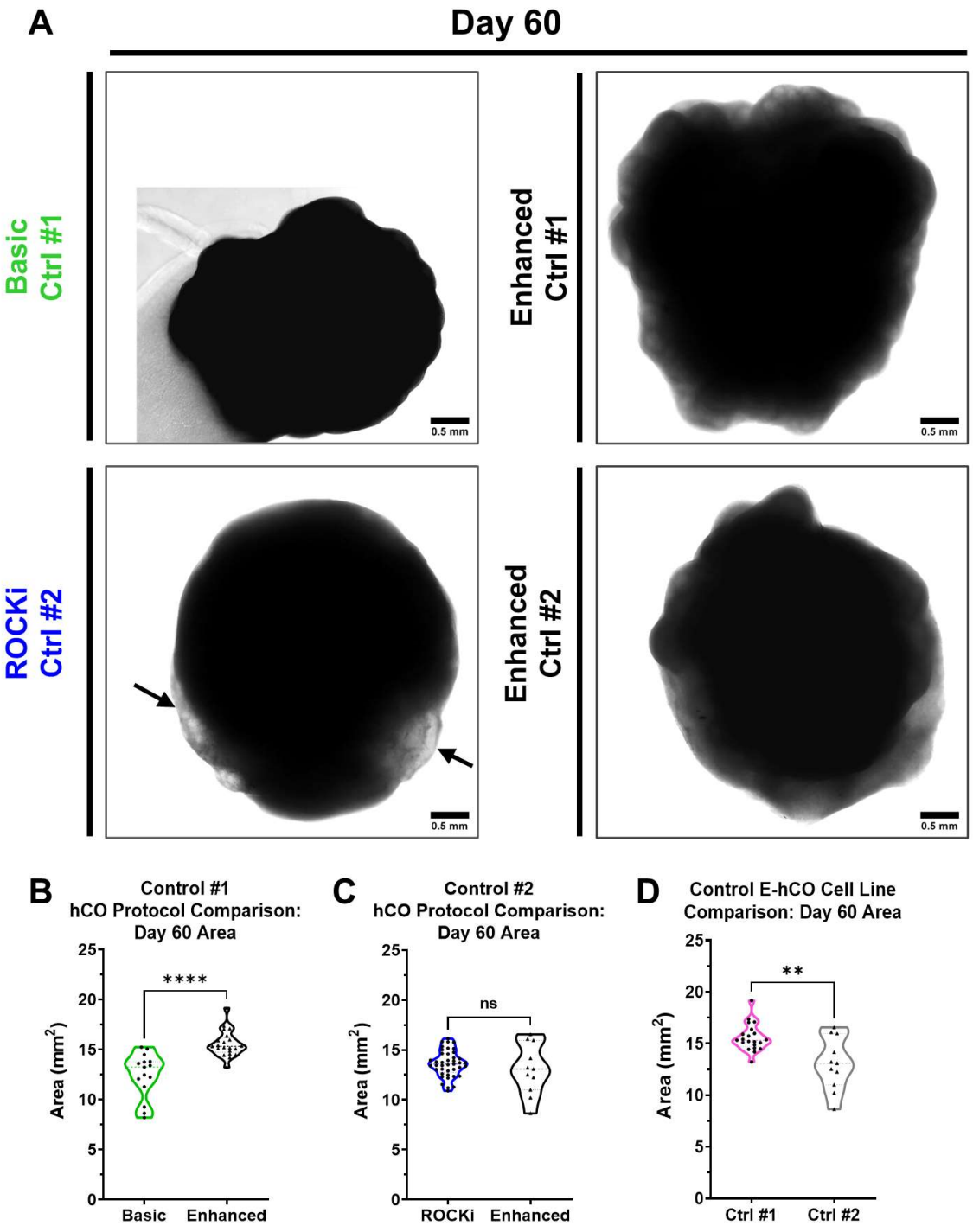

Figure 4.6: Day 60 E-hCOs were larger than B-hCOs, but equal size to Ri-hCOs; significant differences in area found between control E-hCOs.

A) Bright-field images of Day 60 hCOs from across Basic, ROCKi or Enhanced protocols. hCO protocol and control cell line used referenced in image. Annotation of Ri-hCOs refer to cystic regions. Scale bar = 500 µm. **B-D)** Truncated violin plots of hCO area at Day 60, comparing either hCO protocols using Control #1 **(B)** or Control #2 **(C)**, or comparing E-hCOs from both control cell lines **(D)**. Statistical analysis conducted using unpaired, two-tailed t-tests with Welch's correction. All data used n≥11 independent hCOs per group; ns=not significant, **p=<0.005, ****p=<0.0001.

When transferred to RA-supplemented media, hCOs were clustered together into low-attachment, oscillating plates and therefore repeat batch measurements were no longer possible. As such, area measurements were taken as a batch at Day 30 and Day 60. At Day 30, all protocols and cell lines had the expected characteristic of visible neuronal migration into the Matrigel® (Figure 4.5). However, Control #2 Ri-hCOs continued to be substantially larger than their E-hCO counterparts (Figure 4.5.C), and Control #1 E-hCOs were significantly larger than B-hCOs (Figure 4.5.B). There was no difference in area between Control #1 and #2 E-hCOs (Figure 4.5.D). At Day 60, compacted, lobe-like structures should be visible across the hCO, as exhibited by B-hCOs and E-hCOs (Figure 4.6.A). Instead of lobes, semi-transparent cystic regions were found in Ri-hCOs (Figure 4.6.A - annotated). Control #2 E-hCOs had increased in area to match Ri-hCO area and continued to be significantly larger than B-hCOs (Figure 4.6.B-C). Day 60 E-hCOs also had significant changes in area when comparing cell lines, where Control #1 was considerably larger than Control #2 (Figure 4.6.D).

As evidenced above, hCO protocol design affected hCO growth and visible external morphology, the impact of which was either in keeping with Table 4.1.1 requirements (E-hCOs and B-hCOs), or was not (Ri-hCOs). It was also noticeable that control cell lines created variance in the data, regardless of protocol.

4.3.2 Proliferation and Lumen Characteristics, Although Vary Between Cortical Organoid Protocols, are Not Responsible for the Excessive Size of Lumen-Deficient Cortical Organoids

Day 30 hCOs should exhibit unique internal cytoarchitecture that begins with the apical-basal-orientated, proliferative NPCs in the VZ-like region (Figure 4.1.J and Table 4.1.2). At Day 30, B-hCOs and E-hCOs were capable of generating the essential neuroepithelial loops, defined by orientated $SOX2^{+}$ NPC nuclei, with appropriate localisation of KI67 near and around the lumen (Figure 4.7.A and 4.7.C-D). Day 60 B-hCOs and E-hCOs had a similar observation, but larger neuroepithelial loops were observed in Day 60 B-hCOs than in E-hCOs (Figure 4.8.A and 4.8.C-D).

Ri-hCOs, on the other hand, were substantially different than the other two protocols. Day 30 Ri-hCOs were characterised by an unstructured internal mass of $SOX2^+$ cells with few neuroepithelial loops, surrounded by large, unoccupied space that was outlined by a thin band of nuclei, indicating cystic formation (Figure 4.7.B). $KI67^+$ cell abundance was predominantly found in the few neuroepithelial loops that were present, but was otherwise dispersed throughout the Ri-hCO (Figure 4.7.B). Furthermore, it was observed that Day 60 Ri-hCOs had greater cell density than Day 30, but the density was not uniform across the Ri-hCO (Figure 4.8.B); there were also no visible neuroepithelial loops (Figure 4.8.B). SOX2 and KI67 expression in cells was scattered indiscriminately around the “live border” region of the Ri-hCO (Figure 4.8.B). Finally, E-hCOs from both control cell lines showed evidence of neuroepithelial loops with characteristic localisation of $SOX2^+$ and $KI67^+$ cells at Day 30 and Day 60 (Figure 4.7.C-D and 4.8.C-D), but there was substantial difference in organisation of these ventricles at Day 30. Day 30 Control #1 E-hCOs were observed to have greater definition when distinguishing neuroepithelial loops from surrounding cells, as well as larger lumens (Figure 4.7.C-D). On the other hand, Day 60 E-hCOs shared similar morphology with regards to ventricles (Figure 4.8.C-D).

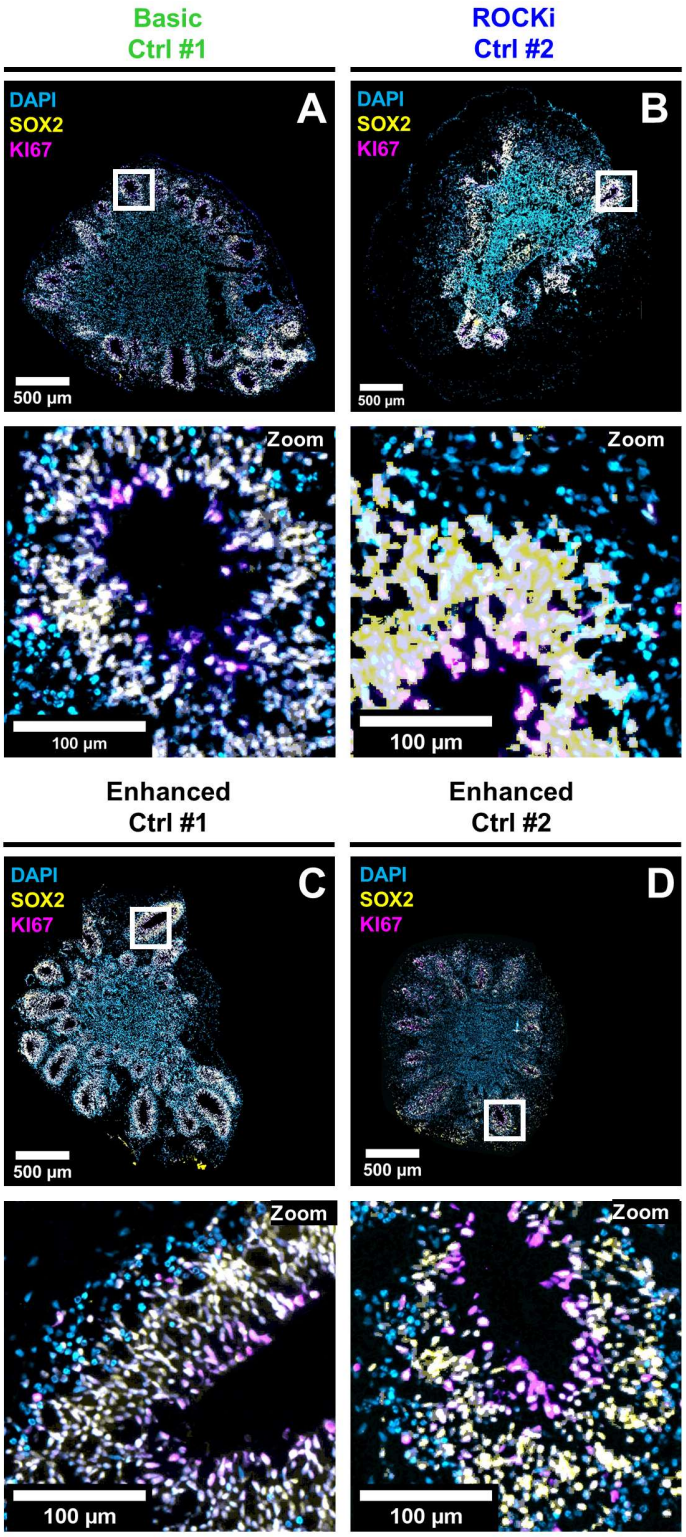

Figure 4.7: Day 30 B-hCOs and E-hCOs exhibited the necessary neuroepithelial loop organisation and localisation of proliferation; cystic formation and few neuroepithelial loops were present in Ri-hCOs.

Fluorescent, slide-scan images of 10 µm hCO slices of Day 30 B-hCOs **(A)**, Ri-hCOs **(B)** and E-hCOs **(C-D).** 20 x magnification with white box annotation referring to zoomed in 250 µm x 250 µm region of interest (ROI). hCO protocol and control cell line used is referenced in image. Proteins identified by colour: KI67 (pink), SOX2 (yellow), DAPI (blue). Scale bar = 500 µm (whole image) or 100 µm (zoomed ROI).

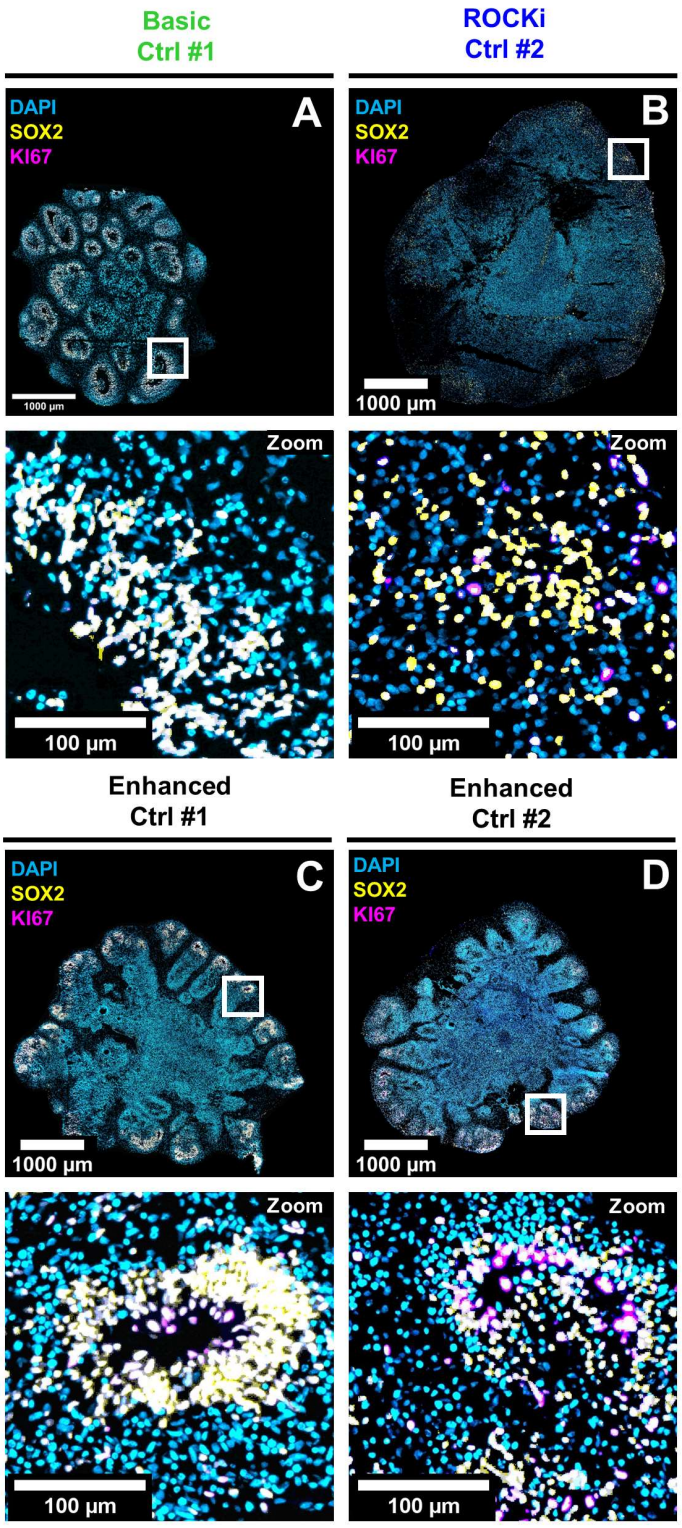

Figure 4.8: Day 60 B-hCOs and E-hCOs exhibited the necessary neuroepithelial loop organisation and localisation of proliferation; scattered proliferation and no neuroepithelial loops were present in Ri-hCOs.

Fluorescent, slide-scan images of 10 µm hCO slices of Day 60 B-hCOs **(A)**, Ri-hCOs **(B)** and E-hCOs **(C-D).** 20 x magnification with white box annotation referring to zoomed in 250 µm x 250 µm region of interest (ROI). hCO protocol and control cell line used is referenced in image. Proteins identified by colour: KI67 (pink), SOX2 (yellow), DAPI (blue). Scale bar = 500 µm (whole image) or 100 µm (zoomed ROI).

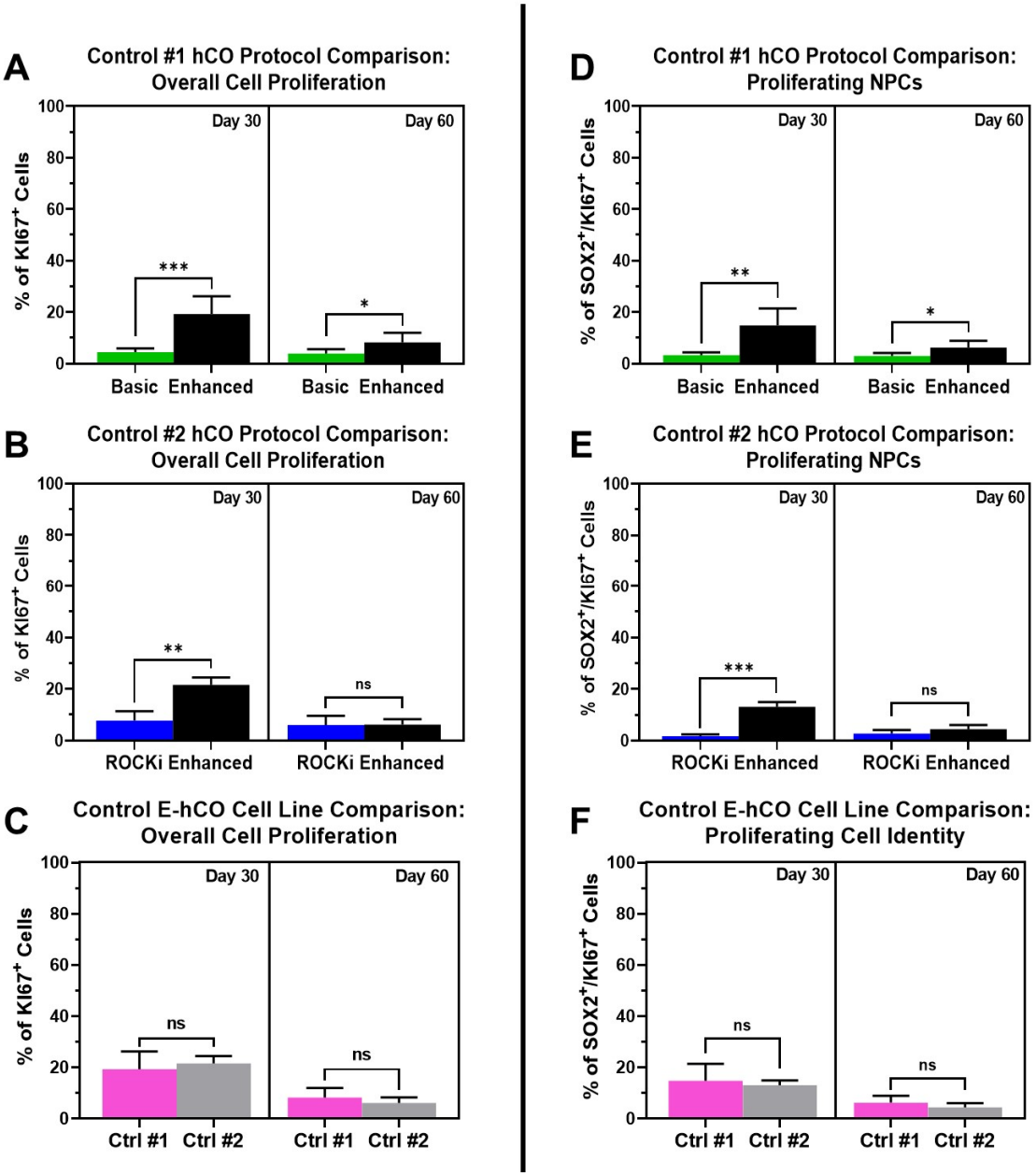

Figure 4.9: E-hCOs had significantly higher proliferation than B-hCOs or Ri-hCOs; no differences in proliferation were found between control E-hCOs.
A-C) Percentage of KI67$^+$/DAPI$^+$ cells at Day 30 and Day 60, comparing hCO protocols that use Control #1 **(A)** or Control #2 **(B)**, or comparing E-hCOs from both control cell lines **(C). D-F)** Percentage of SOX2$^+$/KI67$^+$/DAPI$^+$ cells at Day 30 and Day 60, comparing hCO protocols that use Control # 1 **(D)** or Control #2 **(E)**, or comparing E-hCOs from both control cell lines **(F).** Bar graphs present mean count value as a percentage of total non-apoptotic cells ±standard deviation. Statistical significance determined by Student's t-test with Welch's correction, (n≥3 independent hCOs); ns=not significant, *p=<0.05, **p=<0.005, ***p=<0.0005.

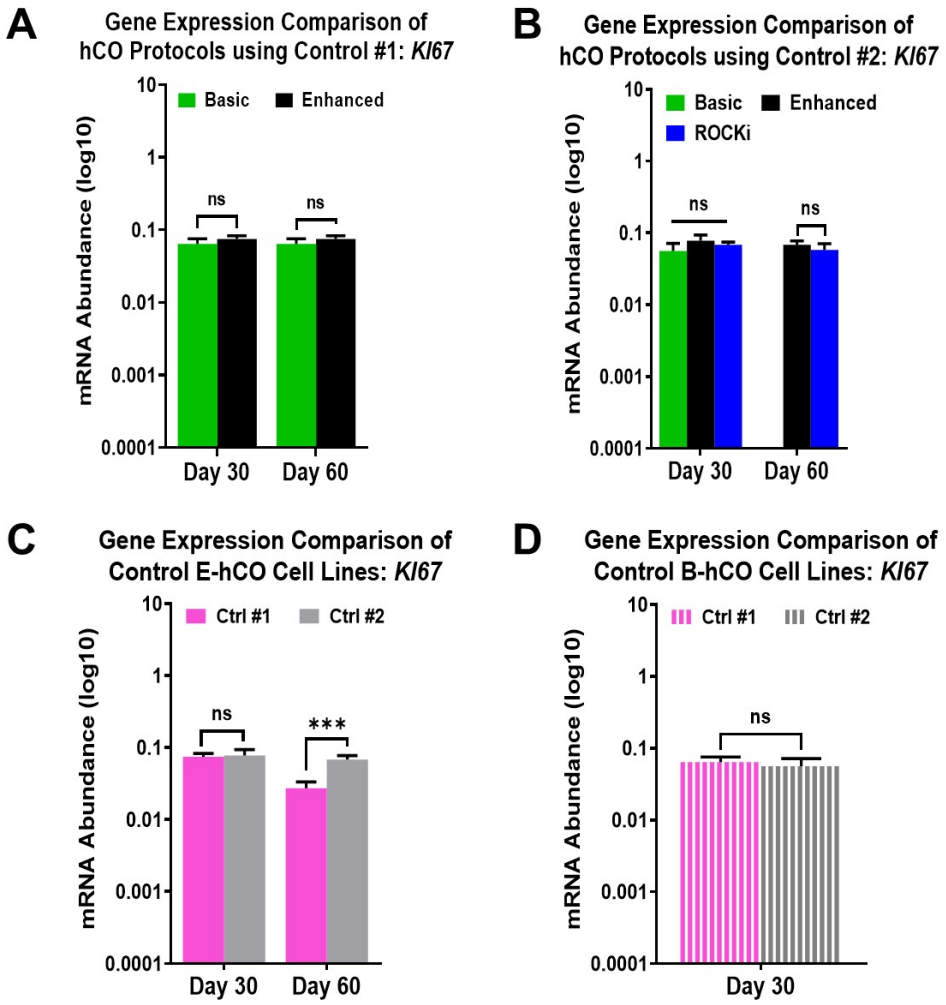

Figure 4.10: *KI67* transcription did not vary between hCO protocols and only varied at Day 60 between control E-hCOs.

mRNA abundance of *KI67* for either hCO protocol comparison using Control #1 **(A)** or Control #2 **(B)**, or comparing both control cell lines in E-hCOs **(C)** or B-hCOs **(D)**. Data is presented as log10 of relative mRNA abundance ($2^{-\Delta CT}$, $\pm 2^{-CI}$). Statistical analysis was conducted on dCTs using either a Student's t-test with Welch's correction **(A, B – Day 60, C-D)** or a one-way ANOVA with Tukey correction for post-hoc tests **(B – Day 30)**, (n≥3 independent hCOs); ns=not significant, ***p=<0.0005.

E-hCOs had consistently more KI67$^+$ cells than the other two hCO protocols, as well as more mitotically active NPCs (SOX2$^+$/KI67$^+$ cells), except when comparing Day 60 for Control #2 Ri-hCOs and E-hCOs (Figure 4.9.A-B and 4.9.D-E). No significant differences in proliferation overall or NPC-specific were found between E-hCOs of the two control cell lines (Figure 4.9.C and 4.9.F). However, hCO protocol and cell line had no effect on *KI67* transcription (Figure 4.10), except at Day 60 in E-hCOs (Figure 4.10.C).

Increased proliferation found in E-hCOs was hypothesised to be related to abundance and organisation of lumens and M phase cells. As shown in Figure 4.11, lumens were defined by ZO1$^+$ expression outlining the apical edge, surrounded by SOX2$^+$, orientated nuclei of NECs/RGs. At the apical edge of the lumen, pVIM$^+$-blebbed nuclei represented cells undertaking the M phase of mitosis. The number of lumens found in each hCO were normalised to APD to avoid bias towards morphological and cell density differences. Additionally, each lumen area measurement, also normalised to APD, was presented as a singular unit (Figure 4.13 and 4.14). At Day 30, Control ‘1 B-hCOs and E-hCOs generated similar quantities of lumens, but of significantly different sizes; B-hCOs were significantly larger (Figure 4.12.A, 4.13.A and 4.13.C); the same could be said of Day 60, (Figure 4.12.A, 4.14.A and 4.14.C), as was observed in whole hCO ICC images (Figure 4.8). Similarly suggested by whole hCO ICC images (Figure 4.7.C-D), E-hCOs had a cell line-specific difference in quantity of lumens at Day 30, but size was comparable (Figure 4.12.C and 4.13.C-D). At Day 60 the control cell lines shared similar quantities of lumens of a similar size (Figure 4.12.C and 4.14.C-D). Conversely to the other two protocols, Ri-hCOs had very little representation of lumens or orientated cells around a defined edge (Figure 4.11.C-D). Day 30 Ri-hCOs had few lumens (Figure 4.12.B), although what lumens were present were comparable in area to Control #2 E-hCOs (Figure 4.13.B and 4.13.D); Day 60 Ri-hCOs had no definable lumens (Figure 4.12.B).

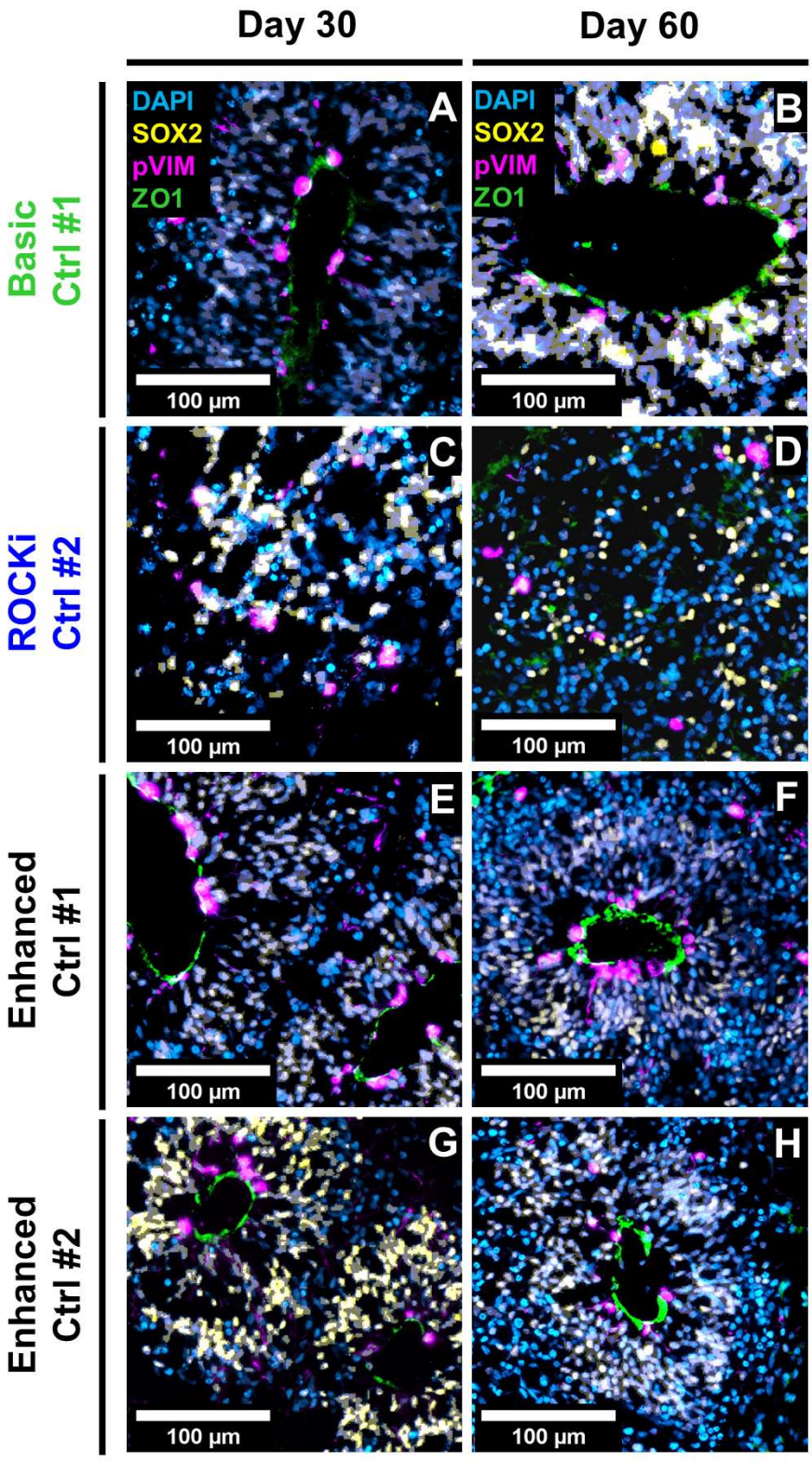

Figure 4.11: E-hCOs and B-hCOs produced neuroepithelial loops containing apical-basal orientated NPCs surrounding a tight junction-bound lumen; Ri-hCOs had no such organisation.

Fluorescent images of 10 µm hCO slices of B-hCOs **(A-B)**, Ri-hCOs **(C-D)** and E-hCOs **(E-H)** at Day 30 and Day 60. 20x magnification, hCO protocol, timepoint and control cell line used is referenced in image. Proteins identified by colour: ZO1 (green), pVIM (pink), SOX2 (yellow), DAPI (blue). Scale bar = 100 µm.

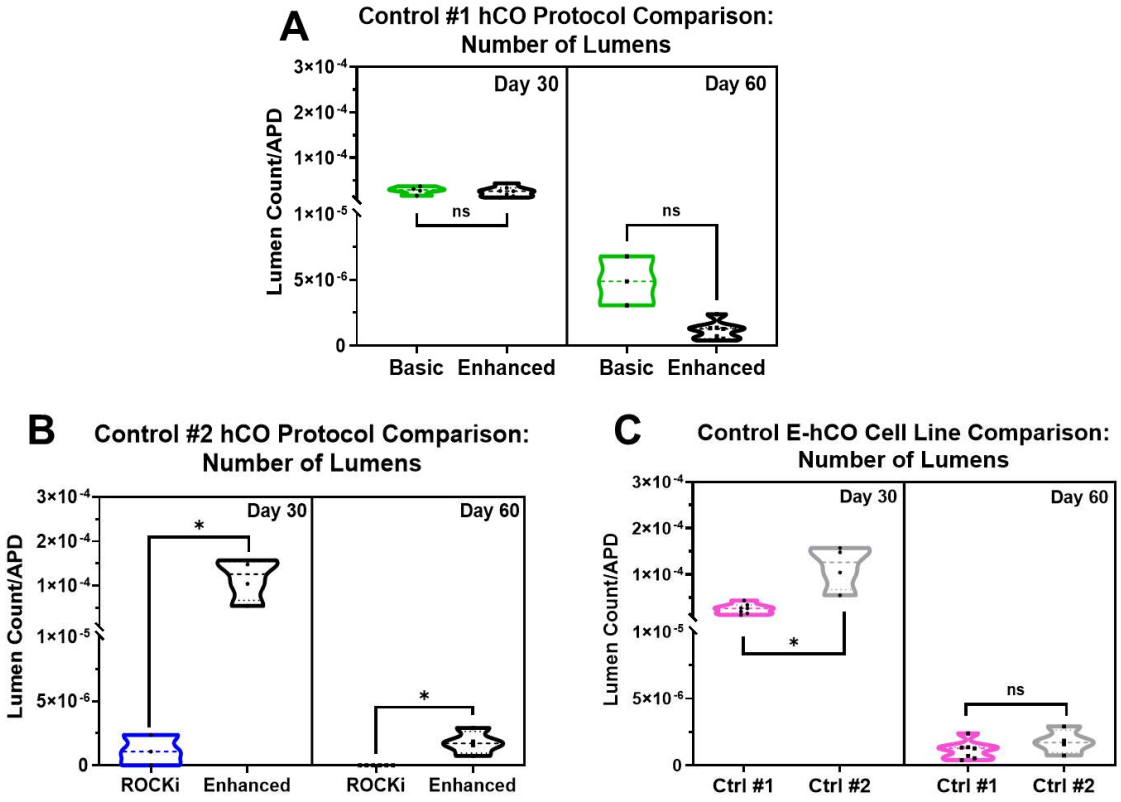

Figure 4.12: E-hCOs and B-hCOs had similar lumen count, whilst Ri-hCOs lacked lumens; control E-hCOs presented some differences in lumen count.

Total number of lumens normalised by APD, comparing hCO protocols using Control #1 **(A)** or Control #2 **(B)**, or comparing E-hCOs from both control cell lines **(C).** Statistical significance defined by Student's t-test with Welch's correction (n≥3 independent hCOs) for all comparisons except for Day 60 comparisons in **(B)** which used a one-sample t-test (μ=0); ns=not significant, *p=<0.05, **p=<0.005, ****p=<0.0001.

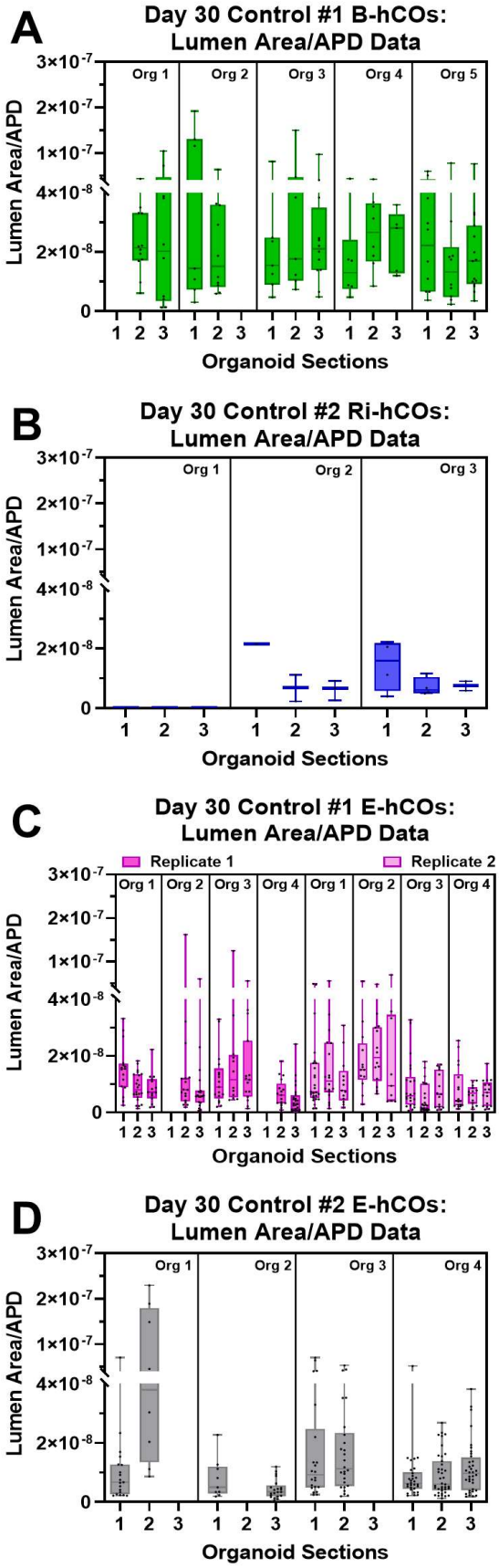

Figure 4.13: Significant differences found between Day 30 B-hCO and E-hCO lumen area, but not between Ri-hCO and E-hCO; lumen area did not change between Day 30 control E-hCOs.

Figure legend on following page.

Figure 4.13 (above): Significant differences found between Day 30 B-hCO and E-hCO lumen area, but not between Ri-hCO and E-hCO; lumen area did not change between Day 30 control E-hCOs.

Measurements of Day 30 raw lumen areas defined by vacuous spaces surrounded by $SOX2^+$ cells and/or $ZO1^+$ aggregation, and divided by APD. hCO lumens presented as individuals (singular dots) within each cryosection, each hCO has ≥2 cryosections; box and whisker plots show full range of points. The following general linear mixed effects model was used for statistical analysis: “lme(log(Lumen_Area) ~ Protocol, random = ~1|Organoid/Section/LumenID, method = “REML”)”. All statistical assumptions of normal residuals and homoscedasticity were met. Pairwise comparisons of estimated marginal means with Bonferroni post-hoc correction were used to determine statistical significance. The following groups were compared: **(A & C)** Control #1 B-hCO/E-hCO protocol comparison: $F(1,11)=15.484$, $p=0.0023$, **(B & D)** Control #2 Ri-hCO/E-hCO protocol comparison: $F(1,4)=0.043$, $p=0.8462$, **(C & D)** E-hCO cell line comparison: $F(1,10)=0.251$, $p=0.6273$.

Figure 4.14 (below): Significant differences found between Day 60 B-hCO and E-hCO lumen area, but not between Ri-hCO and E-hCO or between control E-hCOs.

Measurements of Day 60 raw lumen areas defined by vacuous spaces surrounded by $SOX2^+$ cells and/or $ZO1^+$ aggregation and divided by APD. hCO lumens presented as individuals (singular dots) within each cryosection, each hCO has ≥2 cryosections; box and whisker plots show full range of points. The following general linear mixed effects model was used for statistical analysis: “lme(log(Lumen_Area) ~ Protocol, random = ~1|Organoid/Section/LumenID, method = “REML”)”. All statistical assumptions of normal residuals and homoscedasticity were met. Pairwise comparisons of estimated marginal means with Bonferroni post-hoc correction were used to determine statistical significance. The following groups were compared: **(A & C)** Control #1 B-hCO/E-hCO protocol comparison: $F(1,8)=79.728$, $p=<0.0001$, **(B & D)** Control #2 Ri-hCO/E-hCO protocol comparison required one sample t-test of log(Lumen_Area) [$\mu=0$] concluded: $t(213)=-446.63$, $p=<2.2e-16$, **(C & D)** E-hCO cell line comparison: $F(1,9)=3.629$, $p=0.0892$.

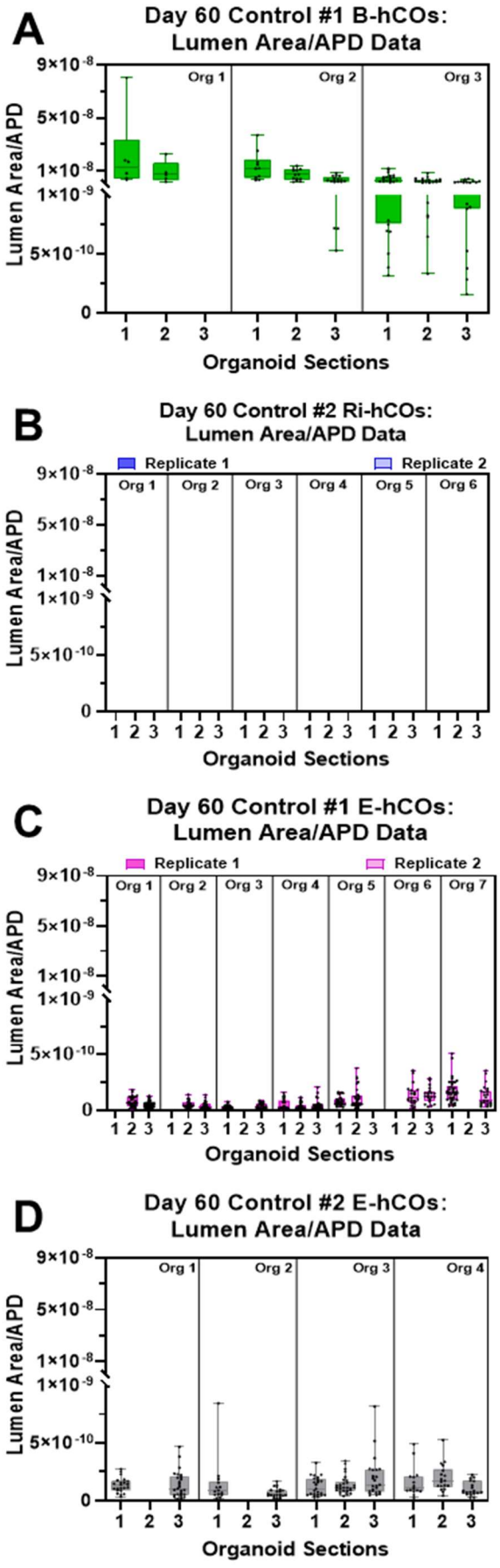

Figure 4.14: Significant differences found between Day 60 B-hCO and E-hCO lumen area, but not between Ri-hCO and E-hCO or between control E-hCOs. Figure legend on previous page.

To supplement lumen observation, transcription of filamentous RG-associated genes *NES* and *VIM* was examined. There was no significant within-protocol variation for control E-hCOs or B-hCOs for Day 30 or Day 60 (Figure 4.15.E-G). However, significant differences were found at Day 60 between hCO protocols; Control #1 B-hCOs had substantially less expression of *NES* and *VIM* than E-hCOs, whilst Control #2 E-hCOs expression was less than Ri-hCOs (Figure 4.15.B and 4.15.D).

As significant changes were found in the lumen count, size and potentially organisation, localisation of proliferation was suspected to vary between hCO protocols. The total number of M phase cells in a hCO mostly paralleled the trends observed in KI67 quantification (Figure 4.9); E-hCOs surpassed the other two hCO protocols for quantity of M phase cells, and that there were no cell line-specific differences (Figure 4.16.A-C). However, there were differences between and within protocols of how many M phase cells were bound close to lumens. Despite a similar quantity of lumens of greater size, Control #1 Day 30 B-hCOs had a significantly smaller percentage of the M phase cell population bound to the apical edge of lumens than Day 30 E-hCOs (Figure 4.16.A). However, at Day 60, the difference was resolved (Figure 4.16.A). There was also a significant difference in the quantity of apically-bound M phase cells between Control #1 and #2 E-hCOs at Day 60 (Figure 4.16.F). Finally, in Ri-hCOs, the majority of M phase cells were not bound to Day 30 Ri-hCO lumens (Figure 4.16.E); as there were no lumens in Day 60 Ri-hCO it was not possible to conduct this analysis (Figure 4.16.E). Assessing these results as a whole, it was clear the B-hCOs and E-hCOs represented the requirements of Table 4.1.2 to varying degrees, whilst Ri-hCOs did not.

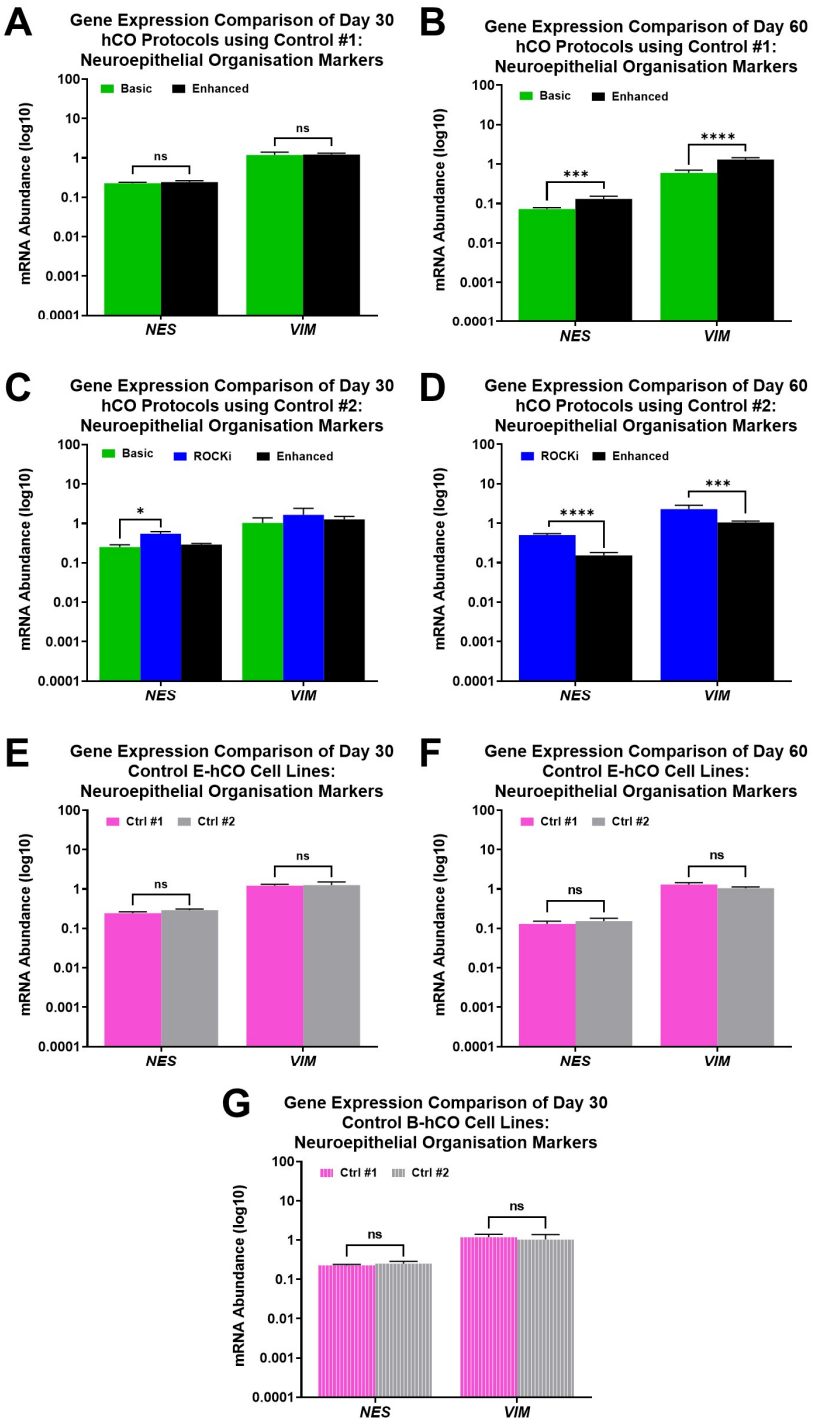

Figure 4.15: *NES* and *VIM* transcription varied between hCO protocols only at Day 60; no variance was found between control E-hCOs.

mRNA abundance of *NES* and *VIM* at Day 30 and Day 60 for either hCO protocol comparison using Control #1 **(A-B)** or Control #2 **(C-D)**, or comparing both control cell lines in E-hCOs **(E-F)** or B-hCOs **(G)**. Data is presented as log10 of relative mRNA abundance ($2^{-\Delta CT}$, $\pm 2^{-CI}$). Statistical analysis was conducted on dCTs using a two-way ANOVA with Geisser-Greenhouse correction with Holm-Šídák correction for post-hoc tests, (n≥3 independent hCOs); unlabelled/ns=not significant, *p=<0.05, ***p=<0.0005, ****p=<0.0001.

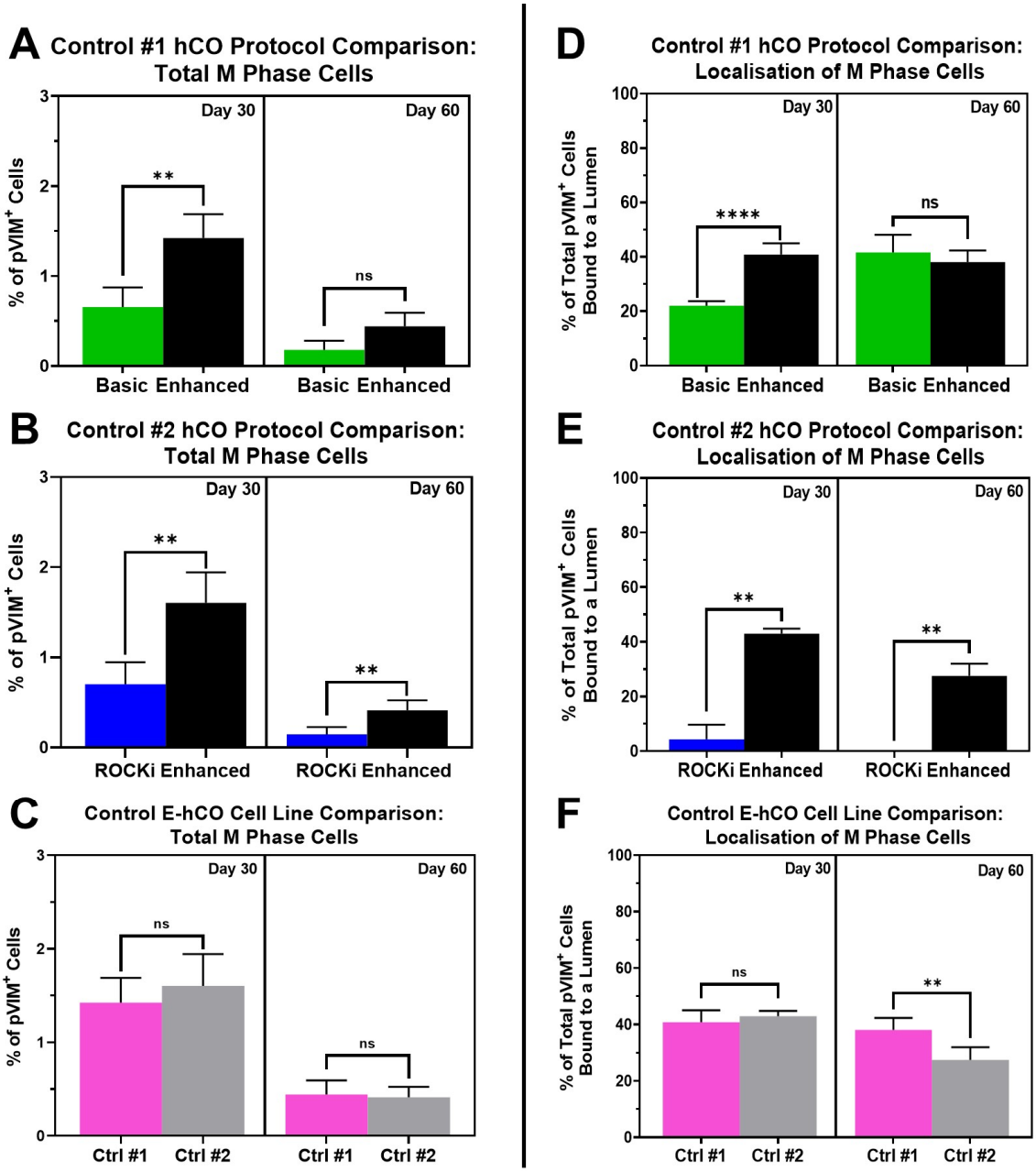

Figure 4.16: E-hCOs had more cells in M phase, of which more were localised to the apical edge of lumens than both B-hCOs and Ri-hCOs; minimal differences were found between control E-hCOs.

A-C) Percentage of pVIM$^+$/DAPI$^+$ cells, comparing hCO protocols that use Control #1 **(A)** or Control #2 **(B)**, or comparing E-hCOs from both control cell lines **(C)**. **D-F)** pVIM$^+$/DAPI$^+$ cell count that are localised to lumens, as a percentage of total pVIM$^+$/DAPI$^+$ cells, comparing protocols using Control #1 **(D)** or Control #2 **(E)**, or comparing E-hCOs from both control cell lines **(F)**. Statistical significance defined by Student's t-test with Welch's correction (n≥3 independent hCOs) for all comparisons except for Day 60 comparisons in **(E)** which used a one-sample t-test (μ=0); ns=not significant, *p=<0.05, **p=<0.005, ****p=<0.0001.

4.3.3 Apoptotic Differences are Observed More Within Cortical Organoid Protocols than Between; the Inverse is Observed for Cell Density

Apoptosis is key to cellular reorganisation during hCO development, particularly in constructing lumens (Hříbková *et al.*, 2018). Minimal variation in apoptosis and NPC-specific apoptosis occurred between Control #1 B-hCOs and E-hCOs at both Day 30 and Day 60 (Figure 4.17.A and 4.17.D). However, when looking at within protocol changes, there was a significantly larger proportion of total apoptosis in Day 30 Control #1 E-hCOs than Control #2; this difference was also observed in NPC-specific apoptosis (Figure 4.17.C and 4.17.F). Additionally, overall and NPC-specific apoptosis was not significantly higher in Control #2 Ri-hCOs than E-hCOs at Day 30, despite the cystic formation (Figure 4.17.B and 4.17.E). However, when the cystic regions had disappeared at Day 60, Control #2 Ri-hCOs had a significantly higher quantity of total apoptotic cells than E-hCOs, but lower NPC-specific apoptosis (Figure 4.17.B and 4.17.E). Although apoptosis remained unchanged between protocols, except for Ri-hCOs at Day 60, E-hCOs were consistently denser than the other protocols (Figure 4.18.A-B). Conversely, no within-protocol variation in cell density is found in E-hCOs (Figure 4.18.C).

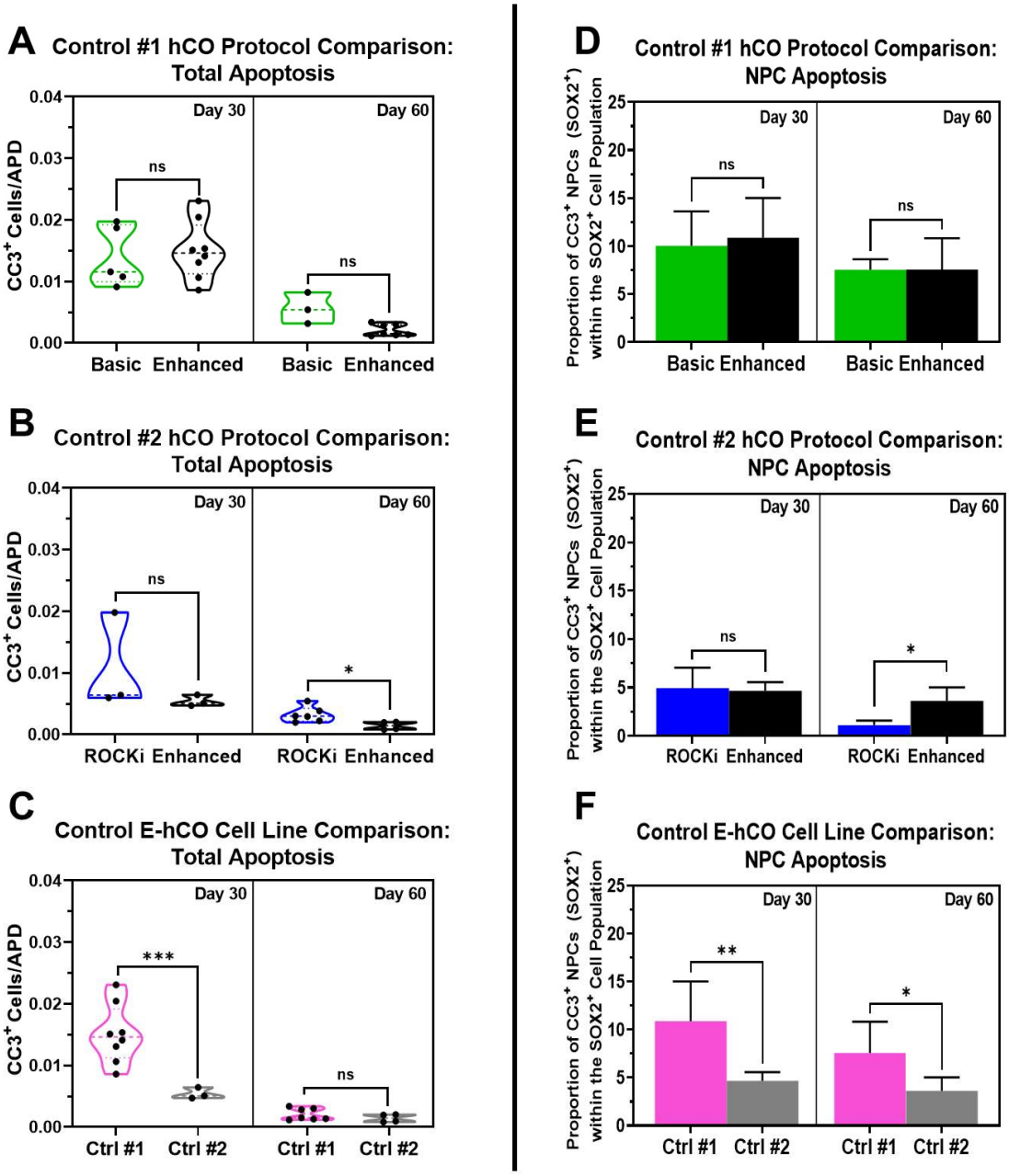

Figure 4.17: Apoptosis did not vary substantially between hCO protocols, but there was within-protocol variation between control E-hCOs.

A-C) $CC3^+/DAPI^+$ count normalised by the APD metric, comparing hCO protocols using Control #1 **(A)** or Control #2 **(B)**, or comparing E-hCOs from both control cell lines **(C)**. **D-F)** Percentage of $SOX2^+/CC3^+/ DAPI^+$ cells within the total $SOX2^+/DAPI^+$ cell population, comparing protocols using Control #1 **(D)** or Control #2 **(E)**, or comparing E-hCOs from both control cell lines **(F)**. Truncated violin plots present all available data; bar graphs present mean counts ±standard deviation. All cell counts were quantified from ICC images. Statistical significance determined by Student's t-test with Welch's correction, (n≥3 independent hCOs); ns=not significant, *p=<0.05, **p=<0.005, ***p=<0.0005.

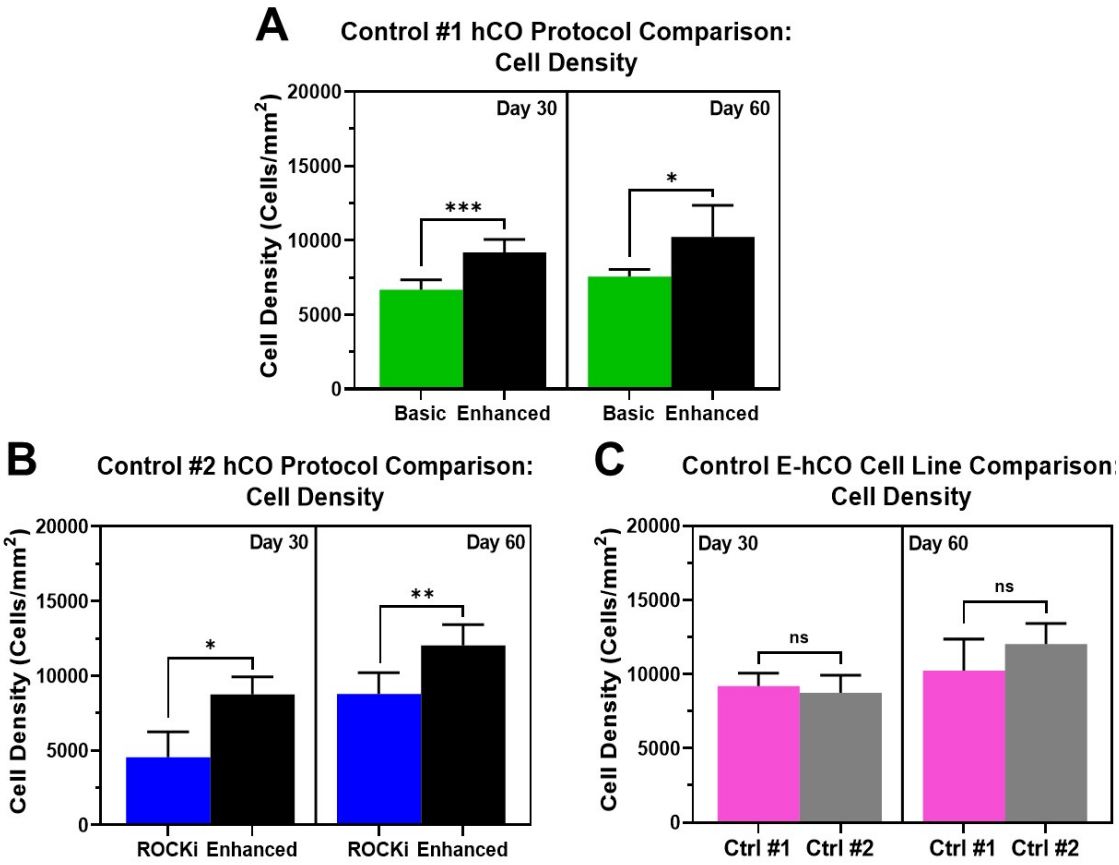

Figure 4.18: E-hCOs had greater cell density than other hCO protocols, without within-protocol variation between control E-hCOs.

Cell density, determined by DAPI^{+} count per mm^2, comparing hCO protocols using Control #1 **(A)** or Control #2 **(B)**, or comparing E-hCOs from both control cell lines **(C)**. Bar graphs present mean counts ±standard deviation. All cell counts were quantified from ICC images. Statistical significance determined by Student's t-test with Welch's correction, (n≥3 independent hCOs); ns=not significant, *p=<0.05, **p=<0.005, ***p=<0.0005.

4.3.4 Dorsal Forebrain Representation Prolific in Cortical Organoids, whilst Significant PAX3 Expression Coincided with FOXG1 Deficit

Cell fate determination needs to be examined in order to confirm hCO dorsal forebrain identity (Table 4.1.3). Firstly, qPCR analysis of key forebrain transcription factors showed that there was little variation in mRNA abundance of both dorsal and ventral forebrain markers between B-hCOs and E-hCOs at Day 30 in Control #1 (Figure 4.19.A). Additionally, there was no difference in number of cells positive for the pan-forebrain marker FOXG1 (Figure 4.24.A). Overall, the transcription of ventral forebrain markers (*NKX2-1, DLX1, OLIG2* and *LHX6*) were low whilst dorsal forebrain markers (*PAX6, EOMES* and *TBR1*) were high for both Control #1 Day 30 B-hCOs and E-hCOs (Figure 4.19.A). This was not the case by Day 60, where Control #1 E-hCOs had greater expression of dorsal forebrain markers than B-hCOs, but also had a trend of increased ventral forebrain markers (Figure 4.19.B). This increase in dorsal forebrain transcription in Day 60 Control #1 E-hCOs was not represented in the percentage of $FOXG1^+$ cells, where B-hCOs exceeded E-hCOs' $FOXG1^+$ cell population at Day 60 (Figure 4.24.B). With regards to non-telencephalic identities, compared to Control #2 E-hCOs, B-hCOs at Day 30 had elevated levels of transcription of midbrain marker *FOXA2,* and of the neural plate border and neural crest cells marker *PAX3* (Figure 4.21.A) (Mehler *et al.*, 2020; So *et al.*, 2020), although there was no increased abundance of $PAX3^+$ cells for B-hCOs (Figure 4.24.A). This was partially reversed at Day 60, where Control #1 E-hCOs had higher transcription of *FOXA2* than B-hCOs, but no other transcriptional differences were observed (Figure 4.21.B).

When reviewing the differences between control cell lines, there was no difference in transcription of any cell identity found between Control #1 and #2 in B-hCOs at Day 30 (Figure 4.19.G and 4.20.G). In E-hCOs, on the other hand, there were a number of significant differences in both dorsal and ventral forebrain markers between Control #1 and #2 at Day 30 (Figure 4.19.E). Interestingly, all of the transcription factors that were significantly different in Figure 4.19.E, i.e., *FOXG1, PAX6, DLX1* and *LHX6*, represented almost all of the differences between Control #2 B-hCOs and E-hCOs at Day 30, except *TBR1* (Figure 4.19.C). The shift towards non-dorsal forebrain identity extended to non-telencephalic identities in Control #2 E-hCOs at Day 30, with increased *HOXB2* and *FOXA2* transcription compared to Control #1 (Figure 4.21.E). These differences dissipated at Day 60, of which the only cell line-specific differences found between control E-

hCOs were the downregulation of *EOMES* and *NKX2-1* in Control #2 E-hCOs (Figure 4.19.F). The Day 30 Control #2 E-hCO-specific trends in non-dorsal forebrain identity were observed only in transcriptional analysis, and did not reflect a difference in cell populations positive for NKX2.1, FOXG1 and TBR2 (Figure 4.20.B, 4.24.E-F and 4.26.E).

Conversely, Ri-hCOs had comparatively low transcription for almost all analysed dorsal forebrain markers, e.g. *FOXG1, PAX6* and *TBR1*, at both Day 30 and Day 60 (Figure 4.19.C-D). Control #2 Ri-hCOs had similar expression of ventral forebrain markers as E-hCOs (*NKX2-1*, *DLX1* and *LHX6*) with a significant increase in *OLIG2*, as well as similar abundance of the $NKX2.1^{+}$ cell population at Day 60 (Figure 4.19.C-D and 4.20.A), despite poor *FOXG1* transcription and $FOXG1^{+}$ cell population across both timepoints (Figure 4.19.C-D and 4.24.C-D, respectively). There were minimal differences in non-telencephalic identity between Ri-hCOs and B-hCOs/E-hCOs at either timepoint, with the exception of increased *HOXB2* transcription at Day 30 and a trend or significant increase in *PAX3* transcription (Figure 4.21.C-D).

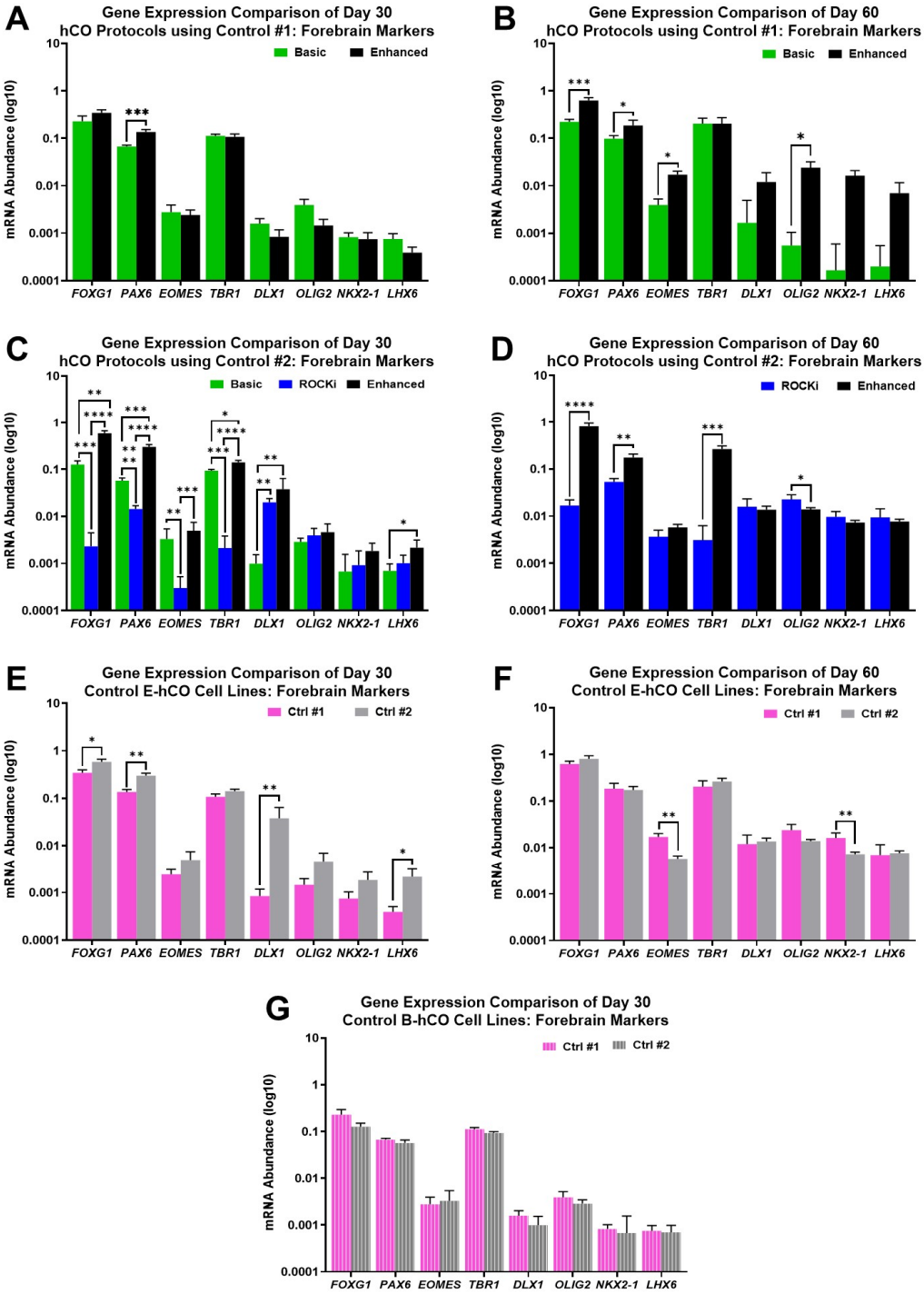

Figure 4.19: B-hCOs and E-hCOs both expressed dorsal forebrain markers, whilst Ri-hCOs did not; significant differences between control E-hCOs were found, but not between control B-hCOs.

Each graph compares the transcription of forebrain markers between hCO protocols that use Control #1 **(A-B)** or Control #2 **(C-D),** or compares both control cell lines in E-hCOs **(E-F)** or B-hCOs **(G).** Data is presented as relative mRNA abundance ($2^{-\Delta CT}$, $\pm 2^{-CI}$). Statistical analysis was conducted on dCTs using a two-way ANOVA with Geisser-Greenhouse correction with Holm-Šídák correction for post-hoc tests, (n≥3 independent hCOs); unlabelled=not significant, *p=<0.05, **p=<0.005, ***p=<0.0005, ****p=<0.0001.

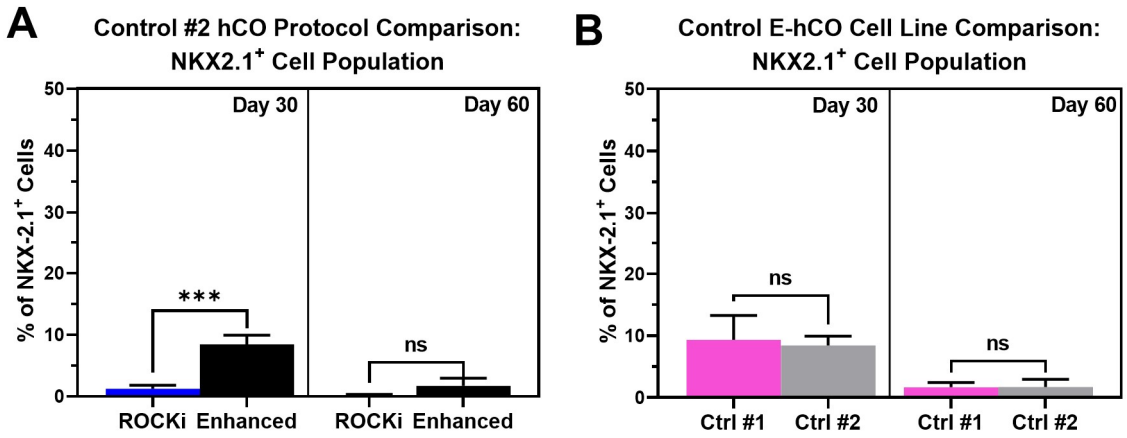

Figure 4.20: Control E-hCOs had a small population of ventral forebrain progenitors, whilst Ri-hCOs did not.

Percentage of NKX2.1$^+$/DAPI$^+$ cells, comparing hCO protocols that use Control #2 **(A)** or comparing E-hCOs from both control cell lines **(B).** Bar graphs present mean count percentage ±standard deviation. All cell counts were quantified from ICC images. Statistical significance determined by Student's t-test with Welch's correction, (n≥3 independent hCOs); ns=not significant, ***p=<0.0005.

As the morphological abnormalities start early in Ri-hCOs (Figure 4.3), and PAX3 is known to cause severe disruption to early neuronal development when dysregulated (Sudiwala *et al.*, 2019; Palmer *et al.*, 2021), this upregulation was investigated further. PAX3 was visible throughout the Day 30 Ri-hCO and intermittently across the live border of Day 60 Ri-hCOs, whilst FOXG1 was not visible at either timepoint (Figure 4.22.B and 4.23.B). This was in stark contrast to what was observed in B-hCOs and E-hCOs, where FOXG1$^+$ cells were abundant, whilst PAX3$^+$ cells had also been found in small populations in E-hCOs (Figure 4.22.A, 4.22.C-D, 4.23.A and 4.23.C-D). FOXG1$^+$ and PAX3$^+$ cell populations arose discretely separate from one another and only had trace levels of colocalisation across all three protocols, even when there were high populations of FOXG1$^+$ cells (Figure 4.24). Additionally, the only observed difference in PAX3$^+$ cell populations between and within protocols was in Control #2 Ri-hCOs, which had consistently elevated populations of PAX3$^+$ cells when compared to E-hCOs, between 5-10% of all non-apoptotic cells (Figure 4.24.C-D).

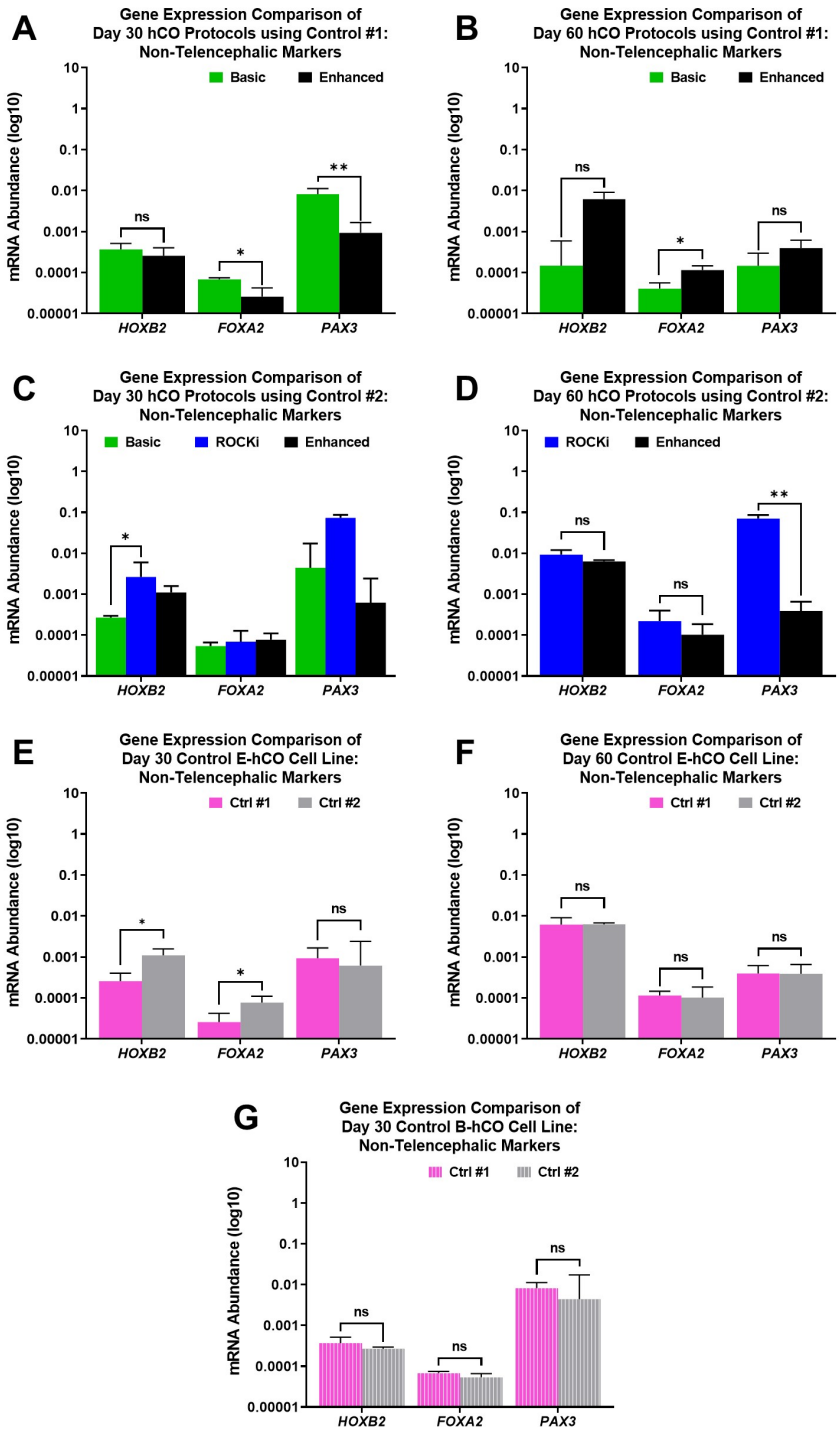

Figure 4.21: Variable expression of non-telencephalic marker expression was found both between and within hCO protocols; *PAX3* expression was substantially higher in B-hCOs and Ri-hCOs.

Each graph compares the transcription of the non-telencephalic markers hindbrain *(HOXB2),* midbrain (*FOXA2*) and neural crest (*PAX3*), between hCO protocols that use Control #1 **(A-B)** or Control #2 **(C-D)**, or compares both control cell lines in E-hCOs **(E-F)** or B-hCOs **(G)**. Data is presented as relative mRNA abundance ($2^{-\Delta CT}$, $\pm 2^{-CI}$). Statistical analysis was conducted on dCTs using a two-way ANOVA with Geisser-Greenhouse correction with Holm-Šídák correction for post-hoc tests, (n≥3 independent hCOs); unlabelled/ns=not significant, *p=<0.05, **p=<0.005.

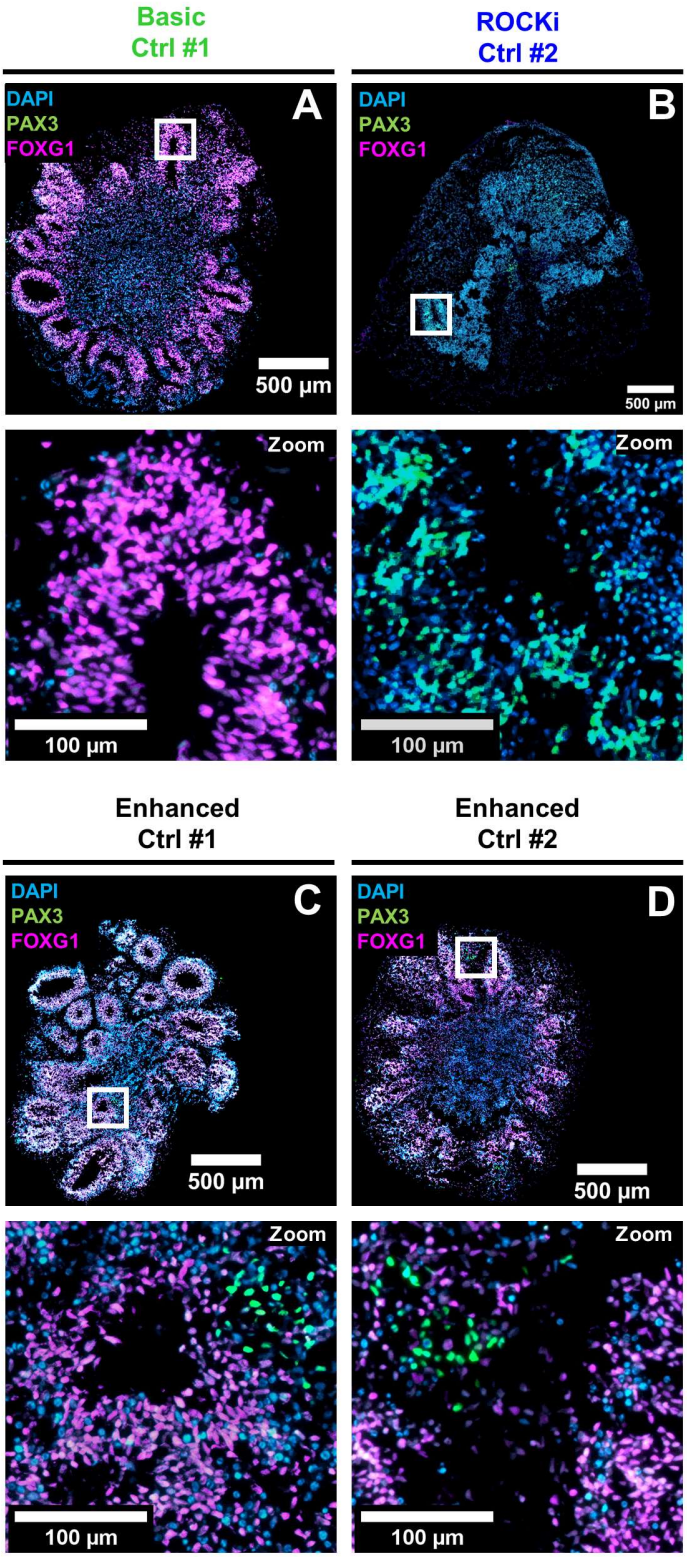

Figure 4.22: FOXG1^{+} cells localised to ventricle regions in Day 30 B-hCOs and E-hCOs, whilst PAX3^{+} cells localised to VZ-like regions in Ri-hCOs.
Fluorescent images of 10 µm hCO slices of B-hCOs **(A)**, Ri-hCOs **(B)** and E-hCOs **(C-D)** at Day 30. 20x magnification with white box annotation referring to zoomed in 250 µm x 250 µm region of interest. hCO protocol, timepoint and control cell line used is referenced in image. Proteins identified by colour: FOXG1 (pink), PAX3 (green), DAPI (blue). Scale bar = 500 µm (whole image) or 100 µm (zoomed ROI).

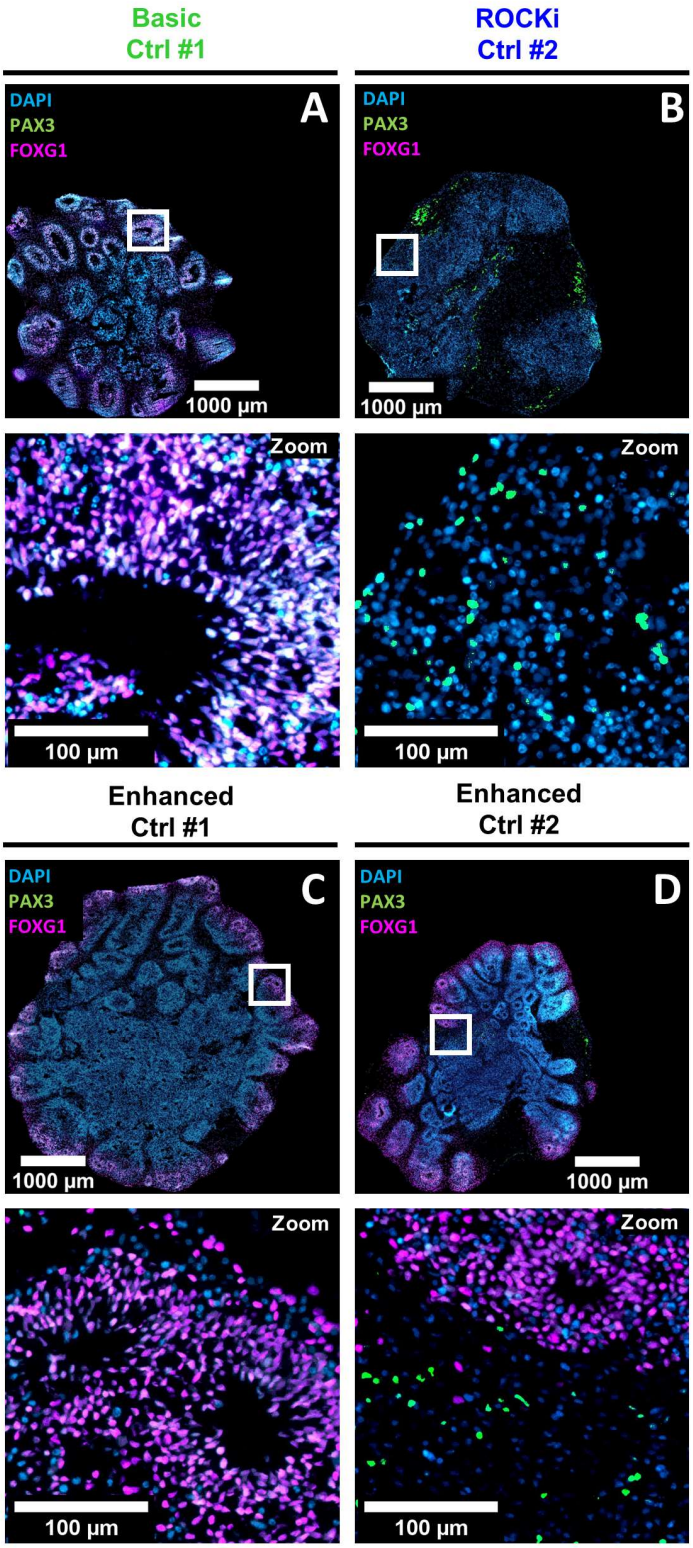

Figure 4.23: FOXG1⁺ cells localised to ventricle regions in Day 60 B-hCOs and E-hCOs, whilst PAX3⁺ cells localised around the border of Ri-hCOs.
Fluorescent images of 10 µm hCO slices of B-hCOs **(A)**, Ri-hCOs **(B)** and E-hCOs **(C-D)** at Day 60. 20x magnification with white box annotation referring to zoomed in 250 µm x 250 µm region of interest. hCO protocol, timepoint and control cell line used is referenced in image. Proteins identified by colour: FOXG1 (pink), PAX3 (green), DAPI (blue). Scale bar = 500 µm (whole image) or 100 µm (zoomed ROI).

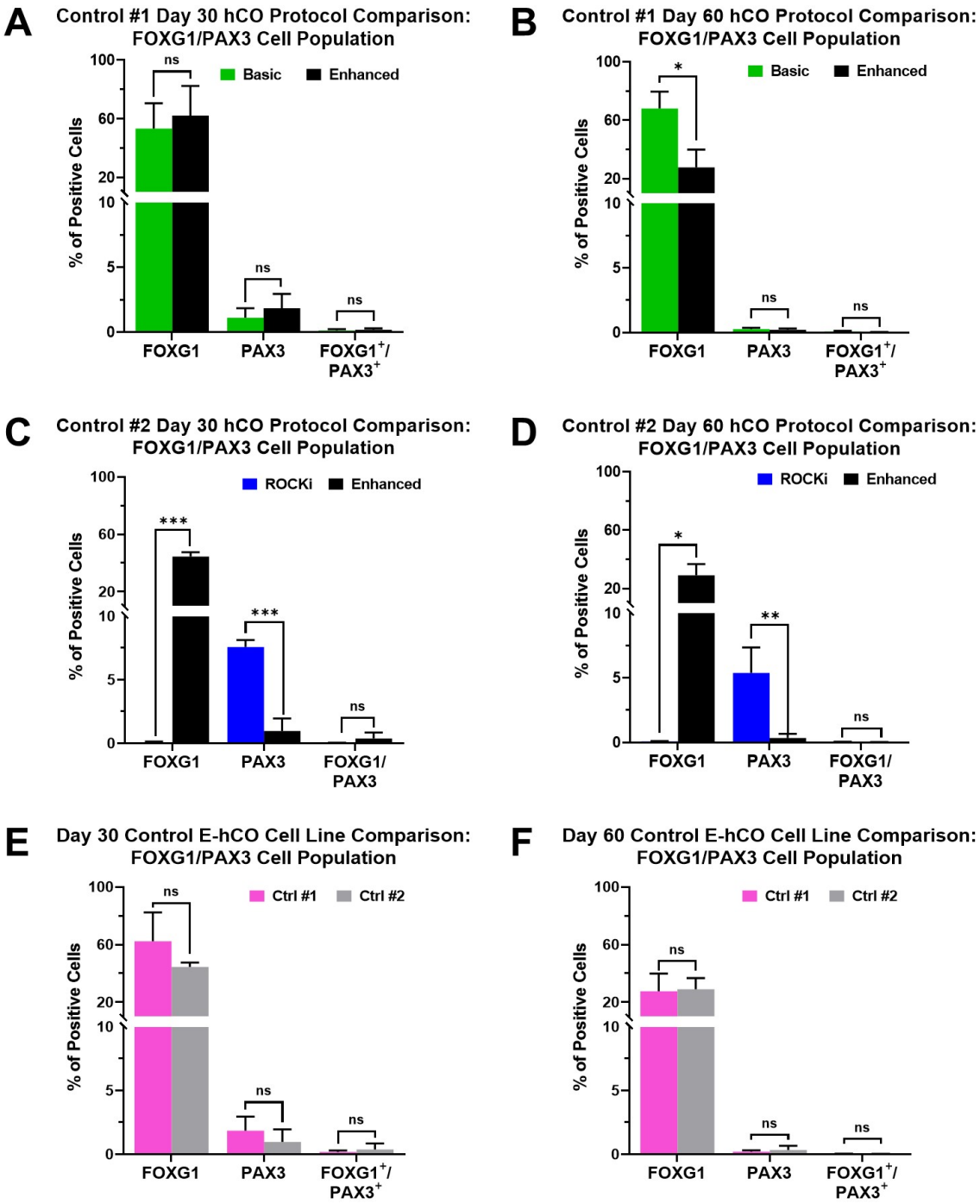

Figure 4.24: FOXG1⁺ cells were abundant in B-hCOs and E-hCOs, whilst Ri-hCOs had few FOXG1⁺ cells but more PAX3⁺ cells.

Each graph compares the percentage of FOXG1, PAX3 and FOXG1/PAX3 positive cells between hCO protocols that use Control #1 **(A-B)** or Control #2 **(C-D),** or compares both control cell lines in E-hCOs **(E-F)** in Day 30 and Day 60 hCOs**.** Bar graphs present mean count percentage ±standard deviation. All cell counts were quantified from ICC images. Statistical significance determined by Student's t-test with Welch's correction, (n≥3 independent hCOs); ns=not significant, *p=<0.05, **p=<0.005, ***p=<0.0005.

4.3.5 Neocortical Layering Occurs in Cortical Organoids, but to Varying Degrees and Not Consistently Between Cell Lines

With confirmation of B-hCOs' and E-hCOs' dorsal forebrain identity, the next requirement was to investigate possible layering organisation that emulates the distinctive cell populations representative of VZ, SVZ and CP (Table 4.1.4). At Day 30, there was minimal organisation of these populations in both B-hCOs and E-hCOs, only clear distinction between VZ and surrounding tissue (Figure 4.25.A, 4.25.D and 4.25.F). Although the $SOX2^+$ NPC pool was consistent across Control #1 B-hCOs and E-hCOs at Day 30, E-hCOs showed increased populations of both $TBR2^+$ IPs and $CTIP2^+$ neurons (Figure 4.26.A). This divergence was similarly observed in mRNA abundance, but only when comparing Day 30 B-hCOs and E-hCOs of Control #2, not in Control #1 (Figure 4.28.A and 4.28.C). There were also elevated numbers of IPs transitioning into neurons in Day 30 E-hCOs compared to B-hCOs (Figure 4.26.B). Day 60 B-hCO ICC images were unavailable, but transcriptional analysis pointed to a reduced NPC pool in Control #1 Day 60 B-hCOs compared to E-hCOs, represented by the significant and trending downregulation of *SOX2, HOPX* and *EOMES* (Figure 4.28.B).

Although both Control #1 and #2 E-hCOs were able to separate into the three distinctive layers of VZ, SVZ and CP by Day 60 (Figure 4.25.D-G), there were a number of cell line-specific differences in E-hCOs across both timepoints. Control #1 E-hCOs had substantially more $SOX2^+$ NPCs and $CTIP2^+$ neurons, and transitioning IPs to neurons, at Day 30 than Control #2 E-hCOs (Figure 4.26.E-F). At Day 60, the $TBR2^+$ IPs, $CTIP2^+$ neurons and transitioning cell populations were similar between E-hCOs of both cell lines, but there was still a significant change in $SOX2^+$ NPCs (Figure 4.27.C-D). Contrasting what was observed at ICC level, transcription of *SOX2, EOMES* and *BCL11B* did not vary between control cell lines for both the Enhanced or Basic protocol for either timepoint, except for *EOMES* at Day 60 in E-hCOs (Figure 4.28.E-G).

Given the previous observation of persistently low dorsal forebrain marker expression (Figure 4.19.C-D), it was unsurprising that there was minimal presence of $TBR2^+$ and $CTIP2^+$ cells in Ri-hCOs at Day 30 or Day 60 (Figure 4.26.C-D and 4.27.A-B). As a result, there was no observable hierarchy of layering structure in Ri-hCOs at either timepoint (Figure 4.25.B-C). This was also reflected in downregulation of transcription of key cortical layer markers at Day 30 (*SOX2,*

EOMES, TBR1, BCL11B and *REELIN*) and at Day 60 (*TBR1* and *BCL11B*) (Figure 4.28.C-D). However, there were a relatively equal number of $SOX2^+$ NPCs in Ri-hCOs compared to E-hCOs at Day 30, and significantly more at Day 60 (Figure 4.26.C and 4.27.A), despite lacking $FOXG1^+$, $CTIP2^+$ or $TBR2^+$ cells at either timepoint (Figure 4.24.C-D, 4.26.C and 4.27.A).

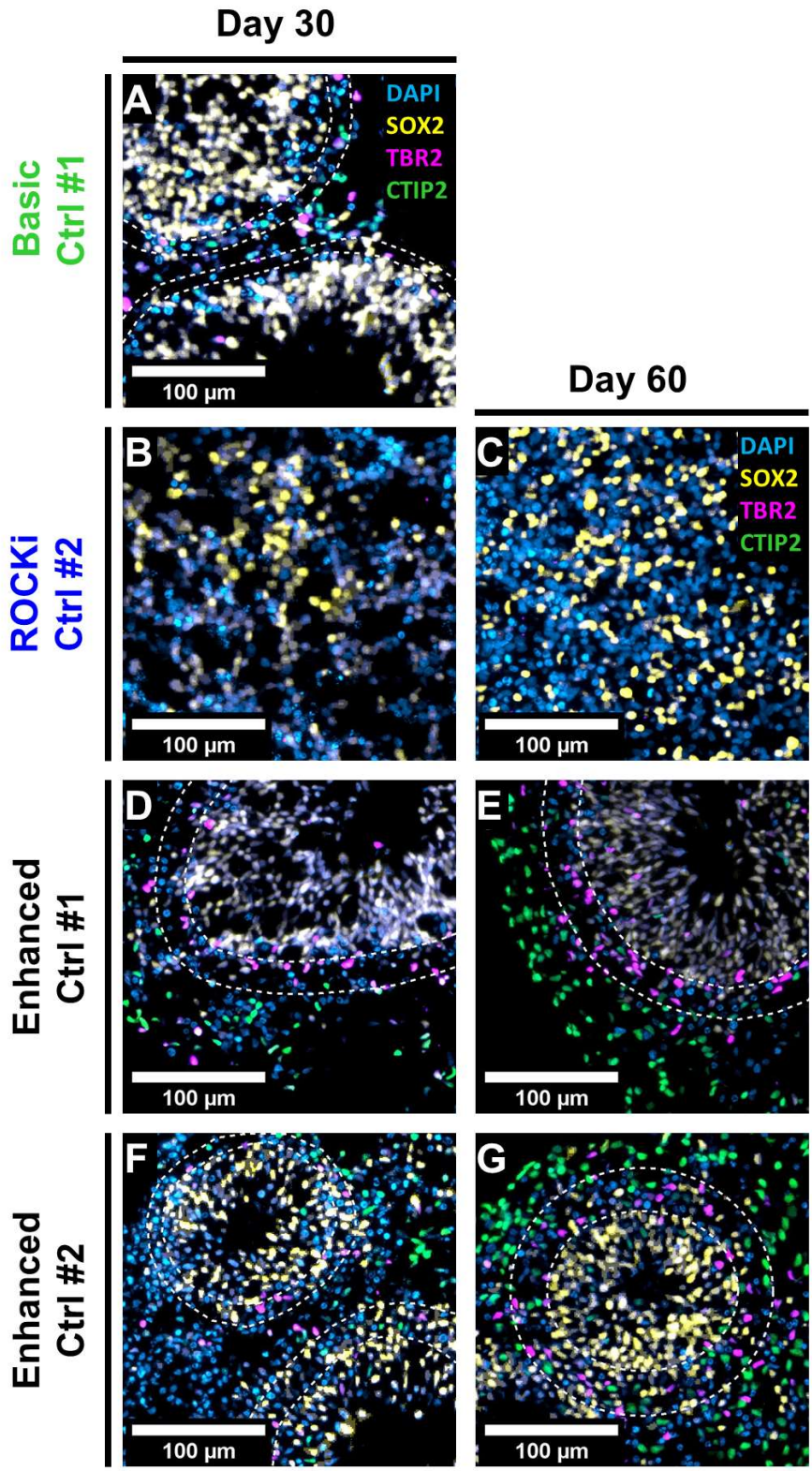

Figure 4.25: B-hCOs and E-hCOs have cellular organisation reminiscent of cortical layers, whilst Ri-hCOs had no distinguishable layering.
Fluorescent images of 10 µm hCO slices of B-hCOs **(A)**, Ri-hCOs **(B-C)** and E-hCOs **(D-G)** at Day 30 and 60. 20x magnification, with white dashed lines annotating VZ ($SOX2^+$), SVZ ($TBR2^+$) and CP ($CTIP2^+$) layers within hCOs. hCO protocol and control cell line used is referenced in image. Proteins identified by colour: CTIP2 (green), TBR2 (pink), SOX2 (yellow), DAPI (blue). Scale bar = 100 µm.

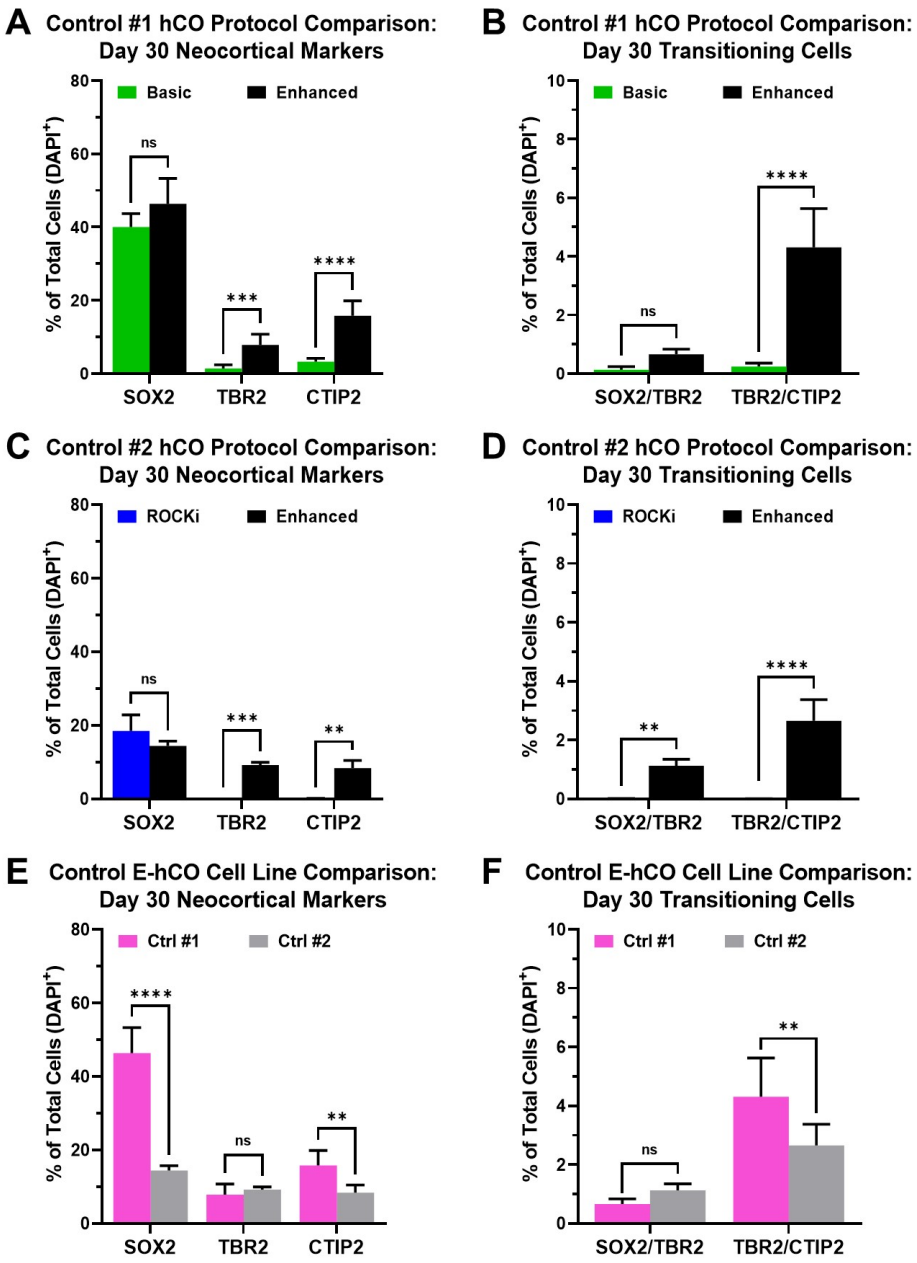

Figure 4.26: E-hCOs had significantly more IPs and neurons than B-hCOs at Day 30, whilst Ri-hCOs only had NPCs; significant variance was found between control E-hCOs.

A, C and E) Percentage of SOX2$^+$/DAPI$^+$, TBR2$^+$/DAPI$^+$ and CTIP2$^+$/DAPI$^+$ cells in Day 30 hCOs, comparing hCO protocols that use Control #1 **(A)** or Control #2 **(C)**, or comparing E-hCOs from both control cell lines **(E). B, D and F)** Percentage of SOX2$^+$/TBR2$^+$/DAPI$^+$ and TBR2$^+$/CTIP2$^+$/DAPI$^+$ cells in Day 30 hCOs, comparing hCO protocols that use Control #1 **(B)** or Control #2 **(D)**, or comparing E-hCOs from both control cell lines at Day 30 **(F).** Bar graphs present mean counts ±standard deviation. All cell counts were quantified from ICC images. Statistical analysis used a two-way ANOVA, with Geisser-Greenhouse correction for **(A), (C)** and **(E)**, with Holm-Šídák correction for post-hoc tests, (n≥3 independent hCOs); ns=not significant, *p=<0.05, **p=<0.005, p***=<0.0005, p****=<0.0001.

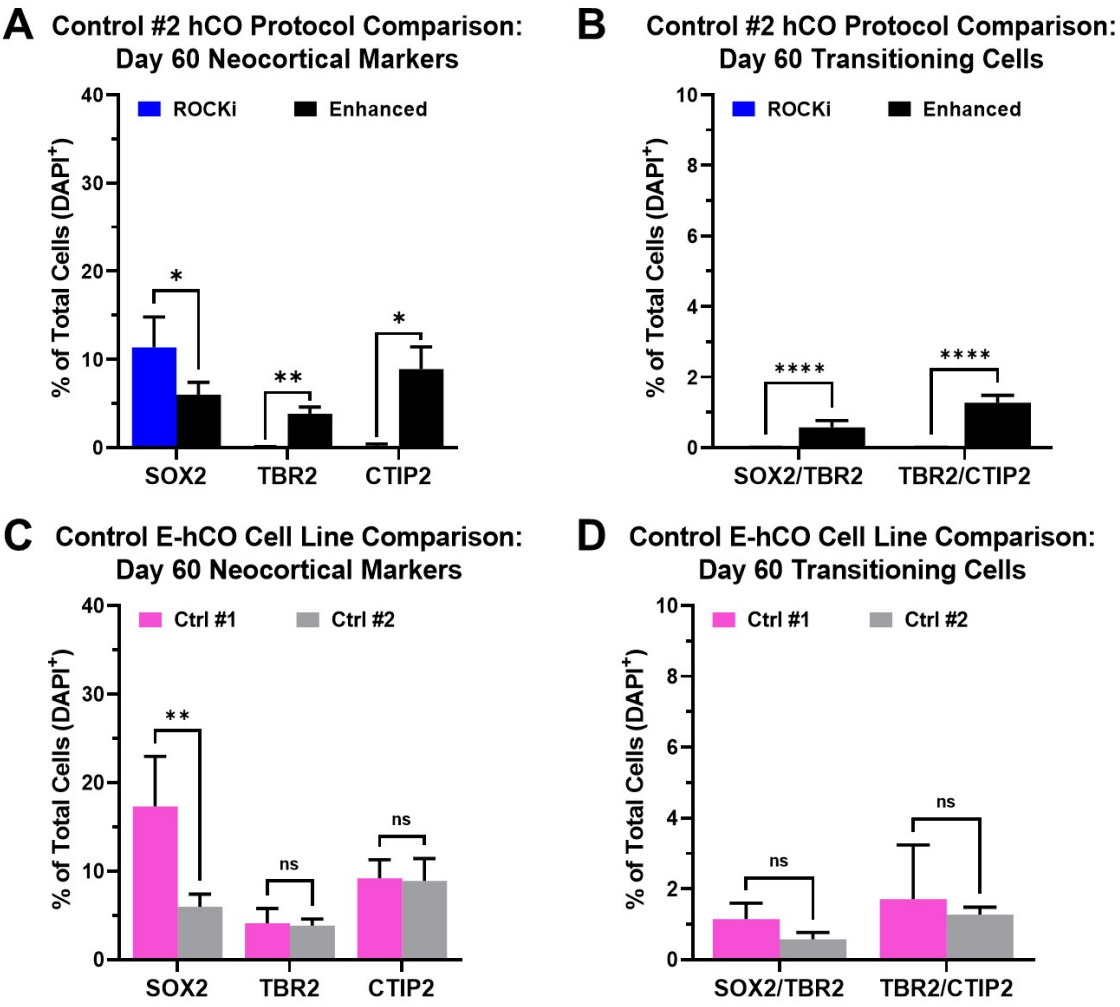

Figure 4.27: Ri-hCOs only had NPCs at Day 60; significant variance was found between control E-hCOs' NPC population.

A and C) Percentage of SOX2$^+$/DAPI$^+$, TBR2$^+$/DAPI$^+$ and CTIP2$^+$/DAPI$^+$ cells in Day 60 hCOs, comparing hCO protocols that use Control #2 **(A)**, or comparing E-hCOs from both control cell lines **(C). B and D)** Percentage of SOX2$^+$/TBR2$^+$/DAPI$^+$ and TBR2$^+$/CTIP2$^+$/DAPI$^+$ cells in Day 60 hCOs, comparing hCO protocols that use Control #1 **(B)** or Control #2 **(D)**, or comparing E-hCOs from both control cell lines at Day 30 **(F).** Bar graphs present mean counts ±standard deviation. Statistical analysis used a two-way ANOVA, with Geisser-Greenhouse correction, with Holm-Šídák correction for post-hoc tests, (n≥3 independent hCOs); ns=not significant, *p=<0.05, **p=<0.005, p****=<0.0001.

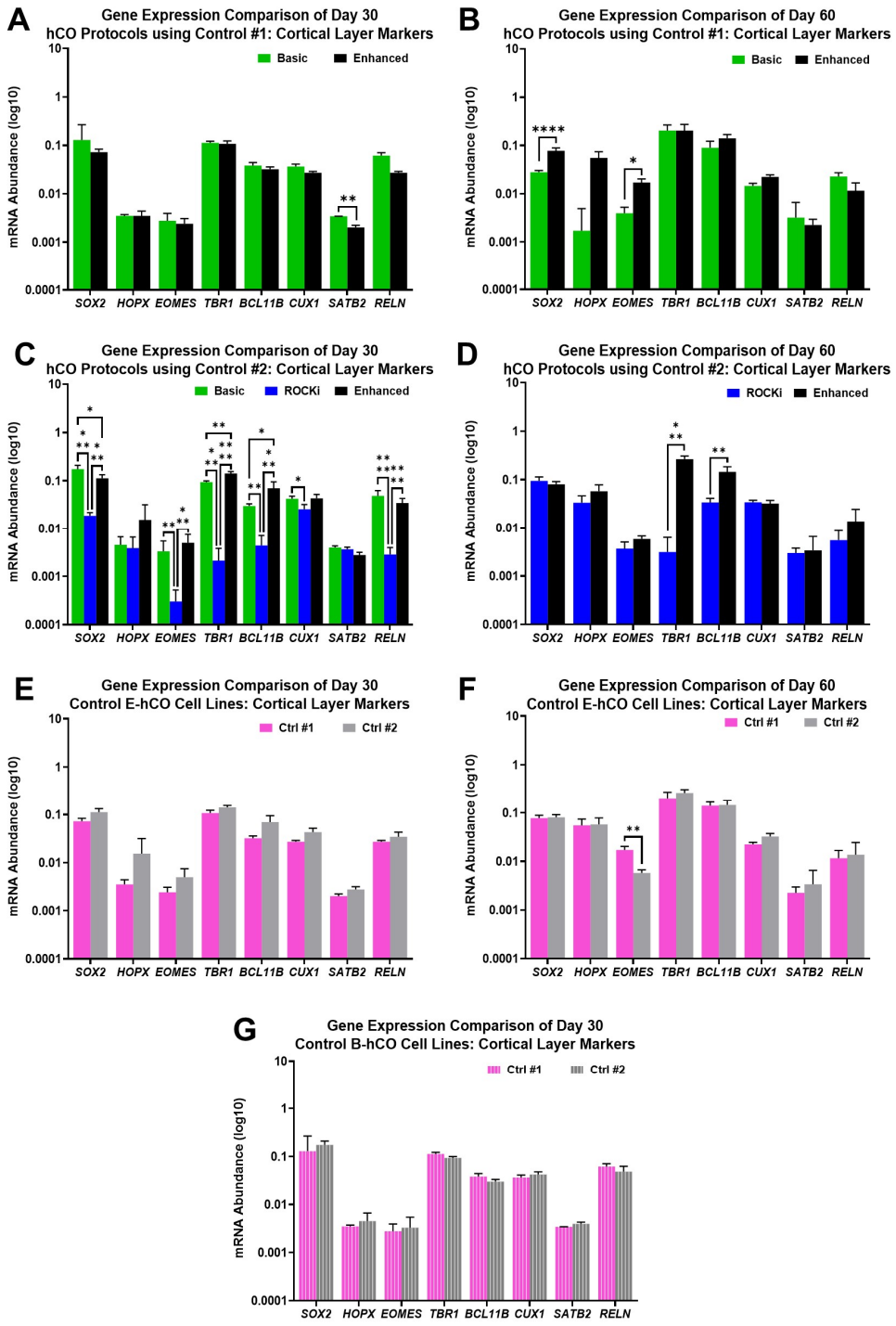

Figure 4.28: B-hCOs and E-hCOs had similar levels of transcription of cortical layer markers, both between and within hCO protocols, whilst Ri-hCOs lacked lower layer representation.

Each graph compares the transcription of cortical layer markers between hCO protocols of either Day 30 and Day 60 that use Control #1 **(A-B)** or Control #2 **(C-D)**, or compares both control cell lines in E-hCOs **(E-F)** or B-hCOs **(G)**. Data is presented as relative mRNA abundance ($2^{-\Delta CT}$, $\pm 2^{-CI}$). Statistical analysis was conducted on dCTs using a two-way ANOVA with Geisser-Greenhouse correction with Holm-Šídák correction for post-hoc tests, (n≥3 independent hCOs); unlabelled=not significant, *p=<0.05, **p=<0.005, ***p=<0.0005, ****p=<0.0001.

4.3.6 Transcriptional Analysis of Pan-Neuronal Markers Suggest that Different Cortical Organoid Protocols Vary in Identity and Quantity of Mature Neuronal Populations

A hCO should produce significant populations of maturing cell types alongside NPCs, including electrophysiologically-active, post-mitotic glutamatergic neurons (Table 4.1.5). When comparing hCO protocols, Control #2 Day 30 E-hCOs had greater transcription of pan-neuronal markers *NCAM1* and *MAP2* than B-hCOs (Figure 4.29.C). This differed to Control #1 hCOs, where B-hCOs had significantly higher transcription of *MAP2*, but not *NCAM1* (Figure 4.29.A). This trend was not maintained at Day 60, as Control #1 E-hCOs had greater expression of *NCAM1, DCX* and *MAP2* than B-hCOs (Figure 4.30.A). Control #1 B-hCOs and E-hCOs also had no differences in mRNA abundance of synaptic markers at Day 30, except *GRIA1* upregulation in B-hCOs (Figure 4.29.B). On the other hand, at Day 60, although no significance could be determined due to variance, there was a consistent trend of heightened transcription of synaptic markers in E-hCOs (Figure 4.30.B).

Control #2 Day 30 Ri-hCOs mirrored B-hCOs' expression of pan-neuronal markers more than E-hCOs, only having significantly greater expression of *DCX* than B-hCOs (Figure 4.29.C). Conversely, Control #2 Day 60 Ri-hCOs reflected similar expression of pan-neuronal markers as E-hCOs (Figure 4.30.C). This temporal pattern of mirroring either B-hCOs (Day 30) or E-hCOs (Day 60) was similarly observed when looking at pre- and postsynaptic markers, regardless of origin (Figure 4.29.D and 4.30.D). However, it was noted that Ri-hCOs consistently had lower *SLC17A7* expression, the gene responsible for coding for the VGLUT1 protein present in glutamatergic cortical and hippocampal neurons specifically (Vigneault *et al.*, 2015) (Figure 4.29.D and 4.30.D). There was also a trend or significant increase in expression of presynaptic GABA-ergic markers in Control #2 Day 60 Ri-hCOs, compared to E-hCOs, that otherwise did not appear in Day 30 Ri-hCOs (Figure 4.29.D and 4.30.D),

Lastly, differences in pan-neuronal marker transcription was found between Day 30 E-hCOs, but not B-hCOs, of the two control cell lines, with *DCX* and *MAP2* significantly upregulated in Control #2 E-hCOs (Figure 4.29.E). There was also a significant upregulation of all pre- and postsynaptic markers of both glutamatergic and GABA-ergic neurons in Day 30 Control #2 E-hCOs, except for *SLC17A7*

which was unchanged (Figure 4.29.F). This increase was not observed when comparing Day 30 B-hCOs from different control cell lines (Figure 4.29.H). Despite the significant differences in pan-neuronal and synaptic markers at Day 30, no such changes were found between control cell lines at Day 60 (Figure 4.30.E-F).

Figure 4.29 (below): Day 30 pan-neuronal, presynaptic and postsynaptic markers varied inconsistently across all three hCO protocols, but Ri-hCOs had significantly less SLC17A7. Day 30 Control #2 E-hCOs had substantially greater GABA-ergic presynaptic markers compared to Control #1, but Control #2 B-hCOs did not. Each graph compares the Day 30 transcription of pan-neuronal or synaptic markers between hCO protocols of either Control #1 **(A-B)** or Control #2 **(C-D)**, or compared both control cell lines in E-hCOs **(E-F)** or B-hCOs **(G-H)**. Data is presented as relative mRNA abundance ($2^{-\Delta CT}$, $\pm 2^{-CI}$). Statistical analysis was conducted on dCTs using a two-way ANOVA with Geisser-Greenhouse correction with Holm-Šídák correction for post-hoc tests (n≥3 independent hCOs); unlabelled/ns=not significant, *p=<0.05, **p=<0.005, ***p=<0.0005, ****p=<0.0001.

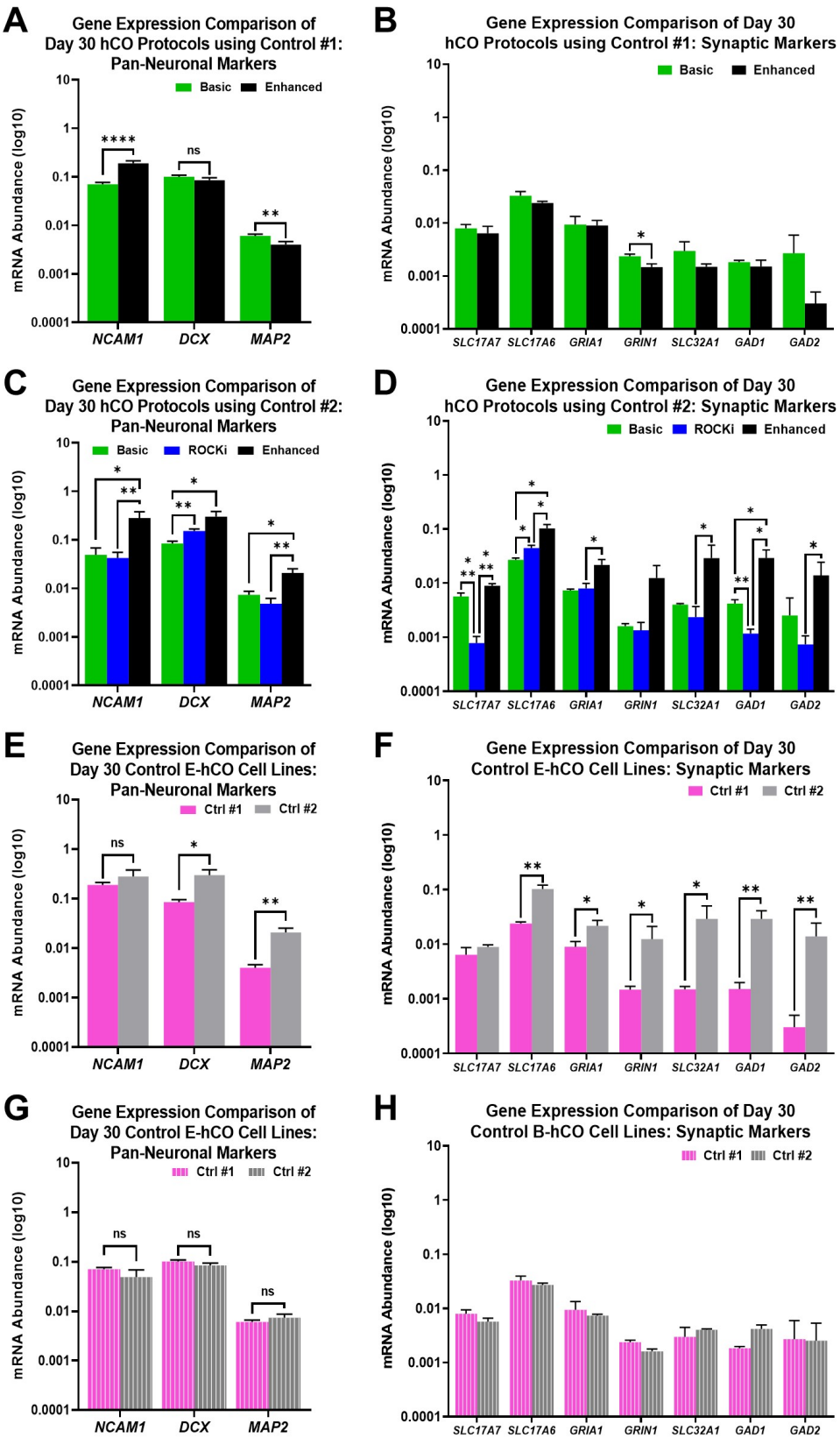

Figure 4.29: Day 30 pan-neuronal, presynaptic and postsynaptic markers varied inconsistently across all three hCO protocols, but Ri-hCOs had significantly less SLC17A7. Day 30 Control #2 E-hCOs had substantially greater GABA-ergic presynaptic markers compared to Control #1, but Control #2 B-hCOs did not. Figure legend on previous page.

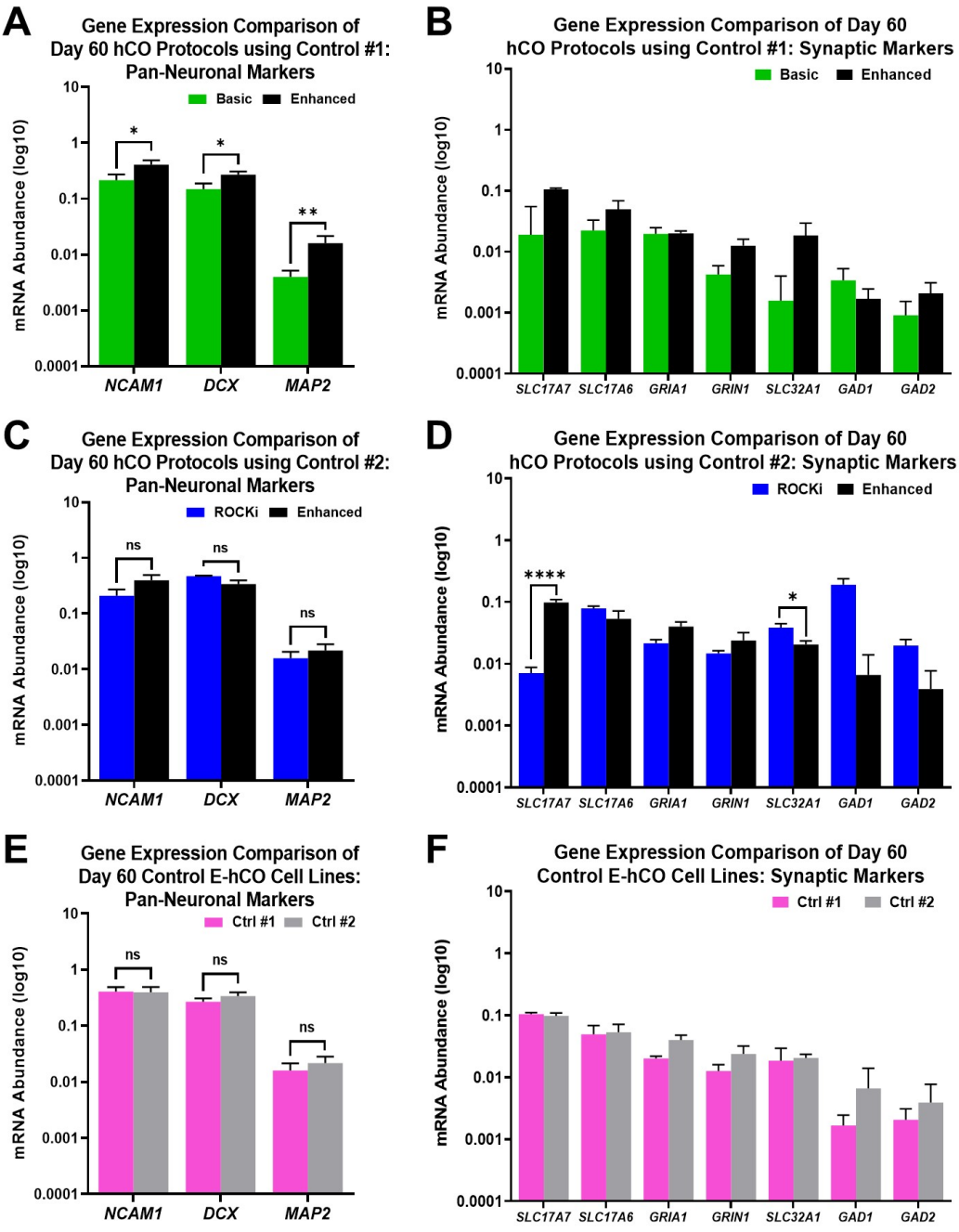

Figure 4.30: Day 60 E-hCOs had consistently higher transcription of pan-neuronal, presynaptic and postsynaptic markers than B-hCOs, but similar to Ri-hCOs, although Ri-hCOs had significantly less SLC17A7. No within-protocol variation found for control E-hCOs.

Each graph compares the Day 60 transcription of pan-neuronal or synaptic markers between hCO protocols of either Control #1 **(A-B)** or Control #2 **(C-D)**, or compared both control cell lines in E-hCOs **(E-F)**. Data is presented as relative mRNA abundance ($2^{-\Delta CT}$, $\pm 2^{-CI}$). Statistical analysis was conducted on dCTs using a two-way ANOVA with Geisser-Greenhouse correction with Holm-Šídák correction for post-hoc tests (n≥3 independent hCOs); unlabelled/ns=not significant, *p=<0.05, **p=<0.005, ***p=<0.0005, ****p=<0.0001.

4.4 Discussion

4.4.1 Substantial Variation Exists Between the Two Validated Cortical Organoid Protocols, Basic and Enhanced

As Ri-hCOs failed to represent any of the required hCO attributes, Ri-hCOs cannot be considered hCOs. However, the remaining two protocols, Basic and Enhanced, fulfilled the requirements set out in Table 4.1, but require further evaluation to determine which protocol is preferable for use in disease modelling.

Firstly, both the Basic and Enhanced protocols presented morphological characteristics akin to classic hCO development (Giandomenico, Sutcliffe and Lancaster, 2021), such as smooth EB formation, neuroectodermal clearing and budding, neuroepithelial loop development and mature lobe structures (Figure 4.3, 4.5.A and 4.6.A). Despite similar visible morphology, substantial deviation in area occurred during the ND phase of differentiation between Control #1 B-hCOs and E-hCOs; there was no significant difference in area at the NE phase (Figure 4.4.A). Although there was a 33% increase in cells seeded in each EB of an E-hCO, compared to B-hCOs (Figure 4.2), this would not have affected the analysis starting at Day 5 as the mixed-effects model took variable initial (Day 5) area measurements into account (Supplementary Figure 1). Increasing EB seeding density, from 3000 (B-hCO) to 4000 (E-hCO) cells, was introduced as low cell number during differentiation can cause disrupted development for microcephalus NDDs (Lancaster *et al.*, 2017). As the Basic and Enhanced protocols did not deviate significantly until the ND phase (Figure 4.4.A), these results could be reflective of the inclusion of thermally-stable FGF in the Enhanced protocol, improving support for neural progenitor proliferation (Bonafina *et al.*, 2018; Ledesma-Terrón, Peralta-Cañadas and Míguez, 2020).

However, the different seeding densities were reflected at Day 30 and Day 60, where Control #1 E-hCOs had a ~25% increase in area compared to B-hCOs (Figure 4.5.B and 4.6.B). Both protocols produce hCOs that fall within the ranges of previously observed cerebral organoid area for Day 30 (Li *et al.*, 2017; Delepine *et al.*, 2021) and Day 60 (Choe *et al.*, 2021), although both B-hCOs and E-hCOs were considerably larger than most cerebral organoids at 2 months (Bershteyn *et al.*, 2017; Srikanth *et al.*, 2018; de Jong *et al.*, 2021; Rosebrock *et al.*, 2022). Cerebral organoids that are not grown in Matrigel have been shown to be smaller than those that are (Bershteyn *et al.*, 2017; Srikanth *et al.*, 2018; de Jong *et al.*,

2021), and differing protocols during neuronal development make area comparison of mature timepoints difficult (Benito-Kwiecinski *et al.*, 2021; Rosebrock *et al.*, 2022). In this circumstance, although external morphology was useful initial information, it was an inconclusive measure of a hCO protocol's ability to generate hCOs with the characteristic internal cytoarchitecture.

The internal morphology of hCOs from the Basic and Enhanced protocols adhered to the second requirement of the hCO validation guidelines (Table 4.1): the capability to generate proliferative NPC-surrounded lumens, including apical edge-localised, M phase cells (Lancaster and Knoblich, 2014; Bershteyn *et al.*, 2017). Both hCO protocols produced neuroepithelia of this description and had similar lumen count at both Day 30 and Day 60 in Control #1 (Figure 4.12.A). However, the area of these lumens differed significantly at both timepoints, with B-hCOs' lumens being substantially larger and more variable in area than E-hCOs (Figure 4.13.A, 4.13.C, 4.14.A and 4.14.C). A possible cause of this change in lumen size may be due to the different culturing conditions during maturation. B-hCOs had a greater 'live cell' border than E-hCOs, which extended considerably further into the hCO, indicating better diffusion and facilitating larger neuroepithelial loops, most notably at Day 60 (Figure 4.23.A-D). However, this does not necessarily indicate that the Basic protocol is overall superior to the Enhanced, but that refinement of maturation techniques is necessary, focusing on restricting size and improving diffusion.

In the context of proliferation, B-hCOs do not benefit from the observed enlarged lobes and improved diffusion. Although *KI67* transcription was unaffected by which hCO protocol was used (Figure 4.10.A-B), KI67^{+} cell abundance was significantly higher in E-hCOs than B-hCOs, at both Day 30 and Day 60 (Figure 4.9.A). The same trend appeared in the KI67^{+}/SOX2^{+} NPC population (Figure 4.9.D). Elevated KI67 in Day 30 E-hCOs' was complimented by an increase in total M phase (pVIM^{+}) cells, of which a larger proportion were bound to lumens, compared to B-hCOs (Figure 4.16.A and 4.16.D). There is a positive linear relationship between KI67 and pVIM abundance in cerebral organoids (Daviaud *et al.*, 2019), and so the elevation of both affirms a higher rate of proliferation in Control #1 Day 30 E-hCOs than B-hCOs; this correlation has also been observed in the developing neocortex of mice (Güven *et al.*, 2020; Fabra-Beser *et al.*, 2021). On the other hand, Control #1 Day 60 B-hCOs and E-hCOs had a comparable number of M phase cells in total, as well as those anchored to the lumens, but

lower overall and NPC-specific KI67$^+$ cells (Figure 4.16.A, 4.16.D, 4.9.A and 4.9.D). This may be related to the long-term maturation technique of Erlenmeyer flasks instead oscillating plates, as it is the only methodological difference between Day 60 B-hCOs and E-hCOs. A possible hypothesis would be that the different rates of diffusion could influence both the number of cells actively proliferating, as well as the length of the cell cycle. However, due to the number of additional differences between the Basic and Enhanced protocol both prior and during maturation, it is difficult to determine if the oscillation technique is the cause of this difference.

Furthermore, recorded proliferation rates from other cerebral organoid studies are closer to E-hCOs than B-hCOs, with ~30-40% of cells within the VZ being KI67$^+$ in cerebral organoids aged between 2 to 6 weeks (Bershteyn *et al.*, 2017; Anastasaki *et al.*, 2020; Wang *et al.*, 2020; Kang *et al.*, 2021; Wegscheid *et al.*, 2021), although these studies analysed the VZ specifically, as opposed to the whole cerebral organoid. As the majority of KI67$^+$ cells were also SOX2$^+$ in both timepoints for both protocols, it is likely that there was a relatively small population of SOX2$^-$ or SOX2^{low} NPCs that are mitotically-active, such as IPs (Hutton and Pevny, 2011). This was evidenced by SOX2$^-$/TBR2$^+$ IPs representing ≤10% of observed cells in both protocols at Day 30 and Day 60 (E-hCO only) (Figure 4.26.A and 4.27.C). The populace of TBR2$^+$ IPs are low in cerebral organoid literature, between 5-10% of total cell count in 1-2 month old cerebral organoids (Mariani *et al.*, 2015; Kang *et al.*, 2021; Rosebrock *et al.*, 2022). Considering IP abundance is so low, the fact that less than 50% of all pVIM$^+$ cells were bound to the lumen in either protocol would suggest that there was a significant number of non-apical NPCs that were also not IPs, such as bRGs (Figure 4.16.D and 4.16.F). Based on the transcriptional representation of *HOPX* across both protocols and timepoints (Figure 4.28.A-B), it is expected that HOPX$^+$ bRGs are at least represented within the hCO cell population to a similar extent as TBR2$^+$ IPs, if not greater.

Cell death is as important to a cerebral organoid as cell proliferation, as it is required for cellular health and reorganisation (Daviaud *et al.*, 2019; Zhang *et al.*, 2019). For B-hCOs and E-hCOs, overall cell death and specifically SOX2$^+$ NPC death did not vary (Figure 4.17.A and 4.17.D). The lack of apoptotic variability between protocols could be a reflection of the conservation of apoptotic activity within the NPC populace. It is difficult to compare total apoptotic values to other

studies, as the APD constant and quantifying the whole hCO is unique to this study. However, other cerebral organoid studies converge on a concept of conserved quantities of apoptosis, regardless of size or protocol. For example, similar quantities of NPC apoptosis found in B-hCOs and E-hCOs were present in the VZ or in $SOX2^+$ NPCs specifically in other cerebral organoid studies (Bershteyn *et al.*, 2017; Daviaud *et al.*, 2019; Zhang *et al.*, 2019; Anastasaki *et al.*, 2020; Notaras, *et al.*, 2021). On the other hand, cell density was significantly higher in E-hCOs than B-hCOs for both timepoints (Figure 4.18.A). As apoptosis did not change significantly, the additional cells likely stem from the elevated levels of proliferation found in E-hCOs (Figure 4.9.A). There is no prerequisite number denoting high or low cell density in cerebral organoids, however other protocol comparison studies, such as Lancaster *et al.*, (2017) illustrate the importance of tight compaction of NPCs in the VZ areas to emulate the striated nature of NPCs *in vivo*, which would suggest greater cell density is optimal.

The striated organisation of NPCs is facilitated by intermediate filaments, such as nestin and vimentin (Xue and Yuan, 2010; Eze *et al.*, 2021) which highlight NPC processes in cerebral organoids (Klaus *et al.*, 2019; Albanese *et al.*, 2020). *NES* and *VIM* transcription was not significantly different between Day 30 B-hCOs and E-hCOs of Control #1 and Control #2 (Figure 4.15.A and 4.15.C). However, at Day 60 Control #1 E-hCOs had significantly greater expression of *NES* and *VIM* than B-hCOs (Figure 4.15.B). This outcome countered the original hypothesis that, as the VZ area in cerebral organoids is NPC-specific (Klaus *et al.*, 2019), the greater lumen area in Day 30 and Day 60 B-hCOs would translate to greater *NES*/*VIM* expression than E-hCOs (Figure 4.13.A, 4.13.C, 4.14.A and 4.14.C). This would only be the case, however, if the depth of the VZ was consistent between both hCO protocols. In addition to the differential expression of *NES* and *VIM*, $SOX2^+$ cell abundance did not increase despite Day 30 B-hCO's greater lumen size, even though lumen count was comparable to E-hCOs (Figure 4.13.A, 4.13.C and 4.26.A). The hypothesis was therefore revised, that in the absence of VZ depth measurements, the visible reduction in VZ depth of B-hCOs compared to E-hCOs was genuine (Figure 4.25.A and 4.25.D). A shallower VZ could be acting as a contributory factor to the reduced cell density observed in B-hCOs, as this is the area of highest cell density within a hCO due to its' striated organisation (Figure 4.18.A).

Although quantification of multiple features differed between hCO protocols, the numerous lumens with striated NPCs, and appropriately localised proliferation and apoptosis thereof, were highly suggestive that both the Basic and Enhanced protocols are capable of generating hCOs of a telencephalic ($FOXG1^{+}$) identity. Disease models have shown the necessity FOXG1's in *in vitro* forebrain progenitor development (Hettige *et al.*, 2022), as well as identity of mature neuronal population (Mariani *et al.*, 2015; Cederquist *et al.*, 2019; Zhu *et al.*, 2019). It was therefore unsurprising that E-hCOs and B-hCOs had high expression of the telencephalic marker FOXG1 in both transcriptional and cell abundance assessments across both timepoints. Although the two protocols did not significantly differ at Day 30 in Control #1 for either analysis of FOXG1 (Figure 4.19.A and 4.24.A), Control #2 B-hCOs and E-hCOs did vary significantly for *FOXG1* transcription, with E-hCOs exhibiting higher mRNA abundance (Figure 4.19.C). Although this difference was only found when comparing Day 30 Control #2 B-hCOs and E-hCOs, at Day 60, Control #1 E-hCOs also had significantly greater *FOXG1* expression than B-hCOs (Figure 4.19.B). However, in ICC analysis, FOXG1 was considerably higher in Day 60 B-hCOs than E-hCOs (Figure 4.24.B). The latter result was considered a consequence of a greater "live cell border" within the Day 60 B-hCO, which led to B-hCOs having an increased number of live cells in ratio to their size compared to E-hCOs (Figure 4.23.A and 4.23.C). However, FOXG1 should be ubiquitously expressed in the vast majority of live cells in a hCO (Lancaster *et al.*, 2013; Renner *et al.*, 2017), regardless of the internal morphology, and so both hCO protocols' exhibition of this protein confirms telencephalic identity.

Expanding further, both Control #1 B-hCOs and E-hCOs had high mRNA abundance of dorsal forebrain markers (*PAX6, EOMES, TBR1*) at both timepoints, with either equal or higher abundance in E-hCOs than in B-hCOs, most notably at Day 60 (Figure 4.19.A-B). B-hCOs and E-hCOs from Control #2 followed this trend at Day 30, but E-hCOs also had significantly higher mRNA abundance of ventral forebrain markers *DLX1* and *LHX6* (Figure 4.19.C). A significant proportion of this variance is attributed to Control #2 E-hCOs cell line and protocol-specific transcriptional differences (Figure 4.19.E), which were not replicated in similar cell line comparisons in Day 30 B-hCOs (Figure 4.19.G). However, Day 60 Control #1 E-hCOs have a similar trend of upregulated ventral forebrain markers when compared to B-hCOs (Figure 4.19.B). As suggested previously, the maturation

technique was suggested to be the cause of this increase, as different maturation vessels and culture techniques are known to introduce variation in cerebral organoids (Quadrato *et al.*, 2017). Unfortunately, it was not possible to stain B-hCOs for NKX2.1 due to slide availability, and therefore not possible to confirm if transcriptional analysis in B-hCOs was representative of a low ventral forebrain cell population.

Overexpression of non-telencephalic identities was relative to the timepoint and protocol. *FOXA2* and *PAX3* were substantially upregulated in Control #1 B-hCOs at Day 30 compared to E-hCOs (Figure 4.21.A). Although *FOXA2* is still very low in abundance, the substantially elevated levels of *PAX3* in Control #1 Day 30 E-hCOs suggests transcriptional changes towards neural crest cell identity, although the increased transcription did not result in greater abundance of $PAX3^+$ cells (Figure 4.24.A). It was noted that there was a reverse trend in *FOXA2* transcription at Day 60, where E-hCOs had higher transcription, although the overall expression was still low (Figure 4.21.B). In contrast with the increased ventral forebrain markers (Figure 4.19.C), all three non-telencephalic markers were not significantly different between the two protocols for Control #2 at Day 30 (Figure 4.20.C). Designation of one specific identity is the cornerstone of guided cerebral organoids and what separates them apart from unguided cerebral organoids. Both B-hCOs and E-hCOs were successful at exhibiting the high dorsal forebrain/low ventral forebrain representation with low representation of other non-telencephalic lineages mentioned in Table 4.1, with minor exceptions for both protocols.

Alongside dorsal forebrain identity, hCOs must exhibit organised cytoarchitecture that emulates neocortex-like layered structure to be considered an adequate reflection of the dorsal forebrain (Table 4.1.4). Control #1 Day 30 hCOs of both the Basic and Enhanced protocols presented $SOX2^+$ NPCs in a ventricular arrangement, surrounded by $TBR2^+$ IPs and $CTIP2^+$ neurons, although E-hCOs had an arguably greater VZ depth and more defined SVZ region (Figure 4.25.A and 4.25.D). Overall, quantification of each individual cell population showed that both hCO protocols had similar numbers of $SOX2^+$ cells at Day 30, but E-hCOs had substantially more IPs and neurons than B-hCOs (Figure 4.26.A) and was closer to cellular population proportions of other cerebral organoid studies (Bershteyn *et al.*, 2017). Transcriptional analysis contradicted this observation, as there was minimal difference in the mRNA abundance of *SOX2* at Day 30 between

B-hCOs and E-hCOs for Control #1, but no difference in *EOMES* or *BCL11B* transcription (Figure 4.28.A). On the other hand, Control #2 B-hCOs and E-hCOs had differing *SOX2* and *BCL11B* expression (Figure 4.28.C), although this could not be confirmed to be representative of differing cell populations due to slide availability of Control #2 Day 30 B-hCOs. Upon review of this data, it could be argued that the VZ structure within hCOs was conserved at Day 30 across the two hCO protocols, despite minor transcriptional discrepancies: the number of $SOX2^+$ cells, predominantly congregating in the VZ, the separation of VZ and SVZ, and the quantity, although not the size, of lumens (Figure 4.12.A, 4.13.A, 4.13.C, 4.25.A, 4.25.D, 4.25.F and 4.26.A-B). However, this initial analysis also identified that the SVZ and CP layers of the two types of hCOs varied significantly.

Firstly, the previously discussed lack of $TBR2^+$ cells in Day 30 Control #1 B-hCOs suggested a smaller SVZ than E-hCOs (Figure 4.26.A), but the depth of an SVZ can also be recognised by the percentage of $SOX2^+/TBR2^+$ and/or $TBR2^+/CTIP2^+$ cells (Bershteyn *et al.*, 2017; R. Li *et al.*, 2017; Zhang *et al.*, 2019; Rosebrock *et al.*, 2022). Control #1 Day 30 B-hCOs had similar quantities of $SOX2^+/TBR2^+$ cells as E-hCOs, but considerably less $TBR2^+/CTIP2^+$ cells, indicating a smaller representation of the SVZ (Figure 4.26.B). On the other hand, Day 30 and 60 E-hCOs had comparable values of $TBR2^+/CTIP2^+$ cells with other cerebral organoid studies, between 4 to 7% of total cells (Figure 4.26.F and 4.27.D) (Kang *et al.*, 2021). However, a greater overlap of progenitors and neurons is not always beneficial, as an increased $TBR2^+/CTIP2^+$ cell population in cerebral organoids has been related to diseases such as Fragile X syndrome (Kang *et al.*, 2021). Due to slide availability Day 60 B-hCOs cellular populations could not be analysed, however, Day 60 Control #1 E-hCOs had significantly or trending elevation of *SOX2, HOPX* and *EOMES* transcription, representative of the VZ and SVZ regions (Figure 4.28.B). This correlates to what was observed for *FOXG1* transcription dorsal forebrain markers; although Control #1 Day 30 hCO protocol comparison varied very little, *FOXG1* was upregulated substantially in Day 60 E-hCOs (Figure 4.19.A-B). This transcriptional analysis suggests that Control #1 Day 60 B-hCOs underperform in maintaining the NPC pool, including aRGs, bRGs and IPs, when in comparison to E-hCOs, a significant setback to the argument of using B-hCOs to emulate NDDs, such as microcephaly, that are known to affect NPCs (Li *et al.*, 2017; Zhang *et al.*, 2019).

Similarly, the quantity and organisation of cortical neurons in the CP is critical to emulating NDDs and therefore correct representation of the CP is a requirement of hCOs (Table 4.1.4). As previously mentioned, CTIP2$^+$ neurons were underrepresented in Day 30 Control #1 B-hCOs compared to E-hCOs (Figure 4.26.A). Although transcription of *BCL11B* was unchanged between B-hCOs and E-hCOs of Control #1, those of Control #2 found E-hCOs to have significantly greater *BCL11B* expression (Figure 4.28.A and 4.28.C); such disparity between the transcription and cellular abundance makes it difficult to theorise about the quantity of both lower- and upper-layer neurons without complementary ICC analysis. However, as the highly transcribed genes of *SOX2* and *CTIP2* represent the abundant cell populations of corresponding identity in ICC quantification (Figure 4.26.A, 4.28.A and 4.28.C), it could be extrapolated that there would be very few upper-layer neurons, such as SATB2$^+$ neurons, in hCOs from both protocols, based on mRNA abundance data (Figure 4.21.A-B).

On the other hand, *CUX1* transcription was as high as *BCL11B* in Day 30 hCOs of both protocols and both cell lines (Figure 4.28.A and 4.28.C). Conversely, CUX1$^+$ neurons span the same upper layers of the developing cortex as SATB2, both *in vivo* (Nieto *et al.*, 2004; Alcamo *et al.*, 2008; Martins *et al.*, 2021) and in cerebral organoids (Qian *et al.*, 2016, 2020; Rosebrock *et al.*, 2022). However, *in vitro* studies have shown that the two can act differently in culture; SATB2$^+$ neurons appear up to 60 days later in culture than CUX1 neurons (Shi *et al.*, 2012). In cerebral organoids, both identities of upper layer neurons are observed in ICC analysis, but much later than Day 60: CUX1 is observed at Day 80-150 (Qian *et al.*, 2016, 2020; Giandomenico *et al.*, 2019; Rosebrock *et al.*, 2022) whilst SATB2 is observed between Day 65-100 (Lancaster *et al.*, 2013; R. Li *et al.*, 2017; Y. Li *et al.*, 2017; Qian *et al.*, 2020; Cho *et al.*, 2021; Rosebrock *et al.*, 2022). This contradiction between research models on timing of upper layer neuron production, alongside this phenotype presenting across hCO protocols, suggests that this is a feature of hCO culture, as opposed to a fault. Extension of differentiation to Day 90 and 120 would aid in distinguishing either hCO protocols' capability of generating and segregating upper and lower layer neurons accordingly (Qian *et al.*, 2016; Li *et al.*, 2017; Li *et al.*, 2017).

From a broader perspective, both hCO protocols exhibited high expression of pan-neuronal markers such as *DCX* and *NCAM1* at both timepoints. These markers are essential for neuronal development in hCOs, as DCX is expressed in

immature neurons, aiding in neuronal migration by regulating microtubules (Moslehi, Ng and Bogoyevitch, 2017) whilst NCAM1 is associated with neuronal development (Sytnyk, Leshchyns'ka and Schachner, 2017), but is also involved with NPC proliferation in the VZ and SVZ during early corticogenesis (Huang *et al.*, 2019). On the other hand, MAP2 is a microtubule-associated protein expressed in the dendrites and cell body of mature neurons (Borsini *et al.*, 2020) and was expressed significantly less than *DCX* and *NCAM1* in both types of hCO at Day 30 (Figure 4.29.A and 4.29.C).

The development of immature and mature neurons in cerebral organoids is staggered and relative to the cerebral organoid protocol; DCX can be prolifically expressed from Day 20 onwards (Li *et al.*, 2017; Zhang *et al.*, 2019; Huang *et al.*, 2022), whilst MAP2 is expressed significantly after Day 30 (Albanese *et al.*, 2020; Wegscheid *et al.*, 2021; Huang *et al.*, 2022). Reviewing the transcriptional analysis of pan-neuronal markers between B-hCOs and E-hCOs provides strong evidence to support the theory that E-hCOs are superior to B-hCOs. At Day 30, Control #1 and #2 E-hCOs consistently had greater expression of *NCAM1* than B-hCOs, with Control #2 E-hCOs also having significantly greater *DCX* and *MAP2* expression (Figure 4.29.A and 4.29.C). At Day 60, Control #1 E-hCOs had consistently greater expression than B-hCOs across all three pan-neuronal markers, whilst exhibiting an increase of *MAP2* expression over time, which B-hCOs did not (Figure 4.30.A). It could therefore be proposed that E-hCOs are transcriptionally primed to create more neurons than B-hCOs, although this requires ICC quantification to confirm.

Definition of which type of neurons are generated is required (Table 4.1.5), although pre-and postsynaptic markers are usually exhibited after Day 60 as neurons mature (Kim *et al.*, 2019; Cho *et al.*, 2021; Samarasinghe *et al.*, 2021; Huang *et al.*, 2022). Both Control #1 B-hCOs' and E-hCOs' transcriptional analysis followed this timeline, with low expression and only one distinguishable difference between hCO protocols at Day 30, *GRIN1* (Figure 4.29.B). Control #2 E-hCOs, on the other hand, had an unexpected significantly higher abundance of synaptic markers that were both glutamatergic (*SLC17A6*) and GABA-ergic in origin (*GAD1*) compared to B-hCOs (Figure 4.29.D); genes that were not significantly increased still exhibited trends of upregulation (*GRIA1, GRIN1, SLC32A1* and *GAD2*). This was believed to be a repercussion of the increased ventral forebrain progenitor representation of *DLX1* and *LHX6* present in Day 30 Control #2 E-

hCOs (Figure 4.19.C). Akin to this increase in ventral forebrain representation, the increase in all pre- and postsynaptic markers, except *SLC17A7*, was a cell line and protocol-specific anomaly, as Control #1 E-hCOs and Control #2 B-hCOs did not reproduce this result. By Day 60, however, pan-neuronal and synaptic marker expression between the two control cell lines became indistinguishable from one another in the Enhanced protocol. In contrast with Day 30, Day 60 Control #1 E-hCOs had a trend of higher abundance of key synaptic markers compared to B-hCOs, particularly of *SLC17A7* which increased in expression ten-fold between the two timepoints in E-hCOs (Figure 4.30.B). *SLC17A7* is responsible for the PFC-specific, presynaptic glutamatergic protein VGLUT1 (Vigneault *et al.*, 2015), and is therefore a strong indicator of the identity and possible volume or quality of neurons being produced in a hCO. Without ICC or multiple electrode arrays to assess quantity, quality and functional activity of the neurons generated from either hCO protocol, it can only be suggested that, compared to B-hCOs, E-hCOs have a greater quantity of glutamatergic synapses and/or neurons at Day 60.

There are two major changes that were likely to have caused the improved development perceived in E-hCOs. Firstly, replacing the standard basic FGF2 (B-hCO) in favour of the thermally-stable FGF2 (E-hCO) during the ND phase of differentiation was believed to improve the hCO protocol substantially. With no additional difference between either hCO protocol except seeding density, the thermally-stable FGF2 could have been responsible for the E-hCOs increased mitotic activity, with greater numbers of proliferative cells at Day 30 and 60, and more M phase cells at Day 30 (Figure 4.9.A and 4.16.A), as well as suggested increased depth of VZ compared to B-hCOs. The impact of adding thermally-stable FGF2 could perpetuate into Day 60, with the hypothesised greater representation of the NPC pool in E-hCOs, supported by transcriptional analysis (Figure 4.28.B). As FGF2 is a commonly used additive in hCO protocols at both EB generation and ND phases of differentiation (Lancaster and Knoblich, 2014; Kang *et al.*, 2021; Urresti *et al.*, 2021; Rosebrock *et al.*, 2022; Sharf *et al.*, 2022), it would be an easy-to-implement revision with a significant, possibly long lasting, impact. Secondly, the addition of BDNF in the first week of maturation (Day 21-30) in the Enhanced protocol was expected to improve the maturation of neurons and long-term synaptic plasticity. Although this result was only observed in Control #2 E-hCOs at Day 30, significantly greater transcription of mature neuronal markers was observed at Day 60 in Control #1 E-hCOs, as was a trend of increased pre-

and postsynaptic glutamatergic markers (Figure 4.29.B, 4.29.D and 4.30.B). It is difficult to distinguish if this was a result of the BDNF, culturing technique during maturation, or both, due to both being different between the Basic and Enhanced protocol. Using E-hCOs bereft of BDNF as a control, ICC assessment of the presence of astrocytes at Day 30 could determine if BDNF is necessary; although unlikely, if astrocytes are present in Day 30 E-hCOs, it is likely unnecessary to supplement maturation media with BDNF. Overall, evidence presented here suggests that these revisions were either valuable or did not detract from E-hCO development.

In summary, these two hCO protocols adhere to the assessment guidelines set out in Table 4.1 and would therefore be considered capable of creating hCOs of quality comparable to current cerebral organoid literature. They both emulate rudimentary cortical layers and have expression of mature neuronal markers. Theoretically, either protocol would be suitable for applying to this research's disease model, 1qDel. Although E-hCOs show cell line-specific variability at Day 30, by Day 60 E-hCOs have proven to be significantly better at NPC and neuronal generation and maintenance compared to B-hCOs. With this evidence, combined with the observations of Ri-hCOs poor performance in generating hCOs, the Enhanced protocol was chosen as the hCO methodology with which to investigate 1qDel.

4.4.2 Extended Exposure to ROCK Inhibition Results in Non-Dorsal Forebrain Identity in ROCKi Protocol Organoids

The ROCKi protocol was designed to improve EB stability and survivability by extending the exposure of ROCK inhibitor Y-27632 from 24 hours to 5 days. Both *in vitro* and cerebral organoid protocols have used ROCK inhibition as a method of EB generation (Lancaster *et al.*, 2013; Watanabe *et al.*, 2017; Zhang *et al.*, 2019; Albanese *et al.*, 2020) or improving cell survival (Chen *et al.*, 2011; Harbom *et al.*, 2019) without significant negative implications. Although there were no observed morphological characteristics to convey unsuccessful EB generation at Day 5 (Figure 4.3), it became apparent during the NE phase of differentiation, after the removal of Y-27632, that the ROCKi protocol was not fit for purpose. hCO area only deviated significantly during the NE stage between Control #2 B-hCOs and Ri-hCOs, and not E-hCOs and Ri-hCOs (Figure 4.4.B). By the end of the NE stage, at Day 11, there were visible differences that depicted a substantial

morphological issue (Figure 4.3). Day 11 Ri-hCOs did not resemble a spheroid and the optical density was inconsistent across the Ri-hCO, depicting a distinctively different morphology than the other two protocols at Day 11 (Figure 4.3). The differentiation of Ri-hCOs continued to be aberrant, with gross expansion throughout the ND phase, resulting in a lack of neuroepithelial loops at Day 21 (Figure 4.3 and 4.4.B). Whilst it is difficult to draw conclusions as to how these issues arose when comparing Ri-hCOs to B-hCOs as the protocols differ substantially, Ri-hCOs and E-hCOs only had one difference for the first 21 days of differentiation: the length of exposure of Y-27632 during EB generation (Figure 4.2).

Y-27632 inhibits the ROCK/RhoA pathway, which is heavily implicated in multiple developmental processes relevant to this study. Despite Y-27632's proven advantages when used in tissue culture, such as increased survivability (Chen *et al.*, 2011; Vernardis *et al.*, 2017) and ability to aggregate cells (Sivitilli *et al.*, 2020), it can also be detrimental. Firstly, significant metabolic changes are observed in hIPSCs across timepoints ranging from initial addition to 96 hours of Y-27632 exposure (Vernardis *et al.*, 2017). In addition, although ROCK inhibition does not have a significant impact in stem cell identity immediately, after 96 hours of Y-27632 exposure, stem cell identity markers are reduced (Vernardis *et al.*, 2017); it was not stated in the study what identity the differentiating hIPSCs became. It is possible to extrapolate information about Day 5 ROCKi protocol EBs (Ri-EBs) from Day 5 Enhanced EBs (E-EBs) (Figure 3.4), given that they are methodologically identical except for the extended Y-27632 exposure. With this in mind, the known population of multipotent primitive NECs likely present within Day 5 Ri-EBs could be significantly affected by prolonged ROCK inhibition similar to that of those in Vernardis *et al.*, (2017), resulting in aberrant differentiation due to reduced multipotency.

Y-27632 is also designed to reduce passage-related apoptosis by inhibiting apoptotic blebbing that is governed by ROCK1 (Gao *et al.*, 2019). Ri-EBs could be negatively affected by this repressed apoptosis caused by extended ROCK inhibition. Developmental stages that undergo cellular morphogenesis require apoptosis to reorganise cells, such as forming lumens in neural rosettes (Hříbková *et al.*, 2018) and undertaking NTC (Yamaguchi *et al.*, 2011), both of which are relevant to early hCO development. Considering apoptosis did not differ between Ri-hCOs and E-hCOs at Day 30, it is possible that Ri-hCOs had physiologically

recovered from the early Y-27632 exposure and resumed typical NPC apoptosis (Figure 4.17.B).

Furthermore, cellular organisation of Ri-EBs would be abnormal due to the effect of ROCK inhibition on the actin cytoskeleton, as Rho kinases play a significant role in its maintenance (Vaezi *et al.*, 2002). When inhibited, ROCK is not capable of initiating actin bundling in stem cells (Gao *et al.*, 2019). Additionally, a collection of studies in neuronal models have illustrated that developmentally-significant cell movement is hampered in the presence of extended ROCK inhibition. In Kadoshima *et al.*, (2013), developmentally-patterned neocortical EBs displayed an inability to "roll" into the neocortical shape when exposed to Y-27632 for 4 days during maturation, but this did not disrupt forebrain identity. This study claimed that this was because the Y-27632 inhibited the Rho-ROCK-myosin pathway from instigating apical constriction thereby stopping cortical formation (Kadoshima *et al.*, 2013). This inability to execute apical constriction due to ROCK inhibition is also observed in a different 3D model that emulates the neural tube (Karzbrun *et al.*, 2021). Within 3 days of exposure, Y-27632 inhibited SHROOM3 aggregation, reducing actin bundling at the apical edge, thereby resulting in a flattened neural tube incapable of curling (Karzbrun *et al.*, 2021); *in vivo* studies have observed similar effects of ROCK inhibition preventing neuropore closure (Butler *et al.*, 2019). The population of primitive NECs within Day 5 Ri-EBs would rely on actin to begin forming the NE (Xue *et al.*, 2018). However, prolonged ROCK inhibition during neuroectodermal differentiation could disrupt the natural organisation of cells around an apical edge, such as neural rosette formation, as this process is facilitated by actin bundling (Beghin *et al.*, 2022). The aforementioned studies do not discuss the impact after removing the Y-27632, but stem cell studies have shown that there is some level of recovery for actin organisation 12 hours after Y-27632 removal (Gao *et al.*, 2019).

The combination of repressed apoptosis, abnormal stem cell identity and disrupted actin cytoskeleton during early Ri-hCO development could be a feasible explanation for the poor forebrain development and area expansion observed in later stages of Ri-hCOs development. Without actin cytoskeletal reorganisation, primitive NECs within the Ri-EBs would be unable to form preliminary neural rosette formation (Hříbková *et al.*, 2018; Fedorova *et al.*, 2019; Beghin *et al.*, 2022). Absence of neural rosette formation would mean that introduction of the proceeding dual-SMAD inhibitors at Day 5 could be instructing the Ri-EB to an

undesirable fate. There has been no known investigation into the ideal Y-27632 exposure time in EBs and some studies argue it is not necessary at all (Pettinato, Wen and Zhang, 2014).

Despite the disarray caused by extended Y-27632 exposure, Ri-hCOs shared certain cellular physiological results with E-hCOs and B-hCOs. Ri-hCOs' proliferation and apoptosis followed similar trends to B-hCOs when compared to E-hCOs. At Day 30, Control #2 Ri-hCOs' overall and NPC-specific proliferation was significantly less than E-hCOs, whilst *KI67* transcription and apoptosis was unaffected (Figure 4.9.B, 4.9.E, 4.10.B and 4.17.B). Conversely, at Day 60, Control #2 Ri-hCOs overall and NPC-specific proliferation, as well as *KI67* transcription, was similar to that of E-hCOs, whilst apoptosis was significantly higher (Figure 4.9.B, 4.9.E, 4.10.B and 4.17.B). Additionally, Control #2 Ri-hCOs present equal or higher proportions of the $SOX2^+$ population at Day 30 and Day 60, respectively, when compared to E-hCOs (Figure 4.26.C and 4.27.A). On the other hand, *SOX2* expression was significantly lower in Control #2 Day 30 Ri-hCOs compared to both B-hCOs and E-hCOs, but increased to E-hCO levels at Day 60 (Figure 4.28.C-D). A similar temporal pattern of expression was observed in transcription of pan-neuronal markers (Figure 4.29.C and 4.30.C). Glial markers *NES* and *VIM* were also expressed to a similar degree in Control #2 Ri-hCOs, B-hCOs and E-hCOs at Day 30, and significantly more so than E-hCOs at Day 60 (Figure 4.15.C-D). This evidence points towards Ri-hCOs being capable of producing neuronal cells and supporting glia to a similar degree to E-hCOs.

Further support for this theory was found when analysing transcription of genes related to synaptic function, where Control #2 Ri-hCOs largely mirrored B-hCOs' expression profile at Day 30 and E-hCOs' at Day 60, except *SLC17A7* (Figure 4.29.D and 4.30.D). In fact, Ri-hCOs show substantial failings in generating forebrain-specific features of hCOs, such as lumens; they are few in number at Day 30 and absent at Day 60 (Figure 4.12.B). Ri-hCOs also significantly downregulated transcription of any genes related to the forebrain (*FOXG1*), particularly dorsal forebrain (*PAX6, EOMES, TBR1, BCL11B, REELIN*); all aforementioned genes were downregulated in Day 30 Ri-hCOs, whilst *FOXG1, PAX6, TBR1* and *BCL11B* expression was still substantially reduced in Day 60 Ri-hCOs (Figure 4.19.C-D and 4.28.C-D). $FOXG1^+$, $TBR2^+$ and $CTIP2^+$ cells were also substantially low in both Day 30 and Day 60 Ri-hCOs (Figure 4.24.C-D, 4.26.C and 4.27.A). There was no visible neocortical layering for either timepoint in

Ri-hCOs (Figure 4.25.B-C). On review of the results, the key distinction between B-hCOs/E-hCOs and Ri-hCOs is the presence or absence of dorsal forebrain identity, respectively. In theory, Ri-hCOs could be used as a negative control hCO, a means of identifying important factors that are important in a hCO, but the question as to what the identity of an Ri-hCOs' is is not clear.

It may be beneficial to use a process of elimination to answer this question. As suggested previously, Ri-hCOs do not represent the dorsal forebrain, although Day 30 Ri-hCOs had a significant increase in the pan-GE, ventral forebrain marker *DLX1* (Figure 4.19.C), as well as *HOXB2* expression (Figure 4.21.C). At Day 60, there was relatively equal mRNA abundance of all ventral forebrain markers and *HOXB2* when compared to E-hCOs (Figure 4.19.D and 4.21.D). In fact, by Day 60, almost all non-dorsal forebrain progenitors are represented equally in both Control #2 Ri-hCOs and E-hCOs, with the exception of *OLIG2* expression which is greater in Ri-hCOs (Figure 4.19.D and 4.21.D); this may be due to the same maturation technique used in both hCO protocols enriching for these progenitors. The unique difference between Control #2 Ri-hCOs and E-hCOs was that across both timepoints, PAX3 was represented excessively, both transcriptionally and in cellular abundance (Figure 4.21.C-D and 4.24.C-D). To understand how PAX3 could reveal Ri-hCOs identity, and how this relates to increases in SOX2, further exploration of PAX3's functionality is necessary.

PAX3 expression is regulated initially by the WNT and SHH pathways from both the dorsoventral and anterior-posterior axis (Moore *et al.*, 2013; Sanchez-Ferras *et al.*, 2014), defining the neural plate border when under the influence of SMAD inhibitors (Degenhardt *et al.*, 2010; Xue *et al.*, 2018). During neural tube formation, the neural plate border cells become the dorsal neural folds closing the neural tube (Sudiwala *et al.*, 2019) and upon closure, disseminate into neural crest cells (NCCs) (Mehler *et al.*, 2020). As hCOs replicate elements of neural plate border designation and neural tube formation (Zheng *et al.*, 2021), it was therefore expected to observe trace values of PAX3 for all hCO protocols (Figure 4.21.A-D and 4.24.A-D). To current knowledge, PAX3 abundance has not been investigated in neuronal-based organoids and therefore it is necessary to rely on alternative models to interpret the results gathered from Ri-hCOs. Firstly, the morphological abnormalities indicate that Ri-hCOs do not successfully form neuroectoderm, implying a possible neural plate border issue (Figure 4.3). Neural plate border cells induced from human fibroblasts had high expression of *PAX3* and *HOXB2* in the

absence of *FOXG1*, similar to Ri-hCOs (Figure 4.21.C-D) (Thier *et al.*, 2019). On the other hand, unique *in vitro* models that emulate the separation between the epidermis and neural ectoderm stated that, after a brief calcium depletion followed by 7 days of Y-27632 exposure, the model was still able to generate NE and PAX3 levels were unaffected (Xue *et al.*, 2018). This conflicting evidence indicates that Ri-hCOs' high PAX3 expression is not enough to conclude Ri-hCOs' abnormalities are a result of neural plate border disturbance alone.

PAX3 is also implicated in NTC, in particular its role in exaggerating NTC disorders such as anencephaly and spina bifida (reviewed by Leduc, Singh and McDermid, (2017)). PAX3 contributes to such disorders by influencing apoptosis during NTC, as inhibition of *Pax3* increases p53-driven apoptosis resulting in an increased likelihood of NTC disorders (Loeken, 2005). This connection between low PAX3 expression and/or heightened caspase-dependent apoptosis with NTC disorders is also observed in both murine live imaging (Yamaguchi *et al.*, 2011) and post-mortem human tissue (Wang *et al.*, 2017). However, in Ri-hCOs whilst there was a significant increase in PAX3, apoptosis varied relevant to the timepoint; Day 30 Ri-hCOs do not significantly differ in level of apoptosis from E-hCOs, but apoptosis is elevated in Day 60 Ri-hCOs (Figure 4.17.B and 4.21.C-D). Although no known *in vivo* study has explored overexpression of PAX3 in the context of NTC, *in vitro* mouse neuroblastoma studies have shown that overexpression of *Pax3* inhibited proliferation and cell viability, as well as altered the length of time for each phase of the cell cycle (Huo *et al.*, 2021); proliferation and M phase cells was significantly lower in Ri-hCOs across both timepoints (Figure 4.9.B and Figure 4.16.B). A tangential connection between NTC and PAX3 can be observed at the roof plate of the E9.5 telencephalon in FOXG1-null mice. PAX3 expression significantly increases in the absence of FOXG1, descending ventrally from the dorsal roof plate (Martynoga *et al.*, 2005). This could be interpreted as FOXG1 acting as a repressive regulator of PAX3, and in its absence, PAX3 becomes more prolific, although no further evidence was provided about the relationship between the two (Martynoga *et al.*, 2005). Although this could be an explanation as to why PAX3 was overrepresented in Ri-hCOs, as FOXG1 was not present to repress it, there is no known evidence linking ROCK inhibition to repression of FOXG1 in NE or neocortex development currently. As PAX3 was overrepresented in Ri-hCOs, current evidence does not support the idea that the lack of lumens observed in Ri-hCOs is caused by NTC failure.

A final theory for explaining what Ri-hCOs identity was revolves around NCCs, with which two questions could be asked: are current NCC-generating protocols similar to the first 2 weeks of Ri-hCO culture and does the resulting mature Ri-hCO represent a likely outcome of 3D NCC culture, in the absence of a reference NCC organoid for comparison. When reviewing NCC protocols, 2D cultures exposed to Knockout Serum Replacement™ and N2 over the course of one week can create NCC precursors, but only when extended use of Y-27632 is applied (Kim, Ossipova and Sokol, 2015). When the endogenously-formed 3D aggregates are removed and tested against the 2D colonies, these 3D aggregates show diffuse ZO1^{+} tight junctions and reduced *PAX6* (Kim, Ossipova and Sokol, 2015), similar to what is observed in Ri-hCOs (Figure 4.11.C-D and 4.19.C-D). These NCCs were cultured in a similar media composition to Ri-hCOs and are provided the same concentration of Y-27632, with two additional days of exposure (Kim, Ossipova and Sokol, 2015). These NCC progenitors were also capable of generating TUJ1^{+} neurons (Kim, Ossipova and Sokol, 2015), similar to Ri-hCOs' suggested ability to produce neurons (Figure 4.29.C and 4.30.C). Other NCC protocols use Y-27632 as extensively as Kim, Ossipova and Sokol, (2015), such as So *et al.*, (2020), both of which can generate NCC progenitors within 7 days, whilst using similar patterning factors used for cerebral organoid protocols, e.g. SB-431542 for TGF-β inhibition and CHIR993021 for Wnt agonism (Lancaster *et al.*, 2017; Mehler *et al.*, 2020; So *et al.*, 2020; Delepine *et al.*, 2021). Contrastingly, neural plate border cell-generating protocols are substantially different to that of Ri-hCOs; there is no use of Y-27632, instead including of SHH agonists (Thier *et al.*, 2019). The evidence presented argues that the extended Y-27632 exposure included in EB generation of Ri-hCOs could have instigated a shifted cell fate to that of NCCs, which are PAX3^{+}, PAX6^{low}, unable to form ZO1^{+} tight junctions and are able to generate neurons (Kim, Ossipova and Sokol, 2015; So *et al.*, 2020).

When investigating the effects of PAX3 and ROCK manipulation experimentally, there are examples of similar scenarios occurring in the general literature. In the *in vivo* model of *Xenopus*, an injection of Y-27632 into the 4-8 cell stage's presumptive ectoderm did not affect *Sox2* expression by the neurula stage; instead, there was an expansion of NCC progenitor markers, such as *Sox8* (Kim, Ossipova and Sokol, 2015). Coincidentally, Control #2 Ri-hCOs also maintained relatively equal levels of SOX2^{+} cells compared to E-hCOs (Figure 4.26.C and 4.27.A). *In vitro* neuronal cultures, when exposed to PAX3

overexpression, exhibit Ri-hCO-like downregulation of proliferation (Figure 4.9.B) (Huo *et al.*, 2021). Additionally, PAX3-deficiency has a similar effect on proliferation in *in vivo* mouse models (Sudiwala *et al.*, 2019), whilst PAX3 overexpression causes cell aggregation *in vivo*, most notably during very early development (Lin *et al.*, 2017), suggesting that PAX3 could be involved in EB generation, as suggested in Section 3.5.2.

Overall, mature Ri-hCOs have a closer similarity to NCCs than neural plate border cells with regards to methodology for cell generation and results thereof. However, this theory is based on the limited information on neural plate border cell generation, as well as the limited bright field imaging data prior to Day 30, plus Day 30 and 60 Ri-hCO samples. It is of note that neural plate border cells precede NCCs in development (Thawani and Groves, 2020), and so generation of neural plate border cells in early Ri-hCO differentiation could have led to NCC development in Day 30 and Day 60 Ri-hCOs. PAX3 is a regularly used marker of successful NCC progenitor differentiation from a variety of stem cell origins (Liu and Cheung, 2016). For example, in So *et al.*, (2020), it was found that 95% of the population of NCC progenitors generated from such protocols are $PAX3^+$, but only after 6 days of exposure to Y-27632. This would explain why <10% of non-apoptotic cells are $PAX3^+$ (Figure 4.24.C-D); these cells could be representing the progenitor portion of the NCC population in Ri-hCOs. However, there is no known dominant identity for the live cells in Ri-hCOs, akin to B-hCOs' and E-hCOs' FOXG1 population (Figure 4.24.A-B). It would be expected that if Ri-hCOs were predominantly NCCs, this could be confirmed by staining for mature/migrating NCC markers such as SNAIL, TWIST, FOXD3 or SOX10, as reviewed by Simões-Costa and Bronner, (2015). Similarly, further analysis on the type of neurons present in Ri-hCOs is necessary. The current panel of glutamatergic and GABA-ergic synaptic markers was not sufficient in this circumstance, and would require targeting neuronal groups descending from NCCs, such as sensory ($TRKA\text{-}C^+$) and cholinergic ($ChAT^+$) neurons (Alshawaf *et al.*, 2018; Granger *et al.*, 2020).

Despite initial observations determining Ri-hCOs unfit for use in hCO modelling, this does not render them useless; three important pieces of information can be extracted from Ri-hCOs. Firstly, PAX3 should be more readily investigated as a deterministic factor for hCO quality. Secondly, Ri-hCOs could be an insight into how to generate neural plate border/NCC-based organoids, which are not currently available. Lastly, Y-27632 should be used sparingly, if at all, in

hCO protocols to avoid undesirable effects on hCO development. In a scenario where validated hCOs were not available to compare Ri-hCOs to, Ri-hCOs' inability to function as a hCO could be overlooked. In future, more emphasis should be placed on morphological hCO evaluation during peer review to minimise the possibility of poor hCO protocols, and the results thereof, being disseminated.

4.4.3 Control Cell Lines Can Exhibit Morphological and Cell Identity Discrepancies in Different Cortical Organoid Protocols

One of the largest arguments against the use of hCOs, is variability. In this study, intra-batch and within genotype variability were put under scrutiny (Table 4.1.6). In most examples, intra-batch variability was low enough to meet the statistical assumptions of normal residuals and Gaussian distribution necessary to use parametric analysis to isolate significant differences between data sets. Within-genotype variability was conducted throughout the quality assessment, comparing the two control cell lines as both E-hCOs and B-hCOs, where data was available.

Firstly, E-hCOs and B-hCOs both showed significant variance in early developmental growth of control cell lines. Control #2 B-hCOs had substantially smaller areas across both the NE and ND stages of development compared to Control #1 (Figure 4.4.C). On the other hand, in E-hCOs the control cell lines' patterns of growth varied significantly, as opposed to one cell line surpassing the other in area,e as exhibited by B-hCOs (Figure 4.4.D). The fact that the two selected control cell lines reacted significantly differently from one another, regardless of methodology, illustrates that accounting for inter-batch variability is a necessity for hCO research. Early developmental growth was the only instance where Control #1 and #2 B-hCOs differed; transcriptional analysis of Day 30 B-hCOs did not locate any one gene that had differential expression between the two control cell lines (Figures 4.10.D, 4.15.G, 4.19.G, 4.21.G, 4.28.G and 4.29.G-H). This is a considerable juxtaposition of what was observed in E-hCOs, where significant differences were found between the two cell lines, predominantly at Day 30. This could lead to the conclusion that B-hCOs were a better choice of protocol than E-hCOs. However, in the absence of ICC stains of Control #2 B-hCOs, it is difficult to make such a conclusion, as a proportion of the variability observed within E-hCOs was observed in results of ICC-based analysis.

Variability between cell lines was also found when examining the relationship between the internal and external morphology of E-hCOs, as a previously study has documented a correlation between lumen count and surface area (Albanese *et al.*, 2020). Day 30 E-hCOs of the two control cell lines did not vary in external area and there were no distinctive morphological differences (Figure 4.5.A and 4.5.D). On the other hand, Day 60 Control #1 E-hCOs had significantly increased external area and more externally-visible lobes than Control #2 (Figure 4.6.A and 4.6.D). As both Ri-hCOs and E-hCOs of Control #2 had similar external area at Day 60 (Figure 4.6.C), it is possible that each cell line had a unique limitation in size when using the oscillating plate method of maturation; there is no known literature investigating the effects of different maturation methodology on organoid culture. On the other hand, Day 30 E-hCOs' lumen count varied between the two control cell lines (Figure 4.12.C), although the size of these lumens did not differ (Figure 4.13.C-D). At Day 60, neither lumen count nor lumen size varied between E-hCOs of the two control cell lines (Figure 4.12.C and 4.14.C-D). Both timepoints are in contradiction with the anticipated correlation between lumen count and surface area, where lumen count increased with expanded surface area (Albanese *et al.*, 2020).

This correlation is under the assumption that nutrient diffusion is pervasive, which in E-hCOs of Day 30 onwards is not the case as evidenced by the absence of neuroepithelia in the centre of the E-hCO (Figure 4.7.C-D and 4.8.C-D). The cerebral organoids produced in the Albanese *et al.*, (2020), generated via the Velasco *et al.*, (2019) protocol, share similar methodology to E-hCOs, including dual SMAD inhibition and oscillating culture during maturation, but vary in key elements such as a drastically shorter ND phases and non-thermally stable FGF. One month-old Albanese *et al.*, (2020) cerebral organoids have similar ratio of NPC to neurons as Day 30 E-hCOs, but have far fewer cells overall due to the reduced NPC pool generated in the ND stage, thereby constraining the cerebral organoid's size whilst maintaining nutrient availability throughout the cerebral organoid. Over time, the Albanese *et al.*, (2020) cerebral organoids do not expand in size substantially, unlike E-hCOs, and therefore the relationship between lumen count and overall area cannot be applied to the excessively expanded Day 60 E-hCOs. Furthermore, Control #1 E-hCOs had significantly different morphology to Control #2 E-hCOs across both timepoints, with Control #1 E-hCOs more closely emulating that of Albanese *et al.*, (2020).

The reduced external size of Day 60 Control #2 E-hCOs could be a direct reflection of one of the most distinguishable differences between Control #1 and Control #2; the NPC pool population. As previously proposed when comparing the Basic and Enhanced protocol, lumen size may be unrelated to the depth of VZ, a hypothesis which is supported by the absence of lumen area differences between Control #1 and #2 E-hCOs, but significant changes in the $SOX2^+$ NPC population. At both Day 30 and Day 60, E-hCOs had significantly more $SOX2^+$ cells in Control #1 than #2 (Figure 4.26.E and 4.27.C); this disparity was not reflected in the transcriptional data (Figure 4.28.E-F). The fewer $SOX2^+$ cells in Control #2 Day 30 E-hCOs existed despite Control #2 having greater numbers of lumens than Control #1 (Figure 4.12.C). This outcome is unlikely a reflection of protocol variability, as both B-hCOs and E-hCOs of Control #1 had similar quantities of $SOX2^+$ cells at Day 30 (Figure 4.26.A), instead is likely to be a variability between the two cell lines themselves.

Despite E-hCOs' variable external size, lumen morphology and NPC population, certain aspects of NPC physiology are relatively comparable. Across both timepoints, E-hCOs had similar quantities of overall proliferation ($KI67^+$) and NPC-specific proliferation ($SOX2^+/KI67^+$) (Figure 4.9.C and 4.9.F), reflected only partially in *KI67* transcription, as Day 60 Control #2 E-hCOs had higher *KI67* expression (Figure 4.10.C). Control cell lines continued to share features of proliferation expanded to M phase cells, where there was no significant difference found in the total number of M phase ($pVIM^+$) cells in either timepoint (Figure 4.16.F), illustrating the same correlation between overall proliferation and cells undergoing M phase as was observed when comparing hCO protocols. Localisation of M phase cells to the apical edge of lumens were also similar in number at Day 30 between the two control E-hCOs, although this varied at Day 60 where less M phase cells were bound to the lumen in Control #2 E-hCOs (Figure 4.16.F). These results suggest that, to an extent, the depth of VZ, represented by $SOX2^+$ NPC population, does not affect the number of actively proliferating, apically-associated NPCs. Cerebral organoid studies analysing proliferation support this hypothesis, as only the first two cell layers of the VZ of a cerebral organoid are apically-associated cycling cells (Bershteyn *et al.*, 2017; Li *et al.*, 2017; Zhang *et al.*, 2019).

Although proliferation had minimal cell line variability, apoptosis, on the other hand, was more significantly different between cell lines. Apoptosis was

most variable at Day 30 in E-hCOs, as both total and NPC-specific apoptosis were significantly different; at Day 60, only NPC-specific apoptosis was varied (Figure 4.17.C and 4.17.F). It was hypothesised based on ICC imaging (Figure 4.7.C-D, 4.8.C-D and 4.25.D-G), that Day 30 E-hCOs had a greater ratio of NPCs to neurons than Day 60 and therefore the increased overall apoptosis was significantly greater due to the increased NPC-specific apoptosis (Figure 4.17.C and 4.17.F). Unfortunately, the NPC/neuron ratio could not be compared directly due to the dead core distorting cell count. Furthermore, the consistent NPC-specific difference between the two cell lines could indicate that there is a limit to the support E-hCOs can provide for deeper VZs, and that an excess of $SOX2^+$ NPCs may not be favourable to an E-hCOs development (Figure 4.20.C and 4.20.H). This hypothesis is further supported by the absence of difference between Day 30 B-hCOs and E-hCOs of Control #1, which also have share similar volumes of $SOX2^+$ NPCs (Figure 4.17.D), indicating that this difference in NPC apoptosis between E-hCOs is not a result of the Enhanced protocol specifically. Evolutionarily, it is beneficial to have a large NPC population and is attributed to the improvement in cerebral complexity in humans (Benito-Kwiecinski *et al.*, 2021), so the inability to support an expanded VZ may be an unfortunate repercussion of the hCO model.

Lastly, although proliferation and apoptosis had different responses to the two control cell lines, cell density does not vary between cell lines at either timepoint (Figure 4.18.C). The increased apoptosis alongside increased $SOX2^+$ NPC population, and therefore hypothesised VZ depth, of Control #1 E-hCOs possibly negated one another in terms of cell density, resulting in equal cell density at both timepoints in control E-hCOs (Figure 4.18.C). Overall, E-hCOs of the two control cell lines had distinctive morphological differences, and that changes in cellular physiology, such as apoptosis, were likely a response to those morphological changes. However, it was necessary to determine that there were no further ramifications of morphological differences with regards to cellular identity or neuronal development.

With regards to cellular identity, both control E-hCOs depict dorsal forebrain (Figure 4.22.C-D and 4.23.C-D). Additionally, ventral forebrain marker NKX2.1 expression remained consistently low across transcription and cell abundance for both control E-hCOs at both timepoints (Figure 4.19.E-F and 4.20.B). This would suggest that there was minimal representation of progenitors descended from the

VZ of the MGE (Stoykova *et al.*, 2000; Germain *et al.*, 2013; Minocha *et al.*, 2017). On the other hand, other ventral forebrain markers, such as *DLX1* and *LHX6* were significantly upregulated in Day 30 Control #2 E-hCOs (Figure 4.19.E). The ventral progenitor marker DLX1 is functionally similar to DLX2 (Petryniak *et al.*, 2007; Alzu'bi and Clowry, 2019), both of which are expressed across the VZ and SVZ in neural progenitors of the LGE and MGE in the rostral portion of the telencephalon (Stoykova *et al.*, 2000; Alzu'bi and Clowry, 2019). DLX1 and DLX2 are also responsible for regulating LHX6 (Alzu'bi and Clowry, 2019), a protein found in GABA-ergic interneurons that are located in both the LGE and MGE (Stoykova *et al.*, 2000), as well as in the cortex after GABA-ergic interneurons migration (Alzu'bi and Clowry, 2019; F. Yuan *et al.*, 2020). LHX6 expression is also regulated by NKX2.1 (Du *et al.*, 2008), but in the absence of any change in *NKX2-1* transcription and translation, it can be assumed that the rise in *LHX6* expression found in Control #2 Day 30 E-hCOs was likely due to the increase in *DLX1* (Figure 4.19.E). By process of elimination of GE locales, Control #2 Day 30 E-hCOs were enriched for LGE progenitors and possibly also the GABA-ergic interneurons that descend from them. For confirmation of the LGE identity, it would be beneficial to confirm LGE identity using LGE-specific markers such as *GSX2* (Pei *et al.*, 2011).

In addition to this LGE enrichment, Day 30 Control #2 E-hCOs had significantly upregulated *FOXG1* and *PAX6* (Figure 4.19.E), but there was no change in the abundance of $FOXG1^{+}$ cells (Figure 4.24.E-F). These increases in dorsal forebrain markers are not necessarily representative of greater dorsal forebrain identity, but instead could further evidence of increased LGE prominence. *PAX6* can be found in the lateral portion of the LGE (Englund *et al.*, 2005; Mi *et al.*, 2013) and if there was greater representation of other forebrain regions, increases in the telencephalic marker FOXG1 could be expected (Renner *et al.*, 2017). By Day 60, *DLX1*, *LHX6, PAX6* and *FOXG1* had similar mRNA abundance across E-hCOs of the two control cell lines, with *NKX2-1* elevated to similar levels as other GE markers, although it was downregulated in Control #2 E-hCOs (Figure 4.19.F). It is possible that Control #2 E-hCOs are sensitive to the oscillating method of maturation, and respond to the stress by shifting cellular identity, which is a known cerebral organoid response to environmental stress (Bhaduri *et al.*, 2020); despite different cellular identities, similarly cultured Ri-hCOs shared mRNA abundance of ventral forebrain markers with Control #2 E-hCOs (Figure 4.19.C-D). This cellular identity shift was not confined to

telencephalic identity. Both midbrain (*FOXA2*) and hindbrain (*HOXB2*) progenitor markers were upregulated in Day 30 Control #2 E-hCOs but the mRNA abundance was still low overall (Figure 4.21.E). In review, the overall increase in non-dorsal forebrain identity representation, particularly the LGE, was perceived to be an unfortunate response of Control #2 to the oscillating culture during maturation.

It would be anticipated that a cell population of non-dorsal forebrain identity would disrupt the neocortical layer development in Control #2 E-hCOs. Transcriptional analysis showed no significant differences between cell lines, at either timepoint, for markers representing the scope of the neocortex, from VZ to Layer I, with the exception of *EOMES* at Day 60 (Figure 4.29.E-F). Outside of the $SOX2^+$ VZ, the only significant change in neocortical cell abundance was $CTIP2^+$ neurons in Day 30 Control #2 E-hCOs (Figure 4.26.E). $TBR2^+$ IPs were unaffected by cell line at both timepoints (Figure 4.26.E and 4.27.C). Subsequent changes were found in related transitioning NPC populations, as Day 30 Control #1 E-hCOs had more $TBR2^+/CTIP2^+$ NPCs than Control #2 (Figure 4.26.F). It is unknown why there would be significantly fewer $CTIP2^+$ neurons as a result of fewer IPs terminally differentiating in Day 30 Control #2 E-hCOs, as $CTIP2^+$ neurons are generated in both the dorsal forebrain's cortical plate and LGE's mantle zone (Arlotta *et al.*, 2008).

One possible explanation is that with more types of neurons being generated, produced by the LGE progenitors, there is competition for space and resources; this would not occur in Control #1 Day 30 E-hCOs as only cortical neurons were generated. Such a scenario is depicted in Mariani *et al.*, (2015), where outcroppings of $DLX1^+$ and $GAD67^+$ cells situate themselves in the space surrounding VZs. This requires further investigation to determine what is occupying the percentage of the cell population left absent by low $SOX2^+$ cells in Control #2 E-hCOs, if it is neither dorsal nor ventral forebrain progenitors. It would be assumed that the ventral forebrain associated-cells would occupy the areas of less cellular arrangement, as ventricular structure is not required for generating ventral forebrain progenitors in cerebral organoids (Bagley *et al.*, 2017; Cederquist *et al.*, 2019). It is interesting, however, that SOX2 is present in both dorsal and ventral forebrain progenitors (Ferri *et al.*, 2013), and yet SOX2 was still significantly lower in Day 30 Control #2 E-hCOs.

It would be expected that a diverse pool of progenitors would generate a greater variety of neurons, possibly maturing at different speeds. Day 30 Control #2 E-hCOs had greater representation of maturing neurons than its Control #1 counterpart, with elevated *DCX* and *MAP2* transcription (Figure 4.29.E); this was not observed at Day 60 (Figure 4.30.E). Although transcriptional analysis can only suggest an increase in maturing neuronal populations, these hypothesised additional neurons were unlikely to be VGLUT1^{+} glutamatergic neurons, as the mRNA abundance of *SLC17A7* remained unchanged between the two control cell lines at Day 30 (Figure 4.29.F). Instead, pre- and postsynaptic markers that are not specific to the developing cerebral cortex were significantly upregulated (Figure 4.29.F). This included genes coding for hippocampal- and brainstem-specific glutamate-refuelling proteins, *SLC17A6,* and ubiquitously expressed subunits of glutamate receptors, *GRIA1* and *GRIN1* (Enoch *et al.*, 2014; Vigneault *et al.*, 2015; Shen, Zeppillo and Limon, 2020). Presynaptic GABA-ergic interneuron markers involved with vesicular loading and synthesising GABA (*VGAT, GAD1* and *GAD2*) were also upregulated (Pla *et al.*, 2018); these GABA-related markers are known to be influenced by DLX1 expression (Pla *et al.*, 2018). Arguably, the altered transcriptional dynamics of synaptic markers may not be a representation of quantity of neurons of a specific lineages, but instead a reflection of adjusted synaptic transmission of each neuron (Glynn *et al.*, 2011; Lazarus, Krishnan and Huang, 2015), i.e. same number and type of neurons, different synaptic activity. Without further investigation it is difficult to conclude any singular hypothesis. Regardless of the interpretation, however, this result is uniquely specific to the timepoint, protocol and cell line, as B-hCOs did not exhibit this phenomenon and at Day 60 the disparity in mRNA abundance associated with ventral forebrain was resolved (Figure 4.29.F, 4.29.H and 4.30.F).

The importance of accounting for variability between cell lines cannot be overstated, as shown here. In this circumstance, a singular facet, such as an abundance of non-dorsal forebrain progenitors, can have inadvertent effects on other features within a model, such as VZ depth and type of neurons generated. Although there are few studies that investigate within-genotype variability in cerebral organoids, their results bear a similarity to what is observed in Control #1 and #2 E-hCOs. Yoon *et al.*, (2019) analysed cerebral organoids from more than 5 hIPSC lines and found significant transcriptional diversity in *FOXG1*, *PAX6* and *NKX2-1*, as well as differences in gene clusters responsible for radial glia and

GABA-ergic neurons, whilst intermediate progenitors were unaffected by the differing hIPSC lines. Transcription of cortical layers were also unaffected by differentiation from different hIPSCs, but the quantification of proportional representation of cortical layers illustrated up to 20% variance between cell lines (Yoon *et al.*, 2019). The within-genotype variability observed in Control #1 and #2 E-hCOs mirror all of these traits, indicating that the results discussed here are in keeping with current expectation of within-genotype variability (Yoon *et al.*, 2019; Hernández *et al.*, 2021). Although further refinements in the hCO protocol may minimise the within-genotype variability, ideally more control cell lines are necessary to conclusively isolate disease phenotypes. In the absence of such measures, the two control cell lines will be compared to the 1qDel cell line separately, so as not to skew conclusions.

4.5 Conclusion

Given cerebral organoids' relatively short time in circulation, there has been a wealth of literature utilising the cerebral organoids' unique attributes in a variety of research questions. Unfortunately, there has been significantly less focus on creating consistent protocols and validating current systems. The variety of cerebral organoids protocols currently in literature has made cross-paper examination difficult, and has resulted in conflicting conclusions when applied to disease modelling, such as FOXG1 overexpression in ASD patient-derived cerebral organoids where either an increase (Mariani *et al.*, 2015) or a decrease (Zhu *et al.*, 2019) in GABA-ergic neurons was observed. This weakens the argument for using cerebral organoids, despite the solution being relatively simple; to use a universal, validated cerebral organoid protocol. However, as illustrated in this chapter, different cerebral organoids protocols can meet the requirements of a broad validation assessment to varying degrees, such as B-hCOs and E-hCOs. On the other hand, small variations in protocol can create organoids that are unsuitable for use, such as Ri-hCOs. Within-protocol variability is also a continuing issue, as demonstrated by the two pluripotent control cell lines of this study. Evidently, cerebral organoids are highly sensitive to methodological change (Quadrato *et al.*, 2017) and stress (Bhaduri *et al.*, 2020), affecting their physiology, and therefore future quality assessments should be designed more stringently. Ideally, the next iteration of a cerebral organoid quality assessment would be a combination of Table 4.1 and the Sivitilli *et al.*, (2020) assessment of cerebral organoids, which included substantial more information on functionality of neurons,

longer differentiation times and broader transcriptional and proteomic analysis. The endeavour of this chapter was to provide a foundation from which to develop such an assessment, such as Table 4.1 and the results herein, with the aim that methodological discrepancies are kept to a minimum in future cerebral organoid research. Using Table 4.1 as a guide, the Enhanced protocol was chosen for modelling 1qDel, as it is telencephalic in identity, unlike Ri-hCOs, and outperforms the Basic protocol in key hCO physiology such as localised proliferation, as well as significantly increased representation of cortical layers and improved neuronal maturity.

5 Characterisation of 1q21.1 Deletion in Validated Human Cortical Organoids

5.1 Introduction

Cerebral organoids have proven to be suitable research models for recapitulating the phenotypes seen in patients of CNV disorders, including changes in brain size (Lancaster *et al.*, 2013; Qian *et al.*, 2016; Li *et al.*, 2017; Zhang *et al.*, 2019) and increased risk of developing neuropsychiatric disorders (Iefremova *et al.*, 2017; Wang *et al.*, 2017; Stachowiak *et al.*, 2017). As the E-hCO has proven capable of producing a rudimentary *in vivo*-like structure of a neocortex (Section 4), it was therefore used to investigate the impact of 1qDel on dorsal forebrain development. As previously mentioned, 1qDel exhibits microcephaly in a reported 22-72% of patients (Mefford *et al.*, 2008; Bernier *et al.*, 2016) and patients have a significantly increased likelihood of developing SCZ (Stefansson *et al.*, 2008; Stone *et al.*, 2008; Crespi and Crofts, 2012). Understanding how these two phenotypes present in current research models may provide insight into what abnormal mechanisms may present in 1qDel E-hCOs.

5.1.1 Presentation of Microcephaly in Current Research Models

Microcephaly is defined by an occipitofrontal circumference of the head that is more than 3 standard deviations away from the average, the occurrence of which affects 2-3% of the worldwide population (Hagen, 2017). Microcephaly is split into specific categories based on time of onset: prenatal underdevelopment of cortical thickness (primary microcephaly) or postnatal truncation of brain growth (secondary microcephaly) (reviewed by Gabriel *et al.*, (2017)). Microcephaly is further categorised by its additional features: conditions that are solely characterised by intellectual disability and microcephaly are considered non-syndromic, whilst those that have a wider spectrum of cognitive and physiological defects as well as microcephaly are called syndromic. In this regard, the categorisation of 1qDel's microcephaly is unknown at present (Sønderby *et al.*, 2021). As cerebral organoids have proven capable of emulating both primary and secondary microcephaly (Lancaster *et al.*, 2013; Gomes *et al.*, 2020), despite predominantly resembling prenatal development (Camp *et al.*, 2015; Luo *et al.*, 2016), the delineation between microcephalus onset was investigated.

5.1.1.1 Primary Microcephaly

Cranial magnetic resonance imaging of primary microcephaly (both syndromic and non-syndromic) has illustrated common features of brain morphology of the phenotype, including abnormal gyral pattern, extra-axial space, pachygyria, agenesis of corpus callosum and small size of cerebellum and brainstem (Basel-Vanagaite and Dobyns, 2010; Shaheen *et al.*, 2019). Primary microcephaly is often comorbid with intellectual disability, with a positive correlation in the severity of both symptoms (Boonsawat *et al.*, 2019). Primary microcephaly can be significantly heterogenous in its presentation (Boonsawat *et al.*, 2019; Shaheen *et al.*, 2019), however autosomal recessive primary microcephaly disorder (MCPH) has been well documented due to its phenotypic homogeneity. MCPH is defined by the appearance of non-syndromic primary microcephaly which occurs in 1 in 250,000 births in non-consanguineous populations; incidence rates are considerably higher in consanguineous populations (Van Den Bosch, 1958). MCPH pathogenesis is attributed to a series of genes, which are clustered into groups based on their protein functions: centriole biogenesis template recruitment (*STIL, CENPJ, CEP63/135152, SASS6*), microtubule organisation (*ASPM, WDR62* and *CDK5RAP2*) or DNA damage regulation (*MCPH1*) (Jean, Stuart and Tarailo-Graovac, 2020).

The majority of MCPH-associated genes have key roles within the same pathways, namely centriole biogenesis. As reviewed by Jean, Stuart and Tarailo-Graovac, (2020) and displayed in Figure 5.1, the process of centriole biogenesis coordinates with the S phase of the cell cycle, where the majority of MCPH-inducing proteins have been identified. At the beginning of G1-S phase, the maturation of daughter centrioles into mother centrioles is catalysed by the microtubule scaffold protein WDR62, recruiting CEP63 & CEP152 to form a ring-structure at the proximal end of the mother centriole (Sir *et al.*, 2011; Kim *et al.*, 2013). Once the ring structure is formed on each mother centriole, PLK4 binds to the ring, acting as the site for future daughter centriole generation (Kim *et al.*, 2013). PLK4 is responsible for the recruitment of two other MCPH-related proteins, STIL and SASS6, to form a rudimentary template of the daughter centriole (Tang *et al.*, 2011). CENPJ and CEP135 are recruited to the daughter centriole template, with the aid of WDR62 and ASPM (Jayaraman *et al.*, 2016), and begin fleshing out the template with microtubules (Lin *et al.*, 2013). The new daughter centrioles require additional space within the centrosome to organise microtubules prior to

mitosis. Microtubule-associated proteins such as CDK5RAP2 recruit γ-tubulin to the centrosome to accommodate the new daughter centrioles (Issa *et al.*, 2013), in preparation for ASPM-mediated astral microtubule formation during M phase (González-Martínez *et al.*, 2021), as the cell transitions into G2.

There are a number of additional proteins that contribute to the processes of centriole generation and maintenance, however, the fact that this pathway is punctuated at each stage by MCPH-related proteins is informative as to why there are phenotypic parallels in MCPH cases with different genetic mutations (Jean, Stuart and Tarailo-Graovac, 2020). Neural progenitors are repetitively cited as vulnerable to mutations in these genes and are directly attributed to the resulting microcephaly (Jean, Stuart and Tarailo-Graovac, 2020). Key aspects of neuronal progenitor physiology, such as proliferation and apoptosis, can be substantially affected by abnormal expression of MCPH proteins involved in daughter centriole generation, such as STIL, CENPJ and CEP135 (Hussain *et al.*, 2012; David *et al.*, 2014; Ding *et al.*, 2019; Jean, Stuart and Tarailo-Graovac, 2020). Furthermore, microtubule-associated MCPH genes, such as WD6R2, ASPM and CDK5RAP2, are similarly impactful on NPC physiology.

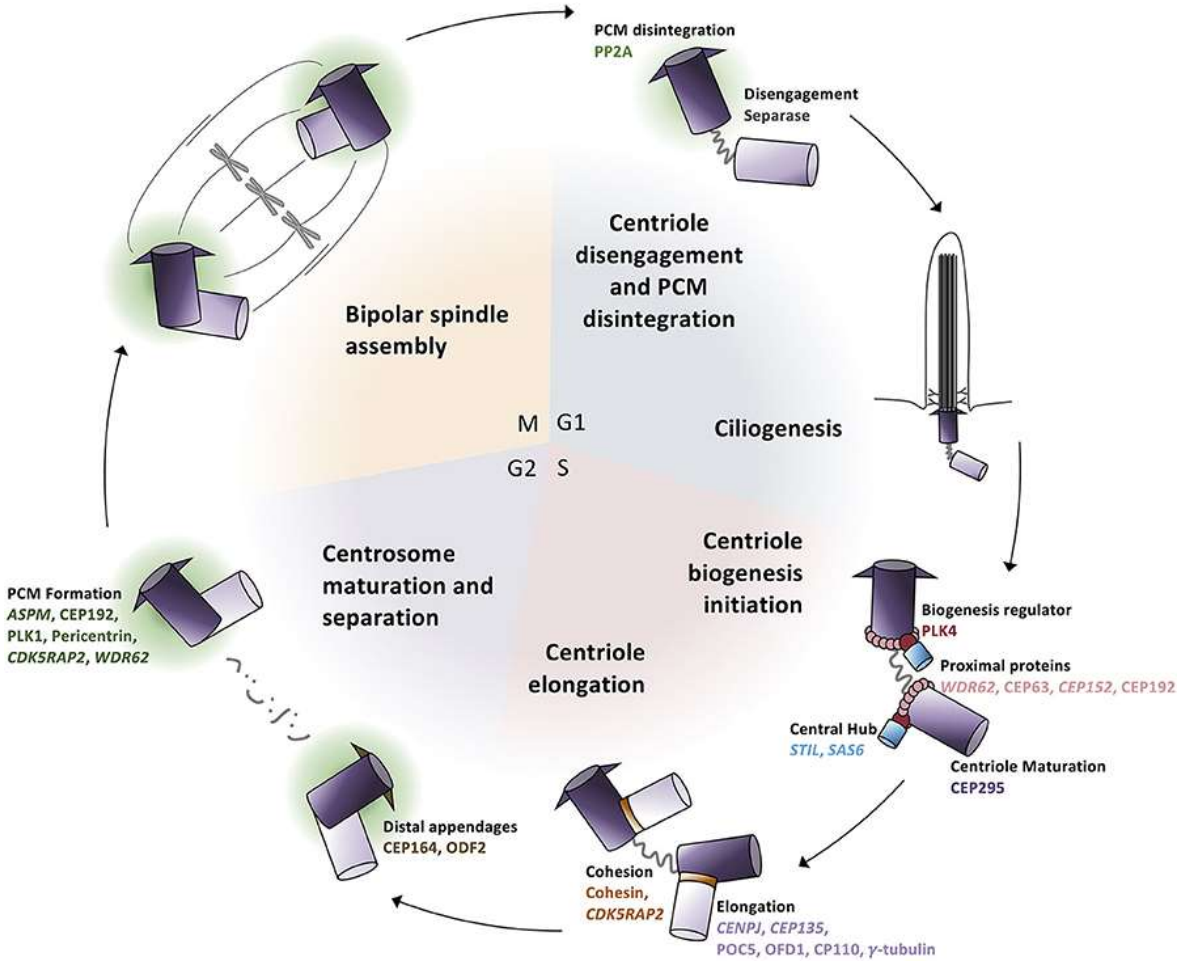

Figure 5.1: The process of centrosomal biogenesis in relation to the cell cycle. Key proteins and their localisation are referenced in image. Figure from Jean, *et al.*, (2020): PCM – pericentriolar material.

WDR62 mutant mice with human-specific missense mutations have microcephaly, alongside embryonic lethality, dwarfism and anophthalmia (Shohayeb *et al.*, 2020). The cilia, as opposed to the centrioles, were scrutinised in these mouse models, as the basal body of the RG's cilia did not recruit all necessary proteins to maintain cilia formation, thereby undermining RG's self-proliferation. The knock-on effect of poor cilia formation was premature neuronal differentiation, with overall cortical thinning from the fewer neurons (Shohayeb *et al.*, 2020). Corroborating results of WDR62's specific localisation to RGs and role in mitotic spindle and centrosome organisation was also found in post-mortem MCPH patients' brains (Nicholas *et al.*, 2010; Yu *et al.*, 2010). Although also targeting microtubules, the centrosome maturation-associated ASPM acts redundantly with CDK5RAP2, as spindle morphology in the M phase of *ASPM* knockout human cell lines is only affected when CDK5RAP2 is exogenously

reduced in tandem (Tungadi *et al.*, 2017). Similarly, *ASPM*$^{+/-}$ mice have considerably less severe cortical thinning and neuronal progenitor reduction than *CDK5RAP2*$^{-/-}$ and *CEP135*$^{-/-}$ mice (González-Martínez *et al.*, 2021). This would indicate that there is a hierarchy of severity associated within the groups of functionally-similar MCPH proteins, where those involved with initial steps of centriole biogenesis are at greater risk of severe phenotypes, although this requires further examination to confirm.

As discussed previously, a large proportion of the MCPH-associated genes are associated with centriole construction and so MCPH was originally considered a “centriolopathy”. However, additional genes are being uncovered that are less involved with centriole manufacture and more related to overall cell cycle regulation (Jean, Stuart and Tarailo-Graovac, 2020), it is no longer considered as such. One such example is the DNA damage response regulator, MCPH1, that can affect the timing of entry into M phase, inducing asymmetric division of neural progenitors and resulting in cortical thinning (Peng *et al.*, 2009; Gruber *et al.*, 2011). These converging features of MCPH phenotypes depict a common shared pathogenesis across the different categories of MCPH genes; MCPH-associated microcephaly is a reduction of neurons in the neocortex, caused by abnormal cell cycle dynamics in neural progenitors, although how this dysregulation occurs is specific to the affected MCPH gene. It should be stated that MCPH shares key risk genes (*CENPJ*, *CENPE, CEP152*) with other syndromic, secondary microcephaly disorders such as primordial dwarfism (Jean, Stuart and Tarailo-Graovac, 2020), and therefore reassessment of the definition of primary/secondary microcephaly may be necessary in the future.

Primary microcephaly can occur as inherited or *de novo* genetic mutations, as shown by MCPH (Boonsawat *et al.*, 2019), but can also be caused by non-genetic factors including viral infections, one of the most recent examples being the Zika virus. Whilst pregnant, maternal infection of the virus can have serious negative effects on foetal neurodevelopment, resulting in substantially high risks of brain malformations such as cerebral atrophy, ventriculomegaly and overall abnormal cerebral cortex development (Lage *et al.*, 2019). The gestational time of maternal infection relates to the severity of the symptoms (Huang *et al.*, 2016), and an infection in the first trimester can cause primary microcephaly in foetuses by the second trimester (Vesnaver *et al.*, 2017). The pathology of the Zika virus in the cerebral cortex follows MCPH’s theme of increased direct neurogenesis at the

expense of forming sufficient neuronal progenitor populations (Huang *et al.*, 2016; Gladwyn-Ng *et al.*, 2018). However, as opposed to a centrosome/mitotic issue, current research states that the shift to direct neurogenesis, and the infection-specific increase in widespread apoptosis, are the repercussions of an unfolding protein response, prompted by endoplasmic reticulum (ER) stress (Huang *et al.*, 2016; Gladwyn-Ng *et al.*, 2018; Muthuraj *et al.*, 2021). This pathology of ER stress and elevated apoptosis is shared with cases of neonatal diabetes patients that also exhibit primary microcephaly (Poulton *et al.*, 2011; Franco *et al.*, 2020). This suggests that primary microcephaly's theme of increased direct neurogenesis at the behest of neuronal progenitor expansion is shared between non-syndromic and syndromic disorders, but deviates significantly in which pathways contribute to this result.

Although primary microcephaly is a common phenotype in neurodevelopmental disorders, the heterogeneity within its genotype and phenotype makes researching causative factors difficult. The method in which primary microcephaly is described and monitored in literature makes it all the more complex to identify the mechanisms responsible. As an example, there are currently >1500 entries for "Microcephaly" in the clinical resource Online Mendelian Inheritance in Man, but only <100 entries for "Primary Microcephaly". As new tools and better clinical cohort management becomes available, these resources should aim to provide more detailed patient information with the intention of understanding the development and improving the prognosis of primary microcephaly patients.

5.1.1.2 Secondary Microcephaly

Secondary microcephaly differs significantly from primary, as it is defined by average neonatal head size that is followed by developmental regression; there is no correlation between the severity of intellectual disability and secondary microcephaly (Boonsawat *et al.*, 2019). Secondary microcephaly is often syndromic, observed in cases such as Rett syndrome and Angelman syndrome. Shared symptoms of these syndromes include intellectual disability, postnatal microcephaly, difficulties with language, repetitive behavioural patterns, epilepsy and impairment in fine motor skills (reviewed by Seltzer and Paciorkowski, (2014)). However, these disorders have distinctly different causative factors for dysregulation of cortical development.

To begin, Rett syndrome is the result of *MECP2* loss, an X-linked gene responsible for methylating genomic DNA. Accompanying the shared symptoms of other secondary microcephaly syndromes, between 54-80% of children with Rett syndrome suffer from postnatal truncation of head growth in the first 18 months (Sandweiss, Brandt and Zoghbi, 2020), predominantly affecting the frontal, parietal and temporal lobes (Carter *et al.*, 2008). The complexity of Rett syndrome is partially attributed to the hundreds of variants of *MECP2* identified, which contributes to the severity of the disorder (Townend *et al.*, 2018). MECP2's role in neurodevelopment has been investigated to elucidate how Rett syndrome symptoms occur, including microcephaly (reviewed by Ip, Mellios and Sur, (2018)). There is a resemblance in pathology of Rett syndrome microcephaly to MCPH, as neural progenitors are significantly affected by relinquished MECP2 function in the cerebral cortex. MECP2 facilitates microRNAs (miRNAs) regulation of neural progenitors, and the repression of this process can result in microcephaly (Nakashima *et al.*, 2021).

Further investigation using cerebral organoids studies have related the mutation of *MECP2* to a shifted cell fate ratio towards neurogenesis at the expense of the neural progenitor pool (Gomes *et al.*, 2020). However, there is conflicting evidence to this conclusion from *in vitro* literature, as some studies have shown greater neural progenitor populations (Morelli *et al.*, 2022), whilst others have observed a significantly greater astrocytic populations at the expense of neural progenitors (Nakashima *et al.*, 2021). Further elaboration on the molecular/cellular relationship between *MECP2* and *MECP2*-associated microcephaly is necessary, with emphasis on comparing the same *MECP2* variants. On the other hand, considerably more information is available on the postnatal brain development of *MECP2* patients. *MECP2*-associated microcephaly is associated with shortened, compacted neurons with simplified dendritic branching and spine density in adult patients (Armstrong *et al.*, 1995). These morphological mutations coincide with a loss of forebrain-specific neurons (Zhang *et al.*, 2014). Overall this results in dysfunctional neuronal connectivity, observed as hyperexcitation and seizures (Zhang *et al.*, 2014), as well as poor experience-based refinements of these circuits (Banerjee *et al.*, 2016). Both of these functional deficits become greater issues during postnatal brain development and directly contribute to symptom presentation (Ip, Mellios and Sur, 2018).

Much like Rett syndrome, Angelman syndrome is also associated with the maternal/paternal divide of gene activity, but in the form of an imprinting syndrome as opposed to an X-linked syndrome. Angelman syndrome presents the aforementioned secondary microcephalus syndromic symptoms, the majority of which do not usually present neonatally, taking up to two years to become evident (Williams, Driscoll and Dagli, 2010). Angelman syndrome is caused by the loss of expression of the maternal copy of the imprinting gene *UBE3A*. There are four classes of Angelman syndrome, relevant to the method of *UBE3A* loss, including *de novo* deletion, failure to inherit the maternal copy, abnormal methylation and loss-of-function mutations of *UBE3A* (Seltzer and Paciorkowski, 2014). Although UBE3A is bi-allelically expressed in most tissues, only the maternal copy is expressed in the brain during development (Landers *et al.*, 2005). Although *UBE3A* and *MECP2* are not currently associated with one another (Lawson-Yuen *et al.*, 2007), Rett syndrome and Angelman's syndrome share the fluctuating impact of gene loss relative to the region of the brain (Ip, Mellios and Sur, 2018; Rotaru *et al.*, 2018). This is because MECP2 and UBE3A are expressed in the majority of neurons, including those which are glutamatergic and GABA-ergic (Ip, Mellios and Sur, 2018; Rotaru *et al.*, 2018).

As a result of their ubiquitous expression in neurons, *MECP2* and *UBE3A* cause significant neuronal circuitry disruption, coincidentally in a similar fashion to one another, which provides some explanation for the significant overlap in clinical presentation. *MECP2*$^{-/-}$ murine pyramidal neurons have reduced calcium transmission due to affected potassium/chloride co-transporter channels (Banerjee *et al.*, 2016). This induces a polarity switch of GABA receptors, thereby reducing response of parvalbumin (PV)-specific inhibitory neurons and inducing a hyperexcitable network (Banerjee *et al.*, 2016). *UBE3A*$^{-/-}$ mice have a similar hyperexcitable phenotype to *MECP2*$^{-/-}$ neurons, as there is a significant reduction in spontaneous inhibitory transmission with an opposing increase of spontaneous excitatory transmission in the PFC (Rotaru *et al.*, 2018). UBE3A suppresses this hyperexcitability in neurotypical patients by regulating calcium and voltage-dependent potassium channels (Sun *et al.*, 2019).

Unfortunately, none of the aforementioned studies reported brain size in disease models, and there is a lack of data on the relationship between Angelman or Rett syndrome-associated microcephaly and cortical dysfunction. However, the structural abnormalities of Rett syndrome, such as regional volume reduction,

have been suggested to be a result of altered neural progenitor populations similar to MCPH (Gomes *et al.*, 2020; Nakashima *et al.*, 2021; Takeguchi *et al.*, 2022), although this is under dispute (Morelli *et al.*, 2022). Conversely, different structural anomalies are observed in Angelman syndrome, where there is an absence of differences in brain structure compared to controls, but delayed and repressed growth of white matter tracts which has been suggested to drive the observed microcephaly (Harting *et al.*, 2009; Judson *et al.*, 2017). There is, however, evidence to suggest that Angelman syndrome-associated microcephaly also originates in neural progenitor health, as UBE3A has been found to interact with the MCPH gene, *ASPM* (Singhmar and Kumar, 2011). Further shared genetic associations have been found between primary and secondary microcephaly, with functions associated with DNA repair, neuronal migration and transcriptional regulation in evidence (Alcantara and O'Driscoll, 2014; Seltzer and Paciorkowski, 2014; Boonsawat *et al.*, 2019). Overall, comparison of the molecular pathways between the two presentations of microcephaly is difficult due to the heterogeneity of secondary microcephaly syndromes, as well as minimal investigations into the cause of secondary microcephaly. It would therefore be beneficial to focus efforts into comparing these two types of microcephaly in early development, with the intention of identifying how and why secondary microcephaly has a postnatally-delayed time interval prior to presentation.

5.1.1.3 Cerebral Organoids' Ability to Represent Microcephaly

Contradictions between human patients and mouse models in primary microcephalus studies have slowed progress in elucidating these disorders; heterozygous/homozygous deletion of *ASPM, NDE1* or *CDK5RAP2* in mice does not replicate the primary microcephaly observed in patients (Gabriel *et al.*, 2020). Conflicting results across different research models of secondary microcephaly have also made defining pathology difficult (Gomes *et al.*, 2020; Nakashima *et al.*, 2021; Morelli *et al.*, 2022). This disconnect between research models could be due to the human-specific features that are affected in most microcephaly cases, namely neuronal progenitor type and proliferation and more defined separation of cortical layers (Cadwell *et al.*, 2019). Even within the primate order, there are considerable differences in neurodevelopment, such as the expansion of the neural progenitor pool, vulnerable to microcephaly-associated deficits (Benito-Kwiecinski *et al.*, 2021). Additionally, the catalogue of variants for each microcephalus disorder or syndrome, e.g. Rett syndrome, can be difficult to

emulate efficiently if not directly descended from a patient (Ip, Mellios and Sur, 2018). Cerebral organoids have proven to be significantly useful in filling the niche of a prenatal, human-specific, multi-cellular research model capable of exploring the mechanisms suggested to be involved in both forms of microcephaly (Lancaster *et al.*, 2013; Li *et al.*, 2017; Sun *et al.*, 2019; Gomes *et al.*, 2020).

There are a number of MCPH-associated genes modelled in cerebral organoids that exhibit disruptions to the neural progenitor pool, resulting in aberrant neurogenesis (Lancaster *et al.*, 2013; Li *et al.*, 2017; Zhang *et al.*, 2019). *ASPM*-mutated patient-derived cerebral organoids present structural degradation of the neuroepithelium, lacking VZ formation, resulting in sporadic and undefined Ca^{2+} activity in neurons (Li *et al.*, 2017). *WDR62*-deleted cerebral organoids have abnormal neuronal progenitor activity and impaired symmetric/asymmetric radial glia division ratio as a result of poorly forming cilia (Zhang *et al.*, 2019). Finally, loss of *CDK5RAP2* in cerebral organoids replicated the patient's phenotype of microcephaly from which the cerebral organoids were derived from and rendered patient-derived embryoid bodies incapable of developing during neural induction (Lancaster *et al.*, 2013). With increased seeding density, the patient-derived cerebral organoids were capable of developing neuroepithelia, however these had considerably fewer RGs, driven by reduced horizontal division of the radial glia, with greater neuronal populations and outgrowth compared to controls (Lancaster *et al.*, 2013). All three MCPH cerebral organoid examples documented here exhibited substantial microcephaly similar to what is observed in patients, but this was not necessarily replicated in mouse models (Nicholas *et al.*, 2010; Lancaster *et al.*, 2013; Tungadi *et al.*, 2017; Gabriel *et al.*, 2020).

There is also a growing list of non-MCPH-related primary microcephaly studies using cerebral organoids as a model system, but disrupted neural progenitors continue to be a causative factor for microcephaly. Non-syndromic, primary microcephaly disorders have been investigated using cerebral organoids generated from either targeted gene overexpression (*PTEN*) or patient-derived mutations (*NARS1*) (Wang *et al.*, 2020; Dhaliwal *et al.*, 2021). Both cerebral organoid types exhibit microcephaly similar to what is observed in patients. *PTEN* sacrifices the neural progenitor population for lower layer neurons (Dhaliwal *et al.*, 2021), whilst mutations in *NARS1* resulted in fewer neural rosettes forming, with single cell, RNA sequencing illustrating that RGs are vulnerable to change when NARS1 is reduced (Wang *et al.*, 2020).

Syndromic primary microcephaly disorders exhibit more detrimental results than those of non-syndromic primary microcephaly in cerebral organoid studies. Targeted p53 knockdown, representing the p53 deficit in Nijmegen Breakage syndrome, illustrates poor retention of neuroepithelia structure, detrimental to both IP and Layer 6 neuron production (Marin Navarro *et al.*, 2020). In addition, the G1 phase of the cell cycle was extended to the detriment of the S phase (Marin Navarro *et al.*, 2020), which was supported by abnormal cell cycle appearing in RNAseq data from other Nijmegen Breakage syndrome patient-derived cerebral organoids (Martins *et al.*, 2022). Interestingly, Nijmegen Breakage syndrome patient-derived cerebral organoids do not show a decrease in cycling cells, but do show significantly shrunken VZs coinciding with a substantial reduction in forebrain markers such as *FOXG1* and *PAX6* (Martins *et al.*, 2022). This would suggest that the cell cycle of telencephalic-origin neural progenitors specifically are affected by Nijmegen Breakage syndrome. When modelled in cerebral organoids, another syndromic primary microcephaly disorder, Seckel syndrome, unifies the majority of features observed in both MCPH and Nijmegen Breakage syndrome cerebral organoids; as cilia disassembly is inhibited due to mutated CPAP, thereby extending the G1 phase, with the outcome being a depleted NPC pool caused by premature differentiation (Gabriel *et al.*, 2016; An, Kuo and Tang, 2022). As evidenced by the aforementioned syndromic and non-syndromic primary microcephaly cerebral organoid studies, cerebral organoids are able to replicate many of the common molecular, cellular and clinical phenotypes observed in the patient cohorts, however further exploration is necessary with regards to the functional deficits.

Cerebral organoids proved to be successful at emulating primary microcephaly immediately after their creation, by emulating the Zika virus. When the Zika virus was introduced into developing cerebral organoids, the viral infiltration increases overall apoptosis, reducing the neural progenitor population and resulting in disrupted VZ regions (Gabriel *et al.*, 2017; Setoh *et al.*, 2019). This structural disorganisation was caused by RGs shifting to asymmetric division, instigating premature neuronal differentiation thereby causing cortical thinning (Gabriel *et al.*, 2017). Although cerebral organoids already exhibit significant ER stress (Bhaduri *et al.*, 2020), the ER was manipulated by the Zika virus to endogenously manufacture a greater viral load (Qian *et al.*, 2016; Gabriel *et al.*, 2017). This conflated the phenotypes observed initially in cerebral organoids,

culminating in cerebral organoids mimicking the patients prenatal microcephaly in culture (Dang *et al.*, 2016; Setoh *et al.*, 2019). Unfortunately, efforts made to isolate key attachment factors for the virus' entry to NPCs were unsuccessful (Wells *et al.*, 2016), but pharmaceutical interference and manipulation of immune receptors have reversed the pathological mechanisms of the Zika virus-induced microcephaly in cerebral organoids (Dang *et al.*, 2016; Watanabe *et al.*, 2017). As evidenced by the accurate emulation of the Zika virus' targeting of the structural organisation of NPCs, cerebral organoids are a substantially improved choice of research model than 2D culture for investigating viral infections (Krenn *et al.*, 2021).

As cerebral organoids are intended to be a close representation of the developing neocortex, it is therefore unsurprising that cerebral organoids derived from primary microcephaly patients mimic aspects of the disorder's pathology. However, in circumstances such as secondary microcephaly where the repression of growth is postnatal, it would be reasonable to question if cerebral organoids are capable of representing this. Cerebral organoid models of Angelman syndrome suggest that cerebral organoids are poor representations of secondary microcephaly, as no distinguishable size difference was observed between control and *UBE3A*-knockout cerebral organoids (Sun *et al.*, 2019). However, these cerebral organoids were successful as a model for electrical activity, acting as a facsimile of patient-like seizures whereupon the pharmaceutical trialling on cerebral organoids successfully translated to mice, ameliorating them of their seizure phenotype (Sun *et al.*, 2019).

On the other hand, Rett syndrome organoids have proven to successfully recapitulate the characteristic microcephaly (Nakashima *et al.*, 2021), although this is not mentioned in all cerebral organoids representations of Rett syndrome (Mellios *et al.*, 2018; Gomes *et al.*, 2020). When microcephaly is referenced, it becomes apparent earlier in development than would be expected for postnatal, secondary microcephaly, from Day 5 of cerebral organoid differentiation onwards (Nakashima *et al.*, 2021). This microcephaly was resolved once inhibition of BMP signalling was introduced after a month of culture, using previous exploration of the causative pathways in *in vitro* neuronal monoculture as a guide (Nakashima *et al.*, 2021). Conversely, other patient-derived cerebral organoid representations of Rett syndrome make reference to a recovery of neural progenitors during maturity without interference (Mellios *et al.*, 2018). These Rett syndrome patient-derived

cerebral organoids showed expansion of RGs at the detriment to populations of intermediate progenitors and neurons, particularly targeting those related to GABA-ergic neurons (Mellios *et al.*, 2018). Coincidentally, cerebral organoids have been able to emulate other features of Rett syndrome, including stature abnormalities. They have been found to overlap transcriptional pathways with myotonic dystrophy patient-derived cerebral organoids, sharing similar pathologies and response to rescue treatments, as well as exhibiting microcephaly (Morelli *et al.*, 2022). A comparative review of these postnatal, syndromic studies suggests that microcephalus features of cerebral organoids are lost when individual genes are targeted, i.e. *UBE3A*, as opposed to using patient-derived hIPSCs. It should therefore be actively encouraged to use patient-derived hIPSCs where possible to reflect the complex genetic aetiology, and therefore be of the most benefit for translational research.

Due to the lack of current information on clinical cohorts (Mefford *et al.*, 2008; Bernier *et al.*, 2016; Linden *et al.*, 2021; Sønderby *et al.*, 2021), it is not known if the microcephaly observed in 1qDel patients is pre- or postnatal. With the combined information of cerebral organoids' proclivity to capture both primary and secondary microcephaly, it was believed that 1qDel-associated microcephaly would occur in cerebral organoids regardless of time of onset in patients. Although few other CNVs have been modelled in cerebral organoids, this assumption was supported by observations of 16p11.2 duplication patient-derived cerebral organoids that were microcephalus from induction onwards; 16p11.2 duplication-induced microcephaly is prenatal in origin (Urresti *et al.*, 2021). Despite the microcephalus outcome, the predominant deficit presented was truncated migration of neurons which was rescued by supplementing cerebral organoids with RhoA agonists (Urresti *et al.*, 2021). There was little information on the mechanisms contributing to the phenotype, although no significant changes in RGs or neurons populations were reported, with few differentially expressed genes and proteins between 16p11.2 duplication cerebral organoids and controls (Steinman *et al.*, 2016). In the absence of literature investigating the development of abnormal head size in CNV patients further, it was therefore considered advantageous to model 1qDel in cerebral organoids to shed light on the question as to when, how and why microcephaly occurs in 1qDel.

5.1.2 Presentation of Schizophrenia in Current Research Models

SCZ risk is significantly heightened in 1qDel cohorts (Crespi and Crofts, 2012), but it is not inevitable that patients will develop SCZ. It is therefore necessary to examine the aspects of SCZ pathogenesis, particular those that has been previously established in cerebral organoids, to determine if 1qDel patient-derived E-hCOs emulate SCZ features. SCZ is diagnosed on the presentation of positive and negative symptoms, in the form of hallucinations and absence or repression of emotions, respectively, with additional cognitive dysfunction properties (Kay, Fiszbein and Opler, 1987). The negative symptoms of SCZ are associated with an underrepresented dopamine activity in the PFC (Slifstein *et al.*, 2015), whilst, the positive symptoms are connected to the excessive synthesis of dopamine in the striatum (Avram *et al.*, 2019). SCZ affects ~1% of the general population and is a significant contributor to global disability (Charlson *et al.*, 2018). The average diagnosis age is over 30, with a gender difference in diagnosis of 4 years between men and women (Sommer *et al.*, 2020). There is a significant heritability relationship (~79%) when examined in twin studies (Hilker *et al.*, 2018) and the familial risk as a first-degree relative of a SCZ patient is 6.3 fold higher than in the general population (Chou *et al.*, 2017). Despite the average diagnosis age occurring in adulthood, SCZ was proposed as an NDD in 1987 by Dr Weinberger due to its similarities to congenital encephalopathies that did not exhibit psychotic symptoms until adolescence (Weinberger, 2017). Since proposed, this has been supported by reports of increased SCZ incidences in cases of prenatal infection, hypoxia during labour, maternal stress and poor nutrition (Ursini *et al.*, 2018; Eyles, 2021). Although cerebral organoids are not representative of the adolescent/adult cortex when symptoms of SCZ would most likely arise, they can shed light on the developmental underpinnings to support the categorisation of SCZ as a NDD.

5.1.2.1 Pathology of Schizophrenia

Despite Dr Weinberger's hypothesis, the pathology of schizophrenia has historically focussed on the onset and trajectory of the developing adult. As a result, two key hypotheses have been suggested to act independently or collaboratively in SCZ patients; the dopamine hypothesis and the glutamate hypothesis (Gründer and Cumming, 2016; Uno and Coyle, 2019). Firstly, the dopamine hypothesis is defined by the altered dopamine system observed in SCZ, originally discovered in traditional anti-psychotic treatment of the positive

symptoms of SCZ (Gründer and Cumming, 2016). The expansion of this hypothesis has been hampered by the contradicting observations seen in human molecular imaging studies and *in vivo* mouse studies (Kesby *et al.*, 2018), such as patients that are resistant to anti-psychotic treatment (Howes *et al.*, 2011; Demjaha *et al.*, 2012). What is known is that elevated dopamine in the associative striatum correlates to the severity of SCZ symptoms, as well as precludes SCZ-associated psychosis onset (Howes *et al.*, 2009). However, guided cerebral organoids, such as E-hCOs, do not generate dopaminergic neurons; guided striatum organoids have been designed to fulfil this purpose (Miura *et al.*, 2020). As such, this aspect of SCZ pathology will not be investigated in E-hCOs at this time.

Given guided cerebral organoids' proclivity to generate glutamatergic neurons, investigation of the glutamate hypothesis of SCZ pathology could be more fruitful. The glutamate hypothesis of SCZ proposes that SCZ is a result of faulty glutamate neurotransmission originating during development, and can be responsible for both the positive and negative symptoms of SCZ (Sumiyoshi *et al.*, 2004; Edwards *et al.*, 2016). This hypothesis was suggested originally because of the parallel between SCZ-associated psychosis and the acute psychosis observed under the influence of phencyclidine and ketamine, which are N-methyl-D-aspartate (NMDA) receptor antagonists (Kapur and Seeman, 2002). Expansion of this idea has led to examination of the NMDA receptor itself in the context of SCZ pathogenesis. The NMDA receptor is comprised of the subunits GLUN1-3, encoded by the glutamate ionotropic receptor NMDA type subunit 1-3 genes (*GRIN1A-3D*). Each subunit has shown connections to SCZ via pathogenic SNPs (Fromer *et al.*, 2014), autoimmunity (Tong *et al.*, 2019) and *in vivo* studies (Lee *et al.*, 2018; Bygrave *et al.*, 2019). NMDA receptors' counterpart, α-amino-3-hydroxy-5-methyl-4-isoxazolepropionic acid (AMPA), could be contributing to NMDA receptor hypofunction, as activated AMPA receptors disperse the magnesium blockade that prevents NMDA receptor permeability (Pochwat *et al.*, 2014). AMPA receptors are also impaired in adult SCZ patients (Zeppillo *et al.*, 2020) and miRNAs capable of inhibiting AMPA receptor-mediated synaptic transmission are significantly enriched in the PFC of SCZ patients (Panja *et al.*, 2021). Both types of receptors have been targeted for SCZ therapeutics, but have not been brought forward for commercial use (Cadinu *et al.*, 2018; Tanaka *et al.*, 2019). It has been proposed that using NMDA receptor antagonist drugs such as phencyclidine to

model the hypoglutamate property of SCZ is inappropriate, given its non-selective binding to dopamine and serotonin receptors (Kapur and Seeman, 2002), as well as its instigation of depolarisation of GABA currents in the PFC (H. R. Kim *et al.*, 2021).

It has been argued that the dopamine and glutamate hypotheses do not act separately but are intrinsically linked. Studies have shown that NMDA receptor hypofunction in PV^+ interneurons results in reversed dopamine transmission in the nucleus accumbens and PFC when exposed to amphetamine-associated dopamine release, but only during adolescence (Nakao *et al.*, 2019). This feeds into the observations that the success of dopamine transmission in SCZ patients is relevant to the brain region, i.e. there is hyperactive dopamine transmission in the striatum and hypoactive transmission in the PFC (Brisch *et al.*, 2014). This concern is exemplified by the impact of SCZ-associated loci on glutamatergic pyramidal neurons and medium spiny neurons, despite there being no convergence on individual genetic risk (Skene *et al.*, 2018). This evidence points to the activity of two or more pathways acting in tandem, as opposed to one mechanism governing all SCZ symptoms. The E/I imbalance hypothesis encapsulates this multi-level interaction between these pathways, without restricting the integration of other mechanisms (Davenport *et al.*, 2019). This hypothesis accommodates for the inclusion of the GABA-ergic inhibitory pathway into understanding SCZ. Evidence of the importance of the inhibitory system in SCZ pathology has mounted substantially: there is disrupted connectivity caused by reductions of GABA in the anterior cingulate cortex and thalamus (Shukla *et al.*, 2019; Quiñones *et al.*, 2021), enriched gene variants of members of the GABA system (Magri *et al.*, 2018) and reduced quantity and abnormal properties of SCZ cortical PV^+ interneurons (Beasley and Reynolds, 1997; Fung *et al.*, 2010; Ni *et al.*, 2020; Shen *et al.*, 2021) with inhibitory synaptic transmission deficits (Kathuria *et al.*, 2019). As cerebral organoids have also been proven to emulate aspects of E/I imbalance in other NDDs (Mariani *et al.*, 2015; Paulsen *et al.*, 2022), SCZ-specific disruption of synaptic transmission between excitatory and inhibitory neurons is therefore key to the investigation of 1qDel in E-hCOs.

E/I balance hangs on appropriate synaptic transmission, however, one key feature of SCZ pathology is the substantially reduced synapse density found in post-mortem adult SCZ patients (reviewed by Moyer, Shelton and Sweet, (2015)). Recent studies have shown reduced synaptic vesicle density in a range of brain

regions in SCZ patients, based on measurements of the synaptic vesicle and neurotransmitter modulator SV2A, as well as its correlation with positive symptom severity (Onwordi *et al.*, 2021; Radhakrishnan *et al.*, 2021). Additionally, significant synaptic pruning occurs during adolescence, the age range of which SCZ is commonly diagnosed (Feinberg, 1982). However, synaptic pruning's role in SCZ has been questioned, as SCZ patients have a loss of small, immature dendritic spines, rather than larger mature spines, suggesting that fewer spines reach maturity, as opposed to dendritic spines being overly pruned (MacDonald *et al.*, 2017). Regardless of maturity, it is clear that the end result is a substantial decrease of dendritic spine density in a number of cortical regions that could contribute to reduced synaptic transmission and an E/I imbalance (Moyer, Shelton and Sweet, 2015).

SCZ pathology has not only been tied to abnormal neuronal physiology, but also oligodendrocyte and astrocyte dysfunction, cell populations observed in mature guided cerebral organoids (Dezonne *et al.*, 2017; Madhavan *et al.*, 2018). Firstly, models of SCZ exhibit poor viability of oligodendrocyte precursors, reduced oligodendrocyte density in PFC regions and altered ultrastructures of oligodendrocytes (Uranova *et al.*, 2018; de Vrij *et al.*, 2019; Kolomeets and Uranova, 2019). SCZ patients also present white matter abnormalities, with diffusion metrics such as fractional anisotropy reduced in a multitude of white matter regions (de Vrij *et al.*, 2019; Domínguez-Iturza *et al.*, 2019), regardless of age of onset or medication (Kelly *et al.*, 2018). An overall volume reduction specifically in the corpus callosum is a consistent feature of SCZ (Rotarska-Jagiela *et al.*, 2008; Walterfang *et al.*, 2009; del Re *et al.*, 2019), which has an inverse relationship with positive SCZ symptoms (del Re *et al.*, 2019), and correlates to another common phenotype of SCZ: enlarged ventricles (del Re *et al.*, 2019; Eom *et al.*, 2020). SCZ's impact is not isolated to the white matter alone; there is a reduction in whole brain volume, including specific regions of grey and white matter (Olabi *et al.*, 2011) and the response to treatment correlates with subcortical volume (Tronchin *et al.*, 2020). It has also been observed that there is significant acceleration of brain age from the onset of SCZ (Schnack *et al.*, 2016). Contrasting the oligodendrocyte deficit, cortical astrocytes are overrepresented in bulk sequencing of SCZ cohorts (Toker *et al.*, 2018). However a meta-analysis of recent studies has muddied the waters with regards to a clear, overarching conclusion on the impact of these glial cells; how, and if, these cells are involved in

SCZ depends on the brain region, age of onset and death and genetic background (Trépanier *et al.*, 2016). This information would suggest that SCZ neurons are vulnerable as individual cells, but also vulnerable in the absence of supporting glia.

How each SCZ feature manifests is likely to be relative to the genetic background of the patient and it therefore may require a variety of techniques to define pathological components of SCZ. Such research would provide a framework with which to separate additive effects of high-risk genes and environmental factors and aid in documenting genotype-to-phenotype relationships. Developmental models such as cerebral organoids could provide such details of SCZ pathology during development, due to their patient origin and 3D, self-organising format.

5.1.2.2 Developmental Origins of Schizophrenia as Depicted by Cerebral Organoids

In recent years, genetic analysis has substantially supported Dr Weinberger's hypothesis of SCZ as a neurodevelopmental disorder (Sanders *et al.*, 2022). SCZ's high heritability suggests a strong genetic influence to SCZ pathology, but SCZ has a complex genetic background. Currently, over one hundred genomic loci are enriched in SCZ cohorts (Ripke *et al.*, 2014), a number of which are involved in early neurodevelopment (Howell and Law, 2020), and so specific candidate genes have been examined to unravel their involvement with SCZ pathology. One of the first candidate genes, disrupted-in-schrizophenia-1 (*DISC1*), was found in a rare case of familial schizophrenia where multiple members exhibited psychosis-related conditions (Millar *et al.*, 2000). Examination of this gene found *DISC1*-deleted, patient-derived cortical neurons undergo normal development but exhibit reduced glutamatergic synaptic transmission (Wen *et al.*, 2014). The same 4 bp *DISC1* deletion was induced in mice which supported the previously observed synaptic deficits, alongside behavioural abnormalities indicative of SCZ (Kim *et al.*, 2021); there was no changes observed in gross brain structure in murine models (Kim *et al.*, 2021). On the other hand, *DISC1*-disrupted cerebral organoids had substantially smaller VZs, which was accompanied by abnormal cortical layering, as well as reduced transcription of NMDA receptors and GABA transporters (Srikanth *et al.*, 2018). Although cerebral organoids are incapable of providing behavioural information, the affected structural architecture combined with the suggestion of glutamate hypofunction and disrupted E/I balance

was reminiscent to what is seen in adult SCZ patients (Arnold, Ruscheinsky and Han, 1997).

Similar to the *DISC1* cohort, cerebral organoids derived from SCZ patients of a different genetic background exhibited detrimental organisation of the VZ which was attributed to the disaggregation of proliferating neural progenitors within the first 2 weeks of differentiation (Stachowiak *et al.*, 2017). Additionally, after 1 month, substantially fewer $TBR1^+$ neurons were visible in SCZ cerebral organoids (Stachowiak *et al.*, 2017). This research was followed up with investigations into the relationship between SCZ patient-derived cerebral organoids and maternal immune activation, whereupon similar dispersed, cycling NPCs were observed in both models after exposure (Benson *et al.*, 2020). Furthermore, SCZ patient-derived cerebral organoids were more vulnerable than controls to developmental deficits when exposed to immune activation-replicating stimuli (Benson *et al.*, 2020). Although the representation of sensitivity to neuroinflammatory conditions is in keeping with current SCZ literature (Khokhar *et al.*, 2018; Weinstein *et al.*, 2018; Purves-Tyson *et al.*, 2021), the additional results of increased oligodendrocyte quantity did not concur with the reduced white matter phenotype observed in SCZ patients (de Vrij *et al.*, 2019; Domínguez-Iturza *et al.*, 2019). The contradiction in results between research models illustrates the necessity to explore cerebral organoids' recapitulation of SCZ.

An alternative SCZ patient-derived cerebral organoid study documented substantial apoptosis within the neuroepithelium, as well as considerable repression of $MAP2^+$ cells (Notaras, *et al.*, 2021). With single cell RNA sequencing, it became evident that cell fate decisions were skewed against telencephalic or neuronal origin, in favour of neuroendothelial and pluripotent identity, shifting progenitor differentiation away from neurogenesis (Notaras, *et al.*, 2021). Genes associated with upper layer neuron production (*BRN2*) and neural progenitor survival (*PTN*) were identified as being significantly differentially expressed in SCZ patient-derived cerebral organoids (Notaras, *et al.*, 2021). Modulation of these two genes related to their functions; viral-activated BRN2 rescued the neurogenic deficit, but not the previously discovered apoptosis, whilst exogenous PTN rescued both observations (Notaras, *et al.*, 2021). In review, comparing the different cohorts of SCZ patient-derived cerebral organoids illustrates the phenotypic heterogeneity amongst individuals of different genetic

background, which could be an issue in future when attempting to distinguish key mechanisms of SCZ pathology.

There are a number of methods to alleviate this issue, such as expanding the patient cohort considerably (Kathuria *et al.*, 2020; Notaras, *et al.*, 2021), using parallel twin studies instead of neurotypical controls (Sawada *et al.*, 2020), or investigating SCZ-associated syndromes (Khan *et al.*, 2020). Proteomic analysis of large SCZ patient cohorts support the phenotypes seen in other SCZ cerebral organoids studies as well as SCZ patients, by both observing similarly differentially expressed genes (*PTN, GRIN2A, GRIA1*) or by downregulation of relevant gene ontology terms, e.g. axonal development, cellular morphogenesis and projection and neuronal differentiation (Kathuria *et al.*, 2020; Notaras, *et al.*, 2021). Additionally, metabolic regulation of lipids dominates the gene ontology processes upregulated in these larger cohorts, supporting a growing hypothesis of metabolic dysfunction in SCZ (Goldsmith *et al.*, 2021). In smaller cohorts, twin SCZ patient-derived cerebral organoids have the advantage of minimal genetic heterogeneity (Sawada *et al.*, 2020), with the outcome of the study supporting non-twin SCZ cerebral organoid studies (Kathuria *et al.*, 2020; Notaras, *et al.*, 2021). These twin study organoids, at the expense of neural rosette size caused by an under-proliferating NPC pool, had a shift of neuronal identity to a GABA-ergic fate (Sawada *et al.*, 2020). An increased representation of the GABA-ergic neuronal population is the opposite of what is observed in both SCZ patients and patient-derived neuronal models (Kathuria *et al.*, 2019), and so this result in twin studies may be attributed to the bipolar disorder also experienced by the observed patients (Sawada *et al.*, 2020). However, similar to what is observed in *DISC1*-mutated cerebral organoids (Srikanth *et al.*, 2018), Wnt agonism rescues these phenotypes in SCZ-affected twin cerebral organoids (Sawada *et al.*, 2020).

In the context of CNVs that have elevated risk of SCZ similar to 1qDel (Crespi and Crofts, 2012), 22q11.2 deletion patient-derived cerebral organoids are highly enriched for SCZ-associated gene expression specifically, but only after Day 50 (Khan *et al.*, 2020). Although glutamate levels were unchanged, unlike what is observed in SCZ patients (Uno and Coyle, 2019), hyperexcitability and increased resting membrane potential of neurons was observed across both 2D neurons and cerebral organoids of 22q11.2 deletion patients (Khan *et al.*, 2020). Lentiviral delivery of key genes identified within the 22q11.2 loci resolved the functional phenotypes, as did pharmaceutical treatment using a dopamine-

associated D2 receptor blocker (Khan *et al.*, 2020). This supported evidence that not only was the D2 receptor functional in a subset of pyramidal neurons in the cortex (Gee *et al.*, 2012), but that this neuronal population was present in cerebral organoids as well (Khan *et al.*, 2020).

Although Khan *et al.*, (2020) provides evidence that the dopamine and glutamate hypothesis of SCZ could be investigated in CNV-associated cerebral organoids, it is unknown if E-hCOs replicate similar subsets of $DRD2^{+}$ neurons to those in Khan *et al.*, (2020), and therefore the dopamine aspect of SCZ pathology was not the focus of 1qDel E-hCOs characterisation. Additionally, E-hCO differentiation was limited to two months, and so neurons were the key cell population examined, as the development of glia such as astrocytes and oligodendrocytes were likely to be in their infancy during this timeframe (Gonzalez *et al.*, 2018; Madhavan *et al.*, 2018; Huang *et al.*, 2022). With these factors taken into account, key pathological features of SCZ were identified as targets for investigation in 1qDel E-hCOs: glutamate hypofunction, E/I imbalance and whole brain volume reduction.

5.1.3 Research Aims & Hypothesis

The aim of this chapter was to characterise phenotypes exhibited in 1qDel patient-derived E-hCOs and begin deconstructing the mechanisms responsible for said phenotypes to determine how they relate to 1qDel patients.

The hypothesis of this chapter was that E-hCOs would accurately capture the two core neurological phenotypes displayed in 1qDel cohorts, microcephaly and SCZ-associated cortical dysfunction. It was anticipated that the microcephaly would present prior to Day 30, as illustrated in other cerebral organoid studies of both primary and secondary microcephaly disorders (Lancaster *et al.*, 2013; Li *et al.*, 2017; Zhang *et al.*, 2019; Gomes *et al.*, 2020; Urresti *et al.*, 2021; Martins *et al.*, 2022). As evidenced by such studies, aspects of cellular physiology, such as apoptosis and cell cycle of NPCs or efficiency of neuronal differentiation and maturation, were expected to be significantly different in 1qDel E-hCOs compared to controls, either as a result of the microcephaly, or contributing to the microcephaly's induction. Finally, it was expected that the mature neuronal identity of 1qDel E-hCOs would reflect either E/I imbalance and/or glutamate hypofunction as a result of the elevated SCZ risk in 1qDel patients (Stachowiak *et al.*, 2017;

Srikanth *et al.*, 2018; Davenport *et al.*, 2019; Notaras, *et al.*, 2021; Sønderby *et al.*, 2021).

5.2 Methodology

E-hCOs and all methodologies mentioned in Section 2.2 were used throughout Section 5. In addition, at Day 5, between two to five E-EBs were moved from the EB media to a 1.5 mL Eppendorf tube and washed with PBS. All liquid was removed and 1 mL of 37ºC Accutase was added to the tube and incubated at 37ºC for 10 minutes. After incubation, EBs were homogenised into single cells using a 200 µL tip. Cells were counted using a 60 µm Scepter™ cell counter sensor in a Scepter™ 2.0 automatic cell counter, counting those between the size range of 10.09 µm to 18.07 µm. The resulting number was divided by the number of EBs used to gain an estimated number of cells per EB.

In addition, APD of E-hCOs was used for normalising non-count or non-live cell count data where mentioned. ICC quantification of live cell counts was reported as a percentage of non-apoptotic cells, determined by subtracting cell line-specific, APD-predicted, CC3-based apoptosis values from total DAPI count (Control #1 and #2 – Figure 3.9.E, 3.9.J, 3.9.O, 3.10.E, 3.10.J and 3.10.O, 1qDel – Supplementary Figure 7).

5.3 Results

5.3.1 Bright Field Imaging Shows 1q21.1 Deletion Cortical Organoids Immediately Exhibit Microcephaly Phenotype Until Day 30

E-hCOs of both Control #1 and #2 were previously validated in Section 4 and therefore were known to exhibit appropriate hCO growth and morphology. The 1qDel patient-derived hIPSCs were differentiated into E-hCOs and characterised, firstly through bright field imaging. No significant differences were found in external area or morphology between Control #1 or #2 at the EB stage of differentiation; differences in external area were previously established at the NE and ND stages (Figure 5.2.B). 1qDel E-hCOs were significantly different in external area compared to both control cell lines at all stages of E-hCO differentiation prior to Day 30 (Figure 5.2.A-B). Although smaller, there were no observed differences in morphology of Day 1 to Day 11 1qDel E-hCOs compared to control E-hCOs (Figure 5.2.A). At Day 21, 1qDel E-hCOs were visibly smaller, but also had less visible definition of the neuroepithelial loops otherwise visible in both control E-hCOs (Figure 5.2.A). In the absence of visible neuroepithelial loops, excessive dispersion of cells was seen around the periphery of Day 30 1qDel E-hCOs (Figure 5.3.A). When quantified, there were no significant differences between control and 1qDel E-hCOs' external areas at Day 30 and Day 60 (Figure 5.3.B-C). It was noted, however, that 1qDel lacked the numerous lobular structures present in the control E-hCOs at Day 60 (Figure 5.3.A).

Figure 5.2 (below): 1qDel E-hCOs exhibited visible and quantifiable microcephaly in the first 21 days of E-hCO differentiation.

A) Bright field images of key stages of early E-hCO differentiation, including Day 1 (aggregation), Day 5 (EB), Day 11 (NE) and Day 21 (ND), across Control #1, #2 and 1qDel E-hCOs. Cell line and timepoint is referenced in image. Scale bar = 500 μm. B) Growth of area during early E-hCO differentiation across Control #1, #2 and 1qDel E-hCOs. Data for area was collected from individually-tracked, repeat-batch bright field imaging; mean ±95%CI presented in line graphs. Statistical analysis used mixed effects models on datasets of ≥15 independent hCOs per independent differentiation, ≥1 independent differentiations per cell line (for full information on spread of data and mixed effects models see Supplementary Figure 6 and 7, respectively). After two-way ANOVA determined significant variation among cell lines, pairwise, Tukey-corrected post-hoc comparison that accommodated for interaction with Media was used to determine significant differences in area relative to either the NE or ND stages of E-hCO differentiation; unlabelled=not significant, *p=<0.05, **p=<0.005, ****p=<0.0001.

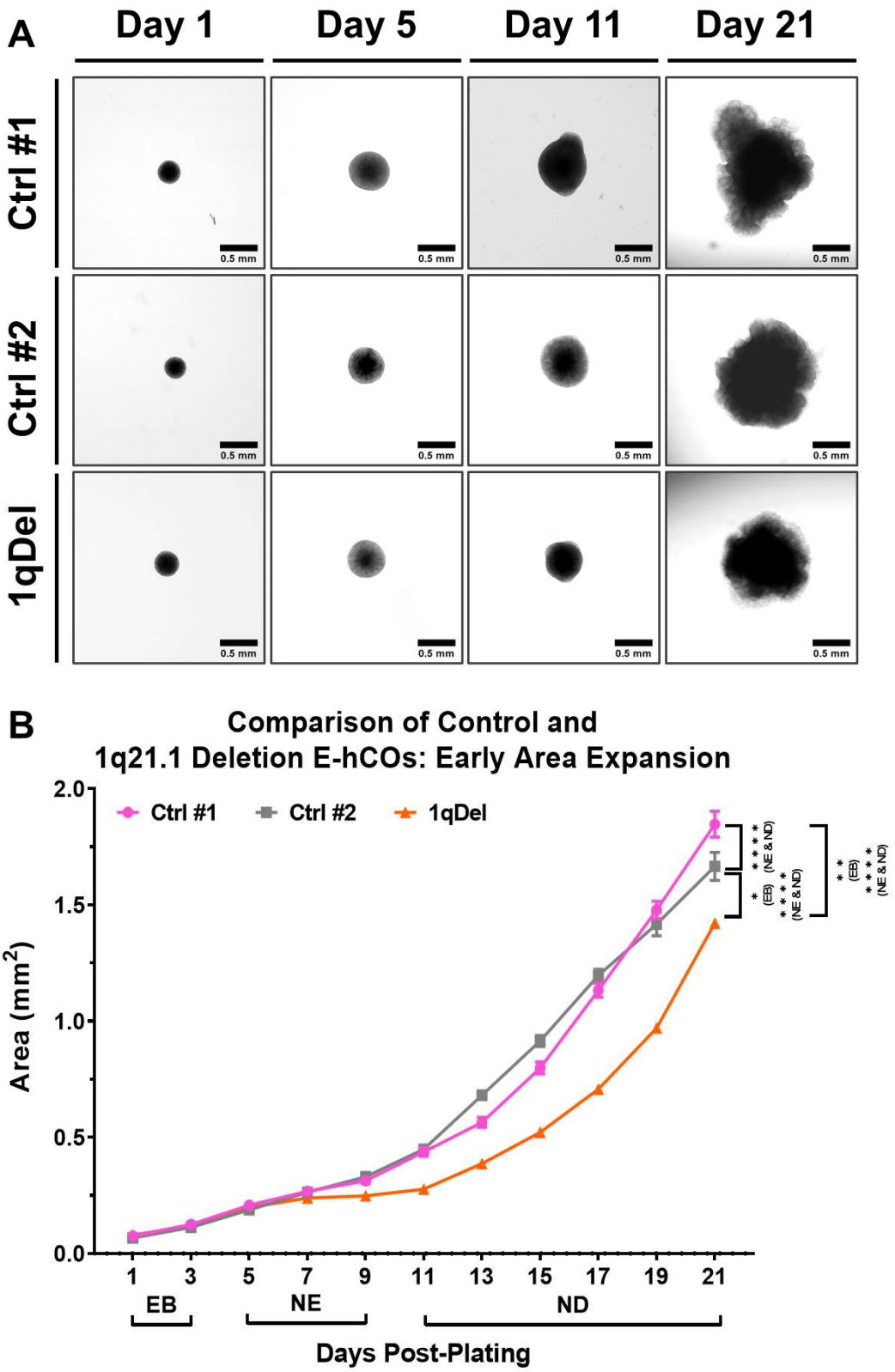

Figure 5.2: 1qDel E-hCOs exhibited visible and quantifiable microcephaly in the first 21 days of E-hCO differentiation.

Figure legend on the previous page.

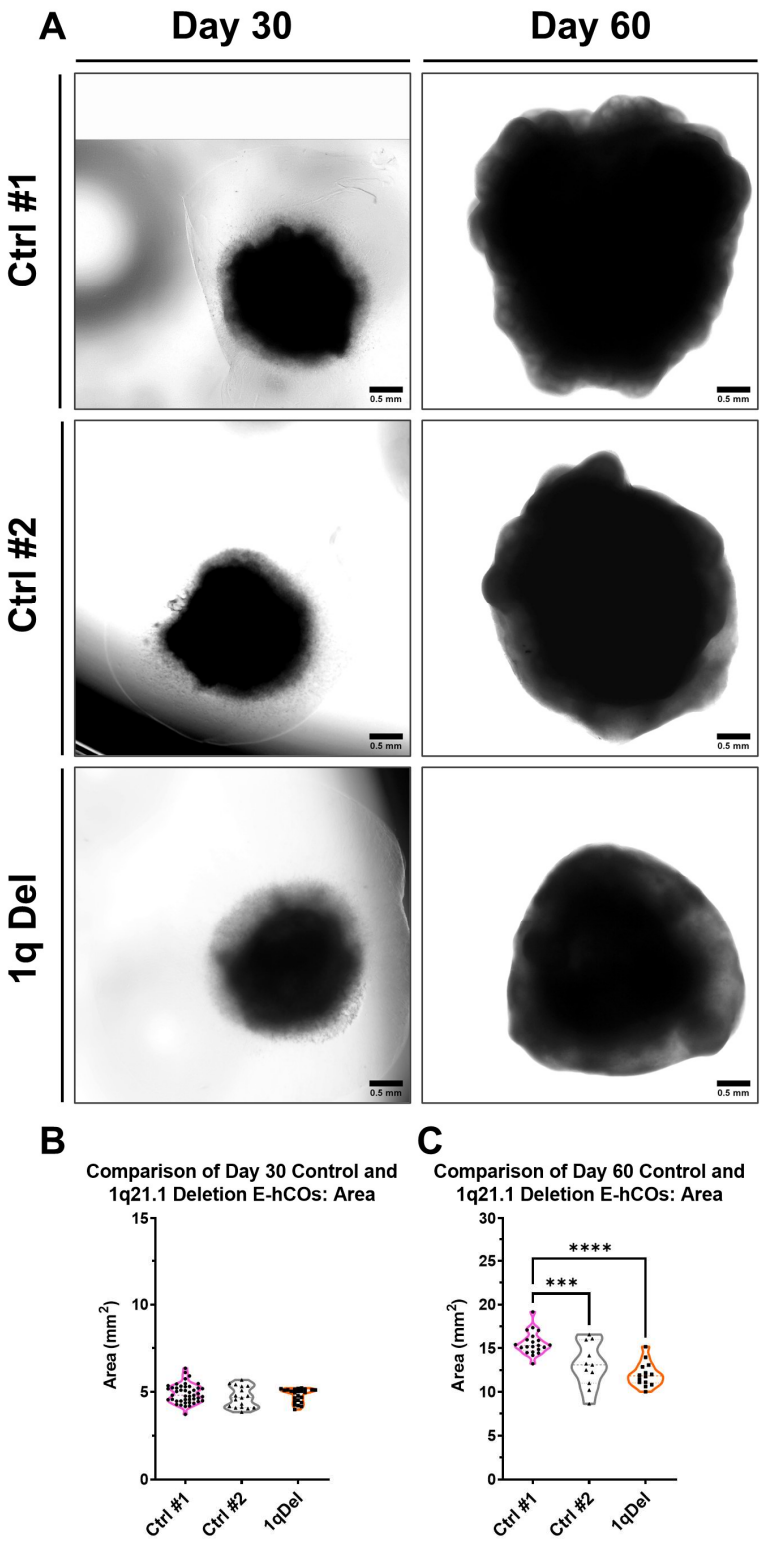

Figure 5.3: 1qDel E-hCOs had a comparable area to control E-hCOs at Day 30 and Day 60.

A) Bright-field images of Day 30 and Day 60 Control #1, #2 and 1qDel E-hCOs. Scale bar = 500 µm. **B-C)** Truncated violin plots of Control #1, #2 and 1qDel E-hCO external area at Day 30 **(B)** and Day 60 **(C).** Statistical analysis used a one-way ANOVA with Holm-Šídák correction for post-hoc tests. All data used n≥17 independent hCOs per group, unlabelled=>0.05, *p=<0.05, ****p=<0.0001.

5.3.2 Gene Dosage Effects of 1q21.1 Deletion Evident in Early Cortical Organoid Differentiation

The 1qDel E-hCO phenotype of early microcephaly suggested that the 1q21.1 region was required for 1qDel E-hCO development from the onset of E-hCO differentiation. Establishing at what timepoint during E-hCO differentiation 1q21.1-specific gene's dosage changed was key to identifying possible genes responsible for the early-born microcephalus phenotype. The genes were selected based on their counterpart protein's function. *BCL9*, *PRKAB2* and *CHD1L* have been connected to neuronal development (Xu *et al.*, 2013; Kimura *et al.*, 2015; Dou *et al.*, 2017; Nagy *et al.*, 2018), whilst *ACP6* acted as non-neuronal-associated control within the 1qDel region, as little is known outside of its connection to metabolism (Chryplewicz *et al.*, 2019). Finally, *GJA5* and *GPR89B* were chosen as 1qDel controls, as they are within the 1q21.1 distal region but not deleted in the 1qDel patient cell line (Table 2.1).

Transcriptional analysis using qPCR reported that certain genes shared similar patterns of reduced expression in 1qDel E-hCOs across E-hCO differentiation: *CHD1L* and *ACP6* expression was significantly reduced between Day 0 to Day 11 (Figure 5.4.C-D), *BCL9* and *PRKAB2* expression was affected at Day 5, 11, 21 and 60 (Figure 5.4.A-B) and there was minimal to no reduction across all timepoints of *GJA5* and *GPR89B* (Figure 5.4.E-F). These, however, were trends, and there were some exceptions, including significantly lower *CHD1L* expression in Day 30 1qDel E-hCOs (Figure 5.4.C). Overall, it was noted that Day 5 and Day 11 had substantially lower mRNA expression across four of the six genes selected: *CHD1L, ACP6, BCL9* and *PRKAB2* (Figure 5.4.A-D). All other timepoints either had fewer genes' dosage affected by 1q21.1 deletion, had cell line-specific variability between control cell lines or were not significantly different.

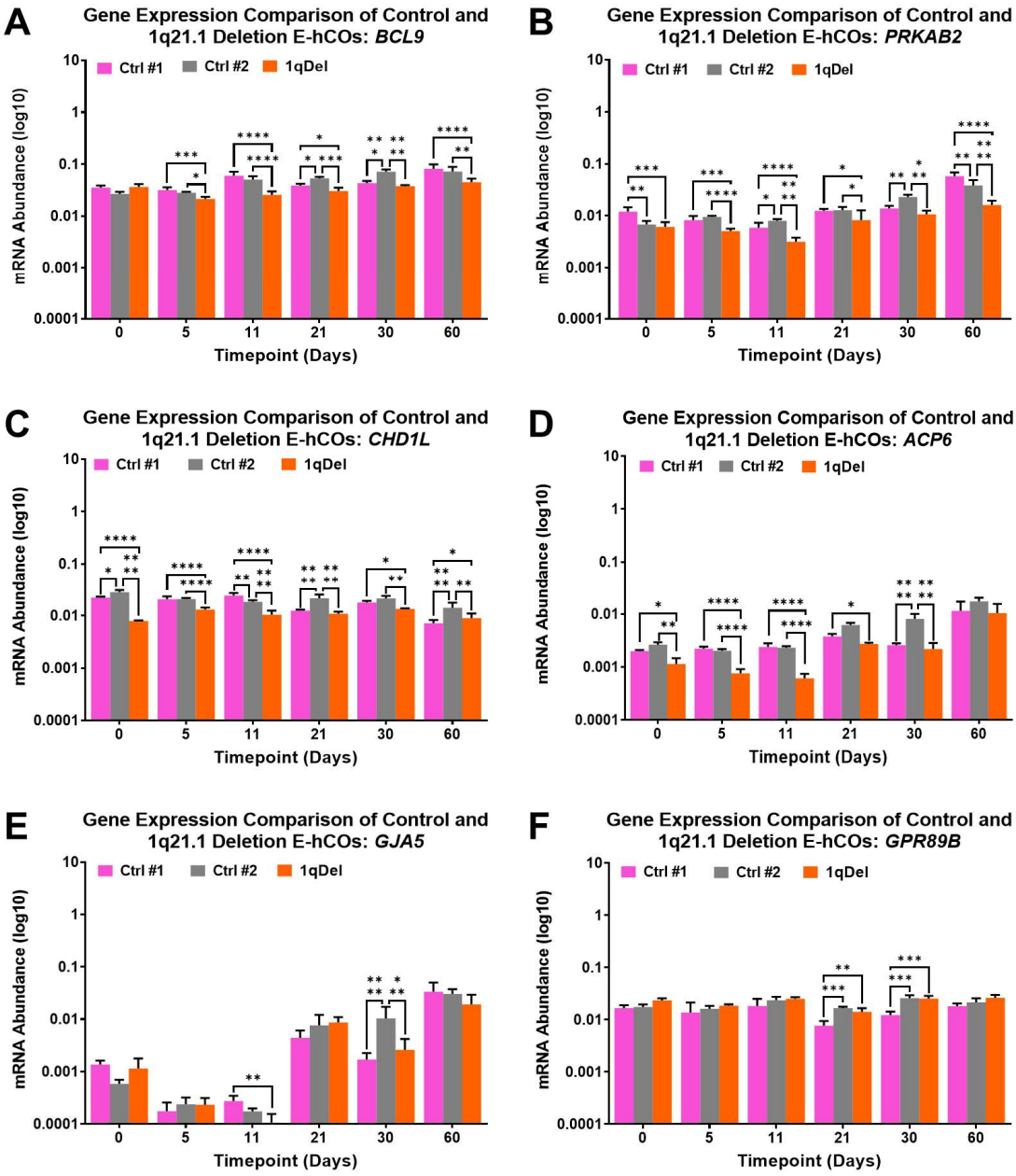

Figure 5.4: Expression of genes within the distal region of 1q21.1 were significantly reduced in 1qDel E-hCOs, predominantly in the first 11 days of E-hCO differentiation.

mRNA abundance of 1q21.1 distal region genes in Control #1, #2 and 1qDel samples across E-hCO differentiation: *BCL9* **(A)**, *PRKAB2* **(B)**, *CHD1L* **(C)**, *ACP6* **(D)**, *GJA5* **(E)** and *GPR89B* **(F)**. Data is presented as relative mRNA abundance ($2^{-\Delta CT}$, $\pm 2^{-CI}$), (n≥3 wells or independent E-hCOs). Statistical analysis was conducted on dCTs using a two-way ANOVA with Geisser-Greenhouse correction with Holm-Šídák correction for post-hoc tests, unlabelled=>0.05, *p=<0.05, **p=<0.005, ***p=<0.0005, ****p=<0.0001.

5.3.3 Early 1q21.1 Deletion Cortical Organoids Have Dysregulation of Gene Transcription Related to Pluripotency, Neuroepithelia & Proliferation

In order to determine which early cell populations were affected by 1qDel microcephaly, transcription of genes representing pluripotency and neural markers were examined in control and 1qDel samples of Day 0, 5 and 11 (Figure 5.5). These timepoints had already been identified to represent hIPSCs, primitive NECs and mature NECs, respectively (Figure 3.4). Pluripotency markers' expression was predominantly unaffected by the reduced gene dosage of 1q21.1 (Figure 5.5.A-C). *OCT4* was the consistent exception, downregulated in 1qDel samples across the three timepoints (Figure 5.5.A-C); *SOX2* transcription was also significantly downregulated at Day 11 (Figure 5.5.C). Transcription of neuroectodermal markers were also unaffected by the reduction in 1q21.1 genes in early 1qDel E-hCO development, with the exception of the neuroectodermal border marker *PAX3* at Day 11 (Figure 5.5.F). Expression of non-ectodermal markers *TBXT* (mesoderm) and *SOX17* (endoderm) was significantly greater in 1qDel hIPSCs compared to control hIPSCs (Figure 5.6.A). At Day 5, E-EBs of both genotypes only registered transcriptional expression for *TBXT*, not *SOX17*, of which no significant changes were observed (Figure 5.6.B). No transcription was quantifiable of either non-ectodermal marker at Day 11 for all cell lines (data not shown).

In addition to investigating cellular identity, aspects of cell proliferation were documented. Expression of the proliferative marker *KI67* was consistently upregulated from Day 0 to Day 11 in 1qDel samples (Figure 5.6.C), however there were considerably fewer cells in Day 5 1qDel E-EBs than in controls (Figure 5.6.D). This was not normalised to area of EB and therefore it was unknown if this was an example of reduced cell density or a reflection of the reduced external area.

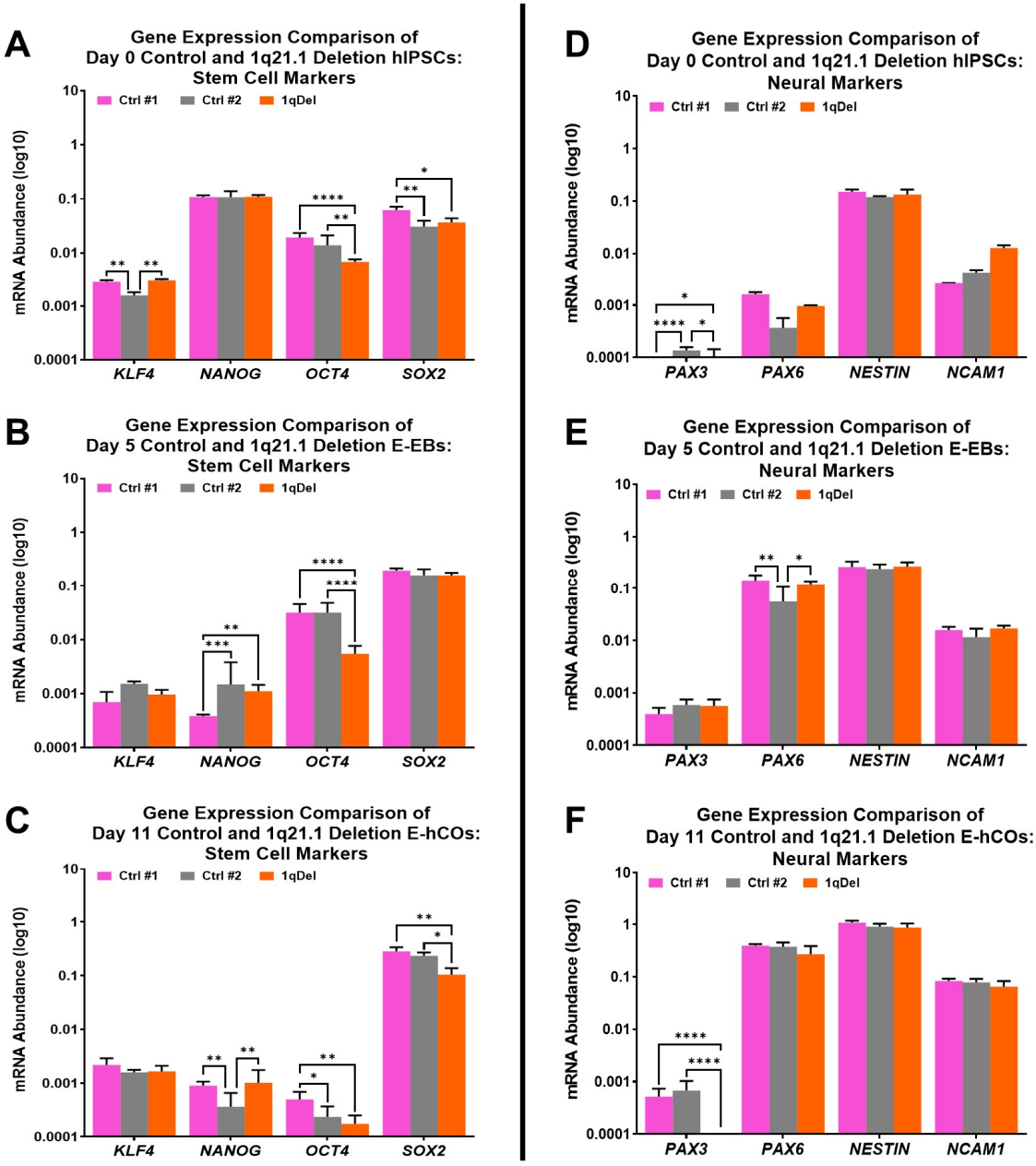

Figure 5.5: Changes in cell identity in early 1qDel samples included consistent downregulation of *OCT4* and Day 11-specific downregulation of *SOX2* and *PAX3*. **A-C)** Transcription of stem cell markers in Control #1, #2 and 1qDel across three timepoints: Day 0 **(A)**, Day 5 **(B)** and Day 11 **(C)**. **D-F)** Transcription of neural markers in Control #1, #2 and 1qDel samples across three timepoints: Day 0 **(D)**, Day 5 **(E)** and Day 11 **(F)**. Data is presented as relative mRNA abundance ($2^{-\Delta CT}$, $\pm 2^{-CI}$), (n≥3 hIPSC wells or independent E-hCOs, n≥6 independent E-EBs). Statistical analysis was conducted on dCTs using a two-way ANOVA with Geisser-Greenhouse correction with Holm-Šídák correction for post-hoc tests, unlabelled=>0.05, *p=<0.05, **p=<0.005,

5.3.4 Overall Apoptosis and Proliferation Unchanged in Day 21 – Day 60 1q21.1 Deletion Cortical Organoids

The microcephalus phenotype found in 1qDel E-hCOs began from Day 1 and persisted until Day 30 (Figure 5.2.B and 5.3.B-C), with indicators that cell proliferation and/or apoptosis may be a causative factor (Figure 5.6.C-D). The quantity of total mitotically active cells ($KI67^+$) and mitotically active NPCs ($SOX2^+/KI67^+$) did not significantly change between the three cell lines from Day 21 onwards (Figure 5.7.B-C and Supplemental Figure 9). This was in contrast to what was observed in *KI67* transcription, which followed the pattern observed from the onset of E-hCO differentiation; 1qDel E-hCOs either had a significant or trending increase in *KI67* transcription, although this resolved at Day 60 (Figure 5.7.A.). There was also no change in overall apoptosis and NPC-specific apoptosis, nor cell density for all three cell lines at the observed timepoints; only cell line-specific variability was significant (Figure 5.7.D-F and Supplemental Figure 10).

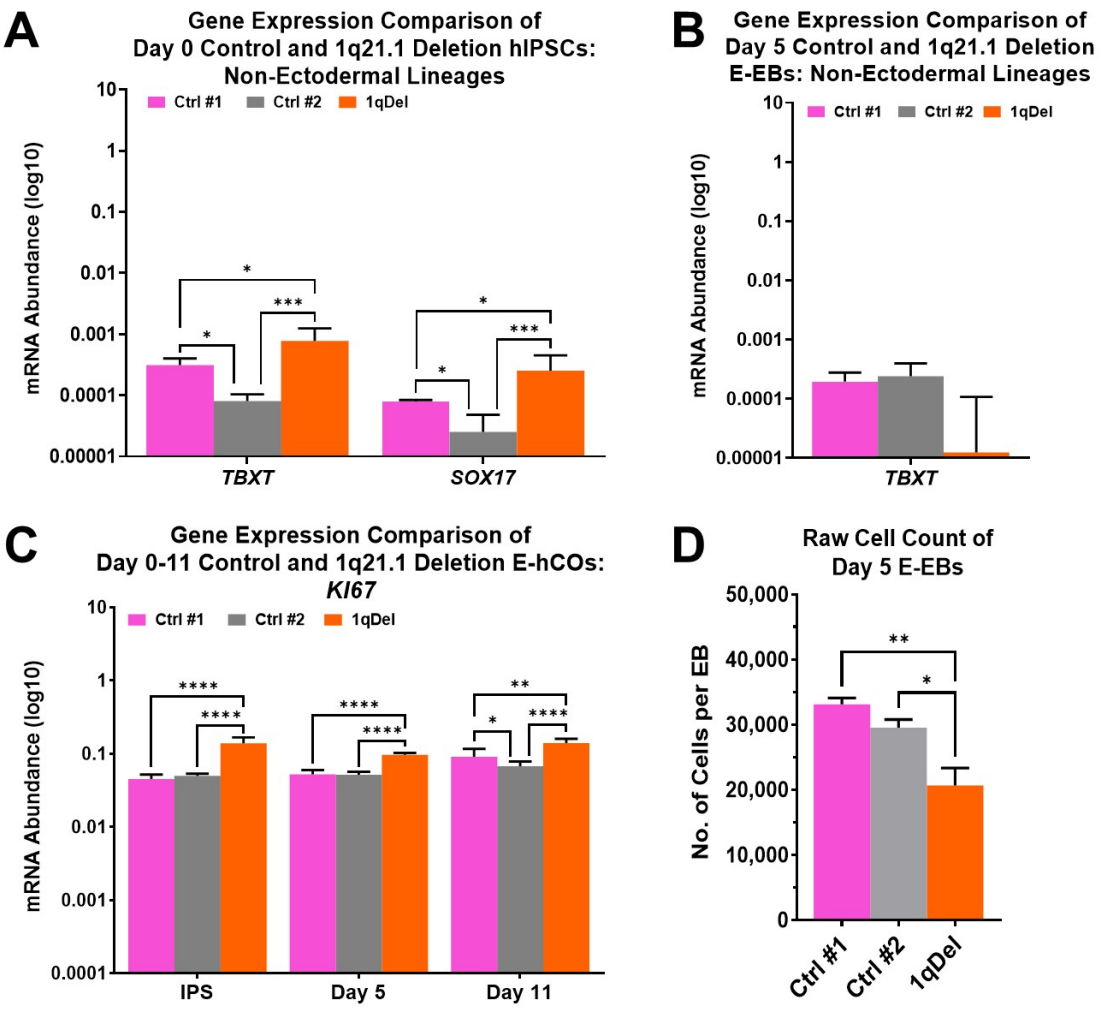

Figure 5.6: Non-ectodermal markers were significantly higher in 1qDel hIPSCs; consistent overexpression of *KI67* in 1qDel samples was evident across early timepoints, despite reduced total cell count at Day 5.

A-B) Transcriptional analysis of Control #1, #2 and 1qDel samples' expression of mesodermal *(TBXT*) and endodermal *(SOX17*) markers in Day 0 hIPSCs **(A)** and Day 5 EBs **(B)**. **C)** Transcriptional analysis of Control #1, #2 and 1qDel samples' expression of *KI67* across Day 0, 5 and 11. Data is presented as relative mRNA abundance ($2^{-\Delta CT}$, $\pm 2^{-CI}$), (n≥3 hIPSC wells or independent E-hCOs, n≥6 independent E-EBs). Statistical analysis was conducted on dCTs using a two-way ANOVA with Geisser-Greenhouse correction with Holm-Šídák correction for post-hoc tests, except for **(B)** which used a One-way ANOVA with Brown-Forsythe and Welch correction, with Dunnett correction for post-hoc test. **D)** Raw cell count of Control #1, #2 and 1qDel dissociated Day 5 E-EBs (n≥1 EB per differentiation, ≥2 independent differentiations). Statistical analysis used a one-way ANOVA with Holm-Šídák correction for post-hoc tests, unlabelled=>0.05, *p=<0.05, **p=<0.005, ****p=<0.0001.

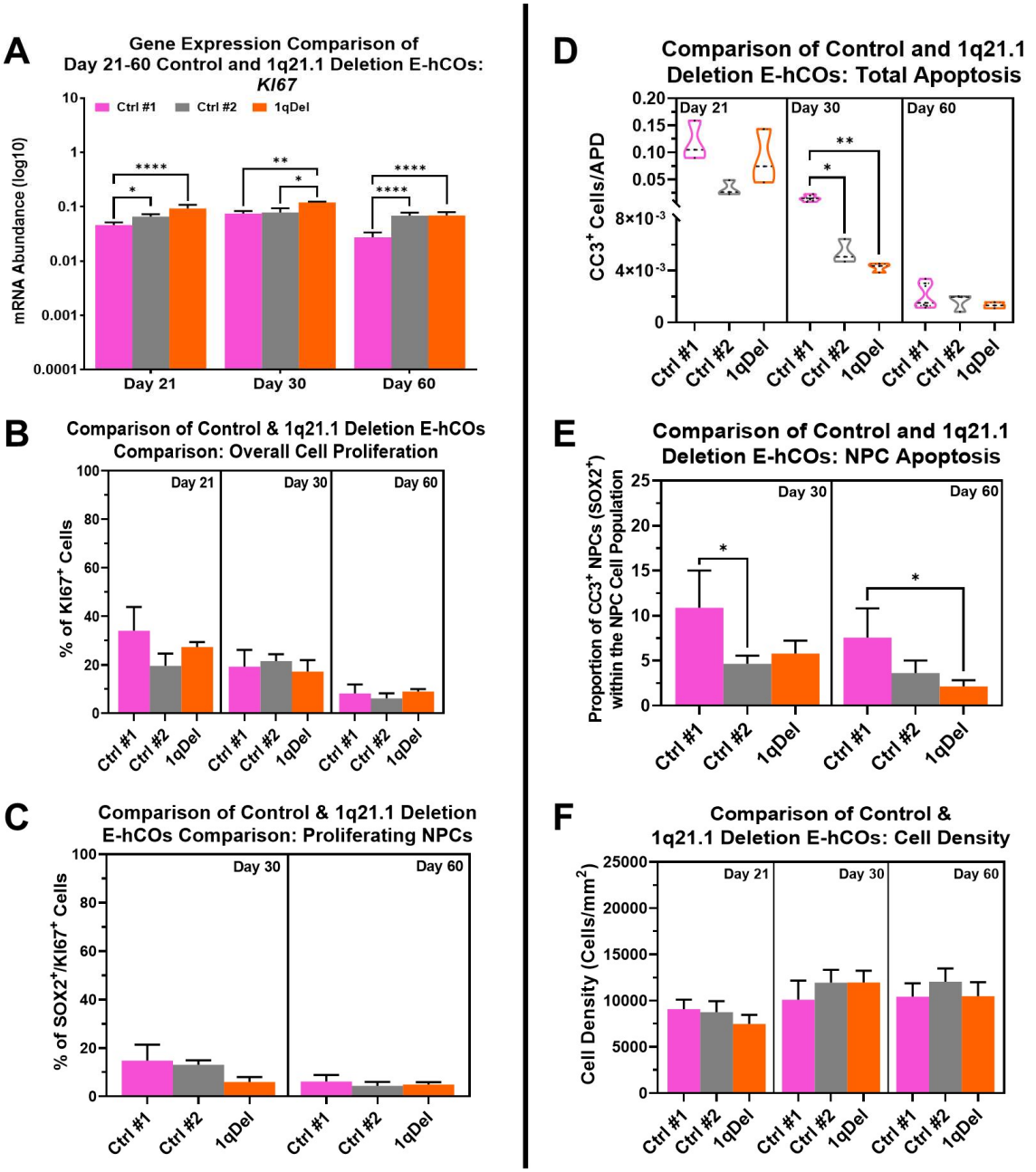

Figure 5.7: Quantities of overall cells, mitotically-active cells and dead cells were comparable in 1qDel and control E-hCOs between Day 21 to Day 60, except KI67 expression which was significantly higher in 1qDel E-hCOs.

Figure legend on following page.

Figure 5.7 (above): Quantities of overall cells, mitotically-active cells and dead cells were comparable in 1qDel and control E-hCOs between Day 21 to Day 60, except KI67 expression which was significantly higher in 1qDel E-hCOs.

A) *KI67* transcription in Control #1, #2 and 1qDel E-hCOs across Day 21, 30 and 60. Data is presented as relative mRNA abundance ($2^{-\Delta CT}$, $\pm 2^{-CI}$), (n≥3 independent hCOs). Statistical analysis was conducted on dCTs using a two-way ANOVA with Geisser-Greenhouse correction with Holm-Šídák correction for post-hoc tests. **B)** Percentage of $KI67^+/DAPI^+$ cells in Control #1, #2 and 1qDel E-hCOs across Day 21, 30 and 60. **C)** Percentage of $SOX2^+/KI67^+/DAPI^+$ cells in Control #1, #2 and 1qDel E-hCOs across Day 21, 30 and 60. **D)** $CC3^+/DAPI^+$ count, normalised to APD, of Control #1, #2 and 1qDel E-hCOs across Day 21, 30 and 60. **E)** Percentage of $SOX2^+/CC3^+/ DAPI^+$ cells within the total $SOX2^+/DAPI^+$ cell population, in Control #1, #2 and 1qDel E-hCOs across Day 21, 30 and 60. **F)** Cell density, determined by $DAPI^+$ count per mm^2, of Control #1, #2 and 1qDel E-hCOs across Day 21, 30 and 60. Truncated violin plots present all available data; bar graphs present mean counts ±standard deviation. Statistical significance determined by One-Way ANOVA with Holm-Šídák's correction, (n≥3 independent hCOs); unlabelled=>0.05, *p=<0.05, **p=<0.005, ****p=<0.0001.

5.3.5 Day 21 1q21.1 Deletion Cortical Organoids Exhibit Altered Neuroepithelial Structure

1qDel E-hCOs exhibited no signs of atypical $KI67^+$ or apoptotic cell count that would contribute to the observed microcephaly (Figure 5.7). As such, the bright field phenotype of abnormal neuroepithelial structure was the next observation to be investigated. Lumen count was comparable across cell lines over time, after APD normalisation (Figure 5.11.A). However, ICC imaging of these characteristics illustrated significant differences between the control and 1qDel E-hCOs. Firstly, 1qDel E-hCOs' lumen area was significantly smaller than control E-hCOs at Day 30 specifically, after APD normalisation (Figure 5.11.B-D and 5.12). Additionally, increases in *NES* and *VIM* expression, responsible for organising radial glia within the neuroepithelium, were only evidenced in Day 30 1qDel E-hCOs, with *NES* expression still significantly elevated at Day 60 (Figure 5.13.A-C). However, there were no significant changes in the quantity of lumens found between E-hCOs at any other timepoint, after APD normalisation (Figure 5.11.A).

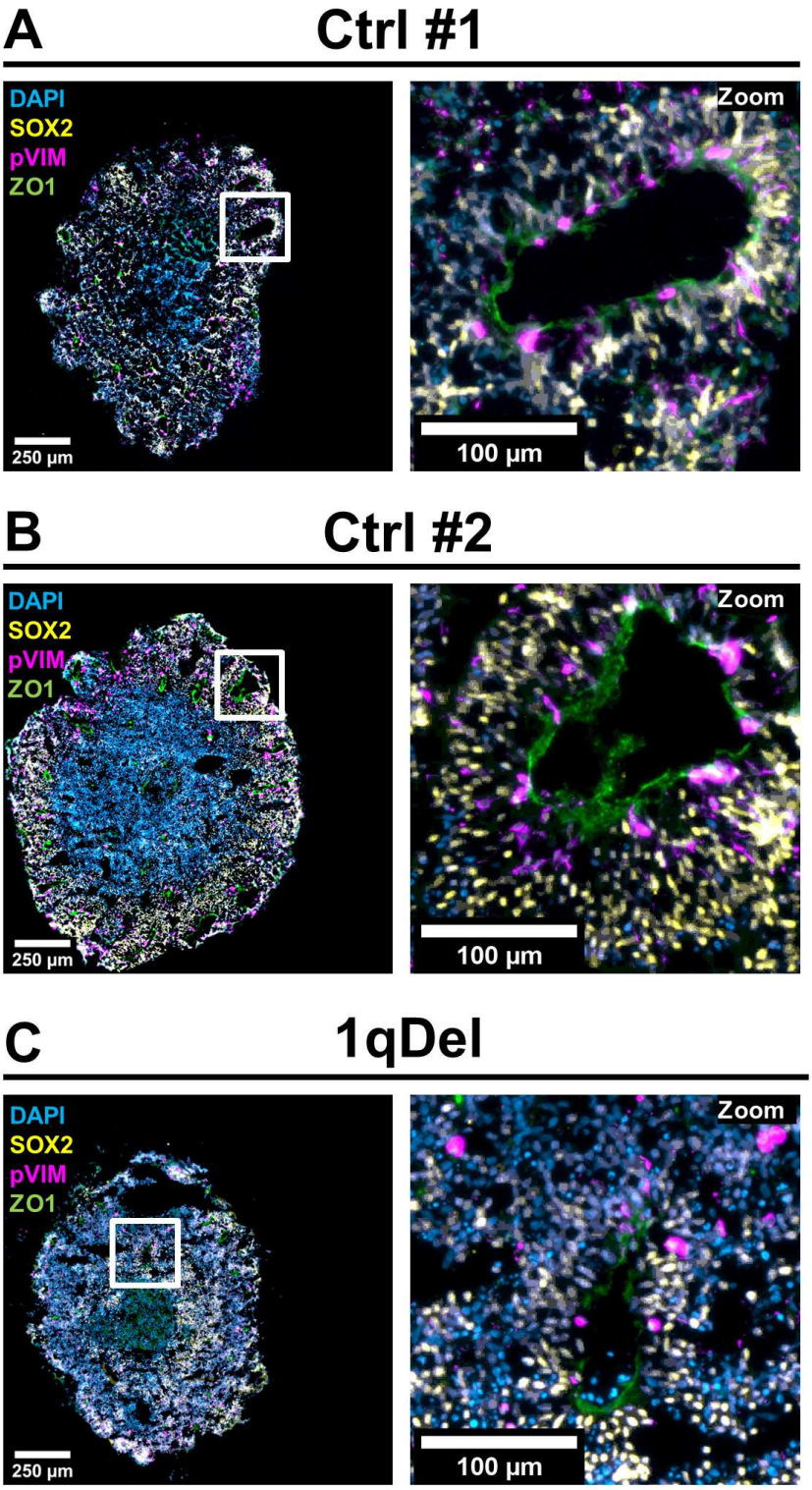

Figure 5.8: Day 21 1qDel E-hCOs had visibly similar neuroepithelial loop features as control E-hCOs, but less apically-bound M phase cells.

Fluorescent images of 10 µm E-hCO slices of Day 21 Control #1 **(A)**, #2 **(B)** and 1qDel **(C)**. 20x magnification, with white box annotation referring to zoomed in 250 µm x 250 µm region of interest (ROI). Proteins identified by colour: ZO1 (green), pVIM (pink), SOX2 (yellow), DAPI (blue). Scale bar = 250 µm (whole image) or 100 µm (zoomed in ROI).

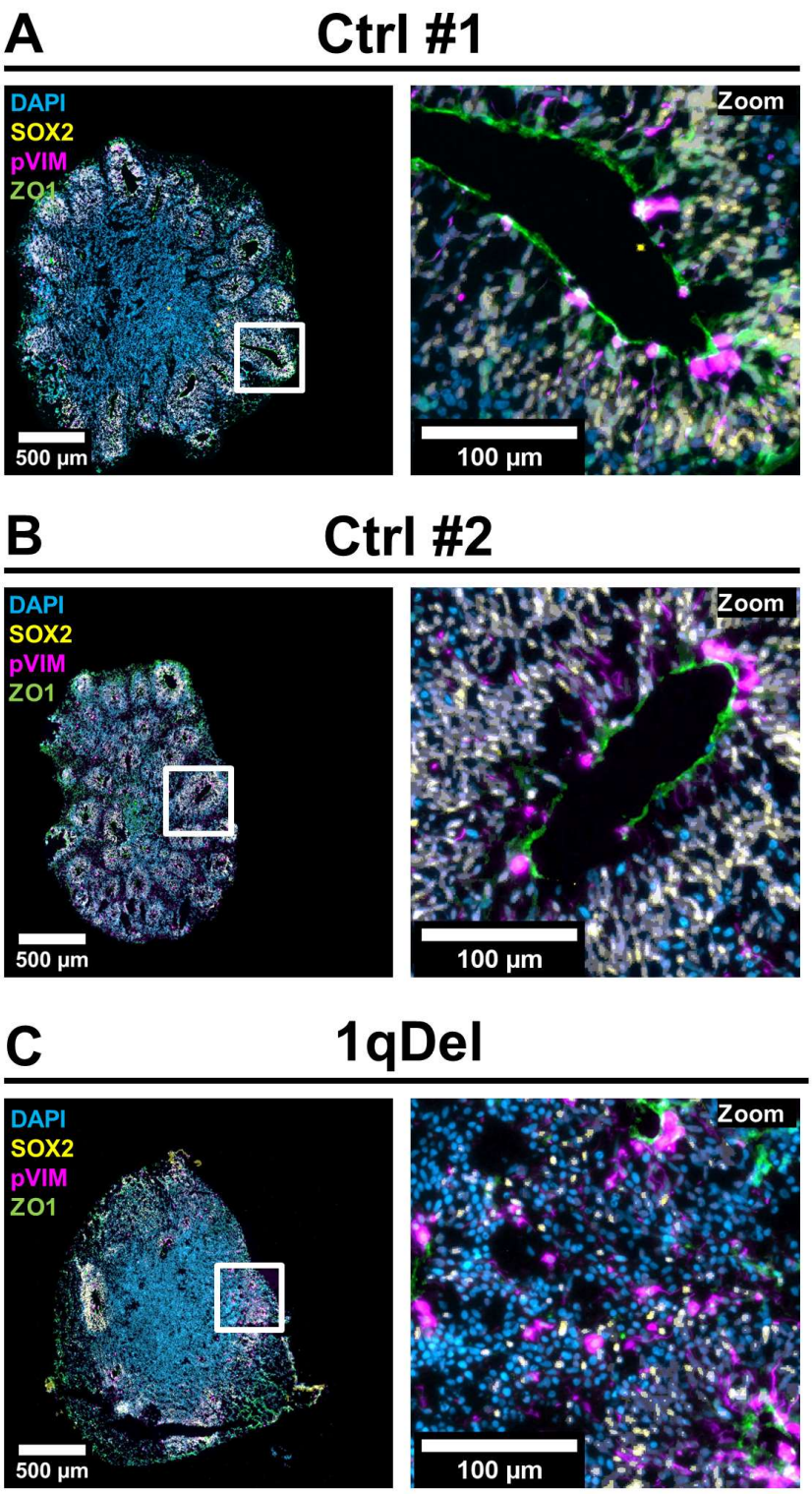

Figure 5.9: Day 30 1qDel E-hCOs had visible migration of cells away from the main body of the E-hCOs, as well as smaller lumens and significant disaggregation of M phase cells.

Fluorescent images of 10 µm E-hCO slices of Day 30 Control #1 **(A)**, #2 **(B)** and 1qDel **(C)**. 20x magnification, with white box annotation referring to zoomed in 250 µm x 250 µm region of interest (ROI). Proteins identified by colour: ZO1 (green), pVIM (pink), SOX2 (yellow), DAPI (blue). Scale bar = 250 µm (whole image) or 100 µm (zoomed in ROI).

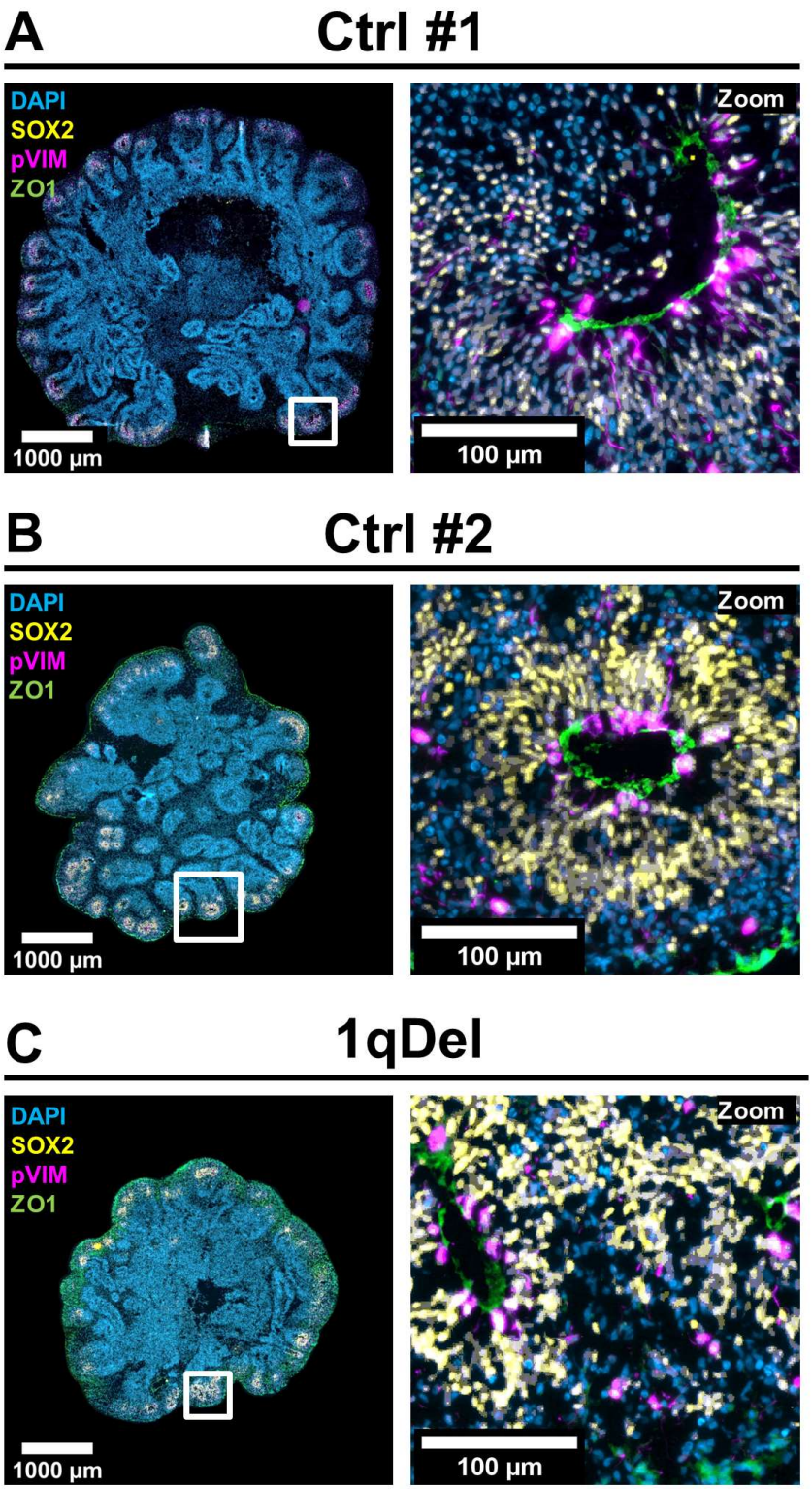

Figure 5.10: Day 60 1qDel E-hCOs exhibited visibly similar neuroepithelial formation as control E-hCOs.

Fluorescent images of 10 µm E-hCO slices of Day 60 Control #1 **(A)**, #2 **(B)** and 1qDel **(C)**. 20x magnification, with white box annotation referring to zoomed in 250 µm x 250 µm region of interest (ROI). Proteins identified by colour: ZO1 (green), pVIM (pink), SOX2 (yellow), DAPI (blue). Scale bar = 250 µm (whole image) or 100 µm (zoomed in ROI).

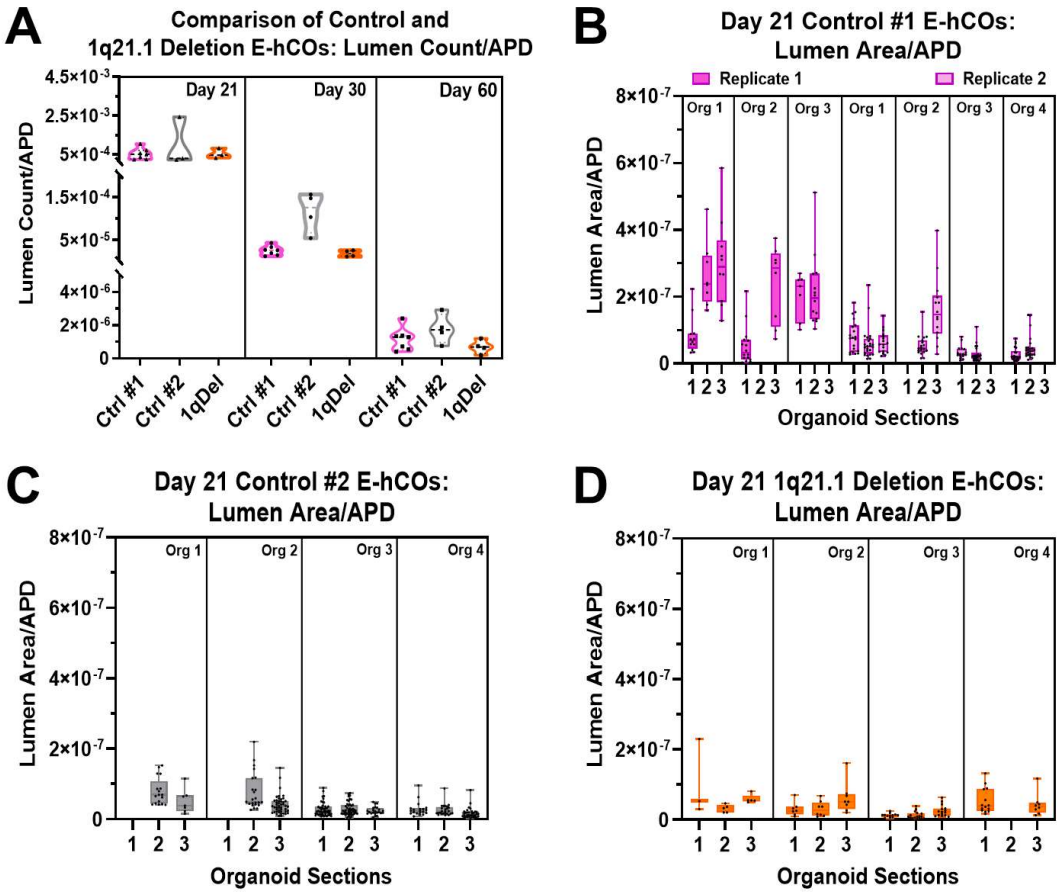

Figure 5.11: Control and 1qDel E-hCOs had comparable lumen count from Day 21 to Day 60, and lumen area at Day 21.

A) Total number of lumens, normalised by APD, in Control #1, #2 and 1qDel E-hCOs across Day 21, 30 and 60. Truncated violin plots present all available data. Statistical significance determined by One-Way ANOVA with Holm-Šídák's correction, (n≥3 independent hCOs); unlabelled=>0.05. **B-D)** Measurements of raw lumen areas defined by vacuous spaces surrounded by $SOX2^+$ cells and/or $ZO1^+$ aggregation. Lumens presented as individuals (singular dots) within each cryosection, each E-hCO has ≥2 cryosections; box and whisker plots show full range of points. The following general linear mixed effects model was used for statistical analysis: "lme(log(Lumen_Area) ~ CellLine, random = ~1|Organoid/Section/LumenID, method = "REML")". All statistical assumptions of normal residuals and homoscedasticity were met. Pairwise comparisons of estimated marginal means with Bonferroni post-hoc correction were used to determine statistical significance. The following groups were compared: Control #1 & #2 at Day 21 **(B & C):** $F(2,12)=1.810$, $p=0.8923$. Control #1 & 1qDel at Day 21 **(B & D)**: $F(2,12)=1.810$, $p=0.2655$. Control #2 and 1qDel at Day 21 **(C & D)**: $F(2,12)=1.810$, $p=1.0000$.

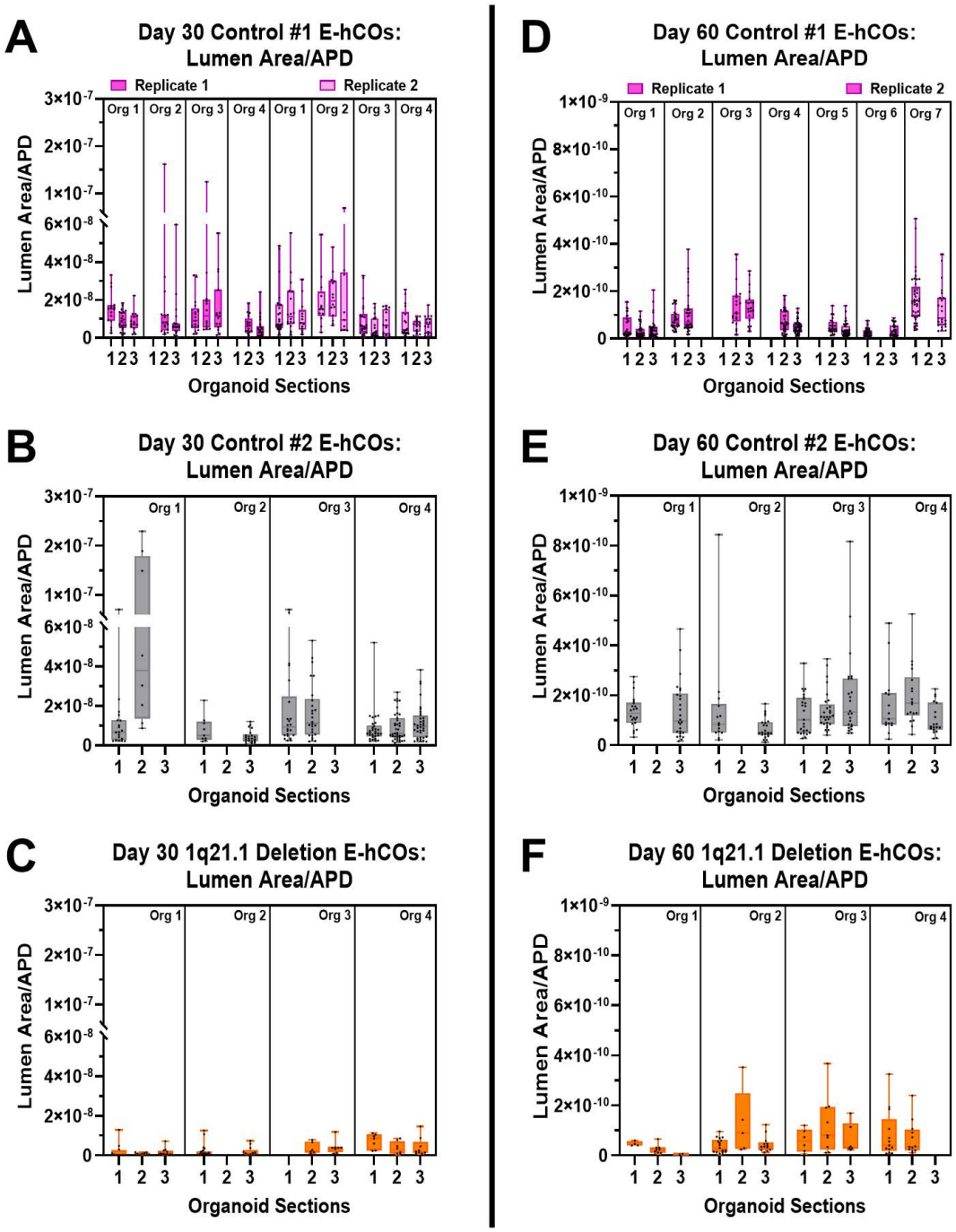

Figure 5.12: Day 30 1qDel E-hCOs' lumen areas were substantially smaller than control E-hCOs, unlike at Day 60 where lumen areas were comparable across cell lines.

Figure legend on following page.

Figure 5.12 (above): Day 30 1qDel E-hCOs' lumen areas were substantially smaller than control E-hCOs, unlike at Day 60 where lumen areas were comparable across cell lines.

Measurements of raw lumen areas, normalised by APD, defined by vacuous spaces surrounded by $SOX2^+$ cells and/or $ZO1^+$ aggregation. Lumens presented as individuals (singular dots) within each cryosection, each E-hCO has ≥2 cryosections; box and whisker plots show full range of points. The following general linear mixed effects model was used for statistical analysis: "lme(log(Lumen_Area) ~ CellLine, random = ~1|Organoid/Section/LumenID, method = "REML")". All statistical assumptions of normal residuals and homoscedasticity were met. Pairwise comparisons of estimated marginal means with Bonferroni post-hoc correction were used to determine statistical significance. The following groups were compared: Control #1 & #2 at Day 30 **(A & B):** $F(2,13)=11.302$, $p=1.0000$, Day 60 **(D & E):** $F(2,12)=4.058$, $p=0.1976$. Control #1 & 1qDel at Day 30 **(A & C)**: $F(2,13)=11.302$, $p=0.0024$, Day 60 **(D & F)**: $F(2,12)=4.058$, $p=0.8208$. Control #2 and 1qDel at Day 30 **(B & C)**: $F(2,13)=11.302$, $p=0.0037$, Day 60 **(E & F)**: $F(2,12)=4.058$, $p=0.0488$.

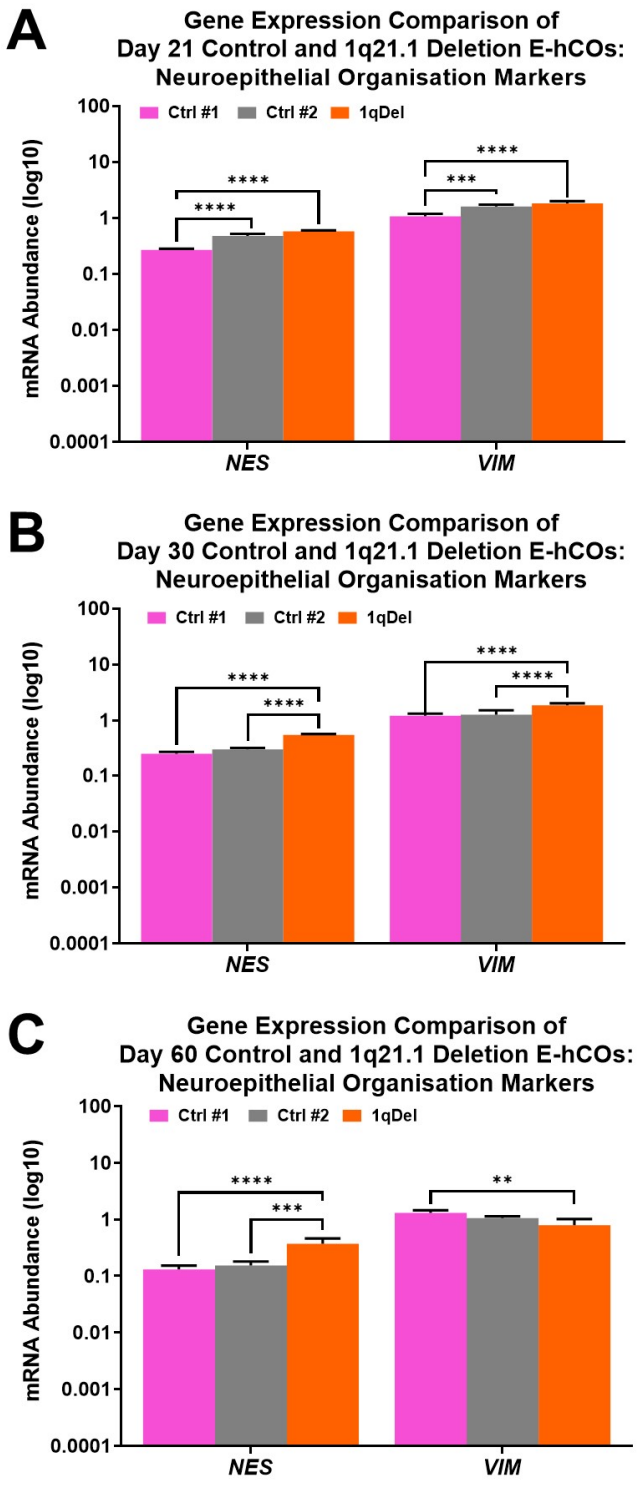

Figure 5.13: Neuroepithelial organisation markers significantly increased in Day 30 and Day 60 1qDel E-hCOs.

Transcriptional analysis of Control #1, #2 and 1qDel E-hCOs' expression of neuroepithelial organisation markers at Day 21 **(A)**, Day 30 **(B)** and Day 60 **(C)**. Data is presented as relative mRNA abundance ($2^{-\Delta CT}$, $\pm 2^{-CI}$), (n≥3 independent hCOs). Statistical analysis was conducted on dCTs using a two-way ANOVA with Geisser-Greenhouse correction with Holm-Šídák correction for post-hoc tests; unlabelled=>0.05, *p=<0.05, **p=<0.005, ***p=<0.0005, ****p=<0.0001.

5.3.6 Day 21 1q21.1 Deletion Cortical Organoids Characterised by Faulty Cell Cycle and Premature Neuronal Differentiation

Alongside lumen area variability, abnormal localisation of M phase cells was visible from Day 21 to Day 60 in 1qDel E-hCOs (Figures 5.8, 5.9 and 5.10). 1qDel E-hCOs had significantly more M phase ($pVIM^+$) cells at Day 21 (Figure 5.14.A), whilst the population of M phase cells localised to the apical edge of the lumen was reduced at all timepoints in 1qDel E-hCOs (Figure 5.14.B). Further exploration into cell cycle disruption uncovered that Day 21 1qDel E-hCOs had significantly increased $KI67^+/p53^+$ cells after APD normalisation, a reflection of a greater population of actively cycling cells in a state of cell cycle arrest (Figure 5.14.C and Supplemental Figure 9). Finally, Day 21 1qDel E-hCOs exhibited greater quantities of $TUNEL^+$ cells, normalised to APD (Figure 5.14.D). As CC3 quantities were unchanged (Figure 5.7.D), an increase in $TUNEL^+$ cells identified a heightened level of DNA DSBs as opposed to apoptosis (Figure 5.14.D). The three Day 21-specific characteristics of 1qDel E-hCOs, increased total M phase cells, arrested cycling cells and DNA DSBs, resolved after Day 21 when microcephaly was no longer present (Figure 5.3.B and 5.14).

Due to the observations of bright field imaging and changes in elements of the cell cycle, and the knowledge that the cell cycle changes relative to the orientation of division of aRG (Arai *et al.*, 2011), it was proposed that Day 21 1qDel E-hCOs were undertaking early neurogenesis. DCX is a protein associated with immature, migrating neurons, the ICC stain of which revealed that the bright field imaging of Day 30 1qDel E-hCOs' disorganised border was a collection of immature neurons (Figure 5.15.H). Quantitative analysis of DCX staining, normalised to APD, did not identify significant changes between control and 1qDel E-hCOs at Day 30, however Day 21 1qDel E-hCOs showed substantial greater coverage of DCX (Figure 5.16.A). This result was supported by significantly increased *DCX* and *NCAM1* expression, both associated with immature neurons and neuronal migration, in Day 21 and Day 30 1qDel E-hCOs (Figure 5.16.B-D).

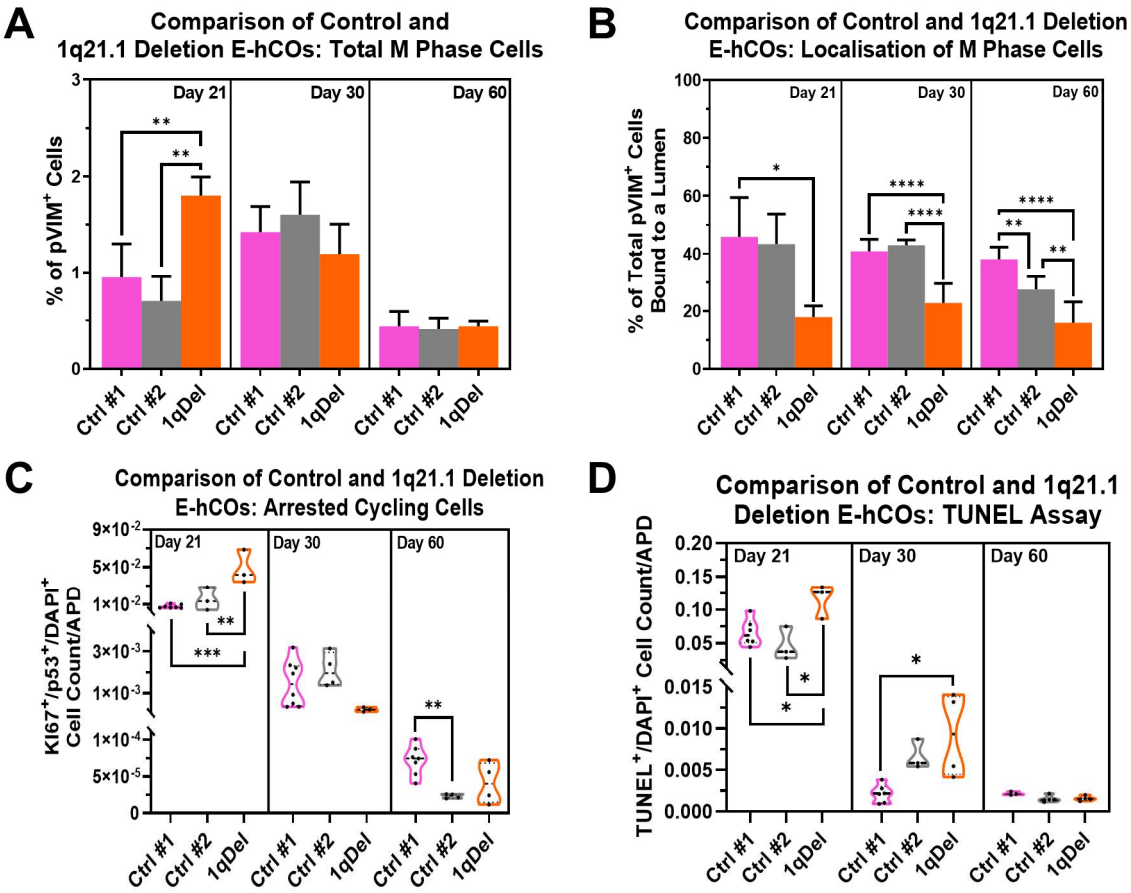

Figure 5.14: Day 21-specific phenotypes found in 1qDel E-hCOs, including increased M phase cell population, arrested cycling cells and DNA DSBs, as well as cross-timepoint phenotype of poor localisation of RGs in 1qDel E-hCOs.
A) Percentage of pVIM$^+$/DAPI$^+$ cells in Control #1, #2 and 1qDel E-hCOs across Day 21, 30 and 60. **B)** pVIM$^+$/DAPI$^+$ cell count that are localised to lumens, as a percentage of total pVIM$^+$/DAPI$^+$ cells, in Control #1, #2 and 1qDel E-hCOs across Day 21, 30 and 60. **C)** KI67$^+$/p53$^+$/DAPI$^+$ count, normalised to APD, of Control #1, #2 and 1qDel E-hCOs across Day 21, 30 and 60. **D)** TUNEL$^+$/DAPI$^+$ count, normalised to APD, in Control #1, #2 and 1qDel E-hCOs across Day 21, 30 and 60. Truncated violin plots present all available data; bar graphs present mean counts ±standard deviation. Statistical significance determined by One-Way ANOVA with Holm-Šídák's correction, (n≥3 independent hCOs); unlabelled=>0.05, *p=<0.05, **p=<0.005, ***p=<0.0005.

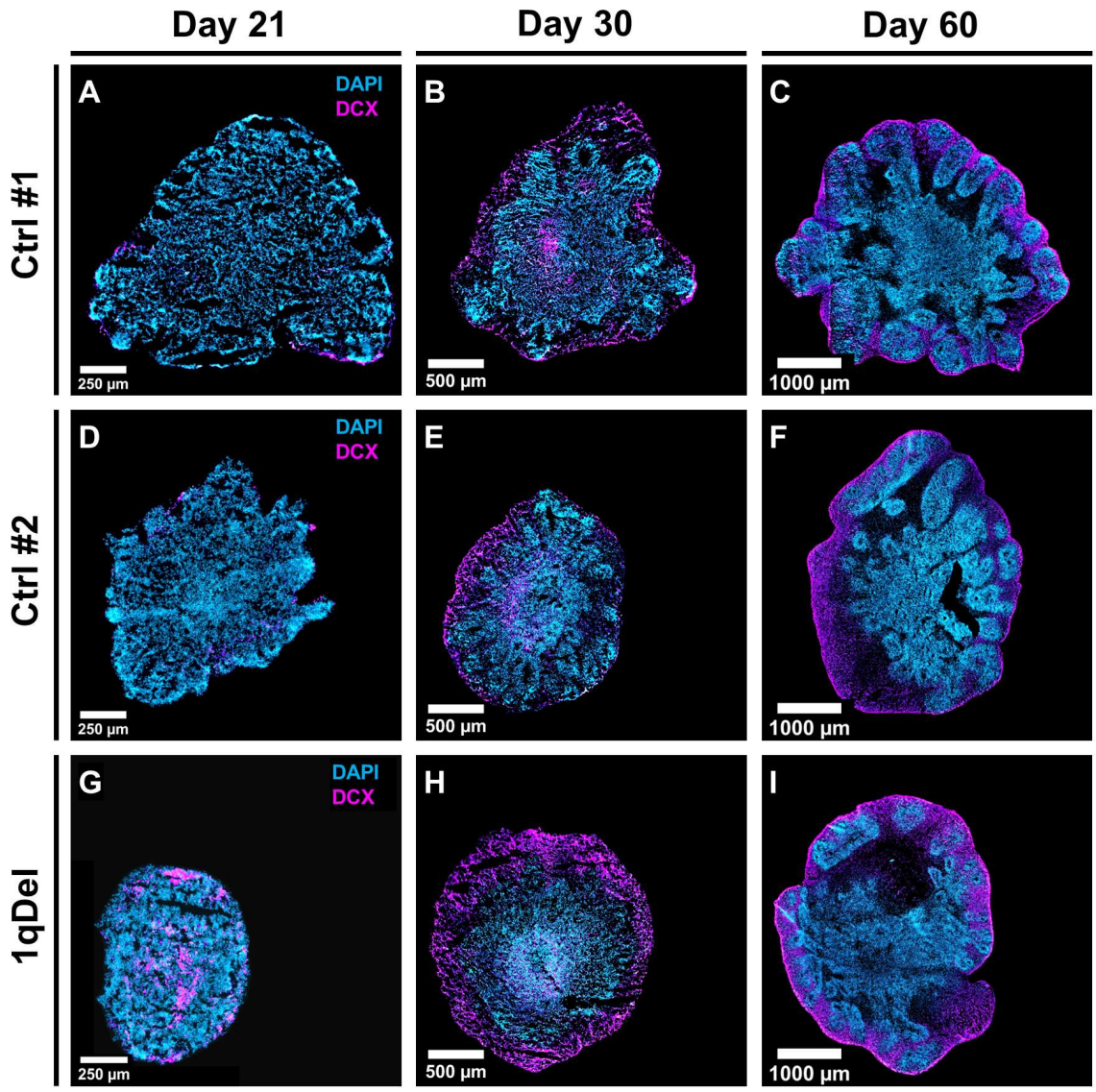

Figure 5.15: Visibly greater DCX representation found in Day 21 1qDel E-hCOs, whilst Day 30 1qDel E-hCOs were surrounded by migratory neurons.

20x magnification fluorescent images of 10 µm slices of Control #1 **(A-C),** #2 **(D-F)** and 1qDel **(G-I)** E-hCOs at Day 21, 30 and 60. Cell line and timepoint is referenced in image. Proteins identified by colour: DCX (pink), DAPI (blue). Scale bar = 250 µm (Day 21), 500 µm (Day 30) or 1000 µm (Day 60).

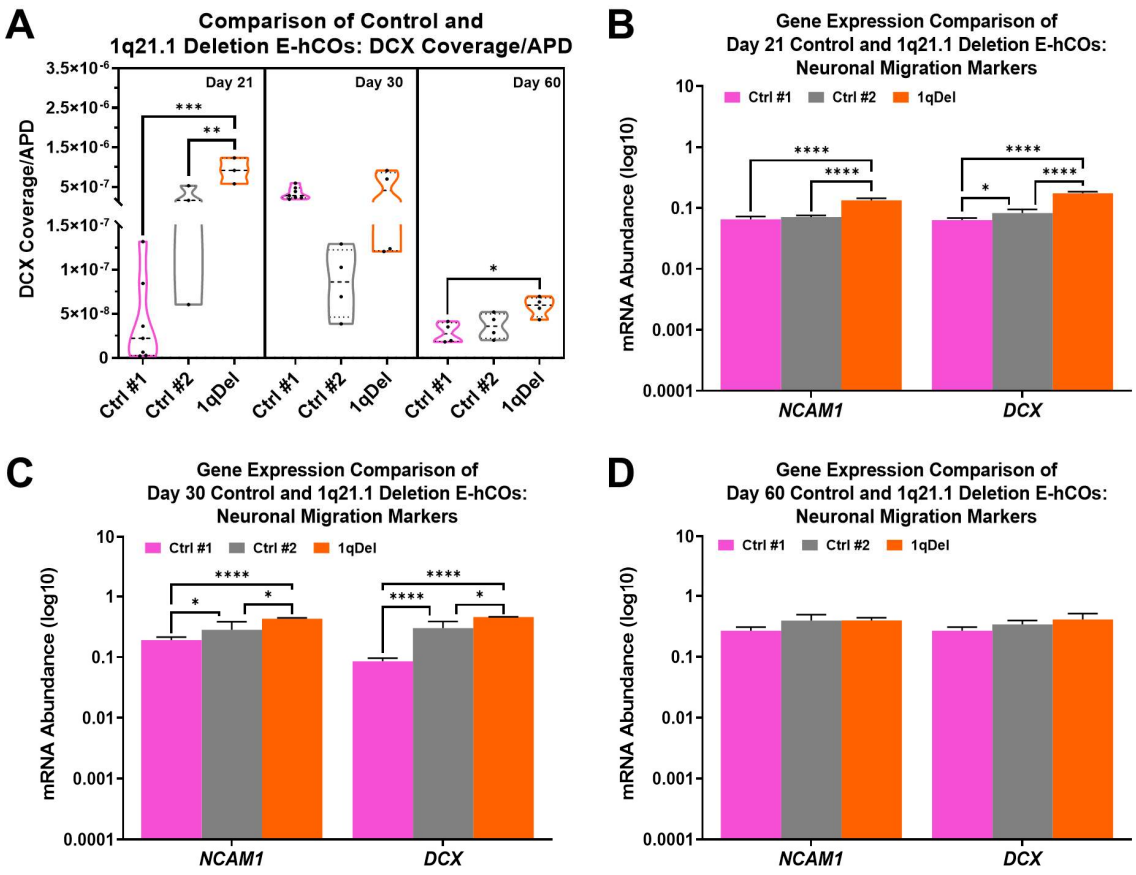

Figure 5.16: DCX coverage and transcription of *DCX* and *NCAM1* were increased in Day 21 1qDel E-hCOs, whilst *DCX* and *NCAM1* continued to be upregulated at Day 30.

A) DCX coverage, normalised to APD, of Control Line #1, #2 and 1qDel E-hCOs across Day 21, 30 and 60. Truncated violin plots present all available data. Statistical significance determined by One-Way ANOVA with Holm-Šídák's correction, (n≥3 independent hCOs). **B-D)** Transcriptional analysis of Control #1, #2 and 1qDel E-hCOs' expression of neuronal migration markers at Day 21 **(B)**, Day 30 **(C)** and Day 60 **(D)**. Data is presented as relative mRNA abundance ($2^{-\Delta CT}$, $\pm 2^{-CI}$), (n≥3 independent hCOs). Statistical analysis was conducted on dCTs using a two-way ANOVA with Geisser-Greenhouse correction with Holm-Šídák correction for post-hoc tests; unlabelled=>0.05, *p=<0.05, **p=<0.005, ***p=<0.0005, ****p=<0.0001.

5.3.7 Limited Changes in Quantity of Neuronal Progenitors, Intermediate Progenitors and CTIP2⁺ Neurons in 1q21.1 Deletion Cortical Organoids

It was expected that the alteration to M phase cell localisation and neuroepithelial localisation, accompanied by premature neuronal differentiation, would likely disrupt other structure-oriented features of E-hCO development in 1qDel E-hCOs, including definition of cortical layers. All Day 21 E-hCOs had organisation of SOX2⁺ NPCs in the VZ, but minimal organisation of TBR2⁺ IPs in the SVZ region and no CTIP2⁺ neurons, with no discernible differences in cortical layer morphology (Figure 5.17.A, 5.17.D and 5.17.G). Although there was a trend for reduced TBR2⁺ IPs in Day 21 1qDel E-hCOs, there were no other distinguishing features or significant changes in cell type quantities between the three cell lines at Day 21 (Figure 5.18.A). At Day 30, TBR2⁺ IPs were significantly lower in 1qDel E-hCOs than controls, which impacted on transitionary cells colocalised for TBR2 and CTIP2 (Figure 5.18.B and 5.18.E). More IPs were also observed outside of the close parameter of SOX2⁺ VZ regions in 1qDel E-hCOs (Figure 5.17.B). At Day 60, there were no significant changes in quantity of cell types between 1qDel and control E-hCOs that could be distinguished from cell line-specific variability (Figure 5.18.C and 5.18.F). There was, however, visibly less discrete separation between the VZ, SVZ and CP in Day 60 1qDel E-hCOs (Figure 5.17.I). Transcriptional analysis of cortical layer markers showed few significant changes across the three timepoints that could not be attributed to cell line-specific variability (Figure 5.19). However, in Day 21 and Day 30 1qDel E-hCOs, *CUX1, BCL11B* and *RELN* transcription had an inclined trend, if not a significant increase, compared to controls (Figure 5.19.A-B). The preplate/Layer VI gene *TBR1*, on the other hand, trended downwards across all three timepoints (Figure 5.19.A-C).

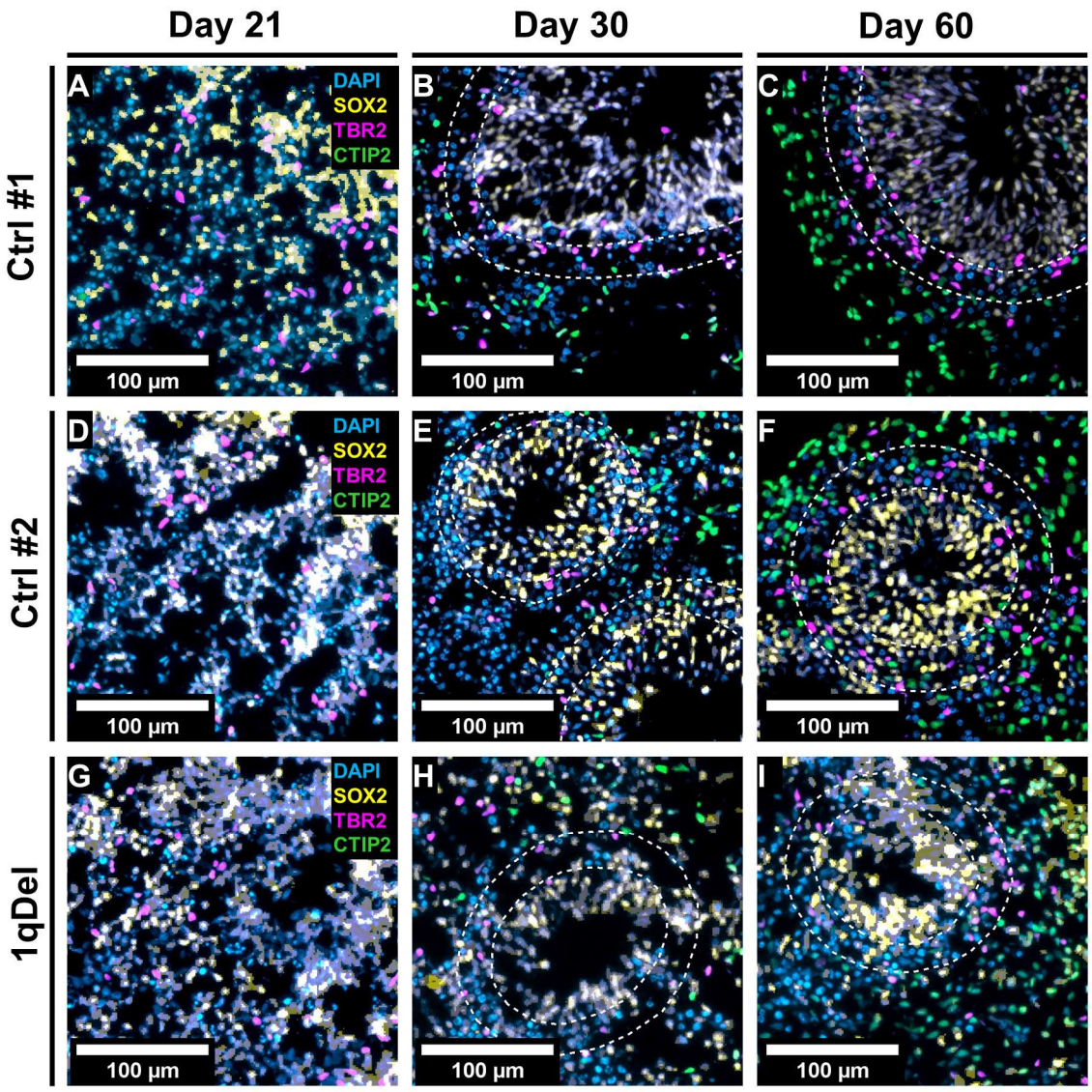

Figure 5.17: Less defined cortical layers were visible in Day 30 and Day 60 1qDel E-hCOs.

Fluorescent images of 10 µm slices of Control #1 **(A-C),** #2 **(D-F)** and 1qDel **(G-I)** E-hCOs at Day 21, 30 and 60. 20x magnification, with white dashed lines, annotating VZ ($SOX2^+$) and SVZ ($TBR2^+$) layers within E-hCO, visible from Day 30 onwards. Cell line and timepoint is referenced in image. Proteins identified by colour: CTIP2 (green), TBR2 (pink), SOX2 (yellow), DAPI (blue). Scale bar = 100 µm.

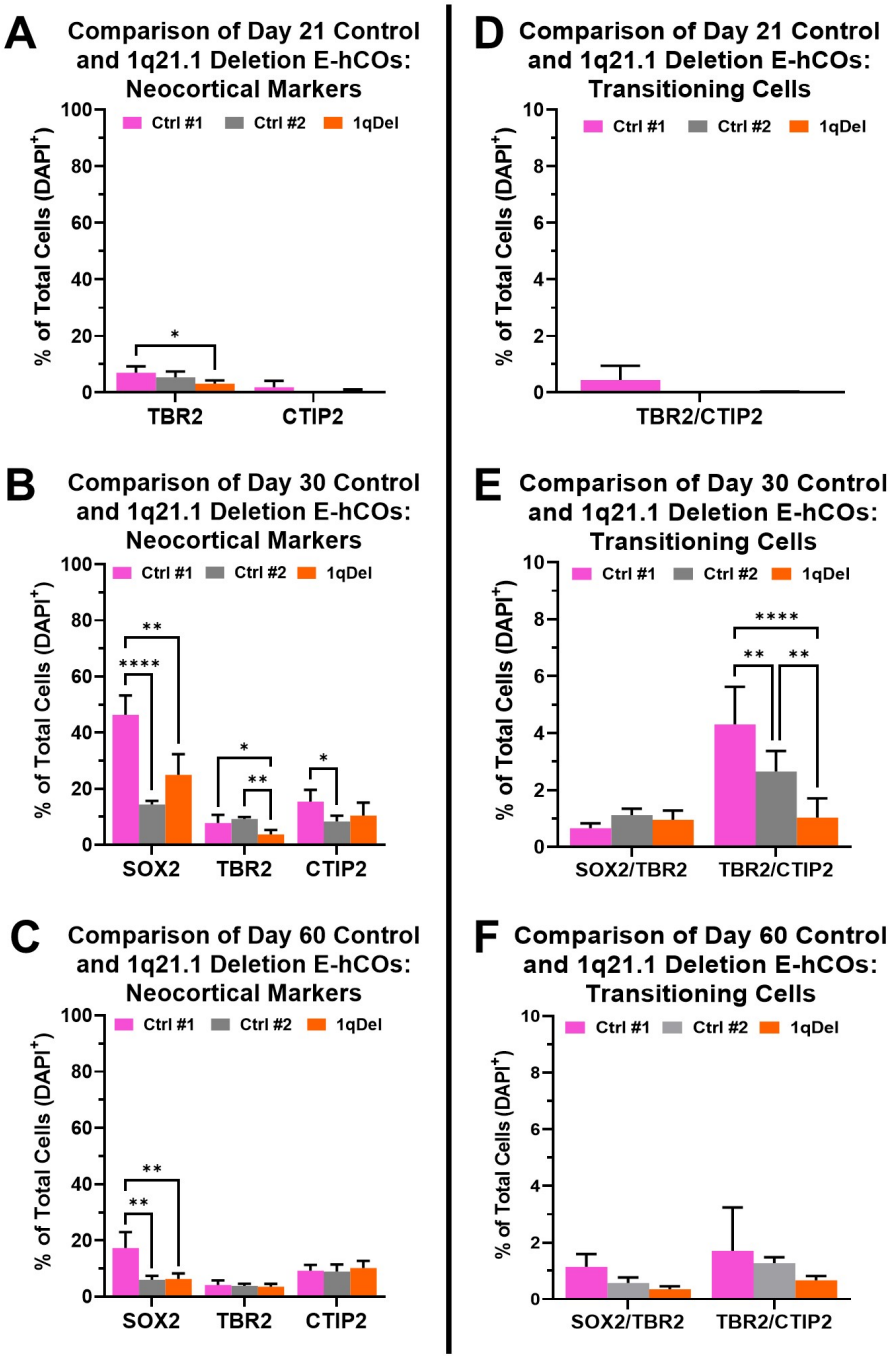

Figure 5.18: TBR2⁺ IP population underrepresented in Day 21 and Day 30 1qDel E-hCOs, whilst CTIP2⁺ neurons and SOX2⁺ NPCs were comparable to control E-hCOs from Day 21 to Day 60.

A-C) Percentage of SOX2⁺/DAPI⁺, TBR2⁺/DAPI⁺ and CTIP2⁺/DAPI⁺ cells in Control #1, #2 and 1qDel E-hCOs across three timepoints: Day 21 (TBR2⁺, CTIP2⁺ only) **(A)**, Day 30 **(B)** and Day 60 **(C)**. **D-F)** Percentage of SOX2⁺/TBR2⁺/DAPI⁺ and TBR2⁺/CTIP2⁺/DAPI⁺ cells in Control #1, #2 and 1qDel E-hCOs across three timepoints: Day 21 (TBR2⁺/CTIP2⁺ only) **(D)**, Day 30 **(E)** and Day 60 **(F)**. Bar graphs present mean counts ±standard deviation. Statistical significance determined by One-Way ANOVA with Holm-Šídák's correction, (n≥3 independent hCOs); unlabelled=>0.05, *p=<0.05, **p=<0.005, ****p=<0.0001.

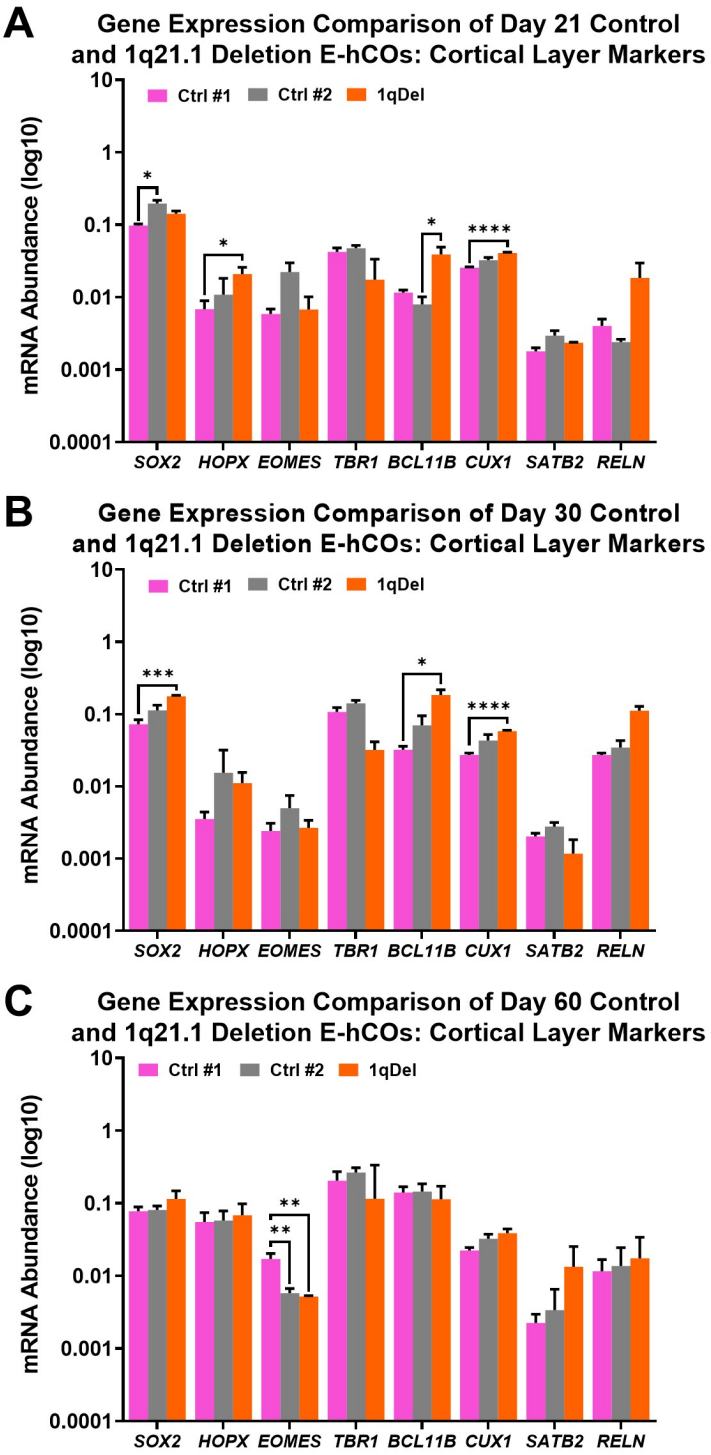

Figure 5.19: Overexpression of *BCL11B, CUX1* and *RELN* found between control and 1qDel E-hCOs at Day 21 and Day 30; no significant differences between cell lines at Day 60.

Transcriptional analysis of Control #1, #2 and 1qDel E-hCOs' expression of cortical layer markers at Day 21 **(A)**, Day 30 **(B)** and Day 60 **(C)**. Data is presented as relative mRNA abundance ($2^{-\Delta CT}$, $\pm 2^{-CI}$), (n≥3 independent hCOs). Statistical analysis was conducted on dCTs using a two-way ANOVA with Geisser-Greenhouse correction with Holm-Šídák correction for post-hoc tests, unlabelled=>0.05, *p=<0.05, **p=<0.005, ***p=<0.0005, ****p=<0.0001.

5.3.8 Recovery of Microcephaly Phenotype and Reduction in Lumen Area in Day 30 1q21.1 Deletion Cortical Organoids Coincides with the Expansion of Ventral Forebrain Progenitors

One hypothesis for the disrupted neuroepithelial organisation at Day 30 was a reduction in dorsal forebrain-specific progenitors in favour of other brain regions, such as ventral forebrain. Ventral forebrain was consistently represented in 1qDel E-hCOs from Day 21 onwards, in particular the pan-GE marker *DLX1*, which was either significantly or trending towards an increase in transcription compared to controls (Figure 5.20.A-C). There was also a trend at Day 21 and Day 30 of increased *OLIG2* expression, an oligodendrocyte precursor marker present in the GE, and *NKX2-1*, an MGE NPC marker (Figure 5.20.A-B) (Alzu'bi and Clowry, 2019). To assess if there was a shift to the MGE identity in 1qDel E-hCOs, the abundance of $NKX2.1^+$ cells was investigated. Such a shift was observed at Day 30 in 1qDel E-hCOs, where a significant number of $NKX2.1^+$ progenitors were present in non-lumen orientated spaces (Figure 5.21.A-C and 5.22.A). This change in MGE progenitors was not found at Day 21 or Day 60 (Figure 5.22.A), nor was *NKX2-1* expression found prior to Day 21 in E-hCOs of any cell line (data not presented).

Other significant changes were found in the expression of different brain region markers, notably *FOXG1*, *PAX3*, *FOXA2* and *HOXB2*. Although all were difficult to delineate significant changes between genotypes due to cell line-specific variability, there was a trend of increased *FOXG1* at Day 21 and Day 30, accompanied by increased *HOXB2* and *FOXA2* mRNA abundance at Day 21 (Figure 5.21). It is of note that non-telencephalic identity markers were at low abundance at all timepoints (Figure 5.21.D-F). A consistent trend in downregulated *PAX3* transcription at Day 21 and Day 30 in 1qDel E-hCOs was also noted (Figure 5.21.D-F). However, no changes were observed in FOXG1 or PAX3 between control and 1qDel E-hCOs at any timepoint (Figure 5.22.B-C).

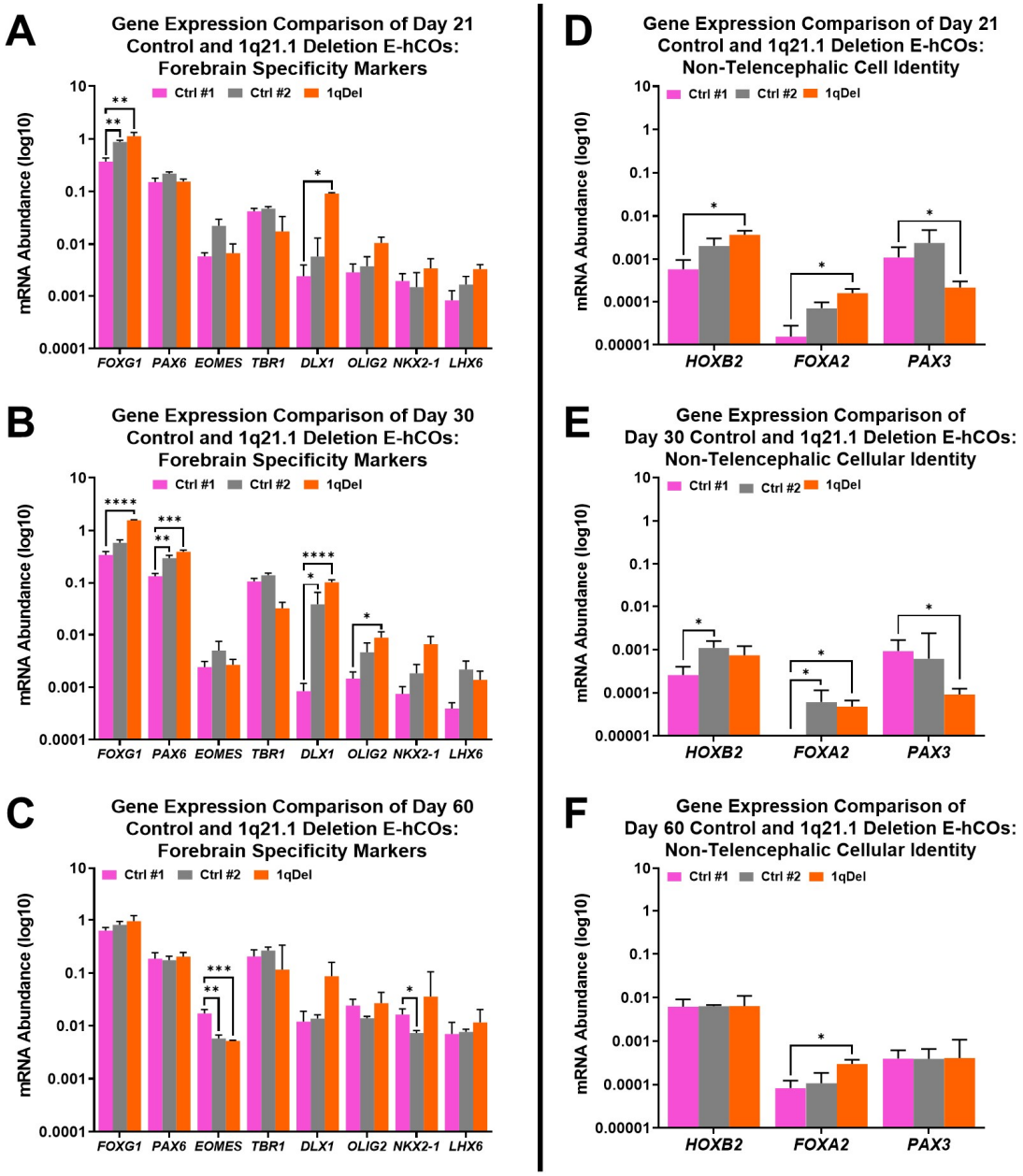

Figure 5.20: Prior to Day 60, 1qDel E-hCOs had a trend of overexpression of all three major brain regions, with significantly less *PAX3*.

A-C) Transcriptional analysis of Control #1, #2 and 1qDel E-hCOs' expression of forebrain markers at Day 21 **(A)**, Day 30 **(B)** and Day 60 **(C)**. **D-F)** Transcriptional analysis of Control #1, #2 and 1qDel E-hCOs' expression of non-telencephalic markers at Day 21 **(D)**, Day 30 **(E)** and Day 60 **(F)**. Data is presented as relative mRNA abundance ($2^{-\Delta CT}$, $\pm 2^{-CI}$), (n≥3 independent hCOs). Statistical analysis was conducted on dCTs using a two-way ANOVA with Geisser-Greenhouse correction, with Holm-Šídák correction for post-hoc tests, unlabelled=>0.05, *p=<0.05, **p=<0.005, ***p=<0.0005, ****p=<0.0001.

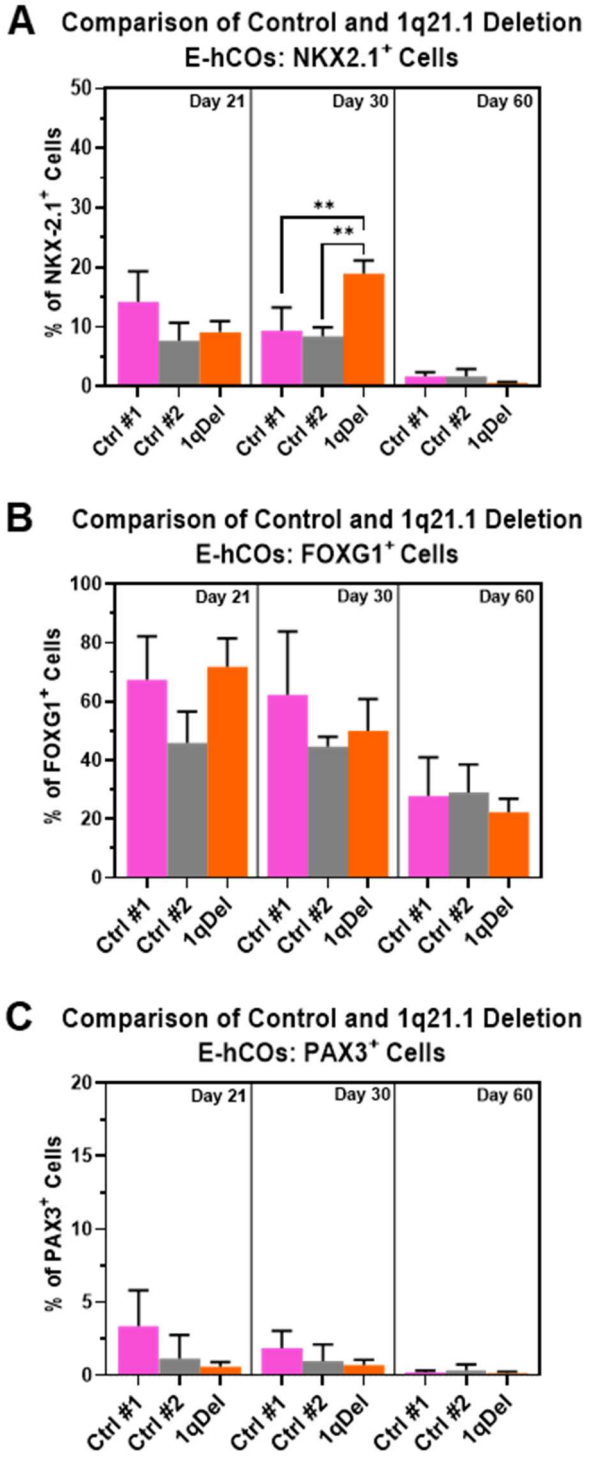

Figure 5.21: NKX2.1⁺ cells significantly overrepresented in Day 30 1qDel E-hCOs only; FOXG1⁺ and PAX3⁺ cell populations unchanged between Day 21 to Day 60 control and 1qDel E-hCOs.

A) Percentage of NKX2.1⁺/DAPI⁺ cells in Control #1, #2 and 1qDel E-hCOs across Day 21, Day 30 and Day 60. **B)** Percentage of FOXG1⁺/DAPI⁺ cells in Control #1, #2 and 1qDel E-hCOs across Day 21, Day 30 and Day 60. **C)** Percentage of PAX3⁺/DAPI⁺ cells in Control #1, #2 and 1qDel E-hCOs across Day 21, Day 30 and Day 60. Bar graphs present mean counts ±standard deviation. Statistical significance determined by One-Way ANOVA with Holm-Šídák's correction, (n≥3 independent hCOs); unlabelled=>0.05,**p=<0.005.

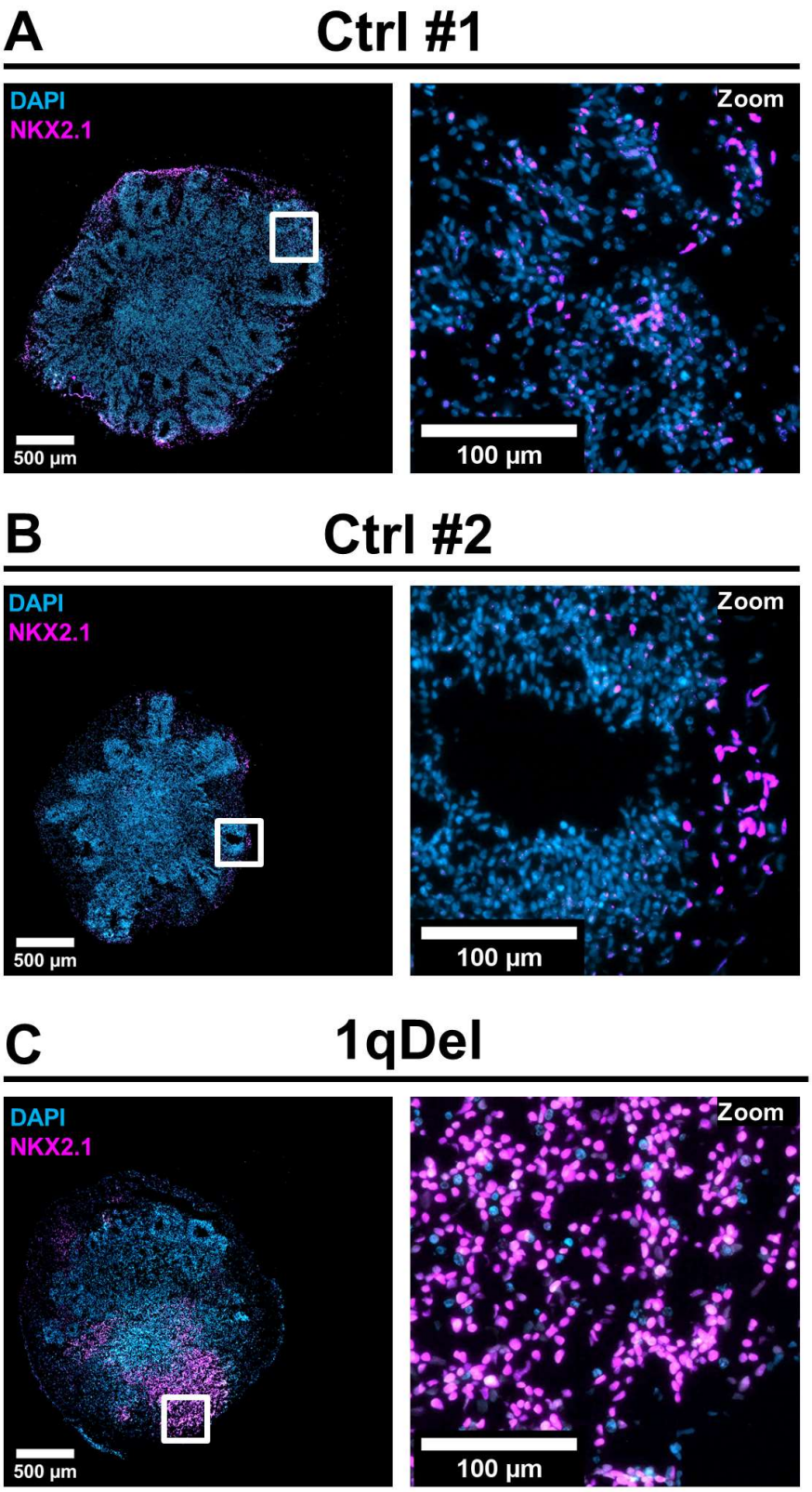

Figure 5.22: Visible greater representation of NKX2.1^{+} cells found in unorganised areas of Day 30 1qDel E-hCOs.

Fluorescent images of 10 µm slices of Control #1 **(A)**, #2 **(B)** and 1qDel **(C)** E-hCOs at Day 30. 20x magnification, with white box annotation referring to zoomed in 250 µm x 250 µm region of interest (ROI). Proteins identified by colour: NKX2.1 (pink), DAPI (blue). Scale bar = 500 µm (whole image) or 100 µm (zoomed in ROI).

5.3.9 Increased Transcription of GABA-ergic Presynaptic Markers Found in Neurogenic 1q21.1 Deletion Cortical Organoids

With an increase in MGE progenitors at Day 30, 1qDel E-hCOs were expected to have altered mature neuronal populations as well. Transcription of synaptic markers were not analysed until after anticipated onset of neuronal maturation, from Day 30 onwards. Only cell line-specific changes were reported for mature neuronal marker *MAP2* (Figure 5.23.A-B). Transcriptional analysis of pre- and postsynaptic markers illustrated an increase in presynaptic markers associated with GABA-ergic neurons, i.e., *SLC32A1*, *GAD1* and *GAD2*, in 1qDel E-hCOs at both Day 30 and Day 60, either significantly or by noticeable trends in gene expression (Figure 5.23.A-B). It was also of note that *SLC17A7* abundance was either significantly, or trended towards, a decrease at both timepoints in 1qDel E-hCOs (Figure 5.23.A-B). Transcription of postsynaptic NMDA or AMPA receptors (*GRIN1* and *GRIA1*, respectively) were unchanged at both timepoints, either due to cell line-specific variability skewing statistical conclusions or overall comparable mRNA abundance (Figure 5.23.A-B).

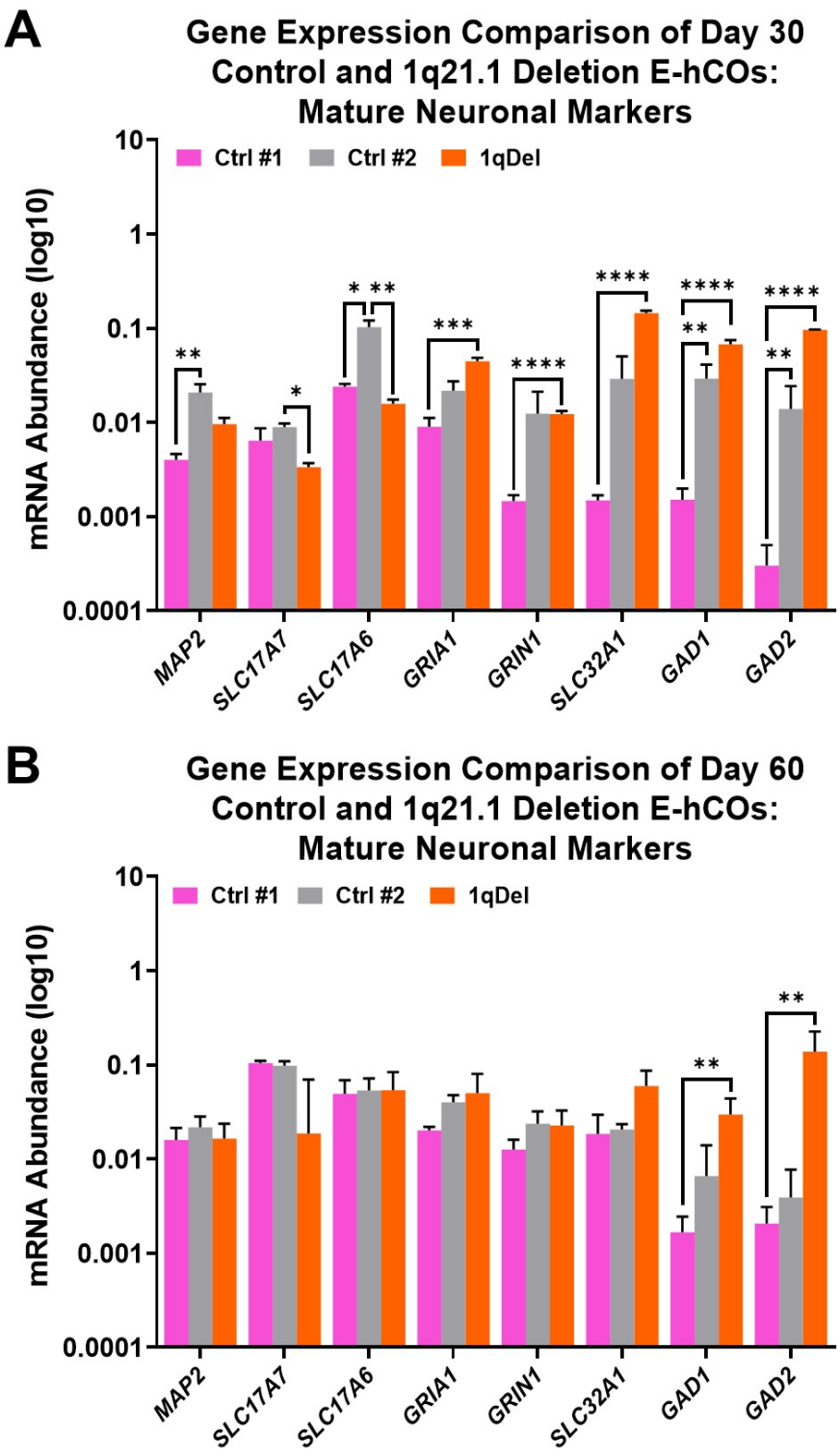

Figure 5.23: Consistent upregulation of presynaptic GABA-ergic markers was found in Day 30 and Day 60 1qDel E-hCOs.

Transcriptional analysis of Control #1, #2 and 1qDel E-hCOs' expression of mature neuronal markers at Day 30 **(A)** and Day 60 **(B)**. Data is presented as relative mRNA abundance ($2^{-\Delta CT}$, $\pm 2^{-CI}$), (n≥3 independent hCOs). Statistical analysis was conducted on dCTs using a two-way ANOVA with Geisser-Greenhouse correction with Holm-Šídák correction for post-hoc tests, unlabelled=>0.05, *p=<0.05, **p=<0.005, ***p=<0.0005, ****p=<0.0001.

5.4 Discussion

Neither 1qDel-associated microcephaly or SCZ has been examined from a cortical organoid perspective previously. Throughout the development of 1qDel E-hCOs, distinct phenotypes appeared at specific timepoints in relation to microcephaly and SCZ, predominantly those associated with the abnormal generation of NPCs, premature neuronal differentiation at Day 21 and E/I imbalance at Day 30 onwards. Using developmental pseudotime and 1q21.1 gene dosage as guides, identification of affected cell types and associated mechanisms in 1qDel E-hCOs could provide insight into the mechanisms attributing to the increased presentation of microcephaly and SCZ in 1qDel patients.

5.4.1 Patient-derived Induced Pluripotent Stem Cells are Primed to Produce Abnormal Neuroepithelial Cells, Contributing to Microcephaly in 1q21.1 Deletion Cortical Organoids

Reviewing the features of each timepoint in early 1qDel E-hCO differentiation aids in formulating a hypothesis as to the cause of microcephaly found in early developing 1qDel E-hCOs (Figure 5.2.B and 5.24). At the onset of 1qDel E-hCO differentiation (Day 0), there were substantial transcriptional changes to 1qDel hIPSCs, including upregulation of non-ectodermal markers (*TBXT* and *SOX17*), suggesting spontaneous differentiation (Figure 5.5.A, 5.6.A and 5.6.C). The microcephaly phenotype was initially observed in Day 1 1qDel E-EBs with worsening severity through to Day 11 (Figure 5.2.B). This observation was accompanied by reduced cell quantity in 1qDel E-EBs at Day 5 (Figure 5.6.D). By Day 11, 1qDel E-hCOs had the same features as Day 5 1qDel E-EBs, with the addition of downregulated *SOX2* and *PAX3* (Figure 5.E-F).

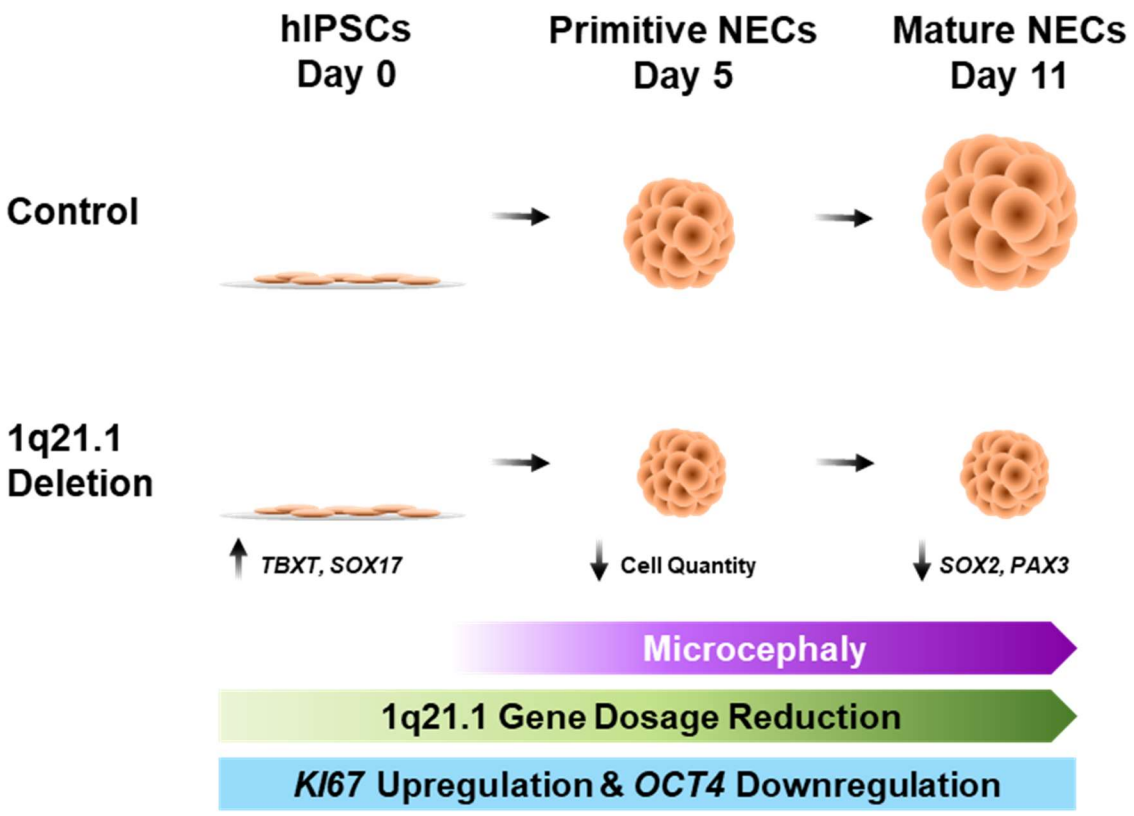

Figure 5.24: Schematic summary of results possibly contributing, or as a result of, the early onset of microcephaly in 1qDel samples.
Day 0 1qDel hIPSCs exhibited significant expression of mesodermal and endodermal markers. Day 5 1qDel E-EBs, constituting of primitive NECs, were substantially smaller than controls, with a reduced cell quantity. Day 11 1qDel E-hCOs, containing mature NECs, were also significantly smaller, with significantly less *SOX2* and *PAX3* expression. *KI67* upregulation and *OCT4* downregulation was consistent from Day 0 to Day 11, and 1q21.1 gene dosage reduced substantially at Day 5 and Day 11.

1q21.1 dosage was significantly affected by the transition from 2D to 3D culture and the induction of neuroectoderm. Only two of the four deleted 1q21.1 genes showed significant transcriptional downregulation in 1qDel hIPSCs; this increased at Day 5 and Day 11 to all four genes (*BCL9, PRKAB2, CHD1L* and *ACP6*) in 1qDel samples (Figure 5.4.A-D). Additionally, *OCT4* downregulation/*KI67* upregulation was consistent between Day 0 and Day 11 (Figure 5.5.C). When assessed as a collective, it is likely that there are a multitude of pathways, as well as individual factors, instigating or facilitating the early-born microcephalus phenotype of 1qDel E-hCOs. As such, each timepoint requires investigation to piece together what are likely causative players, and how best to assess such phenotypes in the future.

Beginning with 1qDel hIPSCs, 1q21.1 dosage of specific genes significantly deviated from controls. From the genes chosen from within the 1q21.1 locus for transcriptional analysis, only *CHD1L* and *ACP6* dosage was affected by the heterozygous deletion of 1q21.1 at the hIPSC stage (Figure 5.4.C-D). This pair of genes were consistently reduced over the first three timepoints, a temporal pattern only mirrored by two other genes: *KI67* and *OCT4*. The substantial reduction of *OCT4* expression to trace levels could have been sufficient to transition primitive NECs (Day 5 control E-EBs) into mature NECs (Day 11 control E-hCOs) (Figure 5.5.A-C). This transition would likely significantly increase the rate of cell proliferation (upregulation of *KI67*), as NECs' cell cycle is roughly half that of hIPSCs (~8 hours to 16-18 hours, respectively (Ghule *et al.*, 2011; Liu *et al.*, 2019)). Theoretically, an early transition to mature NECs could be an explanation for the changes in *KI67* and *OCT4* transcription that was observed in 1qDel hIPSCs and the E-hCO differentiation thereafter. However, at the hIPSC stage, transcription of *PAX6* was sufficiently low across all three cell lines, whilst naïve and universal stem cell markers of *KLF4, NANOG* and *SOX2* remain unchanged amongst control and 1qDel samples, with only cell line-specific variability as a cause for variation (Figure 5.5.A and 5.5.D). This would suggest that 1qDel hIPSCs are still pluripotent naïve stem cells prior to differentiation, despite the reduction in *OCT4* and increase in *KI67* expression, and therefore the "accelerated neuroectodermal differentiation" hypothesis should be rejected.

A more likely possibility as to what could have caused the consistent transcriptional repression of *OCT4* can be gleaned from looking at how *OCT4* is regulated. Stem cell factors, including *OCT4*, are hypomethylated in hIPSCs, but become silenced by hypermethylation as primitive NECs mature (Akamatsu *et al.*, 2009; Lee *et al.*, 2010), and reverting primitive NECs back to hIPSCs is possible when *OCT4* is demethylated (Lee *et al.*, 2010). However, investigations into the downstream effects of *OCT4* expression concluded that downregulation of *OCT4* caused a decrease in expression of DNA methyltransferase, thereby reducing the expression of cell cycle markers *p16* and *p21* in mesenchymal stem cells (Tsai *et al.*, 2012; Lu *et al.*, 2019). The reduction of *p16* and/or *p21* resulted in reduced proliferation and efficiency of targeted differentiation and increases in spontaneous differentiation. These results are supported by *OCT4* knockdown studies in human ESCs, which similarly reported that *OCT4* is necessary for suppressing spontaneous differentiation (Zhang *et al.*, 2014).

In contradiction to what would be expected given the reduced expression of *OCT4,* 1qDel hIPSCs' increased *KI67* transcription suggests elevated proliferation rather than reduced (Figure 5.6.C). Additionally, they exhibit hallmarks of spontaneous differentiation, although this is purely segregated to non-ectodermal lineages (Figure 5.5.A), with no significant changes in any ectodermal markers (*PAX6, NES*) (Figure 5.4.D). At present, it is not possible to determine the methylation state of *OCT4*, however, one of the aforementioned genes, *p21*, is a downstream target of both *OCT4* and *CHD1L*, of which both genes have been attributed to increased proliferation (Tsai *et al.*, 2012; Sun *et al.*, 2016; Lu *et al.*, 2019). CHD1L has also been shown to be involved with *OCT4* regulation as part of a pluripotency-regulating complex with PARP1. The CHD1L/PARP1 complex occupies the loci of stem cell factors including *OCT4*, and the reduction of CHD1L results in the blocking of PARP1 to binding to these loci, inducing chromatin compaction and, by extension, transcriptional repression of stem cell factors (Jiang *et al.*, 2015). The results of Jiang *et al.*, (2015) supported the hypothesis that the downregulation of *OCT4* observed in 1qDel hIPSCs and the developing E-hCOs was likely to be at least partially caused by the reduced dosage of *CHD1L* (Figure 5.4.C). In addition, this evidence suggests that the *CHD1L* dosage reduction was also likely responsible for the observed elements of spontaneous differentiation in non-ectodermal lineages (Figure 5.6.A).

However, it would be expected that other stem cell factors, such as *NANOG* or *SOX2*, would be affected similarly to *OCT4* in 1qDel hIPSCs based on the results of the aforementioned study and the autoregulatory feedback loop between the three transcription factors (Navarro *et al.*, 2012; Merino *et al.*, 2014; Swaidan *et al.*, 2020). It would also be expected that the downregulation of *OCT4*, caused by dosage reduction in *CHD1L*, would result in reduced hIPSC proliferation, although this is the opposite of what was suggested by the elevated *KI67* transcription found in 1qDel hIPSCs (Figure 5.6.C). On the other hand, transcriptional analysis does not yield absolute answers with regards to the proliferative activity of 1qDel hIPSCs and developing E-hCOs, as later timepoints show that the increased *KI67* transcription did not translate to greater $KI67^{+}$ cell abundance (Figure 5.7.A-B). Similarly, it is also unknown if the transcriptional repression of *OCT4* in 1qDel hIPSCs results in reduced translation. However, the sole reduction of *OCT4* expression may not be detrimental to 1qDel E-hCOs' development, as the conditional inactivation of *OCT4* between E9.5-E15.5 has

negligible effects on murine brain development, including neural progenitor activity in the adult mouse cortex (Lengner *et al.*, 2007). *OCT4* is also not necessary for the proliferation or maintenance of mature NECs (Akamatsu *et al.*, 2009). If *OCT4* was the only gene affected by 1qDel throughout the early timepoints of E-hCO differentiation 1qDel E-hCOs could develop as controls, however it is not the only affected gene.

As CHD1L knockdown is known to reduce human ES cells' capability to differentiate into NECs, as well as playing a possible role in *PAX6* regulation (Dou *et al.*, 2017), it was anticipated that the differentiation of hIPSCs into primitive and mature NECs would be detrimentally affected in 1qDel samples. Transcriptional analysis did not support this hypothesis, as Day 5 1qDel E-EBs shared the same differential transcription of genes as 1qDel hIPSCs (Figure 5.5.B and 5.5.E). 1qDel E-EBs no longer presented spontaneous differentiation from non-ectodermal lineages, but it had significantly fewer cells per EB (Figure 5.6.B-D). This coincided with the onset of the microcephaly (Figure 5.2.B). Although the reduction in cell quantity in Day 5 1qDel E-EBs could point to a miscalculated translation of the increased *KI67* transcription (Figure 5.6.C), it is possible that a reduction in cells was a repercussion of *CHD1L* dosage reduction, as *CHD1L* is considered anti-apoptotic (Sun *et al.*, 2016; Wang *et al.*, 2021). In this context, it could be suggested that less CHD1L would result in more apoptosis. However, the cell quantity was not normalised to the size of the EB, and therefore the reduced quantity could be a reflection of the reduced size, not explicitly a reduction in cell density or increased apoptosis. Conversely to *CHD1L*, no evidence was found that could tie *ACP6* to any phenotypes observed in 1qDel samples, however the transition from hIPSCs to primitive and mature NECs was also accompanied with dosage reduction of two other 1q21.1 genes: *PRKAB2* and *BCL9* (Figure 5.4.A-B).

There is a common functionality between *BCL9*, *CHD1L* and *PRKAB2*; when each gene's expression is reduced, the result is downregulated proliferation and/or upregulated apoptosis (Dasgupta and Milbrandt, 2009; Chen *et al.*, 2018; Nagy *et al.*, 2018; Panja *et al.*, 2021; Orikasa *et al.*, 2022). With this in mind, it is reasonable to suggest that the combined dosage reduction of *BCL9*, *CHD1L* and *PRKAB2* induces significant disruption to cell activity and, by extension, the initiation of the microcephaly phenotype, observed in 1qDel E-EBs (Figure 5.2.B). Extending beyond Day 5, these three genes, alongside *ACP6*, continued to be significantly reduced at Day 11 in 1qDel E-hCOs, and therefore are likely

contributing to its ceased growth. However, there are a number of additional factors identified in Day 11 1qDel E-hCOs that suggest how this balance of proliferation and apoptosis halts the growth of 1qDel E-hCOs during the maturing NEC stage.

As previous research has illustrated, mature NEC aggregates are capable of generating neural rosettes, or lumens, with a significant vacuous internal volume (Beghin *et al.*, 2022). This was also observed in high magnification of bright field imaging of control Day 11 E-hCOs (Figure 5.2.A). These rosettes are analogous to the neural rosettes observed in 2D *in vitro* neuronal culture, and therefore have similar features, including actin bundling, tight junctions, adherens junctions and cellular morphology changes (Fedorova *et al.*, 2019; Benito-Kwiecinski *et al.*, 2021; Beghin *et al.*, 2022). However, in the case of Day 11 1qDel E-hCOs, these features are likely dysregulated due to the dosage reduction of *BCL9*, *CHD1L* and *PRKAB2*; all three genes are associated to some degree with one target, β-catenin (Brack *et al.*, 2009; Ziegler *et al.*, 2020; Xiong *et al.*, 2021).

β-catenin is a core component necessary for creating the belt-like adherens junctions necessary for neural rosette formation (Hříbková *et al.*, 2018; Fedorova *et al.*, 2019). The reduction of the 1q21.1 genes in question may result in either dampened overall β-catenin production (reduction in *PRKAB2*) or poor β-catenin localisation (reduction in *BCL9*) (Ziegler *et al.*, 2020; Orikasa *et al.*, 2022). It is not clear exactly how *CHD1L* interacts with β-catenin, as it varies between tumour cell types and has not been tested in hIPSC or neuronal cultures (Xiong *et al.*, 2021). However, in 1qDel samples, the abnormal control of β-catenin could be coupled with the previously suggested imbalance of proliferation and apoptosis, also caused by the dosage reduction of the aforementioned 1q21.1 genes. The cumulative effect of poor adherens junction formation failing to establish lumens and abnormal cell apoptosis and proliferation could result in a reduction in overall lumen size. Excessive apoptosis, repressed proliferation and poorly formed/shrunken lumens have proven to result in small NEC aggregates (Dang *et al.*, 2016; Garcez *et al.*, 2016, 2017; Sun *et al.*, 2020; Benito-Kwiecinski *et al.*, 2021; Krenn *et al.*, 2021), and so any combination of the three could be the cause of the halted growth observed in Day 11 1qDel E-hCO.

Two additional genes were differentially expressed specifically at Day 11 in 1qDel E-hCOs that coincided with halted growth: *SOX2* and *PAX3*. *SOX2* has a

multitude of functions in early development, namely as a regulator of pluripotency and NE/neuroepithelial differentiation (Hutton and Pevny, 2011; Merino *et al.*, 2014). However, in the context of 1qDel samples, only at Day 11 was there a significant downregulation of *SOX2* transcription (Figure 5.5.C). This would suggest that *SOX2* expression was only affected in mature NECs, not stem cells or primitive NECs. However, there is no difference in the quantity of SOX2 generated in primitive and mature NECs (Shin *et al.*, 2006). An explanation for this downregulation may not stem from the type of cell being affected, but could be as a result of the dosage reduction of 1q21.1 genes. Only one chosen 1q21.1 gene substantially changed between Day 5 and Day 11 in 1qDel samples, *BCL9*, which is reduced considerably more at Day 11 (Figure 5.4.A). There is a positive correlation in the degradation of SOX2 and β-catenin during neuronal differentiation (Kuwabara *et al.*, 2009), and there is evidence of a regulatory feedback loop between canonical Wnt signalling and SOX2 in maintaining self-replication of neural progenitor in *in vivo* models (Agathocleous *et al.*, 2009). An exacerbated reduction of *BCL9* transcription at Day 11 in 1qDel E-hCOs could lead to reduced β-catenin activity, thereby detrimentally affecting *SOX2* transcription only in Day 11 1qDel E-hCOs. This could be a contributory factor to the halting of Day 11 1qDel E-hCO growth, as reduced SOX2 has contributed to other microcephalus neurospheres (Garcez *et al.*, 2017).

Accompanying this, Day 11 1qDel E-hCOs had trace levels of *PAX3* transcription (Figure 5.5.F). *PAX3* is associated with neuroectodermal plate border allocation (Xue *et al.*, 2018) and NTC (Pani, Horal and Loeken, 2002; Wang *et al.*, 2017). The two developmental processes are featured in a unique way in E-hCOs in the form of neural rosettes, and therefore there is a requirement for *PAX3* as evidenced by its significant increase after EB formation (Figure 5.5.D-F). Although present in Day 5 E-EBs, the absence of *PAX3* expression in Day 11 1qDel E-hCOs suggests that there was a significant disruption to morphological rearrangement when mature NECs were arranging into neural rosettes. This could be caused by two factors: disrupted β-catenin-associated adherens junction proteins unable to form the lumen of the neural rosette and/or abnormal apoptosis resulting in poor neural rosette organisation. Firstly, *PAX3* is a downstream target for the Wnt pathway in a β-catenin-dependent manner during NTC and in glioma cells (Zhao *et al.*, 2014; Liang *et al.*, 2019; Palmer *et al.*, 2021). As proposed for reduced *SOX2* expression in Day 11 1qDel E-hCOs, the exacerbated reduction of

Wnt pathway activity could cause a reduction in adherens junctions being formed. This could result in smaller/fewer neural rosettes and an overall smaller E-hCO. The severity of this result would be amplified if the suggested abnormal apoptosis, also as a result of reduced β-catenin activity, could be disrupting the requirement for *PAX3; PAX3* functions as an apoptotic regulator, specific to NTC (Wang *et al.*, 2017). Assessed together, the additional decline in transcription of two key NEC markers indicate that the repression of the Wnt pathway could become more extreme over exogenous NE induction, resulting in the halting of growth between Day 5 and Day 11 in 1qDel E-hCOs.

Although *BCL9, CHD1L* and *PRKAB2* affect different pathways, the Wnt pathway is a shared target/regulator of these genes' activities, and is therefore likely to be vulnerable to the 1q21.1 genes' reduced dosage at multiple timepoints. However, there are other pathways that could be contributing to the 1qDel microcephalus E-hCO phenotype. Certain 1q21.1 genes are Wnt-independent, but were not chosen for qPCR analysis due to their paralogous nature, i.e. the *NOTCH2NL* and *NBPF* paralogs. These paralogs have been directly attributed to human-specific cortical development, particularly in the first trimester, and are found to be expressed in abundance in neural progenitors (Dumas *et al.*, 2012; Fiddes *et al.*, 2018, 2019; Florio *et al.*, 2018; Suzuki *et al.*, 2018). Based on the known location of the 1qDel in the 1qDel patient hIPSC line, it was expected that one allele of the NBPF paralogs, *NBPF11/12/14*, as well as one of two NOTCH2NL paralogs (*NOTCH2NLA*), was deleted. It is important to note what impact these two groups of genes could have throughout early E-hCO differentiation to assess if they were likely contributing to the microcephalus phenotype of 1qDel samples.

The NBPF paralogs, NBPF11/12/14, have little information as to their function in cortical development, but are expressed in the neocortex, are human-specific, and that lacking a copy number of these paralogs positively correlates with severity of microcephaly in 1qDel patients (Popesco *et al.*, 2006; Dumas *et al.*, 2012). Similarly, there is minimal information about the NOTCH2NL paralogs and their role in NOTCH regulation during hIPSC/NEC development, as NOTCH2NLA and NOTCH2NLB have been predominantly assessed for their supportive role in RG differentiation (Fiddes *et al.*, 2018; Suzuki *et al.*, 2018). There is, however, evidence that the deletion of *NOTCH2NLA* induces microcephalus phenotypes during NEC development in human ESC-based

cerebral organoids, although this initial observation was not expanded upon to date (Fiddes *et al.*, 2018). Although little else is known of these paralogs' involvement with NECs, it is known that the NOTCH2NL paralogs have been shown to enhance NOTCH receptor activation, including NOTCH1 and NOTCH2 (Fiddes *et al.*, 2018). The NOTCH pathway is readily active in hIPSCs to maintain pluripotency and then gradually decreases over NEC differentiation (Chen *et al.*, 2014), oscillating in expression over the first trimester and increasing as NECs transition to RGs (Eze *et al.*, 2021). Conversely, NOTCH1 expression has also been observed consistently in primitive NEC aggregates (Hitoshi *et al.*, 2004) and overstimulation of the NOTCH pathway is associated with increased production of NPCs from stem cells (Androutsellis-Theotokis *et al.*, 2006; Salewski *et al.*, 2013). Based on these studies, the $NOTCH^{low}$ environment would likely affect 1qDel E-EBs/E-hCOs' transition from hIPSCs to NECs, however how exactly is unclear.

NOTCH has also been known to work in collaboration with the Wnt pathway, targeting the same cells and following relatively similar expression profiles during early human neurodevelopment (Eze *et al.*, 2021). This would add supporting information to what could be the causative pathways for 1qDel samples' early microcephaly. It is likely that *NOTCH2NLA* would be required for NOTCH pathway regulation from the onset of E-hCO differentiation and therefore the dosage reduction would detrimentally affect 1qDel hIPSC pluripotency, as well as 1qDel E-hCO development, based on previous studies' results (Fiddes *et al.*, 2018). The revised hypothesis for 1qDel E-hCO microcephaly would be that of a dual downregulation of both the Wnt and NOTCH pathways in 1qDel samples. Unfortunately, there is little evidence in mammalian models to support or deny this hypothesis. In addition, there are currently no known examples of the four differentially-expressed 1q21.1 genes in 1qDel samples, *ACP6*, *BCL9*, *CHD1L* and *PRKAB2*, having a direct association with the NOTCH pathway. In order to determine if and how the NOTCH pathway is affected during 1qDel E-hCO differentiation, and whether there is an interaction with Wnt mediators, more sensitive transcriptional and translational network analysis is necessary to ascertain the dosage reduction of each gene over time.

In summation, the heterozygous deletion of the 1q21.1 region has considerable impact on the pluripotency, proliferation, apoptosis and differentiation of both hIPSCs and developing E-hCOs. The developmental trajectory of 1qDel E-hCOs was significantly negatively affected from the onset of E-hCO differentiation,

with microcephaly becoming evident from EB formation, graduating to a suppression of growth as the EB transitioned into a mature NEC aggregate (Figure 5.2.B). Dosage of genes within the 1q21.1 region gradually reduced over this timeframe, notably those associated with the Wnt pathway i.e., *BCL9*, *CHD1L* and *PRKAB2*. Disruptions to Wnt/β-catenin activity were believed to be responsible for both the consistent issues in 1qDel samples from the onset of E-hCO differentiation (*OCT4* downregulation/*KI67* upregulation), as well as the accruing issues unique to each timepoint, e.g. increased *TBXT* and *SOX17* expression at Day 0 and *SOX2* and *PAX3* downregulation at Day 11. It was also believed that NOTCH downregulation, caused by *NOTCH2NLA* deletion, could have contributed to these results, although this will require further investigation to confirm. It was expected that by Day 11, 1qDel E-hCOs were likely to have a reduced cell density, disrupted apoptosis and/or proliferation, and poor organisation of neural rosettes due to dysfunctional adherens junction proteins. Substantial further investigation is necessary to confirm this dual-mechanism, microcephaly-inducing hypothesis. However, these initial results do provide insight into the mechanisms that are vulnerable to disruption of genes from the 1q21.1 locus when modelled in hIPSCs and NECs. It also informs possible repercussions for the cell types that proceed them, such as RGs, IPs and neurons.

5.4.2 Aberrant Neuroepithelial Cells Beget Aberrant Radial Glia that Prematurely Differentiate into Neurons in Microcephalus 1q21.1 Deletion Cortical Organoids

Although 1qDel E-hCOs continued to be microcephalus throughout the ND stage (Day 11 to Day 21), the microcephaly phenotype dissipated after Day 21 in 1qDel E-hCOs (Figure 5.2.B and 5.3.B). As a turning point for both microcephaly recovery and the onset of neurogenesis, Day 21 was investigated substantially to ascertain what was contributing to the microcephaly. The information gleaned from this timepoint could shed light on the possible causes of early-born microcephaly, as well as work as a benchmark to determine the recovery of microcephaly at later timepoints (Figure 5.25).

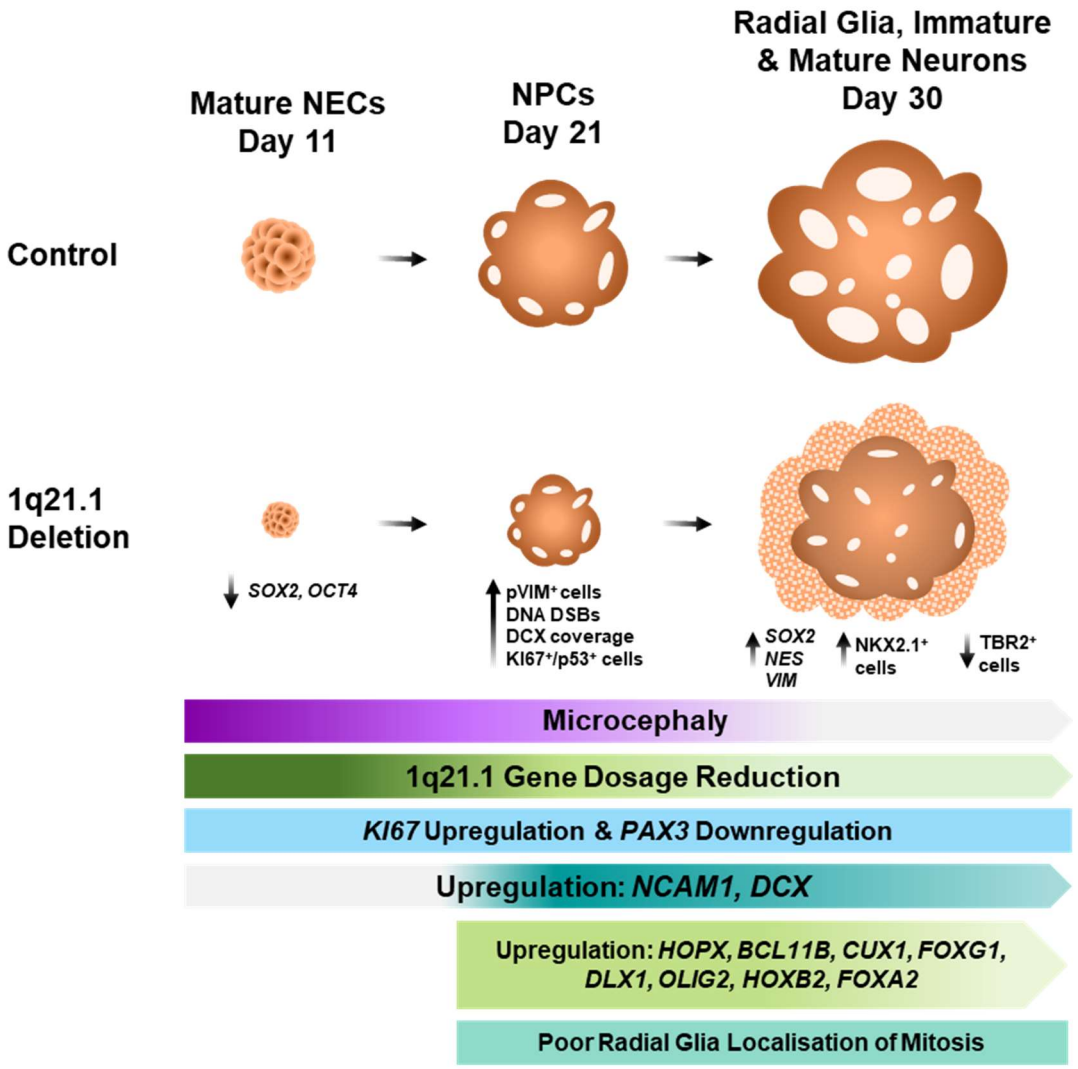

Figure 5.25: Schematic summary of results monitoring from the peak (Day 11) to the resolution (Day 30) of microcephaly in 1qDel E-hCOs.

Day 11 1qDel E-hCOs containing mature NECs were significantly smaller, with significantly less SOX2 and *OCT4* expression. At Day 21, 1qDel E-hCOs were still microcephalus and displayed signs of abnormal cell cycle and arrest, particularly with M phase. Accompanying this, there was a greater representation of immature neurons, despite this stage representing NPCs only in control E-hCOs. By Day 30, 1qDel E-hCOs no longer exhibited the aforementioned Day 21-specific phenotypes, including microcephaly. Instead, Day 30 1qDel E-hCOs had substantially smaller lumens, generated more NKX2.1^{+} cells with fewer TBR2^{+} IPs, and had greater transcriptional representation of radial glia. Consistent cross-timepoint features of 1qDel E-hCOs include: *KI67* upregulation and *PAX3* downregulation (Day 11 to Day 30), upregulation of brain region and cortical layer markers (Day 21 to Day 30) and poor M phase radial glia localisation to the apical edge of lumens (Day 21 to Day 30). Lastly, 1q21.1 gene dosage reduction became less severe after Day 11.

Theoretically, Day 21 is a pre-neurogenic timepoint due to its lack of RA to support neuronal production. As of yet, NECs would not have transitioned into RGs, as having the capacity to produce neurons is one of the key distinguishing features between the two types of NPCs (Subramanian *et al.*, 2017; Benito-Kwiecinski *et al.*, 2021; Eze *et al.*, 2021). However, substantial increases in DCX coverage in Day 21 1qDel E-hCOs would suggest this transition has already occurred (Figure 5.15 and 5.16). It would therefore be informative to assess when and why this transition has occurred earlier than anticipated, and how this would relate to prospective causes of 1qDel-associated microcephaly.

Firstly, it is plausible that there is an association between 1q21.1 gene dosage and NPC identity, as the relative difference between control and 1qDel E-hCOs' transcription of 1q21.1 genes shrinks at Day 21 compared to Day 11 despite the continuing microcephaly phenotype (Figure 5.2.B and 5.4.A-D). One example of such a relationship is *SOX2* and *BCL9*. *SOX2* was only significantly downregulated at Day 11, when *BCL9* was at its lowest relative expression compared to control E-hCOs (Figure 5.4.A and 5.5.C). This scenario is unlikely to be instigated by other 1q21.1 genes, such as *ACP6*, *CHD1L* or *PRKAB2*, as these genes had similar relative dosage reduction across more timepoints than Day 11 alone with no accompanying change of *SOX2* transcription (Figure 5.4.A-D, 5.5.A-B, 5.19.A and 5.19.C). The change in 1q21.1 gene dosage across Day 11 and Day 21 is therefore possibly related to the requirement of the Wnt pathway (represented by *BCL9*) for the type of NPC present; for example, NECs have low dependence on the Wnt pathway compared to RGs *in vivo* (Eze *et al.*, 2021). By transitioning into RGs early, Day 21 1qDel E-hCOs would require increased activation of the Wnt pathway, more so than its Day 21 control E-hCO counterparts that were still predominantly populated by NECs; this is one interpretation of the diminishing 1q21.1 gene dosage reduction between Day 11 and Day 21 1qDel E-hCOs (Figure 5.4.A-D). If the early RG transition hypothesis is true, it is therefore necessary to avoid assuming NECs and RGs exhibit microcephaly for the same reason, as NECs and RGs share, but also diverge, on specific features (Section 1.1.4), some of which may be key to understanding 1qDel E-hCO microcephaly.

The discrepancy between 1qDel NECs and RGs was substantiated when using the hypotheses speculated for Day 11 1qDel E-hCOs' microcephaly as starting points for investigating Day 21 1qDel E-hCOs. Firstly, it was suggested

that overall proliferation was abnormal in Day 11 1qDel E-hCOs. Similarly to Day 0-11, Day 21-30 1qDel E-hCOs shared the upregulated of *KI67* transcription (Figure 5.7.A). However, from Day 21 to Day 60, 1qDel E-hCOs had similar overall and NPC-specific quantities of KI67$^+$ cells to control E-hCOs (Figure 5.7.B-C). It was therefore clear that a reduction in the population of cycling cells was not contributing to Day 21 1qDel E-hCO microcephaly, despite upregulation of *KI67*. The alternative hypothesis postulated as a cause for Day 11 1qDel E-hCO microcephaly was heightened overall apoptosis. Again, this theory did not apply to Day 21-60 1qDel E-hCOs, as there was no definitive change in total or NPC-specific CC3-dependent apoptosis (Figure 5.7.D-E). In conjunction with no significant changes to quantity of proliferating cells (KI67$^+$ cells) (Figure 5.7.B), the lack of change in cell density of the three cell lines across the three timepoints was to be expected (Figure 5.7.F). This did not necessarily contradict with the reduced cell quantity observed in Day 5 1qDel E-EBs (Figure 5.6.D), as the cell count was not normalised to size and therefore could be a reflection of the reduced overall size of the EB, rather than a reduction in overall cell density.

Finally, the lumen disorganisation hypothesis of Day 5 and Day 11 1qDel E-hCOs was only partially observed in Day 21 1qDel E-hCOs. Lumen size and quantity were unchanged in Day 21 1qDel E-hCOs, as was *SOX2* transcription (Figure 5.11 and 5.19.A), although the Day 11 1qDel E-hCO phenotype of reduced *PAX3* transcription continued at Day 21 and Day 30, supported by a trend of decreased PAX3$^+$ cells (Figure 5.5.F, 5.20.D-E and 5.22.C). A reduction of PAX3 would likely affect the VZ and lumen structure, as PAX3 is associated with NTC (Wang *et al.*, 2017) and organising lateral ventricles (Zhou and Conway, 2016). Although lumen size and number were unaffected, on observation, the depth of striated neuroepithelium was visibly less in Day 21 1qDel E-hCOs (Figure 5.8.C), although SOX2 quantification was not possible at Day 21 due to poor ICC clarity. This would suggest that Day 21 1qDel E-hCOs had disrupted neuroepithelium to a degree. However, this is not suggested by *NES* and *VIM* expression (Figure 5.13.A). Furthermore, it is unlikely that the β-catenin-regulated adherens junctions of Day 21 1qDel E-hCOs are as severely affected as Day 5 and Day 11 1qDel samples, as *BCL9*, *CHD1L* and *PRKAB2* have all substantially increased in expression in Day 21 1qDel E-hCOs compared to controls, although *BCL9* and *PRKAB2* are still significantly lower (Figure 5.4.A-C). This highlights that, as

predicted, some of the results and hypotheses surrounding Day 5-11 1qDel E-hCOs are not transferable to Day 21, possibly due to the differences in NPC type.

With the knowledge that the Day 5-11 1qDel E-hCO hypotheses do not provide substantial insight into the cause of Day 21 1qDel E-hCOs' microcephaly, a fresh approach was taken, investigating the excessive immature neuron production observed in Day 21 1qDel E-hCOs (Figure 5.15.G and 5.16.A-B). This transition would be expected in a $NOTCH^{low}$ environment as a result of RA exposure (Janesick, Wu and Blumberg, 2015; Haushalter *et al.*, 2017), and this therefore would imply that the dosage of *NOTCH2NLA* was reduced significantly at Day 21. This could not be confirmed with transcriptional data collected from qPCR analysis due to the paralogous nature of *NOTCH2NLA*. Instead, supporting evidence was found in previous studies that investigated the *NOTCH2NLA/B* paralogs. When *NOTCH2NLB* is overexpressed in *in vitro* neurons, there is an increase in symmetrical NPC proliferation but also more cells exiting the cell-cycle; there was no effect on cell cycle phase length (Suzuki *et al.*, 2018). In contrast, deletion of *NOTCH2NLA/B* causes early-born microcephaly, but also increased CTIP2 accumulation per cell and accelerated differentiation and maturation of neurons in human ESC-derived cerebral organoids (Fiddes *et al.*, 2018). From a broader perspective, multiple microcephaly-presenting cerebral organoids have illustrated shifted asymmetric/symmetric RG division ratio in favour of neurogenic asymmetric division (Lancaster *et al.*, 2013; Bershteyn *et al.*, 2017; Iefremova *et al.*, 2017; Zhang *et al.*, 2019). Furthermore, certain SCZ patient-derived cerebral organoids have also exhibited preference to early neurogenesis (Sawada *et al.*, 2020). These studies, particularly those of Fiddes *et al.*, (2018), are a close representation of Day 21 1qDel E-hCOs, supporting the hypothesis of an early NEC-to-RG transition, as the observed neuronal production would require asymmetrically dividing RGs.

To better understand the characteristics of the early RG population in Day 21 1qDel E-hCOs, more detailed investigations were undertaken. Both NECs and RGs undergo apical-basal orientated, interkinetic nuclear migration, however, 1qDel E-hCOs consistently have fewer M phase NPCs anchored to the apical edge of lumens (Figure 5.14.B). Furthermore, significantly more $pVIM^{+}$ M phase NPCs were found in Day 21 1qDel E-hCOs, specifically (Figure 5.14.A). Recent cerebral organoids studies have illustrated that modified cell cycle phase length can be a phenotype of microcephaly, such as either increased or decreased

numbers of cells in M phase (Zhang *et al.*, 2019; Wang *et al.*, 2020); no such observation has been reported in SCZ-presenting cerebral organoids currently. One hypothesis was that the NPCs were arresting in M phase, therefore extending it. Coincidentally, substantially more $p53^{+}$ cycling ($KI67^{+}$) cells were found in Day 21 1qDel E-hCOs than controls (Figure 5.14.C). APD was used to normalise $KI67^{+}/p53^{+}$ cell count as it was observed that p53 stained both live and dead (pyknotic) nuclei, and therefore it would be inaccurate to use the post-hoc apoptosis modification used in other live cell ICC quantification. Although there was a lack of evidence to suggest that cell cycle arrest was occurring in M phase, despite increases in both M phase cells and cell cycle arrests coinciding, it was expected that this cell cycle arrest would cause significant cell stress. Despite CC3-associated apoptosis remaining unchanged (Figure 5.7.D), the number of DNA DSBs were found to be significantly higher at Day 21 in 1qDel E-hCOs (Figure 5.14.D). This result is in keeping with the well-known association of p53 activation with cell cycle arrest in response to cell stress, such as DNA DSBs (Tedeschi and Di Giovanni, 2009). As evidenced here, Day 21 1qDel E-hCOs have a cluster of timepoint-specific outcomes that could be contributing to the observed microcephaly, with DNA DSBs possibly linking these features together.

There are a variety of ways DNA DSBs could be induced in 1qDel E-hCOs, although DNA DSBs are a natural part of neurodevelopment and can be found in clusters on genes associated with neural cell adhesion and synaptogenesis (Wei *et al.*, 2016). Endogenous factors such as oxidative stress can influence the formation of these DNA DSBs,; inhibition of *PRKAB2*-regulated AMPK activity can induce oxidative stress-based DNA damage during M phase for mouse zygotic cells for example (He *et al.*, 2020). Additionally, *in vivo* models under excessive oxidative stress have a significant increase in aRG pHH3 activity in the developing dorsal forebrain, of which did not constitute in increased apoptosis, paralleling what was observed in Day 21 1qDel E-hCOs (Chui *et al.*, 2020). These two studies suggest a direct link between the Day 21-specific features of increased M phase cells and DNA DSBs in 1qDel E-hCOs (Figure 5.14.A and 5.14.D). However, oxidative stress intensifies in the VZ during development (Chui *et al.*, 2020) and Day 21 was the only timepoint with excessive DNA DSBs. It would also be expected that if 1qDel E-hCOs were vulnerable to oxidative stress this would exacerbate during maturation due to the cellular stress of the hCO model itself (Bhaduri *et al.*, 2020).

Instead, an alternative stressor may be causing this timepoint-specific issue, such as DNA replication stress, whereby cells can accumulate DNA DSBs due to altered progression of DNA synthesis (reviewed by Zeman and Cimprich, (2014)). The unprecedented transition from NECs to RGs in Day 21 1qDel E-hCOs would likely induce DNA replication stress as asymmetric and symmetric division greatly vary in cell cycle dynamics; S phase is four times longer in symmetric RG divisions than asymmetric (Arai *et al.*, 2011). Variabilities in cell cycle dynamics have also been found to be key elements of NDD pathologies. DNA DSBs have been found alongside increased asymmetric division of RGs in microcephalus cerebral organoids (Zhang *et al.*, 2019), whilst autistic patient-derived NPCs experience DNA replication stress by progressing quickly through S phase, resulting in poor adherens junction formation, abnormal cell adhesion, poor apical-basal polarity of NPCs and DNA DSBs (Wang *et al.*, 2020); all of these features are either hypothesised or observed in Day 21 1qDel E-hCO.

How the 1q21.1 genes could influence DNA replication in NPCs is unclear; the NOTCH pathway is expected to be underactive in 1qDel E-hCOs, but there have been discrepancies between research models as to how NOTCH can affect the cell cycle prior to neurogenesis (De Blasio *et al.*, 2019; Zhou *et al.*, 2020). What is known, however, is that NOTCH maintains RG adhesion and so its suppression results in faulty interkinetic nuclear migration (Li *et al.*, 2008; Jiang *et al.*, 2021), a phenotype consistently observed in 1qDel E-hCOs and likely contributing to abnormal cell cycle features as a result (Figure 5.14.B). Furthermore, previous studies have shown that RA-deficient neurogenesis, as well as transitioning to asymmetric divisions, could result in the observed increase in DNA replication stress (Haushalter *et al.*, 2017; Zhang *et al.*, 2019).

On the other hand, downregulation of the Wnt pathway could repress innate cellular responses to DNA damage, as p53 and β-catenin act in a positive feedback loop upon DNA damage, activating DNA damage response machinery once β-catenin is overexpressed (Karimaian *et al.*, 2017). This is in contradiction of what is observed, as p53-mediated arrest increased in cycling cells of Day 21 1qDel E-hCOs, likely in response to the elevated DNA DSBs, despite underexpressed β-catenin as the Wnt pathway was still significantly affected by 1qDel (Figure 5.4.A-C and 5.14.C-D). However, repression of Wnt is known to encourage NPCs to retain forebrain identity and exit the cell cycle as neurons (Moya *et al.*, 2014) and so could be directly, or indirectly, involved in Day 21 1qDel

E-hCOs' accelerated neuron generation (Figure 5.15 and 5.16). Despite these discrepancies, DNA replication stress was still considered the most likely source of DNA DSBs due to the context of early RG transition and accelerated neurogenesis observed in Day 21 1qDel E-hCOs (Figure 5.15 and 5.16).

As proposed, DNA DSBs link the multiple Day 21-specific phenotypes into a feedback loop, herein termed the DSB/p53/M phase cascade. Beginning with NOTCH2NL-influenced reduction in NOTCH signalling, NECs transition to RGs that undergo asymmetric cell division in Day 21 1qDel E-hCOs. As a result, this could be instigating DNA replication stress, shown as $TUNEL^+$ cells (Figure 5.14.D), that prompts p53 to induce transient cell cycle arrest, possibly extending M phase temporarily (Figure 5.14.A and 5.14.C); permanent cell cycle arrest would likely induce cell death (Chen *et al.*, 2014). Mitotic delay has been found to increase DNA damage response in the form of γH2AX aggregation, as well as increase neuronal differentiation from NPCs, relative to p53-mediation which induces apoptosis (Pilaz *et al.*, 2016). If M phase was extended in Day 21 1qDel E-hCOs as a result of DNA DSB-related cell cycle arrest, this could feed back into the increase in immature neuron production, as well as increase the number of DNA DSBs (Pilaz *et al.*, 2016). However, an extension of M phase and cell cycle arrest did not cause apoptosis in Day 21 1qDel E-hCOs (Figure 5.7.D). Elongated M phase without apoptotic changes has been seen as features in other models of microcephaly (Ito *et al.*, 2015), as has altered cell cycles (Zeman and Cimprich, 2014). Increased quantity of M phase cells has also been observed in microcephalus cerebral organoids that shift to neurogenic differentiation, although this does come at the cost of greater apoptosis (Zhang *et al.*, 2019). Upon review, certain facets of the DSB/p53/M phase cascade hypothesis are not clear with current 1qDel E-hCO results and will require significantly greater investigation to confirm, although this is an evidence-based foundation for future research.

The results presented here suggest an overlapping set of dysfunctional attributes in Day 21 1qDel E-hCOs' NPCs, that reduce the NPC pool in favour of early neurogenesis, resulting in the observed microcephaly phenotype (Figure 5.26). The hypothesised faulty processes can be attributed to 1qDel through the repression of the Wnt and/or NOTCH pathways (Figure 5.26). Although these two signalling pathways are also associated to the proposed microcephaly hypothesis of Day 5-11 1qDel E-hCOs, the two hypotheses are distinctly different. Day 21 1qDel E-hCOs do not exhibit heightened apoptosis, shrunken lumens or reduced

proliferation. Instead, the faulty cell cycle of Day 21 1qDel E-hCOs was evidenced by increased DNA damage, observed as DNA DSBs, of which was suggested to be a direct DNA replication stress response to the early transition of NECs to RGs that are undergoing asymmetric division. The shift from NECs to RGs was not believed to have begun until after Day 11, in consideration of the multiple NPC-based transcriptional differences between Day 11 and Day 21, i.e., *SOX2* and *NCAM1* (Figure 5.5.F, 5.13.A and 5.16.B). However, if the DNA replication stress is caused by an altered cell cycle of self-proliferation, NECs are likely to suffer substantially worse than RGs, as they are more vulnerable to DNA replication stress (Kalogeropoulou *et al.*, 2022). This could be serving as a key contributor to the severe microcephaly observed in Day 5-11 1qDel E-hCOs. It is also worth stating that the poor localisation of M phase cells could be shared by 1qDel E-hCOs prior to Day 21, as the M phase cellular disorganisation is universal from Day 21 to Day 60 in 1qDel E-hCOs regardless of 1q21.1 dosage. There are multiple examples of repressed Wnt and NOTCH pathways causing apical-basal polarity issues for NECs or causing NECs to proliferate away from the apical edge of lumens, respectively (Ohata *et al.*, 2011; Herrera *et al.*, 2014; Mase *et al.*, 2021). It is therefore reasonable to assume that Day 21 1qDel E-hCO phenotypes of NPC disorganisation are representative of longstanding issues in 1qDel E-hCO development, possibly prior to Day 21. In summation, considerably more investigations targeting corrupted cell cycle, neuroepithelial disorganisation and accelerated differentiation are necessary to validate the Day 21-specific hypotheses. However, there is a strong argument to suggest that an early transition to neurogenic RGs is the key to understanding 1qDel E-hCO microcephaly at Day 21.

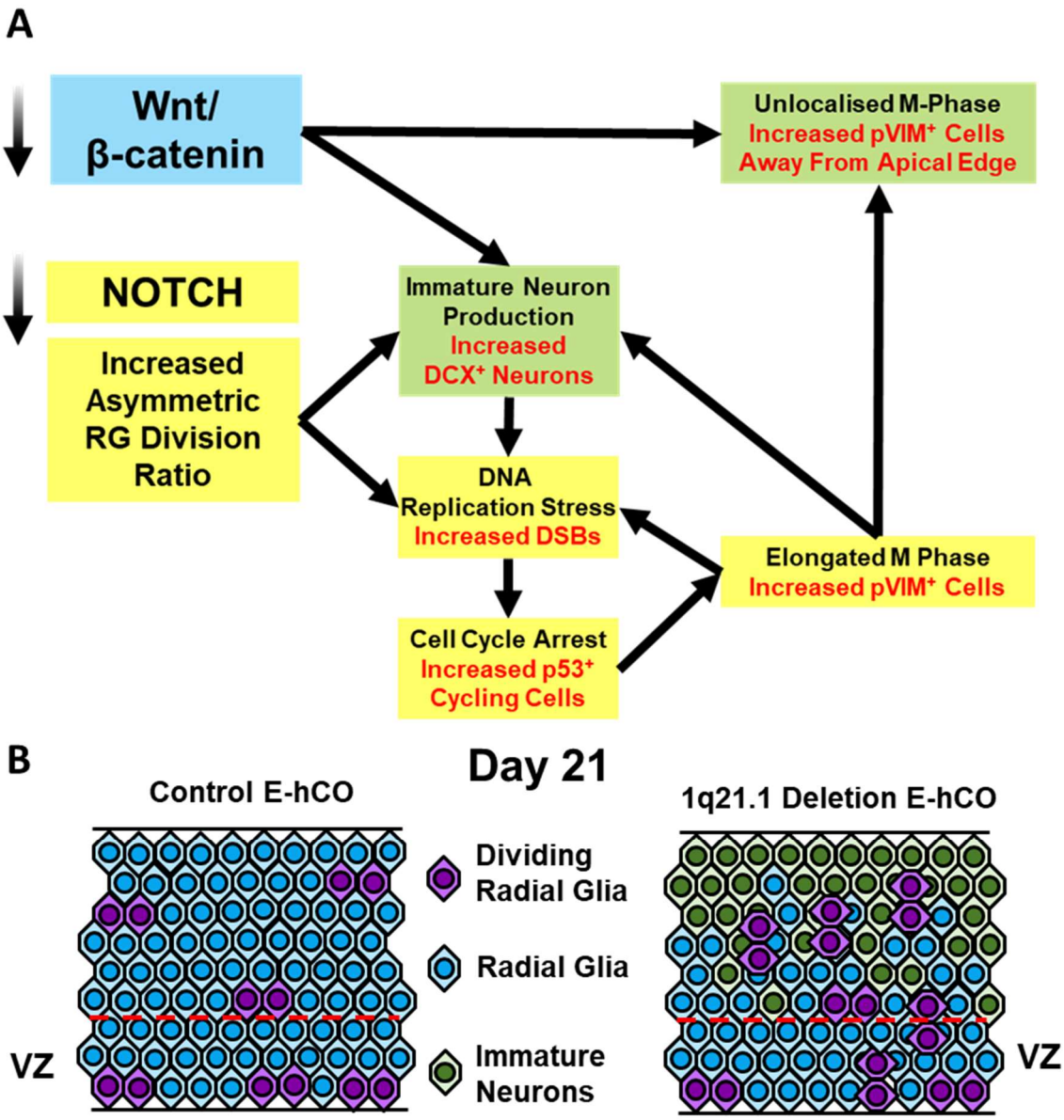

Figure 5.26: Hypothesised mechanisms and structural deficits suggested as responsible for observed phenotypes in Day 21 1qDel E-hCOs.

A) Hypothesised mechanistic pathway of observed phenotypes in Day 21 1qDel E-hCOs. Annotations: Wnt-related (blue), NOTCH-related (yellow), Wnt and NOTCH-related (green), hypothetical features (black) and confirmed phenotypes (red). **B)** Proposed organisation of developing neocortex, including ventricular zone (VZ) in Day 21 1qDel E-hCOs, suggesting induction of neurogenesis due to increased horizontally-orientated radial glia, the total population of which are less bound to the apical edge of the VZ.

5.4.3 Microcephaly Recovery Coincides with Increased Ventral Forebrain Representation in Day 30 1q21.1 Deletion Cortical Organoids

Microcephaly is still present at Day 21, where 1qDel E-hCOs have an overgrowth of immature neurons, as well as cell cycle alterations and substantial changes to the organisation of the neuroepithelium. However, 1qDel E-hCO microcephaly recovers from Day 30 onwards as the culturing media switches to maturation media that induces and supports neuronal growth (Figure 5.3.A-B). Previously established phenotypes of Day 30 1qDel E-hCOs include small lumens, external aggregations of immature neurons and *NES*/*VIM* upregulation, with minimal 1q21.1 gene dosage differences and the resolution of the DSB/p53/M phase cascade (Figure). These phenotypes suggested that, although the majority of Day 21 phenotypes had resolved, there was neuroepithelial disorganisation specific to Day 30, but no clear reason as to why the microcephaly had resolved. It was therefore hypothesised that a phenotype, unique to Day 30, was compensating for the early developmental losses in order to recover overall size, but possibly not without repercussions (Figure 5.27).

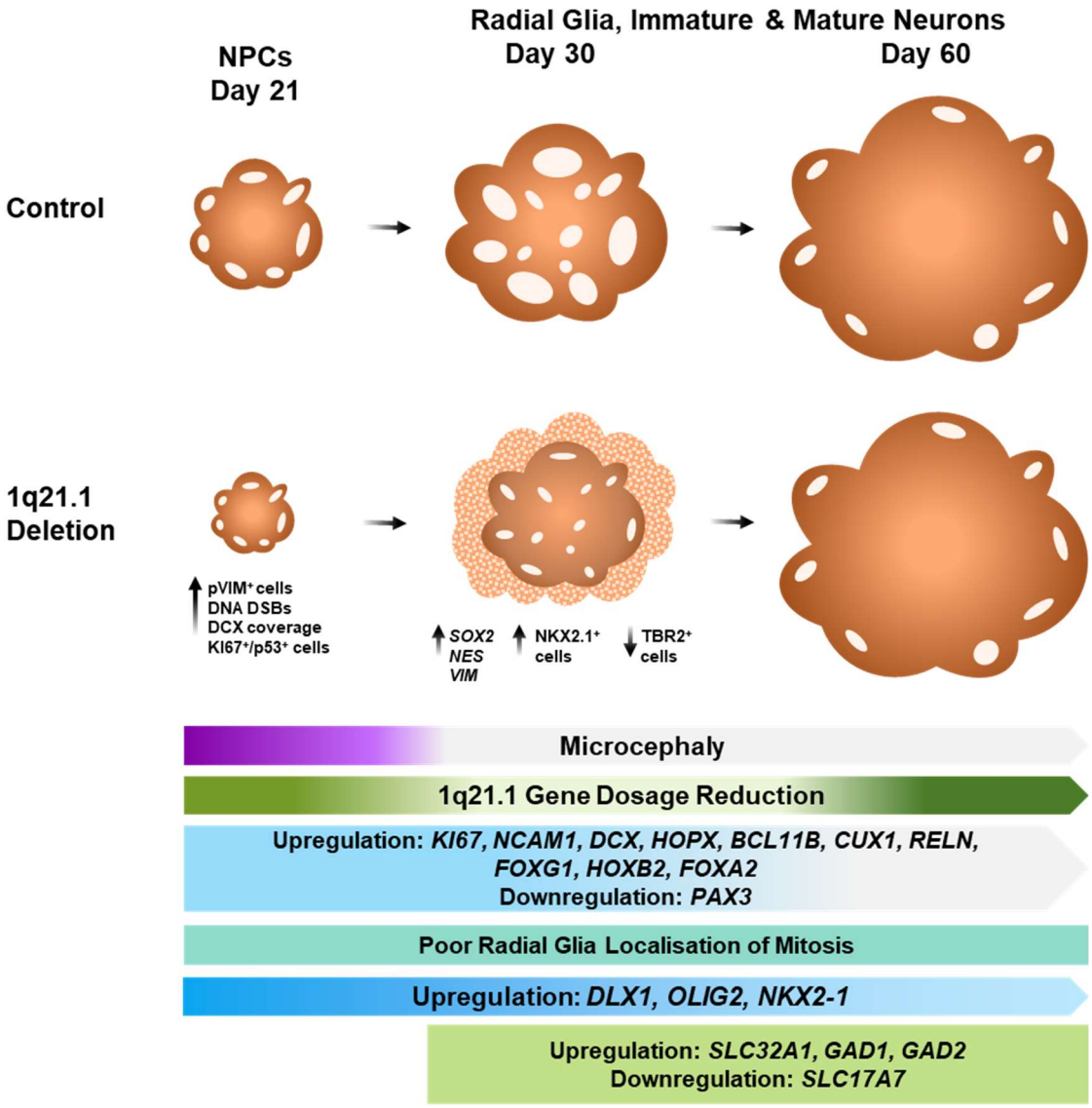

Figure 5.27: Schematic summary of results of 1qDel E-hCOs prior to neurogenesis (Day 21) to neuronal maturation (Day 60).

At Day 21, 1qDel E-hCOs were microcephalus and displayed signs of abnormal cell cycle and arrest, particularly with M phase. Accompanying this, there was a greater representation of immature neurons, despite this stage representing NPCs only in control E-hCOs. By Day 30, 1qDel E-hCOs no longer exhibited the aforementioned Day 21-specific phenotypes, including microcephaly. Instead, Day 30 1qDel E-hCOs had substantially smaller lumens, generated more NKX2.1^{+} cells with fewer TBR2^{+} IPs, and had greater transcriptional representation of RG. Unlike previous timepoints, Day 60 1qDel E-hCOs did not vary considerably from control E-hCOs, resolving multiple previous transcriptional differences, and had no timepoint-specific features. Consistent cross-timepoint features of 1qDel E-hCOs include: *PAX3* downregulation (Day 21 to Day 30), upregulation of *KI67*, brain region and cortical layer markers (Day 21 to Day 30) and poor M phase radial glia localisation to the apical edge of lumens (Day 21 to Day 60). Lastly, 1q21.1 gene dosage reduction became less severe at Day 30, but became substantial again at Day 60.

The causative factors of 1qDel E-hCOs' recovery from microcephaly is not immediately obvious as there is a significant amount of variability between control cell line E-hCOs from Day 30 onwards; possible reasons for and examples of inter-genotype variation of E-hCOs have been previously discussed throughout Section 4. Although it would be preferable to have a homogenous response from control cell lines when differentiated into E-hCOs, it was considered beneficial to investigate the noticeable resemblance in experimental outcomes between Control #2 E-hCOs and 1qDel E-hCOs at Day 30. Both Control #2 and 1qDel E-hCOs had reduced $SOX2^+$ cells and apoptosis, upregulated *PAX6,* and an overall increase in transcriptional representation of both LGE progenitors and mature GABA-ergic neurons (Figure 5.7.D, 5.18.B, 5.20.B and 5.23.A). Of these phenotypes, only reduced $SOX2^+$ cells were shared in Control #2 and 1qDel E-hCOs by Day 60 (Figure 5.18.C). Although it could be suggested that there is a potential link between NPC ($SOX2^+$) quantity and dorsal forebrain identity, Control #2 results undermine this hypothesis by not retaining the Day 30 results through to Day 60 (Figure 5.18.C and 5.20.C).

The Control #2/1qDel E-hCO comparison was also beneficial as it highlighted a consistent increase in ventral forebrain progenitor markers, proceeded by increased GABA-ergic markers in 1qDel E-hCOs, most poignantly at Day 30 when microcephaly resolves. If the consistently heightened transcription of *DLX1* (Figure 5.20.A-C) translated to greater $DLX1^+$ cells, 1qDel E-hCOs could resemble other ventral forebrain-shifted cerebral organoids, such as macrocephalus ASD patient-derived cerebral organoids (Mariani *et al.*, 2015). $DLX1^+$ cells would occupy non-dorsal, non-neuroepithelial-structured space, thereby reducing space dedicated to dorsal forebrain-derived neuroepithelia generation and expansion (Mariani *et al.*, 2015). Coincidentally, Day 30 was the only timepoint where lumen area was significantly reduced (Figure 5.12.A-C), coinciding with an outcrop of $NKX2.1^+$ cells in the disorganised areas of Day 30 1qDel E-hCOs (Figure 5.21 and 5.22.A). Additionally, *VIM* and *NES* were significantly upregulated, without cell line-specific variability, in Day 30 1qDel E-hCOs specifically (Figure 5.13.B). Ideally, filamentous proteins such as vimentin and nestin would span in and around areas of NPCs, which in hCOs would be around the VZ (Cho *et al.*, 2021). The disruption of nestin filaments has been observed previously as a phenotype of periventricular heterotopia-emulating cerebral organoids, demonstrating that when the neuroepithelium is disrupted it

drastically affects the depth of the VZ (Klaus *et al.*, 2019). Similarly, Miller-Dieker syndrome cerebral organoids show significant disruption in acetylated tubulin, part of the microtubule framework upholding NPC organisation, resulting in small cerebral organoids (Iefremova *et al.*, 2017).

Observations from ICC imaging, upregulation of *NES* and *VIM* transcription, as well as smaller lumens and reduced $SOX2^+$ cells, demonstrated that the 1qDel E-hCOs' neuroepithelium was likely to have been poorly organised at Day 30 in particular (Figure 5.9, 5.12.A-C, 5.13.B, 5.15.H and 5.18.B-C). It is unclear whether the MGE NPCs caused the possible neuroepithelial disorganisation, or vice versa, but it is reasonable to suggest a link between these two features considering the timepoint specificity, similar to that of the DSB/p53/M phase cascade. Furthermore, 1qDel E-hCOs' microcephaly was unlikely to be caused by this form of neuroepithelial disorganisation, as there were no significant changes in lumen size, *NES*, *VIM* or NKX2.1 until Day 30, compared to other timepoints (Figure 5.5.D-F, 5.11.B-D, 5.13.A, 5.20.A and 5.22.A). Instead, it was suggested that the microcephaly was restored in part due to the neuroepithelial disarray, as cells were no longer constrained to the striated neuroepithelium. Additionally, the alleviation of the DSB/p53/M phase cascade and early neurogenesis were likely to contribute to resolving microcephaly, as neurons were now supported by the pro-neurogenic media at Day 30, and therefore 1qDel E-hCOs were no longer in a state of excessive stress.

It was unknown if 1qDel E-hCOs' ventral forebrain enrichment was a by-product of the microcephaly or an isolated phenotype; no evidence was found to support a connection. It was therefore thought useful to frame the ventral forebrain enrichment as an independent phenotype to microcephaly, as a potential representation of the cortical dysfunction present in 1qDel-associated SCZ, a key phenotype of 1qDel. This could open avenues to potentially explain the expansion of ventral forebrain cells, but also how this new cell population could have arisen as a result of the microcephaly.

Altered representation of forebrain identity is not common in SCZ patient-derived cerebral organoids, but one cohort produced fewer forebrain progenitors and neurons, replacing them with other cellular identities spanning endothelial, retinal and choroid plexus, whilst also having anomalous downregulation of upper layer neuron marker *BRN2* (Notaras, *et al.*, 2021), a known feature of SCZ

patients (Batiuk *et al.*, 2022). The patient-derived cerebral organoids were also in a heightened state of stress with poor neuroepithelial construction but also elevated apoptosis (Notaras, *et al.*, 2021). Some of the phenotypes exhibited by this SCZ cohort bore resemblance to 1qDel E-hCOs, such as poor neuroepithelial organisation and non-dorsal forebrain identities, but the results of Notaras et al., (2021) were phenocopied by *DISC1*-mutant cerebral organoids (Srikanth *et al.*, 2018); this suggests 1qDel E-hCOs do not represent SCZ pathology. The results of *DISC1*-mutant cerebral organoids characterisation elaborated further, illustrating that *GAD1*, *GAD2* and *SLC32A1* were also significantly underrepresented, as were NMDA receptors *GRIN1* and *GRIN2B* (Srikanth *et al.*, 2018). Although these results tie into what is already known of SCZ with regards to GABA-ergic neurons and NMDA hypofunction in patients (Bygrave *et al.*, 2019; Tong *et al.*, 2019; Batiuk *et al.*, 2022), not all SCZ patient-derived cerebral organoid cohorts report the same phenotypes. Although reduced expression of NMDA receptor-associated pathways and core neuronal markers (MAP2/TUBB3/NCAM1) were also found in other cerebral organoids derived from SCZ cohorts, there was no mention of altered NPC identities (Kathuria *et al.*, 2020; Notaras, Lodhi, Fang, *et al.*, 2021). Even cerebral organoids generated from SCZ-risk CNVs such as 22q11.2 deletion, which has similar heightened risk of SCZ and microcephaly as 1qDel, exhibited no mention of heightened GABA-ergic synaptic transmission, instead referring to the downregulation of voltage-gated Ca^{2+} channels (Khan *et al.*, 2020). Currently, the only evidence of divergent neuronal differentiation in SCZ cerebral organoids that mimic 1qDel E-hCOs' shift to ventral forebrain identity, is twin studies that exhibit both SCZ and bipolar disorder (Sawada *et al.*, 2020). Although this phenotype was also supported in RNAseq results of SCZ-only patients compared to their twin (Sawada *et al.*, 2020), this was not elaborated on further. This data would suggest that 1qDel E-hCOs' ventral forebrain enrichment is not in keeping with SCZ hypothesis formulated from both patient and cerebral organoid studies.

Investigations into microcephaly-presenting cerebral organoids was similarly fruitless in finding answers of how and why the ventral forebrain outcrop occurred. The results of such studies either presented upregulation of astrocytes or RGs to the detriment of neurons (Mellios *et al.*, 2018; Wang *et al.*, 2020; Nakashima *et al.*, 2021). Additionally, dramatically reduced expression of ventral forebrain markers were found in some circumstances, i.e. *DLX1, GAD1*, *SST* (Mellios *et al.*, 2018), comparatively similar to SCZ cerebral organoid studies

(Srikanth *et al.*, 2018). However, one connecting element was found in the form of FOXG1, which is significantly upregulated at Day 30 in 1qDel E-hCOs (Figure 5.20.B), but is also associated with atypical Rett syndrome and head size variability (Kortüm *et al.*, 2011; Hettige *et al.*, 2022). Gradual reduction of FOXG1 correlated with reduced cerebral organoid diameter (Zhu *et al.*, 2019; Hettige *et al.*, 2022) as well as premature neuronal differentiation (Hettige *et al.*, 2022). This is likely due to FOXG1's affiliation with microcephalus-related processes, such as quantity of primary cilia, alterations to cell cycle and reduction in proliferation (Hettige *et al.*, 2022).

On the other hand, when overexpressed in macrocephalus ASD patient-derived cerebral organoids, FOXG1 has been found to endorse GABA-ergic neuronal production, alongside elevated progenitor populations of $DLX1^+$ and $NKX2.1^+$ cells in regions of dorsal forebrain marker deficit (Mariani *et al.*, 2015); the results of this study bear a striking resemblance to Day 30 1qDel E-hCOs. Interestingly, the macrocephalus ASD-derived cerebral organoids exhibited the ventral forebrain phenotype in a vacuum, absent of accelerated neuronal differentiation or proliferative differences, although cell cycle was significantly shorter (Mariani *et al.*, 2015). Other macrocephalus ASD patient-derived cerebral organoids have bolstered FOXG1's importance in cerebral organoid size, as it was identified to be part of the upregulated module of proliferation and neurogenesis attributed to cerebral organoid overgrowth (de Jong *et al.*, 2021). Furthermore, this was supported by recent analysis of multiple high-risk ASD genes in cerebral organoids that also reported enriched development of GABA-ergic neurons (Paulsen *et al.*, 2022). However, in the ASD-risk 16p11.2 CNV, there was no mention of abnormal NPC or neuronal identity, instead pinning the microcephaly/macrocephaly phenotypes of the two rearrangements on accelerated neuronal maturation and regressive neuronal migration (Urresti *et al.*, 2021).

With the combined information of *FOXG1* upregulation, reduced lumen size, increase in overall size, accelerated neuronal differentiation, increased ventral forebrain progenitors and GABA-ergic neuron markers as 1qDel E-hCOs transition from Day 21 to Day 30 (Figure 5.2.B, 5.3.B, 5.12.A-C, 5.16.A, 5.17.E, 5.20.A-B, 5.22.A and 5.23.A), it could be suggested that Day 30 1qDel E-hCOs bear a closer resemblance to ASD patient-derived cerebral organoids than SCZ- or microcephaly-presenting cerebral organoids. The basis of this hypothesis is

predominantly rooted in the transcriptional analysis, as the number of FOXG1$^+$ cells does not vary at any timepoint (Figure 5.22.B). However, the quantity of FOXG1$^+$ cells would not necessarily be expected to change as it represents both the dorsal and ventral axis of the telencephalon (Mariani *et al.*, 2015), whilst transcriptional changes trending towards inflated ventral forebrain representation are confirmed by the abundance of NKX2.1$^+$ cells in Day 30 1qDel E-hCOs (Figure 5.20.A-B and 5.22.A).

In summary, the current hypothesis for how mature 1qDel E-hCOs recover from microcephaly is by exhibiting ASD-like, not SCZ-like, features. Although likely key elements to this hypothesis have been identified, including neuroepithelial disorganisation, increased ventral forebrain representation and *FOXG1* upregulation, further exploration is needed of the dorsal forebrain-specific components of mature 1qDel E-hCOs in the context of alleviating microcephaly. Similarly, exploration of the possible functional activity of mature 1qDel E-hCOs could support or reject the ASD-like hypothesis suggested for mature 1qDel E-hCOs.

5.4.4 Dorsal Forebrain-Specific Features of Mature 1q21.1 Deletion Cortical Organoids are Affected by the Resolution of Microcephaly

The dorsal forebrain-specific features of mature 1qDel E-hCOs, such as cortical layering and radial migration, were affected by 1qDel, although whether this was a result of the previous microcephaly, ventral forebrain representation or neither was unknown. There was a temporal correlation between the increase in NKX2.1$^+$ progenitors and the reduction in TBR2$^+$ IPs (Figure 5.18.B and 5.22.A). TBR2$^+$ IPs are specific to the dorsal forebrain and are correlated to neurogenic proliferation from RGs, and therefore a NOTCH^{low} environment encourages IP production (Eze *et al.*, 2021). This was not what was observed in 1qDel E-hCOs, where TBR2$^+$ IPs were consistently trending lower than control E-hCOs, significantly so at Day 30 (Figure 5.18.A-C). However, TBR2$^+$ IPs are known to be a vulnerable cell type in primary microcephaly mouse models, often found to be considerably reduced alongside PAX6$^+$ NPCs (Zhang *et al.*, 2019) or neurons (Mellios *et al.*, 2018). Other dorsal forebrain cell types, such as TBR1$^+$ or SLC17A7$^+$ neurons, had a trend of transcriptional downregulation in neurogenic 1qDel E-hCO differentiation (Figure 5.19.A-C and 5.23.A-B). Similar morphology

and attributes were found in *p53*^{KD} cerebral organoids, which showed significantly fewer TBR1^{+} and TBR2^{+} cells, with no change in NPC proliferation or apoptosis, but had severely degraded ventricular organisation (Marin Navarro *et al.*, 2020); Day 30 1qDel E-hCOs disrupted neuroepithelium was likely contributing to the deterioration of the SVZ layer.

Conversely, the universally telencephalic neuronal gene *BCL11B* (Leid *et al.*, 2004) was significantly greater in Day 21-30 1qDel E-hCOs (Figure 5.19.A-B), albeit not partnered with a change in CTIP2^{+} neuronal populations (Figure 5.18.A-C). The lack of increased CTIP2^{+} neurons in Day 21 1qDel E-hCOs indicate that the immature neurons being generated by early neurogenesis are not capable of maturation until after RA exposure (Figure 5.18.A). One possibility could be that the CTIP2^{+} neurons originating in the dorsal forebrain are fewer in 1qDel E-hCOs, but the deficit resolved itself by increased ventral forebrain-originating CTIP2^{+} neurons. This would not necessarily explain why *BCLL1B* transcription is heightened. However, post-transcriptional modifications could be complicating the transcript-to-protein procedure, as observed in other incidences in 1qDel E-hCOs, i.e. *KI67* transcription and KI67^{+} cell abundance (Figure 5.7.A-B). ASD-presenting syndromes such as Fragile X syndrome, have shown post-transcriptional regulators, like FMRP, to be key in understanding pathogenesis of such disorders (Kang *et al.*, 2021). In fact, FMRP targets *CHD2* in cerebral organoid studies (Kang *et al.*, 2021), a member of the same protein family as *CHD1L* (Xiong *et al.*, 2021), which could suggest CHD1L and other 1q21.1 genes are vulnerable to similar modulation. As such, the change in *CTIP2* transcription should be treated as an indicator of an anomaly in either forebrain identity or overall cortical lamination, not conclusive evidence of such, until further examined.

The representation of upper layer neurons in Day 30 1qDel E-hCOs suggest that not just lower neurons are affected by 1qDel. There was an increased transcription of *CUX1* (Layer II-IV) and *RELN* (Layer I) that match the temporal changes in *CTIP2* transcription; all three were either visibly or significantly overexpressed at Day 21 and Day 30 in 1qDel E-hCOs, but less so at Day 60 (Figure 5.19.A-C). This could mean that there is biased neurogenesis in favour of upper layer neurons to the detriment of the lower layers. This bias aligns with current information on adult SCZ patients' cortical composition, of upper layer neurons taking precedent over lower layer neurons (Batiuk *et al.*, 2022). However, BRN2^{+} neurons, which are present in the same upper cortical layers as CUX1^{+}

neurons, were under-represented in multiple SCZ cerebral organoids studies, which contributed to neuronal loss (Srikanth *et al.*, 2018; Notaras, *et al.*, 2021). This would suggest that there is a developmentally-specific fault in upper cortical layer neurons in SCZ. Microcephaly is less clear than SCZ with regards to affected neocortical lamination, as it is dependent on the affected gene(s) (Zhou *et al.*, 2013; Phan *et al.*, 2021). ASD is similarly complex, with both over- and under-production of lower layer neurons culminating in ASD-like behaviours in mice (Fang *et al.*, 2014; Sacai *et al.*, 2020). Despite conflicting results between different mouse models, correlation has been found amongst ASD patients that ASD severity positively associates with upper layer neuron enrichment (Velmeshev *et al.*, 2019). However, when reviewing ASD patient-derived cerebral organoids there is either no reported investigation (Mariani *et al.*, 2015; de Jong *et al.*, 2021), or no differential expression of upper layer neurons found (Paulsen *et al.*, 2022). 1qDel E-hCOs presented no suggestion of overall neuron loss; instead, there are indicators of an enriched population of upper layer neurons, with a deprecated expression of lower layer neuron marker (Figure 5.19.A-C and 5.23.A-B). This observation coincides with both ASD and SCZ examples presented here, but the literature on such NDDs currently has no consensus for any one trait. It is therefore difficult to discern how and if 1qDel associates with these conditions.

There is, however, support evidence for 1qDel E-hCOs bias for upper layer neurons. The possibly increased presence of Layer I reelin^{+} neurons, proposed by *RELN* upregulation in Day 21 and Day 30 1qDel E-hCOs, would suggest that there was not only an enrichment of upper layer neurons, but also faulty neuronal radial migration in 1qDel E-hCOs (Figure 5.19.A-B). Reelin's role in neuronal radial migration through the neocortex is directly linked to NOTCH signalling, where the overexpression of the cleaved intracellular domain of NOTCH rescues neuronal migration defects in reelin-deficient mice (Hashimoto-Torii *et al.*, 2008). 1qDel E-hCOs were suspected to be in a NOTCH^{low} state perpetually, causing phenotypes such as early neurogenesis in Day 21 1qDel E-hCOs (Figure 5.16.A). In fact, the temporal changes of *RELN* transcription match that of *DCX* and *NCAM1* in 1qDel E-hCOs, where high expression of neuronal migration markers at Day 21 reduced in severity over time until reaching control levels by Day 60 (Figure 5.16.B-D and 5.19.A-C). This would suggest that there was a significant issue with the migration of neurons in Day 21-30 1qDel E-hCOs, as previously suggested by bright field images (Figure 5.2.A and 5.3.A). A neuronal migration issue could be a

contributory factor to the differences in upper (CUX1/reelin) and lower (TBR1) neurons, the separation of which is a key role for reelin during early neocortical development (Faini, Del Bene and Albadri, 2021).

Cortical neuronal migration abnormalities are considered a frequent phenotype of microcephaly (Mellios *et al.*, 2018), ASD (Peñagarikano *et al.*, 2011; de Jong *et al.*, 2021) and SCZ (Teixeira *et al.*, 2011; Muraki and Tanigaki, 2015). Neuronal migration-associated transcription factors, such as TCF4 and ASCL1, are enriched in both upper and lower cortical layer neurons in SCZ adults (Batiuk *et al.*, 2022), whilst SCZ patient-derived cerebral organoids have downregulation of tubule proteins (MAP2, TUBB3) and NCAM1 (Notaras, *et al.*, 2021), proposing that insufficient radial migration is part of SCZ pathology. However, as previously determined, 1qDel E-hCOs are arguably unlikely to be an accurate representation of SCZ, due to increased ventral forebrain representation. These results support this hypothesis, as SCZ patients have been documented to have less reelin in the PFC and that overexpression of reelin alleviates symptoms (Teixeira *et al.*, 2011), the opposite of what is found in Day 21-60 1qDel E-hCOs.

However, 1qDel E-hCOs have shown closer representation to ASD, particularly at the point of microcephaly recovery (Day 30). Although reelin's role in ASD pathology is less clear than SCZ (Scala *et al.*, 2022), high-risk ASD genes, such as *CHD8*, have illustrated that the disrupted organisation of layer-specific neurons in ASD can be a consequence of faulty neuronal migration (Xu *et al.*, 2018). ASD-like *Cntnap2*$^{-/-}$ mice illustrate an abundance of CUX1^{+} neurons present in Layers VI-V, as well as Layers II-IV (Peñagarikano *et al.*, 2011), whilst cerebral organoids of similar genetic background demonstrate macrocephaly with significantly fewer neurons of lower layer identity (de Jong *et al.*, 2021); upper layer cell quantity was not mentioned. Conversely, microcephaly-presenting disorders do not share aspects of ASD's faulty neuronal radial migration features, instead exhibiting minimal changes to Layer I, but substantial deficits to neuronal populace in Layer II-III, indicative of poor radial columnar organisation (Yu *et al.*, 2010; Zhou *et al.*, 2013). In review of these studies, the overarching theme of NDDs is that they are susceptible to neuronal migration abnormalities, but are vastly heterogenous in their presentation.

Radial migration of cortical neurons is difficult to define in cerebral organoids, unlike in *in vivo* models, as cerebral organoids' cortical layering

structure is a greatly simplified version of the developing neocortex (Li *et al.*, 2017); the same issue would likely arise when trying to model more nuanced cortical layering phenotypes. It is therefore difficult to determine how relevant any 1qDel E-hCOs cortical layer and migration phenotypes would be in relation to 1qDel patients, if substantiated. However, deprecated numbers of $TBR2^+$ IPs suggest the SVZ is vulnerable during early neurogenesis, whilst transcriptional analysis in Day 21-60 1qDel E-hCOs alludes to disproportionate cortical layer expression alongside heightened neuronal migration before reaching a control-like plateau at Day 60 after recovery of microcephaly. This would suggest that 1qDel syndrome could have a cortical layer disruption and a radial migration phenotype, that either resolves naturally or due to the size limitation of the E-hCO model. To determine if these hypotheses have merit in future, an extended E-hCO differentiation time, possibly to Day 120, as well as substantial, targeted analysis using ICC guided by the transcriptional analysis provided in this study, would be necessary. Additionally, if the cause of the enrichment of ventral forebrain progenitors is found, it would be auspicious to manipulate 1qDel E-hCOs to remain dorsal and then revaluate 1qDel E-hCOs neocortical organisation.

5.4.5 Evidence of E/I Imbalance in 1q21.1 Deletion Cortical Organoids

A number of the phenotypes in Day 21 and Day 30 1qDel E-hCOs decrease by Day 60, e.g., decreased IP population, lumen size variability and neuroepithelial disorganisation, enrichment for ventral forebrain progenitors, differential cortical layer representation and possible abnormal radial neuronal migration, but the increase in presynaptic GABA-ergic interneuron markers was consistent (Figure 5.27). In the absence of electrophysiological analysis such as whole-cell patch clamp, Ca^{2+} imaging or multiple electrode arrays however, hypothesis on the functional activity of 1qDel E-hCOs requires interpretation of the presented evidence: overrepresented ventral forebrain progenitors and transcription of GABA-ergic presynaptic markers, coupled with reduced glutamatergic synaptic markers (Figure 5.22.A and 5.23). Using current knowledge of microcephaly, ASD and SCZ neuronal activity, it may be possible to form a hypothesis on the neuronal activity of 1qDel E-hCOs and how this may relate to 1qDel patients.

As discussed, SCZ has a complex aetiology with regards to electrical activity, with the two hypothesis of fluctuating dopamine receptor activity (Gründer and Cumming, 2016) and NMDA hypofunction (Cadinu *et al.*, 2018). Although it

has previously been proven that cortical pyramidal neurons have DRD2 receptors (Khan *et al.*, 2020), E-hCOs were not investigated for their dopamine function. However, the transcription of subunits of NMDA (*GRIN1*) and AMPA (*GRIA1*) receptors in Day 30 and Day 60 1qDel E-hCOs were found to be either not significantly different from control E-hCOs or difficult to discern statistical significance due to cell line-specific variability (Figure 5.23). There was a trend of reduced *SLC17A7*, which would indicate repressed glutamatergic transmission, one attribute found in the PFC of SCZ patients (Panja *et al.*, 2021). However, SCZ cerebral organoids from multiple genetic lineages do not replicate the mature neuronal phenotypes 1qDel E-hCOs including over-representation of GABA-ergic presynaptic markers, and therefore it is reasonable to conclude that mature 1qDel E-hCOs are not depicting SCZ functionality (Srikanth *et al.*, 2018; Kathuria *et al.*, 2020; Notaras, *et al.*, 2021; Notaras, *et al.*, 2021).

In ASD, cortical hyperexcitability can be found as a result of increased cortical neurons or reduced quantities of PV^+ interneurons in the PFC (Courchesne *et al.*, 2011; Hashemi *et al.*, 2017). RNAseq data highlights ASD-risk genes' connections to both of the major neuronal subtypes in CNS tissues (Reilly *et al.*, 2020), although inhibitory neurons were more substantially implicated than glutamatergic neurons (Wang *et al.*, 2018; Velmeshev *et al.*, 2019). ASD phenotypes in adults can be traced back to developmental changes in ASD patient-derived cerebral organoids, where GABA-ergic lineage cells are enriched during cerebral organoid differentiation (Mariani *et al.*, 2015; Paulsen *et al.*, 2022). Other *in vitro* and *in vivo* research models, including hIPSC-derived neurons, support both the developmental observations and the resulting adult phenotype of altered balance of E/I signals (Culotta and Penzes, 2020; Park *et al.*, 2022). MCPH-emulating mouse models also present cortical hyperexcitability, but as a result of abnormalities such as increased density of glutamatergic synapses on Layer II/III pyramidal, neocortical neurons (Zaqout *et al.*, 2019). Some MCPH models also share similar traits to ASD that would contribute to E/I imbalance, for example PV^+ interneurons were significantly reduced in truncated ASPM mouse models, but only in non-cortical structures (Garrett *et al.*, 2020). These mouse models were analysed postnatally, whilst prenatal-modelling, microcephalus cerebral organoids have exhibited repressed electrical activity, both in MCPH and secondary microcephaly cerebral organoids models (Li *et al.*, 2017; Gomes *et al.*,

2020), supported by previously established hIPSC model results (Marchetto *et al.*, 2010).

Albeit a simplified synopsis, evidence suggests that ASD and microcephaly share similar trajectories in pathology, from greater inhibition (prenatal) to greater excitation (postnatal). Additionally, other factors may also be influencing the synaptic transmission of 1qDel E-hCOs. For example, reelin is associated with neuronal migration, but is also linked to GABA-ergic transmission by actively repressing GABA receptor activity at the presynaptic cell surface (Faini, Del Bene and Albadri, 2021). Upregulation of *RELN,* if translated in 1qDel, could be contributing to a hypoactive network (Faini, Del Bene and Albadri, 2021). Coincidentally, as *RELN* transcription resolves to control levels by Day 60 in 1qDel E-hCOs, the significance of GABA-ergic presynaptic markers also reduces (Figure 5.19.C and 5.23.B).

It is difficult to detract a working theory of the functional activity of 1qDel E-hCOs due to the heterogenous outcomes from current literature, as well as the limited data available for 1qDel E-hCOs. However, it is likely that 1qDel E-hCOs have a dysfunctional network due to differential glutamate and GABA inputs, alongside abnormal cortical pyramidal neuron generation and *RELN* expression. There is also a possibility that there is a greater population of GABA-ergic interneurons, although without additional experiments this cannot be confirmed. Similarly, whether the 1qDel E-hCO network is hyper- or hypo-active is uncertain, and requires further exploration to determine how closely it associates with other NDDs. On reflection upon the patient from which the 1qDel hIPSC line is derived from, they suffer from neither SCZ or ASD nor is there any mention of microcephaly; instead, there are a myriad of other neuropsychiatric disorders (major depressive disorder) and physical anomalies (short stature). A substantially greater numbers of cell lines, derived from 1qDel patients that exhibit these NDDs, is required to determine not only the pathology of 1qDel but also which facets of its pathology contribute to heightened risk of SCZ and/or ASD. In the absence of such resources, scrutiny of current 1qDel models, both *in vitro* and *in vivo* could provide context for the myriad of phenotypes observed in 1qDel E-hCOs.

5.4.6 1q21.1 Deletion Cerebral Organoids Have Model-Specific Features Compared to Other 1q21.1 Deletion Research Models

As cerebral organoids are a relatively new tool in *in vitro* disease modelling, determining whether they can be used as a complement for *in vitro* monoculture or *in vivo* animal modelling is essential to support their use in translational research. Only one study has documented 1qDel in *in vitro* (2D) cortical neurons (Chapman *et al.*, 2021); this study was conducted using the same hIPSC lines as those used in this thesis. Chapman *et al.*, (2021) did not investigate the microcephaly phenotype in 2D 1qDel NPCs or neurons, however Nielsen *et al.*, (2017) reported smaller head-to-tail length of mice, whilst Reinwald *et al.*, (2020) reported smaller overall brain volume, but in midbrain regions. Other findings from *in vivo* models were largely of little benefit in comparison to 1qDel E-hCOs, as they predominantly focus on dopaminergic pathways (Nielsen *et al.*, 2017; Gordon *et al.*, 2019; Reinwald *et al.*, 2020). Although informative for the SCZ aspect of 1qDel pathology, the collective information on the 1qDel *in vivo* mouse model unfortunately provides little insight into the results and hypotheses of 1qDel E-hCOs.

On the other hand, Chapman *et al.*, (2021) examined features of 1qDel NPCs and neurons similarly to the study presented here on 1qDel E-hCOs. Firstly, both 2D 1qDel NPCs and 1qDel E-hCOs have proliferative abnormalities, but they present differently. 2D 1qDel NPCs had fewer KI67^{+} cells and *KI67* transcription (Chapman *et al.*, 2021), whilst 1qDel E-hCOs had no change in KI67^{+} NPC cell abundance but did observe increased *KI67* transcription and changes in pVIM^{+} cell abundance and M phase orientation (Figure 5.7.A and 5.14.A-B); cell cycle changes were not investigated in Chapman *et al.*, (2021). As the protocols used in Chapman *et al.*, (2021) and E-hCO differentiation did not vary substantially during NPC differentiation, these proliferative differences are likely due to the change in differentiation format, i.e. 2D neuronal monoculture to 3D cerebral organoids. This may or may not also contribute to the varying dosage of 1q21.1 genes observed across the two models at comparable timepoints of Day 50-60; *BCL9* and *PRKAB2* expression was found to be significantly lower in 1qDel E-hCOs than in 2D 1qDel neurons (Figure 5.4.C-D) (Chapman *et al.*, 2021). Milder dosage reduction of 1q21.1 genes in 2D 1qDel neurons could be replicated in 2D 1qDel NPCs, which would explain why 2D 1qDel NPCs do not exhibit features of premature neurogenesis, such as upregulation of *DCX* transcription, prior to RA

induction (Chapman *et al.*, 2021); the premature neurogenesis in 1qDel E-hCOs was believed to be a result of *NOTCH2NLA* dosage reduction. As premature neurogenesis was a key phenotype of 1qDel E-hCOs' early development, this adds weight to the argument that cerebral organoids should be used in conjunction with *in vitro* modelling of NDDs.

The protocols do change significantly during neuronal maturation however, in such a manner that makes cross-model comparison complex. The 2D 1qDel neurons generated in Chapman *et al.*, (2021) follow a similar composition of media and timeline for the induction of 2D NPCs and neurons as E-hCOs. However, at Day 24, four days after neuronal maturation induction (the addition of RA), the small molecule DAPT was added to differentiate all 2D NPCs into neurons by NOTCH inhibition, so as to facilitate neuronal maturation and halt NPC proliferation (Qi *et al.*, 2017; Sato *et al.*, 2021). As a result, distinctive phenotypes occur in the 2D 1qDel neurons that deviate substantially from 1qDel E-hCOs, including increases in $TBR1^+$ cell abundance and transcription of *TBR1*; the same can be said of CTIP2 translation and transcription of *SATB2* and *RELN* (Chapman *et al.*, 2021). Upregulation of transcription and translation of these cortical layer genes suggest that in a NOTCH-inhibited environment, 2D 1qDel neurons retain dorsal forebrain identity and have accelerated, but not early, neurogenesis (Chapman *et al.*, 2021). This would also explain why 1qDel mice, that do not retain the human-specific NOTCH2NL paralogs, reproduced similar differential abundance of $TBR1^+$ neurons to the 2D 1qDel neurons (Chapman *et al.*, 2021).

In 1qDel E-hCOs, where the NOTCH pathway is only altered by RA, not completely inhibited by DAPT, there was elevated *CUX1, RELN* and *BCL11B* transcription during early neurogenesis (Figure 5.19.A-B), similar to 2D 1qDel neurons (Chapman *et al.*, 2021). However, this increase in transcription was not accompanied by an increase in the population of $CTIP2^+$ neurons (Figure 5.18.A-C). Additionally, the consistent trend in downregulation of the dorsal forebrain-specific *TBR1* observed in 1qDel E-hCOs (Figure 5.19) contradicted the increase in $TBR1^+$ cells in both 2D and *in vivo* 1qDel models (Chapman *et al.*, 2021). Lastly, Chapman *et al.*, (2021) does not document the forebrain identity of 2D NPCs. Given the abundance of dorsal forebrain-specific cortical neurons in 2D 1qDel monoculture, it is reasonable to assume that 2D 1qDel NPCs are predominantly dorsal forebrain in identity (Chapman *et al.*, 2021), but to what percentage is unknown.

Cross-model comparison of 1qDel neurons in 2D monoculture and E-hCOs suggests that the exogenous inhibition of NOTCH significantly changed synaptic networks as mRNA abundance of postsynaptic NMDA (*GRIN1*) and AMPA (*GRIA1*) receptors were significantly greater in expression in 2D 1qDel neurons compared to controls (Chapman *et al.*, 2021), but not in 1qDel E-hCOs (Figure 5.23). Both results are in contrast with what would be expected in a model of SCZ, as one documented hypothesis of SCZ pathology is NMDA hypofunction (Nakao *et al.*, 2019). On the other hand, 1qDel mice emulate the SCZ patient's hypersensitivity to NMDA receptor antagonists (Kapur and Seeman, 2002; Nielsen *et al.*, 2017), whilst 2D 1qDel neurons act as controls when exposed to similar antagonists (Chapman *et al.*, 2021). This calls into question whether the electrophysiological network produced by 2D 1qDel neurons and 1qDel E-hCOs can reflect 1qDel patients' cortical dysfunction. Instead of the cortical hypoexcitability anticipated as a result of NMDA hypofunction, 2D 1qDel neurons illustrate a hyperexcitable network with significantly greater number of spikes per electrode, as well as bursts per minute (Chapman *et al.*, 2021). This is accompanied by a greater number of cortical neurons present in 2D 1qDel neuron cultures, as well significant increases in mRNA and protein expression of pre- and postsynaptic proteins at Day 50 (Chapman *et al.*, 2021). However, it was not documented which type of synaptic protein was increased, either glutamatergic or GABA-ergic in nature (Chapman *et al.*, 2021). It can be assumed that the hyperexcitability is a result of increased glutamatergic synaptic transmission, considering the increase in cortical neurons and pre- and postsynaptic markers (Chapman *et al.*, 2021).

Comparing these functional attributes of 2D 1qDel neurons to 1qDel E-hCOs exposed little commonality. Although pan-neuronal pre- and postsynaptic markers were not investigated in 1qDel E-hCOs, there was no suggestion of an increased abundance of neurons (Figure 5.23), whilst GABA-ergic activity was unknown in Chapman *et al.*, (2021). Unfortunately, there is no functional characterisation of 1qDel E-hCOs but it is reasonable to assume it would be dysregulated, although how is not clear. There are arguments in favour of hypoexcitability, with the assumption that the increase in ventral forebrain progenitors and presynaptic GABA-ergic markers translate to a greater abundance of GABA-ergic inhibitory interneurons within the 1qDel E-hCOs; this is evidenced in SCZ as glutamate hypofunction (Nakao *et al.*, 2019; Uno and Coyle, 2019).

However, in light of 2D 1qDel neurons' hyperexcitability, there is an alternative hypothesis. It is known that GABA is used as an excitatory transmitter in early neurodevelopment; only in later development do GABA receptors make a "polarity switch" wherein GABA transmission serves to be inhibitory (Zafeiriou *et al.*, 2020). Increased GABA transmission could therefore constitute in a hyperactive cortical network in 1qDel E-hCOs, similar to that seen in 2D 1qDel neurons (Chapman *et al.*, 2021). This suggestion is bolstered by evidence that the GABA polarity switch is absent or abnormal in other pathogenic CNVs (Amin *et al.*, 2017), as well as SCZ (Toritsuka *et al.*, 2021).

Evidently, there are significant differences between all three research models of 1qDel. Discrepancies are to be expected, given the differences in culture and development, although there is a common theme of abnormal neurogenesis coinciding with cortical dysfunction (Nielsen *et al.*, 2017; Reinwald *et al.*, 2020; Chapman *et al.*, 2021). 1qDel E-hCOs do overlap certain aspects of the 2D 1qDel neuronal model, including NPC proliferation abnormalities (Chapman *et al.*, 2021). To their credit, 1qDel E-hCOs emulate characteristic features of 1qDel such as microcephaly of PFC structures that are only otherwise seen in patients (Sønderby *et al.*, 2021). As different aspects of 1qDel are explored across multiple models, it is difficult to discern a clear picture of its pathology. It would therefore be advantageous to bring all research models together to target individual features of 1qDel collaboratively.

5.5 Conclusion

The aim of this investigation was to recapitulate 1qDel patient phenotypes in patient-derived E-hCOs of microcephaly and SCZ, of which the former was observed and analysed in detail. Microcephaly was pinpointed to begin from the onset of 1qDel E-hCO differentiation and proceed until maturity, whereupon addition of media that supported neurogenesis resolved the microcephaly. Significant detrimental effects impacted each predominant cell type relevant to the timepoint, most notably those responsible for expanding the proliferative NPC pool, NECs and RGs. Each cell type had distinctive characteristics that contributed to the microcephaly observed, with disrupted neuroepithelium and altered cell cycle being consistent phenotypes throughout 1qDel E-hCO differentiation. A suggested mechanism of adverse apoptosis, proliferation and cell organisation were proposed for the microcephaly observed in EB and NE stages of 1qDel E-

hCO differentiation, whilst an evidence-based mechanism was hypothesised for the microcephaly occurring during the ND stage. Overall size was limited at Day 21 as a result of hypothesised deprecated NOTCH signalling from the deleted *NOTCH2NLA*, inducing premature neurogenesis and a feedback loop of DNA DSBs, cell cycle arrest and M phase disruption that was believed to reduce the NPC pool. Recovery of microcephaly was a result of excessive representation of ventral forebrain progenitors at Day 30, to the suspected detriment of cortical lamination and neuronal radial migration, culminating in an expansion of presynaptic GABA-ergic markers thereafter. Although the outcomes of modelling 1qDel in E-hCOs resembled a number of other primary and secondary microcephaly cerebral organoid studies (Lancaster *et al.*, 2013; R. Li *et al.*, 2017; Zhang *et al.*, 2019), they do not represent the majority of SCZ phenotypes in both cerebral organoid or patient studies. Instead, 1qDel E-hCOs have a closer resemblance to ASD cerebral organoids, particularly during maturation as the E-hCO expands and the GABA-ergic synapses become more prevalent (Mariani *et al.*, 2015). Evidently, there is substantial exploration necessary to fully characterise 1qDel E-hCOs and determine the mechanisms contributing to the observed phenotypes, but the results provided here provide insight into what those next steps should be.

6 General Discussion

6.1 Refinement of Cerebral Organoid Culture, Analysis and Experimental Design is Necessary for Disease Modelling

Evidence within current literature has illustrated that there are various methodologies to choose from to generate cerebral organoids (Lancaster *et al.*, 2013; Watanabe *et al.*, 2017; Yoon *et al.*, 2019; Giandomenico, Sutcliffe and Lancaster, 2021). More recently, however, certain versions of these methodologies have been called into question and examined for both replicability and quality of mimicking neurodevelopment (Velasco *et al.*, 2019; Yoon *et al.*, 2019; Hernández *et al.*, 2021; Uzquiano *et al.*, 2022). Similarly, questions are arising with regards to the analysis of cerebral organoids (Albanese *et al.*, 2020; Beghin *et al.*, 2022). The research presented in this thesis supports such scrutiny of both analysis and generation of cerebral organoids. Firstly, this research illustrated the inconsistencies of using current methods of cerebral organoid ICC analysis, including the flaws of using random field for image acquisition, using

individual measurements such as area for normalisation and ignoring the influence of the dead core in total cell count (Figure 3.5 and 3.6). These flaws would have been detrimental to finding the phenotypes of 1qDel E-hCOs. 1qDel E-hCOs are heterogenous in arrangement and size of ventricles, as well as have large areas of homogenous neuronal outgrowth (Figure 5.8-5.10); this would skew any random field measurements of ICC images. Similarly, using individual measurements for normalisation of ICC quantification and ignoring the dead core bias in total cell count would have been less successful in identifying 1qDel phenotypes than using the APD metric and the predicted CC3 count derived from it. Some analysis such as DCX coverage and M phase cell quantity of 1qDel E-hCOs (Figure 5.14.A and 5.16.A) showed the same significant differences between control and 1qDel E-hCOs at Day 21 when measured using both traditional and adapted methods of analysis. However, the outcome of Day 21 TUNEL and p53/Ki67^{+} analysis varied substantially depending on what was chosen, whether it be raw count values, raw count values as a percentage of total cells or raw count values normalised to APD. Lastly, in the absence of the high throughput analysis pipeline and unique approaches to NPC analysis, the persistent 1qDel phenotype of M phase NPC disassociation from the apical edge of lumens was unlikely to be found without significant manual input. In summary, more investigation is necessary on how best to quantify cerebral organoids, but adapted methodology such as those presented here are a good choice for cerebral organoid analysis in future.

Although the development of analysis methodology for cerebral organoids resolved a number of issues within current methodology, the protocol assessment of Basic, ROCKi and Enhanced hCOs was more limited in its scope when compared to the likes of current cerebral organoid protocol validation (Lancaster *et al.*, 2017; Velasco *et al.*, 2019; Yoon *et al.*, 2019; Sivitilli *et al.*, 2020). However, such studies that are dedicated to refining cerebral organoid generation use a range of protocols for comparison, but neglect outcomes such as the Ri-hCOs that are otherwise unsuccessful. As discussed, Ri-hCOs' inconsistent density, excessive growth and absence of telencephalic lineage make them a poor choice of hCO (Figure 4.4.B, 4.7.B, 4.8.B, 4.19.C-D and 4.24.C-D). Erroneous results such as these are nevertheless informative, and could be the foundation from which to build new organoids; the ROCKi protocol could be the start point from which to develop neural crest cell organoids, for example. Conclusions on the best choice of hCO protocol were based on incremental improvements exhibited by the

Enhanced protocol, such as proliferation and NPC/IP/CP cell populations (Figure 4.9 and 4.26-4.27). However, unquantified observations of B-hCOs also found B-hCOs more unstable in culture than their E-hCO counterparts, undertaking destructive cystic formation after exposure to RA. 1qDel B-hCOs were particularly affected when trialled, losing 60-70% of a single differentiation before Day 30. With this observation combined with the quantified improved characteristics, it was therefore clear that the E-hCO was ultimately a better choice for modelling 1qDel.

Finally, experimental design of cerebral organoids would benefit from a longitudinal analysis approach as opposed to ≤3 timepoints. Although many cerebral organoid studies have multiple timepoints (Mariani *et al.*, 2015; Iefremova *et al.*, 2017; Zhang *et al.*, 2019; Khan *et al.*, 2020; Bowles *et al.*, 2021), pre-neurogenic timepoints of cerebral organoids have largely been overlooked in favour of analysing the developing cortex due to its relevance in disease modelling (Dang *et al.*, 2016; Fiddes *et al.*, 2018). However, results from within and across timepoints between Day 0 - 21 of the Enhanced protocol acts as evidence in support of such analysis. Comparing control samples to themselves clarified what cellular populations were present at early stages of E-hCO development (Figure 3.4), and therefore which were vulnerable to 1qDel (Figure 5.5 and 5.6). It has also proved beneficial to target early timepoints when pinpointing the onset of microcephaly in 1qDel samples (Figure 5.2.B), of which only a few other cerebral organoid papers are known to investigate size so early on (Iefremova *et al.*, 2017; Fiddes *et al.*, 2018). The research presented here therefore supports the necessity of looking at such timepoints for disease modelling NDDs.

6.2 Disease Model Phenotypes can be Misconstrued due to Within-Genotype Variation in Cerebral Organoids

Although homogeneity within genotypes is key to dissecting disease phenotypes, cerebral organoids are known to be susceptible to variation, even within controls (Yoon *et al.*, 2019; Hernández *et al.*, 2021). Control #1 and #2 E-hCOs were found to diverge on a number of morphological and physiological features, including overall growth (Figure 4.4.C-D) and cell death (Figure 4.17.C and 4.17.F). The changes continue with cellular composition, with large variations in $SOX2^{+}$ NPC abundance (Figure 4.26.E and 4.27.C) and transcription of forebrain and synaptic markers (Figure 4.19.E and 4.29.E-F). These differences are despite both control cell lines illustrating pluripotency as stem cells (Figure 3.1-

2). However, it was noted that Control #2 hIPSCs had significant downregulation of *NES* after ectodermal differentiation using the trilineage kit (Figure 3.2), a possible indicator of future ectodermal-specific differentiation issues, such as those observed in E-hCO differentiation. Arguably this divergence in outcomes is as tied to the Enhanced protocol as it is the cell line; B-hCOs of the two control cell lines did not exhibit transcriptional differences, but did see deviations in growth (Figure 4.4.C, 4.10.D, 4.15.G, 4.19.G, 4.21.G, 4.28.G and 4.29.G-H). Despite the variability caused by the protocol and/or the cell line, the differences between the two control E-hCOs are in keeping with known within-genotype variations observed in cerebral organoids (Yoon *et al.*, 2019; Hernández *et al.*, 2021). For example, there is a correlation where control cerebral organoids that have fewer radial glia also report having greater astroglia and GABA-ergic interneurons (Yoon *et al.*, 2019); a similar outcome to Control #2 E-hCOs.

Such variability presents a number of concerns when disease modelling however. As discussed previously, there are two core features that Control #2 E-hCOs and 1qDel E-hCOs share that distinguish them from Control #1 E-hCOs: substantial reductions in NPC ($SOX2^{+}$) populations and heightened transcription of ventral forebrain progenitors and presynaptic GABA-ergic interneuron markers (Figure 5.18.B-C, 5.20.A-C, 5.22.A and 5.23.A-B). In the absence of Control #1 E-hCOs, it would be difficult to dissect these phenotypes presented by 1qDel E-hCOs when comparing to Control #2 E-hCOs alone. On the other hand, it is useful to have all three cell lines in comparison to one another, to observe if different phenotypes could be interconnected, e.g., NPC quantity and ventral forebrain representation. Overall, there is a requirement for greater numbers of control and patient cell lines to ensure that the conclusions about 1qDel pathology is accurate. However, the limited cell line number per genotype is not unusual in cerebral organoid literature, with many examples of fewer than three cell lines being used per genotype, including controls (Allende *et al.*, 2018; Mellios *et al.*, 2018; Daviaud *et al.*, 2019; Klaus *et al.*, 2019; Wang *et al.*, 2020; Dhaliwal *et al.*, 2021; Kyrousi *et al.*, 2021; Martins *et al.*, 2022; Wang *et al.*, 2022); some of these studies even report differences amongst their controls (Martins *et al.*, 2022; Wang *et al.*, 2022). The research presented here should therefore be taken as a cautionary example as to why considerably greater numbers of both control and patient cell lines are necessary.

6.3 Future Considerations for 1q21.1 CNV Research

The next experimental step for understanding 1qDel microcephaly is to manipulate the signalling pathways suggested to be affecting 1qDel E-hCO development: NOTCH and Wnt. This would be achieved by first using rescue experiments, applying exogenous pathway modulators that are agonists of the NOTCH and Wnt pathway and are likely to engage with 1q21.1 genes, e.g. NOTCH2 and CP21, respectively (Suzuki *et al.*, 2018; Y. Zhang *et al.*, 2018). In consideration of the timepoints affected by Wnt and NOTCH, a reasonable course of action would be to introduce these agonists to 1qDel cells upon EB aggregation (Day 0) to neutralise 1qDel's influence on these pathways. Maintaining the exposure to the agonists until Day 11 would provide evidence of which pathway, if not both, is contributing to 1qDel E-hCO microcephaly. Cerebral organoid studies on related NDDs have attempted similar signalling pathway manipulations for resolving early phenotypes with effective success (Iefremova *et al.*, 2017; Srikanth *et al.*, 2018; Zhang *et al.*, 2019, 2020; Kang *et al.*, 2021). Studies bearing significant relevance to 1qDel pathology illustrated that Wnt antagonism in SCZ patient-derived cerebral organoids improved proliferation to control levels (Srikanth *et al.*, 2018) and GSK3β inhibition/Wnt activation substantially improving lumen size and M phase organisation in microcephalus Miller-Dieker syndrome cerebral organoids (Iefremova *et al.*, 2017). The agonist-exposed 1qDel E-hCOs would continue to grow in culture, absent of exogenous input, to determine whether subverting the microcephaly phenotype alleviates the abundance of ventral forebrain progenitors and improve the suspected cortical dysfunction outcome.

An alternative idea would be to replicate the *NOTCH2NL* knockdown created by Fiddes *et al.*, (2019), but expand substantially on the perfunctory investigation conducted in the study. As *NOTCH2NLA* is expected to be a 1.5 copy reduction (Fiddes *et al.*, 2018; Suzuki *et al.*, 2018) as opposed to a heterozygous or homozygous knockout, it would be necessary to monitor NOTCH reduction. The aim of the knockdown would be to see if the $NOTCH^{low}$ environment caused by *NOTCH2NL* knockdown emulates aspects of 1qDel E-hCOs, such as the abnormal cell cycle, early neurogenesis or shift to ventral forebrain cellular identity. If the *NOTCH2NL* knockdown does not replicate 1qDel E-hCO results, similar experimental manipulations would target the 1q21.1 genes associated with the Wnt pathway, namely *BCL9* because of its association to β-catenin. Alongside these knockout experiments, it would be significantly beneficial

to create isogenic hIPSC lines of 1qDel patients, as opposed to using standard control hIPSCs, to minimise genetic heterogeneity from age, gender, etc. Because of the vast complexity of the 1q21.1 locus, and the multiple paths that could be contributing to 1qDel E-hCO phenotypes, having a concise, evidence-based approach for future investigations would progress 1qDel research forward.

From a broader perspective, future 1q21.1 CNV research should focus on cohesive studies that can be cross-analysed across models, with the intention of addressing key patient phenotypes. For example, *in vivo* 1qDel mouse models assess the association of SCZ with 1qDel by examining dopaminergic transmission (Nielsen *et al.*, 2017). However, *in vivo* 1qDel mouse models do not exhibit any functional differences in the PFC and despite reduced overall brain volume, only subcortical structures were morphologically affected (Reinwald *et al.*, 2020). Non-primate *in vivo* models also lack the multiple human-specific, cortical-development-related genes, such as the paralogs *NOTCH2NL* and *NBPF* (Fiddes *et al.*, 2019). On the other hand, 1qDel patient-derived *in vitro* cortical neurons identify cellular and functional aberrations not observed in mouse models (Chapman *et al.*, 2021), but do not exhibit SCZ-associated glutamate hypofunction (Uno and Coyle, 2019) or reference microcephaly (Sønderby *et al.*, 2021). 1qDel E-hCOs reinforce *in vitro* 1qDel studies' conclusion of differential attributes of human-derived 1qDel cortical neurons and NPCs, but 1qDel E-hCO are the only model to exhibit the PFC-specific microcephaly presented in 1qDel patients (Sønderby *et al.*, 2021). However, as discussed previously, 1qDel E-hCOs do not pose a significant similarity to characteristic SCZ phenotypes (Nielsen *et al.*, 2017; Cadinu *et al.*, 2018; Uno and Coyle, 2019).

Other CNV disorders with genetic arrangement reciprocity, such as 16p11.2, have similar cross-model conflict. Models of 16p11.2 deletion, including patients, *in vivo* models and patient-derived cerebral organoids, all exhibit macrocephaly (Pucilowska *et al.*, 2015; Steinman *et al.*, 2016; Urresti *et al.*, 2021). However, cerebral organoids also observe accelerated cortical neuron maturation and impaired migration that had been otherwise unobserved in 16p11.2 deletion 2D neurons or mouse models (Urresti *et al.*, 2021). Although these features were not observed in *in vitro* 2D neurons, different phenotypes of cerebral organoids and 2D neurons were rescued by RhoA inhibition, suggesting a shared mechanism across models despite phenotypic variance (Sundberg *et al.*, 2021; Urresti *et al.*, 2021). The combined overview of 16p11.2 deletion research mirrors

the collective results from various models of 1qDel; although shared mechanisms are likely, each research model represents distinct aspects of CNV pathology. In summation, both the research presented here and current evidence suggests that no singular research model is capable of encapsulated the array of clinical phenotypes presented in CNV disorders, including those of 1qDel.

It would be valuable to incorporate the lessons learnt from the 1qDel research presented and referenced here to future investigations of 1qDup. Although 1qDup has been modelled in 2D neurons (Chapman *et al.*, 2021), there is no *in vivo* counterpart. 2D 1qDup neurons have minimal pre-neurogenesis phenotypes compared to 1qDel, but exhibit substantial loss of neurons, with minimal electrical activity reported of those remaining (Chapman *et al.*, 2021). As such it is unknown if the macrocephalus phenotype presented by 1qDup patients persists into *in vivo* models; few NPC phenotypes were found in 2D 1qDup neurons which sheds doubt on this possibility. However, 1qDel E-hCOs emulate the 1qDel-associated microcephaly more closely to patient phenotypes than 1qDel *in vivo* models, as well as exhibiting more NPC phenotypes than 2D 1qDel neurons. It is therefore reasonable to choose E-hCOs for future 1qDup research, to investigate NPC phenotypes for potential ties to 1qDup patient-associated macrocephaly, as well as attempting to corroborate the severe neuronal loss found in 2D 1qDup neurons (Chapman *et al.*, 2021).

6.4 Experimental Improvements for Cerebral Organoid Research Encompassing Both Protocol Validation and Disease Modelling

As discussed in each Section of the research presented here, there are individual experiments relevant to each Section that would lead to fulfilling unresolved questions. However, there are overarching improvements across this body of work that can, and should, be made in future.

Most importantly, each chapter of this research would benefit from an increase in independent differentiations (biological replicates), as well as an increase in cell lines of both controls and 1qDel patients. More biological replicates would improve the predictability of the apoptotic post-hoc correction for cell count. Conclusions over hCO protocol validation would be more statistically significant, as all three hCO protocols could be compared to one another consistently if all cell lines were represented. It would also determine how variable control cell lines are in different protocols. In a collective of other control cell lines, it would be possible

to determine if Control #2 E-hCOs are an outlier, representative of Control #2 as an underperforming cell line or reflecting possible heterogeneity induced by the Enhanced protocol. Finally, in addition to more control cell lines, more 1qDel patient cell lines are necessary to cement the 1qDel E-hCOs' results of microcephaly, early neurogenesis and ventral forebrain representation. It would also be beneficial to have 1qDel patients who exhibited the SCZ phenotype (Sønderby *et al.*, 2021). These patients could be treated as a separate cohort from non-SCZ 1qDel patients, in order to determine how SCZ changes the already atypical neurodevelopment of 1qDel patients.

In addition to expanding the quantity of cell lines and differentiations, there are a number of productive experimental techniques that would be powerful for both validating cerebral organoid protocol, as well as examining 1qDel pathology in the future. To improve and expand upon information that is already known, RNAseq data should be used, using a similar format to other longitudinal developmental studies for a number of reasons (Kaitetzidou *et al.*, 2019; Wang *et al.*, 2021; Fleck *et al.*, 2022). RNAseq would be able to quantify genes that are difficult to accurately capture via qPCR due to high homology, for example paralogs such as *NOTCH2NLA/B* or *NBPF11/12/14*. RNAseq would also provide the opportunity to observe each timepoint's specific transcriptional nuances by clustering differentially expressed gene sets (Fleck *et al.*, 2022; Paulsen *et al.*, 2022), as opposed to manually selecting genes of interest. RNAseq is quickly becoming a necessary analysis technique for both protocol validation and disease modelling in cerebral organoid literature (Mariani *et al.*, 2015; Velasco *et al.*, 2019; Sivitilli *et al.*, 2020; Paulsen *et al.*, 2022). It would be beneficial for confirming the specificity of dorsal forebrain identity of E-hCOs and B-hCOs, as well as further investigating Ri-hCOs hypothesised NCC identity. In the context of 1qDel, it could uncover unknown shifts in cellular identity prior to Day 21, but also highlight if 1qDel shares similar processes to primary or secondary microcephaly disorders, such as MCPH-related DNA damage repair mechanisms and centrosomal abnormalities (Alcantara and O'Driscoll, 2014).

It should be noted that a trend in mRNA abundance does not necessarily translate to more cells being positive for the protein of interest for a number of reasons, for example, it is possible that more mRNA can be generated per cell or that there is pre-translational regulation by microRNAs (miRNAs). Significant deviations were found when comparing results of transcriptional analysis and cell

abundance in both protocol validation and disease modelling. As an example, it would be useful to known how miRNAs regulate KI67 expression, as the transcription and abundance of KI67^{+} cells vary in both Section 4 and Section 5. Pre-translational miRNAs have been attributed to cell cycle regulation in NPCs (Nigro *et al.*, 2012; Zhang, Zhang and Sun, 2018), and KI67 in NPCs specifically (Wang *et al.*, 2017). Similar examples of diverging aspects of transcription and cell abundance have been found for neocortical layers of SOX2^{+} VZ, TBR2^{+} SVZ and CTIP2^{+} CP spanning both protocol validation and 1qDel investigations (Figure 4.26-4.28 and 5.18-5.19). This could also be connected to miRNA regulation, as miRNAs have also proven capable of regulating transitionary states of NPCs (Bian *et al.*, 2013; Zhang *et al.*, 2016) and neurons (Shu *et al.*, 2019) in the neocortex by targeting the mRNA for degradation or blocking translation via the RNA-induced silencing complex (reviewed by Popovitchenko and Rasin, (2017)). Few cerebral organoid studies have ventured into analysing miRNAs involvement in neurodevelopment, but those that have have shown that miRNAs have significant involvement with governing signalling pathways, and that miRNAs contribute to neurodevelopmental phenotypes such as microcephaly (Mellios *et al.*, 2018). It would also provide conclusive information on both the naïve or primed state of stem cells, as well as concluding whether Day 5 E-EBs are primitive NEC aggregates or not (Dodsworth *et al.*, 2020). It is therefore beneficial in future research to complement miRNA investigations with RNAseq data in cerebral organoid studies, to discern why such differences in transcriptional and translational analysis could appear.

Analysis of cellular abundance and organisation could significantly improve beyond 2D cryosections. Whole cerebral organoid light sheet imaging should become a staple of cerebral organoid disease modelling to ensure non-biased ICC quantification (Albanese *et al.*, 2020), and to make best use of the 3D structure of cerebral organoids (Albanese *et al.*, 2020; Beghin *et al.*, 2022; Ishihara *et al.*, 2022). Such imaging would have been particularly beneficial for early aggregates where traditional ICC methods were not feasible. For example, visualisation of Day 5 E-EBs and Day 11 E-hCOs through light sheet imaging would provide information about the structural organisation of the spheroid and confirm if rosette formation was a contributing factor to an increase in proliferation (Figure 3.4.D), by using KI67 and ZO1-specific antibodies. Similarly, targeting Ri-hCOs' and 1qDel E-hCOs' during early development with light sheet imaging could have illuminated

the differential features that led to their detrimental outcomes of macro- and microcephaly, respectively (Figure 4.3 and 5.2). Light sheet imaging would provide data comparative to later timepoints, for features such as lumen morphology, apoptosis, proliferation and cell cycle, the likes of which have been conducted in similar EB/neurosphere studies (Odenwald *et al.*, 2017; Adhya *et al.*, 2021; Beghin *et al.*, 2022). For Ri-hCOs, this would be informative with regards to confirming the absence of lumens and the hypothesis of reduced apoptosis inducing the amorphous growth of early Ri-hCOs (Figure 4.3). In the context of investigating causative factors of 1qDel, it may also be beneficial to also image TUNEL staining for DNA DSBs (Klaus *et al.*, 2019), or include a sparsely-labelled GFP construct to analyse the changing morphology between NEC and RG, i.e. columnar to pyramidal (Benito-Kwiecinski *et al.*, 2021), to determine if there is a change in timing for the transition between these two NPCs. It would also be important that, given the Wnt association in 1qDel E-hCOs at early timepoints, β-catenin should be analysed both for lumen organisation by adherens junctions but also if β-catenin is cytoplasmic or nuclear in localisation, which is regulated by BCL9 (Takada *et al.*, 2012). As these early timepoints hold key information for both successful and unsuccessful hCO differentiation, as well as crucial evidence to answer the question of 1qDel E-hCOs microcephaly, this would be essential for future NDD research in cerebral organoids.

Significant ICC quantification was conducted in this report for timepoints from Day 21 onwards, that utilised the high throughput analysis pipeline and adapted post-hoc methodology. However, hCOs have a vast array of cellular identities and therefore not all cell populations of hCOs have been reported herein. Future research on both protocol validation and 1qDel investigations would benefit greatly from the additional investigation into different cell populations, the likes of which have already been examined in other cerebral organoid studies (Lancaster *et al.*, 2013; Li *et al.*, 2017; Albanese *et al.*, 2020; Arzua *et al.*, 2020).

Firstly, although NPCs were investigated in this report, bRGs were only represented in transcriptional analysis (*HOPX*) (Figure 4.28 and 5.19). It would be beneficial to know if E-hCOs are capable of generating $HOPX^{+}$ bRGs as they reside in the oSVZ predominantly and, if so, whether they were responsible for the increased number of M phase NPCs dissociated from the apical edge of the lumen in 1qDel E-hCOs (Figure 5.14.B). Furthermore, future research should focus on defining E-hCOs ability to display RG-specific asymmetric/symmetric division for

neuronal production and substantiation of the NPC pool. This is particularly relevant in the context of Day 21 1qDel E-hCO, as it would provide weight to the hypothesis of early neurogenesis. By combining either pVIM or pHH3 with centrosome-specific pericentrin and a lumen marker (ZO1, β-catenin, actin, etc.), the angle of nuclei cleavage can be determined (Bershteyn *et al.*, 2017; An, Kuo and Tang, 2022). However, there is a known affiliation of centriole disruption in MCPH (Alcantara and O'Driscoll, 2014), and so it would be preferable to use live imaging using a sparsely labelled GFP to monitor the division planes of early born RGs (Bershteyn *et al.*, 2017; Benito-Kwiecinski *et al.*, 2021). To complement this data, as well as previous M phase data, a pulse-chase approach using EdU labelling would provide information about the length of both S phase and the total cell cycle of Day 21 1qDel E-hCOs (Zhang *et al.*, 2019; Marin Navarro *et al.*, 2020). These experiments would provide a comprehensive scope of the abnormal cell cycle in Day 21 1qDel E-hCOs and how it could contribute to the microcephaly.

The research presented here would also benefit from increased investigation of mature neuronal populations, specifically cortical layer formation. Although CTIP2 was used as a representation of lower layer neurons, this should be replaced in future with TBR1, as TBR1 is dorsal forebrain-specific and in circumstances such as the ventral forebrain-favouring 1qDel E-hCO, it is important to make that distinction (Englund *et al.*, 2005). Only transcriptional analysis of upper layer neurons were represented in this report, as Day 60 hCOs were believed to be unlikely to generate them (Sivitilli *et al.*, 2020); in future it would be suggested to at least investigate this timepoint for upper layers (SATB2/BRN2) to confirm when they arise in E-hCOs or other hCO protocols. Additionally, this could provide evidence to confirm or deny if 1qDel E-hCOs produce upper layer neurons at an abnormal rate, akin to what is observed in SCZ patient-derived cerebral organoids and patients (Srikanth *et al.*, 2018; Notaras, Lodhi, Dündar, *et al.*, 2021; Batiuk *et al.*, 2022). Lastly, the Layer I marker reelin should be included in a revised plan for future investigations, to identify how E-hCOs undergo early cortical layer splitting, as well as examine the support provided for radial neuronal migration (Hashimoto-Torii *et al.*, 2008). Investigations of reelin in 1qDel E-hCOs would confirm if the elevated *RELN* transcription found in Day 21 and 30 1qDel E-hCOs was represented on a cellular level. As a result, this could lead to determining if there is a neuronal migration phenotype in 1qDel E-hCO, suggested by the association of 1qDel to SCZ

(Teixeira *et al.*, 2011), as well as the organisation of neurons surrounding the outer edges of Day 30 1qDel E-hCOs (Figure 5.15.H). The collection of such cortical layer data would provide the necessary information to construct a full picture of cortical layer organisation in hCOs, a useful tool for disease modelling as certain NDDs affect such organisation, including possibly 1qDel (Bershteyn *et al.*, 2017; de Jong *et al.*, 2021; Kang *et al.*, 2021; Paulsen *et al.*, 2022).

Finally, the functionality of the mature neurons in cerebral organoids are vital in disease modelling scenarios similar to that of 1qDel, as cortical dysregulation may be a key phenotype of the disease (Chapman *et al.*, 2021). Experimental techniques used to analyse both the quantity and functional capacity vary relative to the research question. Multiple electrode arrays of cerebral organoids have proved informative for documenting their global neuronal activity (Pelkonen *et al.*, 2022; Schröter *et al.*, 2022); the same can be said of Ca^{2+} imaging or whole-cell patch clamping and individual neuronal activity (Lancaster *et al.*, 2017; Gordon *et al.*, 2021; Saberi *et al.*, 2022). In addition to electrophysiological recordings, alternative methodologies can be used to document mature neuronal activity in cerebral organoids. This could include using confocal microscopy to acquire high magnification ICC images of synaptic markers, such as GABA (Sawada *et al.*, 2020; Kang *et al.*, 2021), vGLUT1 (Mariani *et al.*, 2015; Samarasinghe *et al.*, 2021) or PSD95 (Ormel *et al.*, 2018; Yakoub and Sadek, 2019), colocalised with MAP2 to confirm localisation of synapses on mature neurons. Multiple electrode arrays and/or Ca^{2+} imaging would accompany ICC quantification, and one of the key revisions of Table 4.1 from which future hCO protocols would be judged. However, documenting functional activity would not have replaced the current qPCR results of pre- and postsynaptic markers (Figure 4.29 and 4.30). Instead, the qPCRs would be treated as complementary data to the electrophysiological analysis.

In the context of future 1qDel investigations, multiple electrode arrays would be key to illustrating the cortical dysfunction phenotype, by defining what global shortcomings were occurring in 1qDel E-hCOs. Previous work on 1qDel *in vitro* cortical neurons have already proved significant changes in local and global neuronal activity using Ca^{2+} imaging and multiple electrode arrays, respectively (Chapman *et al.*, 2021). Although it has not been attempted in any known cerebral organoid literature, it would be greatly beneficial to separate global synchronicity from local regions of synchronicity, distinguished by the characteristics of

epicentres of electrical activity. As the knowledge of sliced cerebral organoids' network capability is in its infancy (Giandomenico *et al.*, 2019; Sharf *et al.*, 2022), it would be informative to see if there are different quantities, spatial organisation or functionality of epicentres of synchronicity between control and 1qDel E-hCOs and how this would contribute to the cortical dysfunction phenotype. This would be of particular interest given the localised regions of abundant MGE progenitors in Day 30 1qDel E-hCOs (Figure 5.21.C). Overall, electrophysiological data of 1qDel E-hCOs would be an asset to further compare 2D 1qDel neurons to 1qDel E-hCOs, as well as extrapolating the information in reference to 1qDel patients.

The proposed future experiments of multi-omic analysis, in-depth 3D imaging and functional analysis, as well as substantially expanding the differentiation and cell line quantity, is a significant undertaking for the future. However, recent cerebral organoid publications are already utilising this volume of information and therefore such future experiments should be held to similar standards (Beghin *et al.*, 2022; Fleck *et al.*, 2022; Uzquiano *et al.*, 2022). As a result, some, if not all, of these improvements and future experiments are necessary to provide the best reflection of the E-hCO model, whilst utilising it to its fullest for deciphering 1qDel pathology in greater detail than what is reported in this study.

7 Conclusion

In conclusion, the research presented here supports the requirement for comprehensive examination of cerebral organoid generation and analysis prior to disease modelling. It does so by highlighting ill-suited practices of quantifying cell death, live cellular composition and morphological data, as well as the repercussions of poor cerebral organoid protocol design. To replace these inefficient methodologies, a high throughput ICC analysis pipelines and adapted methodologies were developed. This required use of a new normalising constant, APD, which was able to normalise dead cell count and morphological analysis, whilst predicting apoptotic cells to adjust total cell count to better represent live cell populations. Development of a new hCO protocol utilised these new resources, as well as previous cerebral organoid literature, to critically evaluate key aspects of hCO development, pinpointing one hCO protocol that was both stable in culture and presented all requested features. The Enhanced protocol was therefore chosen, and the 1qDel patient-derived hIPSC line was differentiated into E-hCOs.

Similarities in phenotype between 1qDel patient and cerebral organoid were found immediately, namely microcephaly. Microcephaly was observed during the first 21 days of culture, either believed or confirmed to be a result of faulty cell cycle due to the impact of 1qDel on Wnt and NOTCH signalling pathways. By Day 30, the microcephaly had resolved but indicators of cortical dysfunction were found in the form of disrupted dorsal forebrain structures and increased ventral forebrain progenitors and presynaptic GABA-ergic markers during neuronal maturity. Microcephaly of cortical structures has not been observed in any other research model except in clinical 1qDel patient cohorts (Sønderby *et al.*, 2021), whilst preliminary evidence of cortical dysfunction in 1qDel E-hCOs is reflective of other *in vitro* 1qDel studies (Chapman *et al.*, 2021) but not of SCZ specifically. As illustrated by the successful recapitulation of 1qDel patient microcephaly, cerebral organoids are a favourable choice of research model when researching NDDs.

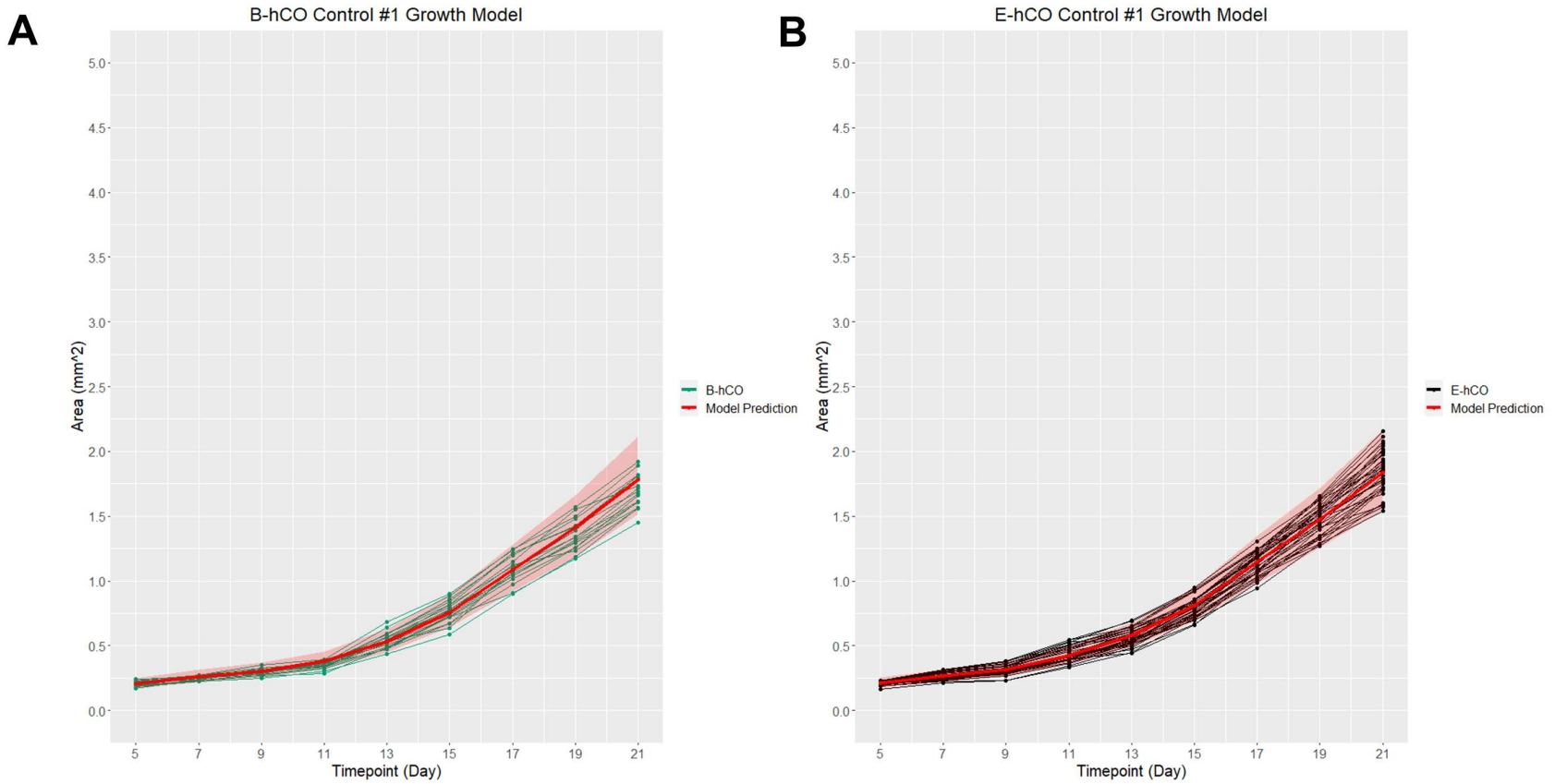

Supplementary Figure 1.A: Simulated prediction of mixed-effects model to validate statistical conclusions made in Figure 4.4.A. Mixed-effects model used was as follows "lmer(log(Area) ~ Protocol*Timepoint*Media + (1|Individual) + (1|Timepoint:Media))". The model was optimised to fit statistical assumptions including homoscedasticity and normal distribution of residuals. Graphs represent Control #1 B-hCOs' **(A)** and E-hCOs' **(B)** raw area values as a dot-line plot, overlaid with a predicted value ± 95% CIs (colour = red). Libraries used: readxl, car, data.table, performance, multcomp, mgcv, emmeans, merTools, patchwork, lme4, tidyverse, ggplot.

A

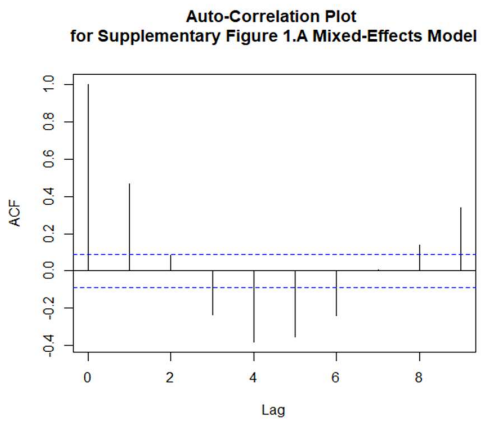

B

Parameter	Estimates (95% CI)	*F* value	P value
Supplementary Figure 1.A: Fixed Effect Variance			
(Intercept)	0.068 (0.057, 0.080)	*NA*	*NA*
Protocol	1.235 (1.127, 1.353)	$11.939_{1,53}$	$5.499e^{-4}$
Timepoint	1.171 (1.159, 1.183)	$1912.849_{1,485}$	$< 2.2e^{-16}$
Media	1.883 (1.423, 2.492)	$1.261_{1,485}$	0.262
Protocol: Timepoint	0.992 (0.987, 0.997)	$0.845_{1,485}$	$9.348e^{-3}$
Protocol: Media	0.811 (0.707, 0.930)	$14.450_{1,485}$	$1.439e^{-4}$
Timepoint: Media	0.940 (0.910, 0.971)	$8.122_{1,485}$	$4.372e^{-3}$
Protocol: Timepoint: Media	1.014 (0.998, 1.030)	$2.748_{1,485}$	0.097

C

Parameter	Variance (95% CI)
Supplementary Figure 1.A: Random Effect Variance	
(Intercept) Individual	0.067 (0.053, 0.082)
(Intercept) Timepoint:Media	0.049 (0.023, 0.065)
Residual	0.076 (0.071, 0.081)

Supplementary Figure 1.B: ACF plots and statistical reporting of mixed-effects models generated in Supplementary Figure 1.A. A) ACF plots denoting autocorrelation of model presented in Supplementary Figure 1.A. **B-C)** Reports of fixed **(B)** and random **(C)** effects from mixed-effects model presented in Supplementary Figure 1.A , including estimates/variance, 95% confidence intervals and *F* and *p* values. Two-way ANOVA stated that the Protocol significantly contributed to change in area ($F(1,53)=11.939$, $p=5.499e^{-4}$), (n≥20 individuals observed per protocol). Tukey post-hoc pairwise comparison determined Control #1 E-hCOs' and B-hCOs' area differed significantly in the ND phase of differentiation only (p=<0.0001) after accommodating for Media interaction.

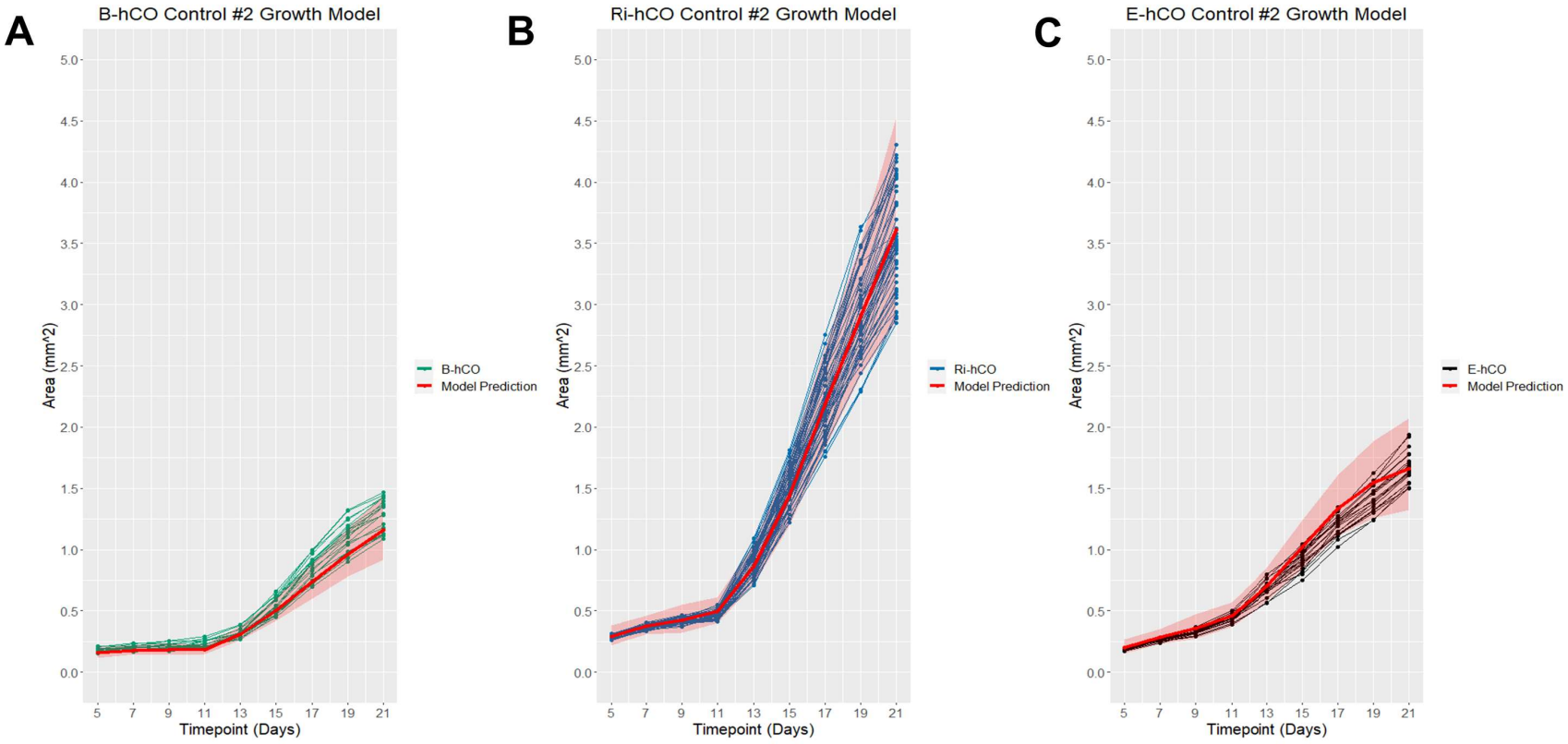

Supplementary Figure 2.A: Simulated prediction of mixed-effects models to validate statistical conclusions made in Figure 4.4.B. Mixed-effects model used was as follows: "lmer(log(Area) ~ Protocol*Timepoint*Media + (1|Individual) + (1|Timepoint:Media)". The model was optimised to fit statistical assumptions including homoscedasticity and normal distribution of residuals. Graphs represent Control #2 B-hCOs' **(A)** Ri-hCOs **(B)** and E-hCOs' **(C)** raw area values as a dot-line plot, overlaid with a predicted value ± 95% CIs (colour = red). Libraries used: readxl, car, data.table, performance, multcomp, mgcv, emmeans, merTools, patchwork, lme4, tidyverse, ggplot.

A

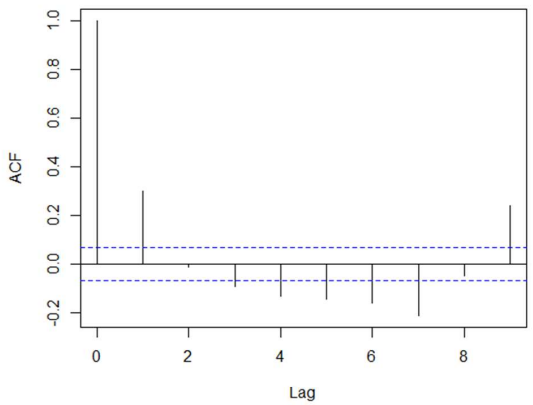

B

Parameter	Estimates (95% CI)	*F* value	P value
Supplementary Figure 1.A: Fixed Effect Variance			
(Intercept)	0.030 (0.020, 0.046)	*NA*	*NA*
Protocol ROCKi	2.114 (1.952, 2.290)	1168.379 $_{2,90}$	$< 2e^{-16}$
Protocol Enhanced	4.054 (3.684, 4.462)		
Timepoint	1.205 (1.175, 1.237)	350.883 $_{1,818}$	$< 2e^{-16}$
Media	4.851 (2.428, 9.691)	1.251 $_{1,818}$	0.263
Protocol Ri: Timepoint	1.013 (1.009, 1.018)	468.327 $_{1,818}$	$< 2e^{-16}$
Protocol E: Timepoint	0.944 (0.939, 0.949)		
Protocol Ri: Media	0.607 (0.539, 0.684)	213.403 $_{1,818}$	$< 2e^{-16}$
Protocol E: Media	0.160 (0.138, 0.184)		
Timepoint: Media	0.863 (0.796, 0.935)	3.398 $_{1,818}$	0.065
Protocol Ri: Media: Timepoint	1.041 (1.027, 1.056)	200.780 $_{1,818}$	$< 2e^{-16}$
Protocol E: Media: Timepoint	1.174 (1.154, 1.193)		

C

Parameter	Variance (95% CI)
Supplementary Figure 2.A: Random Effect Variance	
Individual (Intercept)	0.064 (0.054, 0.075)
(Intercept) Timepoint:Media	0.131 (0.065, 0.169)
Residual	0.072 (0.068, 0.076)

Supplementary Figure 2.B: ACF plots and statistical reporting of mixed-effects models generated in Supplementary Figure 2.A. A) ACF plots denoting autocorrelation of model presented in Supplementary Figure 2.A. **B-C)** Reports of fixed **(B)** and random **(C)** effects from mixed-effects model presented in Supplementary Figure 2.A , including estimates/variance, 95% confidence intervals and *F* and *p* values. Two-way ANOVA stated that Protocol significantly contributed to change in area ($F(2,90)=1168.379$, $p=<2e^{-16}$), ($n\geq20$ individuals observed per protocol). Tukey post-hoc pairwise comparison determined Protocol Basic, ROCKi and Enhanced differed significantly in area from each other at the NE and ND phases of differentiation ($p=<0.0001$) after accommodating for Media interaction, except the NE phase comparison between ROCKi and Enhanced, which was not significant.

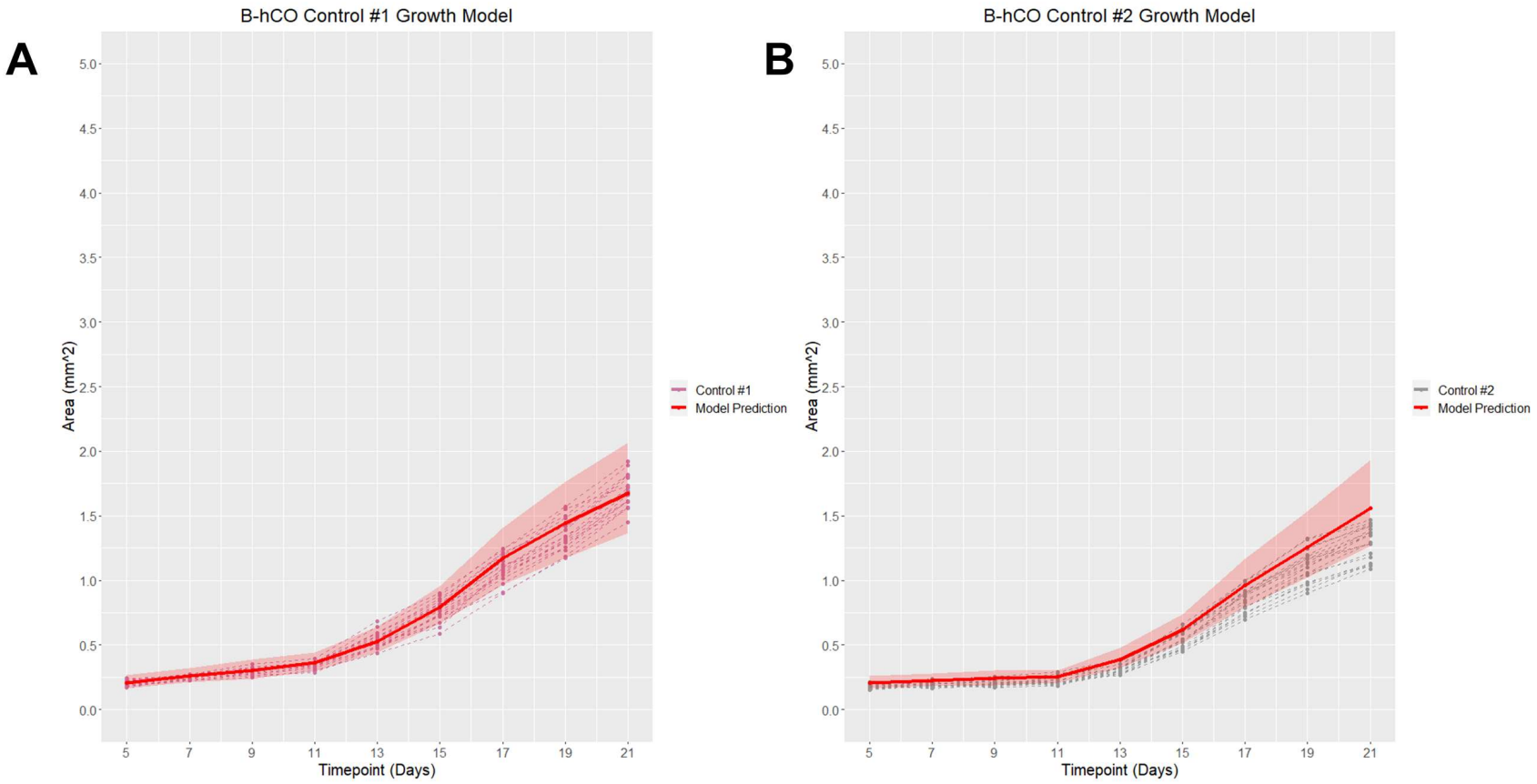

Supplementary Figure 3.A: Simulated prediction of mixed-effects model to validate statistical conclusions made in Figure 4.4.C. Mixed-effects model used was as follows "lmer(log(Area) ~ CellLine*Timepoint*Media + (1|Individual) + (1|Timepoint:Media))". The model was optimised to fit statistical assumptions including homoscedasticity and normal distribution of residuals. Graphs represent B-hCOs from Control #1 **(A)** and Control #2 **(B)** raw area values as a dot-line plot, overlaid with a predicted value ± 95% CIs (colour = red). Libraries used: readxl, car, data.table, performance, multcomp, mgcv, emmeans, merTools, patchwork, lme4, tidyverse, ggplot.

A

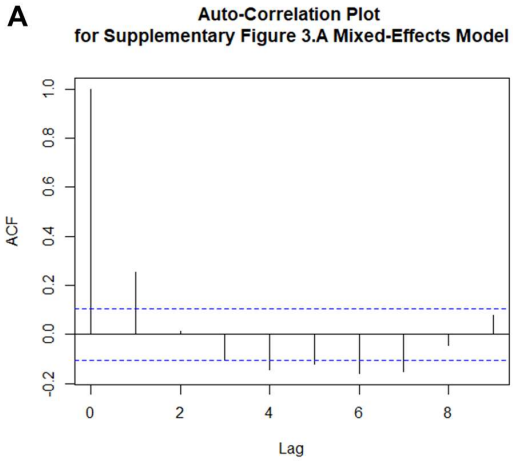

B

Parameter	Estimates (95% CI)	*F* value	P value
Supplementary Figure 3.A: Fixed Effect Variance			
(Intercept)	0.068 (0.049, 0.093)	*NA*	*NA*
Cell Line	0.445 (0.400, 0.494)	$165.026_{1,37}$	$< 2.2e^{-16}$
Timepoint	1.171 (1.148, 1.194)	$482.387_{1,341}$	$< 2.2e^{-16}$
Media	1.883 (1.108, 3.200)	$5.164_{1,341}$	0.023
Cell Line: Timepoint	1.030 (1.024, 1.036)	$0.035_{1,341}$	$6.133e^{-13}$
Cell Line: Media	2.577 (2.201, 3.017)	$74.497_{1,341}$	$< 2.2e^{-16}$
Timepoint: Media	0.940 (0.883, 0.999)	$8.372_{1,341}$	$3.809e^{-3}$
Cell Line: Timepoint: Media	0.918 (0.901, 0.935)	$82.921_{1,341}$	$< 2.2e^{-16}$

C

Parameter	Variance (95% CI)
Supplementary Figure 3.A: Random Effect Variance	
Individual (Intercept)	0.071 (0.054, 0.091)
(Intercept) Timepoint:Media	0.099 (0.048, 0.129)
Residual	0.077 (0.071, 0.084)

Supplementary Figure 3.B: ACF plots and statistical reporting of mixed-effects models generated in Supplementary Figure 3.A. A) ACF plots denoting autocorrelation of model presented in Supplementary Figure 3.A. **B-C)** Reports of fixed **(B)** and random **(C)** effects from mixed-effects model presented in Supplementary Figure 3.A, including estimates/variance, 95% confidence intervals and *F* and *p* values. Two-way ANOVA stated that the Cell Line significantly contributed to change in area ($F(1,37)=165.026$, $p=<2.2e^{-16}$), ($n\geq20$ individuals observed per cell line). Tukey post-hoc pairwise comparison determined Control #1 and #2 B-hCOs differed significantly in area ($p=<0.0001$) from each other at both the NE and ND phases of differentiation after accommodating for Media interaction.

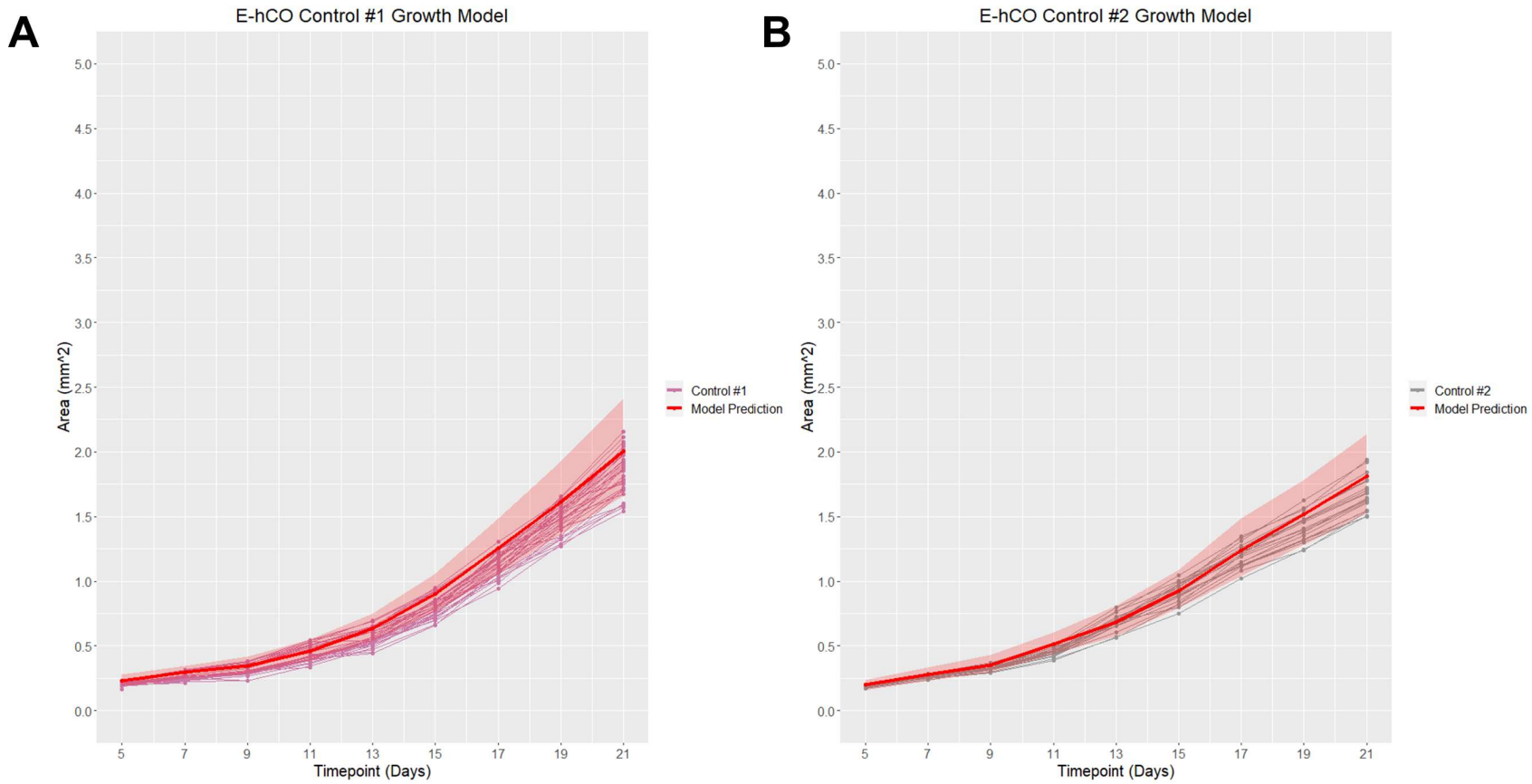

Supplementary Figure 4.A: Simulated prediction of mixed-effects models to validate statistical conclusions made in Figure 4.4.D. Mixed-effects model used was as follows: "lmer(log(Area) ~ CellLine*Timepoint*Media + (1|Individual) + (1|Timepoint:Media))". The model was optimised to fit statistical assumptions including homoscedasticity and normal distribution of residuals. Graphs represent E-hCOs from Control #1 **(A)** and Control #2 **(B)** raw area values as a dot-line plot, overlaid with a predicted value ± 95% CIs (colour = red). Libraries used: readxl, car, data.table, performance, multcomp, mgcv, emmeans, merTools, patchwork, lme4, tidyverse, ggplot.

A

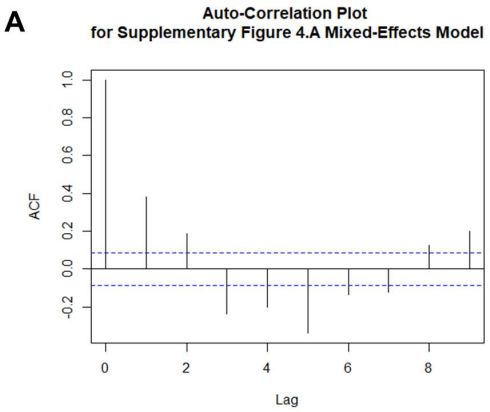

B

Parameter	Estimates (95% CI)	*F* value	P value
Supplementary Figure 4.A: Fixed Effect Variance			
(Intercept)	0.083 (0.070, 0.100)	*NA*	*NA*
Cell Line	1.459 (1.335, 1.594)	$1.910_{1,53}$	0.167
Timepoint	1.162 (1.149, 1.174)	$1684.349_{1,503}$	$<2.2e^{-16}$
Media	1.526 (1.144, 2.035)	$0.255_{1,503}$	0.613
Cell Line: Timepoint	0.979 (0.974, 0.984)	$0.000_{1,503}$	$3.53e^{-9}$
Cell Line: Media	0.507 (0.443, 0.581)	$51.605_{1,503}$	$6.787 e^{-13}$
Timepoint: Media	0.952 (0.921, 0.985)	$1.820_{1,503}$	0.177
Cell Line: Timepoint: Media	1.063 (1.046, 1.080)	$56.956_{1,503}$	$4.456 e^{-14}$

C

Parameter	Variance (95% CI)
Supplementary Figure 4.A: Random Effect Variance	
Individual (Intercept)	0.056 (0.044, 0.070)
(Intercept) Timepoint:Media	0.053 (0.025, 0.069)
Residual	0.078 (0.073, 0.083)

Supplementary Figure 4.B: ACF plots and statistical reporting of mixed-effects models generated in Supplementary Figure 4.A. A) ACF plots denoting autocorrelation of model presented in Supplementary Figure 4.A. **B-C)** Reports of fixed **(B)** and random **(C)** effects from mixed-effects model presented in Supplementary Figure 4.A, including estimates/variance, 95% confidence intervals and *F* and *p* values. Two-way ANOVA stated that Cell Line as an individual variable did not significantly contributed to change in area however all interactions with Cell Line were significant (n≥20 individuals observed per protocol). Tukey post-hoc pairwise comparison determined Control #1 and #2 E-hCOs differed significantly from each other in area at both phases of differentiation (p=<.0001) after accommodating for Media interaction.

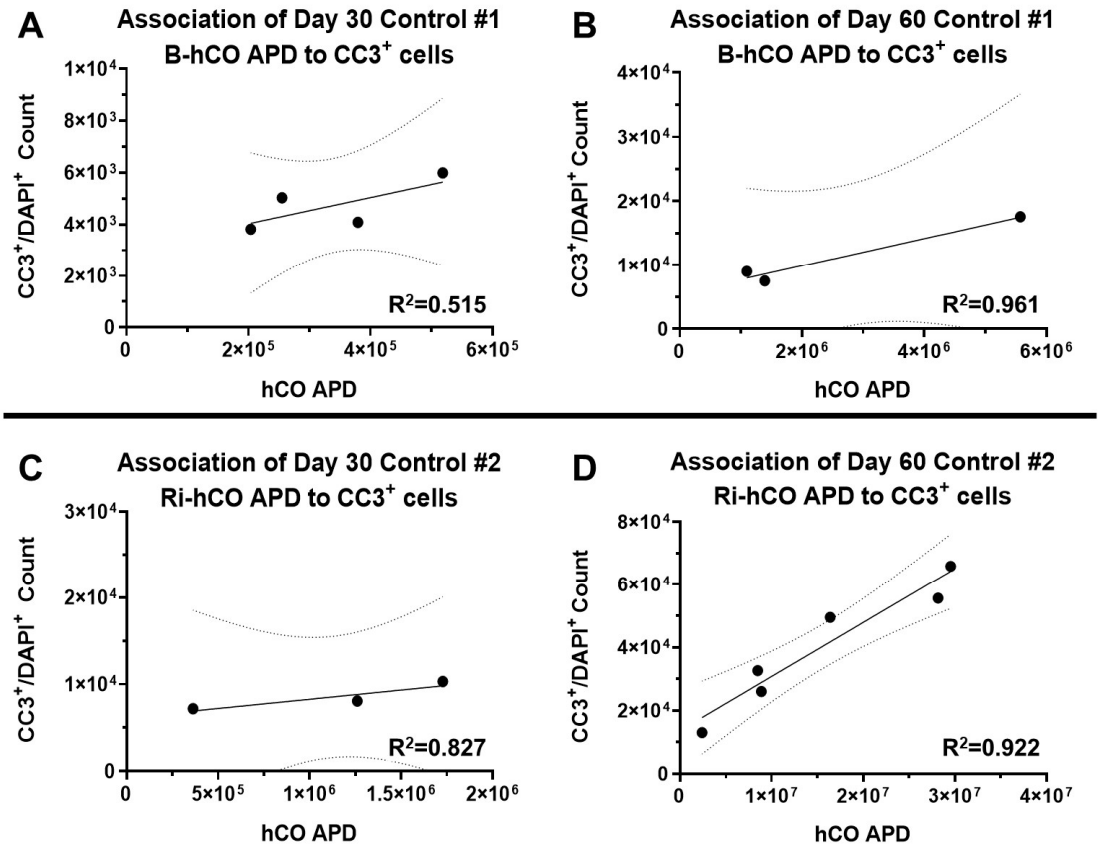

Supplementary Figure 5: Linear regression analysis of cleaved-caspase 3 ICC staining against APD of Day 30 and Day 60 B-hCOs and R-hCOs. A) Day 30 – B-hCO: F(1,2)=2.1, p=0.283. **B)** Day 60 – B-hCO: F(1,1)=4.8, p=0.273. **C)** Day 30 – Ri-hCO: F(1,1)=24.9, p=0.126. **D)** Day 60 – Ri-hCO: F(1,4)=47.4, p=0.0023. Bold line represents line of best fit, dashed lines represent 95% CIs, R^2 value is referenced within image.

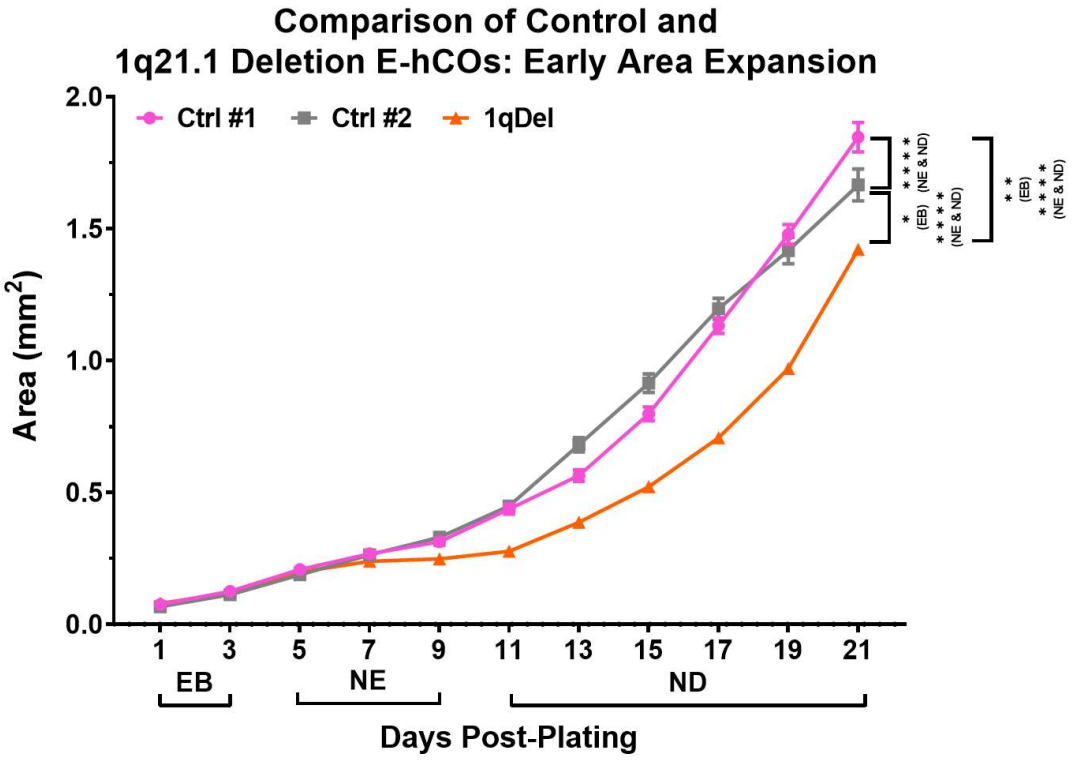

Supplemental Figure 6: Comparison of 1qDel E-hCO's area to Control #1 and #2 E-hCOs, plotted using mean and standard deviation.

Growth of area during early E-hCO differentiation across Control #1, #2 and 1qDel E-hCOs. Data for area was collected from individually-tracked, repeat-batch bright field imaging; mean ±SD presented in line graphs. Statistical analysis used mixed effects models on datasets of ≥15 independent hCOs per independent differentiation, ≥1 independent differentiations per cell line (for full information on models see Supplementary Figure 7). After two-way ANOVA determined significant variation among cell lines, pairwise, Tukey-corrected post-hoc comparison that accommodated for interaction with Media was used to determine significant differences in area relative to either the NE or ND stages of E-hCO differentiation; unlabelled=not significant, *p=<0.05, **p=<0.005, ****p=<0.0001.

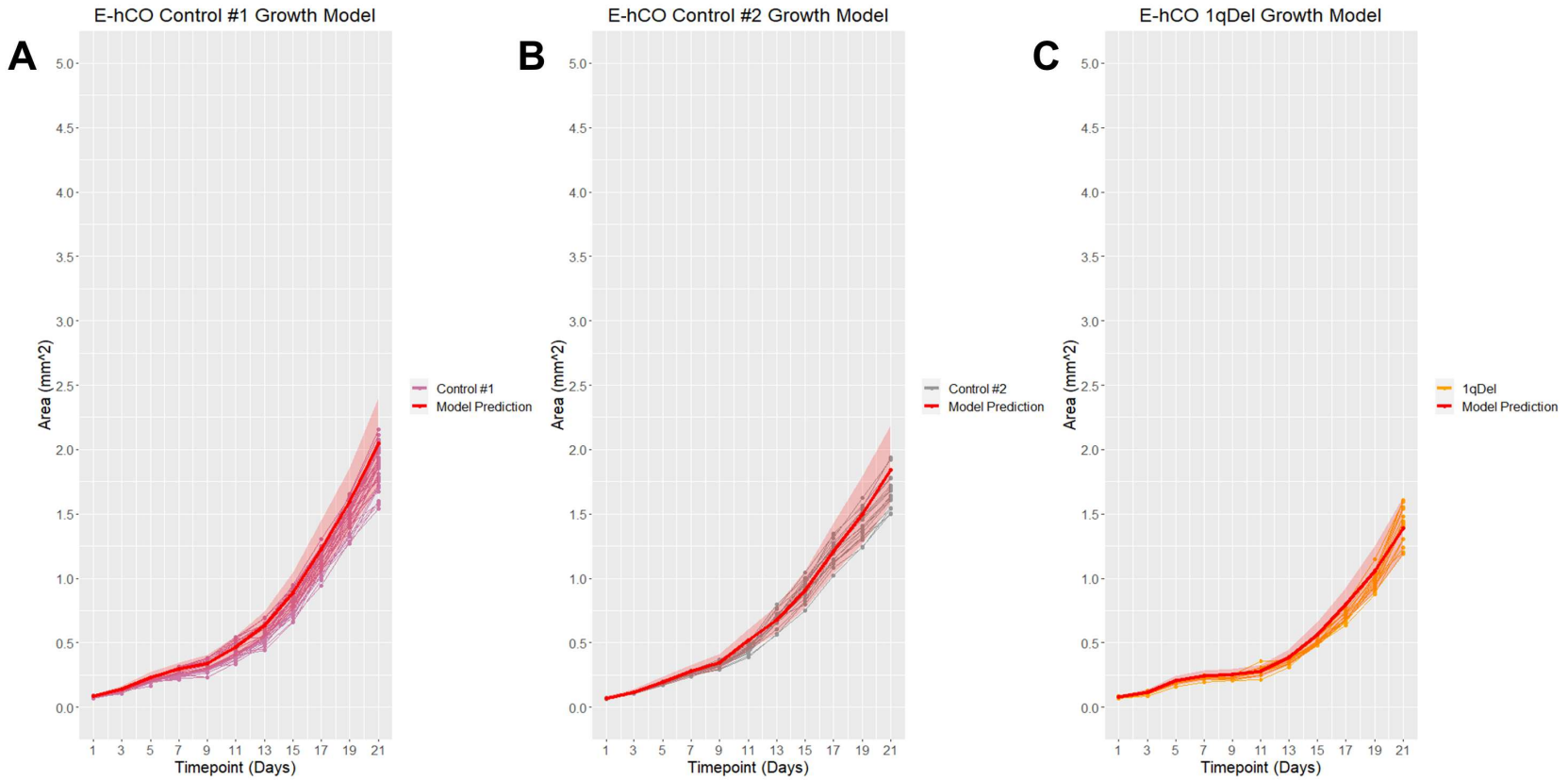

Supplemental Figure 7.A: Simulated prediction of mixed-effects models to validate statistical conclusions made in Figure 1.A. Mixed-effects model used was as follows: "lmer(log(Area) ~ CellLine*Timepoint*Media + (1|Individual) + (1|Timepoint:Media)". The model was optimised to fit statistical assumptions including homoscedasticity and normal distribution of residuals. Graphs represent cell lines differentiated into E-hCOs' **(A)** Control Line #1, **(B)** Control Line #2 and **(C)** 1q21.1 deletion raw area values as a dot-line plot, overlaid with a predicted value ± 95% CIs (colour = red). Libraries used: readxl, car, data.table, performance, multcomp, mgcv, emmeans, merTools, patchwork, lme4, tidyverse, ggplot.

A

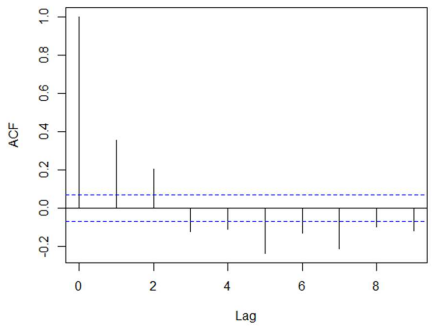

C

Parameter	Variance (95% CI)
Supplementary Figure 6.A: Random Effect Variance	
Individual (Intercept)	0.048 (0.039, 0.058)
(Intercept) Timepoint:Media	0.040 (0.017, 0.044)
Residual	0.075 (0.071, 0.079)

B

Parameter	Estimates (95% CI)	*F* value	P value
Supplementary Figure 4.A: Fixed Effect Variance			
(Intercept)	0.059 (0.053, 0.065)	*NA*	*NA*
Cell Line Ctrl #2	0.880 (0.821, 0.944)	180.248 $_{2,70}$	$<2.2e^{-16}$
Cell Line 1qDel	1.009 (0.937, 1.086)		
Timepoint	1.285 (1.230, 1.342)	6031.595 $_{1,802}$	$<2.2e^{-16}$
Media NE	2.165 (1.800, 2.603)	21.215 $_{1,802}$	$6.118e^{-10}$
Media ND	1.418 (1.214, 1.656)		
Cell Line Ctrl #2: Timepoint	1.008 (0.979, 1.038)	244.642 $_{1,802}$	$6.607e^{-13}$
Cell Line 1qDel : Timepoint	0.957 (0.928, 0.987)		
Cell Line Ctrl #2: Media NE	0.841 (0.744, 0.951)		
Cell Line 1qDel : Media NE	1.197 (1.052, 1.362)	80.246 $_{1,802}$	$<2.2e^{-16}$
Cell Line Ctrl #2: Media ND	1.658 (1.496, 1.838)		
Cell Line 1qDel : Media ND	0.531 (0.476, 0.592)		
Timepoint: Media NE	0.860 (0.820, 0.904)	10.761 $_{1,802}$	$2.121e^{-5}$
Timepoint: Media ND	0.904 (0.865, 0.945)		
Cell Line Ctrl #2: Media NE: Timepoint	1.033 (1.000, 1.067)		
Cell Line Ctrl #2: Media ND: Timepoint	0.971 (0.943, 1.000)	49.739 $_{1,802}$	$<2.2e^{-16}$
Cell Line 1qDel : Media NE: Timepoint	0.994 (0.960, 1.028)		
Cell Line 1qDel : Media ND: Timepoint	1.059 (1.026, 1.092)		

Supplementary Figure 7.B: ACF plots and statistical reporting of mixed-effects models generated in Supplementary Figure 7.A. A) ACF plots denoting autocorrelation of model presented in Supplementary Figure 7.A. **B-C)** Reports of fixed **(B)** and random **(C)** effects from mixed-effects model presented in Supplementary Figure 7.A, including estimates/variance, 95% confidence intervals and *F* and *p* values. Two-way ANOVA stated that Cell Line significantly contributed to change in area ($F(2,70)= 180.248$, $p= <2e^{-16}$), ($n\geq17$ individuals observed per protocol). After accommodating for Media interaction, Tukey post-hoc pairwise comparison determined Control #1 and #2 did not differ at the EB stage of differentiation (p=0.9564), but did significantly deviate at NE and ND phases of differentiation (p=<0.0001). Control #1 and 1qDel differed significantly from each other at the EB, NE and ND phases of differentiation (p=0.0028, p=<0.0001 and p=<0.0001, respectively). Control #2 and 1qDel differed significantly from each other at the EB, NE and ND phases of differentiation (p=0.0189, p=<0.0001 and p=<0.0001, respectively).

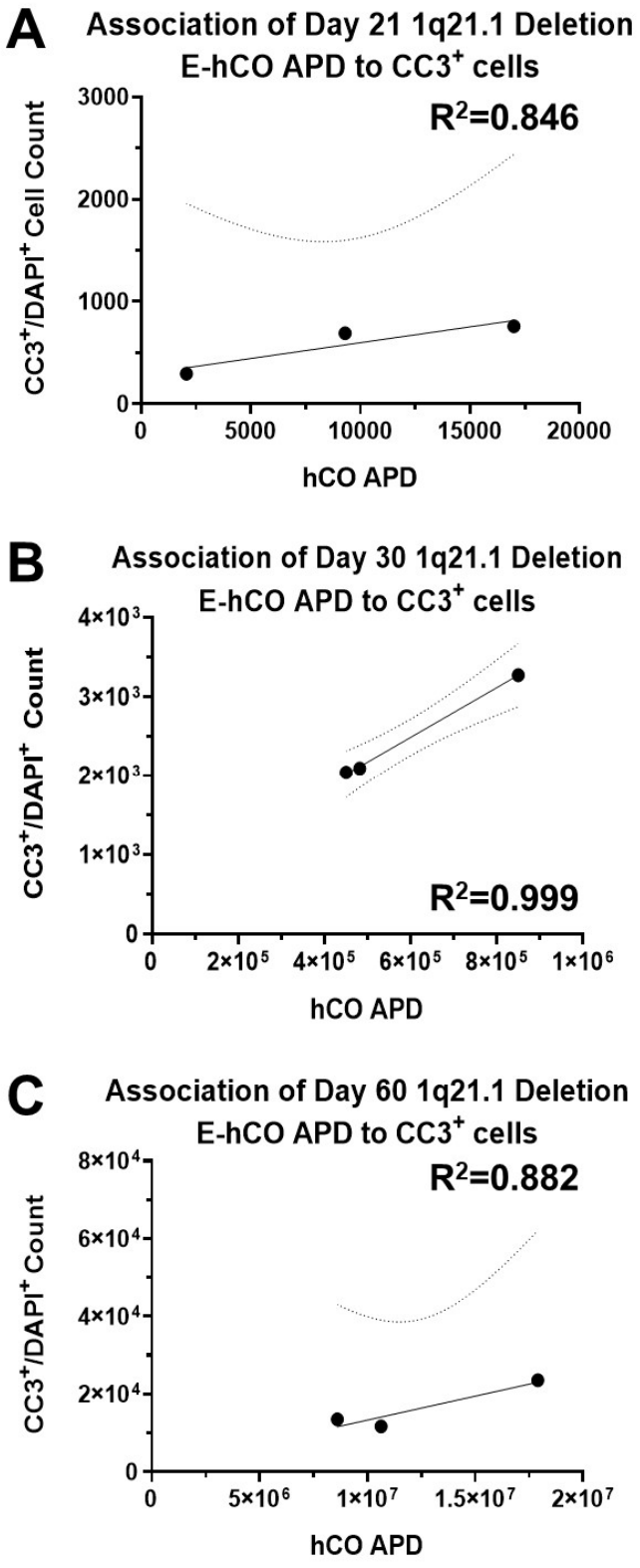

Supplementary Figure 8: Linear regression analysis of cleaved-caspase 3 ICC staining against APD of Day 21, 30 and Day 60 1qDel E-hCOs. A) Day 21: F(1,1)=5.5, p=0.257. **B)** Day 30: F(1,1)=983.4, p=0.0203. **C)** Day 60: F(1,1)=7.48, p=0.257. Bold line represents line of best fit, dashed lines represent 95% CIs, R^2 value is referenced within image.

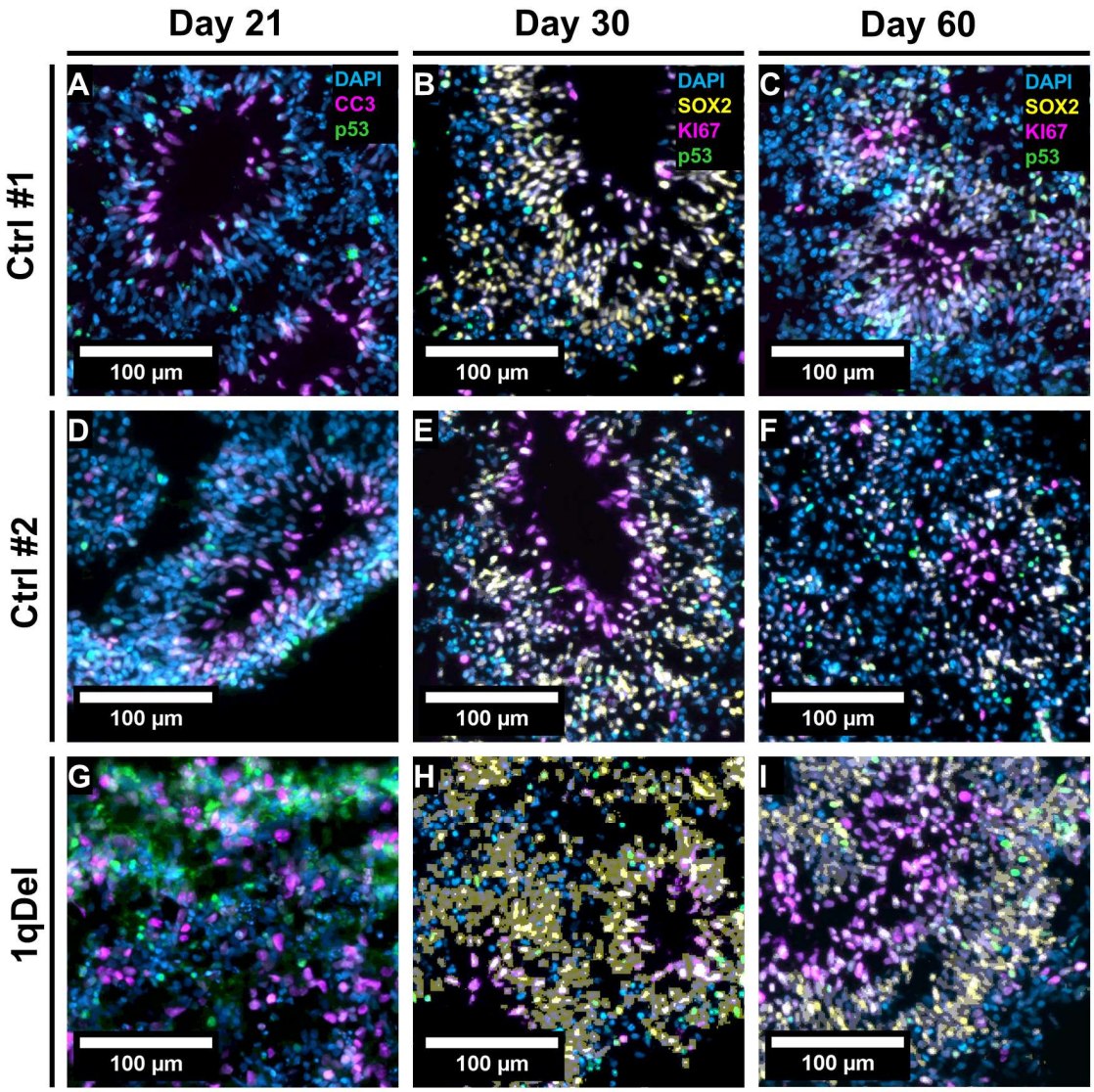

Supplemental Figure 9: Fluorescent images of proliferation and cell cycle arrest in SOX2⁺ NPCs and/or all cells in E-hCOs, with respect to Figure 5.7.B, 5.7.C and 5.14.C. Fluorescent images of 10 µm slices of Control #1 **(A-C),** #2 **(D-F)** and 1qDel **(G-I)** E-hCOs at Day 21, 30 and 60. Cell line and timepoint is referenced in image (20x magnification). Proteins identified by colour: p53 (green), KI67 (pink), SOX2 (yellow), DAPI (blue). Scale bar = 100 µm.

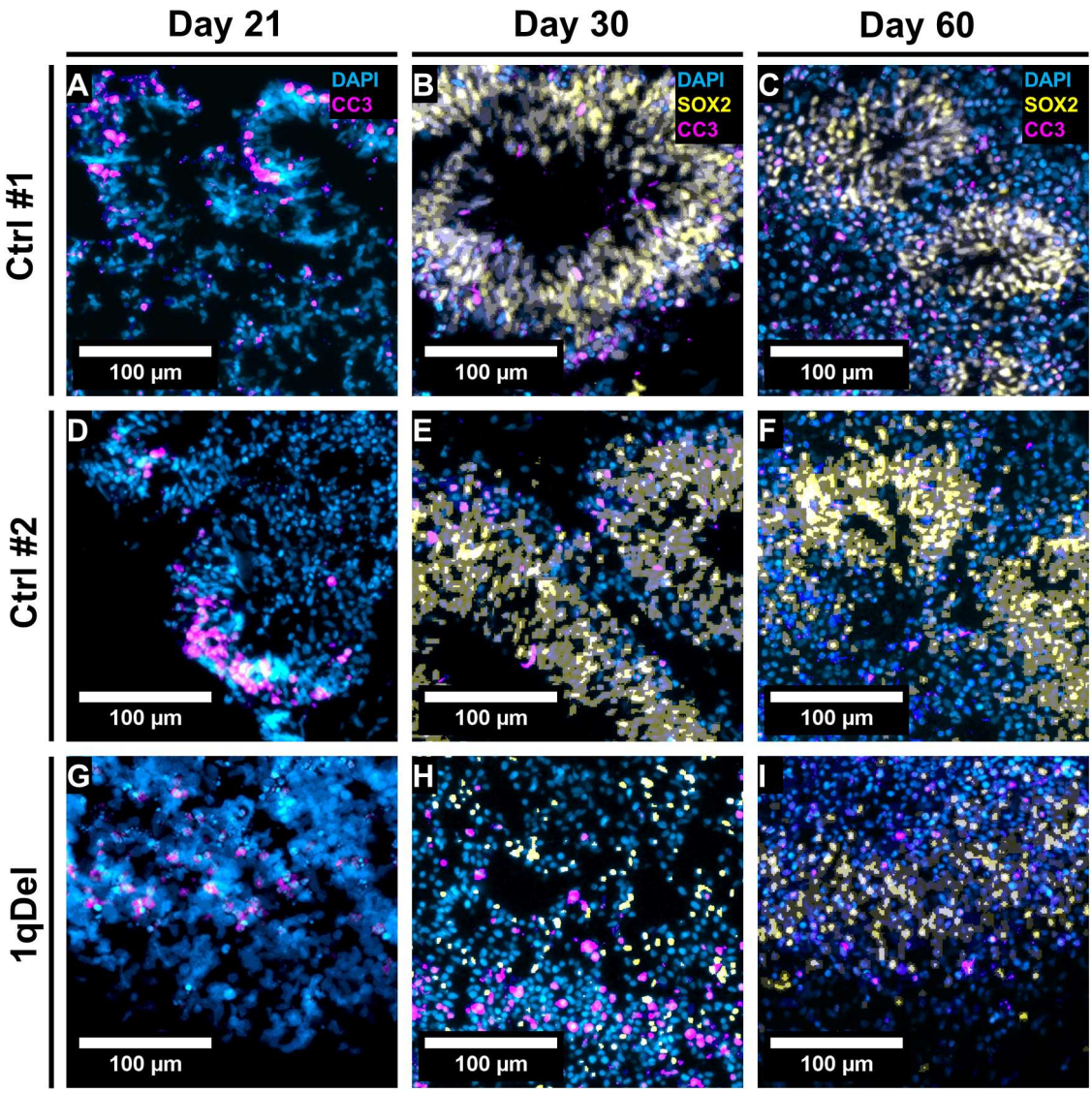

Supplemental Figure 10: Fluorescent images of cell death in SOX2$^+$ NPCs and/or all cells in E-hCOs, with respect to Figure 5.7.D and 5.7.E. Fluorescent images of 10 µm slices of Control #1 **(A-C),** #2 **(D-F)** and 1qDel **(G-I)** E-hCOs at Day 21, 30 and 60. Cell line and timepoint is referenced in image (20x magnification). Proteins identified by colour: CC3 (pink), SOX2 (yellow), DAPI (blue). Scale bar = 100 µm.

9 References

Aaku-Saraste, E., Hellwig, A. and Huttner, W.B. (1996) 'Loss of Occludin and Functional Tight Junctions, but Not ZO-1, during Neural Tube Closure—Remodeling of the Neuroepithelium Prior to Neurogenesis', *Developmental Biology*, 180(2), pp. 664–679. Available at: https://doi.org/10.1006/dbio.1996.0336.

Abdel Fattah, A.R. *et al.* (2021) 'Actuation enhances patterning in human neural tube organoids', *Nature Communications*, 12(1), p. 3192. Available at: https://doi.org/10.1038/s41467-021-22952-0.

Abdyyev, V.K. *et al.* (2020) 'In vitro derived female hPGCLCs are unable to complete meiosis in embryoid bodies', *Experimental Cell Research*, 397(2), p. 112358. Available at: https://doi.org/10.1016/j.yexcr.2020.112358.

Abranches, E. *et al.* (2014) 'Stochastic NANOG fluctuations allow mouse embryonic stem cells to explore pluripotency', *Development*, 141(14), pp. 2770–2779. Available at: https://doi.org/10.1242/dev.108910.

Acampora, D. *et al.* (2017) 'Functional Antagonism between OTX2 and NANOG Specifies a Spectrum of Heterogeneous Identities in Embryonic Stem Cells', *Stem Cell Reports*, 9(5), pp. 1642–1659. Available at: https://doi.org/10.1016/j.stemcr.2017.09.019.

Adhya, D. *et al.* (2021) 'Application of Airy beam light sheet microscopy to examine early neurodevelopmental structures in 3D hiPSC-derived human cortical spheroids', *Molecular Autism*, 12(1), p. 4. Available at: https://doi.org/10.1186/s13229-021-00413-1.

Agathocleous, M. *et al.* (2009) 'A directional Wnt/β-catenin-Sox2-proneural pathway regulates the transition from proliferation to differentiation in the Xenopusretina', *Development*, 136(19), pp. 3289–3299. Available at: https://doi.org/10.1242/dev.040451.

Ahel, D. *et al.* (2009) 'Poly(ADP-ribose)–Dependent Regulation of DNA Repair by the Chromatin Remodeling Enzyme ALC1', *Science*, 325(5945), pp. 1240–1243. Available at: https://doi.org/10.1126/science.1177321.

Aisenbrey, E.A. and Murphy, W.L. (2020) 'Synthetic alternatives to Matrigel', *Nature Reviews Materials*. Nature Research, pp. 539–551. Available at: https://doi.org/10.1038/s41578-020-0199-8.

Akamatsu, W. *et al.* (2009) 'Suppression of Oct4 by Germ Cell Nuclear Factor Restricts Pluripotency and Promotes Neural Stem Cell Development in the Early Neural Lineage', *Journal of Neuroscience*, 29(7), pp. 2113–2124. Available at: https://doi.org/10.1523/JNEUROSCI.4527-08.2009.

Al Shehhi, M. *et al.* (2019) 'NRXN1 deletion syndrome; phenotypic and penetrance data from 34 families', *European Journal of Medical Genetics*, 62(3), pp. 204–209. Available at: https://doi.org/10.1016/j.ejmg.2018.07.015.

Albanese, A. *et al.* (2020) 'Multiscale 3D phenotyping of human cerebral organoids', *Scientific Reports*, 10(1), p. 21487. Available at: https://doi.org/10.1038/s41598-020-78130-7.

Alcamo, E.A. *et al.* (2008) 'Satb2 Regulates Callosal Projection Neuron Identity in the Developing Cerebral Cortex', *Neuron*, 57(3), pp. 364–377. Available at: https://doi.org/10.1016/j.neuron.2007.12.012.

Alcantara, D. and O'Driscoll, M. (2014) 'Congenital microcephaly', *American Journal of Medical Genetics Part C: Seminars in Medical Genetics*, 166(2), pp. 124–139. Available at: https://doi.org/10.1002/ajmg.c.31397.

Alfieri, P. *et al.* (2020) 'Further insight into the neurobehavioral pattern of children carrying the 2p16.3 heterozygous deletion involving NRXN1: Report of five new cases', *Genes, Brain and Behavior*, 19(7), p. e12687. Available at: https://doi.org/10.1111/gbb.12687.

Allende, M.L. *et al.* (2018) 'Cerebral organoids derived from Sandhoff disease-induced pluripotent stem cells exhibit impaired neurodifferentiation[S]', *Journal of Lipid Research*, 59(3), pp. 550–563. Available at: https://doi.org/10.1194/jlr.M081323.

Alsanie, W.F. *et al.* (2020) 'Generating homogenous cortical preplate and deep-layer neurons using a combination of 2D and 3D differentiation cultures', *Scientific Reports*, 10(1), p. 6272. Available at: https://doi.org/10.1038/s41598-020-62925-9.

Alshawaf, A.J. *et al.* (2018) 'Phenotypic and Functional Characterization of Peripheral Sensory Neurons derived from Human Embryonic Stem Cells', *Scientific Reports*, 8(1), p. 603. Available at: https://doi.org/10.1038/s41598-017-19093-0.

Alzu'bi, A. and Clowry, G.J. (2019) 'Expression of ventral telencephalon transcription factors ASCL1 and DLX2 in the early fetal human cerebral cortex', *Journal of Anatomy*, 235(3), pp. 555–568. Available at: https://doi.org/10.1111/joa.12971.

Amadei, G. *et al.* (2022) 'Embryo model completes gastrulation to neurulation and organogenesis', *Nature*, 610(7930), pp. 143–153. Available at: https://doi.org/10.1038/s41586-022-05246-3.

Amin, H. *et al.* (2017) 'Developmental excitatory-to-inhibitory GABA-polarity switch is disrupted in 22q11.2 deletion syndrome: a potential target for clinical therapeutics', *Scientific Reports*, 7, p. 15752. Available at: https://doi.org/10.1038/s41598-017-15793-9.

An, H.-L., Kuo, H.-C. and Tang, T.K. (2022) 'Modeling Human Primary Microcephaly With hiPSC-Derived Brain Organoids Carrying CPAP-E1235V Disease-Associated Mutant Protein', *Frontiers in Cell and Developmental Biology*, 10. Available at: https://www.frontiersin.org/articles/10.3389/fcell.2022.830432 (Accessed: 7 October 2022).

Anastasaki, C. *et al.* (2020) 'Human iPSC-Derived Neurons and Cerebral Organoids Establish Differential Effects of Germline NF1 Gene Mutations', *Stem Cell Reports*, 14(4), pp. 541–550. Available at: https://doi.org/10.1016/j.stemcr.2020.03.007.

Androutsellis-Theotokis, A. *et al.* (2006) 'Notch signalling regulates stem cell numbers in vitro and in vivo', *Nature*, 442(7104), pp. 823–826. Available at: https://doi.org/10.1038/nature04940.

Ao, Z. *et al.* (2020) 'One-Stop Microfluidic Assembly of Human Brain Organoids To Model Prenatal Cannabis Exposure', *Analytical Chemistry*, 92(6), pp. 4630–4638. Available at: https://doi.org/10.1021/acs.analchem.0c00205.

Arai, Y. *et al.* (2011) 'Neural stem and progenitor cells shorten S-phase on commitment to neuron production', *Nature Communications*, 2(1), p. 154. Available at: https://doi.org/10.1038/ncomms1155.

Arai, Y. and Taverna, E. (2017) 'Neural Progenitor Cell Polarity and Cortical Development', *Frontiers in Cellular Neuroscience*, 11, p. 384. Available at: https://doi.org/10.3389/fncel.2017.00384.

Arellano, J.I. *et al.* (2021) 'Radial Glial Cells: New Views on Old Questions', *Neurochemical research*, 46(10), pp. 2512–2524. Available at: https://doi.org/10.1007/s11064-021-03296-z.

Arlotta, P. *et al.* (2008) 'Ctip2 Controls the Differentiation of Medium Spiny Neurons and the Establishment of the Cellular Architecture of the Striatum', *Journal of Neuroscience*, 28(3), pp. 622–632. Available at: https://doi.org/10.1523/JNEUROSCI.2986-07.2008.

Armstrong, D. *et al.* (1995) 'Selective Dendritic Alterations in the Cortex of Rett Syndrome', *Journal of Neuropathology & Experimental Neurology*, 54(2), pp. 195–201. Available at: https://doi.org/10.1097/00005072-199503000-00006.

Arnold, S.E., Ruscheinsky, D.D. and Han, L.-Y. (1997) 'Further Evidence of Abnormal Cytoarchitecture of the Entorhinal Cortex in Schizophrenia Using Spatial Point Pattern Analyses', *Biological Psychiatry*, 42(8), pp. 639–647. Available at: https://doi.org/10.1016/S0006-3223(97)00142-X.

Arzua, T. *et al.* (2020) 'Modeling alcohol-induced neurotoxicity using human induced pluripotent stem cell-derived three-dimensional cerebral organoids', *Translational Psychiatry*, 10(1), pp. 1–21. Available at: https://doi.org/10.1038/s41398-020-01029-4.

Avram, M. *et al.* (2019) 'Reduced striatal dopamine synthesis capacity in patients with schizophrenia during remission of positive symptoms', *Brain*, 142(6), pp. 1813–1826. Available at: https://doi.org/10.1093/brain/awz093.

Bagley, J.A. *et al.* (2017) 'Fused cerebral organoids model interactions between brain regions', *Nature Methods*, 14(7), pp. 743–751. Available at: https://doi.org/10.1038/nmeth.4304.

Baldwin, I. *et al.* (2021) 'Genomic, Clinical, and Behavioral Characterization of 15q11.2 BP1-BP2 Deletion (Burnside-Butler) Syndrome in Five Families', *International Journal of Molecular Sciences*, 22(4), p. 1660. Available at: https://doi.org/10.3390/ijms22041660.

Ballif, B.C. *et al.* (2008) 'Expanding the clinical phenotype of the 3q29 microdeletion syndrome and characterization of the reciprocal microduplication', *Molecular Cytogenetics*, 1(1), p. 8. Available at: https://doi.org/10.1186/1755-8166-1-8.

Banerjee, A. *et al.* (2016) 'Jointly reduced inhibition and excitation underlies circuit-wide changes in cortical processing in Rett syndrome', *Proceedings of the National Academy of Sciences*, 113(46), pp. E7287–E7296. Available at: https://doi.org/10.1073/pnas.1615330113.

Barnevik Olsson, M. *et al.* (2013) 'Autism before diagnosis: crying, feeding and sleeping problems in the first two years of life', *Acta Paediatrica*, 102(6), pp. 635–639. Available at: https://doi.org/10.1111/apa.12229.

Basel-Vanagaite, L. and Dobyns, W.B. (2010) 'Clinical and Brain Imaging Heterogeneity of Severe Microcephaly', *Pediatric Neurology*, 43(1), pp. 7–16. Available at: https://doi.org/10.1016/j.pediatrneurol.2010.02.015.

Batiuk, M.Y. *et al.* (2022) 'Upper cortical layer–driven network impairment in schizophrenia', *Science Advances*, 8(41), p. eabn8367. Available at: https://doi.org/10.1126/sciadv.abn8367.

Bayatti, N. *et al.* (2008) 'A Molecular Neuroanatomical Study of the Developing Human Neocortex from 8 to 17 Postconceptional Weeks Revealing the Early Differentiation of the Subplate and Subventricular Zone', *Cerebral Cortex (New York, NY)*, 18(7), pp. 1536–1548. Available at: https://doi.org/10.1093/cercor/bhm184.

Bayerl, J. *et al.* (2021) ‘Principles of signaling pathway modulation for enhancing human naive pluripotency induction’, *Cell Stem Cell*, 28(9), pp. 1549-1565.e12. Available at: https://doi.org/10.1016/j.stem.2021.04.001.

Beasley, C.L. and Reynolds, G.P. (1997) ‘Parvalbumin-immunoreactive neurons are reduced in the prefrontal cortex of schizophrenics’, *Schizophrenia Research*, 24(3), pp. 349–355. Available at: https://doi.org/10.1016/S0920-9964(96)00122-3.

Beghin, A. *et al.* (2022) ‘Automated high-speed 3D imaging of organoid cultures with multi-scale phenotypic quantification’, *Nature Methods*, 19(7), pp. 881–892. Available at: https://doi.org/10.1038/s41592-022-01508-0.

Benito-Kwiecinski, S. *et al.* (2021) ‘An early cell shape transition drives evolutionary expansion of the human forebrain’, *Cell*, 184(8), pp. 2084-2102.e19. Available at: https://doi.org/10.1016/j.cell.2021.02.050.

Benson, C.A. *et al.* (2020) ‘Immune Factor, TNFα, Disrupts Human Brain Organoid Development Similar to Schizophrenia—Schizophrenia Increases Developmental Vulnerability to TNFα’, *Frontiers in Cellular Neuroscience*, 14. Available at: https://www.frontiersin.org/articles/10.3389/fncel.2020.00233 (Accessed: 14 October 2022).

Berghe, T.V. *et al.* (2010) ‘Necroptosis, necrosis and secondary necrosis converge on similar cellular disintegration features’, *Cell Death & Differentiation*, 17(6), pp. 922–930. Available at: https://doi.org/10.1038/cdd.2009.184.

Berghe, T.V. *et al.* (2014) ‘Regulated necrosis: the expanding network of non-apoptotic cell death pathways’, *Nature Reviews Molecular Cell Biology*, 15(2), pp. 135–147. Available at: https://doi.org/10.1038/nrm3737.

Bernier, R. *et al.* (2016) ‘Clinical phenotype of the recurrent 1q21.1 copy-number variant’, *Genetics in Medicine*, 18(4), pp. 341–349. Available at: https://doi.org/10.1038/gim.2015.78.

Bershteyn, M. *et al.* (2017) ‘Human iPSC-derived cerebral organoids model cellular features of lissencephaly and reveal prolonged mitosis of outer radial glia’, *Cell stem cell*, 20(4), pp. 435-449.e4. Available at: https://doi.org/10.1016/j.stem.2016.12.007.

Bertet, C., Sulak, L. and Lecuit, T. (2004) ‘Myosin-dependent junction remodelling controls planar cell intercalation and axis elongation’, *Nature*, 429(6992), pp. 667–671. Available at: https://doi.org/10.1038/nature02590.

Bhaduri, A. *et al.* (2020) ‘Cell stress in cortical organoids impairs molecular subtype specification’, *Nature* [Preprint]. Available at: https://doi.org/10.1038/s41586-020-1962-0.

Bian, S. *et al.* (2013) ‘MicroRNA Cluster miR-17-92 Regulates Neural Stem Cell Expansion and Transition to Intermediate Progenitors in the Developing Mouse Neocortex’, *Cell Reports*, 3(5), pp. 1398–1406. Available at: https://doi.org/10.1016/j.celrep.2013.03.037.

Bian, S. *et al.* (2018) ‘Genetically engineered cerebral organoids model brain tumor formation’, *Nature Methods*, 15(8), pp. 631–639. Available at: https://doi.org/10.1038/s41592-018-0070-7.

Birey, F. *et al.* (2017) ‘Assembly of functionally integrated human forebrain spheroids.’, *Nature*, 545(7652), pp. 54–59. Available at: https://doi.org/10.1038/nature22330.

Blair, J.D., Hockemeyer, D. and Bateup, H.S. (2018) 'Genetically engineered human cortical spheroid models of tuberous sclerosis', *Nature Medicine*, 24(10), pp. 1568–1578. Available at: https://doi.org/10.1038/s41591-018-0139-y.

Blanken, L.M.E. *et al.* (2018) 'A prospective study of fetal head growth, autistic traits and autism spectrum disorder', *Autism Research*, 11(4), pp. 602–612. Available at: https://doi.org/10.1002/aur.1921.

Bonafina, A. *et al.* (2018) 'GDNF/GFRα1 Complex Abrogates Self-Renewing Activity of Cortical Neural Precursors Inducing Their Differentiation', *Stem Cell Reports*, 10(3), pp. 1000–1015. Available at: https://doi.org/10.1016/j.stemcr.2018.01.019.

Bond, A.M., Bhalala, O.G. and Kessler, J.A. (2012) 'The dynamic role of bone morphogenetic proteins in neural stem cell fate and maturation', *Developmental Neurobiology*, 72(7), pp. 1068–1084. Available at: https://doi.org/10.1002/dneu.22022.

Boonsawat, P. *et al.* (2019) 'Elucidation of the phenotypic spectrum and genetic landscape in primary and secondary microcephaly', *Genetics in Medicine*, 21(9), pp. 2043–2058. Available at: https://doi.org/10.1038/s41436-019-0464-7.

Borsini, A. *et al.* (2020) 'The role of omega-3 fatty acids in preventing glucocorticoid-induced reduction in human hippocampal neurogenesis and increase in apoptosis', *Translational Psychiatry*, 10(1), pp. 1–12. Available at: https://doi.org/10.1038/s41398-020-00908-0.

Borten, M.A. *et al.* (2018) 'Automated brightfield morphometry of 3D organoid populations by OrganoSeg', *Scientific Reports*, 8(1). Available at: https://doi.org/10.1038/s41598-017-18815-8.

Bowles, K.R. *et al.* (2021) 'ELAVL4, splicing, and glutamatergic dysfunction precede neuron loss in MAPT mutation cerebral organoids', *Cell*, 184(17), pp. 4547-4563.e17. Available at: https://doi.org/10.1016/j.cell.2021.07.003.

Boxman, J. *et al.* (2016) 'Integrated live imaging and molecular profiling of embryoid bodies reveals a synchronized progression of early differentiation', *Scientific Reports*, 6(1), p. 31623. Available at: https://doi.org/10.1038/srep31623.

Brack, A.S. *et al.* (2009) 'BCL9 is an essential component of canonical Wnt signaling that mediates the differentiation of myogenic progenitors during muscle regeneration', *Developmental Biology*, 335(1), pp. 93–105. Available at: https://doi.org/10.1016/j.ydbio.2009.08.014.

Brenes, A.J. *et al.* (2021) 'Erosion of human X chromosome inactivation causes major remodeling of the iPSC proteome', *Cell Reports*, 35(4), p. 109032. Available at: https://doi.org/10.1016/j.celrep.2021.109032.

Brisch, R. *et al.* (2014) 'The Role of Dopamine in Schizophrenia from a Neurobiological and Evolutionary Perspective: Old Fashioned, but Still in Vogue', *Frontiers in Psychiatry*, 5, p. 47. Available at: https://doi.org/10.3389/fpsyt.2014.00047.

Britton, G. *et al.* (2019) 'A novel self-organizing embryonic stem cell system reveals signaling logic underlying the patterning of human ectoderm', *Development*, 146(20), p. dev179093. Available at: https://doi.org/10.1242/dev.179093.

Brownjohn, P.W. *et al.* (2018) 'Functional Studies of Missense TREM2 Mutations in Human Stem Cell-Derived Microglia', *Stem Cell Reports*, 10(4), pp. 1294–1307. Available at: https://doi.org/10.1016/j.stemcr.2018.03.003.

Brunetti-Pierri, N. *et al.* (2008) 'Recurrent reciprocal 1q21.1 deletions and duplications associated with microcephaly or macrocephaly and developmental and behavioral abnormalities', *Nature Genetics*, 40(12), pp. 1466–1471. Available at: https://doi.org/10.1038/ng.279.

Budisteanu, M. *et al.* (2021) 'The Phenotypic Spectrum of 15q13.3 Region Duplications: Report of 5 Patients', *Genes*, 12(7), p. 1025. Available at: https://doi.org/10.3390/genes12071025.

Burke, E.E. *et al.* (2020) 'Dissecting transcriptomic signatures of neuronal differentiation and maturation using iPSCs', *Nature Communications*, 11(1), p. 462. Available at: https://doi.org/10.1038/s41467-019-14266-z.

Butler, M.B. *et al.* (2019) 'Rho kinase-dependent apical constriction counteracts M-phase apical expansion to enable mouse neural tube closure', *Journal of Cell Science*, 132(13), p. jcs230300. Available at: https://doi.org/10.1242/jcs.230300.

Butler, M.G. (2017) 'Clinical and genetic aspects of the 15q11.2 BP1-BP2 microdeletion disorder', *Journal of Intellectual Disability Research*, 61(6), pp. 568–579. Available at: https://doi.org/10.1111/jir.12382.

Bygrave, A.M. *et al.* (2019) 'Gene-Environment Interaction in a Conditional NMDAR-Knockout Model of Schizophrenia', *Frontiers in Behavioral Neuroscience*, 12, p. 332. Available at: https://doi.org/10.3389/fnbeh.2018.00332.

C. Lage, M.-L. *et al.* (2019) 'Clinical, Neuroimaging, and Neurophysiological Findings in Children with Microcephaly Related to Congenital Zika Virus Infection', *International Journal of Environmental Research and Public Health*, 16(3), p. 309. Available at: https://doi.org/10.3390/ijerph16030309.

Cadinu, D. *et al.* (2018) 'NMDA receptor antagonist rodent models for cognition in schizophrenia and identification of novel drug treatments, an update', *Neuropharmacology*, 142, pp. 41–62. Available at: https://doi.org/10.1016/j.neuropharm.2017.11.045.

Cadwell, C.R. *et al.* (2019) 'Development and Arealization of the Cerebral Cortex', *Neuron*, 103(6), pp. 980–1004. Available at: https://doi.org/10.1016/j.neuron.2019.07.009.

Cajal, M. *et al.* (2012) 'Clonal and molecular analysis of the prospective anterior neural boundary in the mouse embryo', *Development*, 139(2), pp. 423–436. Available at: https://doi.org/10.1242/dev.075499.

Cakir, B. *et al.* (2022) 'Expression of the transcription factor PU.1 induces the generation of microglia-like cells in human cortical organoids', *Nature Communications*, 13(1), p. 430. Available at: https://doi.org/10.1038/s41467-022-28043-y.

Camp, J.G. *et al.* (2015) 'Human cerebral organoids recapitulate gene expression programs of fetal neocortex development', *Proceedings of the National Academy of Sciences of the United States of America* [Preprint]. Available at: https://doi.org/10.1073/pnas.1520760112.

Caronia-Brown, G. *et al.* (2014) 'The cortical hem regulates the size and patterning of neocortex', *Development (Cambridge)*, 141(14), pp. 2855–2865. Available at: https://doi.org/10.1242/dev.106914.

Carter, J.C. *et al.* (2008) 'Selective Cerebral Volume Reduction in Rett Syndrome: A Multiple-Approach MR Imaging Study', *American Journal of Neuroradiology*, 29(3), pp. 436–441. Available at: https://doi.org/10.3174/ajnr.A0857.

Castro, M. *et al.* (2001) ‘High-affinity sodium–vitamin C co-transporters (SVCT) expression in embryonic mouse neurons’, *Journal of Neurochemistry*, 78(4), pp. 815–823. Available at: https://doi.org/10.1046/j.1471-4159.2001.00461.x.

Cederquist, G.Y. *et al.* (2019) ‘Specification of positional identity in forebrain organoids’, *Nature Biotechnology*, 37(4), pp. 436–444. Available at: https://doi.org/10.1038/s41587-019-0085-3.

Ceroni, F. *et al.* (2019) ‘New GJA8 variants and phenotypes highlight its critical role in a broad spectrum of eye anomalies’, *Human Genetics*, 138(8), pp. 1027–1042. Available at: https://doi.org/10.1007/s00439-018-1875-2.

Chambers, S.M. *et al.* (2009) ‘Highly efficient neural conversion of human ES and iPS cells by dual inhibition of SMAD signaling.’, *Nature biotechnology*, 27(3), pp. 275–80. Available at: https://doi.org/10.1038/nbt.1529.

Chandrasekaran, A. *et al.* (2016) ‘Astrocyte Differentiation of Human Pluripotent Stem Cells: New Tools for Neurological Disorder Research’, *Frontiers in Cellular Neuroscience*, 10. Available at: https://www.frontiersin.org/articles/10.3389/fncel.2016.00215 (Accessed: 15 August 2022).

Chapman, G. *et al.* (2021) ‘Using induced pluripotent stem cells to investigate human neuronal phenotypes in 1q21.1 deletion and duplication syndrome’, *Molecular Psychiatry*, pp. 1–12. Available at: https://doi.org/10.1038/s41380-021-01182-2.

Charlson, F.J. *et al.* (2018) ‘Global Epidemiology and Burden of Schizophrenia: Findings From the Global Burden of Disease Study 2016’, *Schizophrenia Bulletin*, 44(6), pp. 1195–1203. Available at: https://doi.org/10.1093/schbul/sby058.

Chawner, S.J.R.A. *et al.* (2019) ‘Genotype–phenotype associations in children with copy number variants associated with high neuropsychiatric risk in the UK (IMAGINE-ID): a case-control cohort study’, *The Lancet Psychiatry*, 6(6), pp. 493–505. Available at: https://doi.org/10.1016/S2215-0366(19)30123-3.

Chen, C. *et al.* (2021) ‘A matrigel-free method to generate matured human cerebral organoids using 3D-Printed microwell arrays’, *Bioactive Materials*, 6(4), pp. 1130–1139. Available at: https://doi.org/10.1016/j.bioactmat.2020.10.003.

Chen, C.-Y. *et al.* (2014) ‘Inhibition of Notch signaling facilitates the differentiation of human-induced pluripotent stem cells into neural stem cells’, *Molecular and Cellular Biochemistry*, 395(1), pp. 291–298. Available at: https://doi.org/10.1007/s11010-014-2130-3.

Chen, G. *et al.* (2011) ‘Chemically defined conditions for human iPSC derivation and culture’, *Nature Methods*, 8(5), pp. 424–429. Available at: https://doi.org/10.1038/nmeth.1593.

Chen, J. *et al.* (2018) ‘CDK1-mediated BCL9 phosphorylation inhibits clathrin to promote mitotic Wnt signalling’, *The EMBO Journal*, 37(20), p. e99395. Available at: https://doi.org/10.15252/embj.201899395.

Chen, J.-F. *et al.* (2014) ‘Microcephaly disease gene Wdr62 regulates mitotic progression of embryonic neural stem cells and brain size’, *Nature Communications*, 5(1), p. 3885. Available at: https://doi.org/10.1038/ncomms4885.

Chen, Q. *et al.* (2014) ‘MicroRNA-23a/b and microRNA-27a/b suppress Apaf-1 protein and alleviate hypoxia-induced neuronal apoptosis’, *Cell Death & Disease*, 5(3), pp. e1132–e1132. Available at: https://doi.org/10.1038/cddis.2014.92.

Cho, A.-N. *et al.* (2021) 'Microfluidic device with brain extracellular matrix promotes structural and functional maturation of human brain organoids', *Nature Communications*, 12(1), p. 4730. Available at: https://doi.org/10.1038/s41467-021-24775-5.

Choe, M.S. *et al.* (2021) 'A simple method to improve the quality and yield of human pluripotent stem cell-derived cerebral organoids', *Heliyon*, 7(6), p. e07350. Available at: https://doi.org/10.1016/j.heliyon.2021.e07350.

Chou, I.-J. *et al.* (2017) 'Familial Aggregation and Heritability of Schizophrenia and Co-aggregation of Psychiatric Illnesses in Affected Families', *Schizophrenia Bulletin*, 43(5), pp. 1070–1078. Available at: https://doi.org/10.1093/schbul/sbw159.

Chryplewicz, A. *et al.* (2019) 'Mutant p53 regulates LPA signaling through lysophosphatidic acid phosphatase type 6', *Scientific Reports*, 9(1), p. 5195. Available at: https://doi.org/10.1038/s41598-019-41352-5.

Chui, A. *et al.* (2020) 'Oxidative stress regulates progenitor behavior and cortical neurogenesis', *Development (Cambridge, England)*, 147(5), p. dev184150. Available at: https://doi.org/10.1242/dev.184150.

Chung, W.K. *et al.* (2021) '16p11.2 deletion syndrome', *Current Opinion in Genetics & Development*, 68, pp. 49–56. Available at: https://doi.org/10.1016/j.gde.2021.01.011.

Claassen, D.A., Desler, M.M. and Rizzino, A. (2009) 'ROCK inhibition enhances the recovery and growth of cryopreserved human embryonic stem cells and human induced pluripotent stem cells', *Molecular Reproduction and Development*, 76(8), pp. 722–732. Available at: https://doi.org/10.1002/mrd.21021.

Coleman, M.L. *et al.* (2001) 'Membrane blebbing during apoptosis results from caspase-mediated activation of ROCK I', *Nature Cell Biology*, 3(4), pp. 339–345. Available at: https://doi.org/10.1038/35070009.

Conant, K.D. *et al.* (2014) 'A survey of seizures and current treatments in 15q duplication syndrome', *Epilepsia*. Blackwell Publishing Inc., pp. 396–402. Available at: https://doi.org/10.1111/epi.12530.

Cook, E.H. and Scherer, S.W. (2008) 'Copy-number variations associated with neuropsychiatric conditions', *Nature*. Nature Publishing Group, pp. 919–923. Available at: https://doi.org/10.1038/nature07458.

Corbett, D. *et al.* (2015) 'Lost in translation: Rethinking approaches to stroke recovery', in *Progress in Brain Research*. Elsevier B.V., pp. 413–434. Available at: https://doi.org/10.1016/bs.pbr.2014.12.002.

Costa, M.R. *et al.* (2007) 'The Marginal Zone/Layer I as a Novel Niche for Neurogenesis and Gliogenesis in Developing Cerebral Cortex', *Journal of Neuroscience*, 27(42), pp. 11376–11388. Available at: https://doi.org/10.1523/JNEUROSCI.2418-07.2007.

Cotsmire, S.M., Szczerba, M. and Jacobs, B.L. (2021) 'Detecting Necroptosis in Virus-Infected Cells', in A.R. Lucas (ed.) *Viruses as Therapeutics: Methods and Protocols*. New York, NY: Springer US (Methods in Molecular Biology), pp. 199–216. Available at: https://doi.org/10.1007/978-1-0716-1012-1_11.

Courchesne, E. *et al.* (2011) 'Neuron Number and Size in Prefrontal Cortex of Children With Autism', *JAMA*, 306(18), pp. 2001–2010. Available at: https://doi.org/10.1001/jama.2011.1638.

Crespi, B., Stead, P. and Elliot, M. (2010) 'Comparative genomics of autism and schizophrenia', *Proceedings of the National Academy of Sciences of the United States of*

America, 107(SUPPL. 1), pp. 1736–1741. Available at: https://doi.org/10.1073/pnas.0906080106.

Crespi, B.J. and Crofts, H.J. (2012) 'Association testing of copy number variants in schizophrenia and autism spectrum disorders', *Journal of Neurodevelopmental Disorders*, 4(1). Available at: https://doi.org/10.1186/1866-1955-4-15.

Cristino, A.S. *et al.* (2014) 'Neurodevelopmental and neuropsychiatric disorders represent an interconnected molecular system', *Molecular Psychiatry*, 19(3), pp. 294–301. Available at: https://doi.org/10.1038/mp.2013.16.

Cruz-Acuña, R. *et al.* (2017) 'Synthetic hydrogels for human intestinal organoid generation and colonic wound repair', *Nature Cell Biology*, 19(11), pp. 1326–1335. Available at: https://doi.org/10.1038/ncb3632.

Cruz-Acuña, R. *et al.* (2018) 'PEG-4MAL hydrogels for human organoid generation, culture, and in vivo delivery', *Nature Protocols*, 13(9), pp. 2102–2119. Available at: https://doi.org/10.1038/s41596-018-0036-3.

Cullen, D.K. *et al.* (2019) 'Bundled Three-Dimensional Human Axon Tracts Derived from Brain Organoids', *iScience*, 21, pp. 57–67. Available at: https://doi.org/10.1016/j.isci.2019.10.004.

Culotta, L. and Penzes, P. (2020) 'Exploring the mechanisms underlying excitation/inhibition imbalance in human iPSC-derived models of ASD', *Molecular Autism*, 11(1), p. 32. Available at: https://doi.org/10.1186/s13229-020-00339-0.

D'Aiuto, L. *et al.* (2014) 'Large-scale generation of human iPSC-derived neural stem cells/early neural progenitor cells and their neuronal differentiation', *Organogenesis*, 10(4), pp. 365–377. Available at: https://doi.org/10.1080/15476278.2015.1011921.

Dang, J. *et al.* (2016) 'Zika Virus Depletes Neural Progenitors in Human Cerebral Organoids through Activation of the Innate Immune Receptor TLR3', *Cell Stem Cell*, 19(2), pp. 258–265. Available at: https://doi.org/10.1016/j.stem.2016.04.014.

D'Arcy, M.S. (2019) 'Cell death: a review of the major forms of apoptosis, necrosis and autophagy', *Cell Biology International*, 43(6), pp. 582–592. Available at: https://doi.org/10.1002/cbin.11137.

Dasgupta, B. and Milbrandt, J. (2009) 'AMP-Activated Protein Kinase Phosphorylates Retinoblastoma Protein to Control Mammalian Brain Development', *Developmental Cell*, 16(2), pp. 256–270. Available at: https://doi.org/10.1016/j.devcel.2009.01.005.

Davalos, D.B. *et al.* (2004) 'Neuropsychological deficits in children associated with increased familial risk for schizophrenia', *Schizophrenia Research*, 67(2–3), pp. 123–130. Available at: https://doi.org/10.1016/S0920-9964(03)00187-7.

Davenport, E.C. *et al.* (2019) 'Autism and Schizophrenia-Associated CYFIP1 Regulates the Balance of Synaptic Excitation and Inhibition', *Cell Reports*, 26(8), pp. 2037-2051.e6. Available at: https://doi.org/10.1016/j.celrep.2019.01.092.

Daviaud, N. *et al.* (2019) 'Distinct Vulnerability and Resilience of Human Neuroprogenitor Subtypes in Cerebral Organoid Model of Prenatal Hypoxic Injury', *Frontiers in Cellular Neuroscience*, 13. Available at: https://www.frontiersin.org/article/10.3389/fncel.2019.00336 (Accessed: 10 June 2022).

David, A. *et al.* (2014) 'Lack of centrioles and primary cilia in STIL−/− mouse embryos', *Cell Cycle*, 13(18), pp. 2859–2868. Available at: https://doi.org/10.4161/15384101.2014.946830.

Davy, B.E. and Robinson, M.L. (2003) 'Congenital hydrocephalus in hy3 mice is caused by a frameshift mutation in Hydin, a large novel gene', *Human Molecular Genetics*, 12(10), pp. 1163–1170. Available at: https://doi.org/10.1093/hmg/ddg122.

De Blasio, C. *et al.* (2019) 'PLK1 targets NOTCH1 during DNA damage and mitotic progression', *The Journal of Biological Chemistry*, 294(47), pp. 17941–17950. Available at: https://doi.org/10.1074/jbc.RA119.009881.

Degenhardt, K.R. *et al.* (2010) 'Distinct enhancers at the Pax3 locus can function redundantly to regulate neural tube and neural crest expressions', *Developmental Biology*, 339(2), pp. 519–527. Available at: https://doi.org/10.1016/j.ydbio.2009.12.030.

Dehay, C., Kennedy, H. and Kosik, K.S. (2015) 'The Outer Subventricular Zone and Primate-Specific Cortical Complexification', *Neuron*, 85(4), pp. 683–694. Available at: https://doi.org/10.1016/j.neuron.2014.12.060.

Dekkers, J.F. *et al.* (2019) 'High-resolution 3D imaging of fixed and cleared organoids', *Nature Protocols*, 14(6), pp. 1756–1771. Available at: https://doi.org/10.1038/s41596-019-0160-8.

Delepine, C. *et al.* (2021) 'GSK3ß inhibitor CHIR 99021 modulates cerebral organoid development through dose-dependent regulation of apoptosis, proliferation, differentiation and migration', *PLOS ONE*, 16(5), p. e0251173. Available at: https://doi.org/10.1371/journal.pone.0251173.

Demjaha, A. *et al.* (2012) 'Dopamine Synthesis Capacity in Patients With Treatment-Resistant Schizophrenia', *American Journal of Psychiatry*, 169(11), pp. 1203–1210. Available at: https://doi.org/10.1176/appi.ajp.2012.12010144.

Deng, X. *et al.* (2017) 'TNF-α Mediates the Intrinsic and Extrinsic Pathway in Propofol-Induced Neuronal Apoptosis Via PI3K/Akt Signaling Pathway in Rat Prefrontal Cortical Neurons', *Neurotoxicity Research*, 32(3), pp. 409–419. Available at: https://doi.org/10.1007/s12640-017-9751-8.

Dennis, M.Y. and Eichler, E.E. (2016) 'Human adaptation and evolution by segmental duplication', *Current Opinion in Genetics and Development*. Elsevier Ltd, pp. 44–52. Available at: https://doi.org/10.1016/j.gde.2016.08.001.

Detrait, E.R. *et al.* (2005) 'Human neural tube defects: Developmental biology, epidemiology, and genetics', in *Neurotoxicology and Teratology*. Pergamon, pp. 515–524. Available at: https://doi.org/10.1016/j.ntt.2004.12.007.

Dezonne, R.S. *et al.* (2017) 'Derivation of Functional Human Astrocytes from Cerebral Organoids', *Scientific Reports*, 7(1), p. 45091. Available at: https://doi.org/10.1038/srep45091.

Dhaliwal, N. *et al.* (2021) 'Modeling PTEN overexpression-induced microcephaly in human brain organoids', *Molecular Brain*, 14(1), p. 131. Available at: https://doi.org/10.1186/s13041-021-00841-3.

Dhamne, S.C. *et al.* (2017) 'Replicable in vivo physiological and behavioral phenotypes of the Shank3B null mutant mouse model of autism', *Molecular Autism*, 8(1), p. 26. Available at: https://doi.org/10.1186/s13229-017-0142-z.

Dias, C. and Guillemot, F. (2017) 'Revealing the inner workings of organoids', *The EMBO Journal*, 36(10), pp. 1299–1301. Available at: https://doi.org/10.15252/embj.201796860.

Didenko, V.V., Ngo, H. and Baskin, D.S. (2003) 'Early Necrotic DNA Degradation: Presence of Blunt-Ended DNA Breaks, 3′ and 5′ Overhangs in Apoptosis, but only 5′

Overhangs in Early Necrosis', *The American Journal of Pathology*, 162(5), pp. 1571–1578. Available at: https://doi.org/10.1016/S0002-9440(10)64291-5.

Ding, W. *et al.* (2019) 'Cenpj Regulates Cilia Disassembly and Neurogenesis in the Developing Mouse Cortex', *Journal of Neuroscience*, 39(11), pp. 1994–2010. Available at: https://doi.org/10.1523/JNEUROSCI.1849-18.2018.

Diskin, S.J. *et al.* (2009) 'Copy number variation at 1q21.1 associated with neuroblastoma', *Nature*, 459(7249), pp. 987–991. Available at: https://doi.org/10.1038/nature08035.

Dodsworth, B.T. *et al.* (2020) 'Profiling of naïve and primed human pluripotent stem cells reveals state-associated miRNAs', *Scientific Reports*, 10(1), p. 10542. Available at: https://doi.org/10.1038/s41598-020-67376-w.

Domínguez-Iturza, N. *et al.* (2019) 'The autism- and schizophrenia-associated protein CYFIP1 regulates bilateral brain connectivity and behaviour', *Nature Communications*, 10(1), p. 3454. Available at: https://doi.org/10.1038/s41467-019-11203-y.

Dong, F. *et al.* (2016) 'Deletion of CTNNB1 in inhibitory circuitry contributes to autism-associated behavioral defects', *Human Molecular Genetics*, 25(13), pp. 2738–2751. Available at: https://doi.org/10.1093/hmg/ddw131.

Dong, X. *et al.* (2021) 'Human cerebral organoids establish subcortical projections in the mouse brain after transplantation', *Molecular Psychiatry*, 26(7), pp. 2964–2976. Available at: https://doi.org/10.1038/s41380-020-00910-4.

Dou, D. *et al.* (2017) '*CHD1L* Promotes Neuronal Differentiation in Human Embryonic Stem Cells by Upregulating *PAX6*', *Stem Cells and Development*, 26(22), pp. 1626–1636. Available at: https://doi.org/10.1089/scd.2017.0110.

Dougherty, M.L. *et al.* (2017) 'The birth of a human-specific neural gene by incomplete duplication and gene fusion', *Genome Biology*, 18(1). Available at: https://doi.org/10.1186/s13059-017-1163-9.

Du, T. *et al.* (2008) 'NKX2.1 specifies cortical interneuron fate by activating Lhx6', *Development*, 135(8), pp. 1559–1567. Available at: https://doi.org/10.1242/dev.015123.

Duan, W.R. *et al.* (2003) 'Comparison of immunohistochemistry for activated caspase-3 and cleaved cytokeratin 18 with the TUNEL method for quantification of apoptosis in histological sections of PC-3 subcutaneous xenografts', *The Journal of Pathology*, 199(2), pp. 221–228. Available at: https://doi.org/10.1002/path.1289.

Dumas, L.J. *et al.* (2012) 'DUF1220-Domain Copy Number Implicated in Human Brain-Size Pathology and Evolution', *The American Journal of Human Genetics*, 91(3), pp. 444–454. Available at: https://doi.org/10.1016/j.ajhg.2012.07.016.

Dunyak, B.M. and Gestwicki, J.E. (2016) 'Peptidyl-Proline Isomerases (PPIases): Targets for Natural Products and Natural Product-Inspired Compounds', *Journal of medicinal chemistry*, 59(21), pp. 9622–9644. Available at: https://doi.org/10.1021/acs.jmedchem.6b00411.

Durens, M. *et al.* (2020) 'High-throughput screening of human induced pluripotent stem cell-derived brain organoids', *Journal of Neuroscience Methods*, 335, p. 108627. Available at: https://doi.org/10.1016/j.jneumeth.2020.108627.

Dutta, A. *et al.* (2020) 'A proof of concept "phase zero" study of neurodevelopment using brain organoid models with Vis/near-infrared spectroscopy and electrophysiology',

Scientific Reports, 10(1), p. 20987. Available at: https://doi.org/10.1038/s41598-020-77929-8.

Edwards, A.C. *et al.* (2016) 'Meta-analysis of Positive and Negative Symptoms Reveals Schizophrenia Modifier Genes', *Schizophrenia Bulletin*, 42(2), pp. 279–287. Available at: https://doi.org/10.1093/schbul/sbv119.

Edwards, S.D. *et al.* (2021) 'Clinical characterization of individuals with the distal 1q21.1 microdeletion', *American Journal of Medical Genetics Part A*, 185(5), pp. 1388–1398. Available at: https://doi.org/10.1002/ajmg.a.62104.

Eiraku, M. *et al.* (2008) 'Self-Organized Formation of Polarized Cortical Tissues from ESCs and Its Active Manipulation by Extrinsic Signals', *Cell Stem Cell*, 3(5), pp. 519–532. Available at: https://doi.org/10.1016/j.stem.2008.09.002.

Eiraku, M. *et al.* (2011) 'Self-organizing optic-cup morphogenesis in three-dimensional culture', *Nature*, 472(7341), pp. 51–56. Available at: https://doi.org/10.1038/nature09941.

Elmore, S.A. *et al.* (2016) 'Recommendations from the INHAND Apoptosis/Necrosis Working Group', *Toxicologic pathology*, 44(2), pp. 173–188. Available at: https://doi.org/10.1177/0192623315625859.

Englund, C. *et al.* (2005) 'Pax6, Tbr2, and Tbr1 Are Expressed Sequentially by Radial Glia, Intermediate Progenitor Cells, and Postmitotic Neurons in Developing Neocortex', *Journal of Neuroscience*, 25(1), pp. 247–251. Available at: https://doi.org/10.1523/JNEUROSCI.2899-04.2005.

Enoch, M.-A. *et al.* (2014) 'Expression of glutamatergic genes in healthy humans across 16 brain regions; altered expression in the hippocampus after chronic exposure to alcohol or cocaine', *Genes, Brain and Behavior*, 13(8), pp. 758–768. Available at: https://doi.org/10.1111/gbb.12179.

Enright, H.A. *et al.* (2020) 'Functional and transcriptional characterization of complex neuronal co-cultures', *Scientific Reports*, 10(1), p. 11007. Available at: https://doi.org/10.1038/s41598-020-67691-2.

Eom, D.S. *et al.* (2012) 'Bone morphogenetic proteins regulate hinge point formation during neural tube closure by dynamic modulation of apicobasal polarity', *Birth Defects Research Part A: Clinical and Molecular Teratology*, 94(10), pp. 804–816. Available at: https://doi.org/10.1002/bdra.23052.

Eom, T.-Y. *et al.* (2020) 'Schizophrenia-related microdeletion causes defective ciliary motility and brain ventricle enlargement via microRNA-dependent mechanisms in mice', *Nature Communications*, 11(1), p. 912. Available at: https://doi.org/10.1038/s41467-020-14628-y.

Ewart, J.L. *et al.* (1997) 'Heart and neural tube defects in transgenic mice overexpressing the Cx43 gap junction gene', *Development*, 124(7).

Eyles, D.W. (2021) 'How do established developmental risk-factors for schizophrenia change the way the brain develops?', *Translational Psychiatry*, 11(1), pp. 1–15. Available at: https://doi.org/10.1038/s41398-021-01273-2.

Eze, U.C. *et al.* (2021) 'Single-cell atlas of early human brain development highlights heterogeneity of human neuroepithelial cells and early radial glia', *Nature Neuroscience*, 24(4), pp. 584–594. Available at: https://doi.org/10.1038/s41593-020-00794-1.

Fabra-Beser, J. *et al.* (2021) 'Differential Expression Levels of Sox9 in Early Neocortical Radial Glial Cells Regulate the Decision between Stem Cell Maintenance and

Differentiation', *The Journal of Neuroscience: The Official Journal of the Society for Neuroscience*, 41(33), pp. 6969–6986. Available at: https://doi.org/10.1523/JNEUROSCI.2905-20.2021.

Faini, G., Del Bene, F. and Albadri, S. (2021) 'Reelin functions beyond neuronal migration: from synaptogenesis to network activity modulation', *Current Opinion in Neurobiology*, 66, pp. 135–143. Available at: https://doi.org/10.1016/j.conb.2020.10.009.

Fair, S.R. *et al.* (2020) 'Electrophysiological Maturation of Cerebral Organoids Correlates with Dynamic Morphological and Cellular Development', *Stem Cell Reports*, 15(4), pp. 855–868. Available at: https://doi.org/10.1016/j.stemcr.2020.08.017.

Fang, W.-Q. *et al.* (2014) 'Overproduction of Upper-Layer Neurons in the Neocortex Leads to Autism-like Features in Mice', *Cell Reports*, 9(5), pp. 1635–1643. Available at: https://doi.org/10.1016/j.celrep.2014.11.003.

Farhy-Tselnicker, I. *et al.* (2021) 'Activity-dependent modulation of synapse-regulating genes in astrocytes', *eLife*. Edited by B. Stevens, L. Chen, and B. Stevens, 10, p. e70514. Available at: https://doi.org/10.7554/eLife.70514.

Fedorova, V. *et al.* (2019) 'Differentiation of neural rosettes from human pluripotent stem cells in vitro is sequentially regulated on a molecular level and accomplished by the mechanism reminiscent of secondary neurulation', *Stem Cell Research*, 40, p. 101563. Available at: https://doi.org/10.1016/j.scr.2019.101563.

Feinberg, I. (1982) 'Schizophrenia: Caused by a fault in programmed synaptic elimination during adolescence?', *Journal of Psychiatric Research*, 17(4), pp. 319–334. Available at: https://doi.org/10.1016/0022-3956(82)90038-3.

Ferent, J., Zaidi, D. and Francis, F. (2020) 'Extracellular Control of Radial Glia Proliferation and Scaffolding During Cortical Development and Pathology', *Frontiers in Cell and Developmental Biology*, 8. Available at: https://www.frontiersin.org/articles/10.3389/fcell.2020.578341 (Accessed: 16 November 2022).

Fernández-García, S. *et al.* (2020) 'Astrocytic BDNF and TrkB regulate severity and neuronal activity in mouse models of temporal lobe epilepsy', *Cell Death & Disease*, 11(6), pp. 1–17. Available at: https://doi.org/10.1038/s41419-020-2615-9.

Ferri, A. *et al.* (2013) 'Sox2 is required for embryonic development of the ventral telencephalon through the activation of the ventral determinants Nkx2.1 and Shh', *Development*, 140(6), pp. 1250–1261. Available at: https://doi.org/10.1242/dev.073411.

Fiddes, I.T. *et al.* (2018) 'Human-Specific NOTCH2NL Genes Affect Notch Signaling and Cortical Neurogenesis', *Cell*, 173(6), pp. 1356-1369.e22. Available at: https://doi.org/10.1016/J.CELL.2018.03.051.

Fiddes, I.T. *et al.* (2019) 'Paired involvement of human-specific Olduvai domains and NOTCH2NL genes in human brain evolution', *Human Genetics*, 138(7), pp. 715–721. Available at: https://doi.org/10.1007/s00439-019-02018-4.

Fietz, S.A. *et al.* (2012) 'Transcriptomes of germinal zones of human and mouse fetal neocortex suggest a role of extracellular matrix in progenitor self-renewal', *Proceedings of the National Academy of Sciences*, 109(29), pp. 11836–11841. Available at: https://doi.org/10.1073/pnas.1209647109.

Fischer, J. *et al.* (2022) 'Human-specific ARHGAP11B ensures human-like basal progenitor levels in hominid cerebral organoids', *EMBO reports*, 23(11), p. e54728. Available at: https://doi.org/10.15252/embr.202254728.

Flaherty, E. and Maniatis, T. (2020) 'The role of clustered protocadherins in neurodevelopment and neuropsychiatric diseases', *Current Opinion in Genetics & Development*, 65, pp. 144–150. Available at: https://doi.org/10.1016/j.gde.2020.05.041.

Flaherty, E.K. and Brennand, K.J. (2017) 'Using hiPSCs to model neuropsychiatric copy number variations (CNVs) has potential to reveal underlying disease mechanisms', *Brain Research*. Elsevier B.V., pp. 283–293. Available at: https://doi.org/10.1016/j.brainres.2015.11.009.

Fleck, J.S. *et al.* (2022) 'Inferring and perturbing cell fate regulomes in human brain organoids', *Nature*, pp. 1–8. Available at: https://doi.org/10.1038/s41586-022-05279-8.

Florio, M. *et al.* (2018) 'Evolution and cell-type specificity of human-specific genes preferentially expressed in progenitors of fetal neocortex', *eLife*. Edited by J.G. Gleeson, 7, p. e32332. Available at: https://doi.org/10.7554/eLife.32332.

Franco, E.D. *et al.* (2020) '*YIPF5* mutations cause neonatal diabetes and microcephaly through endoplasmic reticulum stress', *The Journal of Clinical Investigation*, 130(12), pp. 6338–6353. Available at: https://doi.org/10.1172/JCI141455.

Fromer, M. *et al.* (2014) 'De novo mutations in schizophrenia implicate synaptic networks', *Nature*, 506(7487), pp. 179–184. Available at: https://doi.org/10.1038/nature12929.

Fu, Y. *et al.* (2021) 'Heterogeneity of glial progenitor cells during the neurogenesis-to-gliogenesis switch in the developing human cerebral cortex', *Cell Reports*, 34(9), p. 108788. Available at: https://doi.org/10.1016/j.celrep.2021.108788.

Fung, S.J. *et al.* (2010) 'Expression of Interneuron Markers in the Dorsolateral Prefrontal Cortex of the Developing Human and in Schizophrenia', *American Journal of Psychiatry*, 167(12), pp. 1479–1488. Available at: https://doi.org/10.1176/appi.ajp.2010.09060784.

Gabriel, E. *et al.* (2016) 'CPAP promotes timely cilium disassembly to maintain neural progenitor pool', *The EMBO Journal*, 35(8), pp. 803–819. Available at: https://doi.org/10.15252/embj.201593679.

Gabriel, E. *et al.* (2017) 'Recent Zika Virus Isolates Induce Premature Differentiation of Neural Progenitors in Human Brain Organoids.', *Cell stem cell*, 20(3), pp. 397-406.e5. Available at: https://doi.org/10.1016/j.stem.2016.12.005.

Gabriel, E. *et al.* (2020) 'Human Brain Organoids to Decode Mechanisms of Microcephaly', *Frontiers in Cellular Neuroscience*, 14, p. 115. Available at: https://doi.org/10.3389/fncel.2020.00115.

Gao, L. *et al.* (2019) 'Post-Passage rock inhibition induces cytoskeletal aberrations and apoptosis in Human embryonic stem cells', *Stem Cell Research*, 41, p. 101641. Available at: https://doi.org/10.1016/j.scr.2019.101641.

Garcez, P.P. *et al.* (2016) 'Zika virus: Zika virus impairs growth in human neurospheres and brain organoids', *Science*, 352(6287), pp. 816–818. Available at: https://doi.org/10.1126/science.aaf6116.

Garcez, P.P. *et al.* (2017) 'Zika virus disrupts molecular fingerprinting of human neurospheres', *Scientific Reports*, 7(1), p. 40780. Available at: https://doi.org/10.1038/srep40780.

Garrett, L. *et al.* (2020) 'A truncating Aspm allele leads to a complex cognitive phenotype and region-specific reductions in parvalbuminergic neurons', *Translational Psychiatry*, 10(1), pp. 1–14. Available at: https://doi.org/10.1038/s41398-020-0686-0.

Gato, A. *et al.* (2014) 'Embryonic cerebrospinal fluid in brain development: neural progenitor control', *Croatian Medical Journal*, 55(4), pp. 299–305. Available at: https://doi.org/10.3325/cmj.2014.55.299.

Gee, S. *et al.* (2012) 'Synaptic Activity Unmasks Dopamine D2 Receptor Modulation of a Specific Class of Layer V Pyramidal Neurons in Prefrontal Cortex', *Journal of Neuroscience*, 32(14), pp. 4959–4971. Available at: https://doi.org/10.1523/JNEUROSCI.5835-11.2012.

Germain, N.D. *et al.* (2013) 'Derivation and Isolation of NKX2.1-Positive Basal Forebrain Progenitors from Human Embryonic Stem Cells', *Stem Cells and Development*, 22(10), pp. 1477–1489. Available at: https://doi.org/10.1089/scd.2012.0264.

Ghule, P.N. *et al.* (2011) 'Reprogramming the pluripotent cell cycle: restoration of an abbreviated G1 phase in human induced pluripotent stem (iPS) cells', *Journal of cellular physiology*, 226(5), pp. 1149–1156. Available at: https://doi.org/10.1002/jcp.22440.

Giandomenico, S.L. *et al.* (2019) 'Cerebral organoids at the air–liquid interface generate diverse nerve tracts with functional output', *Nature Neuroscience*, 22(4), pp. 669–679. Available at: https://doi.org/10.1038/s41593-019-0350-2.

Giandomenico, S.L., Sutcliffe, M. and Lancaster, M.A. (2021) 'Generation and long-term culture of advanced cerebral organoids for studying later stages of neural development', *Nature Protocols*, 16(2), pp. 579–602. Available at: https://doi.org/10.1038/s41596-020-00433-w.

Gladwyn-Ng, I. *et al.* (2018) 'Stress-induced unfolded protein response contributes to Zika virus–associated microcephaly', *Nature Neuroscience*, 21(1), pp. 63–71. Available at: https://doi.org/10.1038/s41593-017-0038-4.

Glassford, M.R. *et al.* (2016) 'Novel features of 3q29 deletion syndrome: Results from the 3q29 registry', *American Journal of Medical Genetics Part A*, 170(4), pp. 999–1006. Available at: https://doi.org/10.1002/ajmg.a.37537.

Glynn, M.W. *et al.* (2011) 'MHCI negatively regulates synapse density during the establishment of cortical connections', *Nature Neuroscience*, 14(4), pp. 442–451. Available at: https://doi.org/10.1038/nn.2764.

Goldsmith, D.R. *et al.* (2021) 'The interaction of lipids and inflammatory markers predict negative symptom severity in patients with schizophrenia', *npj Schizophrenia*, 7(1), pp. 1–3. Available at: https://doi.org/10.1038/s41537-021-00179-8.

Gomes, A.R. *et al.* (2020) 'Modeling Rett Syndrome With Human Patient-Specific Forebrain Organoids', *Frontiers in Cell and Developmental Biology*, 8. Available at: https://www.frontiersin.org/articles/10.3389/fcell.2020.610427 (Accessed: 12 October 2022).

Gonzalez, C. *et al.* (2018) 'Modeling amyloid beta and tau pathology in human cerebral organoids', *Molecular Psychiatry*, 23(12), pp. 2363–2374. Available at: https://doi.org/10.1038/s41380-018-0229-8.

Gonzalez Malagon, S.G. *et al.* (2015) 'The phenotype of a knockout mouse identifies flavin-containing monooxygenase 5 (FMO5) as a regulator of metabolic ageing', *Biochemical Pharmacology*, 96(3), pp. 267–277. Available at: https://doi.org/10.1016/j.bcp.2015.05.013.

González-Martínez, J. *et al.* (2021) 'Deficient adaptation to centrosome duplication defects in neural progenitors causes microcephaly and subcortical heterotopias', *JCI Insight*, 6(16). Available at: https://doi.org/10.1172/jci.insight.146364.

Gordon, A. *et al.* (2019) 'Transcriptomic networks implicate neuronal energetic abnormalities in three mouse models harboring autism and schizophrenia-associated mutations', *Molecular Psychiatry*, pp. 1–15. Available at: https://doi.org/10.1038/s41380-019-0576-0.

Gordon, A. *et al.* (2021) 'Long-term maturation of human cortical organoids matches key early postnatal transitions', *Nature Neuroscience*, 24(3), pp. 331–342. Available at: https://doi.org/10.1038/s41593-021-00802-y.

Götz, M. and Huttner, W.B. (2005) 'The cell biology of neurogenesis', *Nature Reviews Molecular Cell Biology*, 6(10), pp. 777–788. Available at: https://doi.org/10.1038/nrm1739.

Granger, A.J. *et al.* (2020) 'Cortical ChAT+ neurons co-transmit acetylcholine and GABA in a target- and brain-region-specific manner', *eLife*. Edited by S.P. Brown et al., 9, p. e57749. Available at: https://doi.org/10.7554/eLife.57749.

Gray, J.A. *et al.* (1991) 'The neuropsychology of schizophrenia', *Behavioral and Brain Sciences*, 14(1), pp. 1–20. Available at: https://doi.org/10.1017/S0140525X00065055.

Grego-Bessa, J. *et al.* (2016) 'The tumor suppressor PTEN and the PDK1 kinase regulate formation of the columnar neural epithelium', *eLife*, 5(JANUARY2016). Available at: https://doi.org/10.7554/eLife.12034.

Groza, T. *et al.* (2022) 'The International Mouse Phenotyping Consortium: comprehensive knockout phenotyping underpinning the study of human disease', *Nucleic Acids Research*, p. gkac972. Available at: https://doi.org/10.1093/nar/gkac972.

Gruber, R. *et al.* (2011) 'MCPH1 regulates the neuroprogenitor division mode by coupling the centrosomal cycle with mitotic entry through the Chk1–Cdc25 pathway', *Nature Cell Biology*, 13(11), pp. 1325–1334. Available at: https://doi.org/10.1038/ncb2342.

Gründer, G. and Cumming, P. (2016) 'Chapter 7 - The Dopamine Hypothesis of Schizophrenia: Current Status', in T. Abel and T. Nickl-Jockschat (eds) *The Neurobiology of Schizophrenia*. San Diego: Academic Press, pp. 109–124. Available at: https://doi.org/10.1016/B978-0-12-801829-3.00015-X.

Guerra, M.M. *et al.* (2015) 'Cell Junction Pathology of Neural Stem Cells Is Associated With Ventricular Zone Disruption, Hydrocephalus, and Abnormal Neurogenesis', *Journal of Neuropathology & Experimental Neurology*, 74(7), pp. 653–671. Available at: https://doi.org/10.1097/NEN.0000000000000203.

Gunhanlar, N. *et al.* (2017) 'A simplified protocol for differentiation of electrophysiologically mature neuronal networks from human induced pluripotent stem cells', *Molecular Psychiatry*. Available at: https://doi.org/10.1038/mp.2017.56.

Güven, A. *et al.* (2020) 'Extracellular matrix-inducing Sox9 promotes both basal progenitor proliferation and gliogenesis in developing neocortex', *eLife*. Edited by M.E. Bronner and S. Nicolis, 9, p. e49808. Available at: https://doi.org/10.7554/eLife.49808.

H. Dehkordi, M. *et al.* (2020) 'Apoptosome-dependent myotube formation involves activation of caspase-3 in differentiating myoblasts', *Cell Death & Disease*, 11(5), pp. 1–12. Available at: https://doi.org/10.1038/s41419-020-2502-4.

Hack, M.A. *et al.* (2004) 'Regionalization and fate specification in neurospheres: The role of Olig2 and Pax6', *Molecular and Cellular Neuroscience*, 25(4), pp. 664–678. Available at: https://doi.org/10.1016/j.mcn.2003.12.012.

Hagen, M. von der (2017) ‘Diagnostic Approach to Primary Microcephaly’, *Neuropediatrics*, 48(3), pp. 133–134. Available at: https://doi.org/10.1055/s-0037-1602820.

Haldeman-Englert, C.R. and Jewett, T. (1993) *1q21.1 Recurrent Microdeletion*, *GeneReviews®*. University of Washington, Seattle.

Hall, J.G. (1987) ‘Thrombocytopenia and absent radius (TAR) syndrome.’, *Journal of Medical Genetics*, 24(2), pp. 79–83. Available at: https://doi.org/10.1136/jmg.24.2.79.

Hansen, D.V. *et al.* (2010) ‘Neurogenic radial glia in the outer subventricular zone of human neocortex’, *Nature*, 464(7288), pp. 554–561. Available at: https://doi.org/10.1038/nature08845.

Harbom, L.J. *et al.* (2019) ‘The effect of rho kinase inhibition on morphological and electrophysiological maturity in iPSC-derived neurons’, *Cell and Tissue Research*, 375(3), pp. 641–654. Available at: https://doi.org/10.1007/s00441-018-2942-7.

Haronikova, L. *et al.* (2019) ‘The p53 mRNA: an integral part of the cellular stress response’, *Nucleic Acids Research*, 47(7), pp. 3257–3271. Available at: https://doi.org/10.1093/nar/gkz124.

Harting, I. *et al.* (2009) ‘Abnormal myelination in Angelman syndrome’, *European Journal of Paediatric Neurology*, 13(3), pp. 271–276. Available at: https://doi.org/10.1016/j.ejpn.2008.04.005.

Hashemi, E. *et al.* (2017) ‘The Number of Parvalbumin-Expressing Interneurons Is Decreased in the Prefrontal Cortex in Autism’, *Cerebral Cortex*, 27(3), pp. 1931–1943. Available at: https://doi.org/10.1093/cercor/bhw021.

Hashimoto-Torii, K. *et al.* (2008) ‘Interaction between Reelin and Notch Signaling Regulates Neuronal Migration in the Cerebral Cortex’, *Neuron*, 60(2), pp. 273–284. Available at: https://doi.org/10.1016/j.neuron.2008.09.026.

Haushalter, C. *et al.* (2017) ‘Retinoic acid controls early neurogenesis in the developing mouse cerebral cortex’, *Developmental Biology*, 430(1), pp. 129–141. Available at: https://doi.org/10.1016/j.ydbio.2017.08.006.

He, P. *et al.* (2020) ‘AMPK Activity Contributes to G2 Arrest and DNA Damage Decrease via p53/p21 Pathways in Oxidatively Damaged Mouse Zygotes’, *Frontiers in Cell and Developmental Biology*, 8. Available at: https://www.frontiersin.org/articles/10.3389/fcell.2020.539485 (Accessed: 30 September 2022).

Hernández, D. *et al.* (2021) ‘Culture Variabilities of Human iPSC-Derived Cerebral Organoids Are a Major Issue for the Modelling of Phenotypes Observed in Alzheimer’s Disease’, *Stem Cell Reviews and Reports* [Preprint]. Available at: https://doi.org/10.1007/s12015-021-10147-5.

Herrera, A. *et al.* (2014) ‘Sustained Wnt/β-catenin signalling causes neuroepithelial aberrations through the accumulation of aPKC at the apical pole’, *Nature Communications*, 5(1), p. 4168. Available at: https://doi.org/10.1038/ncomms5168.

Hettige, N.C. *et al.* (2022) ‘FOXG1 dose tunes cell proliferation dynamics in human forebrain progenitor cells’, *Stem Cell Reports*, 17(3), pp. 475–488. Available at: https://doi.org/10.1016/j.stemcr.2022.01.010.

Higuchi, Y. (2003) ‘Chromosomal DNA fragmentation in apoptosis and necrosis induced by oxidative stress’, *Biochemical Pharmacology*, 66(8), pp. 1527–1535. Available at: https://doi.org/10.1016/S0006-2952(03)00508-2.

Hilker, R. *et al.* (2018) ‘Heritability of Schizophrenia and Schizophrenia Spectrum Based on the Nationwide Danish Twin Register’, *Biological Psychiatry*, 83(6), pp. 492–498. Available at: https://doi.org/10.1016/J.BIOPSYCH.2017.08.017.

Hirsch, C. and Schildknecht, S. (2019) ‘In Vitro Research Reproducibility: Keeping Up High Standards’, *Frontiers in Pharmacology*, 10. Available at: https://www.frontiersin.org/articles/10.3389/fphar.2019.01484 (Accessed: 18 August 2022).

Hitoshi, S. *et al.* (2004) ‘Primitive neural stem cells from the mammalian epiblast differentiate to definitive neural stem cells under the control of Notch signaling’, *Genes & Development*, 18(15), pp. 1806–1811. Available at: https://doi.org/10.1101/gad.1208404.

Hodge, R.D. *et al.* (2019) ‘Conserved cell types with divergent features in human versus mouse cortex’, *Nature*, 573(7772), pp. 61–68. Available at: https://doi.org/10.1038/s41586-019-1506-7.

Hodge, R.D., D’Ercole, A.J. and O’Kusky, J.R. (2004) ‘Insulin-Like Growth Factor-I Accelerates the Cell Cycle by Decreasing G1 Phase Length and Increases Cell Cycle Reentry in the Embryonic Cerebral Cortex’, *Journal of Neuroscience*, 24(45), pp. 10201–10210. Available at: https://doi.org/10.1523/JNEUROSCI.3246-04.2004.

Hoerder-Suabedissen, A. and Molnár, Z. (2015) ‘Development, evolution and pathology of neocortical subplate neurons’, *Nature Reviews Neuroscience*, 16(3), pp. 133–146. Available at: https://doi.org/10.1038/nrn3915.

Horiguchi, A. *et al.* (2014) ‘Effective Rho-associated protein kinase inhibitor treatment to dissociate human iPS cells for suspension culture to form embryoid body-like cell aggregates’, *Journal of Bioscience and Bioengineering*, 118(5), pp. 588–592. Available at: https://doi.org/10.1016/j.jbiosc.2014.04.008.

Horner, V.L. and Caspary, T. (2011) ‘Disrupted dorsal neural tube BMP signaling in the cilia mutant Arl13bhnn stems from abnormal Shh signaling’, *Developmental biology*, 355(1), pp. 43–54. Available at: https://doi.org/10.1016/j.ydbio.2011.04.019.

Houeijeh, A. *et al.* (2011) ‘Thrombocytopenia-absent radius (TAR) syndrome: A clinical genetic series of 14 further cases. Impact of the associated 1q21.1 deletion on the genetic counselling’, *European Journal of Medical Genetics*, 54(5), pp. e471–e477. Available at: https://doi.org/10.1016/j.ejmg.2011.05.001.

Howell, K.R. and Law, A.J. (2020) ‘Neurodevelopmental concepts of schizophrenia in the genome-wide association era: AKT/mTOR signaling as a pathological mediator of genetic and environmental programming during development’, *Schizophrenia Research*, 217, pp. 95–104. Available at: https://doi.org/10.1016/j.schres.2019.08.036.

Howes, O. *et al.* (2011) ‘Progressive increase in striatal dopamine synthesis capacity as patients develop psychosis: a PET study’, *Molecular Psychiatry*, 16(9), pp. 885–886. Available at: https://doi.org/10.1038/mp.2011.20.

Howes, O.D. *et al.* (2009) ‘Elevated Striatal Dopamine Function Linked to Prodromal Signs of Schizophrenia’, *Archives of General Psychiatry*, 66(1), pp. 13–20. Available at: https://doi.org/10.1001/archgenpsychiatry.2008.514.

Hříbková, H. *et al.* (2018) ‘Calcium signaling mediates five types of cell morphological changes to form neural rosettes’, *Journal of Cell Science*, 131(3), p. jcs206896. Available at: https://doi.org/10.1242/jcs.206896.

Hsu, C.-C. *et al.* (2020) ‘Ischemia/reperfusion injured intestinal epithelial cells cause cortical neuron death by releasing exosomal microRNAs associated with apoptosis, necroptosis, and pyroptosis’, *Scientific Reports*, 10(1), p. 14409. Available at: https://doi.org/10.1038/s41598-020-71310-5.

Huang, J. *et al.* (2009) ‘More synergetic cooperation of Yamanaka factors in induced pluripotent stem cells than in embryonic stem cells’, *Cell Research*, 19(10), pp. 1127–1138. Available at: https://doi.org/10.1038/cr.2009.106.

Huang, R. *et al.* (2019) ‘NCAM regulates temporal specification of neural progenitor cells via profilin2 during corticogenesis’, *The Journal of Cell Biology*, 219(1), p. e201902164. Available at: https://doi.org/10.1083/jcb.201902164.

Huang, S. *et al.* (2022) ‘Chimeric cerebral organoids reveal the essentials of neuronal and astrocytic APOE4 for Alzheimer’s tau pathology’, *Signal Transduction and Targeted Therapy*, 7(1), pp. 1–10. Available at: https://doi.org/10.1038/s41392-022-01006-x.

Huang, W.-C. *et al.* (2016) ‘Zika virus infection during the period of maximal brain growth causes microcephaly and corticospinal neuron apoptosis in wild type mice’, *Scientific Reports*, 6(1), p. 34793. Available at: https://doi.org/10.1038/srep34793.

Huo, B. *et al.* (2021) ‘Pax3 inhibits Neuro-2a cells proliferation and neurite outgrowth’, *Journal of Cellular and Molecular Medicine*, 25(2), pp. 1252–1262. Available at: https://doi.org/10.1111/jcmm.16195.

Hussain, M.S. *et al.* (2012) ‘A Truncating Mutation of CEP135 Causes Primary Microcephaly and Disturbed Centrosomal Function’, *The American Journal of Human Genetics*, 90(5), pp. 871–878. Available at: https://doi.org/10.1016/j.ajhg.2012.03.016.

Hutton, S.R. and Pevny, L.H. (2011) ‘SOX2 expression levels distinguish between neural progenitor populations of the developing dorsal telencephalon’, *Developmental Biology*, 352(1), pp. 40–47. Available at: https://doi.org/10.1016/j.ydbio.2011.01.015.

Iefremova, V. *et al.* (2017) ‘An Organoid-Based Model of Cortical Development Identifies Non-Cell-Autonomous Defects in Wnt Signaling Contributing to Miller-Dieker Syndrome’, *Cell Reports*, 19(1), pp. 50–59. Available at: https://doi.org/10.1016/J.CELREP.2017.03.047.

Ip, J.P.K., Mellios, N. and Sur, M. (2018) ‘Rett syndrome: insights into genetic, molecular and circuit mechanisms’, *Nature Reviews Neuroscience*, 19(6), pp. 368–382. Available at: https://doi.org/10.1038/s41583-018-0006-3.

Ishihara, K. *et al.* (2022) ‘Topological morphogenesis of neuroepithelial organoids’, *Nature Physics*, pp. 1–7. Available at: https://doi.org/10.1038/s41567-022-01822-6.

Issa, L. *et al.* (2013) ‘Clinical and cellular features in patients with primary autosomal recessive microcephaly and a novel CDK5RAP2 mutation’, *Orphanet Journal of Rare Diseases*, 8(1), p. 59. Available at: https://doi.org/10.1186/1750-1172-8-59.

Ito, H. *et al.* (2015) ‘In utero gene therapy rescues microcephaly caused by Pqbp1-hypofunction in neural stem progenitor cells’, *Molecular Psychiatry*, 20(4), pp. 459–471. Available at: https://doi.org/10.1038/mp.2014.69.

Janesick, A., Wu, S.C. and Blumberg, B. (2015) 'Retinoic acid signaling and neuronal differentiation', *Cellular and Molecular Life Sciences*, 72(8), pp. 1559–1576. Available at: https://doi.org/10.1007/s00018-014-1815-9.

Jayaraman, D. *et al.* (2016) 'Microcephaly Proteins Wdr62 and Aspm Define a Mother Centriole Complex Regulating Centriole Biogenesis, Apical Complex, and Cell Fate', *Neuron*, 92(4), pp. 813–828. Available at: https://doi.org/10.1016/j.neuron.2016.09.056.

Jean, F., Stuart, A. and Tarailo-Graovac, M. (2020) 'Dissecting the Genetic and Etiological Causes of Primary Microcephaly', *Frontiers in Neurology*, 11. Available at: https://www.frontiersin.org/articles/10.3389/fneur.2020.570830 (Accessed: 6 September 2022).

Jennifer Antonchuk *et al.* (2010) 'AggreWell(TM) 400, AggreWell(TM) 800, and AggreWell(TM) Medium provide a platform for generation and culture of human embryoid bodies of defined sizes', in. *ISSCR*, StemCell Technologies. Available at: https://eur03.safelinks.protection.outlook.com/?url=https%3A%2F%2Fcdn.stemcell.com%2Fmedia%2Ffiles%2Fposter%2FSP00003-Aggrewell_400_Aggrewell_800_Aggrewell_Medium_Provide_Platform_Generation_Culture_Human_Embryoid_Bodies_Defined_Sizes.pdf%3F_ga%3D2.115334659.507499622.1583165189-1421009442.1576518566&data=04%7C01%7Clunns%40cardiff.ac.uk%7C689f894a32a7486bdb3108da01d8779d%7Cbdb74b3095684856bdbf06759778fcbc%7C1%7C0%7C637824327932022634%7CUnknown%7CTWFpbGZsb3d8eyJWIjoiMC4wLjAwMDAiLCJQIjoiV2luMzIiLCJBTiI6Ik1haWwiLCJXVCI6Mn0%3D%7C3000&sdata=G2becTrma8hD7L%2BO8Y95baw%2FzAvkKv4EFfy9Yp2Raeo%3D&reserved=0.

Jiang, B.-H. *et al.* (2015) 'CHD1L Regulated PARP1-Driven Pluripotency and Chromatin Remodeling During the Early-Stage Cell Reprogramming', *STEM CELLS*, 33(10), pp. 2961–2972. Available at: https://doi.org/10.1002/stem.2116.

Jiang, M. *et al.* (2020) 'The caspase-3/GSDME signal pathway as a switch between apoptosis and pyroptosis in cancer', *Cell Death Discovery*, 6(1), pp. 1–11. Available at: https://doi.org/10.1038/s41420-020-00349-0.

Jiang, M. *et al.* (2021) 'Maternal sevoflurane exposure induces temporary defects in interkinetic nuclear migration of radial glial progenitors in the fetal cerebral cortex through the Notch signalling pathway', *Cell Proliferation*, 54(6), p. e13042. Available at: https://doi.org/10.1111/cpr.13042.

Jo, J. *et al.* (2016) 'Midbrain-like Organoids from Human Pluripotent Stem Cells Contain Functional Dopaminergic and Neuromelanin-Producing Neurons', *Cell Stem Cell*, 19(2), pp. 248–257. Available at: https://doi.org/10.1016/J.STEM.2016.07.005.

Johnson, M.B. *et al.* (2018) 'Aspm knockout ferret reveals an evolutionary mechanism governing cerebral cortical size', *Nature*, 556(7701), pp. 370–375. Available at: https://doi.org/10.1038/s41586-018-0035-0.

de Jong, J.O. *et al.* (2021) 'Cortical overgrowth in a preclinical forebrain organoid model of CNTNAP2-associated autism spectrum disorder', *Nature Communications*, 12(1), p. 4087. Available at: https://doi.org/10.1038/s41467-021-24358-4.

JUDAS, M., Sedmak, G. and Kostovic, I. (2013) 'The significance of the subplate for evolution and developmental plasticity of the human brain', *Frontiers in Human Neuroscience*, 7. Available at: https://www.frontiersin.org/articles/10.3389/fnhum.2013.00423 (Accessed: 15 November 2022).

Judson, M.C. *et al.* (2017) 'Decreased Axon Caliber Underlies Loss of Fiber Tract Integrity, Disproportional Reductions in White Matter Volume, and Microcephaly in Angelman Syndrome Model Mice', *Journal of Neuroscience*, 37(31), pp. 7347–7361. Available at: https://doi.org/10.1523/JNEUROSCI.0037-17.2017.

Kadoshima, T. *et al.* (2013) 'Self-organization of axial polarity, inside-out layer pattern, and species-specific progenitor dynamics in human ES cell-derived neocortex', *Proceedings of the National Academy of Sciences of the United States of America*, 110(50), pp. 20284–20289. Available at: https://doi.org/10.1073/pnas.1315710110.

Kafkafi, N. *et al.* (2018) 'Reproducibility and replicability of rodent phenotyping in preclinical studies', *Neuroscience & Biobehavioral Reviews*, 87, pp. 218–232. Available at: https://doi.org/10.1016/j.neubiorev.2018.01.003.

Kaitetzidou, E. *et al.* (2019) 'Unravelling paralogous gene expression dynamics during three-spined stickleback embryogenesis', *Scientific Reports*, 9(1), p. 3752. Available at: https://doi.org/10.1038/s41598-019-40127-2.

Kalkan, T. *et al.* (2017) 'Tracking the embryonic stem cell transition from ground state pluripotency', *Development*, 144(7), pp. 1221–1234. Available at: https://doi.org/10.1242/dev.142711.

Kalogeropoulou, A. *et al.* (2022) 'Intrinsic neural stem cell properties define brain hypersensitivity to genotoxic stress', *Stem Cell Reports*, 17(6), pp. 1395–1410. Available at: https://doi.org/10.1016/j.stemcr.2022.04.018.

Kang, Y. *et al.* (2021) 'A human forebrain organoid model of fragile X syndrome exhibits altered neurogenesis and highlights new treatment strategies', *Nature Neuroscience*, 24(10), pp. 1377–1391. Available at: https://doi.org/10.1038/s41593-021-00913-6.

Kapur, S. and Seeman, P. (2002) 'NMDA receptor antagonists ketamine and PCP have direct effects on the dopamine D2 and serotonin 5-HT2 receptors—implications for models of schizophrenia', *Molecular Psychiatry*, 7(8), pp. 837–844. Available at: https://doi.org/10.1038/sj.mp.4001093.

Karimaian, A. *et al.* (2017) 'The crosstalk between Wnt/β-catenin signaling pathway with DNA damage response and oxidative stress: Implications in cancer therapy', *DNA Repair*, 51, pp. 14–19. Available at: https://doi.org/10.1016/j.dnarep.2017.01.003.

Karzbrun, E. *et al.* (2018) 'Human brain organoids on a chip reveal the physics of folding', *Nature Physics*, 14(5). Available at: https://doi.org/10.1038/s41567-018-0046-7.

Karzbrun, E. *et al.* (2021) 'Human neural tube morphogenesis in vitro by geometric constraints', *Nature*, 599(7884), pp. 268–272. Available at: https://doi.org/10.1038/s41586-021-04026-9.

Kathuria, A. *et al.* (2019) 'Synaptic deficits in iPSC-derived cortical interneurons in schizophrenia are mediated by NLGN2 and rescued by N-acetylcysteine', *Translational Psychiatry*, 9(1), pp. 1–13. Available at: https://doi.org/10.1038/s41398-019-0660-x.

Kathuria, A. *et al.* (2020) 'Transcriptomic Landscape and Functional Characterization of Induced Pluripotent Stem Cell–Derived Cerebral Organoids in Schizophrenia', *JAMA Psychiatry*, 77(7), pp. 745–754. Available at: https://doi.org/10.1001/jamapsychiatry.2020.0196.

Kay, S.R., Fiszbein, A. and Opler, L.A. (1987) 'The Positive and Negative Syndrome Scale (PANSS) for Schizophrenia', *Schizophrenia Bulletin*, 13(2), pp. 261–276. Available at: https://doi.org/10.1093/schbul/13.2.261.

Kayagaki, N. *et al.* (2021) 'NINJ1 mediates plasma membrane rupture during lytic cell death', *Nature*, 591(7848), pp. 131–136. Available at: https://doi.org/10.1038/s41586-021-03218-7.

Keeley, J.W. *et al.* (2016) 'Developing a Science of Clinical Utility in Diagnostic Classification Systems Field Study Strategies for ICD-11 Mental and Behavioral Disorders', *American Psychologist*, 71(1), pp. 3–16. Available at: https://doi.org/10.1037/a0039972.

Kelava, I. *et al.* (2022) 'Androgens increase excitatory neurogenic potential in human brain organoids', *Nature*, 602(7895), pp. 112–116. Available at: https://doi.org/10.1038/s41586-021-04330-4.

Kelly, S. *et al.* (2018) 'Widespread white matter microstructural differences in schizophrenia across 4322 individuals: results from the ENIGMA Schizophrenia DTI Working Group', *Molecular Psychiatry*, 23(5), pp. 1261–1269. Available at: https://doi.org/10.1038/mp.2017.170.

Kesby, J.P. *et al.* (2018) 'Dopamine, psychosis and schizophrenia: the widening gap between basic and clinical neuroscience', *Translational Psychiatry*, 8(1), pp. 1–12. Available at: https://doi.org/10.1038/s41398-017-0071-9.

Khan, T.A. *et al.* (2020) 'Neuronal defects in a human cellular model of 22q11.2 deletion syndrome', *Nature Medicine*, 26(12), pp. 1888–1898. Available at: https://doi.org/10.1038/s41591-020-1043-9.

Khattabi, L.A.E. *et al.* (2020) '16p13.11 microduplication in 45 new patients: refined clinical significance and genotype–phenotype correlations', *Journal of Medical Genetics*, 57(5), pp. 301–307. Available at: https://doi.org/10.1136/jmedgenet-2018-105389.

Khokhar, J.Y. *et al.* (2018) 'The link between schizophrenia and substance use disorder: A unifying hypothesis', *Schizophrenia Research*, 194, pp. 78–85. Available at: https://doi.org/10.1016/j.schres.2017.04.016.

Khoo, T.S. *et al.* (2020) 'Retention of Somatic Memory Associated with Cell Identity, Age and Metabolism in Induced Pluripotent Stem (iPS) Cells Reprogramming', *Stem Cell Reviews and Reports*, 16(2), pp. 251–261. Available at: https://doi.org/10.1007/s12015-020-09956-x.

Kibschull, M. *et al.* (2016) 'Quantitative large scale gene expression profiling from human stem cell culture micro samples using multiplex pre-amplification', *Systems Biology in Reproductive Medicine*, 62(1), pp. 84–91. Available at: https://doi.org/10.3109/19396368.2015.1062578.

Kilens, S. *et al.* (2018) 'Parallel derivation of isogenic human primed and naive induced pluripotent stem cells', *Nature Communications*, 9(1), p. 360. Available at: https://doi.org/10.1038/s41467-017-02107-w.

Kim, H. *et al.* (2019) 'Pluripotent Stem Cell-Derived Cerebral Organoids Reveal Human Oligodendrogenesis with Dorsal and Ventral Origins', *Stem Cell Reports*, 12(5), pp. 890–905. Available at: https://doi.org/10.1016/j.stemcr.2019.04.011.

Kim, H.-M. *et al.* (2021) 'The epidermal growth factor receptor variant type III mutation frequently found in gliomas induces astrogenesis in human cerebral organoids', *Cell Proliferation*, 54(2), p. e12965. Available at: https://doi.org/10.1111/cpr.12965.

Kim, H.R. *et al.* (2021) 'Depolarizing GABAA current in the prefrontal cortex is linked with cognitive impairment in a mouse model relevant for schizophrenia', *Science Advances* [Preprint]. Available at: https://doi.org/10.1126/sciadv.aba5032.

Kim, I.S. *et al.* (2020) 'Parallel Single-Cell RNA-Seq and Genetic Recording Reveals Lineage Decisions in Developing Embryoid Bodies', *Cell Reports*, 33(1), p. 108222. Available at: https://doi.org/10.1016/j.celrep.2020.108222.

Kim, K., Ossipova, O. and Sokol, S.Y. (2015) 'Neural Crest Specification by Inhibition of the ROCK/Myosin II Pathway', *Stem Cells*, 33(3), pp. 674–685. Available at: https://doi.org/10.1002/stem.1877.

Kim, N.-S. *et al.* (2021) 'Pharmacological rescue in patient iPSC and mouse models with a rare DISC1 mutation', *Nature Communications*, 12(1), p. 1398. Available at: https://doi.org/10.1038/s41467-021-21713-3.

Kim, T.-S. *et al.* (2013) 'Hierarchical recruitment of Plk4 and regulation of centriole biogenesis by two centrosomal scaffolds, Cep192 and Cep152', *Proceedings of the National Academy of Sciences*, 110(50), pp. E4849–E4857. Available at: https://doi.org/10.1073/pnas.1319656110.

Kimura, H. *et al.* (2015) 'Association study of BCL9 gene polymorphism rs583583 with schizophrenia and negative symptoms in Japanese population', *Scientific Reports*, 5(1), pp. 1–6. Available at: https://doi.org/10.1038/srep15705.

Kitahara, T. *et al.* (2020) 'Axonal Extensions along Corticospinal Tracts from Transplanted Human Cerebral Organoids', *Stem Cell Reports*, 15(2), pp. 467–481. Available at: https://doi.org/10.1016/j.stemcr.2020.06.016.

Kitazumi, I. and Tsukahara, M. (2011) 'Regulation of DNA fragmentation: the role of caspases and phosphorylation', *The FEBS Journal*, 278(3), pp. 427–441. Available at: https://doi.org/10.1111/j.1742-4658.2010.07975.x.

Klaus, J. *et al.* (2019) 'Altered neuronal migratory trajectories in human cerebral organoids derived from individuals with neuronal heterotopia', *Nature Medicine*, 25(4), pp. 561–568. Available at: https://doi.org/10.1038/s41591-019-0371-0.

Klingler, E. *et al.* (2021) 'Mapping the molecular and cellular complexity of cortical malformations', *Science*, 371(6527), p. eaba4517. Available at: https://doi.org/10.1126/science.aba4517.

Kobayashi, A. *et al.* (2016) 'Morphometric human embryonic brain features according to developmental stage', *Prenatal Diagnosis*, 36(4), pp. 338–345. Available at: https://doi.org/10.1002/pd.4786.

Kobayashi, G.S. *et al.* (2020) 'Recapitulation of Neural Crest Specification and EMT via Induction from Neural Plate Border-like Cells', *Stem Cell Reports*, 15(3), pp. 776–788. Available at: https://doi.org/10.1016/j.stemcr.2020.07.023.

Koledova, Z. *et al.* (2019) 'Fibroblast Growth Factor 2 Protein Stability Provides Decreased Dependence on Heparin for Induction of FGFR Signaling and Alters ERK Signaling Dynamics', *Frontiers in Cell and Developmental Biology*, 7. Available at: https://www.frontiersin.org/articles/10.3389/fcell.2019.00331 (Accessed: 16 August 2022).

Kolomeets, N.S. and Uranova, N.A. (2019) 'Reduced oligodendrocyte density in layer 5 of the prefrontal cortex in schizophrenia', *European Archives of Psychiatry and Clinical Neuroscience*, 269(4), pp. 379–386. Available at: https://doi.org/10.1007/s00406-018-0888-0.

Kong, Y. *et al.* (2017) 'Pseudogene PDIA3P1 promotes cell proliferation, migration and invasion, and suppresses apoptosis in hepatocellular carcinoma by regulating the p53 pathway', *Cancer Letters*, 407, pp. 76–83. Available at: https://doi.org/10.1016/j.canlet.2017.07.031.

Kortüm, F. *et al.* (2011) 'The core FOXG1 syndrome phenotype consists of postnatal microcephaly, severe mental retardation, absent language, dyskinesia, and corpus callosum hypogenesis', *Journal of Medical Genetics*, 48(6), pp. 396–406. Available at: https://doi.org/10.1136/jmg.2010.087528.

von Kortzfleisch, V.T. *et al.* (2020) 'Improving reproducibility in animal research by splitting the study population into several "mini-experiments"', *Scientific Reports*, 10(1), p. 16579. Available at: https://doi.org/10.1038/s41598-020-73503-4.

Kowalczyk, T. *et al.* (2009) 'Intermediate Neuronal Progenitors (Basal Progenitors) Produce Pyramidal–Projection Neurons for All Layers of Cerebral Cortex', *Cerebral Cortex*, 19(10), pp. 2439–2450. Available at: https://doi.org/10.1093/cercor/bhn260.

Kramps, T. *et al.* (2002) 'Wnt/Wingless Signaling Requires BCL9/Legless-Mediated Recruitment of Pygopus to the Nuclear β-Catenin-TCF Complex', *Cell*, 109(1), pp. 47–60. Available at: https://doi.org/10.1016/S0092-8674(02)00679-7.

Krefft, O. *et al.* (2018) 'Generation of Standardized and Reproducible Forebrain-type Cerebral Organoids from Human Induced Pluripotent Stem Cells', *JoVE (Journal of Visualized Experiments)*, (131), p. e56768. Available at: https://doi.org/10.3791/56768.

Krenn, V. *et al.* (2021) 'Organoid modeling of Zika and herpes simplex virus 1 infections reveals virus-specific responses leading to microcephaly', *Cell Stem Cell*, 28(8), pp. 1362-1379.e7. Available at: https://doi.org/10.1016/j.stem.2021.03.004.

Krieger, T.G. *et al.* (2020) 'Modeling glioblastoma invasion using human brain organoids and single-cell transcriptomics', *Neuro-Oncology*, 22(8), pp. 1138–1149. Available at: https://doi.org/10.1093/neuonc/noaa091.

Kuijlaars, J. *et al.* (2016) 'Sustained synchronized neuronal network activity in a human astrocyte co-culture system', *Scientific Reports*, 6. Available at: https://doi.org/10.1038/srep36529.

Kuwabara, T. *et al.* (2009) 'Wnt-mediated activation of NeuroD1 and retro-elements during adult neurogenesis', *Nature Neuroscience*, 12(9), pp. 1097–1105. Available at: https://doi.org/10.1038/nn.2360.

Kuwana, T. and Newmeyer, D.D. (2003) 'Bcl-2-family proteins and the role of mitochondria in apoptosis', *Current Opinion in Cell Biology*, 15(6), pp. 691–699. Available at: https://doi.org/10.1016/j.ceb.2003.10.004.

Kyrousi, C. *et al.* (2021) 'Extracellular LGALS3BP regulates neural progenitor position and relates to human cortical complexity', *Nature Communications*, 12(1), p. 6298. Available at: https://doi.org/10.1038/s41467-021-26447-w.

Lancaster, M.A. *et al.* (2013) 'Cerebral organoids model human brain development and microcephaly', *Nature*, 501(7467), pp. 373–379. Available at: https://doi.org/10.1038/nature12517.

Lancaster, M.A. *et al.* (2017) 'Guided self-organization and cortical plate formation in human brain organoids', *Nature Biotechnology*, 35(7), pp. 659–666. Available at: https://doi.org/10.1038/nbt.3906.

Lancaster, M.A. and Knoblich, J.A. (2014) 'Generation of cerebral organoids from human pluripotent stem cells', *Nature Protocols*, 9(10), pp. 2329–2340. Available at: https://doi.org/10.1038/nprot.2014.158.

Landers, M. *et al.* (2005) 'Maternal disruption of Ube3a leads to increased expression of Ube3a-ATS in trans', *Nucleic Acids Research*, 33(13), pp. 3976–3984. Available at: https://doi.org/10.1093/nar/gki705.

LaVaute, T.M. *et al.* (2009) 'Regulation of Neural Specification from Human Embryonic Stem Cells by BMP and FGF', *Stem Cells*, 27(8), pp. 1741–1749. Available at: https://doi.org/10.1002/stem.99.

Lawson-Yuen, A. *et al.* (2007) 'Ube3a mRNA and protein expression are not decreased in Mecp2R168X mutant mice', *Brain Research*, 1180, pp. 1–6. Available at: https://doi.org/10.1016/j.brainres.2007.08.039.

Lazarus, M.S., Krishnan, K. and Huang, Z.J. (2015) 'GAD67 Deficiency in Parvalbumin Interneurons Produces Deficits in Inhibitory Transmission and Network Disinhibition in Mouse Prefrontal Cortex', *Cerebral Cortex*, 25(5), pp. 1290–1296. Available at: https://doi.org/10.1093/cercor/bht322.

Ledesma-Terrón, M., Peralta-Cañadas, N. and Míguez, D.G. (2020) 'FGF2 modulates simultaneously the mode, the rate of division and the growth fraction in cultures of radial glia', *Development*, 147(14), p. dev189712. Available at: https://doi.org/10.1242/dev.189712.

Leduc, R.Y.M., Singh, P. and McDermid, H.E. (2017) 'Genetic backgrounds and modifier genes of NTD mouse models: An opportunity for greater understanding of the multifactorial etiology of neural tube defects', *Birth Defects Research*, 109(2), pp. 140–152. Available at: https://doi.org/10.1002/bdra.23554.

Lee, J.H. *et al.* (2018) 'Impaired social behaviors and minimized oxytocin signaling of the adult mice deficient in the N-methyl-d-aspartate receptor GluN3A subunit', *Experimental Neurology*, 305, pp. 1–12. Available at: https://doi.org/10.1016/j.expneurol.2018.02.015.

Lee, S.-H. *et al.* (2010) 'Dynamic methylation and expression of Oct4 in early neural stem cells', *Journal of Anatomy*, 217(3), pp. 203–213. Available at: https://doi.org/10.1111/j.1469-7580.2010.01269.x.

Lehtinen, M.K. *et al.* (2011) 'The cerebrospinal fluid provides a proliferative niche for neural progenitor cells', *Neuron*, 69(5), pp. 893–905. Available at: https://doi.org/10.1016/j.neuron.2011.01.023.

Leid, M. *et al.* (2004) 'CTIP1 and CTIP2 are differentially expressed during mouse embryogenesis', *Gene expression patterns : GEP*, 4(6), p. 733. Available at: https://doi.org/10.1016/j.modgep.2004.03.009.

Lemcke, H. and Kuznetsov, S.A. (2013) 'Involvement of connexin43 in the EGF/EGFR signalling during self-renewal and differentiation of neural progenitor cells', *Cellular Signalling*, 25(12), pp. 2676–2684. Available at: https://doi.org/10.1016/j.cellsig.2013.08.030.

Lengner, C.J. *et al.* (2007) 'Oct4 Expression Is Not Required for Mouse Somatic Stem Cell Self-Renewal', *Cell Stem Cell*, 1(4), pp. 403–415. Available at: https://doi.org/10.1016/j.stem.2007.07.020.

Lepski, G. *et al.* (2013) 'cAMP promotes the differentiation of neural progenitor cells in vitro via modulation of voltage-gated calcium channels', *Frontiers in Cellular Neuroscience*, 7, p. 155. Available at: https://doi.org/10.3389/fncel.2013.00155.

Levy, T. *et al.* (2021) 'Strong evidence for genotype–phenotype correlations in Phelan-McDermid syndrome: results from the developmental synaptopathies consortium', *Human Molecular Genetics*, p. ddab280. Available at: https://doi.org/10.1093/hmg/ddab280.

Li, F.C.H. *et al.* (2012) 'Bioenergetics Failure and Oxidative Stress in Brain Stem Mediates Cardiovascular Collapse Associated with Fatal Methamphetamine Intoxication', *PLOS ONE*, 7(1), p. e30589. Available at: https://doi.org/10.1371/journal.pone.0030589.

Li, H. *et al.* (2008) 'Activated Notch1 maintains the phenotype of radial glial cells and promotes their adhesion to laminin by upregulating nidogen', *Glia*, 56(6), pp. 646–658. Available at: https://doi.org/10.1002/glia.20643.

Li, J. *et al.* (2011) 'Common variants in the BCL9 gene conferring risk of schizophrenia', *Archives of General Psychiatry*, 68(3), pp. 232–240. Available at: https://doi.org/10.1001/archgenpsychiatry.2011.1.

Li, R. *et al.* (2017) 'Recapitulating cortical development with organoid culture in vitro and modeling abnormal spindle-like (ASPM related primary) microcephaly disease', *Protein and Cell*, 8(11), pp. 823–833. Available at: https://doi.org/10.1007/s13238-017-0479-2.

Li, Y. *et al.* (2017) 'Induction of Expansion and Folding in Human Cerebral Organoids', *Cell Stem Cell*, 20(3), pp. 385-396.e3. Available at: https://doi.org/10.1016/j.stem.2016.11.017.

Li, Z. *et al.* (2018) 'The LINC01138 drives malignancies via activating arginine methyltransferase 5 in hepatocellular carcinoma', *Nature Communications*, 9(1), pp. 1–14. Available at: https://doi.org/10.1038/s41467-018-04006-0.

Li, Z. *et al.* (2021) 'Gain of LINC00624 Enhances Liver Cancer Progression by Disrupting the Histone Deacetylase 6/Tripartite Motif Containing 28/Zinc Finger Protein 354C Corepressor Complex', *Hepatology*, 73(5), pp. 1764–1782. Available at: https://doi.org/10.1002/hep.31530.

Liang, X. *et al.* (2019) 'PAX3 Promotes Proliferation of Human Glioma Cells by WNT/β-Catenin Signaling Pathways', *Journal of Molecular Neuroscience*, 68(1), pp. 66–77. Available at: https://doi.org/10.1007/s12031-019-01283-2.

Libby, A.R.G. *et al.* (2021) 'Axial elongation of caudalized human organoids mimics aspects of neural tube development', *Development*, 148(12), p. dev198275. Available at: https://doi.org/10.1242/dev.198275.

Lin, J. *et al.* (2017) 'Pax3 overexpression induces cell aggregation and perturbs commissural axon projection during embryonic spinal cord development', *Journal of Comparative Neurology*, 525(7), pp. 1618–1632. Available at: https://doi.org/10.1002/cne.24146.

Lin, Y.-C. *et al.* (2013) 'Human microcephaly protein CEP135 binds to hSAS-6 and CPAP, and is required for centriole assembly', *The EMBO Journal*, 32(8), pp. 1141–1154. Available at: https://doi.org/10.1038/emboj.2013.56.

Lin, Y.-T. *et al.* (2018) 'APOE4 Causes Widespread Molecular and Cellular Alterations Associated with Alzheimer's Disease Phenotypes in Human iPSC-Derived Brain Cell Types', *Neuron*, 98(6), pp. 1141-1154.e7. Available at: https://doi.org/10.1016/j.neuron.2018.05.008.

Lindborg, B.A. *et al.* (2016) 'Rapid Induction of Cerebral Organoids From Human Induced Pluripotent Stem Cells Using a Chemically Defined Hydrogel and Defined Cell Culture Medium', *Stem Cells Translational Medicine*, 5(7), pp. 970–979. Available at: https://doi.org/10.5966/sctm.2015-0305.

Linden, S.C. *et al.* (2021) 'The psychiatric phenotypes of 1q21 distal deletion and duplication', *Translational Psychiatry*, 11(1), pp. 1–10. Available at: https://doi.org/10.1038/s41398-021-01226-9.

Linkous, A. *et al.* (2019) 'Modeling Patient-Derived Glioblastoma with Cerebral Organoids', *Cell Reports*, 26(12), pp. 3203-3211.e5. Available at: https://doi.org/10.1016/j.celrep.2019.02.063.

Liu, C. *et al.* (2017) 'CHD1L Expression Increases Tumor Progression and Acts as a Predictive Biomarker for Poor Prognosis in Pancreatic Cancer', *Digestive Diseases and Sciences*, 62(9), pp. 2376–2385. Available at: https://doi.org/10.1007/s10620-017-4641-8.

Liu, J.A. and Cheung, M. (2016) 'Neural crest stem cells and their potential therapeutic applications', *Developmental Biology*, 419(2), pp. 199–216. Available at: https://doi.org/10.1016/j.ydbio.2016.09.006.

Liu, L. *et al.* (2019) 'The cell cycle in stem cell proliferation, pluripotency and differentiation', *Nature Cell Biology*, 21(9), pp. 1060–1067. Available at: https://doi.org/10.1038/s41556-019-0384-4.

Liu, P. *et al.* (2011) 'Frequency of nonallelic homologous recombination is correlated with length of homology: Evidence that ectopic synapsis precedes ectopic crossing-over', *American Journal of Human Genetics*, 89(4), pp. 580–588. Available at: https://doi.org/10.1016/j.ajhg.2011.09.009.

Loeken, M.R. (2005) 'Current perspectives on the causes of neural tube defects resulting from diabetic pregnancy', *American Journal of Medical Genetics Part C: Seminars in Medical Genetics*, 135C(1), pp. 77–87. Available at: https://doi.org/10.1002/ajmg.c.30056.

Logan, S. *et al.* (2020) 'Dynamic Characterization of Structural, Molecular, and Electrophysiological Phenotypes of Human-Induced Pluripotent Stem Cell-Derived Cerebral Organoids, and Comparison with Fetal and Adult Gene Profiles', *Cells*, 9(5), p. 1301. Available at: https://doi.org/10.3390/cells9051301.

Loh, K.M. *et al.* (2016) 'Mapping the Pairwise Choices Leading from Pluripotency to Human Bone, Heart, and Other Mesoderm Cell Types', *Cell*, 166(2), pp. 451–467. Available at: https://doi.org/10.1016/j.cell.2016.06.011.

Lowther, C. *et al.* (2015) 'Delineating the 15q13.3 microdeletion phenotype: A case series and comprehensive review of the literature', *Genetics in Medicine*. Nature Publishing Group, pp. 149–157. Available at: https://doi.org/10.1038/gim.2014.83.

Lu, Y. *et al.* (2019) 'OCT4 maintains self-renewal and reverses senescence in human hair follicle mesenchymal stem cells through the downregulation of p21 by DNA methyltransferases', *Stem Cell Research & Therapy*, 10(1), p. 28. Available at: https://doi.org/10.1186/s13287-018-1120-x.

Luo, C. *et al.* (2016) 'Cerebral Organoids Recapitulate Epigenomic Signatures of the Human Fetal Brain', *Cell Reports*, 17(12), pp. 3369–3384. Available at: https://doi.org/10.1016/j.celrep.2016.12.001.

Ma, L. *et al.* (2021) 'Developmental programming and lineage branching of early human telencephalon', *The EMBO Journal*, 40(21), p. e107277. Available at: https://doi.org/10.15252/embj.2020107277.

Ma, N.-F. *et al.* (2008) 'Isolation and characterization of a novel oncogene, amplified in liver cancer 1, within a commonly amplified region at 1q21 in hepatocellular carcinoma', *Hepatology*, 47(2), pp. 503–510. Available at: https://doi.org/10.1002/hep.22072.

MacDonald, J.R. *et al.* (2013) 'The Database of Genomic Variants: a curated collection of structural variation in the human genome', *Nucleic Acids Research*, 42(D1), pp. D986–D992. Available at: https://doi.org/10.1093/nar/gkt958.

MacDonald, M.L. *et al.* (2017) 'Selective Loss of Smaller Spines in Schizophrenia', *American Journal of Psychiatry*, 174(6), pp. 586–594. Available at: https://doi.org/10.1176/appi.ajp.2017.16070814.

Madhavan, M. *et al.* (2018) 'Induction of myelinating oligodendrocytes in human cortical spheroids', *Nature Methods*, p. 1. Available at: https://doi.org/10.1038/s41592-018-0081-4.

Maeda, Y. *et al.* (2008) 'GPHR is a novel anion channel critical for acidification and functions of the Golgi apparatus', *Nature Cell Biology*, 10(10), pp. 1135–1145. Available at: https://doi.org/10.1038/ncb1773.

Magri, C. *et al.* (2018) 'A novel homozygous mutation in GAD1 gene described in a schizophrenic patient impairs activity and dimerization of GAD67 enzyme', *Scientific Reports*, 8(1), p. 15470. Available at: https://doi.org/10.1038/s41598-018-33924-8.

Mallamaci, A. and Stoykova, A. (2006) 'Gene networks controlling early cerebral cortex arealization', *European Journal of Neuroscience*, 23(4), pp. 847–856. Available at: https://doi.org/10.1111/j.1460-9568.2006.04634.x.

Mansour, A.A. *et al.* (2018) 'An in vivo model of functional and vascularized human brain organoids', *Nature Biotechnology*, 36(5), pp. 432–441. Available at: https://doi.org/10.1038/nbt.4127.

Marchal, L. *et al.* (2009) 'BMP inhibition initiates neural induction via FGF signaling and Zic genes', *Proceedings of the National Academy of Sciences of the United States of America*, 106(41), pp. 17437–17442. Available at: https://doi.org/10.1073/pnas.0906352106.

Marchetto, M.C.N. *et al.* (2010) 'A Model for Neural Development and Treatment of Rett Syndrome Using Human Induced Pluripotent Stem Cells', *Cell*, 143(4), pp. 527–539. Available at: https://doi.org/10.1016/j.cell.2010.10.016.

Mariani, J. *et al.* (2015) 'FOXG1-Dependent Dysregulation of GABA/Glutamate Neuron Differentiation in Autism Spectrum Disorders', *Cell*, 162(2), pp. 375–390. Available at: https://doi.org/10.1016/j.cell.2015.06.034.

Marin Navarro, A. *et al.* (2020) 'p53 controls genomic stability and temporal differentiation of human neural stem cells and affects neural organization in human brain organoids', *Cell Death & Disease*, 11(1), pp. 1–16. Available at: https://doi.org/10.1038/s41419-019-2208-7.

Marshall, C.R. *et al.* (2017) 'Contribution of copy number variants to schizophrenia from a genome-wide study of 41,321 subjects', *Nature Genetics*, 49(1), pp. 27–35. Available at: https://doi.org/10.1038/ng.3725.

Martínez-Martínez, M.Á. *et al.* (2016) 'A restricted period for formation of outer subventricular zone defined by Cdh1 and Trnp1 levels', *Nature Communications*, 7(1), p. 11812. Available at: https://doi.org/10.1038/ncomms11812.

Martins, M. *et al.* (2021) 'A eutherian-specific microRNA controls the translation of Satb2 in a model of cortical differentiation', *Stem Cell Reports*, 16(6), pp. 1496–1509. Available at: https://doi.org/10.1016/j.stemcr.2021.04.020.

Martins, S. *et al.* (2022) 'Impaired p53-Mediated DNA Damage Response Contributes to Microcephaly in Nijmegen Breakage Syndrome Patient-Derived Cerebral Organoids', *Cells*, 11(5), p. 802. Available at: https://doi.org/10.3390/cells11050802.

Martynoga, B. *et al.* (2005) 'Foxg1 is required for specification of ventral telencephalon and region-specific regulation of dorsal telencephalic precursor proliferation and apoptosis', *Developmental Biology*, 283(1), pp. 113–127. Available at: https://doi.org/10.1016/j.ydbio.2005.04.005.

Mase, S. *et al.* (2021) 'Notch1 and Notch2 collaboratively maintain radial glial cells in mouse neurogenesis', *Neuroscience Research*, 170, pp. 122–132. Available at: https://doi.org/10.1016/j.neures.2020.11.007.

McQuin, C. *et al.* (2018) 'CellProfiler 3.0: Next-generation image processing for biology', *PLOS Biology*. Edited by T. Misteli, 16(7), p. e2005970. Available at: https://doi.org/10.1371/journal.pbio.2005970.

McShane, S.G. *et al.* (2015) 'Cellular basis of neuroepithelial bending during mouse spinal neural tube closure', *Developmental Biology*, 404(2), pp. 113–124. Available at: https://doi.org/10.1016/j.ydbio.2015.06.003.

Mefford, H.C. *et al.* (2008) 'Recurrent Rearrangements of Chromosome 1q21.1 and Variable Pediatric Phenotypes', *New England Journal of Medicine*, 359(16), pp. 1685–1699. Available at: https://doi.org/10.1056/NEJMoa0805384.

Mehler, V.J. *et al.* (2020) 'Human iPSC-Derived Neural Crest Stem Cells Exhibit Low Immunogenicity', *Molecular Therapy - Methods & Clinical Development*, 16, pp. 161–171. Available at: https://doi.org/10.1016/j.omtm.2019.12.015.

Mellios, N. *et al.* (2018) 'MeCP2-regulated miRNAs control early human neurogenesis through differential effects on ERK and AKT signaling', *Molecular Psychiatry*, 23(4), pp. 1051–1065. Available at: https://doi.org/10.1038/mp.2017.86.

Merino, F. *et al.* (2014) 'Structural Basis for the SOX-Dependent Genomic Redistribution of OCT4 in Stem Cell Differentiation', *Structure*, 22(9), pp. 1274–1286. Available at: https://doi.org/10.1016/j.str.2014.06.014.

Messmer, T. *et al.* (2019) 'Transcriptional Heterogeneity in Naive and Primed Human Pluripotent Stem Cells at Single-Cell Resolution', *Cell Reports*, 26(4), pp. 815-824.e4. Available at: https://doi.org/10.1016/j.celrep.2018.12.099.

Meyer, G. *et al.* (2000) 'Embryonic and Early Fetal Development of the Human Neocortex', *Journal of Neuroscience*, 20(5), pp. 1858–1868. Available at: https://doi.org/10.1523/JNEUROSCI.20-05-01858.2000.

Mi, D. *et al.* (2013) 'Identification of Genomic Regions Regulating Pax6 Expression in Embryonic Forebrain Using YAC Reporter Transgenic Mouse Lines', *PLOS ONE*, 8(11), p. e80208. Available at: https://doi.org/10.1371/journal.pone.0080208.

Millar, J.K. *et al.* (2000) 'Disruption of two novel genes by a translocation co-segregating with schizophrenia', *Human Molecular Genetics*, 9(9), pp. 1415–1423. Available at: https://doi.org/10.1093/hmg/9.9.1415.

Milone, R. *et al.* (2021) '17q12 Recurrent Deletions and Duplications: Description of a Case Series with Neuropsychiatric Phenotype', *Genes*, 12(11), p. 1660. Available at: https://doi.org/10.3390/genes12111660.

Minocha, S. *et al.* (2017) 'Nkx2.1 regulates the generation of telencephalic astrocytes during embryonic development', *Scientific Reports*, 7(1), p. 43093. Available at: https://doi.org/10.1038/srep43093.

Mitchell, C. and Silver, D.L. (2018) ‘Enhancing our brains: Genomic mechanisms underlying cortical evolution’, *Seminars in Cell and Developmental Biology*. Elsevier Ltd, pp. 23–32. Available at: https://doi.org/10.1016/j.semcdb.2017.08.045.

Miura, Y. *et al.* (2020) ‘Generation of human striatal organoids and cortico-striatal assembloids from human pluripotent stem cells’, *Nature Biotechnology*, 38(12), pp. 1421–1430. Available at: https://doi.org/10.1038/s41587-020-00763-w.

Modenato, C. *et al.* (2021) ‘Effects of eight neuropsychiatric copy number variants on human brain structure’, *Translational Psychiatry*, 11(1), pp. 1–10. Available at: https://doi.org/10.1038/s41398-021-01490-9.

Molyneaux, B.J. *et al.* (2007) ‘Neuronal subtype specification in the cerebral cortex’, *Nature Reviews Neuroscience*, 8(6), pp. 427–437. Available at: https://doi.org/10.1038/nrn2151.

Moore, S. *et al.* (2013) ‘Distinct Regulatory Mechanisms Act to Establish and Maintain Pax3 Expression in the Developing Neural Tube’, *PLOS Genetics*, 9(10), p. e1003811. Available at: https://doi.org/10.1371/journal.pgen.1003811.

Morelli, K.H. *et al.* (2022) ‘MECP2-related pathways are dysregulated in a cortical organoid model of myotonic dystrophy’, *Science Translational Medicine*, 14(651), p. eabn2375. Available at: https://doi.org/10.1126/scitranslmed.abn2375.

Moreno-De-Luca, D. *et al.* (2010) ‘Deletion 17q12 is a recurrent copy number variant that confers high risk of autism and schizophrenia’, *American Journal of Human Genetics*, 87(5), pp. 618–630. Available at: https://doi.org/10.1016/j.ajhg.2010.10.004.

Morgan, E.R. *et al.* (2017) ‘Treatment and outcomes for glioblastoma in elderly compared with non-elderly patients: a population-based study’, *Current Oncology*, 24(2), pp. e92–e98. Available at: https://doi.org/10.3747/co.24.3424.

Morris, C.A. *et al.* (2015) ‘7q11.23 Duplication syndrome: Physical characteristics and natural history’, *American Journal of Medical Genetics Part A*, 167(12), pp. 2916–2935. Available at: https://doi.org/10.1002/ajmg.a.37340.

Morrison, G. *et al.* (2016) ‘Evaluation of inter-batch differences in stem-cell derived neurons’, *Stem Cell Research*, 16(1), pp. 140–148. Available at: https://doi.org/10.1016/j.scr.2015.12.025.

Morriss-Kay, G.M. (1981) ‘Growth and development of pattern in the cranial neural epithelium of rat embryos during neurulation’, *Development*, 65(Supplement).

Moslehi, M., Ng, D.C.H. and Bogoyevitch, M.A. (2017) ‘Dynamic microtubule association of Doublecortin X (DCX) is regulated by its C-terminus’, *Scientific Reports*, 7(1), p. 5245. Available at: https://doi.org/10.1038/s41598-017-05340-x.

Moujalled, D., Strasser, A. and Liddell, J.R. (2021) ‘Molecular mechanisms of cell death in neurological diseases’, *Cell Death & Differentiation*, 28(7), pp. 2029–2044. Available at: https://doi.org/10.1038/s41418-021-00814-y.

Moya, N. *et al.* (2014) ‘Endogenous WNT Signaling Regulates hPSC-Derived Neural Progenitor Cell Heterogeneity and Specifies Their Regional Identity’, *Stem Cell Reports*, 3(6), pp. 1015–1028. Available at: https://doi.org/10.1016/j.stemcr.2014.10.004.

Moyer, C.E., Shelton, M.A. and Sweet, R.A. (2015) ‘Dendritic spine alterations in schizophrenia’, *Neuroscience Letters*, 601, pp. 46–53. Available at: https://doi.org/10.1016/j.neulet.2014.11.042.

Muraki, K. and Tanigaki, K. (2015) ‘Neuronal migration abnormalities and its possible implications for schizophrenia’, *Frontiers in Neuroscience*, 9. Available at: https://www.frontiersin.org/articles/10.3389/fnins.2015.00074 (Accessed: 26 October 2022).

Muthuraj, P.G. *et al.* (2021) ‘Zika virus infection induces endoplasmic reticulum stress and apoptosis in placental trophoblasts’, *Cell Death Discovery*, 7(1), pp. 1–17. Available at: https://doi.org/10.1038/s41420-020-00379-8.

Nagy, S. *et al.* (2018) ‘AMPK signaling linked to the schizophrenia-associated 1q21.1 deletion is required for neuronal and sleep maintenance’, *PLOS Genetics*, 14(12), p. e1007623. Available at: https://doi.org/10.1371/journal.pgen.1007623.

Nakao, K. *et al.* (2019) ‘Schizophrenia-Like Dopamine Release Abnormalities in a Mouse Model of NMDA Receptor Hypofunction’, *Schizophrenia Bulletin*, 45(1), pp. 138–147. Available at: https://doi.org/10.1093/schbul/sby003.

Nakashima, H. *et al.* (2021) ‘MeCP2 controls neural stem cell fate specification through miR-199a-mediated inhibition of BMP-Smad signaling’, *Cell Reports*, 35(7), p. 109124. Available at: https://doi.org/10.1016/j.celrep.2021.109124.

Nascimento, J.M. *et al.* (2019) ‘Human Cerebral Organoids and Fetal Brain Tissue Share Proteomic Similarities’, *Frontiers in Cell and Developmental Biology*, 7. Available at: https://www.frontiersin.org/articles/10.3389/fcell.2019.00303 (Accessed: 14 August 2022).

Nat, R. *et al.* (2007) ‘Neurogenic neuroepithelial and radial glial cells generated from six human embryonic stem cell lines in serum-free suspension and adherent cultures’, *Glia*, 55(4), pp. 385–399. Available at: https://doi.org/10.1002/glia.20463.

Navarro, P. *et al.* (2012) ‘OCT4/SOX2-independent Nanog autorepression modulates heterogeneous Nanog gene expression in mouse ES cells’, *The EMBO Journal*, 31(24), pp. 4547–4562. Available at: https://doi.org/10.1038/emboj.2012.321.

Nery, S., Fishell, G. and Corbin, J.G. (2002) ‘The caudal ganglionic eminence is a source of distinct cortical and subcortical cell populations’, *Nature Neuroscience*, 5(12), pp. 1279–1287. Available at: https://doi.org/10.1038/nn971.

Ni, P. *et al.* (2020) ‘iPSC-derived homogeneous populations of developing schizophrenia cortical interneurons have compromised mitochondrial function’, *Molecular Psychiatry*, 25(11), pp. 2873–2888. Available at: https://doi.org/10.1038/s41380-019-0423-3.

Nicholas, A.K. *et al.* (2010) ‘WDR62 is associated with the spindle pole and is mutated in human microcephaly’, *Nature Genetics*, 42(11), pp. 1010–1014. Available at: https://doi.org/10.1038/ng.682.

Nielsen, J. *et al.* (2017) ‘A mouse model of the schizophrenia-associated 1q21.1 microdeletion syndrome exhibits altered mesolimbic dopamine transmission’, *Translational Psychiatry*, 7(11), pp. 1–12. Available at: https://doi.org/10.1038/s41398-017-0011-8.

Nieto, M. *et al.* (2004) ‘Expression of Cux-1 and Cux-2 in the subventricular zone and upper layers II–IV of the cerebral cortex’, *Journal of Comparative Neurology*, 479(2), pp. 168–180. Available at: https://doi.org/10.1002/cne.20322.

Nigro, A. *et al.* (2012) ‘MiR-30e and miR-181d control Radial Glia cell proliferation via HtrA1 modulation’, *Cell Death & Disease*, 3(8), pp. e360–e360. Available at: https://doi.org/10.1038/cddis.2012.98.

Niklasson, L. *et al.* (2001) ‘Neuropsychiatric disorders in the 22q11 deletion syndrome’, in *Genetics in Medicine*. Nature Publishing Group, pp. 79–84. Available at: https://doi.org/10.1097/00125817-200101000-00017.

Nikolopoulou, E. *et al.* (2017) ‘Neural tube closure: cellular, molecular and biomechanical mechanisms’, *Development (Cambridge, England)*, 144(4), pp. 552–566. Available at: https://doi.org/10.1242/dev.145904.

Nishimura, T., Honda, H. and Takeichi, M. (2012) ‘Planar cell polarity links axes of spatial dynamics in neural-tube closure’, *Cell*, 149(5), pp. 1084–1097. Available at: https://doi.org/10.1016/j.cell.2012.04.021.

Nomura, J. and Takumi, T. (2012) ‘Animal models of psychiatric disorDers that reflect human copy number variation’, *Neural Plasticity*. Hindawi Publishing Corporation. Available at: https://doi.org/10.1155/2012/589524.

Notaras, M., Lodhi, A., Dündar, F., *et al.* (2021) ‘Schizophrenia is defined by cell-specific neuropathology and multiple neurodevelopmental mechanisms in patient-derived cerebral organoids’, *Molecular Psychiatry*, pp. 1–19. Available at: https://doi.org/10.1038/s41380-021-01316-6.

Notaras, M., Lodhi, A., Fang, H., *et al.* (2021) ‘The proteomic architecture of schizophrenia iPSC-derived cerebral organoids reveals alterations in GWAS and neuronal development factors’, *Translational Psychiatry*, 11(1), pp. 1–16. Available at: https://doi.org/10.1038/s41398-021-01664-5.

Nowakowski, T.J. *et al.* (2016) ‘Transformation of the Radial Glia Scaffold Demarcates Two Stages of Human Cerebral Cortex Development’, *Neuron*, 91(6), pp. 1219–1227. Available at: https://doi.org/10.1016/j.neuron.2016.09.005.

Núñez, R. *et al.* (2010) ‘Apoptotic volume decrease as a geometric determinant for cell dismantling into apoptotic bodies’, *Cell Death & Differentiation*, 17(11), pp. 1665–1671. Available at: https://doi.org/10.1038/cdd.2010.96.

Odenwald, M.A. *et al.* (2017) ‘ZO-1 interactions with F-actin and occludin direct epithelial polarization and single lumen specification in 3D culture’, *Journal of Cell Science*. Edited by A. Ewald, 130(1), pp. 243–259. Available at: https://doi.org/10.1242/jcs.188185.

Ogawa, J. *et al.* (2018) ‘Glioblastoma Model Using Human Cerebral Organoids’, *Cell Reports*, 23(4), pp. 1220–1229. Available at: https://doi.org/10.1016/j.celrep.2018.03.105.

Ohata, S. *et al.* (2011) ‘Dual Roles of Notch in Regulation of Apically Restricted Mitosis and Apicobasal Polarity of Neuroepithelial Cells’, *Neuron*, 69(2), pp. 215–230. Available at: https://doi.org/10.1016/j.neuron.2010.12.026.

Olabi, B. *et al.* (2011) ‘Are there progressive brain changes in schizophrenia? A meta-analysis of structural magnetic resonance imaging studies’, *Biological Psychiatry*, 70(1), pp. 88–96. Available at: https://doi.org/10.1016/j.biopsych.2011.01.032.

Olbrich, H. *et al.* (2012) ‘Recessive HYDIN mutations cause primary ciliary dyskinesia without randomization of left-right body asymmetry’, *American Journal of Human Genetics*, 91(4), pp. 672–684. Available at: https://doi.org/10.1016/j.ajhg.2012.08.016.

Oliveira, S.R., Amaral, J.D. and Rodrigues, C.M.P. (2018) ‘Mechanism and disease implications of necroptosis and neuronal inflammation’, *Cell Death & Disease*, 9(9), pp. 1–3. Available at: https://doi.org/10.1038/s41419-018-0872-7.

Olson, E.C. (2014) ‘Analysis of Preplate Splitting and Early Cortical Development Illuminates the Biology of Neurological Disease’, *Frontiers in Pediatrics*, 2, p. 121. Available at: https://doi.org/10.3389/fped.2014.00121.

Onwordi, E.C. *et al.* (2021) ‘The relationship between synaptic density marker SV2A, glutamate and N-acetyl aspartate levels in healthy volunteers and schizophrenia: a multimodal PET and magnetic resonance spectroscopy brain imaging study’, *Translational Psychiatry*, 11(1), pp. 1–9. Available at: https://doi.org/10.1038/s41398-021-01515-3.

O’Rahilly, R. and Müller, F. (2002) ‘The two sites of fusion of the neural folds and the two neuropores in the human embryo’, *Teratology*, 65(4), pp. 162–170. Available at: https://doi.org/10.1002/tera.10007.

Orikasa, S. *et al.* (2022) ‘Hypoxia-inducible factor 1α induces osteo/odontoblast differentiation of human dental pulp stem cells via Wnt/β-catenin transcriptional cofactor BCL9’, *Scientific Reports*, 12(1), p. 682. Available at: https://doi.org/10.1038/s41598-021-04453-8.

Ormel, P.R. *et al.* (2018) ‘Microglia innately develop within cerebral organoids’, *Nature Communications*, 9(1), p. 4167. Available at: https://doi.org/10.1038/s41467-018-06684-2.

Ostenfeld, T. *et al.* (2002) ‘Regional specification of rodent and human neurospheres’, *Developmental Brain Research*, 134(1–2), pp. 43–55. Available at: https://doi.org/10.1016/S0165-3806(01)00291-7.

Otani, T. *et al.* (2016) ‘2D and 3D Stem Cell Models of Primate Cortical Development Identify Species-Specific Differences in Progenitor Behavior Contributing to Brain Size’, *Cell Stem Cell*, 18(4), pp. 467–480. Available at: https://doi.org/10.1016/j.stem.2016.03.003.

Owen, M.J. *et al.* (2011) ‘Neurodevelopmental hypothesis of schizophrenia’, *The British Journal of Psychiatry*, 198(3), pp. 173–175. Available at: https://doi.org/10.1192/bjp.bp.110.084384.

Pak, C.H. *et al.* (2015) ‘Human Neuropsychiatric Disease Modeling using Conditional Deletion Reveals Synaptic Transmission Defects Caused by Heterozygous Mutations in NRXN1’, *Cell Stem Cell*, 17(3), pp. 316–328. Available at: https://doi.org/10.1016/j.stem.2015.07.017.

Palmer, A.J. *et al.* (2021) ‘Genetic interaction of Pax3 mutation and canonical Wnt signaling modulates neural tube defects and neural crest abnormalities’, *genesis*, 59(11), p. e23445. Available at: https://doi.org/10.1002/dvg.23445.

Pani, L., Horal, M. and Loeken, M.R. (2002) ‘Rescue of neural tube defects in Pax-3-deficient embryos by p53 loss of function: implications for Pax-3- dependent development and tumorigenesis’, *Genes & Development*, 16(6), pp. 676–680. Available at: https://doi.org/10.1101/gad.969302.

Panja, D. *et al.* (2021) ‘miR-936 is Increased in Schizophrenia and Inhibits Neural Development and AMPA Receptor-Mediated Synaptic Transmission’, *Schizophrenia Bulletin*, 47(6), pp. 1795–1805. Available at: https://doi.org/10.1093/schbul/sbab046.

Parenti, I. *et al.* (2020) ‘Neurodevelopmental Disorders: From Genetics to Functional Pathways’, *Trends in Neurosciences*, 43(8), pp. 608–621. Available at: https://doi.org/10.1016/j.tins.2020.05.004.

Park, G. *et al.* (2022) ‘Decreased in vivo glutamate/GABA ratio correlates with the social behavior deficit in a mouse model of autism spectrum disorder’, *Molecular Brain*, 15(1), p. 19. Available at: https://doi.org/10.1186/s13041-022-00904-z.

Paşca, A.M. *et al.* (2015) 'Functional cortical neurons and astrocytes from human pluripotent stem cells in 3D culture', *Nature Methods*, 12(7), pp. 671–678. Available at: https://doi.org/10.1038/Nmeth.3415.

Pașca, S.P. *et al.* (2022) 'A nomenclature consensus for nervous system organoids and assembloids', *Nature*, 609(7929), pp. 907–910. Available at: https://doi.org/10.1038/s41586-022-05219-6.

Paulsen, B. *et al.* (2022) 'Autism genes converge on asynchronous development of shared neuron classes', *Nature*, 602(7896), pp. 268–273. Available at: https://doi.org/10.1038/s41586-021-04358-6.

Pei, Z. *et al.* (2011) 'Homeobox genes Gsx1 and Gsx2 differentially regulate telencephalic progenitor maturation', *Proceedings of the National Academy of Sciences*, 108(4), pp. 1675–1680. Available at: https://doi.org/10.1073/pnas.1008824108.

Pelkonen, A. *et al.* (2022) 'Functional Characterization of Human Pluripotent Stem Cell-Derived Models of the Brain with Microelectrode Arrays', *Cells*, 11(1), p. 106. Available at: https://doi.org/10.3390/cells11010106.

Pellegrini, L. *et al.* (2020) 'Human CNS barrier-forming organoids with cerebrospinal fluid production', *Science* [Preprint]. Available at: https://doi.org/10.1126/science.aaz5626.

Peñagarikano, O. *et al.* (2011) 'Absence of CNTNAP2 Leads to Epilepsy, Neuronal Migration Abnormalities, and Core Autism-Related Deficits', *Cell*, 147(1), pp. 235–246. Available at: https://doi.org/10.1016/j.cell.2011.08.040.

Peng, G. *et al.* (2009) 'BRIT1/MCPH1 links chromatin remodelling to DNA damage response', *Nature Cell Biology*, 11(7), pp. 865–872. Available at: https://doi.org/10.1038/ncb1895.

Penisson, M. *et al.* (2019) 'Genes and Mechanisms Involved in the Generation and Amplification of Basal Radial Glial Cells', *Frontiers in Cellular Neuroscience*, 13. Available at: https://www.frontiersin.org/articles/10.3389/fncel.2019.00381 (Accessed: 15 November 2022).

Perry, S.W., Epstein, L.G. and Gelbard, H.A. (1997) 'Simultaneous in situ detection of apoptosis and necrosis in monolayer cultures by TUNEL and trypan blue staining', *BioTechniques*, 22(6), pp. 1102–1106. Available at: https://doi.org/10.2144/97226st01.

Petryniak, M.A. *et al.* (2007) 'Dlx1 and Dlx2 control neuronal versus oligodendroglial cell fate acquisition in the developing forebrain', *Neuron*, 55(3), pp. 417–433. Available at: https://doi.org/10.1016/j.neuron.2007.06.036.

Pettinato, G., Wen, X. and Zhang, N. (2014) 'Formation of Well-defined Embryoid Bodies from Dissociated Human Induced Pluripotent Stem Cells using Microfabricated Cell-repellent Microwell Arrays', *Scientific Reports*, 4(1), p. 7402. Available at: https://doi.org/10.1038/srep07402.

Pfaffl, M.W. (2001) 'A new mathematical model for relative quantification in real-time RT-PCR.', *Nucleic acids research*, 29(9), p. e45. Available at: https://doi.org/10.1093/nar/29.9.e45.

Phan, T.P. *et al.* (2021) 'Centrosome defects cause microcephaly by activating the 53BP1-USP28-TP53 mitotic surveillance pathway', *The EMBO Journal*, 40(1), p. e106118. Available at: https://doi.org/10.15252/embj.2020106118.

Phelan, K. and McDermid, H.E. (2011) 'The 22q13.3 Deletion Syndrome (Phelan-McDermid Syndrome)', *Molecular Syndromology* [Preprint]. Available at: https://doi.org/10.1159/000334260.

Phillips, A.W., Nestor, J.E. and Nestor, M.W. (2017) 'Developing hipsc derived serum free embryoid bodies for the interrogation of 3-D stem cell cultures using physiologically relevant assays', *Journal of Visualized Experiments*, 2017(125). Available at: https://doi.org/10.3791/55799.

Piguel, N.H. *et al.* (2022) 'Lithium rescues dendritic abnormalities in Ank3 deficiency models through the synergic effects of GSK3β and cyclic AMP signaling pathways', *Neuropsychopharmacology*, pp. 1–11. Available at: https://doi.org/10.1038/s41386-022-01502-2.

Pilarowski, G.O. *et al.* (2018) 'Missense variants in the chromatin remodeler CHD1 are associated with neurodevelopmental disability', *Journal of Medical Genetics*, 55(8), pp. 561–566. Available at: https://doi.org/10.1136/jmedgenet-2017-104759.

Pilaz, L.-J. *et al.* (2016) 'Prolonged mitosis of neural progenitors alters cell fate in the developing brain', *Neuron*, 89(1), pp. 83–99. Available at: https://doi.org/10.1016/j.neuron.2015.12.007.

Piotrowski, A. *et al.* (2008) 'Somatic mosaicism for copy number variation in differentiated human tissues', *Human Mutation*, 29(9), pp. 1118–1124. Available at: https://doi.org/10.1002/humu.20815.

Pla, R. *et al.* (2018) 'Dlx1 and Dlx2 Promote Interneuron GABA Synthesis, Synaptogenesis, and Dendritogenesis', *Cerebral Cortex*, 28(11), pp. 3797–3815. Available at: https://doi.org/10.1093/cercor/bhx241.

Plumbly, W. *et al.* (2019) 'L-type voltage-gated calcium channel regulation of in vitro human cortical neuronal networks', *Scientific Reports*, 9(1), pp. 1–12. Available at: https://doi.org/10.1038/s41598-019-50226-9.

Pochwat, B. *et al.* (2014) 'Antidepressant-like activity of magnesium in the chronic mild stress model in rats: alterations in the NMDA receptor subunits', *International Journal of Neuropsychopharmacology*, 17(3), pp. 393–405. Available at: https://doi.org/10.1017/S1461145713001089.

Pollen, A.A. *et al.* (2015) 'Molecular Identity of Human Outer Radial Glia During Cortical Development', *Cell*, 163(1), pp. 55–67. Available at: https://doi.org/10.1016/j.cell.2015.09.004.

Pollen, A.A. *et al.* (2019) 'Establishing Cerebral Organoids as Models of Human-Specific Brain Evolution', *Cell*, 176(4), pp. 743-756.e17. Available at: https://doi.org/10.1016/j.cell.2019.01.017.

Ponting, C.P. (2006) 'BIOINFORMATICS DISCOVERY NOTE A novel domain suggests a ciliary function for ASPM, a brain size determining gene', 22(9), pp. 1031–1035. Available at: https://doi.org/10.1093/bioinformatics/btl022.

Popesco, M.C. *et al.* (2006) 'Human Lineage Specific Amplification, Selection, and Neuronal Expression of DUF1220 Domains', *Science*, 313(5791), pp. 1304–1307. Available at: https://doi.org/10.1126/science.1127980.

Popovitchenko, T. and Rasin, M.-R. (2017) 'Transcriptional and Post-Transcriptional Mechanisms of the Development of Neocortical Lamination', *Frontiers in Neuroanatomy*, 11, p. 102. Available at: https://doi.org/10.3389/fnana.2017.00102.

Poulton, C.J. *et al.* (2011) 'Microcephaly with Simplified Gyration, Epilepsy, and Infantile Diabetes Linked to Inappropriate Apoptosis of Neural Progenitors', *The American Journal of Human Genetics*, 89(2), pp. 265–276. Available at: https://doi.org/10.1016/j.ajhg.2011.07.006.

Pozas, E. and Ibáñez, C.F. (2005) 'GDNF and GFRα1 Promote Differentiation and Tangential Migration of Cortical GABAergic Neurons', *Neuron*, 45(5), pp. 701–713. Available at: https://doi.org/10.1016/j.neuron.2005.01.043.

Pucilowska, J. *et al.* (2015) 'The 16p11.2 Deletion Mouse Model of Autism Exhibits Altered Cortical Progenitor Proliferation and Brain Cytoarchitecture Linked to the ERK MAPK Pathway', *Journal of Neuroscience*, 35(7), pp. 3190–3200. Available at: https://doi.org/10.1523/JNEUROSCI.4864-13.2015.

Purves-Tyson, T.D. *et al.* (2021) 'Increased levels of midbrain immune-related transcripts in schizophrenia and in murine offspring after maternal immune activation', *Molecular Psychiatry*, 26(3), pp. 849–863. Available at: https://doi.org/10.1038/s41380-019-0434-0.

Pyrgaki, C. *et al.* (2010) 'Dynamic imaging of mammalian neural tube closure', *Developmental Biology*, 344(2), pp. 941–947. Available at: https://doi.org/10.1016/j.ydbio.2010.06.010.

Qi, X. *et al.* (2019) 'An integrative analysis of transcriptome-wide association study and mRNA expression profile identified candidate genes for attention-deficit/hyperactivity disorder', *Psychiatry Research*, 282, p. 112639. Available at: https://doi.org/10.1016/j.psychres.2019.112639.

Qi, Y. *et al.* (2017) 'Combined small-molecule inhibition accelerates the derivation of functional cortical neurons from human pluripotent stem cells', *Nature Biotechnology*, 35(2), pp. 154–163. Available at: https://doi.org/10.1038/nbt.3777.

Qian, X. *et al.* (2016) 'Brain-Region-Specific Organoids Using Mini-bioreactors for Modeling ZIKV Exposure.', *Cell*, 165(5), pp. 1238–1254. Available at: https://doi.org/10.1016/j.cell.2016.04.032.

Qian, X. *et al.* (2018) 'Generation of human brain region–specific organoids using a miniaturized spinning bioreactor', *Nature Protocols*, 13(3), pp. 565–580. Available at: https://doi.org/10.1038/nprot.2017.152.

Qian, X. *et al.* (2020) 'Sliced Human Cortical Organoids for Modeling Distinct Cortical Layer Formation', *Cell Stem Cell*, 26(5), pp. 766-781.e9. Available at: https://doi.org/10.1016/j.stem.2020.02.002.

Quadrato, G. *et al.* (2017) 'Cell diversity and network dynamics in photosensitive human brain organoids', *Nature*, 545(7652), pp. 48–53. Available at: https://doi.org/10.1038/nature22047.

Quiñones, G.M. *et al.* (2021) 'Reduced GABA/glutamate in the thalamus of individuals at clinical high risk for psychosis', *Neuropsychopharmacology*, 46(6), pp. 1133–1139. Available at: https://doi.org/10.1038/s41386-020-00920-4.

Raasch, M. *et al.* (2016) 'An integrative microfluidically supported in vitro model of an endothelial barrier combined with cortical spheroids simulates effects of neuroinflammation in neocortex development', *Biomicrofluidics*, 10(4), p. 044102. Available at: https://doi.org/10.1063/1.4955184.

Radhakrishnan, R. *et al.* (2021) 'In vivo evidence of lower synaptic vesicle density in schizophrenia', *Molecular Psychiatry*, pp. 1–9. Available at: https://doi.org/10.1038/s41380-021-01184-0.

Ragheb, R. *et al.* (2020) 'Differential regulation of lineage commitment in human and mouse primed pluripotent stem cells by the nucleosome remodelling and deacetylation complex', *Stem Cell Research*, 46, p. 101867. Available at: https://doi.org/10.1016/j.scr.2020.101867.

Rahimi, M. *et al.* (2018) 'Multi-branched ionic liquid-chitosan as a smart and biocompatible nano-vehicle for combination chemotherapy with stealth and targeted properties', *Carbohydrate Polymers*, 196, pp. 299–312. Available at: https://doi.org/10.1016/j.carbpol.2018.05.059.

Raja, W.K. *et al.* (2016) 'Self-Organizing 3D Human Neural Tissue Derived from Induced Pluripotent Stem Cells Recapitulate Alzheimer's Disease Phenotypes', *PLOS ONE*, 11(9), p. e0161969. Available at: https://doi.org/10.1371/journal.pone.0161969.

Ramalingam, A. *et al.* (2011) '16p13.11 duplication is a risk factor for a wide spectrum of neuropsychiatric disorders', *Journal of Human Genetics*, 56(7), pp. 541–544. Available at: https://doi.org/10.1038/jhg.2011.42.

del Re, E.C. *et al.* (2019) 'Diffusion abnormalities in the corpus callosum in first episode schizophrenia: Associated with enlarged lateral ventricles and symptomatology', *Psychiatry Research*, 277, pp. 45–51. Available at: https://doi.org/10.1016/j.psychres.2019.02.038.

Reillo, I. *et al.* (2011) 'A Role for Intermediate Radial Glia in the Tangential Expansion of the Mammalian Cerebral Cortex', *Cerebral Cortex*, 21, pp. 1674–1694. Available at: https://doi.org/10.1093/cercor/bhq238.

Reilly, J. *et al.* (2020) 'Coupling of autism genes to tissue-wide expression and dysfunction of synapse, calcium signalling and transcriptional regulation', *PLOS ONE*, 15(12), p. e0242773. Available at: https://doi.org/10.1371/journal.pone.0242773.

Reinwald, J.R. *et al.* (2020) 'Separable neural mechanisms for the pleiotropic association of copy number variants with neuropsychiatric traits', *Translational Psychiatry*, 10(1), pp. 1–13. Available at: https://doi.org/10.1038/s41398-020-0771-4.

Ren, D. *et al.* (2021) 'GJA1-20K Enhances Mitochondria Transfer from Astrocytes to Neurons via Cx43-TnTs After Traumatic Brain Injury', *Cellular and Molecular Neurobiology* [Preprint]. Available at: https://doi.org/10.1007/s10571-021-01070-x.

Renner, M. *et al.* (2017) 'Self-organized developmental patterning and differentiation in cerebral organoids', *The EMBO Journal* [Preprint]. Available at: https://doi.org/10.15252/embj.201694700.

Reynolds, B.A. and Weiss, S. (1992) 'Generation of neurons and astrocytes from isolated cells of the adult mammalian central nervous system', *Science*, 255(5052), pp. 1707–1710. Available at: https://doi.org/10.1126/science.1553558.

Reynolds, B.A. and Weiss, S. (1996) *Clonal and Population Analyses Demonstrate That an EGF-Responsive Mammalian Embryonic CNS Precursor Is a Stem Cell*, *DEVELOPMENTAL BIOLOGY*.

Rharass, T. *et al.* (2017) 'Ascorbic acid alters cell fate commitment of human neural progenitors in a WNT/β-catenin/ROS signaling dependent manner', *Journal of Biomedical Science*, 24, p. 78. Available at: https://doi.org/10.1186/s12929-017-0385-1.

Rhee, Y.-H. *et al.* (2013) 'Insulin concentration is critical in culturing human neural stem cells and neurons', *Cell Death & Disease*, 4(8), pp. e766–e766. Available at: https://doi.org/10.1038/cddis.2013.295.

Rice, A.M. and McLysaght, A. (2017) ‘Dosage sensitivity is a major determinant of human copy number variant pathogenicity’, *Nature Communications*, 8(1), p. 14366. Available at: https://doi.org/10.1038/ncomms14366.

Rifes, P. *et al.* (2020) ‘Modeling neural tube development by differentiation of human embryonic stem cells in a microfluidic WNT gradient’, *Nature Biotechnology*, pp. 1–9. Available at: https://doi.org/10.1038/s41587-020-0525-0.

Ripke, S. *et al.* (2014) ‘Biological insights from 108 schizophrenia-associated genetic loci’, *Nature*, 511(7510), pp. 421–427. Available at: https://doi.org/10.1038/nature13595.

Rogers, C. *et al.* (2017) ‘Cleavage of DFNA5 by caspase-3 during apoptosis mediates progression to secondary necrotic/pyroptotic cell death’, *Nature Communications*, 8(1), p. 14128. Available at: https://doi.org/10.1038/ncomms14128.

Romanos, J. *et al.* (2019) ‘Differences in glutamate uptake between cortical regions impact neuronal NMDA receptor activation’, *Communications Biology*, 2(1), pp. 1–15. Available at: https://doi.org/10.1038/s42003-019-0367-9.

Rosebrock, D. *et al.* (2022) ‘Enhanced cortical neural stem cell identity through short SMAD and WNT inhibition in human cerebral organoids facilitates emergence of outer radial glial cells’, *Nature Cell Biology*, 24(6), pp. 981–995. Available at: https://doi.org/10.1038/s41556-022-00929-5.

Rosenfeld, J.A. *et al.* (2012) ‘Proximal microdeletions and microduplications of 1q21.1 contribute to variable abnormal phenotypes’, *European Journal of Human Genetics*, 20(7), pp. 754–761. Available at: https://doi.org/10.1038/ejhg.2012.6.

Rotarska-Jagiela, A. *et al.* (2008) ‘The corpus callosum in schizophrenia-volume and connectivity changes affect specific regions’, *NeuroImage*, 39(4), pp. 1522–1532. Available at: https://doi.org/10.1016/j.neuroimage.2007.10.063.

Rotaru, D.C. *et al.* (2018) ‘Adult Ube3a Gene Reinstatement Restores the Electrophysiological Deficits of Prefrontal Cortex Layer 5 Neurons in a Mouse Model of Angelman Syndrome’, *Journal of Neuroscience*, 38(37), pp. 8011–8030. Available at: https://doi.org/10.1523/JNEUROSCI.0083-18.2018.

Rubin, R., Abbott, L.F. and Sompolinsky, H. (2017) ‘Balanced excitation and inhibition are required for high-capacity, noise-robust neuronal selectivity’, *Proceedings of the National Academy of Sciences*, 114(44), pp. E9366–E9375. Available at: https://doi.org/10.1073/pnas.1705841114.

Rydell-Törmänen, K., Uller, L. and Erjefält, J.S. (2006) ‘Direct evidence of secondary necrosis of neutrophils during intense lung inflammation’, *European Respiratory Journal*, 28(2), pp. 268–274. Available at: https://doi.org/10.1183/09031936.06.00126905.

Saberi, A. *et al.* (2022) ‘In-vitro engineered human cerebral tissues mimic pathological circuit disturbances in 3D’, *Communications Biology*, 5(1), pp. 1–9. Available at: https://doi.org/10.1038/s42003-022-03203-4.

Sacai, H. *et al.* (2020) ‘Autism spectrum disorder-like behavior caused by reduced excitatory synaptic transmission in pyramidal neurons of mouse prefrontal cortex’, *Nature Communications*, 11(1), p. 5140. Available at: https://doi.org/10.1038/s41467-020-18861-3.

Sachet, M., Liang, Y.Y. and Oehler, R. (2017) ‘The immune response to secondary necrotic cells’, *Apoptosis*, 22(10), pp. 1189–1204. Available at: https://doi.org/10.1007/s10495-017-1413-z.

Saito, K. *et al.* (2018) 'Neural Progenitor Cells Undergoing Yap/Tead-Mediated Enhanced Self-Renewal Form Heterotopias More Easily in the Diencephalon than in the Telencephalon', *Neurochemical Research*, 43(1), pp. 180–189. Available at: https://doi.org/10.1007/s11064-017-2390-x.

Sakaguchi, H. *et al.* (2015) 'Generation of functional hippocampal neurons from self-organizing human embryonic stem cell-derived dorsomedial telencephalic tissue', *Nature Communications*, 6(1), p. 8896. Available at: https://doi.org/10.1038/ncomms9896.

Salewski, R.P. *et al.* (2013) 'The Generation of Definitive Neural Stem Cells from PiggyBac Transposon-Induced Pluripotent Stem Cells Can Be Enhanced by Induction of the NOTCH Signaling Pathway', *Stem Cells and Development*, 22(3), pp. 383–396. Available at: https://doi.org/10.1089/scd.2012.0218.

Salmon, I. *et al.* (2022) 'Engineering neurovascular organoids with 3D printed microfluidic chips', *Lab on a Chip*, 22(8), pp. 1615–1629. Available at: https://doi.org/10.1039/D1LC00535A.

Samarasinghe, R.A. *et al.* (2021) 'Identification of neural oscillations and epileptiform changes in human brain organoids', *Nature Neuroscience*, 24(10), pp. 1488–1500. Available at: https://doi.org/10.1038/s41593-021-00906-5.

Sanchez Russo, R. *et al.* (2021) 'Deep phenotyping in 3q29 deletion syndrome: recommendations for clinical care', *Genetics in Medicine*, 23(5), pp. 872–880. Available at: https://doi.org/10.1038/s41436-020-01053-1.

Sanchez-Ferras, O. *et al.* (2014) 'Induction and dorsal restriction of Paired-box 3 (Pax3) gene expression in the caudal neuroectoderm is mediated by integration of multiple pathways on a short neural crest enhancer', *Biochimica et Biophysica Acta (BBA) - Gene Regulatory Mechanisms*, 1839(7), pp. 546–558. Available at: https://doi.org/10.1016/j.bbagrm.2014.04.023.

Sandberg, M. *et al.* (2016) 'Transcriptional Networks Controlled by NKX2-1 in the Development of Forebrain GABAergic Neurons', *Neuron*, 91(6), pp. 1260–1275. Available at: https://doi.org/10.1016/j.neuron.2016.08.020.

Sanders, B. *et al.* (2022) 'Transcriptional programs regulating neuronal differentiation are disrupted in DLG2 knockout human embryonic stem cells and enriched for schizophrenia and related disorders risk variants', *Nature Communications*, 13(1), p. 27. Available at: https://doi.org/10.1038/s41467-021-27601-0.

Sanders, S.J. *et al.* (2011) 'Multiple Recurrent De Novo CNVs, Including Duplications of the 7q11.23 Williams Syndrome Region, Are Strongly Associated with Autism', *Neuron*, 70(5), pp. 863–885. Available at: https://doi.org/10.1016/j.neuron.2011.05.002.

Sanders, S.J. *et al.* (2017) 'Whole Genome Sequencing in Psychiatric Disorders: the WGSPD Consortium', *Nature neuroscience*, 20(12), pp. 1661–1668. Available at: https://doi.org/10.1038/s41593-017-0017-9.

Sandweiss, A.J., Brandt, V.L. and Zoghbi, H.Y. (2020) 'Advances in understanding of Rett syndrome and MECP2 duplication syndrome: prospects for future therapies', *The Lancet Neurology*, 19(8), pp. 689–698. Available at: https://doi.org/10.1016/S1474-4422(20)30217-9.

Sato, H. *et al.* (2016) 'Microfabric Vessels for Embryoid Body Formation and Rapid Differentiation of Pluripotent Stem Cells', *Scientific Reports*, 6(1), pp. 1–13. Available at: https://doi.org/10.1038/srep31063.

Sato, T. *et al.* (2021) ‘Generation of region-specific and high-purity neurons from human feeder-free iPSCs’, *Neuroscience Letters*, 746, p. 135676. Available at: https://doi.org/10.1016/j.neulet.2021.135676.

Sawada, T. *et al.* (2020) ‘Developmental excitation-inhibition imbalance underlying psychoses revealed by single-cell analyses of discordant twins-derived cerebral organoids’, *Molecular Psychiatry*, 25(11), pp. 2695–2711. Available at: https://doi.org/10.1038/s41380-020-0844-z.

Sawai, H. and Domae, N. (2011) ‘Discrimination between primary necrosis and apoptosis by necrostatin-1 in Annexin V-positive/propidium iodide-negative cells’, *Biochemical and Biophysical Research Communications*, 411(3), pp. 569–573. Available at: https://doi.org/10.1016/j.bbrc.2011.06.186.

Scala, M. *et al.* (2022) ‘The Pathophysiological Link Between Reelin and Autism: Overview and New Insights’, *Frontiers in Genetics*, 13. Available at: https://doi.org/10.3389/fgene.2022.869002.

Scesa, G., Adami, R. and Bottai, D. (2021) ‘iPSC Preparation and Epigenetic Memory: Does the Tissue Origin Matter?’, *Cells*, 10(6), p. 1470. Available at: https://doi.org/10.3390/cells10061470.

Schnack, H.G. *et al.* (2016) ‘Accelerated Brain Aging in Schizophrenia: A Longitudinal Pattern Recognition Study’, *American Journal of Psychiatry*, 173(6), pp. 607–616. Available at: https://doi.org/10.1176/appi.ajp.2015.15070922.

Schneider, C.A., Rasband, W.S. and Eliceiri, K.W. (2012) ‘NIH Image to ImageJ: 25 years of image analysis’, *Nature Methods*, 9(7), pp. 671–675. Available at: https://doi.org/10.1038/nmeth.2089.

Schork, A.J. *et al.* (2019) ‘A genome-wide association study of shared risk across psychiatric disorders implicates gene regulation during fetal neurodevelopment’, *Nature Neuroscience*, 22(3), pp. 353–361. Available at: https://doi.org/10.1038/s41593-018-0320-0.

Schröter, M. *et al.* (2022) ‘Functional imaging of brain organoids using high-density microelectrode arrays’, *MRS Bulletin* [Preprint]. Available at: https://doi.org/10.1557/s43577-022-00282-w.

Schumacher, M. *et al.* (2016) ‘Progesterone neuroprotection: The background of clinical trial failure’, *Journal of Steroid Biochemistry and Molecular Biology*. Elsevier Ltd, pp. 53–66. Available at: https://doi.org/10.1016/j.jsbmb.2015.11.010.

Schwab, B.L. *et al.* (2002) ‘Cleavage of plasma membrane calcium pumps by caspases: a link between apoptosis and necrosis’, *Cell Death & Differentiation*, 9(8), pp. 818–831. Available at: https://doi.org/10.1038/sj.cdd.4401042.

Seitz-Holland, J. *et al.* (2021) ‘Opposing white matter microstructure abnormalities in 22q11.2 deletion and duplication carriers’, *Translational Psychiatry*, 11(1), pp. 1–11. Available at: https://doi.org/10.1038/s41398-021-01703-1.

Seltzer, L.E. and Paciorkowski, A.R. (2014) ‘Genetic disorders associated with postnatal microcephaly’, *American Journal of Medical Genetics Part C: Seminars in Medical Genetics*, 166(2), pp. 140–155. Available at: https://doi.org/10.1002/ajmg.c.31400.

Setoh, Y.X. *et al.* (2019) ‘Determinants of Zika virus host tropism uncovered by deep mutational scanning’, *Nature Microbiology*, 4(5), pp. 876–887. Available at: https://doi.org/10.1038/s41564-019-0399-4.

Shaheen, R. *et al.* (2019) 'Genomic and phenotypic delineation of congenital microcephaly', *Genetics in Medicine*, 21(3), pp. 545–552. Available at: https://doi.org/10.1038/s41436-018-0140-3.

Sharf, T. *et al.* (2022) 'Functional neuronal circuitry and oscillatory dynamics in human brain organoids', *Nature Communications*, 13(1), p. 4403. Available at: https://doi.org/10.1038/s41467-022-32115-4.

Shcheglovitov, A. *et al.* (2013) 'SHANK3 and IGF1 restore synaptic deficits in neurons from 22q13 deletion syndrome patients', *Nature*, 503(7475), pp. 267–271. Available at: https://doi.org/10.1038/nature12618.

Shen, K., Zeppillo, T. and Limon, A. (2020) 'Regional transcriptome analysis of AMPA and GABAA receptor subunit expression generates E/I signatures of the human brain', *Scientific Reports*, 10(1), p. 11352. Available at: https://doi.org/10.1038/s41598-020-68165-1.

Shen, M. *et al.* (2021) 'FXR1 regulation of parvalbumin interneurons in the prefrontal cortex is critical for schizophrenia-like behaviors', *Molecular Psychiatry*, pp. 1–23. Available at: https://doi.org/10.1038/s41380-021-01096-z.

Shi, Y. *et al.* (2012) 'Human cerebral cortex development from pluripotent stem cells to functional excitatory synapses', *Nature Neuroscience*, 15(3), pp. 477–486. Available at: https://doi.org/10.1038/nn.3041.

Shi, Y. *et al.* (2020) 'Vascularized human cortical organoids (vOrganoids) model cortical development in vivo', *PLOS Biology*, 18(5), p. e3000705. Available at: https://doi.org/10.1371/journal.pbio.3000705.

Shin, S. *et al.* (2006) 'Long-Term Proliferation of Human Embryonic Stem Cell–Derived Neuroepithelial Cells Using Defined Adherent Culture Conditions', *Stem Cells*, 24(1), pp. 125–138. Available at: https://doi.org/10.1634/stemcells.2004-0150.

Shinawi, M. *et al.* (2010) 'Recurrent reciprocal 16p11.2 rearrangements associated with global developmental delay, behavioural problems, dysmorphism, epilepsy, and abnormal head size', *Journal of Medical Genetics*, 47(5), pp. 332–341. Available at: https://doi.org/10.1136/jmg.2009.073015.

Shohat, S., Ben-David, E. and Shifman, S. (2017) 'Varying Intolerance of Gene Pathways to Mutational Classes Explain Genetic Convergence across Neuropsychiatric Disorders', *Cell Reports*, 18(9), pp. 2217–2227. Available at: https://doi.org/10.1016/j.celrep.2017.02.007.

Shohayeb, B. *et al.* (2020) 'The association of microcephaly protein WDR62 with CPAP/IFT88 is required for cilia formation and neocortical development', *Human Molecular Genetics*, 29(2), pp. 248–263. Available at: https://doi.org/10.1093/hmg/ddz281.

Shu, P. *et al.* (2019) 'Opposing Gradients of MicroRNA Expression Temporally Pattern Layer Formation in the Developing Neocortex', *Developmental Cell*, 49(5), pp. 764-785.e4. Available at: https://doi.org/10.1016/j.devcel.2019.04.017.

Shukla, D.K. *et al.* (2019) 'Anterior Cingulate Glutamate and GABA Associations on Functional Connectivity in Schizophrenia', *Schizophrenia Bulletin*, 45(3), pp. 647–658. Available at: https://doi.org/10.1093/schbul/sby075.

Sidhaye, J. and Knoblich, J.A. (2020) 'Brain organoids: an ensemble of bioassays to investigate human neurodevelopment and disease', *Cell Death and Differentiation*. Springer Nature, pp. 1–16. Available at: https://doi.org/10.1038/s41418-020-0566-4.

Silva, A.I. *et al.* (2019) 'Cyfip1 haploinsufficient rats show white matter changes, myelin thinning, abnormal oligodendrocytes and behavioural inflexibility', *Nature Communications*, 10(1), p. 3455. Available at: https://doi.org/10.1038/s41467-019-11119-7.

Silva, M.T. (2010) 'Secondary necrosis: The natural outcome of the complete apoptotic program', *FEBS Letters*, 584(22), pp. 4491–4499. Available at: https://doi.org/10.1016/j.febslet.2010.10.046.

Simões-Costa, M. and Bronner, M.E. (2015) 'Establishing neural crest identity: a gene regulatory recipe', *Development (Cambridge, England)*, 142(2), pp. 242–257. Available at: https://doi.org/10.1242/dev.105445.

Singec, I. *et al.* (2006) 'Defining the actual sensitivity and specificity of the neurosphere assay in stem cell biology', *Nature Methods*, 3(10), pp. 801–806. Available at: https://doi.org/10.1038/nmeth926.

Singhmar, P. and Kumar, A. (2011) 'Angelman Syndrome Protein UBE3A Interacts with Primary Microcephaly Protein ASPM, Localizes to Centrosomes and Regulates Chromosome Segregation', *PLOS ONE*, 6(5), p. e20397. Available at: https://doi.org/10.1371/journal.pone.0020397.

Sir, J.-H. *et al.* (2011) 'A primary microcephaly protein complex forms a ring around parental centrioles', *Nature Genetics*, 43(11), pp. 1147–1153. Available at: https://doi.org/10.1038/ng.971.

Sivitilli, A.A. *et al.* (2020) 'Robust production of uniform human cerebral organoids from pluripotent stem cells', *Life science alliance*, 3(5). Available at: https://doi.org/10.26508/lsa.202000707.

Skene, N.G. *et al.* (2018) 'Genetic identification of brain cell types underlying schizophrenia', *Nature Genetics*, 50(6), pp. 825–833. Available at: https://doi.org/10.1038/s41588-018-0129-5.

Slifstein, M. *et al.* (2015) 'Deficits in Prefrontal Cortical and Extrastriatal Dopamine Release in Schizophrenia: A Positron Emission Tomographic Functional Magnetic Resonance Imaging Study', *JAMA Psychiatry*, 72(4), pp. 316–324. Available at: https://doi.org/10.1001/jamapsychiatry.2014.2414.

Sloan, S.A. *et al.* (2017) 'Human Astrocyte Maturation Captured in 3D Cerebral Cortical Spheroids Derived from Pluripotent Stem Cells', *Neuron*, 95(4), pp. 779-790.e6. Available at: https://doi.org/10.1016/j.neuron.2017.07.035.

Sloan, S.A. *et al.* (2018) 'Generation and assembly of human brain region–specific three-dimensional cultures', *Nature Protocols*, 13(9), pp. 2062–2085. Available at: https://doi.org/10.1038/s41596-018-0032-7.

Snider, A.C. *et al.* (2012) 'The chromatin remodeling factor Chd1l is required in the preimplantation embryo', *Biology Open*, 2(2), pp. 121–131. Available at: https://doi.org/10.1242/bio.20122949.

So, S. *et al.* (2020) 'The Rho-associated kinase inhibitor fasudil can replace Y-27632 for use in human pluripotent stem cell research', *PLOS ONE*, 15(5), p. e0233057. Available at: https://doi.org/10.1371/journal.pone.0233057.

Soemedi, R. *et al.* (2012) 'Phenotype-specific effect of chromosome 1q21.1 rearrangements and GJA5 duplications in 2436 congenital heart disease patients and 6760 controls', *Human Molecular Genetics*, 21(7), pp. 1513–1520. Available at: https://doi.org/10.1093/hmg/ddr589.

Sommer, I.E. *et al.* (2020) 'The clinical course of schizophrenia in women and men—a nation-wide cohort study', *npj Schizophrenia*, 6(1), pp. 1–7. Available at: https://doi.org/10.1038/s41537-020-0102-z.

Sønderby, I.E. *et al.* (2021) '1q21.1 distal copy number variants are associated with cerebral and cognitive alterations in humans', *Translational Psychiatry*, 11(1), pp. 1–16. Available at: https://doi.org/10.1038/s41398-021-01213-0.

Sønderby, I.E. *et al.* (2022) 'Effects of copy number variations on brain structure and risk for psychiatric illness: Large-scale studies from the ENIGMA working groups on CNVs', *Human Brain Mapping*, 43(1), pp. 300–328. Available at: https://doi.org/10.1002/hbm.25354.

Srikanth, P. *et al.* (2018) 'Shared effects of DISC1 disruption and elevated WNT signaling in human cerebral organoids', *Translational Psychiatry*, 8(1). Available at: https://doi.org/10.1038/s41398-018-0122-x.

Stachowiak, E.K. *et al.* (2017) 'Cerebral organoids reveal early cortical maldevelopment in schizophrenia-computational anatomy and genomics, role of FGFR1', *Translational psychiatry*, 7(11), p. 6. Available at: https://doi.org/10.1038/s41398-017-0054-x.

Stefansson, H. *et al.* (2008) 'Large recurrent microdeletions associated with schizophrenia', *Nature*, 455(7210), pp. 232–236. Available at: https://doi.org/10.1038/nature07229.

Steinman, K.J. *et al.* (2016) '16p11.2 deletion and duplication: Characterizing neurologic phenotypes in a large clinically ascertained cohort', *American Journal of Medical Genetics Part A*, 170(11), pp. 2943–2955. Available at: https://doi.org/10.1002/ajmg.a.37820.

Stone, J.L. *et al.* (2008) 'Rare chromosomal deletions and duplications increase risk of schizophrenia', *Nature*, 455(7210), pp. 237–241. Available at: https://doi.org/10.1038/nature07239.

Stoykova, A. *et al.* (2000) 'Pax6 Modulates the Dorsoventral Patterning of the Mammalian Telencephalon', *Journal of Neuroscience*, 20(21), pp. 8042–8050. Available at: https://doi.org/10.1523/JNEUROSCI.20-21-08042.2000.

Subramanian, L. *et al.* (2017) 'Dynamic behaviour of human neuroepithelial cells in the developing forebrain', *Nature Communications*, 8(1), p. 14167. Available at: https://doi.org/10.1038/ncomms14167.

Sudiwala, S. *et al.* (2019) 'Cellular mechanisms underlying Pax3-related neural tube defects and their prevention by folic acid', *Disease Models & Mechanisms*, 12(11), p. dmm042234. Available at: https://doi.org/10.1242/dmm.042234.

Sudmant, P.H. *et al.* (2015) 'Global diversity, population stratification, and selection of human copy-number variation.', *Science (New York, N.Y.)*, 349(6253), p. aab3761. Available at: https://doi.org/10.1126/science.aab3761.

Sumiyoshi, T. *et al.* (2004) 'Plasma glycine and serine levels in schizophrenia compared to normal controls and major depression: relation to negative symptoms', *International Journal of Neuropsychopharmacology*, 7(1), pp. 1–8. Available at: https://doi.org/10.1017/S1461145703003900.

Sun, A.X. *et al.* (2019) 'Potassium channel dysfunction in human neuronal models of Angelman syndrome', *Science*, 366(6472), pp. 1486–1492. Available at: https://doi.org/10.1126/science.aav5386.

Sun, G. *et al.* (2015) '1q21.1 microduplication in a patient with mental impairment and congenital heart defect', *Molecular Medicine Reports*, 12(4), pp. 5655–5658. Available at: https://doi.org/10.3892/mmr.2015.4166.

Sun, G. *et al.* (2020) 'Modeling Human Cytomegalovirus-Induced Microcephaly in Human iPSC-Derived Brain Organoids', *Cell Reports Medicine*, 1(1), p. 100002. Available at: https://doi.org/10.1016/j.xcrm.2020.100002.

Sun, J. *et al.* (2016) 'CHD1L Regulates Cell Cycle, Apoptosis, and Migration in Glioma', *Cellular and Molecular Neurobiology*, 36(4), pp. 565–576. Available at: https://doi.org/10.1007/s10571-015-0237-z.

Sundberg, M. *et al.* (2021) '16p11.2 deletion is associated with hyperactivation of human iPSC-derived dopaminergic neuron networks and is rescued by RHOA inhibition in vitro', *Nature Communications*, 12(1), p. 2897. Available at: https://doi.org/10.1038/s41467-021-23113-z.

Sutherland, A., Keller, R. and Lesko, A. (2020) 'Convergent extension in mammalian morphogenesis', *Seminars in Cell & Developmental Biology*, 100, pp. 199–211. Available at: https://doi.org/10.1016/j.semcdb.2019.11.002.

Suzuki, I.K. *et al.* (2018) 'Human-Specific NOTCH2NL Genes Expand Cortical Neurogenesis through Delta/Notch Regulation', *Cell*, 173(6), pp. 1370-1384.e16. Available at: https://doi.org/10.1016/J.CELL.2018.03.067.

Swaidan, N.T. *et al.* (2020) 'Identification of potential transcription factors that enhance human iPSC generation', *Scientific Reports*, 10(1), p. 21950. Available at: https://doi.org/10.1038/s41598-020-78932-9.

Sytnyk, V., Leshchyns'ka, I. and Schachner, M. (2017) 'Neural Cell Adhesion Molecules of the Immunoglobulin Superfamily Regulate Synapse Formation, Maintenance, and Function', *Trends in Neurosciences*, 40(5), pp. 295–308. Available at: https://doi.org/10.1016/j.tins.2017.03.003.

Takada, K. *et al.* (2012) 'Targeted disruption of the BCL9/β-catenin complex inhibits oncogenic Wnt signaling', *Science Translational Medicine*, 4(148), pp. 148ra117-148ra117. Available at: https://doi.org/10.1126/scitranslmed.3003808.

Takada, S., Watanabe, T. and Mizuta, R. (2020) 'DNase γ-dependent DNA fragmentation causes karyolysis in necrotic hepatocyte', *Journal of Veterinary Medical Science*, 82(1), pp. 23–26. Available at: https://doi.org/10.1292/jvms.19-0499.

Takata, N. *et al.* (2017) 'Self-patterning of rostral-caudal neuroectoderm requires dual role of Fgf signaling for localized Wnt antagonism', *Nature Communications*, 8(1), pp. 1–16. Available at: https://doi.org/10.1038/s41467-017-01105-2.

Takeguchi, R. *et al.* (2022) 'Structural and functional changes in the brains of patients with Rett syndrome: A multimodal MRI study', *Journal of the Neurological Sciences*, 441, p. 120381. Available at: https://doi.org/10.1016/j.jns.2022.120381.

Takumi, T. and Tamada, K. (2018) 'CNV biology in neurodevelopmental disorders', *Current Opinion in Neurobiology*. Elsevier Ltd, pp. 183–192. Available at: https://doi.org/10.1016/j.conb.2017.12.004.

Tanaka, D.H. *et al.* (2006) 'Multidirectional and multizonal tangential migration of GABAergic interneurons in the developing cerebral cortex', *Development*, 133(11), pp. 2167–2176. Available at: https://doi.org/10.1242/dev.02382.

Tanaka, M. *et al.* (2019) 'Preclinical characterization of AMPA receptor potentiator TAK-137 as a therapeutic drug for schizophrenia', *Pharmacology Research & Perspectives*, 7(3), p. e00479. Available at: https://doi.org/10.1002/prp2.479.

Tang, C.-J.C. *et al.* (2011) 'The human microcephaly protein STIL interacts with CPAP and is required for procentriole formation', *The EMBO Journal*, 30(23), pp. 4790–4804. Available at: https://doi.org/10.1038/emboj.2011.378.

Tao, Y. and Zhang, S.-C. (2016) 'Neural Subtype Specification from Human Pluripotent Stem Cells', *Cell Stem Cell*, 19(5), pp. 573–586. Available at: https://doi.org/10.1016/j.stem.2016.10.015.

Taylor, L.E. *et al.* (2018) 'Young Adult Outcomes for Children With 22q11 Deletion Syndrome and Comorbid ADHD', *Journal of Pediatric Psychology*, 43(6), pp. 636–644. Available at: https://doi.org/10.1093/jpepsy/jsy002.

Team, Rs. (2019) 'RStudio'. Boston, MA: RStudio, Inc.

Tedeschi, A. and Di Giovanni, S. (2009) 'The non-apoptotic role of p53 in neuronal biology: enlightening the dark side of the moon', *EMBO reports*, 10(6), pp. 576–583. Available at: https://doi.org/10.1038/embor.2009.89.

Teixeira, C.M. *et al.* (2011) 'Overexpression of Reelin Prevents the Manifestation of Behavioral Phenotypes Related to Schizophrenia and Bipolar Disorder', *Neuropsychopharmacology*, 36(12), pp. 2395–2405. Available at: https://doi.org/10.1038/npp.2011.153.

Terashi, T. *et al.* (2019) 'Neuroprotective effects of different frequency preconditioning exercise on neuronal apoptosis after focal brain ischemia in rats', *Neurological Research*, 41(6), pp. 510–518. Available at: https://doi.org/10.1080/01616412.2019.1580458.

Thawani, A. and Groves, A.K. (2020) 'Building the Border: Development of the Chordate Neural Plate Border Region and Its Derivatives', *Frontiers in Physiology*, 11. Available at: https://www.frontiersin.org/articles/10.3389/fphys.2020.608880 (Accessed: 5 August 2022).

Thier, M.C. *et al.* (2019) 'Identification of Embryonic Neural Plate Border Stem Cells and Their Generation by Direct Reprogramming from Adult Human Blood Cells', *Cell Stem Cell*, 24(1), pp. 166-182.e13. Available at: https://doi.org/10.1016/j.stem.2018.11.015.

Tian, T. *et al.* (2022) 'Hypermethylation of PI3K-AKT signalling pathway genes is associated with human neural tube defects', *Epigenetics*, 17(2), pp. 133–146. Available at: https://doi.org/10.1080/15592294.2021.1878725.

Toker, L. *et al.* (2018) 'Transcriptomic Evidence for Alterations in Astrocytes and Parvalbumin Interneurons in Subjects With Bipolar Disorder and Schizophrenia', *Biological Psychiatry*, 84(11), pp. 787–796. Available at: https://doi.org/10.1016/j.biopsych.2018.07.010.

Tong, J. *et al.* (2019) 'Elevated serum anti-NMDA receptor antibody levels in first-episode patients with schizophrenia', *Brain, Behavior, and Immunity*, 81, pp. 213–219. Available at: https://doi.org/10.1016/j.bbi.2019.06.017.

Toritsuka, M. *et al.* (2021) 'Developmental dysregulation of excitatory-to-inhibitory GABA-polarity switch may underlie schizophrenia pathology: A monozygotic-twin discordant case analysis in human iPS cell-derived neurons', *Neurochemistry International*, 150, p. 105179. Available at: https://doi.org/10.1016/j.neuint.2021.105179.

Townend, G.S. *et al.* (2018) 'MECP2 variation in Rett syndrome—An overview of current coverage of genetic and phenotype data within existing databases', *Human Mutation*, 39(7), pp. 914–924. Available at: https://doi.org/10.1002/humu.23542.

Trautmann, S., Rehm, J. and Wittchen, H.-U. (2016) 'The economic costs of mental disorders', *EMBO reports*, 17(9), pp. 1245–1249. Available at: https://doi.org/10.15252/embr.201642951.

Tremblay, R., Lee, S. and Rudy, B. (2016) 'GABAergic interneurons in the neocortex: From cellular properties to circuits', *Neuron*, 91(2), pp. 260–292. Available at: https://doi.org/10.1016/j.neuron.2016.06.033.

Tremble, K.C. *et al.* (2021) 'Sox2 modulation increases naïve pluripotency plasticity', *iScience*, 24(3), p. 102153. Available at: https://doi.org/10.1016/j.isci.2021.102153.

Trépanier, M.O. *et al.* (2016) 'Postmortem evidence of cerebral inflammation in schizophrenia: a systematic review', *Molecular Psychiatry*, 21(8), pp. 1009–1026. Available at: https://doi.org/10.1038/mp.2016.90.

Tronchin, G. *et al.* (2020) 'Progressive subcortical volume loss in treatment-resistant schizophrenia patients after commencing clozapine treatment', *Neuropsychopharmacology*, 45(8), pp. 1353–1361. Available at: https://doi.org/10.1038/s41386-020-0665-4.

Tropepe, V. *et al.* (1999) 'Distinct Neural Stem Cells Proliferate in Response to EGF and FGF in the Developing Mouse Telencephalon', *Developmental Biology*, 208(1), pp. 166–188. Available at: https://doi.org/10.1006/dbio.1998.9192.

Tsai, C.-C. *et al.* (2012) 'Oct4 and Nanog Directly Regulate Dnmt1 to Maintain Self-Renewal and Undifferentiated State in Mesenchymal Stem Cells', *Molecular Cell*, 47(2), pp. 169–182. Available at: https://doi.org/10.1016/j.molcel.2012.06.020.

Tungadi, E.A. *et al.* (2017) 'Human microcephaly ASPM protein is a spindle pole-focusing factor that functions redundantly with CDK5RAP2', *Journal of Cell Science*, 130(21), pp. 3676–3684. Available at: https://doi.org/10.1242/jcs.203703.

Union, O. (2018) *Health at a Glance: Europe 2018*. OECD (Health at a Glance: Europe). Available at: https://doi.org/10.1787/health_glance_eur-2018-en.

Uno, Y. and Coyle, J.T. (2019) 'Glutamate hypothesis in schizophrenia', *Psychiatry and Clinical Neurosciences*, 73(5), pp. 204–215. Available at: https://doi.org/10.1111/pcn.12823.

Uranova, N.A. *et al.* (2018) 'Ultrastructural pathology of oligodendrocytes adjacent to microglia in prefrontal white matter in schizophrenia', *npj Schizophrenia*, 4(1), pp. 1–10. Available at: https://doi.org/10.1038/s41537-018-0068-2.

Urraca, N. *et al.* (2013) 'The Interstitial Duplication 15q11.2-q13 Syndrome Includes Autism, Mild Facial Anomalies and a Characteristic EEG Signature', *Autism Research*, 6(4), pp. 268–279. Available at: https://doi.org/10.1002/aur.1284.

Urresti, J. *et al.* (2021) 'Cortical organoids model early brain development disrupted by 16p11.2 copy number variants in autism', *Molecular Psychiatry*, pp. 1–21. Available at: https://doi.org/10.1038/s41380-021-01243-6.

Ursini, G. *et al.* (2018) 'Convergence of placenta biology and genetic risk for schizophrenia', *Nature Medicine*, 24(6), pp. 792–801. Available at: https://doi.org/10.1038/s41591-018-0021-y.

Uzquiano, A. *et al.* (2022) ‘Proper acquisition of cell class identity in organoids allows definition of fate specification programs of the human cerebral cortex’, *Cell*, 185(20), pp. 3770-3788.e27. Available at: https://doi.org/10.1016/j.cell.2022.09.010.

Vaezi, A. *et al.* (2002) ‘Actin cable dynamics and Rho/Rock orchestrate a polarized cytoskeletal architercture in the early steps of assembling a stratified epithelium’, *Developmental Cell*, 3(3), pp. 367–381. Available at: https://doi.org/10.1016/S1534-5807(02)00259-9.

Vafaizadeh, V. *et al.* (2021) ‘The interactions of Bcl9/Bcl9L with β-catenin and Pygopus promote breast cancer growth, invasion, and metastasis’, *Oncogene*, 40(43), pp. 6195–6209. Available at: https://doi.org/10.1038/s41388-021-02016-9.

Valiulahi, P. *et al.* (2021) ‘Generation of caudal-type serotonin neurons and hindbrain-fate organoids from hPSCs’, *Stem Cell Reports*, 16(8), pp. 1938–1952. Available at: https://doi.org/10.1016/j.stemcr.2021.06.006.

Van Den Bosch, J. (1958) ‘Microcephaly in the Netherlands: A Clinical and Genetical Study’, *Annals of Human Genetics*, 23(2), pp. 91–116. Available at: https://doi.org/10.1111/j.1469-1809.1958.tb01455.x.

Vanden Berghe, T. *et al.* (2013) ‘Determination of apoptotic and necrotic cell death in vitro and in vivo’, *Methods*, 61(2), pp. 117–129. Available at: https://doi.org/10.1016/j.ymeth.2013.02.011.

Vandepoele, K. *et al.* (2005) ‘A novel gene family NBPF: intricate structure generated by gene duplications during primate evolution’, *Molecular Biology and Evolution*, 22(11), pp. 2265–2274.

Vanlangenakker, N., Vanden Berghe, T. and Vandenabeele, P. (2012) ‘Many stimuli pull the necrotic trigger, an overview’, *Cell Death & Differentiation*, 19(1), pp. 75–86. Available at: https://doi.org/10.1038/cdd.2011.164.

Varshavi, Dorsa *et al.* (2018) ‘Metabolic Biomarkers of Ageing in C57BL/6J Wild-Type and Flavin-Containing Monooxygenase 5 (FMO5)-Knockout Mice’, *Frontiers in Molecular Biosciences*, 5, p. 28. Available at: https://doi.org/10.3389/fmolb.2018.00028.

Velasco, S. *et al.* (2019) ‘Individual brain organoids reproducibly form cell diversity of the human cerebral cortex’, *Nature*, 570(7762), pp. 523–527. Available at: https://doi.org/10.1038/s41586-019-1289-x.

Velmeshev, D. *et al.* (2019) ‘Single-cell genomics identifies cell type–specific molecular changes in autism’, *Science*, 364(6441), pp. 685–689. Available at: https://doi.org/10.1126/science.aav8130.

Vernardis, S.I. *et al.* (2017) ‘Human embryonic and induced pluripotent stem cells maintain phenotype but alter their metabolism after exposure to ROCK inhibitor’, *Scientific Reports*, 7(1), p. 42138. Available at: https://doi.org/10.1038/srep42138.

Vesnaver, T.V. *et al.* (2017) ‘Zika virus associated microcephaly/micrencephaly—fetal brain imaging in comparison with neuropathology’, *BJOG: An International Journal of Obstetrics & Gynaecology*, 124(3), pp. 521–525. Available at: https://doi.org/10.1111/1471-0528.14423.

Vigneault, É. *et al.* (2015) ‘Distribution of vesicular glutamate transporters in the human brain’, *Frontiers in Neuroanatomy*, 9. Available at: https://www.frontiersin.org/articles/10.3389/fnana.2015.00023 (Accessed: 3 August 2022).

Volpato, V. *et al.* (2018) 'Reproducibility of Molecular Phenotypes after Long-Term Differentiation to Human iPSC-Derived Neurons: A Multi-Site Omics Study', *Stem Cell Reports*, 11(4), pp. 897–911. Available at: https://doi.org/10.1016/j.stemcr.2018.08.013.

de Vrij, F.M. *et al.* (2019) 'Candidate CSPG4 mutations and induced pluripotent stem cell modeling implicate oligodendrocyte progenitor cell dysfunction in familial schizophrenia', *Molecular Psychiatry*, 24(5), pp. 757–771. Available at: https://doi.org/10.1038/s41380-017-0004-2.

Walsh, T. *et al.* (2008) 'Rare structural variants disrupt multiple genes in neurodevelopmental pathways in schizophrenia', *Science*, 320(5875), pp. 539–543. Available at: https://doi.org/10.1126/science.1155174.

Walterfang, M. *et al.* (2009) 'Corpus callosum size and shape in first-episode affective and schizophrenia-spectrum psychosis', *Psychiatry Research: Neuroimaging*, 173(1), pp. 77–82. Available at: https://doi.org/10.1016/j.pscychresns.2008.09.007.

Wang, G. *et al.* (2021) 'CHD1L prevents lipopolysaccharide-induced hepatocellular carcinomar cell death by activating hnRNP A2/B1-nmMYLK axis', *Cell Death & Disease*, 12(10), pp. 1–11. Available at: https://doi.org/10.1038/s41419-021-04167-9.

Wang, J. *et al.* (2017) 'MicroRNA-138-5p regulates neural stem cell proliferation and differentiation in vitro by targeting TRIP6 expression', *Molecular Medicine Reports*, 16(5), pp. 7261–7266. Available at: https://doi.org/10.3892/mmr.2017.7504.

Wang, L. *et al.* (2017) 'Apoptosis, Expression of PAX3 and P53, and Caspase Signal in Fetuses with Neural Tube Defects', *Birth Defects Research*, 109(19), pp. 1596–1604. Available at: https://doi.org/10.1002/bdr2.1094.

Wang, L. *et al.* (2020) 'Loss of NARS1 impairs progenitor proliferation in cortical brain organoids and leads to microcephaly', *Nature Communications*, 11(1), p. 4038. Available at: https://doi.org/10.1038/s41467-020-17454-4.

Wang, M. *et al.* (2020) 'Increased Neural Progenitor Proliferation in a hiPSC Model of Autism Induces Replication Stress-Associated Genome Instability', *Cell Stem Cell*, 26(2), pp. 221-233.e6. Available at: https://doi.org/10.1016/j.stem.2019.12.013.

Wang, P. *et al.* (2017) 'CRISPR/Cas9-mediated heterozygous knockout of the autism gene CHD8 and characterization of its transcriptional networks in cerebral organoids derived from iPS cells', *Molecular Autism*, 8(1). Available at: https://doi.org/10.1186/s13229-017-0124-1.

Wang, P. *et al.* (2018) 'Enriched expression of genes associated with autism spectrum disorders in human inhibitory neurons', *Translational Psychiatry*, 8(1), pp. 1–10. Available at: https://doi.org/10.1038/s41398-017-0058-6.

Wang, S. *et al.* (2021) 'Longitudinal single-cell RNA-seq of hESCs-derived retinal organoids', *Science China Life Sciences*, 64(10), pp. 1661–1676. Available at: https://doi.org/10.1007/s11427-020-1836-7.

Wang, Y. *et al.* (2017) 'Chemotherapy drugs induce pyroptosis through caspase-3 cleavage of a gasdermin', *Nature*, 547(7661), pp. 99–103. Available at: https://doi.org/10.1038/nature22393.

Wang, Y. *et al.* (2022) 'Modeling human telencephalic development and autism-associated SHANK3 deficiency using organoids generated from single neural rosettes', *Nature Communications*, 13(1), p. 5688. Available at: https://doi.org/10.1038/s41467-022-33364-z.

Ward, K.E. *et al.* (1996) 'Meta-analysis of brain and cranial size in schizophrenia', *Schizophrenia Research*, 22(3), pp. 197–213. Available at: https://doi.org/10.1016/S0920-9964(96)00076-X.

Watanabe, K. *et al.* (2005) 'Directed differentiation of telencephalic precursors from embryonic stem cells', *Nature Neuroscience*, 8(3), pp. 288–296. Available at: https://doi.org/10.1038/nn1402.

Watanabe, M. *et al.* (2017) 'Self-Organized Cerebral Organoids with Human-Specific Features Predict Effective Drugs to Combat Zika Virus Infection', *Cell Reports*, 21(2), pp. 517–532. Available at: https://doi.org/10.1016/j.celrep.2017.09.047.

Wegscheid, M.L. *et al.* (2021) 'Patient-derived iPSC-cerebral organoid modeling of the 17q11.2 microdeletion syndrome establishes CRLF3 as a critical regulator of neurogenesis', *Cell Reports*, 36(1), p. 109315. Available at: https://doi.org/10.1016/j.celrep.2021.109315.

Wei, P.-C. *et al.* (2016) 'Long Neural Genes Harbor Recurrent DNA Break Clusters in Neural Stem/Progenitor Cells', *Cell*, 164(4), pp. 644–655. Available at: https://doi.org/10.1016/j.cell.2015.12.039.

Weinberger, D.R. (1987) 'Implications of Normal Brain Development for the Pathogenesis of Schizophrenia', *Archives of General Psychiatry*, 44(7), pp. 660–669. Available at: https://doi.org/10.1001/archpsyc.1987.01800190080012.

Weinberger, D.R. (2017) 'Future of Days Past: Neurodevelopment and Schizophrenia', *Schizophrenia Bulletin*, 43(6), pp. 1164–1168. Available at: https://doi.org/10.1093/schbul/sbx118.

Weinstein, Y. *et al.* (2018) 'Association of maternal exposure to terror attacks during pregnancy and the risk of schizophrenia in the offspring: A population-based study', *Schizophrenia Research*, 199, pp. 163–167. Available at: https://doi.org/10.1016/j.schres.2018.04.024.

Wells, M.F. *et al.* (2016) 'Genetic Ablation of AXL Does Not Protect Human Neural Progenitor Cells and Cerebral Organoids from Zika Virus Infection', *Cell Stem Cell*, 19(6), pp. 703–708. Available at: https://doi.org/10.1016/j.stem.2016.11.011.

Wen, Z. *et al.* (2014) 'Synaptic dysregulation in a human iPS cell model of mental disorders', *Nature*, 515(7527), pp. 414–418. Available at: https://doi.org/10.1038/nature13716.

Wenger, T.L. *et al.* (2016) '22q11.2 duplication syndrome: Elevated rate of autism spectrum disorder and need for medical screening', *Molecular Autism*, 7(1). Available at: https://doi.org/10.1186/s13229-016-0090-z.

Wickman, G.R. *et al.* (2013) 'Blebs produced by actin–myosin contraction during apoptosis release damage-associated molecular pattern proteins before secondary necrosis occurs', *Cell Death & Differentiation*, 20(10), pp. 1293–1305. Available at: https://doi.org/10.1038/cdd.2013.69.

Williams, C.A., Driscoll, D.J. and Dagli, A.I. (2010) 'Clinical and genetic aspects of Angelman syndrome', *Genetics in Medicine*, 12(7), pp. 385–395. Available at: https://doi.org/10.1097/GIM.0b013e3181def138.

Williams, M. *et al.* (2014) 'Distinct apical and basolateral mechanisms drive planar cell polarity-dependent convergent extension of the mouse neural plate', *Developmental Cell*, 29(1), pp. 34–46. Available at: https://doi.org/10.1016/j.devcel.2014.02.007.

Wörsdörfer, P. *et al.* (2020) 'Do not keep it simple: recent advances in the generation of complex organoids', *Journal of Neural Transmission*. Springer, pp. 1–9. Available at: https://doi.org/10.1007/s00702-020-02198-8.

Wu, H. *et al.* (2007) 'Integrative genomic and functional analyses reveal neuronal subtype differentiation bias in human embryonic stem cell lines', *Proceedings of the National Academy of Sciences*, 104(34), pp. 13821–13826. Available at: https://doi.org/10.1073/pnas.0706199104.

Wu, H. *et al.* (2020) 'Phenotype-to-genotype approach reveals head-circumference-associated genes in an autism spectrum disorder cohort', *Clinical Genetics*, 97(2), pp. 338–346. Available at: https://doi.org/10.1111/cge.13665.

Wu, Y. *et al.* (2021) 'Organoids as a new model system to study neural tube defects', *FASEB journal : official publication of the Federation of American Societies for Experimental Biology*, 35(4), p. e21545. Available at: https://doi.org/10.1096/fj.202002348R.

Xavier, J. *et al.* (2018) '1q21.1 microduplication: large verbal–nonverbal performance discrepancy and ddPCR assays of HYDIN/HYDIN2 copy number', *npj Genomic Medicine*, 3(1), pp. 1–6. Available at: https://doi.org/10.1038/s41525-018-0059-2.

Xiang, Y. *et al.* (2017) 'Fusion of Regionally Specified hPSC-Derived Organoids Models Human Brain Development and Interneuron Migration.', *Cell stem cell*, 21(3), pp. 383-398.e7. Available at: https://doi.org/10.1016/j.stem.2017.07.007.

Xiang, Y. *et al.* (2019) 'hESC-Derived Thalamic Organoids Form Reciprocal Projections When Fused with Cortical Organoids', *Cell Stem Cell*, 24(3), pp. 487-497.e7. Available at: https://doi.org/10.1016/j.stem.2018.12.015.

Xie, A.W. *et al.* (2017) 'Controlled Self-assembly of Stem Cell Aggregates Instructs Pluripotency and Lineage Bias', *Scientific Reports*, 7(1), p. 14070. Available at: https://doi.org/10.1038/s41598-017-14325-9.

Xiong, X. *et al.* (2021) 'Diversity roles of CHD1L in normal cell function and tumorigenesis', *Biomarker Research*, 9(1), p. 16. Available at: https://doi.org/10.1186/s40364-021-00269-w.

Xu, C. *et al.* (2013) 'BCL9 and C9orf5 Are Associated with Negative Symptoms in Schizophrenia: Meta-Analysis of Two Genome-Wide Association Studies', *PLoS ONE*, 8(1). Available at: https://doi.org/10.1371/journal.pone.0051674.

Xu, J.-C. *et al.* (2016) 'Cultured networks of excitatory projection neurons and inhibitory interneurons for studying human cortical neurotoxicity', *Science Translational Medicine*, 8(333), pp. 333ra48-333ra48. Available at: https://doi.org/10.1126/scitranslmed.aad0623.

Xu, Q. *et al.* (2018) 'Autism-associated CHD8 deficiency impairs axon development and migration of cortical neurons', *Molecular Autism*, 9(1), p. 65. Available at: https://doi.org/10.1186/s13229-018-0244-2.

Xue, X. *et al.* (2018) 'Mechanics-guided embryonic patterning of neuroectoderm tissue from human pluripotent stem cells', *Nature Materials*, 17(7), pp. 633–641. Available at: https://doi.org/10.1038/s41563-018-0082-9.

Xue, X. and Yuan, X. (2010) 'Nestin is essential for mitogen-stimulated proliferation of neural progenitor cells', *Molecular and Cellular Neuroscience*, 45(1), pp. 26–36. Available at: https://doi.org/10.1016/j.mcn.2010.05.006.

Yakoub, A.M. and Sadek, M. (2019) 'Analysis of Synapses in Cerebral Organoids', *Cell Transplantation*, 28(9–10), pp. 1173–1182. Available at: https://doi.org/10.1177/0963689718822811.

Yamaguchi, Y. *et al.* (2011) 'Live imaging of apoptosis in a novel transgenic mouse highlights its role in neural tube closure', *Journal of Cell Biology*, 195(6), pp. 1047–1060. Available at: https://doi.org/10.1083/jcb.201104057.

Yamamoto, H. *et al.* (2013) 'Genetic Deletion of Afadin Causes Hydrocephalus by Destruction of Adherens Junctions in Radial Glial and Ependymal Cells in the Midbrain', *PLOS ONE*, 8(11), p. e80356. Available at: https://doi.org/10.1371/journal.pone.0080356.

Yamasaki, M. *et al.* (2020) 'Sensitivity to gene dosage and gene expression affects genes with copy number variants observed among neuropsychiatric diseases', *BMC Medical Genomics*, 13(1), p. 55. Available at: https://doi.org/10.1186/s12920-020-0699-9.

Ybot-Gonzalez, P. *et al.* (2002) 'Sonic hedgehog and the molecular regulation of mouse neural tube closure', *Development*, 129(10).

Ybot-Gonzalez, P., Savery, D., *et al.* (2007) 'Convergent extension, planar-cell-polarity signaling and initiation of mouse neural tube closure', *Development*, 134(4), pp. 789–799. Available at: https://doi.org/10.1242/dev.000380.

Ybot-Gonzalez, P., Gaston-Massuet, C., *et al.* (2007) 'Neural plate morhogenesis during mouse neurulation is regulated by antagonism of Bmp signalling', *Development*, 134(17), pp. 3203–3211. Available at: https://doi.org/10.1242/dev.008177.

Yoon, J. and Mao, Y. (2021) 'Dissecting Molecular Genetic Mechanisms of 1q21.1 CNV in Neuropsychiatric Disorders', *International Journal of Molecular Sciences*, 22(11), p. 5811. Available at: https://doi.org/10.3390/ijms22115811.

Yoon, S.J. *et al.* (2019) 'Reliability of human cortical organoid generation', *Nature Methods*, 16(1), pp. 75–78. Available at: https://doi.org/10.1038/s41592-018-0255-0.

Yu, T.W. *et al.* (2010) 'Mutations in WDR62, encoding a centrosome-associated protein, cause microcephaly with simplified gyri and abnormal cortical architecture', *Nature Genetics*, 42(11), pp. 1015–1020. Available at: https://doi.org/10.1038/ng.683.

Yuan, B. *et al.* (2020) 'Inhibition of AIM2 inflammasome activation alleviates GSDMD-induced pyroptosis in early brain injury after subarachnoid haemorrhage', *Cell Death & Disease*, 11(1), pp. 1–16. Available at: https://doi.org/10.1038/s41419-020-2248-z.

Yuan, F. *et al.* (2020) 'LHX6 is essential for the migration of human pluripotent stem cell-derived GABAergic interneurons', *Protein & Cell*, 11(4), pp. 286–291. Available at: https://doi.org/10.1007/s13238-019-00686-6.

Yuan, Y. *et al.* (2018) 'Cadmium-induced apoptosis in neuronal cells is mediated by Fas/FasL-mediated mitochondrial apoptotic signaling pathway', *Scientific Reports*, 8(1), p. 8837. Available at: https://doi.org/10.1038/s41598-018-27106-9.

Zafeiriou, M.-P. *et al.* (2020) 'Developmental GABA polarity switch and neuronal plasticity in Bioengineered Neuronal Organoids', *Nature Communications*, 11, p. 3791. Available at: https://doi.org/10.1038/s41467-020-17521-w.

Zaqout, S. *et al.* (2019) 'Altered inhibition and excitation in neocortical circuits in congenital microcephaly', *Neurobiology of Disease*, 129, pp. 130–143. Available at: https://doi.org/10.1016/j.nbd.2019.05.008.

Zarrei, M. *et al.* (2019) 'A large data resource of genomic copy number variation across neurodevelopmental disorders', *npj Genomic Medicine*, 4(1), pp. 1–13. Available at: https://doi.org/10.1038/s41525-019-0098-3.

Zeman, M.K. and Cimprich, K.A. (2014) 'Causes and Consequences of Replication Stress', *Nature cell biology*, 16(1), pp. 2–9. Available at: https://doi.org/10.1038/ncb2897.

Zeppillo, T. *et al.* (2020) 'Functional impairment of cortical AMPA receptors in schizophrenia', *Schizophrenia Research* [Preprint]. Available at: https://doi.org/10.1016/j.schres.2020.03.037.

Zhang, F. *et al.* (2009) 'Copy Number Variation in Human Health, Disease, and Evolution', *Annual Review of Genomics and Human Genetics*, 10(1), pp. 451–481. Available at: https://doi.org/10.1146/annurev.genom.9.081307.164217.

Zhang, H., Zhang, L. and Sun, T. (2018) 'Cohesive Regulation of Neural Progenitor Development by microRNA miR-26, Its Host Gene Ctdsp and Target Gene Emx2 in the Mouse Embryonic Cerebral Cortex', *Frontiers in Molecular Neuroscience*, 11. Available at: https://www.frontiersin.org/articles/10.3389/fnmol.2018.00044 (Accessed: 8 October 2022).

Zhang, L. *et al.* (2017) 'Efficient CNV breakpoint analysis reveals unexpected structural complexity and correlation of dosage-sensitive genes with clinical severity in genomic disorders', *Human molecular genetics*, 26(10), pp. 1927–1941. Available at: https://doi.org/10.1093/hmg/ddx102.

Zhang, L. *et al.* (2021) 'Extracellular vesicles from hypoxia-preconditioned microglia promote angiogenesis and repress apoptosis in stroke mice via the TGF-β/Smad2/3 pathway', *Cell Death & Disease*, 12(11), pp. 1–14. Available at: https://doi.org/10.1038/s41419-021-04363-7.

Zhang, M. *et al.* (2018) 'Highly efficient methods to obtain homogeneous dorsal neural progenitor cells from human and mouse embryonic stem cells and induced pluripotent stem cells', *Stem Cell Research & Therapy*, 9(1), p. 67. Available at: https://doi.org/10.1186/s13287-018-0812-6.

Zhang, W. *et al.* (2014) 'Loss of MeCP2 From Forebrain Excitatory Neurons Leads to Cortical Hyperexcitation and Seizures', *The Journal of Neuroscience*, 34(7), pp. 2754–2763. Available at: https://doi.org/10.1523/JNEUROSCI.4900-12.2014.

Zhang, W. *et al.* (2016) 'MiRNA-128 regulates the proliferation and neurogenesis of neural precursors by targeting PCM1 in the developing cortex', *eLife*. Edited by E. Kim, 5, p. e11324. Available at: https://doi.org/10.7554/eLife.11324.

Zhang, W. *et al.* (2019) 'Modeling microcephaly with cerebral organoids reveals a WDR62–CEP170–KIF2A pathway promoting cilium disassembly in neural progenitors', *Nature Communications*, 10(1). Available at: https://doi.org/10.1038/s41467-019-10497-2.

Zhang, W. *et al.* (2020) 'Cerebral organoid and mouse models reveal a RAB39b-PI3K-mTOR pathway-dependent dysregulation of cortical development leading to macrocephaly/autism phenotypes', *Genes & development*, 34(7–8), pp. 580–597. Available at: https://doi.org/10.1101/gad.332494.119.

Zhang, X. *et al.* (2010) 'Pax6 is a human neuroectoderm cell fate determinant', *Cell Stem Cell*, 7(1), pp. 90–100. Available at: https://doi.org/10.1016/j.stem.2010.04.017.

Zhang, X. *et al.* (2018) 'The LINC01138 interacts with PRMT5 to promote SREBP1-mediated lipid desaturation and cell growth in clear cell renal cell carcinoma', *Biochemical*

and Biophysical Research Communications, 507(1), pp. 337–342. Available at: https://doi.org/10.1016/j.bbrc.2018.11.036.

Zhang, Y. *et al.* (2018) 'BCL9 promotes epithelial mesenchymal transition and invasion in cisplatin resistant NSCLC cells via β-catenin pathway', *Life Sciences*, 208, pp. 284–294. Available at: https://doi.org/10.1016/j.lfs.2018.07.023.

Zhang, Z.-N. *et al.* (2014) 'Oct4 Maintains the Pluripotency of Human Embryonic Stem Cells by Inactivating p53 Through Sirt1-Mediated Deacetylation', *Stem Cells*, 32(1), pp. 157–165. Available at: https://doi.org/10.1002/stem.1532.

Zhao, H. *et al.* (2019) 'Combined use of bFGF/EGF and all-trans-retinoic acid cooperatively promotes neuronal differentiation and neurite outgrowth in neural stem cells', *Neuroscience Letters*, 690, pp. 61–68. Available at: https://doi.org/10.1016/j.neulet.2018.10.002.

Zhao, J. *et al.* (2020) 'APOE4 exacerbates synapse loss and neurodegeneration in Alzheimer's disease patient iPSC-derived cerebral organoids', *Nature Communications*, 11(1), p. 5540. Available at: https://doi.org/10.1038/s41467-020-19264-0.

Zhao, T. *et al.* (2014) 'β-catenin regulates Pax3 and Cdx2 for caudal neural tube closure and elongation', *Development*, 141(1), pp. 148–157. Available at: https://doi.org/10.1242/dev.101550.

Zhao, X. *et al.* (2021) 'Methamphetamine exposure induces neuronal programmed necrosis by activating the receptor-interacting protein kinase 3 -related signalling pathway', *The FASEB Journal*, 35(5), p. e21561. Available at: https://doi.org/10.1096/fj.202100188R.

Zhao, Y. *et al.* (2020) 'Complete Sequence of the 22q11.2 Allele in 1,053 Subjects with 22q11.2 Deletion Syndrome Reveals Modifiers of Conotruncal Heart Defects', *American Journal of Human Genetics*, 106(1), pp. 26–40. Available at: https://doi.org/10.1016/j.ajhg.2019.11.010.

Zheng, Y. *et al.* (2021) 'Advances in neural organoid systems and their application in neurotoxicity testing of environmental chemicals', *Genes and Environment*, 43(1), p. 39. Available at: https://doi.org/10.1186/s41021-021-00214-1.

Zhivotosky, B. and Orrenius, S. (2001) 'Assessment of Apoptosis and Necrosis by DNA Fragmentation and Morphological Criteria', *Current Protocols in Cell Biology*, 12(1), p. 18.3.1-18.3.23. Available at: https://doi.org/10.1002/0471143030.cb1803s12.

Zhou, H.-M. and Conway, S.J. (2016) 'Restricted Pax3 Deletion within the Neural Tube Results in Congenital Hydrocephalus', *Journal of Developmental Biology*, 4(1), p. 7. Available at: https://doi.org/10.3390/jdb4010007.

Zhou, Z.-W. *et al.* (2013) 'DNA damage response in microcephaly development of MCPH1 mouse model', *DNA Repair*, 12(8), pp. 645–655. Available at: https://doi.org/10.1016/j.dnarep.2013.04.017.

Zhou, Z.-W. *et al.* (2020) 'NBS1 interacts with Notch signaling in neuronal homeostasis', *Nucleic Acids Research*, 48(19), pp. 10924–10939. Available at: https://doi.org/10.1093/nar/gkaa716.

Zhu, W. *et al.* (2019) 'Precisely controlling endogenous protein dosage in hPSCs and derivatives to model FOXG1 syndrome', *Nature Communications*, 10(1), p. 928. Available at: https://doi.org/10.1038/s41467-019-08841-7.

Ziegler, N. *et al.* (2020) ‘AMPKβ1 and AMPKβ2 define an isoform-specific gene signature in human pluripotent stem cells, differentially mediating cardiac lineage specification’, *Journal of Biological Chemistry*, 295(51), pp. 17659–17671. Available at: https://doi.org/10.1074/jbc.RA120.013990.

Zwaigenbaum, L. *et al.* (2014) ‘Early Head Growth in Infants at Risk of Autism: A Baby Siblings Research Consortium Study’, *Journal of the American Academy of Child & Adolescent Psychiatry*, 53(10), pp. 1053–1062. Available at: https://doi.org/10.1016/j.jaac.2014.07.007.